UNIVERSITY OF LEEDS

CFD SIMULATION OF TWO-PHASE FLOW IN CLOSE-COUPLED GAS ATOMISATION

Jo Samuel Joseph Subramanian

Submitted in accordance with the requirements for the degree of

Doctor of Philosophy

University of Leeds

School of Chemical and Process Engineering

August 2024

Declaration – Intellectual property and publication statements

I confirm that the work submitted is my own, except where work which has formed part of jointly authored publications has been included. My contribution and the other authors to this work has been explicitly indicated below. I confirm that appropriate credit has been given within the thesis where reference has been made to the work of others.

Parts of Chapter 4 including Sections 4.3, 4.7. and 4.8, and Sections 5.1.1, 5.2.1, and 5.3.1 of Chapter 5 are comprised of jointly authored material. The details of the work, and the authors contributions are summarised below:

'CFD modelling of Close-Coupled Gas Atomisation (CCGA) process by employing the Euler-Lagrange approach to understand melt flow instabilities', jointly authored by *Jo Samuel, Prof. Andrew Mullis, Dr. Duncan Borman*, Published in Chemical Engineering Science in August 2024.

Jo Samuel carried out the CFD simulation and analysis of the two-phase CCGA model, alongside writing and editing the paper. Prof. Andrew Mullis, and Dr. Duncan Borman supervised the work, and reviewed and edited the paper for good quality of English.

This copy has been supplied on the understanding that it is copyright material and that no quotation from the thesis may be published without proper acknowledgement.

The right of *Jo Samuel Joseph Subramanian* to be identified as Author of this work has been asserted by *Jo Samuel Joseph Subramanian* in accordance with the Copyright, Designs and Patents Act 1988.

©2024 The University of Leeds and Jo Samuel Joseph Subramanian

ACKNOWLEDGEMENTS

I thank my Lord and Saviour Jesus Christ for giving me this beautiful life to experience the richness of His mercy, grace, and unfailing love.

I'm deeply grateful to my main supervisor, Prof. Andrew Mullis for his consistent support throughout my research. His profound knowledge on the subject matter, and sound advice has immensely helped me to successfully overcome technical challenges and dead-ends.

I'm also very much grateful to my co-supervisor, Dr. Duncan Borman for his continued help throughout my research. His expertise in CFD was indispensable for carrying out and achieving such a milestone.

I would also like to thank MAPP – The EPSRC Future Manufacturing Hub in Manufacture using Advanced Powder Process (Grant No. EP/P006566/1) for supporting me financially to carry out this research.

Moreover, I'm also thankful for the opportunity to access ARC4, part of the High-Performance Computing facilities at the University of Leeds, UK, which made this work possible.

I also want to take this opportunity to thank my dad for motivating me to excel, and for providing me with valuable life lessons. I also want to thank my mum, a cancer survivor for showering me with her love, caring for me and praying for me. I also want to thank my sister for selflessly dedicating many years of her life, allowing me the opportunity to pursue this research.

I would also like to extend my gratitude to a very special person – Janet – for supporting me throughout my research and in all my endeavours.

Finally, I want to thank my friends and colleagues for being there for me all these years.

ABSTRACT

Gas atomisation is the process of producing melt powders for additive manufacturing applications. The process involves high-speed gas flow to break-up and disintegrate molten melt into ultra-fine metal powders about the order of micrometers (μm). Although gas atomisation is the commercially viable process to produce realisable yield to meet the industrial scale production, yet the process is highly inefficient due to its chaotic and unpredictable gas-melt interaction, resulting in increased particle size distributions.

This thesis presents a series of 22 computational fluid dynamics (CFD) simulations, numerically modelling close-coupled gas atomisation (CCGA) process to investigate the gas-melt interactions and their individual instabilities under varying gas-to-melt ratios (GMRs), and melt temperatures. The premise of these simulations is to understand the coupled nature of the gas-melt interactions resulting in a chaotic and unpredictable process, as typically seen in the physical atomisation process. To capture the gas-melt interactions using a CFD model, the melt flow is coupled to the atomiser's internal pressure (aspiration pressure), which varies over time due to the unsteady behaviour of the gas flow-field, induced by the gas-melt interactions. The CFD simulations are modelled as two-phase flow, with Argon gas as the primary phase, and melt as the secondary phase (particles), modelled via coupled Euler-Lagrange framework. The CFD study was investigated using five different GMRs and melt temperatures: GMRs of 5.5, 2.6, 1.32, 0.88, and 0.44, and melt temperature of 300K, 600K, 1000K, 1500K, and 2000K, and they were run in various combinations. These series of simulations investigated into the gas and melt instabilities and their association with each other.

The study, via CFD models revealed that the atomisation process at higher GMR (5.5 & 2.6) is extremely stable due to the dominance of the gas flow, and that it effectively attenuates any external instability induced into the system. Similarly, investigation into varying GMRs and melt temperatures exhibited that with decreasing GMR or increasing melt temperature, a melt instability was introduced into the process. The melt instability observed across decreasing GMR or increasing melt temperature were profound and displayed multi-layered frequency of fluctuations. However, the effect of melt temperature on the process is more prominent and substantial compared to that of the GMR. This is manifested by the evolving complexity and unpredictability in the process with increase in melt temperature.

Table of Contents

1 Introduction 1

2 Background Science 4

2.1 Gas flow and generation of shock 6

2.2 Generation of supersonic gas flow. 7

2.3 Ideally-expanded, Over-expanded, and under-expanded flows 9

2.4 Melt break-up mechanism 12

2.4.1 Primary break-up mechanism 13

2.4.2 Secondary break-up mechanism 15

2.5 Overview of Computational Fluid Dynamics (CFD) 17

2.5.1 Navier-Stokes equation 17

2.5.2 Reynolds-Averaged Navier-Stokes (RANS) equations 18

2.5.3 Turbulence modelling 19

2.5.4 Major limitations in Turbulence models 22

2.5.5 Two-phase flow: Euler-Euler framework and Euler-Lagrange framework 23

2.5.6 Discrete-Phase Model (DPM) 25

2.5.7 Turbulent dispersion of DPM particles 26

2.5.8 Two-way coupling between primary and secondary phase 27

3 Literature review 30

3.1 Factors and Design parameters affecting CCGA Process 30

3.1.1 Effect of gas inlet pressure 30

3.1.2 Effect of Wake-Closure Pressure (WCP) 33

3.1.3 Design of gas delivery nozzle 35

3.1.4 Design of melt delivery nozzle 39

3.2 CFD study on CCGA 42

3.2.1 Single phase: Gas-only flow 43

3.2.2 Two-phase: Multi-phase flow 46

3.3 Aim and objective of the thesis 54

4 Methodology of the numerical modelling 56

4.1 Establishing the numerical domain of the gas atomiser 56

4.2 Mesh generation 58

4.3 Boundary conditions and assumptions considered for the CFD model 60

4.3.1 Modelling and implementation of the primary phase – gas 61

4.3.2 Modelling and implementation of the secondary phase – melt 63

4.4 Mesh independency study 66

4.5 Domain independency study 67
4.5.1 Domain independency study - Axial direction 68
4.5.2 Domain independency study - Radial direction 69
4.6 Turbulence sensitivity study 70
4.7 DPM sensitivity study 72
4.7.1 DPM sensitivity study - influence of stochasticity 73
4.7.2 DPM sensitivity study - influence of particle size 73
4.8 Coupling of gas and melt mass flow rates via UDF and time-averaging of pressure 74
4.8.1 Implementation of UDF to couple gas and melt mass flow rates 75
4.8.2 Time-averaging of pressure in the UDF to couple with the mass flow rate. 76
4.9 Different GMRs and melt temperatures considered for this study 77
5 Results of the Numerical Simulations. 79
5.1 Results of 1 kg min^{-1} (GMR = 5.5) under increasing melt temperatures. 80
5.1.1 Melt temperature: 300K. 80
5.1.2 Melt temperature: 600K 86
5.1.3 Melt temperature: 1000K 88
5.1.4 Melt temperature: 1500K 91
5.1.5 Melt temperature: 2000K 94
5.1.6 Summary 97
5.2 Results of 2 kg min^{-1} (GMR = 2.6) under increasing melt temperatures. 98
5.2.1 Melt temperature: 300K 98
5.2.2 Melt temperature: 600K 105
5.2.3 Melt temperature: 1000K 108
5.2.4 Melt temperature: 1500K 113
5.2.5 Melt temperature: 2000K 115
5.2.6 Summary 117
5.3 Results of 4 kg min^{-1} (GMR = 1.32) under increasing melt temperatures. 118
5.3.1 Melt temperature: 300K 118
5.3.2 Melt temperature: 600K 128
5.3.3 Melt temperature: 1000K 130
5.3.4 Melt temperature: 1500K 132
5.3.5 Melt temperature: 2000K 136
5.3.6 Summary 139
5.4 Results of 6 kg min^{-1} (GMR = 0.88) under increasing melt temperatures. 140

5.4.1 Melt temperature: 300K 140
5.4.2 Melt temperature: 600K 152
5.4.3 Melt temperature: 1000K 158
5.4.4 Melt temperature: 1500K 164
5.4.5 Summary 168
5.5 Results of 12 kg min^{-1} (GMR = 0.44) under increasing melt temperatures. ... 169
5.5.1 Melt temperature: 300K 169
5.5.2 Melt temperature: 600K 182
5.5.3 Melt temperature: 1000K 188
5.5.4 Summary 194
6 Discussion 195
6.1 Melt fluctuation behaviour over increasing mass flow rates. 195
6.2 Melt fluctuation behaviour over increasing melt temperatures. 197
6.3 The exhibited frequencies of melt fluctuation and its trends and similarities 200
6.4 Trends in melt fluctuation both across increasing mass flow rates and its melt temperatures. 204
6.5 Behaviour of the melt in the wake region during decreasing GMR and increasing melt temperatures. 205
6.6 Effect of GMR with increasing melt temperatures beyond the wake region, and gas - melt interaction far downstream. 208
6.7 Formation of melt-isolated closed-wake (MICW) condition due to increasing mass loading. 210
6.8 Flow-field fluctuation and its mechanism behaviour over increasing melt temperatures. 213
6.9 Summary 226
7 Conclusion 229
8 Research gaps to explore and future work. 231
9 Appendix 233
9.1 Melt-aspiration pressure coupling UDF for 1 kg min^{-1} (0.0166 kg s^{-1}) model 233
9.2 Melt-aspiration pressure coupling UDF for 2 kg min^{-1} (0.033 kg s^{-1}) model .. 234
9.3 Melt-aspiration pressure coupling UDF for 4 kg min^{-1} (0.066 kg s^{-1}) model .. 236
9.4 Melt-aspiration pressure coupling UDF for 6 kg min^{-1} (0.1 kg s^{-1}) model 237
9.5 Melt-aspiration pressure coupling UDF for 12 kg min^{-1} (0.2 kg s^{-1}) model 239
9.6 Review of various CFD studies carried out on the CCGA process. 242
10 Reference 252

List of Figures

Figure 2.1 Schematic representation of close-coupled gas atomiser set-up indicating its key components. 4

Figure 2.2 Types of shock waves. a) normal shock, b) oblique shock, and c) expansion wave (Rathakrishnan, 2019, Moura and Rosa, 2013, Kundu et al., 2012). 7

Figure 2.3 Flow through converging and diverging ducts at subsonic and supersonic speeds.. 8

Figure 2.4 Convergent-Divergent (C-D) nozzle, showing sections of the nozzle having subsonic and supersonic flow (Rathakrishnan, 2019). 9

Figure 2.5 Schematic representation of osver-exypanded flow (Jadidi et al., 2015). 10

Figure 2.6 Schematic representation of under-expanded flow (Rosario, 2012). 11

Figure 2.7 Detailed comparison of shock structures seen in under-expanded and over-expanded flows (not to scale) (Biswas and Qiao, 2017). 12

Figure 2.8 Schematic representation showing the gas-melt interaction and the process of pre-filming at the melt nozzle front (Anderson and Achelis, 2017). 13

Figure 2.9 Schematic representation detailing the different types of melt break-up. 16

Figure 3.1 Schematic illustration of gas flow-field with Mach-disk downstream. 31

Figure 3.2 Schematic representation of closed- and open-wake conditions (Anderson et al., 1991). 31

Figure 3.3 A two-phase flow interaction showing, (a) the gas-only feature at below WCP operation just prior to the introduction of the melt in to the wake, (b) melt entrainment into the wake, and (c) enlargement of wake and retarding melt flow due to the opposing force exerted by stagnation pressure. (Ting, 2003) 33

Figure 3.4 Two phase flow interaction showing, (a) the wake in the closed-wake condition just prior to the introduction of the melt into the wake, (b) the introduction of the melt into the wake drawn in by the deep aspiration pressure, (c) melt disrupting the Mach-disk and entering onto open-wake condition, (d) enlargement of the wake and the high pressure from stagnation point 4 surging into the wake, and (e) the pressure surge temporarily disrupting the melt flow. The wake region begins to neck, leading to the re-establishing of Mach-disk as shown in (a) (Ting, 2003). 34

Figure 3.5 Cut section of annular slit gas nozzle (Zhao et al., 2012). 35

Figure 3.6 The discreet-jet gas-die components and melt delivery nozzle, (b) Melt and discrete gas die assembly (Motaman, 2013). 36

Figure 3.7 A schematic diagram of (a) cylindrical nozzle profile (Antipas, 2009), (b) C-D nozzle profile. (Anderson and Terpstra, 2002). 37

Figure 3.8 Gas nozzle configurations: a) without offset distance, b) with offset distance. 38

Figure 3.9 Cross section of the nozzle having mismatch angle between the gas and melt nozzles (Mi et al., 1997). 38

Figure 3.10 Schematic representation of different protuberance lengths of melt nozzle (Anderson et al., 1991).....39

Figure 3.11 Cut section of different internal profiles of melt nozzles. a) flat tipped, b) flared with lip, c) flared without lip, d) hemi-spherical and e) trumpet (Mullis et al., 2011, McCarthy et al., 2013). 40

Figure 3.12 Velocity contour of gas-only flow simulation for a) gas nozzle without AGN, b) gas nozzle with AGN (Wang et al., 2024b).....46

Figure 3.13 Force balance identifying, the melt break-up mode – a) Umbrella deformation and b) Fountain deformation; and CCGA operation – c) smooth operation and d) melt freeze-off (Liu et al., 2023b, Wang et al., 2021). 48

Figure 4.1 Schematic showing the flowchart of methodology. 56

Figure 4.2 a) Schematic representation of the gas atomiser having annular slit gas-die, showing the gas flow and melt entrainment; b) the schematic diagram of the melt nozzle used in this study showing key dimensions of the design – melt nozzle diameter, 2 mm; gas nozzle diameter, 0.21 mm; and melt nozzle angle, 45°. 57

Figure 4.3 The numerical domain with geometrical dimensions used in this study. 58

Figure 4.4 Schematic representation of compartmentalised numerical domain. 58

Figure 4.5 Mesh for the entire numerical model and for the gas nozzle section showing the refined mesh. 60

Figure 4.6 Boundary conditions applied to the different parts of the numerical domain. 61

Figure 4.7 Velocity magnitude obtained at the domain outlet for the four meshes. 67

Figure 4.8 Velocity contours of domains having axial dimensions of 15, 25 and 35 N_d. 68

Figure 4.9 Velocity contours of domains having radial dimensions of 6, 8 and 12 N_d.....69

Figure 4.10 Velocity contours of four different turbulence model utilised for the sensitivity study. 72

Figure 4.11 Particle trajectories shown for with and without stochastic model with velocity contour in the background. 73

Figure 4.12 Particle trajectories with velocity contour in the background presented for three different partcle size - 390, 500, and 630 μm, all taken at 50 ms. 74

Figure 4.13 Injection mass flow rate plots showing the difference in the three time-averaging period – Instantaneous, 5 μs, and 50 μs. 77

Figure 5.1 Locations of the seven velocity monitor employed in the study to record velocity of the gas flow. 79

Figure 5.2 injection mass flow rate plot of 1 kg min^{-1} with melt temperature, 300K. This shows as time progresses the fluctuation attenuates to become a steady-state mass flow rate. 80

Figure 5.3 Particle trajectories with velocity contours in the background for the 1 kg min^{-1}, 300K case showing the evolvement of particles starting from onset of injection, pre-filming and movement downstream. 81

Figure 5.4 Particle trajectories with velocity contours in the background for the 1 kg min^{-1}, 300K case demonstrating how particle dispersion increases with time. The arrow shown in the frames shows how the less dispersed particles, in frame a, become more dispersed over time, as seen in frame f. 82

Figure 5.5 Mass flow rate of the particles obtained at the outlet of the domain for the 1 kg min^{-1}, 300K case shows the particles takes around 2.4 ms to reach to the outlet, and mass flow rate reaches an approximate steady-state mass flow rate at 64.3 ms. 83

Figure 5.6 velocity contours without particles for the 1 kg min^{-1}, 300 K case showing the initial flow-field fluctuation during the onset of the melt injection, starting at 30 ms. This is illustrated using three guide-lines (i), (ii) and (iii), pinned at frame a, at first Mach-disk, stagnation point, and second Mach-disk, respectively. The melt pool heads of the frames, b-e, are marked in the circle. Using the three guide-lines the to-and-fro motion of the flow-field fluctuation is illustrated. 84

Figure 5.7 velocity contours without the particles for the 1 kg min^{-1}, 300 K case taken at different flow time are presented in sequential order showing the flow-field exist in open-wake condition once it stabilises at t > 36 ms. The melt pool heads of all the frames are marked in red circles. 85

Figure 5.8 Injection mass flow rate plot of 1 kg min^{-1} case with a melt temperature of 600K. After the initial fluctuation, at 42.5 ms there is a gradual rise and fall in the mass flow rate before becoming steady-state at 63 ms. 86

Figure 5.9 Particle trajectories taken at 63 ms exhibiting swirling of the particles in the recirculation zone. Also, at 63 ms the melt pool head penetration downstream also becomes stable. 86

Figure 5.10 Particles' mass flow rate obtained at the outlet of the domain for 1 kg min^{-1}, 600K case, showing the flow rate reaches a near-steady state around 64 ms with a value of 0.01933 kg s^{-1}. 87

Figure 5.11 Injectin mass flow rate plot for the 1000K case, showing onset of a high frequency fluctuation at 60 ms which remains for the remainder of the simulation. The high frequency fluctuation was evaluated to be 28.5 kHz. 88

Figure 5.12 Particle trajectories obtained at 69 ms showing $3N_d$ downstream advancement of melt pool head, where it stabilises. 88

Figure 5.13 Mass flow rate of the particles obtained at the outlet of the domain for the 1 kg min^{-1}, 1000K case. There are two stages of mass flow that is observed: a steep increase as pointed by the green arrow, and a gradual rise pointed by the violet arrow. 89

Figure 5.14 Velocity contours without particles for the 1 kg min^{-1}, 1000 K case showing flow-field fluctuation corresponding to the high frequency fluctuation seen in the injection mass flow rate. End of second shock-cell and stagnation point is seen shifting away and returning back to its original point. The wave propagation due to the flow-field oscillation is traced using ellipse. 91

Figure 5.15 Injection mass flow rate plot of 1 kg min^{-1} case with a melt temperature of 1500K showing an initial steep rise followed by a gradual decline in the mass flow rate in two stages, shown using green and violet arrows.....91

Figure 5.16 Particle trajectories of 1 kg min^{-1} case with melt temperature as 1500K obtained at 72 ms showing the extent of the melt pool head advancement downstream. 92

Figure 5.17 Mass flow rate of the particles recorded at the outlet of the domain for 1 kg min^{-1}, 1500K case showing two stages of continuous rise before reaching steady-state. A steeper rise followed by a gradual one, marked using the green and violet arrows, respectively. In both the stages a rise-and-fall trend is observed, shown using the orange circles. The steep rise indicates increased number of particles being pushed across the exit than the gradual rise. The rise-and-fall indicates a brief fluctuation in the rate of mass outflow.....93

Figure 5.18 Injection mass flow rate of 1 kg min^{-1} case for a melt temperature of 2000K. 94

Figure 5.19 Monitor M1 obtained for the 1 kg min^{-1} , 2000K melt temperature case containing high frequency fluctuation showing the continuous and rapid oscillation of the flow-field.....95

Figure 5.20 Monitors M1 to M7 zoomed in at the injection of the melt and at the high frequency fluctuation. The high frequency for all the 7 monitors is same as the high frequency seen in the injection mass flow rate i.e., 25.5 kHz. The high frequency fluctuation exhibits phase difference between the monitors which is indicated by the red dashed guide-line.....96

Figure 5.21 Particle trajectories obtained at 76 ms showing pointed and protracted downstream movement of the melt pool head. 96

Figure 5.22 Mass flow rate of the melt obtained at the outlet of the domain for the 1 kg min^{-1} case with melt temperature as 2000K. 97

Figure 5.23 Injection mass flow rate plot of 2 kg min^{-1}, 300K melt temperature case, showing initial fluctuation followed by a gradual rise-and-fall trend, indicated using the green and violet arrows, respectively. After this brief change, it transitions into a near constant mass flow rate. 98

Figure 5.24 Particle trajectories with velocity contours in the background showing how the particles evolve after injection. These stacks of particle tracjectories shows the onset of injection, pre-filming, movement downstream, and increased dispersion of particles.....100

Figure 5.25 Particle trajectories with the velocity contour in the background showing melt pool head moving downstream before stabilising at 70 ms. 100

Figure 5.26 Mass flow rate of the particles obtained at the outlet of the domain for 2 kg min^{-1}, 300K case. Two stages of mass build-up is seen: an initial steep mass build-up followed by a secondary gradual build-up, marked using green and violet arrrows, respectively. Following this, around 70 ms the mass flow rate attains an approximate steady-state value. 101

Figure 5.27 Velocity contours for the 2 kg min^{-1}, 300K case, showing the flow-field undergoing fluctuation in the first few milliseconds due to the melt injection. This is shown by the guide-line (i) fixed at the first Mach-disk of frame a) and compared against the rest of the frames. 103

Figure 5.28 Velocity contours showing flow-field continues to exist as open wake from 32.5 ms. Three guide-lines (i), (ii), and (iii) pinned at melt pool head tip, end of second shock-cell, and second Mach-disk, respectively, in frame a. The melt pool head tip continues to move downstream even though the flow-field continues to exist in steady-state condition. 103

Figure 5.29 Velocity contours showing a cycle of the repeated flow-field fluctuation. Two primary guide-lines (i) and (ii) are fixed at the end of the first shock-cell and at the first Mach-disk, respectively, and are used to compare the extent of the flow-field fluctuation against the rest of the frames. Another dashed white line is used to trace the movement of the end of the second shock-cell during the fluctuation. It is seen the first shock-cell didn't change in shape or length whereas the second shock-cell, as marked with the white dashed line, changed in its spatial dimensions. 104

Figure 5.30 Mass flow rate plot of 2 kg min^{-1}, 600K melt temperature case, showing initial fluctuation followed by a gradual rise and steeper fall trend, indicated by the green and violet arrows, respectively. Around 85 ms, it achieves a near constant mass flow rate. 105

Figure 5.31 Particle trajectories with the velocity contours of the flow-field presented at the background, showing the particles evolving over time. At 58 ms the melt pool rejoins the particles that flow downstream pushed by the flow-field. 106

Figure 5.32 Particle trajectories with the velocity contours of the flow-field presented at the background, showing steady flow of particle trajectories. 107

Figure 5.33 Mass flow rate of the particles obtained at the outlet of the domain for 2 kg min^{-1}, 600K case. The mass build-up takes in two stages shown in the green arrow, continuing until 65 ms. Even though the mass build-up is interupted at two instances: 41 to 46 ms, and 59 to 61 ms having a brief period of fall in the mass flow rate, the rate of mass build-up is the same across all the two stages. 107

Figure 5.34 Mass flow rate plot of 2 kg min^{-1}, 1000K melt temperature case. The high-frequency fluctuation initiates at 40 ms. After the momentary rise in the mass flow rate, the fall takes place in two stages: a steep fall followed by a gradual decline, indicated by the green and the violet arrows, respectively. 108

Figure 5.35 Particle trajectories with the velocity contours of the flow-field in the background showing the progressive interaction of the melt pool head with the particles that are pushed

downstream. Frame b & c shows the particles following the path of the recirculation zone. From frame d particles trajectories are stabilised. 109

Figure 5.36 The mass flow rate of the particles obtained at the outlet of the domain for 2 kg min^{-1}, 1000K case. The mass build-up takes place in three stages: two steep build-ups followed by a much gradual build-up, indicated by green and violet arrows, respectively. In between the stages, there is brief period of decline as indicated by the orange circles. After the build-up before the mass flow rate reaches an approximate steady-state, a significant decline in the mass flow rate is observed..... 110

Figure 5.37 Velocity contours of the flow-field stacked in sequential order to elucidate the flow-field fluctuation and the changes in the flow features. Three white guide-lines (i), (ii), and (iii) are pinned at the end of the first shock-cell, at the first Mach-disk, and at the second Mach-disk of the first frame and compared against the rest of the frames. Another secondary white dashed white line is used to trace the end of the second shock-cell during the fluctuation to show the spatial movement of the flow-field. The first shock-cell didn't change in shape or length whereas the second shock-cell, as marked with the white dashed line, changed in its spatial dimensions..... 111

Figure 5.38 Monitors M1 to M7 zoomed in at the injection of the melt and at the high frequency fluctuation. The high frequency fluctuation for all the 7 monitors is same as the high frequency seen in the injection mass flow rate i.e., 25.4kHz. The high frequency fluctuation exhibits phase difference between the monitors indicated by the red guide-line.113

Figure 5.39 Injection mass flow rate of 2 kg min^{-1} with a melt temperature of 1500K. 113

Figure 5.40 Mass flow rate of the particles obtained at the outlet of the domain for 2 kg min^{-1}, 1500K case. Three stages of mass build-up is seen and is indicated by the green arrows. The brief period of decline in between the stages are marked using the orange circles. 114

Figure 5.41 Particle trajectories with the velocity contours in the background, showing the particle dispersion recorded at 82 ms..... 115

Figure 5.42 Injection mass flow rate of 2 kg min^{-1} with a melt temperature of 2000K. 115

Figure 5.43 Particle trajectories with the velocity contours in the background, showing the particle dispersion obtained at 90 ms, where the trajectories stabilise. 116

Figure 5.44 The mass flow rate of the particles obtained at the outlet of the domain for 2 kg min^{-1}, 2000K case. There are three stages of mass build-up: a gradual rise followed by two steeper rises, indicated by the green and violet arrows, respectively..... 117

Figure 5.45 Injection mass flow rate plot of 4 kg min^{-1}, 300K case showing initial fluctuation followed by two high amplitude peaks. At $t > 60$ ms there is an onset of a higher frequency fluctuation that gradually increases in its amplitude and remains constant from $t > 120$ ms. The zoomed section of the initial fluctuation and the regular repeated fluctuation is also presented. 118

Figure 5.46 Particle trajectories with the velocity contour in the background showing the evolvement of particles after being injected into the flow stream. These stacks of particle trajectories show the onset of injection, pre-filming, melt movement downstream, and increased dispersion of particles with time..... 119

Figure 5.47 Particles trajectories with velocity contour in the background showing increasing dispersion of particles with time, and melt pool head plunging through the second Mach-disk. Frame e & f shows flares i.e. particles being propelled radially outwards from the main melt plume in small groups, marked by the red ellipses. 120

Figure 5.48 Mass flow rate of the particles obtained at the outlet of the domain for 4 kg min^{-1}, 300K case. There is an initial steady increase in the flow of particles through the outlet, but decreases briefly, but thereafter it increases rapidly. Subsequently, at t > 70 ms no significant change in the mass flow rate is seen. 121

Figure 5.49 Timeline of flow-field fluctuations observed in 4 kg min^{-1}, 300K case. 122

Figure 5.50 Velocity contours of 4 kg min^{-1}, 300K case showing flow-field fluctuations at the onset of the melt injection into the domain. Two guide-lines (i) and (ii) are fixed at first Mach-disk and second Mach-disk of frame a, to compare the changes with rest of the frames. 123

Figure 5.51 Velocity contours showing a cycle of the continuous flow-field fluctuation. Three guide-lines (i), (ii), and (iii) are fixed at the end of the first, second and third shock-cell, respectively. The lower sonic boundary of the second shock-cell of frames a & e lies close to the atomiser's axis, as marked by the yellow lines, whereas the sonic boundary seen in frame c is far from the axis as shown using the curved red line. Similarly, the third shock-cell seen in frames a & e sparingly touches the axis, whereas, in frame c it seems to engulf the axis to a much larger extent than seen in frame a & e. A wave propagation from the end of third shock-cell is observed, marked using blue ellipses. The frequency of the fluctuation was evaluated to be 20 kHz. 124

Figure 5.52 velocity contours of the flow-field showing a cycle of the repeated fluctuation seen at t > 100 ms. Two vertical guide-lines (i) & (ii) are fixed at frame 'a' at the end of first shock-cell and end of second shock-cell, respectively to compare the extent of fluctuation against other frames. Another two sets of guide-lines are used to trace the movement of the first and second shock-cell ends. The frequency of this fluctuation was found to be 8.3 kHz. 126

Figure 5.53 Monitors M1 to M7 zoomed in at the injection of the melt and at the mid frequency fluctuation. The frequency for all the seven monitors is same as the mid frequency seen in the injection mass flow rate i.e. 8.1 kHz. Existence of phase difference between the monitors is indicated using the red dashed line. 127

Figure 5.54 Injection mass flow rate plot of 4 kg min^{-1}, 600K case showing zoomed-in part of the initial fluctuation in blue and irregular fluctuation around 110 ms in red. There is a rapid decline in the mass flow rate from 50 to 60 ms. Subsequently, the fluctuation continuously attenuates to become a near-constant steady-state mass flow rate with negligible amplitude. 128

Figure 5.55 Mass flow rate of the particles obtained at the outlet of the domain for 4 kg min^{-1}, 600K case. The flow of particles through the outlet rises steadily at first, then decreases briefly, before rapidly increasing till 60 ms. Thereafter, the plot exhibits a low frequency fluctuation and simultaneously dampens out its fluctuations. 129

Figure 5.56 Timeline of flow-field fluctuations observed in 4 kg min^{-1}, 600K case. 129

Figure 5.57 Injection mass flow rate plot of 4 kg min^{-1}, 1000K case showing the initial fluctuation and the high frequency. From t > 39 ms the presence of a higher frequency fluctuation is seen. The high frequency fluctuation is of constant amplitude as seen in the zoomed plot. At t > 60 ms the mass flow rate fluctuation undergoes periodic fluctuation with a time period of ~9 ms. 130

Figure 5.58 Timeline of flow-field fluctuations observed in 4 kg min^{-1}, 1000K case.....131

Figure 5.59 Injection mass flow rate plot of 4 kg min^{-1}, 1500K case showing the onset of high frequency at 36 ms. There is a considerable decline in the mass flow rate at 44 ms. The mass flow rate plot from 50 ms is irregular both in its amplitude and in its frequency of fluctuation. 132

Figure 5.60 Timeline of flow-field fluctuations observed in 4 kg min^{-1}, 1500K case.....133

Figure 5.61 Velocity contours of 4 kg min^{-1}, 1500K case showing flow-field fluctuations. Three guide-lines (i), (ii), and (iii) are pinned in frame a, at the ends of the first, second and third shock-cell, respectively, and are compared against the other frames. It is observed the first and second shock-cells remain fixed throughout the fluctuation, whereas third shock-cell exhibit marginal change in its spatial extent. In frame a, the flow-field exists in closed-wake condition. In the consecutive frames, from frames b till e it is seen the flow-field enters into open-wake condition, and tends to return back to closed-wake condition. However, as seen in frame e, even though the lower sonic boundary is near to the atomiser's axis, still it continues to exist in open-wake condition. Consequently, the sonic boundary moves away from the atomiser's axis before returning to closed-wake condition in frame h. A significant wave propagation from the second Mach-disk is observed which is marked using ellipses. 135

Figure 5.62 Injection mass flow rate plot of 4 kg min^{-1}, 2000K case showing the onset of high frequency around 32.6 ms, and highly irregular fluctuation thereafter. The mass flow rate plot is extremely irregular both in the amplitude and the frequency of the fluctuation. The zoomed section of the high frequency fluctuation shows the extent of the variation in amplitude and frequency.....136

Figure 5.63 FFT analysis of the injection mass flow rate for the 4 $kgmin^{-1}$, 2000K case shows multiple frequencies reflecting the instability in the mass flow rate. 137

Figure 5.64 Timeline of flow-field fluctuations observed in 4 kg min^{-1}, 2000K case.....138

Figure 5.65 Injection mass flow rate plot of 6 kg min^{-1}, 300K case shows the initial fluctuation followed by two high amplitude peaks. At t > 58 ms there is an onset of a higher frequency fluctuation that gradually increases in its amplitude and remains constant from t > 80 ms. The zoomed section of the initial fluctuation and the regular repeated fluctuation is also presented.....140

Figure 5.66 Particle trajectories of the 6 kg min^{-1}, 300K case, with the velocity contour in the background showing the evolvement of particles after being injected into the flow stream. These stacks of particle trajectories show the onset of injection, pre-filming, melt movement downstream, and increased dispersion of particles with time.....143

Figure 5.67 Particles trajectories 6 kg min^{-1}, 300K case with velocity contour in the background showing increasing dispersion of particles with time, and melt pool head

plunging through the second Mach-disk. Frame b - g shows flares i.e. particles being propelled radially outwards from the main melt plume in small groups, marked by ellipses. 144

Figure 5.68 Mass flow rate of the particles obtained at the outlet of the domain for 6 kg min^{-1}, 300K case. There is an initial steady increase in the flow of particles through the outlet, but decreases briefly at 40 ms, but thereafter increases rapidly. Subsequently, at t > 65 ms no significant change in the mass flow rate is seen. 145

Figure 5.69 Timeline of flow-field fluctuations observed in 6 kg min^{-1}, 300K case.....145

Figure 5.70 Velocity contours of 6 kg min^{-1}, 300K case, is presented without particles, showing flow-field fluctuations at the onset of the melt injection into the domain. Two guide-lines (i) and (ii) are fixed at first and second Mach-disk of frame a, to compare the changes with rest of the frames.....146

Figure 5.71 Velocity contours showing a cycle of the continuous flow-field fluctuation. Three guide-lines (i), (ii), and (iii) are fixed at the ends of the first, second and third shock-cell, respectively. The lower sonic boundary of the second shock-cell of frames a & e lies in close proximity to the atomiser's axis, marked using the yellow lines, whereas the sonic boundary seen in frame c is furthest away from the axis, shown using the curved red line. Similarly, the third shock-cell seen in frames a & e sparingly touches the axis, whereas, in frame c seems to engulf the axis to a much larger extent than seen in frame a & e. A wave propagation from the end of third shock-cell is observed and marked using ellipses. The frequency of the fluctuation was evaluated to be 20 kHz. 147

Figure 5.72 velocity contours of the flow-field without particles showing a cycle of the repeated fluctuation that is seen from t > 80 ms. Two vertical guide-lines (i) & (ii) are fixed at the ends of the first and second shock-cell, respectively, of frame a to compare the extent of fluctuation against other frames. Another two sets of guide-lines are used to trace the movement of the first and second shock-cell ends. The frequency of the fluctuation was found to be 8.3 kHz.....150

Figure 5.73 Determination of open- and closed-wake by comparing velocity contours against particle trajectories. (a) the lower sonic boundary of the second shock-cell lies 0.7 mm radially away from the axis, while, the thickness of the melt layer is 0.8 mm indicating the first Mach-disk is immersed in the melt layer, resulting in closed-wake. (b) the lower sonic boundary of the second shock-cell lies 1.37 mm radially away from the axis, while, the thickness of the melt layer is 1.0 mm, resulting in considerable space between the sonic boundary and the melt layer, indicating wake exists in open-wake condition. 151

Figure 5.74 Monitors M1 to M7 zoomed in at the injection of the melt and at the high frequency fluctuation. FFT analysis of the monitors resulted in two dominant frequencies: 8.1 kHz and 16.3 kHz. The high frequency, 8.1 kHz observed in the monitors, corresponded to the high frequency 8.1 kHz, obtained from the injection mass flow rate, confirming the frequency of the flow-field fluctuation. Existence of phase difference between the monitors is indicated using the red dashed line. 152

Figure 5.75 Injection mass flow rate plot of 6 kg min^{-1}, 600K case showing the initial fluctuation followed by two high amplitude peaks between 35-50 ms. At 39 ms there is an

onset of a higher frequency fluctuation that exists for the remainder of the simulation. The zoomed section of the high frequency fluctuation is presented in the blue plot. 152

Figure 5.76 Mass flow rate of the particles obtained at the outlet of the domain for 6 kg min^{-1}, 600K case. The rise in the outlet flow from 45 to 65 ms is observed in three stages; a steep rise, followed by a stalled rise, and again through a steep rise. Subsequently, at t > 80 ms the plot undergoes a regular fluctuation reflecting the injection mass flow rate at t > 55 ms. 154

Figure 5.77 Timeline of flow-field fluctuations observed in 6 kg min^{-1}, 600K case. 155

Figure 5.78 Velocity contours of the flow-field without particles showing a cycle of the repeated fluctuation that is seen at t > 52 ms. Three vertical guide-lines (i), (ii) and (iii) are fixed at the ends of the first, second and third shock-cell, respectively, of frame a to compare the extent of fluctuation against other frames. Another two sets of guide-lines are used to trace the movement of the second shock-cell end. First and third shock-cells remain fixed, whereas the second shock-cell marginally varies in its spatial extent. The frequency of the fluctuation was found to be 20.8 kHz. 157

Figure 5.79 Injection mass flow rate plot of 6 kg min^{-1}, 1000K case showing the initial fluctuation followed by two high amplitude peaks seen between 35-50 ms. At 38 ms there is an onset of a higher frequency fluctuation that exists for the remainder of the simulation. The zoomed section in the blue plot shows one of the many high frequency fluctations observed in the case. 158

Figure 5.80 Timeline of flow-field fluctuations observed in 6 kg min^{-1}, 1000K case. 160

Figure 5.81 Velocity contours of the flow-field without particles showing a cycle of the nested fluctuation that is seen at t > 77.5 ms. Three vertical guide-lines (i), (ii) and (iii) are fixed at the ends of the first, second and third shock-cell, respectively, of frame a to compare the extent of fluctuation against other frames. All the three shock-cells remain fixed. The frequency of the fluctuation was found to be 12.8 kHz. 162

Figure 5.82 Injection mass flow rate plot of 6 kg min^{-1}, 1500K case showing the initial fluctuation and the irregular fluctuation that ensues after it. a) at 36 ms there is an onset of a higher frequency fluctuation that exists for the remainder of the simulation. b) the zoomed section in the blue plot showing the high frequency fluctation. 164

Figure 5.83 Timeline of flow-field fluctuations observed in 6 kg min^{-1}, 1500K case. 166

Figure 5.84 Injection mass flow rate plot of 12 kg min^{-1}, 300K case shows, a) the initial fluctuation followed by multiple peaks between 40 - 70 ms that continue to attenuate. At t > 60 ms an onset of a higher frequency fluctuation is observed that gradually increases in its amplitude and remains constant from t > 110 ms; b) the zoomed section of the initial fluctuation and the regular repeated fluctuation seen at t > 110 ms. 169

Figure 5.85 Particle trajectories of the 12 kg min^{-1}, 300K case, seen with the velocity contours in the background displaying the evolvement of particles after being injected into the flow stream. The particle trajectories show the onset of injection, pre-filming, melt movement downstream, and increased dispersion of particles with time. The pre-filming starts from the circumferential edge of the nozzle and continues to wet the entire nozzle by moving radially inward. 171

Figure 5.86 Particles trajectories 12 kg min^{-1}, 300K case with velocity contours in the background showing increasing dispersion of particles with time and melt pool head plunging through the first and second Mach-disks. Frames e&f shows flares, i.e., particles in small group being propelled radially outwards from the main melt plume, marked by ellipses.....173

Figure 5.87 Mass flow rate of the particles for the 12 kg min^{-1}, 300K case obtained at the outlet of the domain. There is an initial steady increase in the flow of particles through the outlet till 40 ms, but decreases briefly, and thereafter rapidly increases. Subsequently, at t > 67 ms no significant change in the mass flow rate is seen.....174

Figure 5.88 Timeline of flow-field fluctuations observed in 12 kg min^{-1}, 300K case.....174

Figure 5.89 Velocity contours of 12 kg min^{-1}, 300K case, is presented without particles, showing flow-field fluctuations at the onset of the melt injection into the domain. Two guide-lines (i) and (ii) are fixed at first and second Mach-disk of frame a, to compare the changes with rest of the frames.....175

Figure 5.90 Velocity contours of 12 kg min^{-1}, 300K case, is presented without particles, showing flow-field fluctuations existing in open-wake configuration. The downstream movement of the melt pool head is observed, marked using the ellipses. 176

Figure 5.91 Velocity contours of 12 kg min^{-1}, 300K case, is presented without particles, showing the steady gas flow, from 34.2 - 42.5 ms. The two primary guide-lines (i) and (ii), pinned at the first and second Mach-disk, respectively, indicate the flow-field continues as steady state. The downstream movemnt of the melt pool head is marked using the ellipses. White arrows indicate the melt pool head plunging into the first Mach-disk, transforming the flow-field into MICW configuration. The secondary guide-line in frame g pinned at the stagnation point shows the downstream displacement of the stagnation points in frame i&j. This is due to the downstream movemnt of the melt. Melt beginning to plunge into the second Mach-disk is shown using the black arrows. 178

Figure 5.92 Velocity contours of the flow-field without particles for the 12 kg min^{-1}, 300K case, showing a cycle of the repeated fluctuation that is seen at t > 79 ms. Two vertical guide-lines, (i) and (ii) are fixed at the ends of the first and second shock-cell, respectively, of frame a to compare the extent of fluctuation against other frames. Another two sets of guide-lines are used to trace the movement of the first and second shock-cell ends. The second shock-cell undergoes significant spatial fluctuation compared to the first shock-cell. The frequency of the fluctuation was found to be 8.1 kHz. 181

Figure 5.93 Injection mass flow rate plot of 12 kg min^{-1}, 600K case showing the initial fluctuation followed by a rise and fall in the mass flow rate between 40 - 48 ms. A higher frequency fluctuation is observed between 38.4 - 52 ms. At t > 55 ms no significant large amplitude fluctuations are observed. At t > 58 ms, a lower frequency fluctuation is observed. 182

Figure 5.94 Mass flow rate of the particles for the 12 kg min^{-1}, 600K case, obtained at the outlet of the domain. There is an initial steady increase in the flow of particles through the outlet. Following a brief decrease at 41 ms, a sharp rise is observed until 72 ms, after which the plot transforms into a fluctuation similar to the fluctuation seen in injection mass flow rate, at t > 55 ms.....184

Figure 5.95 Timeline of flow-field fluctuations observed in 12 kg min^{-1}, 600K case. 184

Figure 5.96 Velocity contours of the flow-field without particles for the 12 kg min^{-1}, 600K case, showing a cycle of the alternating flow-field fluctuation. Two guide-lines, (i) and (ii) were pinned in frame a, at the ends of the first and second shock-cell, and were compared against the rest of the frames. The first and second shock-cells remain fixed throughout the fluctuation without undergoing any changes to their spatial extent. A wave propagation is observed starting at the end of the third shock-cell, and is marked using ellipses. 187

Figure 5.97 Injection mass flow rate plot of 12 kg min^{-1}, 1000K case. a) The initial and higher frequency fluctuation are shown, with latter becoming prominent at t > 36.5 ms and persisting for the remainder of the simulation. Zoomed section of the plot highlights the repetitive pattern in the melt, b) single frquency of 8.5 kHz followed by, c) varying frequencies in ampplitude modulation. 188

Figure 5.98 Mass flow rate of the particles for the 12 kg min^{-1}, 1000K case, obtained at the outlet of the domain. There is an initial steady increase in the flow of particles through the outlet. Following a brief decrease at 41 ms, a rapid rise is observed until 75 ms, after which the plot transforms into a much lower frequency fluctuation. 189

Figure 5.99 Timeline of flow-field fluctuations observed in 12 kg min^{-1}, 1000K case. 191

Figure 5.100 Velocity contours of the flow-field without particles for the 12 kg min^{-1}, 1000K case, showing a cycle of the alternating flow-field fluctuation. Three guide-lines, (i), (ii), and (iii), were pinned in frame a, at the downstream ends of the first, second and third shock-cell, respectively, and were compared against the rest of the frames. The first shock-cell remained fixed throughout the fluctuation, whereas the second shock-cell reduced in its spatial extent, and the third shock-cell underwent significant spatial movement downstream. The wave propagation is marked using ellipses. 192

Figure 6.1 Mass flow rate plot of the melt injection for cases 4 kg min^{-1} (GMR=1.32), 6 kg min^{-1} (GMR=0.88), and 12 kg min^{-1} (GMR=0.44) all having a melt temperature of 300K; the plots exhibits a constant frequency but increasing amplitude with increasing mass flow rates. 195

Figure 6.2 Stacked melt injection plot of 2 kg min^{-1} (GMR=2.6), 4 kg min^{-1} (GMR=1.32), 6 kg min^{-1} (GMR=0.88), and 12 kg min^{-1} (GMR=0.44) cases, all obtained at 600K, displaying varying frequency and amplitude with decreasing GMR. 196

Figure 6.3 GMR=5.5 (1 kg min^{-1}) case showing all the five different melt injection plots corresponding to melt temperatures, 300K, 600K, 1000K, 1500K, and 2000K.....198

Figure 6.4 GMR=2.6 (2 kg min^{-1}) case showing all the five different melt injection plots corresponding to melt temperatures, 300K, 600K, 1000K, 1500K, and 2000K.....198

Figure 6.5 GMR=1.32 (4 kg min^{-1}) case showing all the five different melt injection plots corresponding to melt temperatures, 300K, 600K, 1000K, 1500K, and 2000K.....200

Figure 6.6 Onset of melt instability in ms observed for different GMRs and melt temperatures. 300K cases exhbited very similar times of onset of melt instability. 201

Figure 6.7 Temperature contours with flow vectors showing the flow direction for the 1 kg min^{-1} 300K and 2000K cases taken at 31 ms. Temperature contour of the 2000K indicates the region of elevated temperature reflecting the higher velocity in that region....206

Figure 6.8 Illustration of melt-isolated closed-wake (MICW) condition seen for different GMR cases, except GMR=5.5. The flow-field immerses into the melt layer, leading to the same condition as observed in regular closed-wake condition. The melt layer thicknes and the gap between lower sonic boundary and aomiser's axis is presented for all the four cases. ..211

Figure 6.9 A schematic diagram illustrating the difference between regular closed-wake and melt isolated closed-wake (MICW). It also illustrates the nature of open-wake condition formed during the presence of melt layer. 212

Figure 6.10 The mechanism of flow-field fluctuation for 300K cases shown using velocity contour in the background and pathlines in the foreground, containing frames a till f. 217

Figure 6.11 The mechanism of flow-field fluctuation for 300K cases shown using velocity contour in the background and pathlines in the foreground, containing frames g till k. 218

Figure 6.12 Pressure plot showing the aspiration pressure and pressures recorded at zone-1 and zone-2. 219

Figure 6.13 The mechanism of flow-field fluctuation for 1000K cases shown using velocity contour in the background and pathlines in the foreground, containing frames a till e.....223

Figure 6.14 The mechanism of flow-field fluctuation for 1000K cases shown using velocity contour in the background and pathlines in the foreground, containing frames f till i.....224

Figure 6.15 Pressure plot showing the aspiration pressure and pressures recorded at zone-1 and zone-2. Zone-1 and aspiration pressure follows the same trend of pressure fluctuaiton.225

Figure 6.16 Schematic diagram showing the back flow of gas seen in the 1000K case of GMR = 1.32 (4 kg min^{-1}). 226

Figure 6.17 Comparison between the pathlines obtained from the simulation results and standard textbook schematic highlighting the complexity in the atomisation process, present in the wake region. The simulation results presents five complex recirculation zones whereas the schematic presents a simple single recirculation zone present at the melt nozzle front. .228

List of Tables

Table 3-1 Inlet gas pressures used in different CCGA process and their respective PSD outcome. 32

Table 3-2 Parameters used by various researchers for studying melt nozzle design 41

Table 4-1 Mesh element sizes used in the different compartments of the numerical domain for the mesh considered for the study. 59

Table 4-2 Boundaries in the domain and their applied conditions. 61

Table 4-3 Computational resource and CPU hours for each of the simulation carried out. 67

Table 4-4 Proportionality constant (K) calculated for the five nominal mass flow rates. 75

Table 4-5 Nominal melt flow rates and their respective GMRs used in the study. 77

Table 4-6 Table of simulation run in this thesis. The blue tick indicates they are simulated, the red cross indicates they are not simulated. 78

Table 5-1 The frequencies obtained from the FFT analysis of 6 kg min^{-1}, 300K case, and their correlation to the flow-field fluctations. 141

Table 5-2 The frequencies obtained from the FFT analysis of 6 kg min^{-1}, 600K case, and their correlation to the flow-field fluctations. 153

Table 5-3 The frequencies obtained from the FFT analysis of 6 kg min^{-1}, 1000K case, and their correlation to the flow-field fluctations. 159

Table 5-4 The frequencies obtained from the FFT analysis of 6 kg min^{-1}, 1500K case, and their correlation to the flow-field fluctations. 165

Table 5-5 The frequencies obtained from FFT analysis of 12 kg min^{-1}, 300K case, and their correlation to the flow-field fluctuations. 170

Table 5-6 The frequencies obtained from FFT analysis of 12 kg min^{-1}, 600K case and their correlation to the flow-field fluctuations. 183

Table 5-7 The frequencies obtained from FFT analysis of of 12 kg min^{-1}, 1000K case and their correlation to the flow-field fluctuations. 190

Table 6-1 Predictive calculation of D_{50} based on different GMRs and model constants. 197

Table 6-2 Onset of melt instability recorded in ms. 201

Table 6-3 Various frequencies obtained via FFT analysis 202

Table 6-4 Melt instability-map, showing the mode of melt fluctuation. 203

Table 6-5 Different modes of melt fluctuation and their characteristcs observed during the melt injection. 204

Table 6-6 Time taken in ms to undergo pre-filming for different simulations. 206

Table 6-7 Table showing the time taken for melt pool head to rejoin with the particles that are pushed after pre-filming for different simulations. 207

Table 6-8 Melt layer thickness measured in millimetres (mm) at 100 ms. 209

Table 6-9 Maximum extent of particles scattering in the radial direction recorded at the domain's outlet, measured in N_d. 209

List of Abbreviations

AGN – Assisted Gas Nozzle
AML – Absence of Melt Layer
AMR – Adaptive Mesh Refinement
AS – Annular Slit
CCGA – Close-Coupled Gas Atomisation
CFD – Computational Fluid Dynamics
DEM – Discrete Element Method
DJ – Discrete Jet
DPM – Discrete-Phase Model
DRW – Discrete Random Walk
EDM – Electrical Discharge Machining
EIGA – Electrode Induction Gas Atomisation
FFT – Fast Fourier Transform
FVM – Finite Volume Method
GMR – Gas-to-Melt Ratio
HIP – Hot Isostatic Pressing
IP – Isentropic Plug
KH – Kelvin-Helmholtz
KHRT – Kelvin-Helmholtz Rayleigh-Taylor
LES – Large Eddy Simulation
LPBF – Laser Powder Bed Fusion
MBJ – Material Binder Jetting
MICW – Melt-Isolated Closed-Wake
MIM – Metal Injection Moulding
MLT – Melt Layer Thickness
NRT – Non-Realisable Thickness
PSD – Particle Size Distribution
R.Z – Recirculation Zones
RANS – Reynolds-Averaged Navier-Stokes
RSM – Reynold Stress Model
RT – Rayleigh-Taylor
SGS – Subgrid-Scale
SLM – Selective Laser Melting
TAB – Taylor Analogy Break-Up
UDF – User-Defined Function
VIGA – Vacuum Inert Gas Atomisation
VOF – Volume of Fluid
WCP – Wake-Closure Pressure

List of Symbols

Symbol	Meaning
M	Mach number of the flow
V	Velocity of the flow in the medium
a	Speed of the sound waves in the same medium
p_1	Static pressure
T_1	Static Temperature
ρ_1	Static Density
p_0	Total pressure
T_0	Total temperature
ρ_0	Total density
γ	Ratio of the specific heats
A	Cross-sectional area
p_{th}	Pressure at throat
A_{th}	Area of the throat
A_e	Exit area
W_e	Weber number
ρ_A	Density of the gas
d_0	Diameter of the liquid column
u_r	Relative velocity
σ	Surface tension
ρ	Density of the fluid

Symbol	Meaning
$\overline{\emptyset}$	Reynolds averaged steady mean value,
$\emptyset'$	Fluctuating part in the Reynolds method
$\widetilde{\emptyset}$	Favre-averaged steady mean value
q_i	Heat flux
κ	Turbulent kinetic energy
ε	Rate of dissipation of turbulent kinetic energy
μ_t	Turbulent viscosity
σ_k	Turbulent Prandtl numbers for κ
σ_ε	Turbulent Prandtl numbers for ε
P_k	Production term of turbulent kinetic energy
L	Turbulent length scale
T	Turbulent time scale
C_1, C_2, & C_L	Model constants
ω	Specific dissipation rate
G_k	Generation of turbulence kinetic energy due to mean velocity gradients
G_ω	Generation of ω
Γ_k	Effective diffusivity of κ
Γ_ω	Effective diffusivity of ω,
y_k	Dissipation of κ
y_ω	Dissipation of ω

u_i	Velocity component along the x_i direction
u_j	Velocity component along the x_j direction
μ	Dynamic viscosity
p	Pressure
τ_{ij}	Viscous stress term
E	Total energy
q_j	Heat flux
H	Enthalpy fluctuations due to turbulence
$\emptyset''$	Fluctuating part in the Favre method
$\emptyset$	Instantaneous value of the flow property
u	Instantaneous fluid velocity
$\bar{u}$	Mean fluid phase velocity
u'	Fluctuating velocity of the fluid phase
T	Integral time scale
$u_{p'}$	Fluctuating component of the particle velocity
τ	Time lag
T_L	Lagrangian integral time
τ_e	Eddy time-scale
ζ	Gaussian distributed random number
v'	Fluctuating velocity along y direction
w'	Fluctuating velocity along z direction
r	Uniform random number
S_k and S_ω	User-defined source terms
G_b & $G_{\omega b}$	Buoyancy terms
α^*	Low-Reynolds number correction coefficient
$\vec{F}$	Other additional forces
m_p	Mass of the particle
g	Acceleration due to gravity
τ_r	Droplet relaxation time,
Re	Relative Reynolds number
C_D	Drag coefficient
$\vec{u}$	Fluid phase velocity
$\vec{u}_p$	Particle velocity
d_p	Diameter of the particle
$\dot{m}_p$	Mass flow rate of the particle
Δt	Timestep
F_{other}	Other interaction forces
$m_{p_{in}}$	Mass of the particle on cell entry
$m_{p_{out}}$	Mass of the particle on cell exit
c_{p_p}	Heat capacity of the particle
H_{pyrol}	Heat of pyrolysis as volatiles are evolved
$T_{p_{in}}$	Temperature of the particle on cell entry
$T_{p_{out}}$	Temperature of the particle on cell exit
T_{ref}	Reference temperature for enthalpy

$\dot{m}_{p,0}$	Initial mass flow rate of the particle injection
$m_{p,0}$	Initial mass of the particle
ρ_p	Density of the particle
d_p	Diameter of the particle
u_p	Velocity of the particle
u	Velocity of the fluid
K	Proportionality constant
N_d	Nozzle-diameter
λ_{RT}	RT Wave number
m	Meter
Pa	Pascal
Hz	Hertz
s	Time
$H_{lat_{ref}}$	Latent heat at reference conditions
β	Gas nozzle's apex angle
α	Melt nozzle's apex angle
F_g	Gravity
F_f	Buoyancy
F_d	Drag force
F_p	Gas pressure
ρ_{melt}	Density of the melt
u_{melt}	Injection velocity
$\dot{m}$	Melt mass flow rate
A_{sp}	Aspiration pressure
K	Temperature
φ	Lubanska model constant

1 Introduction

With the world moving towards more sustainable manufacturing practices like never before in the pursuit to reach the zero-carbon footprint, the manufacturing sector has transformed by adopting the climate-friendly strategy – Industry 4.0. This revolutionised the manufacturing sector to discard the old and conventional manufacturing means of subtractive manufacturing, and to embrace the 'net-zero wastage' method – additive manufacturing. Moreover, unlike conventional subtractive manufacturing where material is wasted in significant proportions, in additive manufacturing intricate and challenging designs, spanning from millimetre to large-scale components, are manufactured with little-to-no wastage at a fraction of the traditional machining time (Aksoy and Ünal, 2006). And in the context of additive manufacturing in the metal industry, the feedstock to produce components is the metal powders. The applications of the metal powders depend on their size – ultra-fine powders having D_{50}[1] ~ 20µm are utilised in Material Binder Jetting (MBJ), Powder Injection Moulding (PIM) (Miyanaji et al., 2020); fine to medium powders having D_{50} ~ 30-50µm are utilised in Laser Powder Bed Fusion (LPBF) and Selective Laser Melting (SLM) (Gallagher et al., 2023); medium to coarse powders having D_{50} ~ 90µm are utilised in Electron Beam Melting (EBM) and Direct Energy Deposition (DED) (Karlsson et al., 2013); coarsest powders having D_{50} > 100µm are utilised in Hot Isostatic Pressing (HIP), Laser Cladding, and Press-and-Sinter Powder Metallurgy processes (Qu et al., 2022).

Although, different methods are adopted to manufacture metal powders, gas atomisation is one of the widely used process to manufacture ultra-fine metal powders owing to its commercially viable yield, and its capability to produce pre-alloyed powders with high purity (Cai et al., 2016). Gas atomisation process uses the principle of converting kinetic energy of a high-speed gas-jet to break-up and disintegrate molten metal stream into fine droplets while solidifying it simultaneously, to produce ultra-fine metal powders smaller than 50µm which are of high quality, purity and sphericity (Ünal and Aydın, 2007, Zeoli and Gu, 2006). The high-pressure gas-jet exiting the gas nozzle rapidly expands downstream, forming a supersonic flow, with typical characteristics flow features like oblique shocks, expansion waves, recompression shocks, and Mach-disk. Owing to the symmetrical arrangement of the gas jets, by virtue of the flow, there is a recirculation zone formed in front of the melt nozzle. This recirculation zone forces the melt to flow over the melt nozzle tip before flowing

[1] D_{50} is the median particle size, a key parameter used in powder characterisation.

downstream, in a process known as pre-filming (Zeoli and Gu, 2008a). As a result of the recirculation zone an aspiration pressure is induced just in front of the melt nozzle which pulls the melt from the melt reservoir proportional to its pressure (Anderson et al., 1991).

Nevertheless, due to the gas-melt interaction between the high-speed gas and molten melt, the process is extremely chaotic, rapid and unpredictable; the entire duration of melt droplet transitioning from its liquid state to a solid powder occurs incredibly quick, in the order of milliseconds (Mullis et al., 2013b, Zhao et al., 2009). The instability in the process is further aggravated by the choice of melt to be atomised, since the alloy in question determines the melt temperature, it directly affects the process instability, leading to variations in output powder size for different alloys. Owing to this chaotic nature of the process, its underlying physics is poorly understood despite the use of high-speed cameras. And this chaotic gas-melt interactions results in increased particle size and particle size distribution (PSD), which is adverse for the process, consequentially leading to significant proportions of out-of-specification powders causing unnecessary energy expenditure. This undesirable outcome in the metal powder yield is also reflected in its undue monetary expenditure. Due to the wider PSD and the fact that most AM processes require particles within specify particle size ranges, the out-of-specifications powders are deemed worthless for that AM process, unless and otherwise targeted by a different industrial application. Moreover, narrow PSD also aids the maximised consumption of the powders; reducing powder wastage, ensures consistency in the powder layers, provides improved flowability, and leads to higher packing density efficiency.

Although numerous experimental and numerical studies have been carried out on the close-coupled gas atomisation (CCGA) process, they have been focussed on primary atomisation mechanism, secondary atomisation mechanism and particle characteristics. However, a full coupling between the gas and melt in a fully coupled atomisation system has not yet been investigated, which is one of the primary reasons for the chaotic and unpredictable instability seen in the process. In this thesis, detailed numerical study is carried out by coupling the melt flow rate to the aspiration pressure to investigate the instabilities in the gas and melt flow, and to analyse their association between them. In addition to the coupling, this research endeavours to explore the effect of two primary factors that substantially affects gas atomisation process – melt flow rate and melt temperature, and how these two parameters change the dynamics of the gas atomisation process. The output of this research will draw the attention of both academics and industries to extend the research by providing academics with

valuable insights into process instability, enabling a deeper exploration of its underlying mechanisms and the influence of key parameters. For industries, this research will serve as a strategic framework to develop optimisation strategies aimed at achieving the desired yield and enhancing overall process efficiency. This research is also a first step towards a full process model for process optimisation and elimination of instabilities, thereby paving the way for substantial improvements to achieve optimal CCGA performance.

2 Background Science

Gas atomisation is the process of manufacturing fine metal powder using kinetic energy of a high-speed gas-jet to break down molten metal into finer particles, and simultaneously solidify it (Antony and Reddy, 2003). The apparatus consists of a crucible (tundish), the atomiser setup and the atomisation chamber as shown in Figure 2.1. Molten metal from the crucible is introduced into the atomisation chamber. The method of melt introduction may be of constant flow rate as in the case of free-fall atomiser, or a function of aspiration pressure as in the case of close-coupled gas atomiser. The atomisation chamber houses the two primary components of an atomiser, the melt delivery nozzle and the gas-die nozzle. As the name suggests, molten melt from the crucible is delivered into the atomisation chamber through the melt delivery nozzle. Similarly, pressurised gas is sent through the gas-die nozzle, which subsequently upon releasing into the atomisation chamber expands to develop into supersonic gas-jet (Yule and Dunkley, 1994). Argon and nitrogen are commonly preferred as the operating gases, depending on the metal in question for production, to prevent oxidation (Uslan et al., 2013).

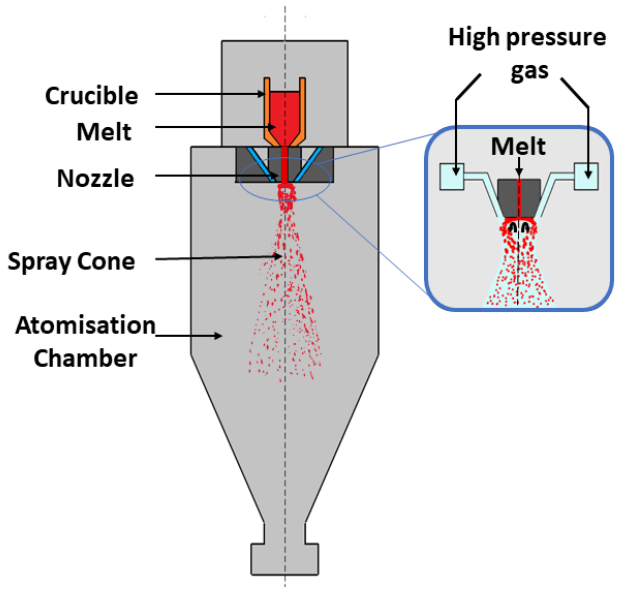

Figure 2.1 Schematic representation of close-coupled gas atomiser set-up indicating its key components.

Generally, the gas atomisation process can be classified into three variants – inert gas atomisation, Vacuum inert gas atomisation (VIGA), and Electrode induction gas atomisation (EIGA). Inert gas atomisation usually yields powders of 30-200µm, and are utilised in LPBF, SLM, MBJ, and PIM; VIGA generally yields powders of 30-90µm, and are utilised in Metal injection moulding (MIM) and HIP; and EIGA produces ultra-pure powders with high

flowability, usually in the range of 15-50µm, utilised in LPBF, SLM, and EBM (Dunkley, 2019). Although there are various other production methods to manufacture metal powders, gas atomised metal powders possess high quality, purity and sphericity, making it ideal for AM and PM applications (Ünal and Aydın, 2007, Zeoli and Gu, 2006).

Based on the method of melt introduction, gas atomisation process can be classified into two types, namely; free-fall gas atomisation and close-coupled gas atomisation (CCGA) (Chang and Zhao, 2013). In free-fall atomisation, the melt falls under its own gravity without the aid of any external force, and travels down for some distance before coming in contact with the gas-jet. Contrastingly, in CCGA, as shown in Figure 2.1, the melt delivery nozzle and the gas nozzle are placed in close proximity with the melt nozzle present in the centre (axis) and the gas nozzle surrounding it axisymmetrically, such that gas nozzle distributes gas symmetrically about the central melt nozzle (Urionabarrenetxea et al., 2022). Owing to the symmetrical arrangement of the gas jets, by virtue of the flow, there is a recirculation zone formed in front of the melt nozzle. As a result of the recirculation zone a region of lower pressure known as aspiration pressure is formed just in front of the melt nozzle tip, which draws out the melt from the crucible proportional to its pressure (Ting and Anderson, 2004). The recirculation zone forces the melt to flow over the melt nozzle tip, wetting it before flowing downstream, in a process known as pre-filming. The melt from the circumferential edge of the melt nozzle tip comes in contact with the gas-jet, and undergoes effective breakdown as ultra-fine particles due to the gas-melt interaction. The major advantage in free-fall atomisation is the established control over the melt and gas interaction. But, on the contrast, this method produces powder with bigger particle size and increased particle-size distribution (PSD) which diminishes its suitability for many applications (Zhao et al., 2012). This is because, the melt in free-fall atomisation undergoes column break-up mechanism, and this disadvantage is effectively overcome by the CCGA process, wherein the melt undergoes film break-up mechanism through the pre-filming mechanism leading to finer particle size and narrow particle-size distribution (PSD). This immense endowing potential makes the commercial atomisation companies prefer CCGA over free-fall atomisation, which also draws the attention of this thesis and research.

The background science of gas and melt flow seen in the atomisation process is further explained in detail in the following sections.

2.1 Gas flow and generation of shock

The gas released from the gas-die nozzle expands from a high-pressure source to develop into a high-speed gas flow, exhibiting supersonic flow, i.e., compressible flow. The behaviour of such high-speed gas flow is characterised by using a dimensionless unit known as Mach number, which is defined as the ratio of the velocity of the moving fluid in a medium to the speed of the sound waves in the same medium. This parameter is vital in understanding the dynamics and effects observed within compressible flows, such as shock waves, expansion fans, and other characteristics such as seen in the gas atomisation process. The Mach number is given by the expression presented in Equation 2.1 (Rathakrishnan, 2019),

$$M = \frac{V}{a} \tag{2.1}$$

where M is the Mach number of the flow, V is the velocity of the flow in the medium, a is the speed of the sound waves in the same medium (Rathakrishnan, 2019). On the basis of Mach number, the flow is divided into subsonic flows ($0 < M < 0.8$), transonic flows ($0.8 < M < 1.2$), supersonic flows ($1.2 < M < 5$) and hypersonic flows ($M > 5$). In subsonic flow the fluid is generally considered incompressible as the kinetic energy contained by the flow is much less significant compared to the thermodynamic properties of the flow, such as pressure, volume and temperature. Whereas for flows having $M > 0.8$, the increase in kinetic energy substantially influences the thermodynamic properties of the flow (Kundu et al., 2012).

Compressible flows, as typically seen in the gas atomisation process is analysed using isentropic flow theory, assuming the flow to be adiabatic and reversible. This helps to understand the relationship between the static and total (stagnation) thermodynamic properties of the flow based on its Mach number. The relationship between the static and total pressure, temperature and density for a given Mach number is given by Equations 2.2, 2.3, and 2.4 (Rathakrishnan, 2019), respectively.

$$\frac{p_1}{p_0} = \left[1 + \frac{\gamma - 1}{2} \cdot M^2\right]^{\frac{-\gamma}{\gamma-1}} \tag{2.2}$$

$$\frac{T_0}{T_1} = 1 + \frac{\gamma - 1}{2} \cdot M^2 \tag{2.3}$$

$$\frac{\rho_0}{\rho_1} = \left[1 + \frac{\gamma - 1}{2} \cdot M^2\right]^{\frac{1}{\gamma-1}} \tag{2.4}$$

where, the p_1, T_1 and ρ_1 are static pressure, temperature and density, respectively; and p_0, T_0 and ρ_0 are total pressure, temperature and density, respectively; and γ is the ratio of the specific heats. Generally, in the industrial atomisation process, nitrogen or argon gases are employed to prevent oxidation on the molten metal during solidification, and their respective γ values are 1.4 and 1.66 (Rathakrishnan, 2019).

In the gas atomisation process, as the high-speed gas-jet exits from the gas nozzle into the ambient atmosphere, oblique shocks, normal shocks and expansion waves are formed. Shocks are formed when the supersonic flow compresses the gas present ahead of them without allowing time to respond to the changes occurring in the flow (Kundu et al., 2012). Normal shocks are formed perpendicular to the flow creating a finite discontinuity in the medium. This is shown in Figure 2.2a. Oblique shocks, presented in Figure 2.2b, occur when the flow is constrained to change its path by a concave corner having a definite angle. This change in path compresses the gas flow and generates an attached shock-wave at an angle known as deflection angle (θ). Similarly, if the flow expands along a convex corner, expansion waves, presented in Figure 2.2c, are formed. A shock can only compress the gas to a high pressure across the flow but can never act as an expanding shock as it violates the second law of thermodynamics which profoundly states that the entropy of a system can never decrease, hence known as expansion waves (or fans) rather than expansion shocks (Rathakrishnan, 2019),

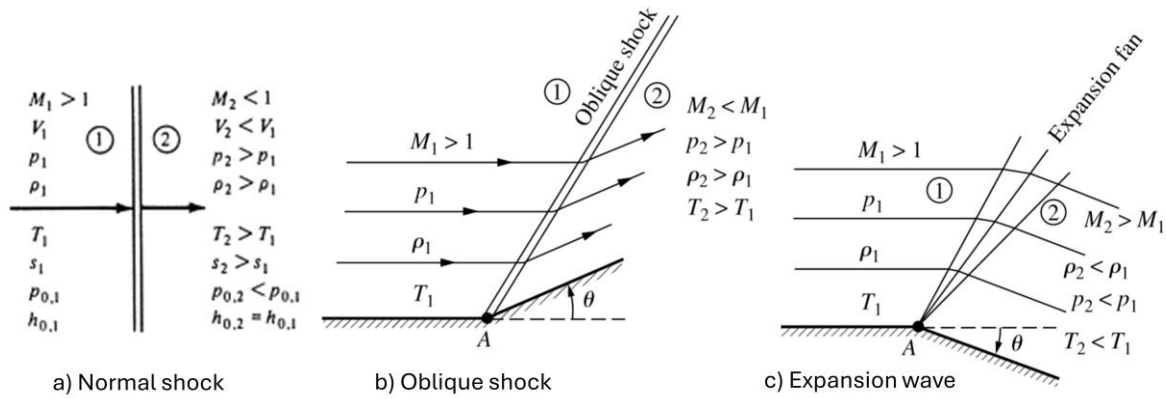

Figure 2.2 Types of shock waves. a) normal shock, b) oblique shock, and c) expansion wave (Rathakrishnan, 2019, Moura and Rosa, 2013, Kundu et al., 2012).

2.2 Generation of supersonic gas flow.

As mentioned earlier, gas atomisation exploits the kinetic energy of high-speed gas to disintegrate molten metal to produce fine metal powders. This is achieved via nozzle flows. It is observed that at subsonic speeds flow through a converging nozzle increases the velocity of

the flow at the outlet of the nozzle. This is dictated by the area-velocity relationship presented in Equation 2.5 (Rathakrishnan, 2019), derived from the continuity equation.

$$\frac{dA}{dV} = -\frac{A}{V}(1 - M^2) \qquad 2.5$$

where, A is the cross-sectional area, and V is the velocity. From Equation 2.5 it is obtained that for subsonic flows for $0 \leq M \leq 1$, a decrease in area as seen in convergent duct, increases the velocity, whereas increase in area as seen in divergent duct, decreases the velocity at the outlet. However, for $M > 1$, Equation 2.5 reveals that decrease in area, decreases the velocity, whereas increase in area, increases the velocity. The flow across convergent and divergent ducts for subsonic and supersonic flows are presented in Figure 2.3.

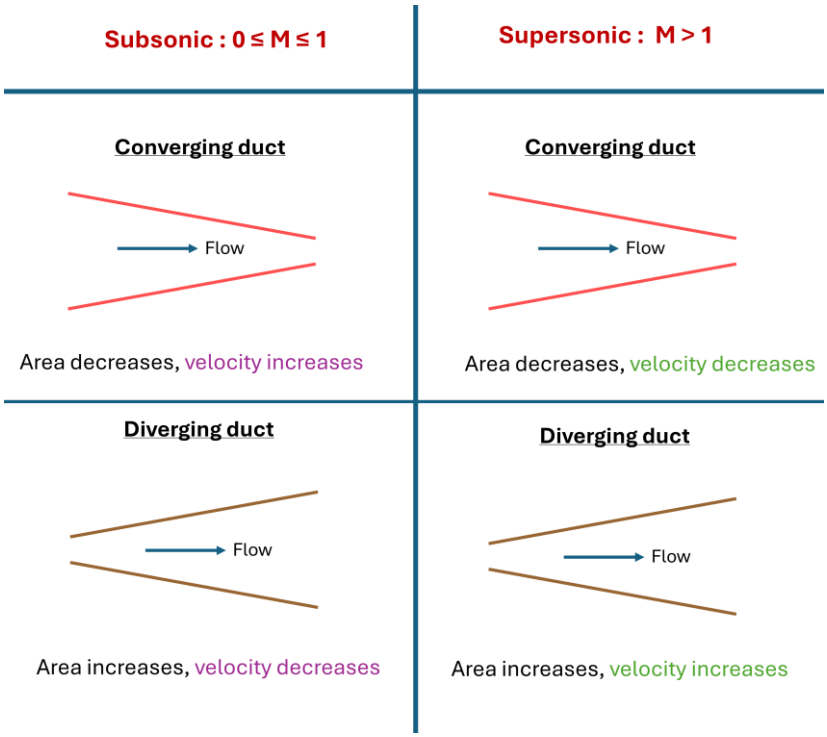

Figure 2.3 Flow through converging and diverging ducts at subsonic and supersonic speeds.

From Equation 2.5 it is also obtained that at $M = 1$ the area of the duct is the least. This led to development of Convergent-Divergent (C-D) nozzle, which has both converging and diverging section in its nozzle (Figure 2.4). In the converging section, the velocity of the flow increases and attains $M = 1$ at the minimum area of the duct, also known as throat. Thereafter, when the flow passes through the diverging section, the velocity further increases to $M > 1$ achieving supersonic speeds. To ensure $M = 1$ at the throat, such that the diverging sections achieves supersonic speeds, a favourable pressure gradient is maintained between the inlet and

the throat. From Equation 2.2, it is calculated that the minimum pressure gradient to ensure $M = 1$ at the throat is $p_{th}/p_0 < 0.528$, were p_{th} is the pressure at throat (Rathakrishnan, 2019). Based on this pressure gradient the area of the throat, A_{th}, is designed. The exit Mach number of the supersonic flow downstream of the throat is governed by the exit area, A_e, of the diverging section of the nozzle, and it is governed by Equation 2.6 (Oosthuizen and Carscallen, 1997).

$$\left(\frac{A_e}{A_{th}}\right)^2 = \frac{1}{M^2}\left[\frac{2}{\gamma+1}\left(1+\frac{\gamma-1}{2}\cdot M^2\right)\right]^{\frac{\gamma+1}{\gamma-1}} \qquad 2.6$$

From Equation 2.6 it is revealed that for a given exit Mach number, there can be only one unique A_e for a C-D nozzle, and if another Mach number is required, then a new A_e is needed, meaning a new C-D nozzle is designed fitting the geometrical calculations. This is a major disadvantage in the C-D nozzle operation, although the manufacturing of the C-D nozzle itself is excruciatingly difficult (Rathakrishnan, 2019). However, in gas atomisation process cylindrical nozzles, i.e., nozzles with constant cross-sectional area are also employed. The disadvantage is that, irrespective of the inlet pressure, the maximum exit Mach number is limited to $M = 1$. Section 3.1.3 discusses more on the operation of C-D and cylindrical nozzles in gas atomisation process.

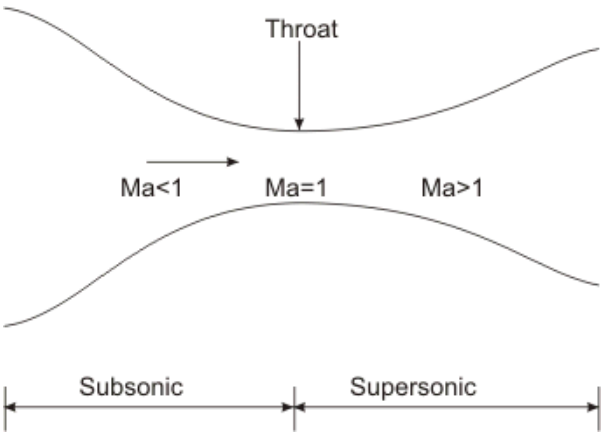

Figure 2.4 Convergent-Divergent (C-D) nozzle, showing sections of the nozzle having subsonic and supersonic flow (Rathakrishnan, 2019).

2.3 Ideally-expanded, over-expanded, and under-expanded flows

Equations 2.2, 2.3, 2.4, and 2.6 describe the isentropic flow through a C-D nozzle designed to produce an ideally-expanded flow. An ideally-expanded flow across a nozzle is a

fully supersonic and isentropically expanded flow, whose exiting pressure is equal to the ambient pressure. In ideally-expanded flow, a normal shock appears precisely at the exit of the nozzle, with the absence of any shocks within the nozzle. To obtain such a flow in C-D nozzles, for a fixed pressure and temperature, a unique throat area and nozzle exit area is designed to result in a Mach number that is ideally-expanded at the exit (Rathakrishnan, 2019). Flows whose exit pressure is not equal to the ambient pressure result in over-expanded or under-expanded flows.

In over-expanded flows, the ambient pressure of the surrounding gas is greater compared to the pressure of the exiting gas and hence the exiting gas flow is compressed. This effectively changes the direction of flow, directing the shocks towards the axis of the nozzle. The oblique shocks produced at the either side of the nozzle edge, as observed in Figure 2.5, meet at the axis of nozzle and is deflected, changing the flow direction. With the shock meeting the boundary where the pressure of the flows is equal to the ambient pressure, the shock gets reflected into an expansion wave (Jadidi et al., 2015). This repetitive formation of oblique shock wave and expansion wave continues till the flow deteriorates, wherein the pressure of the flow merges with the ambient pressure. In the over-expanded flow, a Mach-disk is formed when the incident angle of the oblique shock formed by both edges of the nozzle (in 2D), as seen in Figure 2.5, is beyond a critical angle such that a normal shock, perpendicular to the flow is generated. Since, Mach-disks manifest in the direction perpendicular to the gas flow, they are also considered to be a form of normal shock.

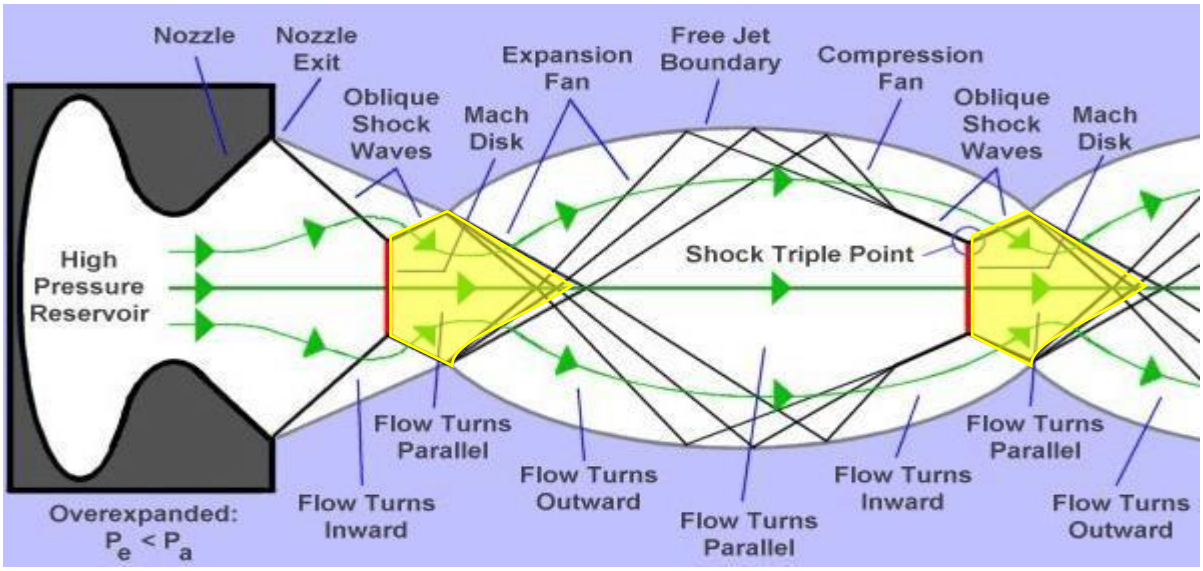

Figure 2.5 Schematic representation of over-expanded flow (Jadidi et al., 2015).

In under-expanded flow a similar fashion is observed but on the contrast, the pressure of flow at the exit is greater than the ambient pressure (Mi et al., 1996). This pressure gradient results in expansion waves occurring at the edge of the exit, causing the gas to expand radially outward, as observed in Figure 2.6. When the pressure drop in the gas flow equalises with the ambient pressure, the expansion waves reflect from the free boundary and coalesce into recompression waves or oblique shocks, resulting in flow turning towards the axis of the nozzle (Jadidi et al., 2015). As mentioned above, when the incident angle of oblique shock is beyond a critical angle, a Mach-disk is formed.

The combination of oblique shock and expansion waves forms a series of diamond shaped shocks known as shock diamonds, illustrated using the yellow shading in Figure 2.5 and Figure 2.6 (Rosario, 2012). Figure 2.7 (only for representation and not scaling) shows the difference between over-expanded and under-expanded flow while comparing the intricate details observed between the type of gas-jets.

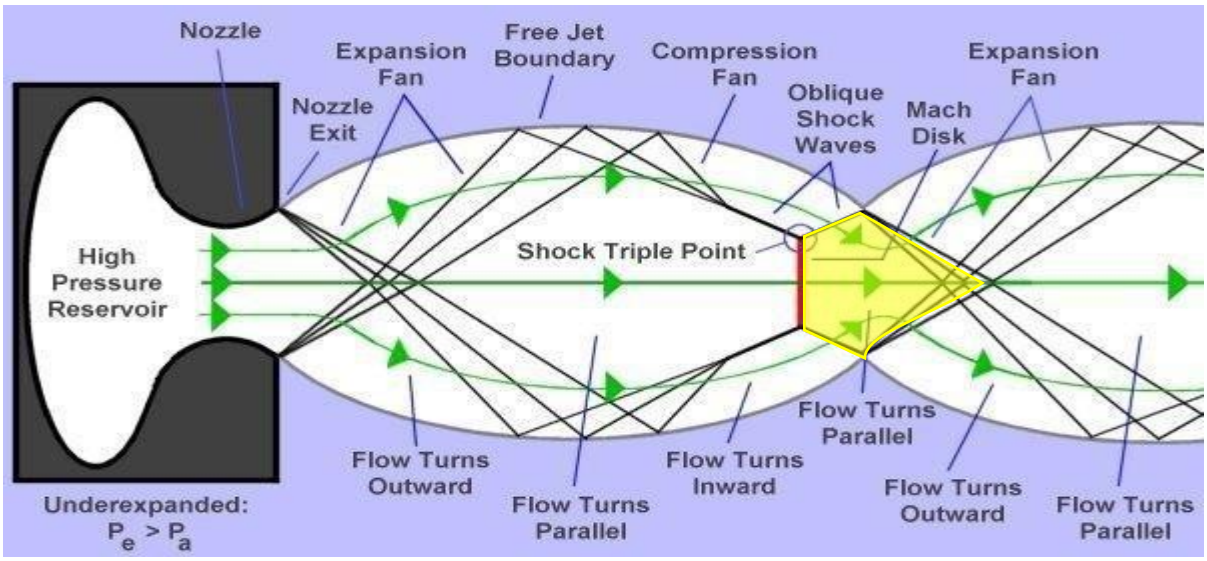

Figure 2.6 Schematic representation of under-expanded flow (Rosario, 2012).

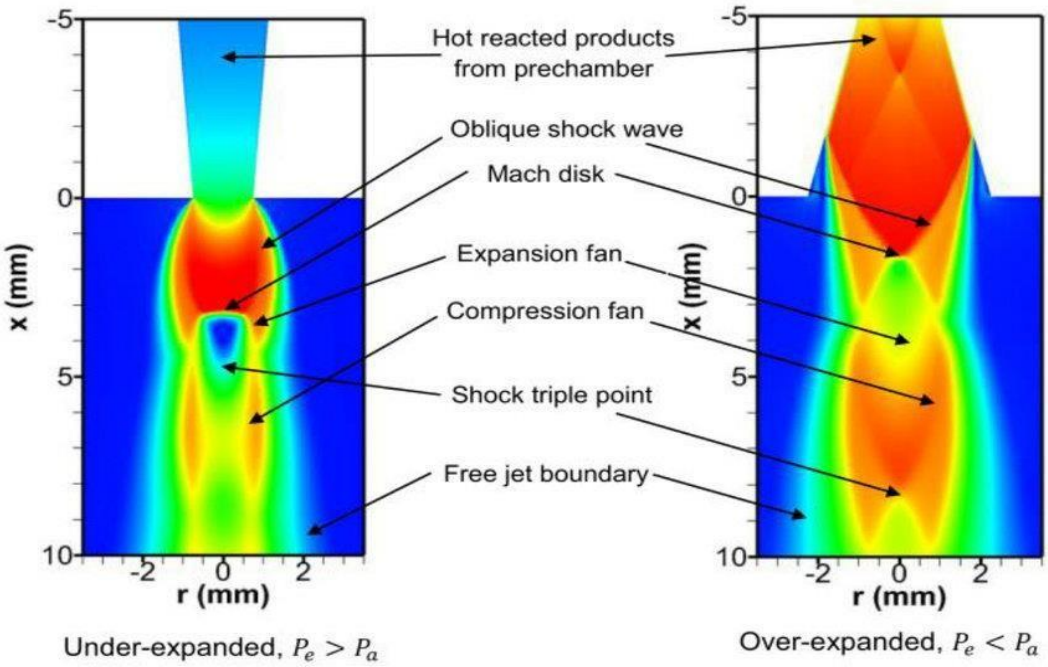

Figure 2.7 Detailed comparison of shock structures seen in under-expanded and over-expanded flows (not to scale) (Biswas and Qiao, 2017).

2.4 Melt break-up mechanism

As mentioned earlier, the transfer of kinetic energy from the high-speed gas-jet on to the molten melt causes the break-up of liquid melt into ligands, and subsequently into fine particles (Ünal, 2006). The melt break-up consists of sequence of events, and it starts with the melt being radially pulled away from the melt nozzle exit due to the presence of recirculation zone. This facilitates the spreading of melt on to the nozzle tip, forming a thin layer of film, in a process known as pre-filming (Mullis et al., 2013a). The illustration of melt being pulled radially away, and undergoing pre-filming is shown in Figure 2.8. The melt break-up takes place in two stages: Primary atomisation, followed by secondary atomisation. The primary atomisation occurs when the aerodynamic forces destabilises the surface tension force and viscous force of the melt film into ligands and sheets (Zeoli and Gu, 2008a). With further continuous agitation on the ligands/sheets due to the aerodynamic force generated by the gas-jet, it breaks-up into droplets. Due to the persistent and strong aerodynamic forces the droplets themselves break-up into smaller and finer droplets. This break-up of liquid melt into ligands, filaments, or droplets is known as primary atomisation; and break-up of droplets into finer droplets is known as secondary atomisation. The final droplet size from secondary atomisation is directly affected by the viscosity, density and surface tension of the melt, and melt with high viscosity, density and surface tension tends to result in increased particle size and particle-size distribution (Jiang

et al., 1988). The primary and secondary atomisation are further classified based on their break-up mechanisms, and are discussed below. A schematic representation detailing the different types of break-up mechanisms are presented in Figure 2.9.

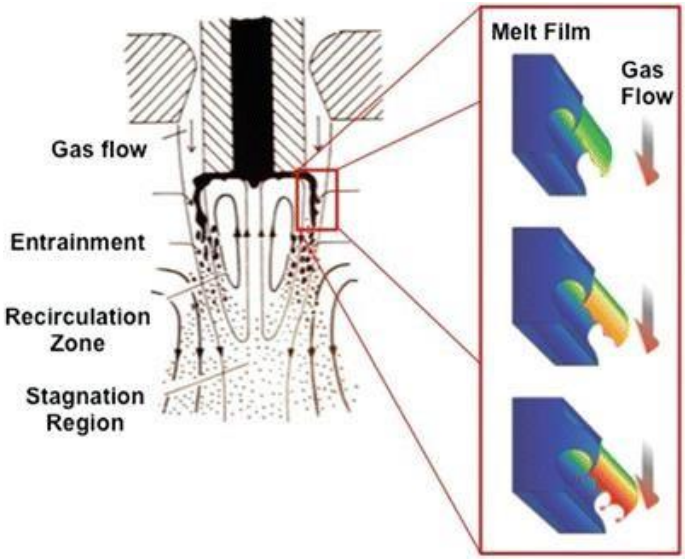

Figure 2.8 Schematic representation showing the gas-melt interaction and the process of pre-filming at the melt nozzle front (Anderson and Achelis, 2017).

2.4.1 Primary break-up mechanism

In CCGA, primary atomisation (primary break-up) takes place at close proximity to the melt nozzle, and during the early stages of the melt being introduced from the melt nozzle exit. Generally, it can be classified into four fundamental break-up mechanisms, namely: liquid dripping break-up, liquid column break-up, liquid film break-up and ligament break-up.

Liquid dripping break-up

This is the most simple and basic mechanism observed in a liquid break-up. The surface tension coalesces the liquid into a spherical shape, and while the liquid accumulates the gravity pulls it downward, causing the droplet to elongate. As it continues to elongate, necking initiates in the droplet, and with sufficient elongation, the region of necking breaks-up into an individual droplet (Xiao, 2012). And this repeats for the rest of the liquid flow. However, it is to be noted, that this mechanism occurs largely due to the effect of gravity, whereas in CCGA, gravity has negligible effect on the process, making this break-up mechanism irrelevant to CCGA process.

Liquid column break-up

This mechanism is observed in both free-fall and close-coupled gas atomisers under low operating pressure conditions. The liquid column is broken-up into smaller droplets or

segments by the relatively low inertial force acting on the liquid column. This break-up mechanism is affected by the intensity of the instability acting on the liquid column. Liquid column break-up mechanism is further divided based on the weber number, which is defined by,

$$W_e = \frac{\rho_A \, \mathrm{d}_0 \, u_r^2}{\sigma} \qquad 2.7$$

where, W_e is the weber number, ρ_A is the density of the gas, d_0 is the diameter of the liquid column, u_r is the relative velocity, and σ is the surface tension (Sa, 2017). Based on Equation 2.7 (Wierzba, 1990), the break-up mechanism is divided into three types, namely: Rayleigh type break-up or normal pulsing for $0 < W_e < 25$; membrane type breakup for $25 < W_e < 70$; and fibre type breakup also known as super pulsing for $70 < W_e < 500$ (Chigier and Farago, 1992). The three types of break-up mechanism are shown in Figure 2.9. In Rayleigh break-up, the lower weber number leads to perturbations in the liquid column to form droplets, while at higher weber number, i.e., the membrane break-up, the liquid undergoes an intermediate bag-like formation before bursting into droplets. Similarly, at significantly high weber number, $0 < W_e < 500$, i.e., fibre break-up, the liquid transforms into fibres, breaking apart into droplets due to the substantial stretching caused by the gas flow.

Liquid film break-up

Liquid film breakup occurs in the CCGA process during pre-filming where the melt slides on the nozzle tip to form thin film sheets, ultimately breaking-up into droplets. There are three types of liquid film break-up namely; a) rim disintegration, b) wave disintegration, and c) perforated film break-up (Mansour and Chigier, 1990). Rim disintegration is observed in fluids with high surface tension and viscosity, where the fluid built-up near the edges of the nozzle edge, breaks up along the free edges as larger droplets. Wave disintegration occurs in fluids where disturbances are in definite patterns possessing distinct segments of wavelengths. The disturbances break the film into wavelengths before breaking them into droplets (Deshpande et al., 2015). Perforated film break-up occurs when holes develop in the fluid film and simultaneously propagate toward the edges until they completely split-up the film, creating droplets. They are observed in liquids with high surface tension which are unstable due to surface tension forces, as small perturbations or instabilities on the film would lead to the growth of the holes in the film, eventually leading to the break-up of the film.

Ligament breakup

In ligament breakup, threads or filaments of liquid melt, also known as ligaments are broken-up prior to becoming smaller droplets (Shao et al., 2018). The mechanism is driven by the instabilities due to the surface tension, primarily due to Rayleigh-Plateau instability, where the instability forces surface tension to minimise the surface area of the ligament, resulting it to break into smaller droplets (Shinjo and Umemura, 2010). In the CCGA process, during pre-filming, the melt undergoes liquid film break-up forming ligaments. Subsequently, the ligaments undergo ligament break-up to produce smaller droplets, which ultimately determine the particle size and PSD, making the ligament thickness and the ligament break-up stage a major importance in the CCGA process.

2.4.2 Secondary break-up mechanism

With the continuous presence of high-speed gas flow in the CCGA process, the larger droplets formed during the primary atomisation undergo further break-up, i.e., secondary atomisation to become fine droplets, which eventually solidifies to form metal powder. The secondary break-up mechanism depends on the weber number (Hsiang and Faeth, 1992). They are divided into six mechanisms, based on their increasing weber number, and they are: no-breakup, vibrational breakup, bag breakup, multimode breakup, film/sheet stripping and catastrophic breakup (Sadhal et al., 2012). The different types of secondary break-up mechanisms and their corresponding weber number is presented in Figure 2.9. The initiation and propagation of the instability with the droplet and until break-up varies uniquely over the mechanism it undergoes. Moreover, the microstructure of the solidified particles depend on the initial cooling rates, which in turn is directly affected by the break-up mechanism (Anderson et al., 2010).

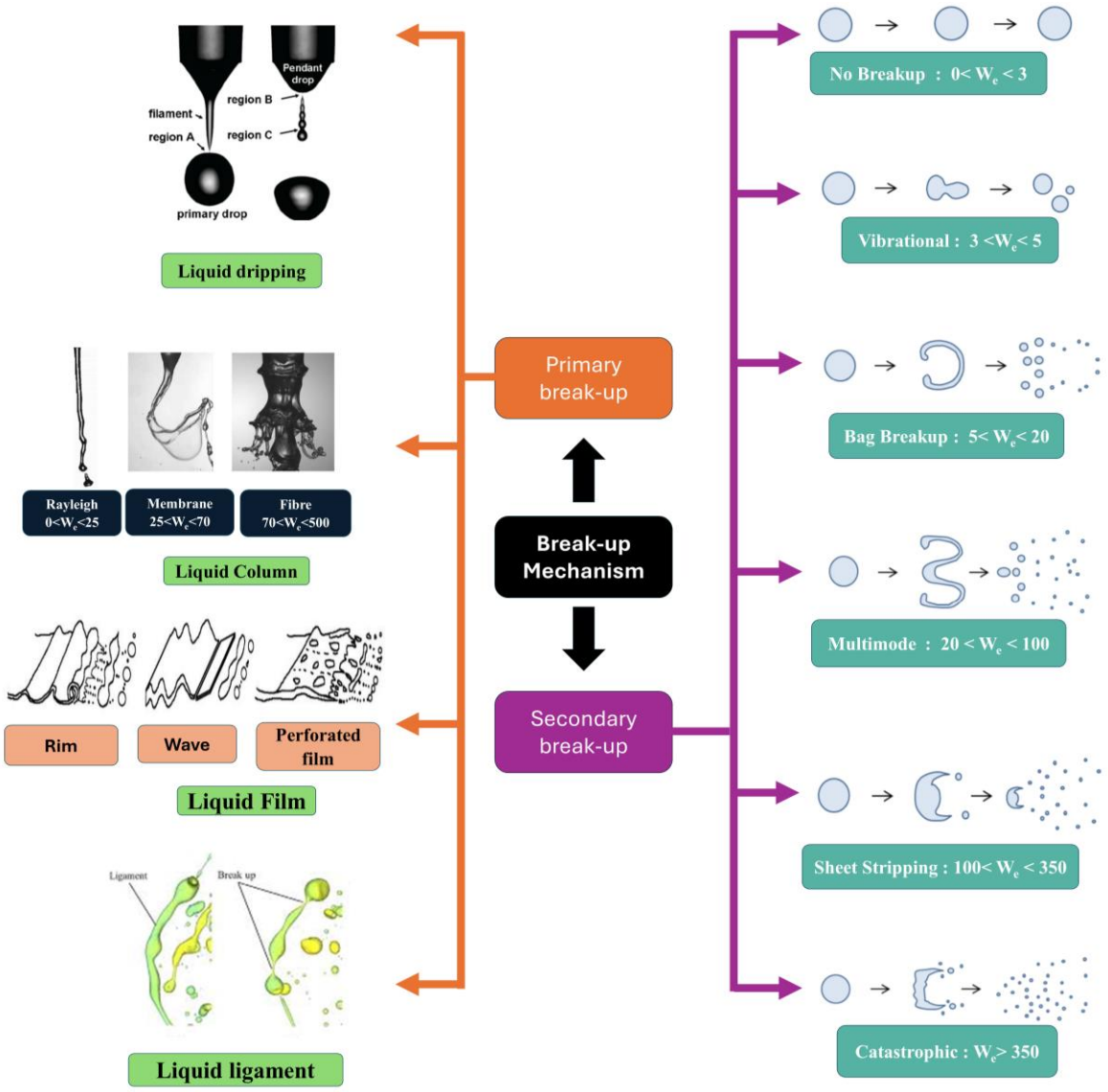

Figure 2.9 Schematic representation detailing the different types of melt break-up.

For $0 < W_e < 3$, the droplet does not undergo any fragmentation or break-up, hence the break-up is also called as no-breakup (Mazumdar et al., 2016). For, $3 < W_e < 5$, the droplet undergoes vibrational break-up, wherein the particles due to the vibrational instability usually split-up into two child droplets. For $5 < W_e < 20$, the droplet undergoes bag break-up, wherein due to the higher weber number the droplet transforms its shape into a hemispherical bag, subsequently it further enlarges before breaking-up into fine droplets. The hemispherical part of the bag atomises finer than the circumferential edge of the bag (Jalaal and Mehravaran, 2012).

For $20 < W_e < 100$, the droplets undergo multimode break-up. They are sub-divided into two types: bag break-up and plume break-up. At the lower range of the weber number, the

droplets undergo bag break-up, with multiple number of bags formed during the break-up (Hsiang and Faeth, 1992). At higher ranges of the weber number, the droplets undergo plume shear break-up.

For 100 < W_e < 350, the droplets undergo sheet-ripping break-up, wherein the edges of the droplet move faster than the centre of the droplet, and hence due to the significant relative speed between the parts of the droplet, the edges are ripped apart from the droplet to produce finer child droplets (Mazumdar et al., 2016).

The final form of the droplet break-up mechanism is the catastrophe break-up, for W_e > 350. This mechanism is similar to the sheet-ripping break-up mechanism; however, due to the immense inertial force, the entire droplet disintegrates into finer droplets, leaving no trace of the parent droplet (Negeed et al., 2011).

2.5 Overview of Computational Fluid Dynamics (CFD)

The research on the CCGA process presented in this thesis is carried out using CFD. This section overviews the various CFD models and their background science which are of importance for this research. The fundamentals of solving a CFD model is in solving the Navier-Stokes equation, since it describes the motion of the fluid within the considered CFD domain. The below sub-sections also elaborate on the various CFD models which are employed in Chapter 4 - Methodology of the numerical modelling.

2.5.1 Navier-Stokes equation

Navier-Stokes equations are a set of partial differential equations that describe the direction and motion of the fluid flow. They are derived from Newton's second law, and provide the time-dependent equations for conservation of mass (continuity), momentum, and energy. The Navier-Stokes equations for compressible flow are:

<u>Continuity equation (conservation of mass):</u>

$$\frac{\partial \rho}{\partial t} + \frac{\partial}{\partial x_i}(\rho u_i) = 0 \qquad 2.8$$

<u>Momentum equation (conservation of momentum):</u>

$$\frac{\partial}{\partial t}(\rho u_i) + \frac{\partial}{\partial x_j}(\rho u_i u_j) = -\frac{\partial p}{\partial x_i} + \frac{\partial \tau_{ij}}{\partial x_j} \qquad 2.9$$

Energy equation (Conservation of energy):

$$\frac{\partial}{\partial t}(\rho E) + \frac{\partial}{\partial x_j}(\rho u_j H) = \frac{\partial}{\partial x_j}(u_i \tau_{ij}) - \frac{\partial q_j}{\partial x_j} \qquad 2.10$$

where, ρ is the density of the fluid, and u_i & u_j are the velocity components along the x_i and x_j directions, p is the pressure, τ_{ij} is the viscous stress term, E is the total energy, q_j is the heat flux, and H is the enthalpy fluctuations due to turbulence (Zhang et al., 2023a).

With the flow being turbulent, characterised by the randomness caused by the instabilities, eddies and swirls, it is infeasible to define every flow path through time using Equations 2.8, 2.9, and 2.10 (Łukaszewicz and Kalita, 2016). Hence the instantaneous physical properties of the fluid are decomposed via a process known as Reynolds decomposition, to split the property into a steady mean (Reynolds-averaged) value and a fluctuating part (Wang et al., 2023a). The flow property at any given point can be described as

$$\emptyset = \overline{\emptyset} + \emptyset' = \widetilde{\emptyset} + \emptyset'' \qquad 2.11$$

where, $\emptyset$ is the instantaneous value of the flow property, $\overline{\emptyset}$ is the Reynolds averaged steady mean value, and $\emptyset'$ is the fluctuating part in the Reynolds method. Density and pressure are usually decomposed using the Reynolds decomposition, whereas other flow variables such as velocity, temperature, and internal energy are decomposed using Favre averaging (density-weighted averaging), where $\widetilde{\emptyset}$ is the Favre averaged steady mean value and $\emptyset''$ is the fluctuating part in the Favre method (Wang et al., 2023a).

2.5.2 Reynolds-Averaged Navier-Stokes (RANS) equations

The Reynolds-averaged Navier-Stokes (RANS) equations for the compressible flows seen in Equations 2.8, 2.9, and 2.10, following the execution of statistical operation in Equation 2.11, are given below:

Continuity equation:

$$\frac{\partial \bar{p}}{\partial t} + \frac{\partial(\bar{\rho}\tilde{u}_i)}{\partial x_i} = 0 \qquad 2.12$$

Momentum equation

$$\frac{\partial(\bar{\rho}\tilde{u}_i)}{\partial t} + \frac{\partial(\bar{\rho}\tilde{u}_j\tilde{u}_i)}{\partial x_i} = -\frac{\partial \bar{p}}{\partial x_i} + \frac{\partial \bar{\tau}_{ij}}{\partial x_j} - \frac{\partial \overline{\rho u''_i u''_j}}{\partial x_j} \qquad 2.13$$

Energy equation

$$\frac{\partial(\bar{\rho}\tilde{E})}{\partial t} + \frac{\partial(\bar{\rho}\tilde{u}_j\tilde{H})}{\partial x_j} = \frac{\partial(\tilde{u}_i\bar{p})}{\partial x_i} + \frac{\partial(\tilde{u}_i\bar{\tau}_{ij})}{\partial x_j} - \frac{\partial q_i}{\partial x_i} - \frac{\partial\left(\tilde{u}_i\overline{\rho u''_i u''_j}\right)}{\partial x_j} \qquad 2.14$$

where, $\frac{\partial(\bar{\rho}\tilde{u}_j\tilde{H})}{\partial x_j}$ is the convective term, $\frac{\partial(\tilde{u}_i\bar{p})}{\partial x_i}$ is the pressure work term, $\frac{\partial(\tilde{u}_i\bar{\tau}_{ij})}{\partial x_j}$ is the viscous work term, $\frac{\partial q_i}{\partial x_i}$ is the heat conduction term, and $\frac{\partial(\tilde{u}_i\overline{\rho u''_i u''_j})}{\partial x_j}$ is the turbulent energy transport term, and $-\overline{\rho u''_i u''_j}$ is the Reynolds stress tensor which represents the turbulent stresses. The variables with bar on the top are Reynolds-averaged (time-averaged) and variables with tilde on the top are Favre-averaged (density-weighted averaged) (Wilcox, 1998).

2.5.3 Turbulence modelling

Equation 2.13 and 2.14 of RANS equation for conservation of momentum and energy, respectively, has an additional term which represent the effect of turbulence, $-\overline{\rho u''_i u''_j}$, which must be modelled in order to close the system of equations and are typically in the form of turbulence models. There are multiple turbulence models to close the Reynolds stress tensor via empirical or semi-empirical formulations, however, these models rely on assumptions, calibrations, and empirical constants, leading to fundamental limitations and constraints in the model. Owing to these limitations, the models perform better in certain flow scenarios, while it fails to perform in certain other flow conditions. Some of the most common turbulence models used in the CFD modelling of fluid flow are κ - ε model, κ - ω model, Reynold Stress model (RSM), and Large Eddy Simulation (LES).

<u>κ - ε model</u>

κ - ε model is one of the most widely used turbulence models owing to its robustness, computational economy, and reasonable accuracy. The model is widely used in industrial flow with heat transfer simulations. The model uses two transport equations to calculate turbulent kinetic energy (κ) and the rate of dissipation of turbulent kinetic energy (ε), based on which the turbulent length and time scales are determined. The transport equations for κ and ε are given as:

Turbulent kinetic energy (κ) equation:

$$\frac{\partial(\rho k)}{\partial t} + \frac{\partial(\rho u_i k)}{\partial x_i} = \frac{\partial}{\partial x_j}\left[\left(\mu + \frac{\mu_t}{\sigma_k}\right)\frac{\partial k}{\partial x_j}\right] + P_k - \rho\varepsilon \qquad 2.15$$

Rate of dissipation (ε) equation:

$$\frac{\partial(\rho\varepsilon)}{\partial t} + \frac{\partial(\rho u_i \varepsilon)}{\partial x_i} = \frac{\partial}{\partial x_j}\left[\left(\mu + \frac{\mu_t}{\sigma_\varepsilon}\right)\frac{\partial \varepsilon}{d x_j}\right] + C_{1\varepsilon}\frac{\varepsilon}{k}P_k - C_{2\varepsilon}\rho\frac{\varepsilon^2}{k} \qquad 2.16$$

Turbulent length scale (L):

$$L = C_L \frac{k^{3/2}}{\varepsilon} \qquad 2.17$$

Turbulent time scale (T):

$$T = \frac{k}{\varepsilon} \qquad 2.18$$

where, μ is the dynamic viscosity, μ_t is the turbulent viscosity, σ_k and σ_ε are the turbulent Prandtl numbers for κ and ε, respectively. P_k is the production term of turbulent kinetic energy, L is the Turbulent length scale, T is the Turbulent time scale, and C_1, C_2, and C_L are model constants (Launder and Spalding, 1974, ANSYSFluent®Theory-Guide).

However, this model has its own disadvantages. The model underpredicts complex flows with swirls and rotation; it resolves the near-wall region less accurately compared to other models; and the model is more tuned for steady-state conditions and hence is less efficient for modelling transient flows (Versteeg, 2007).

***κ - ω* model**

κ - ω model is also one of the most widely used turbulence models, particularly involving complex boundary layer and near-wall flows. It is also employed to model flow separation, pipe flows, and flows containing adverse pressure gradients such as compressible flows with shock waves. Two transport equations are used in this model to calculate the turbulent kinetic energy (κ) and the specific dissipation rate (ω). The transport equations for κ and ω are given as:

Turbulent kinetic energy (κ):

$$\frac{\partial}{\partial t}(\rho k) + \frac{\partial}{\partial x_i}(\rho K u_i) = \frac{\partial}{dx_j}\left(\Gamma_k \frac{\partial k}{\partial x_j}\right) + G_k - y_k + S_k + G_b \qquad 2.19$$

Specific dissipation rate (ω):

$$\frac{\partial}{\partial t}(\rho\omega) + \frac{\partial}{\partial x_i}(\rho\omega u_i) = \frac{\partial}{\partial x_j}\left(\Gamma_\omega \frac{\partial \omega}{\partial x_j}\right) + G_\omega - y_\omega + S_\omega + G_{\omega b} \qquad 2.20$$

Effective Diffusivity

$$\Gamma_k = \mu + \frac{\mu_t}{\sigma_k} \qquad 2.21$$

$$\Gamma_\omega = \mu + \frac{\mu_t}{\sigma_\omega} \qquad 2.22$$

$$\mu_t = \alpha^* \frac{\rho k}{\omega} \qquad 2.23$$

where, G_k represents the generation of turbulence kinetic energy due to mean velocity gradients, G_ω represents the generation of ω, Γ_k and Γ_ω represent the effective diffusivity of κ and ω, respectively. y_k and y_ω represents the dissipation of κ and ω due to turbulence. S_k and S_ω are the user-defined source terms. G_b and $G_{\omega b}$ are the buoyancy terms. σ_k and σ_ω are the turbulent Prandtl numbers for κ and ω, and α^* is the low-Reynolds number correction coefficient (Wilcox, 1998, ANSYSFluent®Theory-Guide).

However, the κ - ω model also poses some disadvantages. The model is sensitive to free-stream values of ω, which might affect the accuracy in external flow problems. The model is complex and computationally expensive compared to the simpler turbulence model, κ - ε model (Versteeg, 2007).

Reynold Stress model (RSM)

Reynold Stress model is a comprehensive turbulence model that closes the RANS equations by solving transport equations for the Reynolds stresses, along with an equation solving the equation for the dissipation rate. Hence, in 2D, the model solves five transport equations, whereas in 3D it solves seven transport equations (ANSYSFluent®Theory-Guide). The RSM is more accurate than the simpler turbulence models, the κ - ε and κ - ω models, as it takes into account the streamline curvature, swirl, rotation, and rapid changes in the strain rate (Jadidi et al., 2015). The model is employed for simulating swirl flows such as cyclone flows, swirling flows as seen in combustors, and rotating flow passages. However, RSM incurs significantly higher computational cost compared to the simpler turbulence models. Moreover, the improvements in results produced by the RSM may not always justify the high computational expense, as it doesn't consistently produce superior results compared to the simpler models.

Large Eddy Simulation (LES)

Large Eddy Simulation is another comprehensive turbulence model that directly resolves the large eddies in turbulent flow, while the small eddies are modelled. In LES an eddy is considered large if the resolved eddies are larger than the grid scale used in the simulation, and the rest of the eddies which are smaller than the grid scale are called small eddies, and are modelled using Subgrid-Scale (SGS) models (Jadidi et al., 2015). To resolve the small eddies, a sufficiently fine computational grid and small timestep size is required to capture the small eddies (Zhao et al., 2012). The direct resolution on the fine grid facilitates LES to provide detailed and more accurate representation of the flow turbulence. LES models are used for

flows characterised by turbulence with unpredictable changes in pressure and velocity, such as airflow over aircraft wings, fuselages, and around engines; airflow around car bodies; flow and wind patterns around buildings; and flow over turbine blades (Ashgriz, 2011). Although the LES model has significant advantages over the simpler models in providing more accurate results, it has much more disadvantages. The LES model demands for exceptionally high computational cost, especially for high Reynolds number flows, which necessitates the use of high-performance computing (Versteeg, 2007). Similarly, the model heavily relies on the grid resolution, especially in the wall boundary layers. Insufficient grid resolution leads to inaccurate results. Owing to the greater challenges posed by the model, the LES model is always used cautiously and only if required.

2.5.4 Major limitations in Turbulence models

Empirical and generalised constants

Turbulence models rely on empirical constants and coefficients derived from experimental studies. Although in a physical flow condition the turbulence in the flow is dictated by the flow configuration, boundary conditions, and Reynolds number, in models, the derived constants/coefficients are fixed and are assumed to be universal, resulting in models being not consistent for all flows. This assumption of universal constants introduces uncertainty and reduces the predictive capability of the turbulence model.

Assumption of isotropy in Reynolds Stress-based models

Many turbulence models such as κ - ε and κ - ω models assume isotropy in the turbulent stress distribution, meaning, in all direction turbulence in the flow behaves the same, which is often incorrect, and are not observed in complex flows. For example, in flow configurations such as boundary layer flows and swirling/rotating flows, the turbulence is anisotropic in nature, and is far from being same in any direction. RSM attempts to address this issue by solving transport equations for each of the Reynolds stress components, but they introduce undue computational cost on the simulation.

Flow separation and adverse pressure gradients

Many RANS based turbulence models fail to accurately capture flow separation, especially under adverse pressure gradients. For example, $\kappa - \varepsilon$, although widely used in industrial CFD, owing to the eddy viscosity assumption, fails to capture the strong anisotropy and non-

equilibrium effects in separating flows having adverse pressure gradients. Although advanced models such as $\kappa - \omega$ SST perform well in predicting flow separation, the model constants require fine tuning and careful calibration. While LES and hybrid RANS-LES, and DES offer better accuracy, it comes with a higher computational cost.

2.5.5 Two-phase flow: Euler-Euler framework and Euler-Lagrange framework

Two-phase flows as typically seen in CCGA process are modelled via two primary numerical frameworks: the Euler-Euler (E-E) framework and the Euler-Lagrange (E-L) framework. In E-E framework, the primary and the secondary phase, the gas and the melt, respectively, are modelled as a continuum and solved. In the E-L framework, the primary phase is modelled as a continuum, whereas the secondary phase is modelled as individual particles or discrete elements, and are solved together.

Euler-Euler (E-E) framework

In Euler-Euler (E-E) framework both the primary and secondary phases are modelled as a continuum, co-existing in the same control volume (Jadidi et al., 2015). Since, the volume of primary phase cannot be occupied by the secondary phase, and vice-versa, the concept of volume fraction is introduced. The volume fraction is an important parameter that indicates the proportion of space (volume) occupied by each phase in a given control volume. The volume fractions are assumed to be continuous functions of space and time, and the sum of volume fractions for primary and secondary phase is equal to one. It involves solving the conservation equations for turbulent flow for each of the phases, and includes an additional term to account for the phase interactions (ANSYSFluent®Theory-Guide). The conservation of mass equation ensures the mass is conserved for each of the phases, while the conservation of momentum equation solves the interaction forces such as drag, lift and turbulence. All the properties, such as velocity, pressure, mass, momentum and energy transfer for both the phases are obtained by averaging over the considered control volume.

The advantage of employing E-E framework in CCGA process helps in the modelling of melt break-up, especially the primary atomisation, facilitating in the understanding of the melt break-up mechanism. It can also be helpful to predict the pre-filming mechanism based on the gas-die design and gas inlet parameters (Jadidi et al., 2015). And also, using E-E framework, there have been efforts to model the satellite formation and gas entrapment within the melt droplets leading to porosity in gas atomised powders. However, the E-E framework also has

major drawbacks. Since, the properties of phases are averaged over a control, the information on trajectory of an individual particle, as typical seen in CCGA process cannot be obtained (Jadidi et al., 2015). Modelling the interactions between the gas and melt phase is highly complex. Fine grid size is required to capture small-scale flow phenomena, such as secondary atomisation or micro-meter droplet formation (Wang et al., 2023d). As E-E framework requires fine spatial resolution of the grid, it is highly computationally intensive and might prevent carrying out parametric studies of real-time applications (Liu et al., 2023b, Wang et al., 2023b).

Euler-Lagrange (E-L) framework

In Euler-Lagrange (E-L) framework the primary phase is modelled as a continuum, whereas the secondary phase is modelled by solving it as individual particles, thereafter integrating it into the solved gas flow-field (ANSYSFluent®Theory-Guide). The interactions between the individual particles and the turbulent eddies of the primary phase are obtained to provide detailed information on the motion of the particles and their trajectories. However, in the E-L framework the flow around the individual particles is not solved and the finite dimensions of the particles are not considered. Hence, the individual particles of the dispersed phase should be smaller than the grid size. Owing to this, the E-L framework can only be employed to flows having a low volume fraction of the dispersed phase (secondary phase), although a higher mass loading ($\dot{m}_{particles} \geq \dot{m}_{fluid}$) is admissible (Pakseresht and Apte, 2019, ANSYSFluent®Theory-Guide).

Some of the widely used CFD models under E-L framework are Discrete Element Method (DEM) and Discrete-Phase model (DPM). In DEM, each particle has definitive properties such as shape, size, and material characteristics. It tracks the particle-particle interaction forces and particle-wall interaction forces such as contact forces, tangential forces, cohesive forces and colliding forces. At each timestep the forces are computed, subsequently their positions and velocities are updated accordingly. In DPM, the individual particles trajectories are predicted by equating the force balance between the particle's inertia and the forces acting on it at specific intervals of the fluid phase. In addition to the particle trajectory, its heat and mass transfer is also computed. DPM also facilitates in the modelling of heating and cooling, boiling and vaporisation, and droplet breakup and coalescence. However, since the model assumes that the dispersed phase is sufficiently dilute, the particle-particle interaction and the effect of dispersed phase volume fraction on the gas phase are negligible. Hence, the model can only be employed for dispersed phase accounting for < 10% of the total

volume fraction, although the mass loading can be greater than that. This makes the model appropriate for modelling atomisation processes, spray dryers, aerosol dispersion, bubble stirring of liquids, and other particle-laden flows.

The DPM model employed can be modelled as uncoupled or coupled DPM. It is divided into four types: one-way, two-way, three-way, and four-way coupling (Vowinckel, 2021). In one-way coupling or uncoupled approach, the influence of the gas flow-field on the particle is taken into account. In two-way coupling, the influence of the particle on the gas flow-field and the influence of the gas flow on the particle is considered. In three-way coupling, in addition to the premise of two-way coupling, it also considers the particle's influence on the localised fluid that affects the motion of another particle. In four-way coupling, in addition to all three above coupling, particle-particle interaction is also considered (Alobaid et al., 2022).

Although modelling the two-phase CCGA process employing DPM via E-L framework is advantageous for providing detailed particle-level insights into the system, its prime advantage is, it is computational tractable compared to E-E framework, enabling longer and more extensive simulations. Since, the research presented in this thesis focusses on the gas-melt interaction rather than the melt break-up, DPM is considered to be the appropriate modelling strategy. The DPM methodology implemented for the research is presented in Section 4.3.2.

2.5.6 Discrete-Phase Model (DPM)

In DPM, the trajectory of an individual particle (discrete phase) is predicted by carrying out force balance on the particle, presented in Lagrangian frame of reference. The force balance is equated between the particle's inertia and the forces acting on the particle. This is presented in Equation 2.24,

$$m_P \frac{d\vec{u}_P}{dt} = m_p \frac{\vec{u} - \vec{u}_p}{\tau_r} + m_p \frac{\vec{g}(\rho_p - \rho)}{\rho_p} + \vec{F} \qquad 2.24$$

$$\tau_r = \frac{\rho_p d_p^2}{18\mu} \frac{24}{C_D Re} \qquad 2.25$$

$$Re \equiv \frac{\rho_p d_p |\vec{u} - \vec{u}_p|}{\mu} \qquad 2.26$$

where, $m_p \frac{\vec{u}-\vec{u}_p}{\tau_r}$ is the drag force acting on the particle, $\vec{F}$ is any other additional forces acting on the particle, m_p is the mass of the particle, ρ_p is the density of the particle, g is the

acceleration due to gravity, τ_r is the droplet relaxation time, Re is the relative Reynolds number, C_D is the drag coefficient, $\vec{u}$ is the fluid phase velocity, $\vec{u}_p$ is the particle velocity, and d_p is the diameter of the particle (Wang et al., 2023c, ANSYSFluent®Theory-Guide).

2.5.7 Turbulent dispersion of DPM particles

In a turbulent flow the trajectories of the DPM particles are predicted by using the mean fluid phase velocity presented in Equation 2.27 derived from Equation 2.11. To include the effect of turbulence on the particle trajectory, in addition to the mean fluid velocity the fluctuating velocity is also considered. This predicts the particle dispersion due to turbulence in the gas flow-field.

$$u = \bar{u} + u' \qquad 2.27$$

where, u is the instantaneous fluid velocity, $\bar{u}$ is the mean fluid phase velocity, u' is the fluctuating velocity of the fluid phase (ANSYSFluent®Theory-Guide).

By introducing the fluctuating velocity term into the particle trajectory, the stochastic tracking aims to capture the unpredictable nature of particle in turbulence flows. The stochastic tracking utilises the probability density function to evaluate the instantaneous components. An integral time scale, T, is introduced to predict the particle dispersion. T is the time a particle retains its initial velocity before changing it due to the effects of turbulence. High values of T indicates the presence of large and persistent turbulent structures in flow, and low values of T indicates the presence of small and inconsistent turbulent structures. Integral time scale, T, is given by

$$T = \int_0^\infty \frac{u_{p'}(t)u_{p'}(t-\tau)}{\overline{u_p{}'^2}} \mathrm{d}\tau \qquad 2.28$$

where, $u_{p'}$ is the fluctuating component of the particle velocity, $\overline{u_p{}'^2}$ is the root mean square of the fluctuating component, and τ is the duration between two instances, known as time lag.

For small particles that move along with the fluid, having zero drift velocity, the integral time scale becomes the fluid Lagrangian integral time, T_L. This time scale can be computed as given by

$$T_L = C_L \frac{k}{\varepsilon} \qquad 2.29$$

where, C_L is the model constant, which is unknown and needs to be determined. For k - ε turbulence model, T_L is the given by Equation 2.30, and for k - ω turbulence model, ε is substituted as $0.09k\omega$ (ANSYSFluent®Theory-Guide).

$$T_L \approx 0.30\frac{k}{\varepsilon} \qquad 2.30$$

The stochastic model employed for DPM particles to capture the particle dispersion is the Discrete Random Walk (DRW) Model which also known as eddy lifetime model. In DRW model, the particle interaction in the turbulent flow is accounted for each of the eddies present, and is simulated based on the eddy characteristics. An eddy is defined by a Gaussian distributed random velocity fluctuation, u', v' and w' in the x, y, and z directions, respectively, and by an eddy time-scale, τ_e. The Gaussian distributed random velocity fluctuation is given by Equation 2.31.

$$u' = \zeta\sqrt{\overline{u'^2}} \qquad 2.31$$

$$\sqrt{\overline{u'^2}} = \sqrt{\overline{v'^2}} = \sqrt{\overline{w'^2}} = \sqrt{2k\,/\,3} \qquad 2.32$$

where, ζ is Gaussian distributed random number. Similarly, the fluctuating velocity, v' and w', along the y, and z direction, respectively, is computed in same manner as presented in Equation 2.31.

The eddy timescale, τ_e, which is the characteristic lifetime of an eddy in the turbulence flow is modelled based on T_L as a constant, or as a variable randomly varying about T_L. Equation 2.33 shows τ_e as a constant, and Equation 2.34 gives τ_e as a random variable, both based on T_L.

$$\tau_e = 2T_L \qquad 2.33$$

$$\tau_e = -T_L \ln(r) \qquad 2.34$$

where, r is a uniform random number, $0 < r < 1$ (ANSYSFluent®Theory-Guide).

2.5.8 Two-way coupling between primary and secondary phase

In Section 2.5.5, the different coupling mechanism available in DPM to predict the particle flow pattern based on the influence of continuum (gas phase) is discussed. There are four ways of coupling, and for the research presented in this thesis, for all of the 22 simulations carried out, two-way coupling is employed. In section 4.3.2, the methodology employing the two-way coupling is discussed.

During a particle's flight, in addition to the particle's trajectory, the mass, momentum and heat-transfer are computed. In two-way coupling, the effect of particle's trajectory on the continuum is computed by employing interface exchange equations of mass, momentum and heat-transfer.

Mass exchange

The mass exchange from the discrete phase to the continuum for the two-way coupling is computed by taking into account the change in mass of a particle as it travels through each control volume. The mass transfer from the discrete phase to the continuous phase is considered as source of mass for the continuous phase (ANSYSFluent®Theory-Guide). The mass transfer is computed as

$$M = \frac{\Delta m_p}{m_{p,0}} \dot{m}_{p,o} \qquad 2.35$$

where, Δm_p = change in mass of a particle,

$\dot{m}_{p,0}$ = initial mass flow rate of the particle injection,

$m_{p,0}$ = initial mass of the particle,

Momentum exchange

Similarly, the momentum exchange between the discrete and continuous phase is computed by calculating the change in momentum of a particle as it travels through each control volume. This momentum exchange is considered as a source of momentum for the continuous phase. The momentum exchange is computed as

$$F = \sum \left(\frac{18\mu C_D Re}{\rho_p d_p^2 24} (u_p - u) + F_{\text{other}} \right) \dot{m}_p \Delta t \qquad 2.36$$

where, ρ_p is the density of the particle, d_p is the diameter of the particle, Re is the relative Reynolds number, u_p is the velocity of the particle, u is the velocity of the fluid, $\dot{m}_p$ is the mass flow rate of the particle, C_D is the drag coefficient, Δt is the timestep, and F_{other} is the other interaction forces (ANSYSFluent®Theory-Guide).

Heat exchange

Similar to the mass and momentum exchange, heat exchange from the discrete phase to the continuum is computed by calculating the change in thermal energy possessed by a particle as it travels through each control volume. The heat transfer appears as a heat source in

the continuous phase (ANSYSFluent®Theory-Guide). The exchange in the thermal energy is given as

$$Q = \frac{\dot{m}_{p,0}}{m_{p,0}}\left[\left[m_{p_{in}} - m_{p_{out}}\right]\left[-H_{lat_{ref}} + H_{pyrol}\right] + m_{p_{in}}\int_{T_{ref}}^{T_{p_{in}}} c_{p_p} dT - m_{p_{out}}\int_{T_{ref}}^{T_{p_{out}}} c_{p_p} dT\right] \quad 2.37$$

where, $m_{p_{in}}$ = mass of the particle on cell entry,

$m_{p_{out}}$= mass of the particle on cell exit,

c_{p_p}= heat capacity of the particle,

H_{pyrol}= heat of pyrolysis as volatiles are evolved,

$T_{p_{in}}$= temperature of the particle on cell entry,

$T_{p_{out}}$= temperature of the particle on cell exit,

T_{ref}= reference temperature for enthalpy, and

$H_{lat_{ref}}$= latent heat at reference conditions.

3 Literature review

In Chapter 2, the general working of the CCGA process and its related CFD models employed to numerically model the process were discussed. This section reviews the operating parameters and the CFD models of the CCGA process, and their influence on the process. The review chapter is divided into two parts: experimental investigations on CCGA process and their outcomes, and theoretical studies on CCGA process using CFD modelling and their model evaluation.

3.1 Factors and Design parameters affecting CCGA Process

The CCGA process is affected by various factors and design parameters such as operating pressure, operation of the atomiser at wake-closure pressure (WCP), gas-die design, melt nozzle design, nozzle angle, protuberance length, and many more. Some of the major parameters are discussed below.

3.1.1 Effect of gas inlet pressure

In CCGA process, based on the gas inlet pressure, the wake can exist in two different configurations: open-wake condition and closed-wake condition. This is because, the pressure variation in the inlet gas results in generation of shocks. At lower operating pressure, the recompression shocks does not cross each other to produce the normal shock perpendicular to direction of flow, known as Mach-disk. However, at higher inlet pressures, the recompression shocks gets reflected from the sonic boundary and crosses each other, producing normal shock, i.e., Mach-disk (Anderson et al., 1991). The region in the flow-field present in front of the melt nozzle outlet, i.e. the region bordered by the inner sonic boundary radially, and the Mach-disk downstream is known as the wake. This is shown in Figure 3.1. At higher gas pressure when the Mach-disk is present downstream, it indicates the wake is in closed-wake condition, and at low pressures, absence of Mach-disk downstream indicates the wake is in open-wake condition. The open-wake and closed-wake condition in gas flow-field is illustrated in Figure 3.2.

In both the wake conditions, the recirculation zones exist because of the close proximity of the gas and melt nozzles, as shown in Figure 3.1. This facilitates the effective pulling of the melt from the melt nozzle (pre-filming), resulting in finer atomisation. Under closed-wake conditions, the introduction of melt disrupts the Mach-disk causing the wake to enter into open-

wake condition. However, this occurs only momentarily since the Mach-disk re-establishes to form closed-wake condition due to the strong gas-jet. This repeats over and over again, and this repeated and continuous shift between open- to closed-wake condition is known as pulsatile phenomenon (Ting et al., 1998).

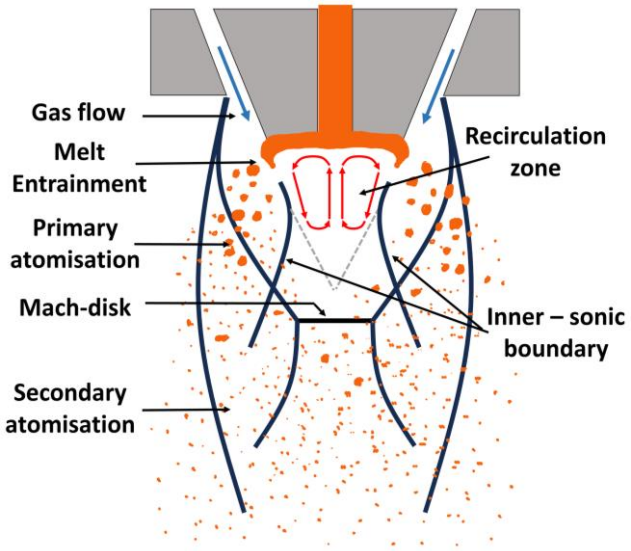

Figure 3.1 Schematic illustration of gas flow-field with Mach-disk downstream.

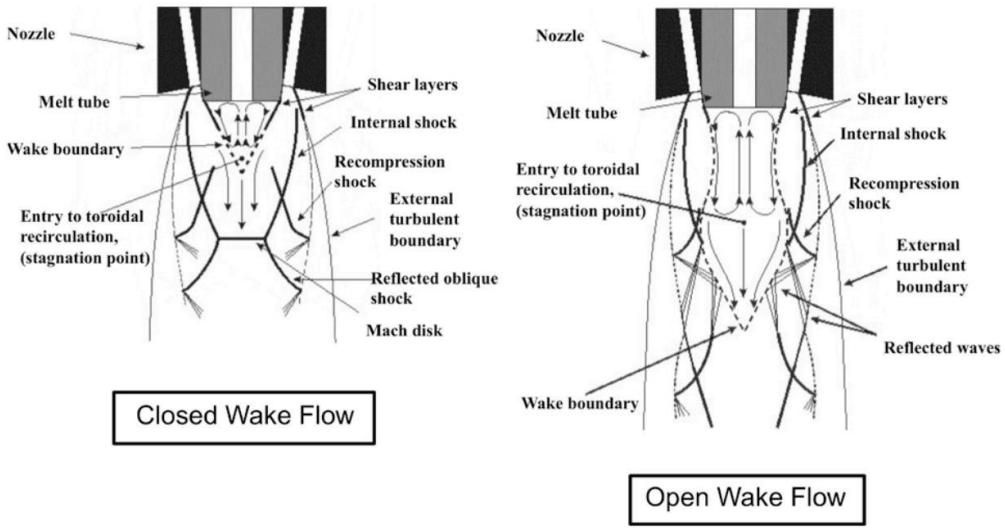

Figure 3.2 Schematic representation of closed- and open-wake conditions (Anderson et al., 1991).

Wide range of research on CCGA were conducted using different inlet gas pressures. It was observed that at lower operating pressures, larger particle sizes were obtained, and higher operating pressures resulted in smaller particle sizes (Wang et al., 2023c). This is because at higher pressure, the particle experiences higher weber number (Figure 2.9), resulting in finer secondary atomisation leading to smaller particle sizes. However, with a retracted melt nozzle

(discussed in Section 3.1.4), it was observed that the particle size increased despite operating at high pressure. This is because a positive pressure develops at the melt nozzle exit, hindering a smooth melt flow from the tundish thereby causing improper atomisation. And at sufficiently high pressure, it possesses the risk of melt freeze-off which is adverse for the process. Table 3-1 presents the various research conducted using different gas inlet pressure and their outcome in PSD. Although, the increase in gas inlet pressure decreases the PSD, it is largely affected by other operating parameters such as GMR, melt temperatures, melt nozzle angle, and many more. Nevertheless, at extreme high inlet pressures of >6 MPa, there is no significant reduction in particle size or PSD (Shi et al., 2022). Additionally, operating at such high pressures also results in substantial energy consumption both during the process and subsequent recompression of the gas. Ideally commercial atomisers operate at a GMR of 1-2 to maximum both the yield and reduce the energy expenditure (Zeoli et al., 2012).

Table 3-1 Inlet gas pressures used in different CCGA process and their respective PSD outcome.

Author	Gas inlet pressure	PSD (µm)
(Wang et al., 2023a)	3 MPa	d_{10}–d_{90} : 11.4 - 105.9
(Luo et al., 2023)	2 MPa	d_{10}–d_{90} : 15 - 53
(Wang et al., 2023b)	1.5 - 4.5 MPa	d_{10}–d_{90}: 25 - 175
(Wang et al., 2023e)	0.5 MPa	D_M : 8.03
	1.5 MPa	D_M : 5.78
	2.5 MPa	D_M : 5.93
(Wang et al., 2021)	2.5 MPa	d_{10}–d_{90} : 22±3 – 50±4.6
(Liu et al., 2023a)	0.5 - 3 MPa	d_{50} : 25.56 - 28.42
(Zhao et al., 2023)	4 MPa	d_{10}–d_{90} : 10 - 100
(Wang et al., 2024b)	4 MPa	d_{10}–d_{90} : 64 - 100
(Zhang et al., 2023a)	2.5 MPa	d_{10}–d_{90} : 25 - 250
(Shi et al., 2022)	5 MPa	d_{10}–d_{90} : 40 - 133
	6 MPa	d_{10}–d_{90} : 35 - 130
	7 MPa	d_{10}–d_{90} : 35 - 120
	8 MPa	d_{10}–d_{90} : 20 - 110
(Wang et al., 2023c)	1.5 MPa	d_{10}–d_{90} : 55 - 179.4
	2.0 MPa	d_{10}–d_{90} : 31.1 - 146.3
	3.0 MPa	d_{10}–d_{90} : 27.2 - 120.4

Predicted | Measured

3.1.2 Effect of Wake-Closure Pressure (WCP)

With the increase in gas inlet pressure, the pressure at which the wake transits from open-wake to closed-wake is known as Wake-Closure Pressure (WCP). Ting (2003) delineated the CCGA operation under open-wake condition just prior to closed-wake condition. It was observed that as the melt was drawn into the wake by the aspiration pressure, the wake region enlarged, owing to which a stronger recirculation zone was developed. The process of melt drawn into the atomisation chamber; it undergoing pre-filming; and wake enlargement are presented in Figure 3.3a-c. Simultaneously, due to the enlargement in the wake, the stagnation pressure flows towards the nozzle creating a backpressure thereby retarding the melt flow (Figure 3.3c). Subsequently, the melt inflow in the wake region reduces, causing the wake to return back to its original configuration as illustrated in Figure 3.3b.

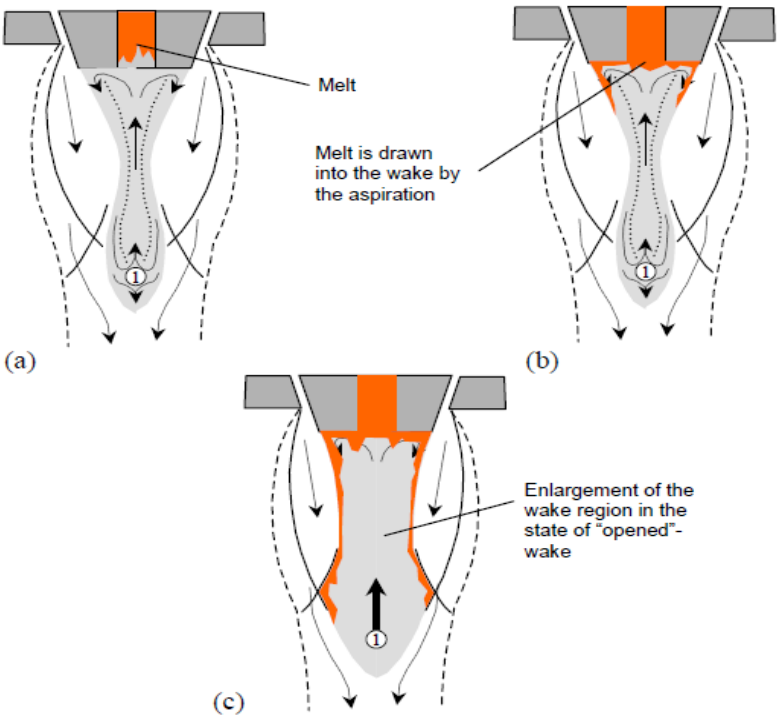

Figure 3.3 A two-phase flow interaction showing, (a) the gas-only feature at below WCP operation just prior to the introduction of the melt in to the wake, (b) melt entrainment into the wake, and (c) enlargement of wake and retarding melt flow due to the opposing force exerted by stagnation pressure. (Ting, 2003)

With further increase in gas inlet pressure, the wake transits from open-wake condition to closed-wake condition. During the closed-wake condition, i.e., with the presence of Mach-disk, as presented in Figure 3.4a, the melt is drawn into the wake by the aspiration pressure. With the continuous entrainment of the melt into the wake, it abruptly disrupts the Mach-disk to enter into open-wake condition. This wake transition from closed-wake condition to open-wake

condition is illustrated in Figure 3.4b and Figure 3.4c. A stronger recirculation zone is developed due to the increased gas flow in the wake, leading to enlargement of the wake, as presented in Figure 3.4d. Simultaneously, the high pressure at stagnation point surges into the wake, temporarily stopping the melt flow. This is shown in Figure 3.4e. With the amount of melt in the wake declined, the wake begins to neck, leading to the re-establishment of the Mack-disk as originally observed in Figure 3.4a. Thus, both operating at and above WCP, the wake continuously alternates between open- to closed-wake condition until the melt reserves exhaust.

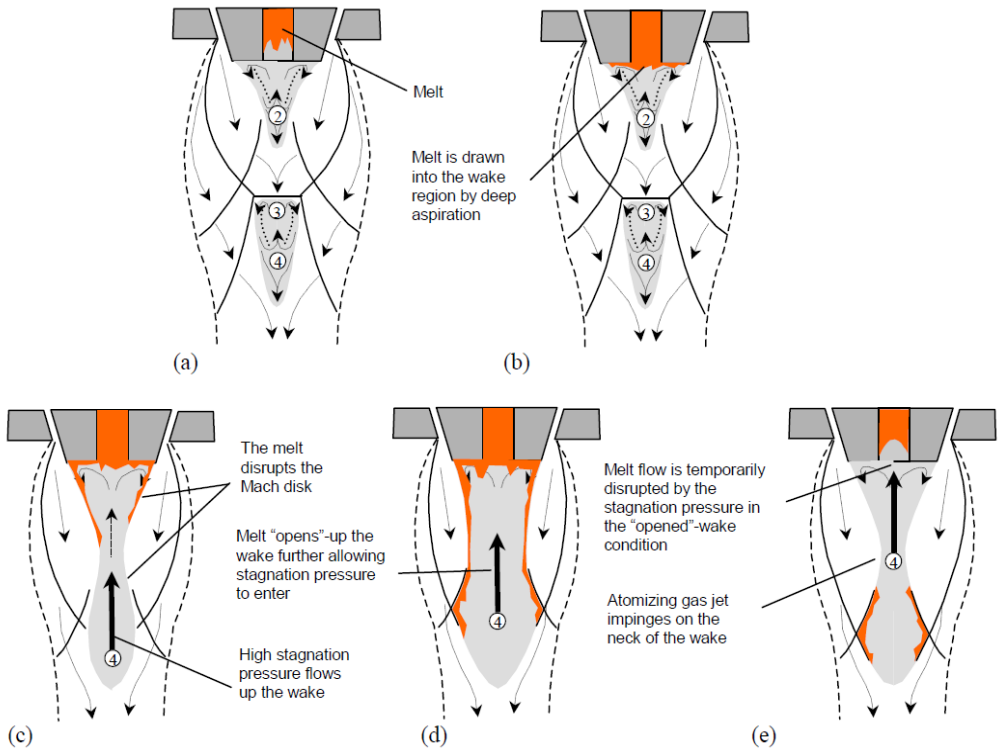

Figure 3.4 Two phase flow interaction showing, (a) the wake in the closed-wake condition just prior to the introduction of the melt into the wake, (b) the introduction of the melt into the wake drawn in by the deep aspiration pressure, (c) melt disrupting the Mach-disk and entering onto open-wake condition, (d) enlargement of the wake and the high pressure from stagnation point 4 surging into the wake, and (e) the pressure surge temporarily disrupting the melt flow. The wake region begins to neck, leading to the re-establishing of Mach-disk as shown in (a) (Ting, 2003).

Atomisation trials were conducted operating both under open-wake condition and closed-wake condition. Ting (2003) observed, atomisation operating above WCP resulted in finer powders compared to atomisation operated below WCP, i.e., open-wake conditions. It was calculated, that the d_{50} reduced from 63.5 to 37 µm, and standard deviation (d_{84}/ d_{50}) reduced from 3.38 to 2.61 when transitioned from open- to closed-wake operation. This is due

to the reduced amounts of melt that is drawn intermittently into the wake during closed-wake condition that the effective atomisation is carried out. Moreover, it was also observed the amount of melt flow rate reduced from 23.2 to 14.5 kg min^{-1} when transitioned from open- to closed-wake operation, confirming the reduced and intermittent inflow of melt. Conversely, during open-wake condition, continuously supply of melt is fed into the wake resulting in larger particle size (Ting, 2003).

3.1.3 Design of gas delivery nozzle

Another factor which influences the PSD is the gas-delivery nozzle design. Pressurised gas when sent through the gas nozzle, expands to develop into supersonic gas. The nozzle plays an important role in the flow mechanics of the impinging jet, creating regions of high and low pressure, shocks, wakes, sonic boundaries, and flow separations. Various designs have been implemented in a continuous effort to improve the powder yield. Some of the important gas nozzle design parameters affecting the powder characteristics are the nozzle configurations, nozzle exit area, and nozzle apex angle (Figure 3.5). This section outlines the nozzle configurations and their characteristics.

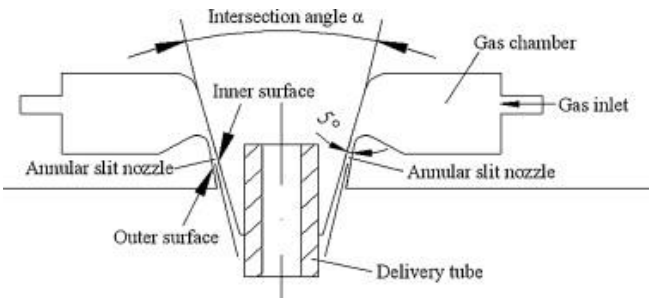

Figure 3.5 Cut section of annular slit gas nozzle (Zhao et al., 2012).

The nozzle configurations are classified into two types: gas-die configuration and nozzle profile. Gas-die configurations are broadly divided into two types: Annular slit (AS) and Discrete jet (DJ). In the annular slit gas nozzle, the melt nozzle lies in the axis of symmetry, i.e., geometrical centre, and the gas nozzle is present around the melt nozzle in the form of circular disk. The outer wall of the melt nozzle acts as the inner wall to the gas nozzle. The cut section of a typical annular slit gas nozzle is presented in Figure 3.5. The opening orifice where gas exits is continuous and circular, forming a slit in the shape of a ring, hence taking the name 'slit'. Although the machining of such nozzles is considered uncomplicated, the nozzles have two significant disadvantages. Firstly, it is extremely tedious to align both melt nozzle and gas nozzle in the same axis of symmetry. Even with minor errors in the alignment of the slit the

width distribution across the slit becomes asymmetrical, resulting in asymmetrical gas flow, thereby deeming the process an adverse failure. Secondly, for a given pressure the mass flow rate of the gas exiting the annular slit nozzle will be considerably higher than that of discrete jet nozzle, resulting in unnecessary usage of gas. These crucial factors led to the construction of better and robust gas nozzle – discrete jet gas nozzle.

Discrete-jet, as the name suggests contains individual slot of holes for gas to flow, forming individual gas-jets. A typical discrete-jet gas nozzle used in the CCGA study conducted by Motaman (2013) is shown in Figure 3.6. Unlike the annular slit nozzle, in this type, both the melt nozzle and gas nozzle are separate entities, and are assembled together as one system. The individual slots are arranged symmetrically around the melt nozzle axis and are positioned equidistant from each other. Different studies have adopted different number of discrete-jet nozzles to construct better nozzle for improved performance. Studies conducted by Anderson et al. (1991), Mullis et al. (2010), McCarthy et al. (2013), and Motaman et al. (2015) have employed 18 discrete nozzles, equidistantly placed at 20° to about the melt nozzle's axis. In a study conducted by Wang et al. (2023e) 36 discrete nozzles were employed, equidistantly placed at 10° to each other. Similarly, in another study, Silva et al. (2022) used 20 discrete nozzles, placed at 18° distribution, and Wang et al. (2024b) used 12 discrete nozzles placed at 30°, in symmetry with the melt nozzle. The advantage in discrete-jet nozzles over annular slit includes increased process control, increased uniformity in particle size and process efficiency. Also, due to the drastically reduced size of the outlet area for gas flow, higher pressures of gas can be used without considerable concern to gas consumption rates which in turn yields finer particles (Urionabarrenetxea et al., 2014).

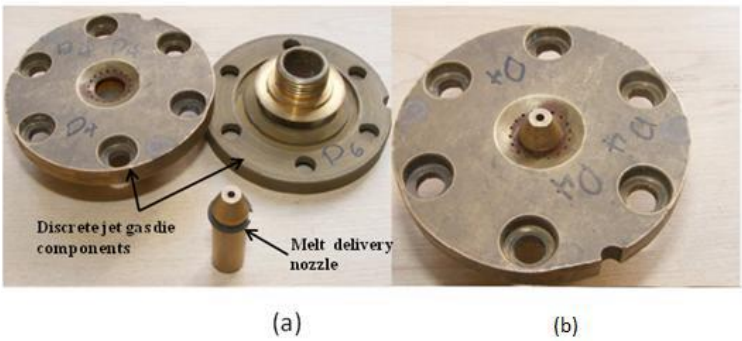

Figure 3.6 The discreet-jet gas-die components and melt delivery nozzle, (b) Melt and discrete gas die assembly (Motaman, 2013).

Just as nozzle gas-die configurations are broadly divided into annular slit and discrete-jet, the nozzle internal profile can also be classified broadly into two types: cylindrical and convergent-divergent (C-D) nozzles. The cut-section of cylindrical and C-D nozzles are

presented in Figure 3.7. Both cylindrical and C-D nozzles, has its own advantages and disadvantages. Cylindrical nozzle profiles are simple in design and are much easier to machine. Albeit, given the nozzle inner diameter is << 1 mm, it requires ultra precision machining. However, it is still simpler compared to the machining of complicated C-D nozzle profiles. The advantage of adopting a cylindrical profile nozzle is, it can be operated over a wide range of pressures (Mullis et al., 2013a). However the major disadvantage is, it develops choked flow in the nozzle, owing to which the flow of the gas is drastically reduced to Mach 1 irrespective of the inlet gas pressure (Mullis et al., 2007).

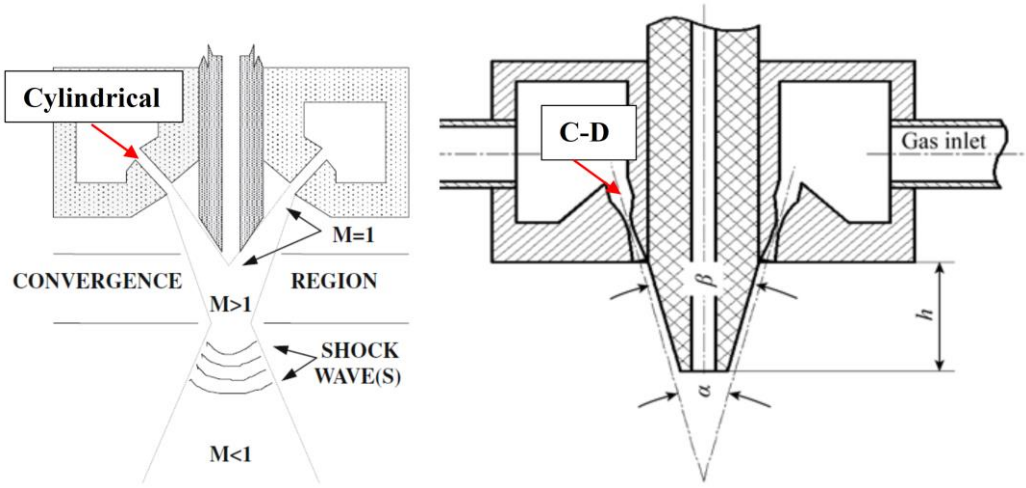

Figure 3.7 A schematic diagram of (a) cylindrical nozzle profile (Antipas, 2009), (b) C-D nozzle profile. (Anderson and Terpstra, 2002).

Similarly, C-D nozzle profiles have their own advantages and disadvantages. Advantages include, higher gas-jet velocity compared to cylindrical nozzle for the same inlet pressure (Srivastava and Ojha, 2006). This results in increased shearing forces on the melt, providing finer atomisation. Also, as a result of higher gas velocity, particles undergo increased cooling rates. The downside of using C-D nozzle profiles is, it is extremely complicated to machine, and needs expensive, non-conventional, ultra precision machining technique such as Wire-cut electrical discharge machining (EDM) to manufacture the nozzle. Moreover, in C-D nozzles for a specified exit Mach number, there is one specific nozzle's exit to throat area (A_e/A_{th}) ratio, and hence if another exit Mach number of interest is required, another C-D nozzle with corresponding exit to throat area ratio has to be designed (Rathakrishnan, 2019).

The gas nozzle performance, and in turn the process performance is also affected by other design parameters such as the nozzle offset distance, and gas and melt nozzle mismatch angle. The nozzle offset distance is the between the gas nozzle's inner wall and the melt nozzle's external wall. Based on this, the nozzle design is classified as gas nozzle with and

without offset. This is shown in Figure 3.8. Gas nozzle without offset distance generates positive aspiration pressure at higher gas inlet pressures leading to potential melt freeze-off. This is avoided in gas nozzle with offset distance, however, it poses another disadvantage; at lower pressures, the gas nozzle is prone to nozzle clogging. Nozzle clogging occurs when molten melt accumulates at the nozzle's exit, blocking the flow of gas. This usually takes places when the melt flows towards the gas nozzle, known as back streaming, and accumulates in the lower pressure region next to the nozzle exit.

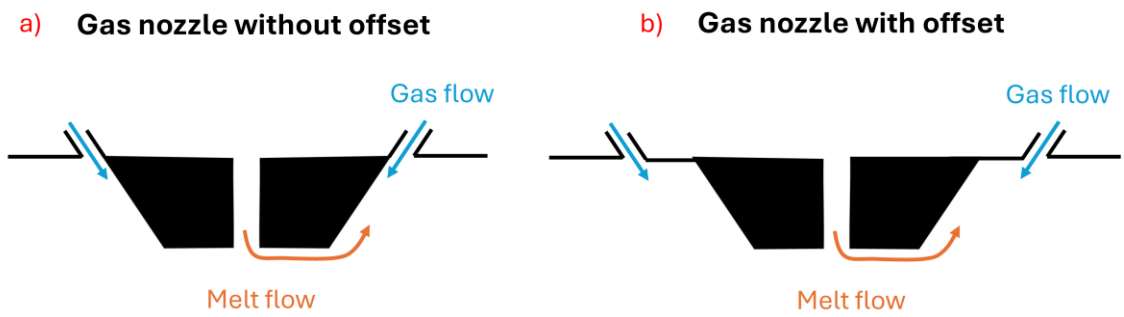

Figure 3.8 Gas nozzle configurations: a) without offset distance, b) with offset distance.

Similarly, another design parameter that affects the process performance is the mismatch between the gas and melt nozzle angle. Mismatch angle is the difference in angle between the gas nozzle's apex angle (β) and melt nozzle's apex angle (α). This is shown in Figure 3.9. A mismatch angle of certain degree generates lower aspiration pressure at the melt nozzle tip due to the strong radial pressure gradient. However, at larger mismatch angle the gas-jet impinges the melt at distance further downstream, resulting in increased particle size (Ünal, 2007b). An extreme case of mismatch angle is the cylindrical melt nozzle, (discussed in Section 3.1.4). Generally, cylindrical melt nozzles have been observed to prevent melt freeze-off, however, the melt nozzle design is not optimum to produce fine powders as seen in tapered melt nozzle designs (Mi et al., 1997).

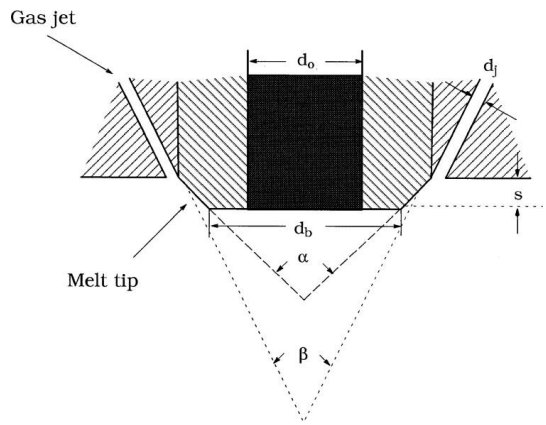

Figure 3.9 Cross section of the nozzle having mismatch angle between the gas and melt nozzles (Mi et al., 1997).

3.1.4 Design of melt delivery nozzle

Accompanying the gas nozzle in the atomiser system is the melt nozzle. Just as how crucial the design parameters of gas nozzle are imperative for efficient operation of the CCGA, so is the melt nozzle design parameters. In CCGA process, as discussed earlier, the melt nozzle is assembled together with the gas nozzle, thereby providing close proximity between the gas and melt nozzle exits. The melt nozzle can be studied broadly on three different aspects: nozzle type, nozzle protuberance length and nozzle internal design.

The nozzle type is generally categorised into two types: cylindrical nozzles and tapered nozzles. Cylindrical nozzles are shown in Figure 3.10a&b, and tapered nozzles are shown in Figure 3.10c&d and Figure 3.11. Cylindrical nozzles were used during earlier stages of CCGA studies (Ünal, 1988, Ünal, 1989a, Ünal, 1989b). Studies conducted by Anderson et al. (1991), Srivastava and Ojha (2006) and Aydin and Unal (2011), reported that nozzles with a tapered profile generate much lower aspiration pressure compared to cylindrical nozzles. Hence cylindrical nozzles are avoided in the current CCGA research due to their aerodynamic disadvantage.

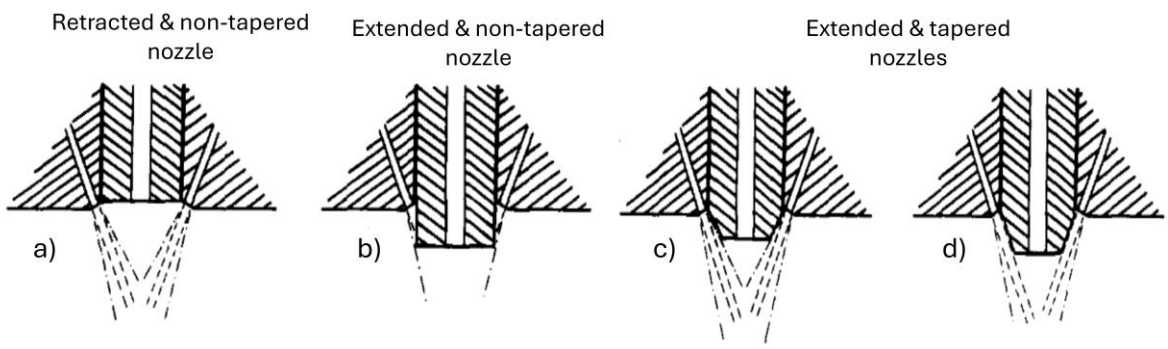

Figure 3.10 Schematic representation of different protuberance lengths of melt nozzle (Anderson et al., 1991).

Protuberance length or protrusion length is the measure of melt nozzle extension beyond the gas-die datum. The variation in protrusion length as shown in Figure 3.10 affects the aspiration pressure of the CCGA process and this in turn affects the melt flow rate. The protrusion can be of two types: retracted or extended. Retracted melt nozzle is shown in Figure 3.10a. In retracted nozzle, the wake closure, i.e., formation of Mach-disk, occurs at a much lower pressure than the extended nozzle, which negatively affects the atomisation efficiency resulting in large particle size. Moreover, in retracted melt nozzles, pressure along the atomiser's axis was reported to be significantly higher compared to extended melt nozzles,

leading to the development of over-ambient (positive) pressure at the melt nozzle tip. Since, CCGA process operates by drawing melt proportional to the aspiration pressure (negative pressure), a positive pressure would be detrimental for the process and can cause adverse melt freeze-off inside the melt nozzle (Mi et al., 1997). An extended melt nozzle on the other hand creates a relatively lower pressure region at the melt nozzle tip owing to the gas flow dynamics, shaped by the nozzle's design. However, for melt nozzles with increased protrusion length, poor atomisation performance were reported, resulting in increased particle size (Ünal, 1988). This is because, with increased protrusion length, the shocks undergo multiple reflection between the melt nozzle outside wall and the sonic boundary, weakening the flow, resulting in flow reaching subsonic speeds (Ünal, 1989b). In a similar study carried out by Aksoy and Ünal (2006) it was observed that at optimal protrusion length, even low inlet gas pressure produces finer particles, whereas at increased protrusion length it resulted in undesirable particle size.

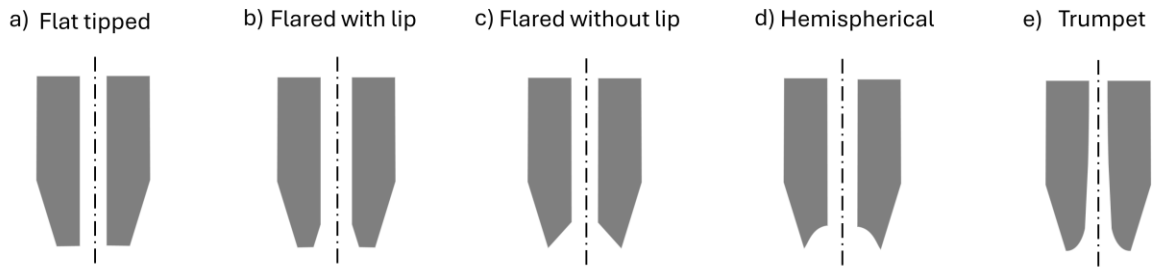

Figure 3.11 Cut section of different internal profiles of melt nozzles. a) flat tipped, b) flared with lip, c) flared without lip, d) hemi-spherical and e) trumpet (Mullis et al., 2011, McCarthy et al., 2013).

Thirdly, the internal design of the melt nozzle also plays an equal role in the CCGA process. The major internal designs present in the literature for the melt nozzle are flat-tipped, flared with lip, flared without lip, hemi-spherical and trumpet shaped (Mullis et al., 2011, McCarthy et al., 2013). Traditionally, flat tipped melt nozzle as shown in Figure 3.11a have been widely adopted for most of the research and commercial production to facilitate a smooth pre-filming. However, nozzles with other designs have also been investigated for pre-filming and atomisation efficiency. Although flared with and without lip (Figure 3.11b-c) have been aimed to increase the pre-filming, study carried out by Mullis et al. (2011) show that the aspiration pressure is higher compared to the flat tipped nozzle, which are generally considered to be of negative impact to the process, since they pose risk of melt freeze-off. However, usually in commercial atomisation this is overcome by applying an over-pressure to the melt reservoir to ensure continuous downward flow of melt.

Table 3-2 Parameters used by various researchers for studying melt nozzle design

Author	Type	Apex angle (Deg)	Protrusion length (mm)	Inner dia (mm)	Tip Dia (mm)	Lip angle (Deg)
(Aksoy and Ünal, 2006)	Tapered	25˚	5	3	-	0
			10			
			15			
(Mates and Settles, 2005)	Tapered	45˚	3.6	2	8	0
	Cylindrical	0	5	2	8	
(Ünal, 1989a)	Cylindrical	0	5	4	10	0
(Mullis et al., 2013b)	Tapered	45˚	-	2	5	0
(Srivastava and Ojha, 2006)	Cylindrical	0	0-6	3	-	0
	Tapered	9˚	0-4	3		0
(Aydin and Unal, 2011)	Tapered	26˚	5	3	-	0
(Mi et al., 1997)	Tapered	63˚	1.93	4.76	8.43	0
		45˚	0		10.03	
			1.93		8.43	
			2.34		8.09	
			3.86		6.83	
		30 ˚	1.93		9	
		0	1.93		10.03	
(Si et al., 2014)	Tapered	45˚	6	4	-	0
(Ünal and Aydın, 2007)	Tapered	44˚	-	3	-	0
(Ünal, 1988)	Cylindrical	0	3	4	10	0
			5		8,10,12	
			8		10	
(Ünal, 2007a)	Tapered	26˚	5	3	5	0
(McCarthy et al., 2013)	Tapered	45˚	-	2	4.9	0
	Flared					30
	Sharp edge					30
	Sharp edge with profile					R-2.5 (radius)
(Mullis et al., 2007)	Tapered	90˚	-	2	5	0
(Mullis et al., 2013a)	Tapered	45˚	-	2	5	0
(Ünal, 1989b)	Cylindrical	0	5	4	8	0
			3,5,8		10	
			5		12	
(Mates and Settles, 1996)	Tapered	45˚	3.6	2	8	0
	Cylindrical	0	5	2	8	0
(Mullis et al., 2010)	Tapered	90˚	-	2	5	0
	Sharp edge					30
	Flared					30

Moreover, melt nozzles with hemi-spherical profile (Figure 3.11d) achieved wake closure at a lesser gas inlet pressure (3 MPa) compared to flat-tipped nozzle (5 MPa) (Mullis et al., 2007). This profile was designed to facilitate the wider spreading of the melt before coming in contact with gas jet, thereby resulting in finer atomisation. On the contrary, the profile posed a challenge, wherein the melt entered into the wake undistributed. Nevertheless, the use of trumpet profile, shown in Figure 3.11de, reduced the particle size by 17% compared to flat-tipped nozzle (Figure 3.11a) (Anderson et al., 2005). By including slots to the trumpet profile, particle size was further reduced another by 16%. However, with an increased exit surface area such as seen in a trumpet profile, the melt is prone to more oxidation (Anderson et al., 2005). Table 3-2 outlines the various CCGA studies carried out with different melt nozzle design parameters.

3.2 CFD study on CCGA

The physical atomisation process is highly complex and chaotic, deeming it too rapid for clear visual observation. Although, high-speed cameras have been utilised to inspect and study the CCGA process, the cameras' ability to capture and record is limited to a 2D plane. Moreover, this 2D observation of the process also does not provide a clear characterisation of the process, since the captured photographic frame in 2D is a superimposed overlap of the 3D process. Furthermore, although photographic capturing of the process has benefited in understanding of some aspects of it, owing to the extremely complex and chaotic nature of the process, they have limited contribution towards the understanding of the background physics. To understand the background physics of the process and to optimise it further, researchers have taken the aid of CFD tools to explore and model the process. This section provides an outline of the various CFD studies carried out on CCGA process, both single-phase (gas-only) and two-phase flow. Overview of the CFD models related to this research is discussed in Section 2.5, and the CFD methodology employed for the current research is presented in Chapter 4. A compilation of various CFD studies carried out on CCGA process, both on single-phase (gas-only) flow and two-phase flow, detailing the key models employed in their study is presented in the Appendix.

3.2.1 Single phase: Gas-only flow

One of the early single-phase CFD studies was carried out by Espina and Piomelli (1998), employing k-ε turbulence model to study the influence of model constants, gas inlet pressure, and gas temperature. The study reported that the model in general under-predicted the flow characteristics. The study reported that with increase in gas inlet pressure, there was a sharp drop in aspiration pressure followed by a steady rise. However, the aspiration pressure measured in this study was in reference to the pressure in the melt delivery tube, rather than the gas pressure obtained at the melt nozzle tip. The sudden drop in the aspiration pressure might be corresponding to the wake-closure pressure; and the steady rise is due to the increase in gas inlet pressure under closed-wake condition which increases the aspiration pressure thereby retarding the melt in-flow. CFD studies carried out by Mi et al. (1997) and Espina and Piomelli (1998) consistently demonstrated that the aspiration pressure decreased with increase in gas inlet pressure while operating under open-wake conditions. And increased with increase in gas inlet pressure while operating under closed-wake conditions. The k-ε turbulence model was also employed by Mi et al. (1996) and Mi et al. (1997). These studies reported one of the earliest flow-field behaviour for closed-wake condition, i.e., with Mach-disk. Mi et al. (1996) reported, with increase in gas inlet pressure the recirculation length increased, however, at >2 MPa, the recirculation length decreased. This is due to the formation of Mach-disk that the recirculation zone shrunk. Mi et al. (1997) extended the CFD model to investigate the effects of melt tip designs under gas-only flow conditions. Increase in melt tip length (protrusion length) did not change the position of Mach-disk downstream, however, it proportionally increased the second recirculation zone length after the Mach-disk. Contrastingly, with increase in melt nozzle taper angle, the Mach-disk location was pushed downstream. Increasing the angle also generated weaker Mach-disk.

Ting and Anderson (2004) also investigated the effect of increasing gas inlet pressure to study the wake-closure phenomenon. The study confirmed the existence of a flow discontinuity both in velocity and pressure, immediate downstream of the Mach-disk. This study corroborated with Mi et al. (1997) and Espina and Piomelli (1998) demonstrating the reduction in the aspiration pressure until wake-closure pressure, and subsequent increasing thereafter. Although, the CFD model captured the general trend in the aspiration pressure with increasing gas inlet pressure, it revealed the existence of mismatch between the CFD model and experimental recordings of the aspiration pressure. This mismatch is due to the non-availability of numerically robust CFD models. Nevertheless, this research is one of the earliest

numerical analyses to include compressibility effect into the CFD model, predicting the behaviour of the gas flow-field and the formation of Mach-disk at and beyond wake-closure pressure. Similarly, Tong and Browne (2009) numerically modelled the compressible gas-only flow, but considered the flow to be transient in nature. However, the model under-predicted the pressure in the gas flow-field. Moreover, the model failed to capture the established trend of aspiration pressure, which typically shows a decrease before the wake-closure and increase afterward. Instead, the model predicted an overall decrease in the aspiration pressure with the increase in gas inlet pressure.

With further advancements in CFD models and computational resources, computationally robust models predicting more reliably were developed. Aydin and Unal (2011) studied the effect of gas inlet pressure in a gas-only (no melt) atomisation process by adopting k-ε turbulence model. The study reported of using an unstructured mesh employing first-order upwind scheme having a total of 629,922 mesh elements. This is because of the extensive mesh refinement near nozzle and wall regions. Using such a refined mesh the study reported a 11-15% difference between the experimental and theoretical results of the aspiration pressure. This difference could be reduced by employing second-order upwind scheme, as it is more robust for unstructured mesh. However, with significant increase in the number of mesh elements, the models require substantially higher computational resources. Although CFD models with such large number of mesh elements might be possible to run in steady-state condition, this would be a cumbersome and strenuous effort to run in transient (unsteady) conditions.

Zhao et al. (2012) compared the k-ε and RSM turbulence models for atomiser with increasing gas nozzle angle, and reported k-ε turbulence model under-predicted the gas expansion thereby resulting in a narrower gas flow-field cone angle compared to that of RSM turbulence model. Although, both the k-ε and RSM turbulence models under-predicted the general flow when compared against the experimental results, RSM model captured the flow and performed better at steep pressure gradients. Motaman et al. (2013) extended the gas atomisation CFD model by employing the k-ω turbulence model and investigated the melt nozzle geometry. A structured mesh with 11,000 elements was employed for this study. The turbulence model effectively captured the compressible flow expanding from a C-D nozzle exit, reflecting the experimentally observed gas flow.

Recent CFD studies, including Kaiser et al. (2018) investigated the comparison between two types of C-D nozzle, annular slit (AS) nozzle and isentropic plug (IP) nozzle. With the considerable development of computational resources, the study solved the CFD

model as a compressible unsteady flow using the RSM turbulence model with a small timestep size of 1e-06 s. However, this computationally intensive simulation was made undemanding by constructing mesh with reduced mesh elements (27,000), although appropriate mesh refinements are applied at the gas nozzle exit and regions of adverse pressure gradient. The study revealed that even though IP nozzle generated gas flow-field with reduced presence of shocks, it generated positive aspiration pressure at the melt nozzle tip which is of negative influence on the process. Similar CFD studies using C-D nozzle were conducted by Zhao et al. (2023), Wang et al. (2023b) and Zhang et al. (2023b).

Zhao et al. (2023) employed k-ε turbulence model to investigate different gas nozzle exit areas. It was found, for a given pressure, at smaller gas nozzle exit area, the flow on exiting, expanded further downstream, and developed a curved Mach-disk. However, with increase in the exit area, the gas expanded relatively less, but developed a distinct Mach-disk. This is because for a given pressure, smaller nozzle exit area leads to increased velocity, and larger nozzle exit area results in reduction in velocity. Similarly, Wang et al. (2023b) also employed the k-ε turbulence model, to investigate the gas inlet pressure on nozzle clogging. It was reported at very low pressure (1.5 MPa) the process would be prone to nozzle clogging due to the negative pressure region formed near the nozzle wall; and at very high pressure (4.5 MPa) because of positive aspiration pressure, the gas flow induces melt freeze-off. However, both of the catastrophes are prevented when an optimum pressure of 3.5 MPa was employed. The results of the study is consistent with the study carried out by Motaman et al. (2013), wherein the back-stream flow was highest at 1 MPa, and at higher pressures of 3-5 MPa the back-stream flow was absent. The study also predicted absence of nozzle clogging when a mismatch angle of 7° is allowed between the melt nozzle and gas nozzle apex angles. These two studies might suggest that an optimum mismatch angle and optimum pressure can simultaneously prevent both gas nozzle clogging and melt freeze-off, facilitating a smooth CCGA working, provided it operates under closed-wake condition for effective atomisation.

In addition to 2D models, CCGA studies in CFD have been extended to 3D to facilitate deeper understanding of the process and its optimisation. Generally, a 3D model is approximated into 2D axisymmetric model to reduce the computational cost and run-time. However, with this approximation, atomiser designs which are radially symmetrical, such as annular slit nozzle and circular melt nozzle tip, can only be modelled. To extend the CFD model to include Discrete-jet gas nozzles and other shapes of melt nozzle profile, 3D modelling is imperative. Ashokkumar (2020) modelled 3D gas-only discrete-jet CCGA process by employing k-ω turbulence model. The study investigated the effect of gas inlet pressure for two

type of gas nozzles: with and without offset distance from the melt nozzle wall. The findings of the study were consistent with that of the 2D CFD study carried out by Motaman et al. (2013) and Wang et al. (2023b), revealing the process is susceptible to nozzle clogging at low gas inlet pressure for the gas nozzle with-offset distance. This adverse nozzle clogging was avoided in the gas nozzle without-offset distance. Wang et al. (2023a) used a gas nozzle without offset distance to investigate into the boundary layer separation and flow circulation by employing the RSM turbulence model. The flow separation results obtained at the melt nozzle tip remained consistent with that of Ashokkumar (2020). The study also revealed that the flow from recirculation zone joins the mainstream flow at the stagnation point. The atomiser model having gas nozzle without-offset distance was further investigated by Wang et al. (2024b) with added design modifications. Secondary set of gas nozzles known as Assisted Gas Nozzles (AGNs) were added in addition to the primary gas nozzle as shown in the Figure 3.12. The model predicted an improvement to the recirculation zone with the implementation of the AGNs. The study reported an 12% increase in its recirculation zone velocity, indicating a decrease in the aspiration pressure. However, its optimal performance resulting in lowest aspiration pressure was observed at lower AGN pressure (1 MPa), rather than higher AGN pressures.

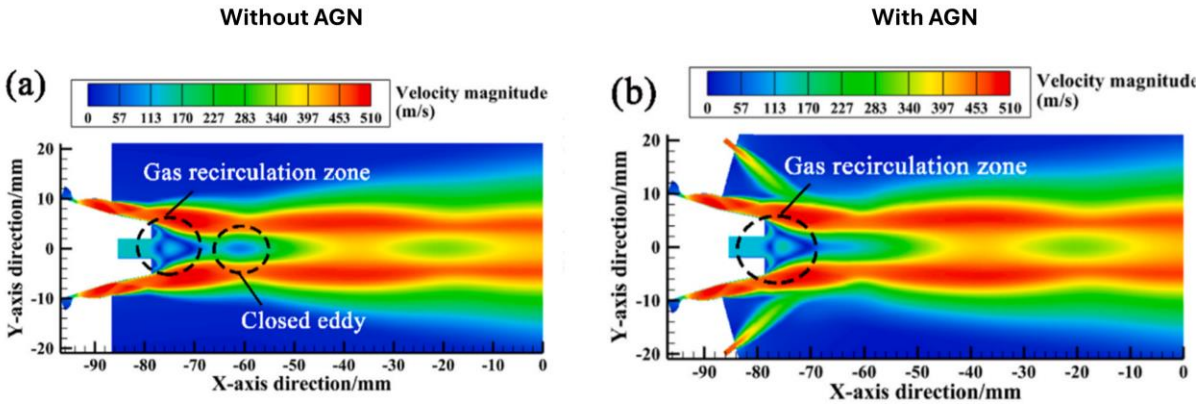

Figure 3.12 Velocity contour of gas-only flow simulation for a) gas nozzle without AGN, b) gas nozzle with AGN (Wang et al., 2024b).

Although gas-only flow studies provide a good insight into the process, it does not provide a deeper understanding of gas-melt interactions and of the physical process. This demands CFD models involving two-phase flow to have a comprehensive understanding of the process and its background physics.

3.2.2 Two-phase: Multi-phase flow

With development of advanced and efficient CFD models and increased computational power, the CCGA simulations were further extended from single-phase flow to two-phase flow

to accurately predict the gas-melt interactions and to deepen the understanding of the background physics. The two-phase flow is simulated broadly via two methods: Euler-Euler framework and Euler-Lagrange framework (Section 2.5.5 discusses more on this). The Euler-Euler framework which is also known as Volume of Fluid (VOF) model considers both the gas and the melt as a continuum, whereas the Euler-Lagrange framework, which is also known as Discrete-Phase model (DPM) considers the gas as a continuum and the melt as a discrete phase. However, both VOF and DPM are widely used in modelling the CCGA process, and the studies which employed these two approaches are discussed in this section. A compilation of various CFD studies carried out on CCGA process, detailing their key models employed in the study is presented in the Appendix.

Zhao et al. (2012) employed 2D VOF model to investigate the melt entrainment and the pre-filming phenomena. The study revealed the formation of liquid sheets from liquid column and also revealed the presence of short-wave propagation in the liquid sheet which facilitated the droplet break-up. The model predicted that, after pre-filming, the liquid sheet would exhibit cyclic alternation in the direction of stripping: first the sheet would be stripped radially inward towards the axis, followed by radially outward stripping away from the axis. This continuous fluctuation in the direction of stripping is primarily due to the gas-melt interaction, ultimately leading to changes in the aspiration pressure as observed by Ashokkumar (2020). The study employing VOF model was further extended by Liu et al. (2023b), and investigated effect of melt flow rate, gas inlet pressure and gas temperature on the primary break-up. A critical force balance was derived to determine the break-up mode based on the experimental study. Based on the different forces – gravity (F_g), buoyancy (F_f), drag force (F_d), and gas pressure (F_p), it was derived that $F_p + F_f > F_d + F_g$ resulted in umbrella deformation (liquid film), whereas $F_p + F_f < F_d + F_g$ resulted in 'fountain' deformation. This is shown in Figure 3.13a-b. Corroborating with the force balance the study revealed, for lower melt flow rate the melt underwent umbrella (liquid-film) break-up, and for higher melt flow rate the melt underwent fountain break-up. This in terms of GMR was evaluated that for GMR ≥ 4.4 the melt underwent umbrella break-up, and for GMR ≤ 4.3 the melt underwent fountain break-up. Based on the force balance, in another study conducted by Wang et al. (2021) it was reported that $F_p + F_g + F_d > F_f$ ensured smooth running of the CCGA process, whereas $F_p + F_g + F_d < F_f$ risked in melt freeze-off. This is shown in Figure 3.13c-d.

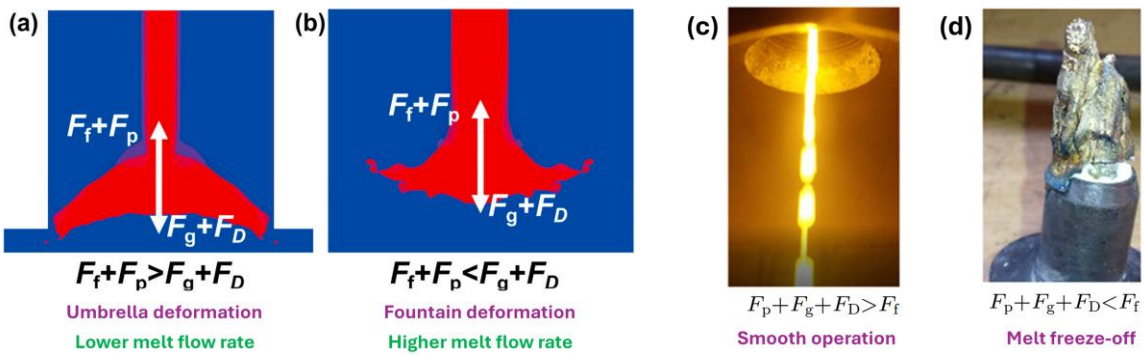

Figure 3.13 Force balance identifying, the melt break-up mode – a) Umbrella deformation and b) Fountain deformation; and CCGA operation – c) smooth operation and d) melt freeze-off (Liu et al., 2023b, Wang et al., 2021).

Additionally, more CFD studies have been conducted employing VOF model to investigate the impact of gas inlet pressure on primary atomisation. Liu et al. (2023b) reported that with increasing gas inlet pressure, the aspiration pressure increases, resulting in delayed melt entrainment from the melt nozzle. The results were consistent with that of the study conducted by Wang et al. (2023b). Moreover, studies carried out by Liu et al. (2023b) and Wang et al. (2023b) captured the phenomenon of nozzle clogging at lower gas inlet pressures as experimentally observed by Motaman et al. (2013). Although the low-pressure region created between the gas nozzle exit and melt nozzle wall facilitates the melt back stream flow leading to nozzle clogging, the nozzle clogging is primarily because of the increased cooling rate due to the low pressure (Wang et al., 2023b). 2D VOF model was employed in another study carried out by Wang et al. (2024a) to further investigate the effect of nozzle clogging using two different melt entrainment sequence: Type1 – gas flow followed by melt introduction, and Type2 – first melt introduction followed by gas flow. The model predicted that under increasing gas pressure, Type1 flow experiences nozzle clogging at low pressures, but Type2 flow do not experience nozzle clogging for any of the pressures, which is attributed to the 'necking' break-up mechanism of the liquid column rather than the liquid sheet formation observed during pre-filming. However, in commercial CCGA process, Type1 melt entrainment is followed, and not Type2. This is because, in type2, molten metal falling to the bottom of the chamber would solidify into a sizeable mass making it difficult to be removed.

Similar to the 2D VOF studies, research were conducted on 3D VOF model. Zeoli et al. (2012) studied the melt entrainment and primary atomisation in CCGA process both under steady and transient conditions. In the study, for the steady-state simulation, RSM turbulence model, and for the transient simulation LES turbulence model, were employed. The transient simulation captured well the instability in the gas-melt interaction, whereas the steady-state

simulation predicted a simple 'fountain' shape melt structure without pre-filming. In the transient simulation, the melt entrainment was far from predictable, and moreover, the model also successfully captured the pre-filming seen in the physical process. In addition to that, the model also captured the complex asymmetrical recirculation zones at the nozzle front, leading to the melt plume being displaced off-axis as experimentally observed by Mullis et al. (2010) and Mullis et al. (2011). Although the model revealed the complexity in the recirculation zones and instability in the gas-melt interaction, the model under-predicted the process in general and did not capture the secondary melt break-up, despite a high GMR of 3.3.

Arachchilage et al. (2019) extended the 3D VOF model to investigate the secondary atomisation in detail under increasing gas pressures using LES as turbulence model. The study revealed that the chaotic interactions close to the gas-melt interface creates perturbations in the melt and leads to interfacial instabilities and ultimately to melt break-up. Moreover, in addition to the interfacial instability it was found that the mechanism of liquid column deformation is also determined by the presence of whether shear force exist either side of the melt stream or not. Although higher gas pressures resulted in finer particles, due to the increased velocity of the gas, the melt column is briefly cut-off at the focal point of the gas-jet, in a process known as pinching, as observed by Wang et al. (2024a). Subsequently, because of the increased aspiration pressure at higher gas pressures, the incoming melt accumulated at the melt nozzle tip, leading to potential melt freeze-off. Similarly, another study carried out by Wang et al. (2023e) extended the same 3D VOF model with LES to investigate the effect of gas pressure on the gas-melt interaction using Adaptive Mesh Refinement (AMR). The study quantitatively validated and corroborated the findings of Arachchilage et al. (2019) – effects of increasing gas pressure. Additionally, the model predicted that during the droplets' flight downstream they undertake two different paths sequentially. Initially they converge towards the axis, and thereafter for the remainder of the distance downstream they disperse radially away. Increasing gas pressure increased more droplets to converge, leading to the increased particle size and satellite formation. However, this adverse effect could be prevented by changing the gas nozzle angle. To study gas nozzle angle effect three different angles were investigated: 20°, 40° and 60°. The study revealed, initially with increasing gas pressure 40° reduced the particle size compared to 20° and 60°. However, further increase in gas pressure resulted in increased particle size, even though the droplets underwent substantial dispersion. At higher pressure, 60° nozzle angle performed well to produce smaller particles even though the model indicates the droplets to undergo more converged and columnated flight downstream (Wang et al., 2023e).

The effect of gas inlet pressure was further investigated using 3D VOF model by Wang et al. (2024b) using secondary gas nozzles as seen in Figure 3.12. The model included both the melt break-up and solidification models to examine the atomisation process under different primary and secondary gas pressures. The model predicted that for lower secondary gas nozzle pressure, the melt underwent only ligament shedding with 35-50% of the melt existing in liquid phase with no droplet formation. With increase in secondary gas pressure, droplets were created from ligaments although the majority of the ligaments transitioned into semi-solid state losing its ability to break-up. With further increase in pressure, significant secondary atomisation was predicted, wherein 40-70% droplets are in liquid phase. Although higher secondary gas pressures resulted in effective atomisation, lower pressures resulted in low aspiration pressure. Contrasting to the force balance outlined by Wang et al. (2021) for a smooth running of the process, i.e., $F_p + F_g + F_d > F_f$, Wang et al. (2024b) also utilised the force balance and reported that $F_p + F_g + F_h > F_d + F_f$ ensured the smooth running of the process, where F_h is the hydraulic pressure force

Similar to the VOF model, various studies have been carried out using discrete-phase model (DPM). DPM is employed to investigate the gas-melt interactions and to analyse the particles' dimensional and thermal properties. Similar to the VOF model, studies have been conducted both in 2D and 3D DPM, including cases with and without particle break-up. A contrasting detail between VOF and DPM is that the VOF model can simulate both primary and secondary atomisation, provided the mesh resolution is fine enough to capture the micro-scale particles, while the DPM model is limited to only simulating secondary atomisation, since the melt is directly injected in the form of particles.

Ashokkumar (2020) investigated the CCGA process under closed-wake condition, i.e., with the presence of Mach-disk in the gas flow-field, employing DPM without droplet break-up, to analyse the melt flow behaviour near the melt nozzle and far-field downstream. The model captured well the pre-filming process and the particle swirl in the recirculation zone. Similarly, Luo et al. (2023) employed DPM without droplet break-up to investigate the elemental loss in the particle during their flight. The study predicted bigger particles lose more of their element compared to the smaller particles. And in addition to it, decrease in melt over-heat resulted in reduced elemental loss. Nevertheless, studies conducted by Zeoli and Gu (2008b), Wang et al. (2023c), and Liu et al. (2023b) predicted that increase in gas temperature reduced the particle size. This is because of the increased kinetic energy in gas leading to higher velocity gas.

DPM model with different droplet break-up models were studied to explore the suitability and to analyse the secondary atomisation behaviour influenced by gas temperature, gas pressure and other operating and design factors. Although there are numerous break-up models such as Taylor Analogy Break-up (TAB) model, Kelvin-Helmholtz (KH) model, Wave model, Rayleigh-Taylor (RT) instability model, Kelvin-Helmholtz Rayleigh-Taylor (KHRT) model, and Schmehl model, in the context and scope of numerical modelling of CCGA process, three break-up models are widely used, and they are TAB, KH, and KHRT models.

Studies conducted by Firmansyah et al. (2014) and Kaiser et al. (2018) employed KH break-up model to investigate the influence of gas on droplet break-up along the radial direction. Both studies indicated that the maximum droplet break-up occur in the gas-jet core region compared to the gas-jet periphery (inner and outer sonic boundary). And in fact, the particles closer to the axis experienced very little influence from the gas-jet, which might be explained as one of the factors for increased particle size. This has been supported by the droplet break-up and Weber number results obtained from the simulation. The KH break-up model was compared against TAB model by Zhang et al. (2023a) and the results were validated against experimental results. The PSD obtained from the two models exhibited two different distributions: The TAB model exhibited a symmetrical distribution about median particle size whereas the KH model exhibited an asymmetrical distribution. The experimentally obtained PSD were closer to the PSD obtained from TAB model, possibly indicating TAB model is more suitable for droplet break-up modelling.

Although the break-up models: TAB model and KH model have been advantageous in modelling the CCGA process, they are each applied to different ranges of Weber number. TAB model worked better for lower Weber number, ranging between 12-100, capturing the bag break-up (Figure 2.9). In contrast, the KH break-up model performed better for higher Weber number, ranging between 80-800, effectively capturing the stripping and catastrophic break-up and were in good agreement with experimental data (Thompson et al., 2016, Wang et al., 2021). To accommodate wider ranges of Weber number into the break-up model, Zeoli and Gu (2006) developed hybrid break-up, TAB-KH model, which activated TAB model for $12 < We < 80$, and KH model for $80 < We < 800$. Comparing the numerical PSD with the experimental results, the predicted mean particle diameter and standard deviation obtained from the simulation matched closely with the experimentally obtained values. Zeoli and Gu (2008a) and Zeoli and Gu (2008b) also employed the same hybrid TAB-KH model to investigate the droplet break-up and droplet cooling for three different particle sizes (1, 3, and 5 mm), and three different gas temperatures (300K, 400K, and 500K). The model predicted all the droplet break-up

occurred within 100 mm downstream along the axial direction, although the solidification of the droplets started at 500 mm downstream, i.e., five times the break-up distance for 1 mm particles, but break-up distance of 200 mm for the 5 mm particle. The above results were contrary to those obtained by Zeoli and Gu (2006), whose study revealed that 1 mm particles solidified at a much earlier distance than 500 mm, while 5 mm particles solidified at a much later distance downstream than 200 mm. Moreover, Firmansyah et al. (2014) reported the KH model was better and closer to the experiment results than hybrid TAB-KH model. This might indicate the hybrid TAB-KH model's inability to robustly capture the cooling and solidification phenomena. Albeit the hybrid model rightly predicted the reduction in particle size with increasing gas temperatures (Zeoli and Gu, 2008a).

Similar to the hybrid TAB-KH model, Wang et al. (2023c) employed KHRT break-up model, which is a combination of KH and RT break-up models. It combines the influence of KH waves affected by aerodynamic force along with the RT instabilities due to the acceleration of shed particles ejected into the free stream. The droplets formed from the liquid column are subjected to sudden acceleration because of the high speed gas-jet, and under such conditions the RT instability becomes the domain effect. The radius of the child droplet is determined by the RT wave number (λ_{RT}), wherein the droplet break-up commenced only when λ_{RT} value is smaller than the parent droplet diameter (Wang et al., 2021). Since the KHRT model is effective for high Weber number (We > 80), it was utilised to investigate the effects of varying gas inlet pressure, gas temperature and melt flow rate. The KHRT model predicted that with increasing melt flow rate from 0.025 to 0.1 kg s^{-1}, i.e., GMR 6.5 to 1.6, the particle mean diameter increased by a factor of 2.7 while the cooling rate reduced by a factor of 2. However, the dispersion cone angle observed in this study was much smaller compared the dispersion cone angle observed in the study conducted by Thompson et al. (2016) who also employed the KHRT model. It was expected that increased gas inlet pressure would result in increased dispersion cone angle. On the contrary, it decreases, which can aggravate the collisions between droplets. The model also correctly captures the trend in the effect of increasing gas temperatures on the droplet break-up; increasing gas temperature from 300K to 500K reduced the particle size by 20% and increased the cooling rate by a factor of 2. A comparative analysis between the two hybrid break-up models, TAB-KH and KHRT models was conducted by Thompson et al. (2016) using an initial droplet size of 1 mm. The study revealed that the TAB-KH model heavily under-predicted the particle break-up and dispersion. Moreover, the model revealed the gas velocity of the flow with the particles is nearly the same as the gas velocity without particles loading. This however would not be true since, the particle loading in the domain would

diminish the energy of the gas flow. However, on the other hand the KHRT model effectively captured the substantial decrease in the gas velocity from ~500 ms^{-1} to ~200 ms^{-1} with particle loading. Similarly, for increasing melt flow rate, i.e., for decreasing GMRs, the KHRT model predicted increase in the particle size, and was consistent with the experimental results. Another finding was that the TAB-KH model predicted a decrease in the particle size with increase in melt flow, which generally would not be true. From these above results, it indicates that the TAB-KH model clearly under-predicted the droplet break-up in the CCGA process.

To further study the primary and secondary atomisation, recently a transitional model was developed which models the melt as a VOF model initially, and thereafter transitions it into DPM depending on the size of the droplet. This allows to capture the primary atomisation – the transition from liquid column to ligaments or sheets via the VOF model; and secondary atomisation – droplet breakup and solidification via the DPM model. The VOF-DPM model for CCGA process was studied by Wang et al. (2021) and Hua et al. (2024). The studies were conducted as 3D transient simulation using LES as turbulence model. These aspects of the simulation clearly indicate an increased requirement of computational resource to run the model compared to the earlier discussed models. Also, the studies have implemented KHRT break-up model for the DPM part of the model, owing to its robustness in predicting the droplet break-up. Results of the VOF part of the VOF-DPM simulation reported by Wang et al. (2021) were consistent with the VOF simulation conducted by Zeoli et al. (2012). Similarly, the DPM part of the simulation effectively predicted the initial converging flow and subsequent dispersion of droplets as reported by Wang et al. (2023e) and Luo et al. (2023). However, unlike the VOF studies reported by Wang et al. (2024b), Zhao et al. (2012), Wang et al. (2023e) and Arachchilage et al. (2019), the VOF-DPM model revealed the melt underwent primary atomisation without pre-filming at the melt nozzle tip.

Similarly, Hua et al. (2024) conducted simulation using the VOF-DPM model and investigated the effect of different GMRs using different break-up models. The study compared KHRT model, Wave model, TAB model, SSD model, and Schmehl break-up model against the experimental results and validated KHRT model to be closer to the experimental results. However, the model generally overestimated the PSD. For lower GMR, the overestimation was well within the tolerance limits. Even for higher GMR cases, the model effectively captured the d_{10} and d_{50} within good tolerance. However, the model significantly over-predicted the d_{90} value for the higher GMR cases. This discrepancy may be attributed to the model's assumption that the gas flow is incompressible, although it would be compressible in nature at pressures of 3.5 and 4.5 MPa.

Based on the insights derived from previous research highlighted in the literature review, and considering the practical feasibility of conducting such computationally intensive simulations, the following CFD methodologies have been selected. The CFD simulation is run using commercial CFD code ANSYS Fluent owing to its enormous resource on public platform and ample existing documentation of gas atomisation simulations. 2D-axisymmetric domain was considered to reduce the computational cost; the primary phase, argon was considered compressible owing to the high pressure and the orifice of the nozzle; secondary phase is considered to be inert particles, as the focus is on gas-melt interaction rather than explicitly understanding the melt breakup. And to introduce melt as particles, DPM is employed; however, particle breakup is not considered to reduce the computational cost. Exploiting the in-built module within ANSYS Fluent, the aspiration pressure and the melt mass flow rate are coupled programmatically via User-Defined Function (UDF). Based on the analysis from literature review, no research has been carried out to understand the effect of melt temperature and melt flow rate in a fully-coupled gas atomisation process. Hence, two important parameters – melt flow rate (via GMR), and melt temperature, were investigated in the fully-coupled model to understand how the parameters affect the process.

3.3 Aim and objective of the thesis

This thesis investigates the CCGA process through numerical modelling to examine the effect of gas-to-melt ratio (GMR) and melt temperature, and their association with the process instability. (GMR is the ratio of the mass flow rate of the gas flow to the mass flow rate of the melt). This thesis specifically focusses on understanding the process instabilities both in the gas and melt flow generated due to the gas-melt interactions, and does not endeavour in the understanding of the primary and secondary melt break-up mechanisms and particle characteristics. The primary objectives of this thesis are:

- To develop a two-dimensional (r-z coordinates) numerical domain based on a physical atomiser design, and model a two-phase flow using two-way coupled Euler-Lagrangian framework.
- To implement a user-defined function (UDF) into the developed model, to couple the melt flow rate with the aspiration pressure, to reflect the physical CCGA process.
- To investigate the gas and melt flow, both quantitatively and qualitatively for varying GMRs and melt temperatures to understand the nature of the process and the type of instability induced in the process.

- To analyse the gas and melt instabilities developed in the process for various combinations of GMR and melt temperature, and to comprehend the association between the instabilities, to map the trend in the instability for varying GMR/melt temperature.
- To conduct comparative study between gas flow-field of the low and high melt temperature cases to elucidate the anomaly in their instabilities reflecting the unpredictable nature as seen in the gas atomisation, thereby illustrating the mechanism of their instabilities.

4 Methodology of the numerical modelling

With the current research focussing on the CFD analysis of a research-scale based CCGA process, it is imperative to transfer the data observed and used in the physical atomisation process, both the primary phase – gas, and the secondary phase – melt, on to a numerical platform to numerically model and solve the atomisation process. It is also important to transfer as much as information possible on to the numerical model so as to meaningfully run a simulation that is a representative and reflection of a physical case. However, in doing so, it usually results in expensive computational cost. Hence, to balance both accuracy of the model within acceptable tolerance and reasonably use the computational resources, the transferred information on to the numerical model is carefully selected.

CFD modelling includes establishing a numerical domain, followed by discretising the numerical domain into smaller parts known as mesh. The boundary conditions are applied to the numerical domain, and the governing equations are solved. After solving, the obtained results are visualised and analysed using appropriate post-processors. Since the CCGA process involves two phases, primary and secondary, in this CFD study they are modelled separately, and the mass flow rate of the secondary phase is coupled together with the aspiration pressure of the primary phase via User-Defined Function (UDF). The CFD model discussed in this thesis is developed using ANSYS Fluent, a Finite Volume Method (FVM) based commercial CFD code. The flow chart of the methodology is presented in Figure 4.1.

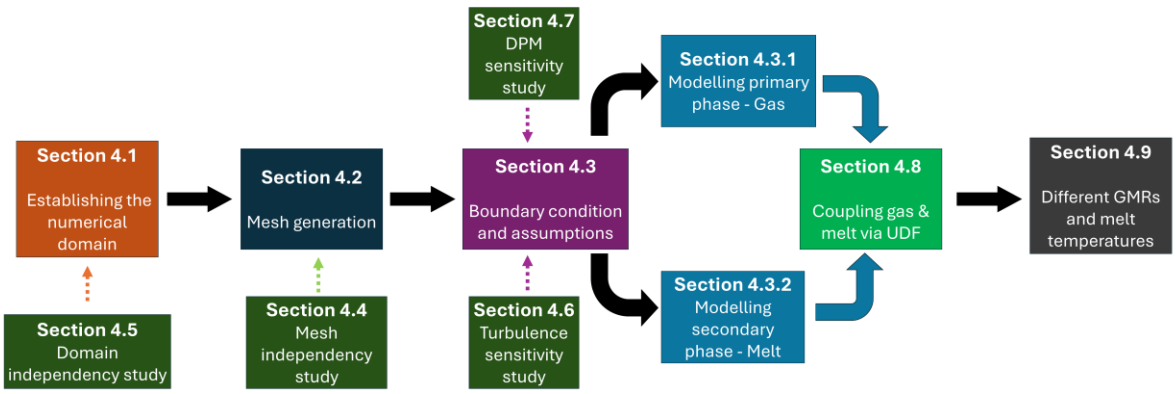

Figure 4.1 Schematic showing the flowchart of methodology.

4.1 Establishing the numerical domain of the gas atomiser

The primary step in the CFD modelling involves creation of a numerical domain replicating a physical atomiser (Figure 4.2a). The numerical domain is created based on the

close-coupled gas atomiser having annular slit gas-die as shown in Figure 4.2b. Owing to the symmetry about the atomiser's axis the numerical domain was modelled as a 2D axisymmetric model. The geometrical extent of the numerical domain is presented in Figure 4.3, wherein its extent is about 12 melt nozzle-diameter (N_d) in the radial direction (r-direction) and 25 N_d in the vertical direction (z-direction). The geometrical dimensions of the numerical domain are thus considered to allow a sufficient far field area, ensuring that the gas-flow is not affected by the extent of the domain or by the boundary condition they possess. The geometrical extent of the numerical domain is decided following a domain sensitivity test investigated in Section 4.5. Although the installation and working of the physical atomiser is about the vertical direction, for presentational purposes the numerical model of the atomiser is presented by rotating it 90° counter-clockwise as shown in Figure 4.3.

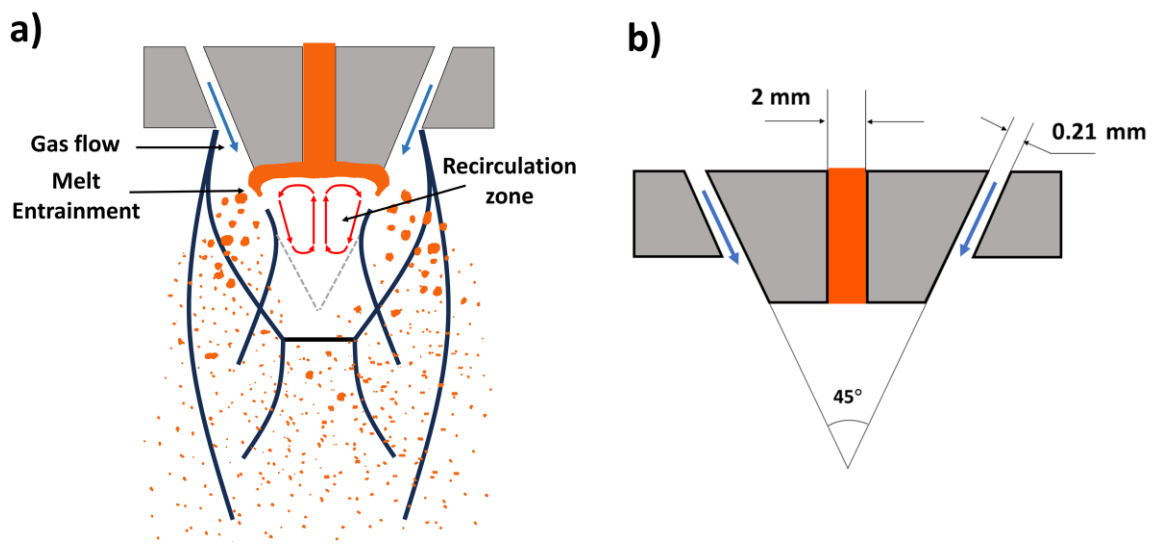

Figure 4.2 a) Schematic representation of the gas atomiser having annular slit gas-die, showing the gas flow and melt entrainment; b) the schematic diagram of the melt nozzle used in this study showing key dimensions of the design – melt nozzle diameter, 2 mm; gas nozzle diameter, 0.21 mm; and melt nozzle angle, 45°.

The adopted atomiser design is based on a CERAM PSI atomiser adopted from (McCarthy et al., 2013) containing 18 discrete gas nozzles, radially equidistant, as shown in Figure 3.6. On observing the schlieren images of the gas flow-field during gas-only condition, irrespective of the type of gas nozzle, whether cylindrical or C-D nozzle, the flow-field was observed to possess a uniform radial profile due to the combination of gas-jet nozzles arranged radially equidistant (Motaman, 2013). Based on this observation, the 3D atomiser domain is approximated into 2D axisymmetric domain, and hence an annular slit gas nozzle is adopted for this CFD study.

Although, in the physical atomiser a melt delivery tube is present to bring in the melt from the tundish, for this CFD study the melt delivery tube is not considered. This is because in the physical atomisation process, the gas in the atomisation chamber will not enter into the melt delivery tube. Hence, the melt delivery tube is eliminated and replaced with a wall where melt is injected. This is discussed in Section 4.3.2 which discusses the boundary condition and implementation of the secondary phase – melt.

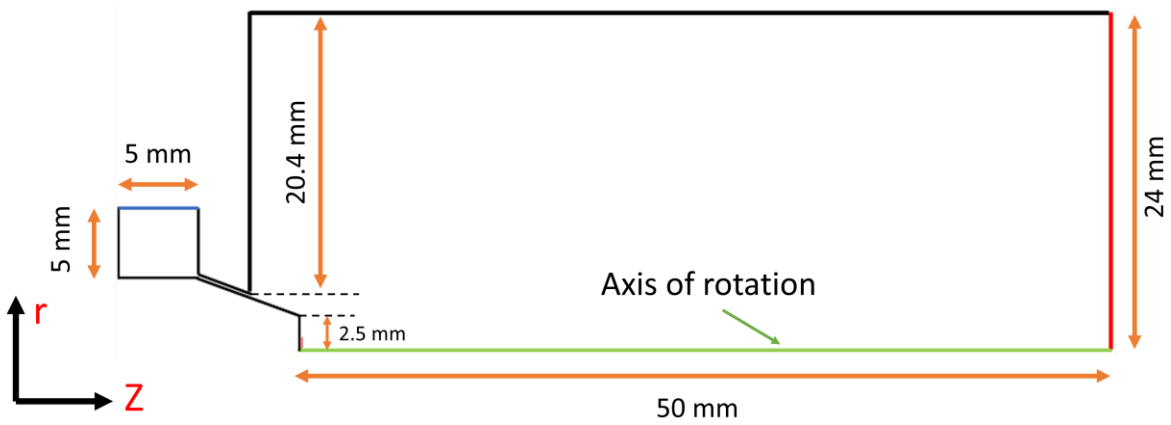

Figure 4.3 The numerical domain with geometrical dimensions used in this study.

4.2 Mesh generation

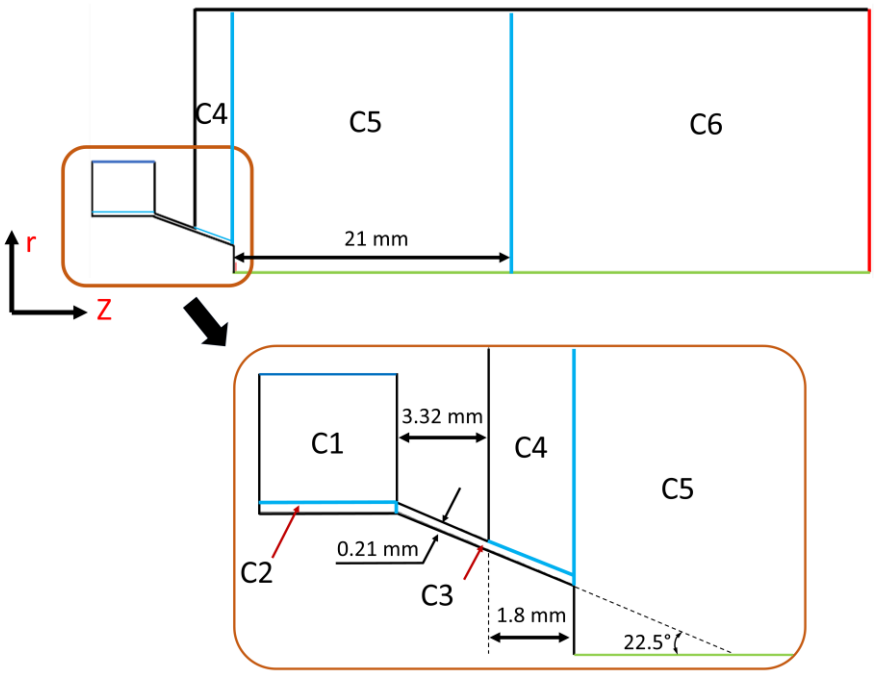

Figure 4.4 Schematic representation of compartmentalised numerical domain.

Following the determination of the numerical domain – geometry and dimension, based on the domain sensitivity study (presented in Section 4.5), the domain is discretised into smaller sub-domains called elements via a process known as meshing. The numerical domain is compartmentalised into six parts before creating the mesh. The compartmentalisation of the domain is shown in Figure 4.4, divided using the light blue lines. Compartmentalisation is carried out to effectively divide the domain into sections of regular shape to produce structured mesh. Although unstructured mesh can be incorporated for the domain, considering the simple geometry of the domain; no movable boundaries; and other advantages such as reduced mesh connectivity data, decreased complexity and higher accuracy, structured mesh is considered and incorporated for this domain (Ashokkumar, 2020). All of the six compartments of the domain were individually meshed with different mesh refinements based on the flow behaviour observed in their respective part. It is vital to generate a fine mesh to capture all the flow characteristics, however, a trade-off should be achieved, so as to not to make the model computationally intense. This process of generating optimum mesh size will be carried out by conducting a mesh independency study, and it is presented in Section 4.4. The mesh element sizes employed for the different compartments are tabulated in Table 4-1. As observed in Table 4-1, compartments C2 and C3, which are the nozzle regions, were meshed finely to capture the supersonic flow characteristics, whereas compartment C6, the far field region was meshed relatively coarser.

Table 4-1 Mesh element sizes used in the different compartments of the numerical domain for the mesh considered for the study.

Compartments	**Mesh element size (z x r)**	**Dimension of the compartment (z x r)**
C1	0.1 mm x 0.1 mm	5 mm x 4.78 mm
C2	0.1 mm x 0.04 mm	5 mm x 0.22 mm
C3	0.1 mm x 0.04 mm	5.12 mm x 0.22 mm
C4	0.1 mm x 0.1 mm	1.8 mm x 20.4/21.5 mm
C5	0.1 mm x 0.1 mm	21 mm x 24 mm
C6	0.15 mm x 0.1 mm	29 mm x 24 mm

The generated mesh based on Table 4-1 is presented in Figure 4.5, showing the mesh of the entire numerical domain and the zoomed in section of the gas nozzle region. This generated mesh observed in Figure 4.5 is employed for all of the simulations and is carried out by iteratively changing the element's size such that the flow characteristics captured by the optimal mesh size do not change with any further with decrease in its mesh size. The mesh independency study carried out to generate this optimal mesh size is discussed in Section 4.4.

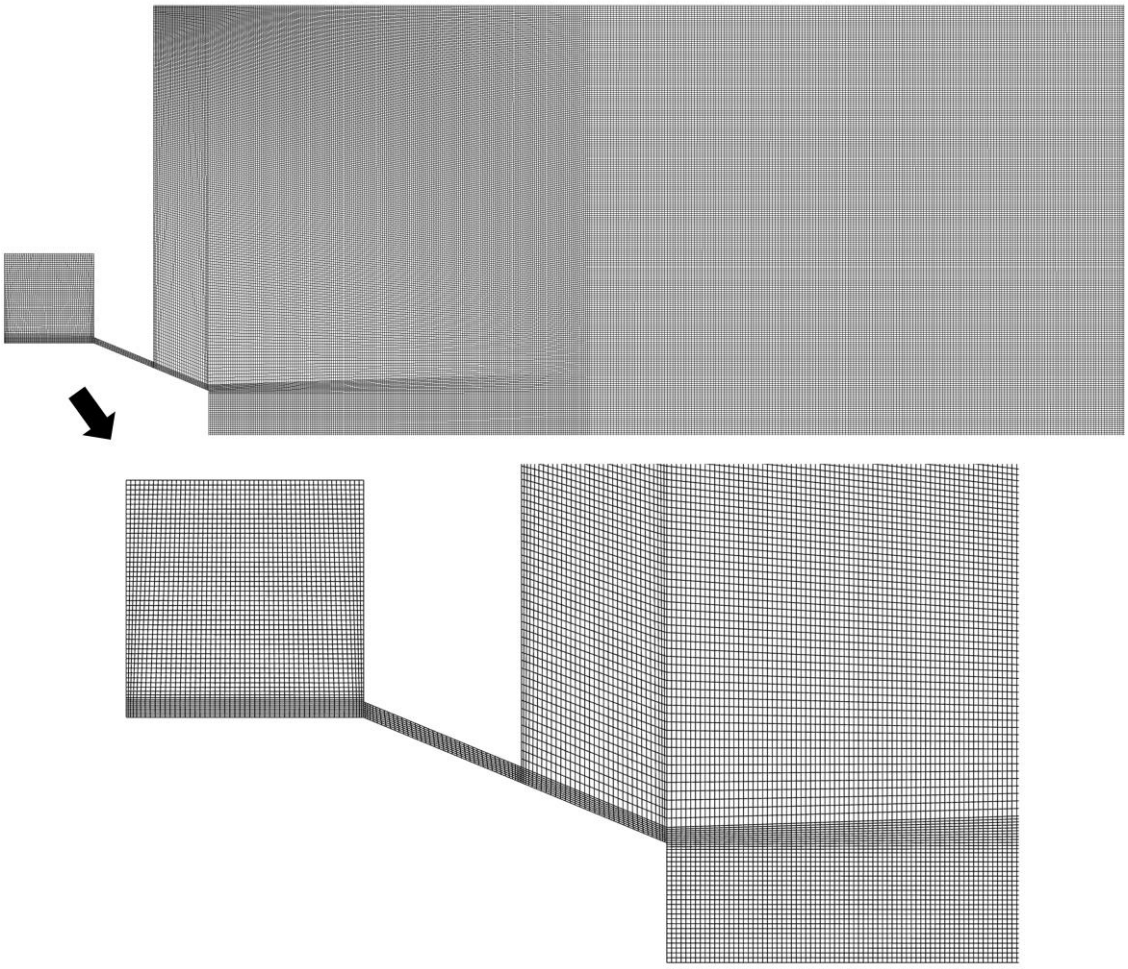

Figure 4.5 Mesh for the entire numerical model and for the gas nozzle section showing the refined mesh.

4.3 Boundary conditions and assumptions considered for the CFD model

Following the mesh generation, the boundary conditions and their appropriate initial values were applied to the different parts of the numerical domain. The part of the domain where the operating gas enters is assigned as the 'Pressure Inlet'. Since, the gas entering is specified in terms of its pressure, it is considered as pressure inlet. Similarly, the part of the domain where the fluid exits the atomiser is assigned as the 'Pressure Outlet'. Usually, the outlet of an atomiser is at atmospheric pressure, hence the same is applied to the model's outlet. It has to be noted both the gas and melt have their separate inlets, but they exit through the same outlet. The other parts of the domain are considered as 'Stationary Wall' with no slip condition, as a physical atomiser setup is a stationary machinery, anchored to the ground. Moreover, the temperature of all the boundaries – inlet, outlet and the wall were set at a constant temperature of 300K. Likewise, the gas temperature at the inlet is also kept at 300K, however,

the gas upon expanding reduces in its temperature. Boundary conditions applied to different parts of the numerical domain are presented in Figure 4.6 and Table 4-2.

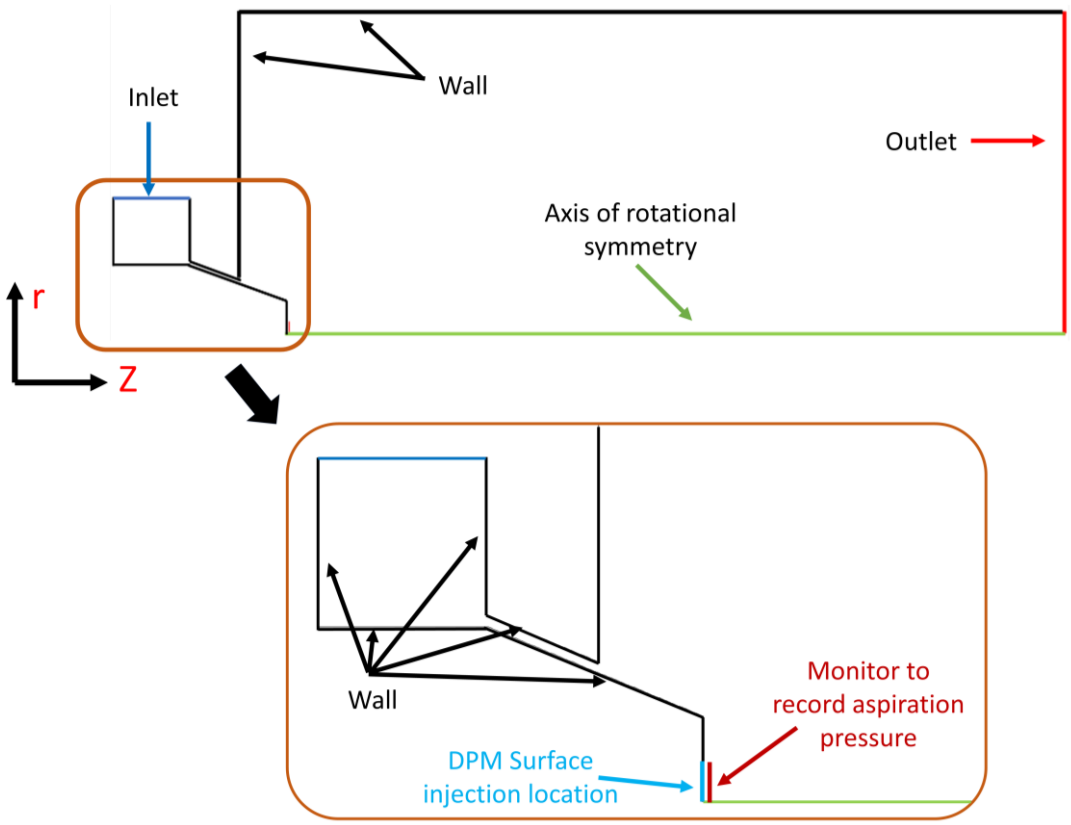

Figure 4.6 Boundary conditions applied to the different parts of the numerical domain.

Table 4-2 Boundaries in the domain and their applied conditions.

Boundary	**Conditions**
Inlet	Pressure Inlet; P = 4.5MPa; Argon; T=300K; ideal-gas law.
Wall	No-slip, stationary wall, u=v=0; T=300K; κ=0, ω=0; DPM particles reflect.
Axis	Axis of rotational symmetry; DPM particles reflect.
Outlet	Pressure outlet; DPM particles escape.
DPM Inlet	Particle size = 500µm; velocity = 1.38 ms^{-1}; density = 3850 kg m^{-3}; particle type = inert; two-way coupling; no droplet breakup; Stochastic tracking.

4.3.1 Modelling and implementation of the primary phase – gas

The primary phase – gas considered for this study is the usually considered ideal gas in the atomisation process, which is Argon. Since the high-pressure gas enters into the plenum at

supersonic speeds, the gas is modelled as a compressible fluid. The conservation equations of continuity, momentum and energy were solved for the compressible fluids using the unsteady Reynolds Averaging Navier-Stokes (RANS) equation. The RANS equations solved for the study are discussed in Section 2.5.2. With the flow occurring within turbulent regime, the gas flow is modelled using k - ω standard turbulence model as they have reliably shown to well-predict the flow, whereas the k - ε and k - ω SST models have shown to underpredict the flow velocity and have failed to develop Mach-disk seen at higher pressures (Ashokkumar, 2020). Furthermore, four different turbulence models were investigated as part of this study to obtain the optimal turbulence model, i.e., k - ω standard, and their results are presented in Section 4.6. Since, the flow is modelled as a compressible flow, density is solved using the compressible ideal-gas equation and hence a density-based solver is utilised. The model is solved using implicit second order formulation, a higher order formulation, to reduce the error, and to obtain accurate results.

An inlet operating pressure of 4.5 MPa is used so as to run the model under closed-wake condition. This operating pressure was determined after carrying out preliminary gas-only flow simulations at different operating pressures. Also, the results of the study carried out by Ashokkumar (2020) corroborates with the results of gas only-flow study conducted for this work. The temperature of the operating gas is set to 300K. In addition to this, a monitor is set up near the melt nozzle exit, as shown in Figure 4.6 to record the aspiration pressure, which is then coupled with the melt mass flow rate. The coupling between the aspiration pressure and melt flow rate is discussed in Section 4.8.

The following assumptions were made for the primary phase (gas) to simplify the numerical calculations and to reduce the computational cost:

- The gas flow is considered to be transient.
- The gas flow is considered to be 2D axisymmetric.
- The operating gas is considered to be Argon and is modelled as a compressible ideal gas with an inlet temperature of 300K.
- The presence of secondary phase – melt is not considered for the preliminary gas-only flow studies, such as mesh independency and domain independency studies.

4.3.2 Modelling and implementation of the secondary phase – melt

With the introduction of the secondary phase – melt, the model becomes a two-phase flow, and two-phase flows can be modelled in two ways: in the Eulerian - Eulerian (E-E) approach and the Eulerian - Lagrangian (E-L) approach. In the former approach, the melt is modelled as a fluid, whereas in the latter, the melt is modelled as particles. Using the E-E approach, the melt break-up and the trajectory of the melt droplet downstream is modelled. However, this comes with some significant disadvantages; very fine mesh would be necessary to capture the melt break-up and the droplets movement; increased computational cost to run such a refined mesh; and increased run-time, but reduced simulation time (flow-time) resulting in inefficient capturing of the gas-melt interactions. The other approach, i.e., E-L approach, which is also known as Discrete-Phase Model (DPM), where the melt is modelled as particles, the mesh size required is bigger than the particle size, hence resulting in lesser computational resources, facilitating longer simulation time. Moreover, this study focusses on the coupling between the gas and the melt, and their interactions rather than explicitly attempting to resolve the highly complex melt breakup. Hence the E-L approach using the DPM model is adopted for this study. More details on the above two approaches are discussed in Section 2.5.5.

In the physical atomisation process, the melt is introduced from the tundish (reservoir) into the atomisation chamber via the melt delivery tube. However, the atomising gas do not enter into the melt delivery tube. Hence, the melt delivery tube is eliminated and is replaced with a wall. The wall is the melt delivery tube's exit, which is also known as melt nozzle exit, and is assigned as the location where the melt is injected in the form of particles into the atomisation chamber. This is shown in Figure 4.6. The method adopted to inject particles into the atomisation chamber is via surface injection, this is because in the physical atomisation, the melt is present as a continuum filling the entire melt delivery tube. The light blue line in Figure 4.6 which constitutes the melt delivery tube's exit is assigned as the surface to inject the particles. Although the term 'surface injection' might make one to think as a continuum, the particles are injected from every mesh edge of the surface assigned.

Even though the size of metal powders obtained from the atomisation process varies between 15 and 500 μm (Anderson et al., 2018), for this work the DPM particles were modelled as a constant-diameter particle of 500 μm. This diameter is considered so as to reduce the computational load and at the same time utilise the particle size that is within the yield size range i.e. 15-500 μm. With the decrease in particle size, there would be an increase in number

of tracked particles within the domain, correspondingly leading to an increased computational load and longer run-time. Moreover, particle size of 500 µm is employed, as that's the order of size of the particles existing in the primary atomisation zone (Ashokkumar, 2020), and this will be supplementing towards the understanding of the gas-melt interactions in the wake region more specifically. DPM sensitivity study on particle size is investigated as part of the study and is discussed in Section 4.7. The particles are considered to be inert and to understand the interaction between gas and the melt, two-way coupling is employed along with Discrete Random Walk (DRW) model. DRW model reintroduces the random flow fluctuations that are averaged in RANS equations, thereby facilitating in the capturing of the particle dispersion in the wake and far downstream region reflecting the physical process. The DRW model is discussed in Section 2.5.7. Although higher order of coupling, such as three-way or four-way coupling could be employed, considering the computational cost they are not employed. The mechanism of the two-way coupling between the Eulerian phase and the Lagrangian (DPM) phase is presented in Section 2.5.8. The particles on impacting the wall and axis of the atomiser get reflected and do not adhere to it; for the domain outlet, the particles escape.

Since the velocity and trajectory of the particles within the gas flow will be determined by the nature of the drag force upon those droplets, in this work the spherical drag law that scales based upon the Reynolds number approximation of Morsi and Alexander (1972) is employed. With the shape and diameter of the particle fixed, drag coefficient (C_d) remains constant. Also, in order to ensure the model accurately reflects actual atomisation process, the magnitude of the drag force is set so as to reflect typical velocities actually observed in atomisation melt plume. For this purpose, this study referred to the work of Bigg & Mullis (Bigg and Mullis, 2020), who used a statistical image tracking technique to map velocities within an atomization plume, and the findings showed that these varied from a few metres per second in the plume centre to a few tens of metres per second on the plume margins where the interaction of the gas and melt is strongest. Allowing for a slight underestimation of velocity in the work of Bigg & Mullis, due to loss of tracking as the particles cool (personal communication) and that the atomizing gas pressure used in this present study is more than twice that in the study by Bigg & Mullis, it is believed that the measured melt velocities of around 70 ms^{-1} on the plume margins are realistic for the atomisation conditions prevailing, validating the drag model that is employed.

The secondary phase – melt considered for this study is Ni-50wt%Al, is adopted from the work carried out by (McCarthy et al., 2013), (from where also the atomiser design is

adopted as discussed in Section 4.1) and its corresponding density is evaluated to be 3850 kg m^{-3}. The average mass flow rate of the injection for the N_d = 2 mm (Figure 4.2) is determined based on an experimental run carried out on the research-scale atomiser. The injection velocity of the particles is calculated based on an estimate of the actual velocity of the melt in the 2 mm bore nozzle. From the density of the melt (ρ_{melt}) and the mass flow rate (of 1 kg min^{-1}), the volumetric flow rate is found. Using the volumetric flow rate and the cross-sectional area (A) of the nozzle bore, the injection velocity (u_{melt}) of the particles is calculated. And the velocity was found out to be 1.38 m s^{-1}, and the same is assigned as the particles' velocity.

As mentioned earlier, this study focusses on the instability present in the gas and the melt flow, by examining the gas-melt interaction. Hence, five different melt flow rates and five melt temperatures were considered to investigate the instability, to gain deeper understanding of the gas-melt interactions around the wake region and downstream. The different melt flow rates and melt temperatures are 1, 2, 4, 6, and 12 kg min^{-1} and 300K, 600K, 1000K, 1500K and 2000K, respectively. However, these five melt mass flow rates are only nominal values. With the melt mass flow rate coupled to the aspiration pressure that is obtained at the melt nozzle exit (Figure 4.6), the melt flow rate changes continuously with change in the recorded aspiration pressure as the simulation progresses. This is discussed in Section 4.8.

For the two-phase flow simulation, the melt particles are not injected along with the onset of the gas flow, i.e., time, t = 0 s. Rather, initially the simulation is run as gas-only flow for 30 milliseconds (ms) until it reaches steady-state, and thereafter the particles are injected into the steady gas flow. This helps to understand how the gas flow-field behaves with the injection of melt. Moreover, this also provides insight into how changes in the gas flow field affect fluctuations in the aspiration pressure.

A very small timestep size of $5x10^{-8}$ s is required for this highly complex coupled multiphase flow simulation. This was empirically determined as the largest timestep under which simulation results were stable and insensitive to further reductions in step-size. The complexity of these simulations reflected on the run-time it took to simulate these models – it took 13 months to simulate the 12 kg min^{-1} models (Section 5.5). To ensure good solution convergence and to avoid any numerical instability, the residuals and mass imbalances were monitored. The residuals' tolerances were found to be consistently below $1x10^{-4}$ for continuity

and x-velocity; $1x10^{-5}$ for y-velocity; and $1x10^{-7}$ for energy. Also, the mass imbalance was observed to be less than 1%.

The following assumptions were considered for the DPM particles used in this study:

- The gas flow with the particles is considered to be transient.
- The melt break-up is not considered.
- The particles are inert, spherical in shape having constant diameter of 500 μm.
- Gravity is not considered, as it would be irrelevant to such processes.
- Stochastic modelling using Discrete Random Walk (DRW) model is applied to the particles.
- Particles are injected at t = 30 ms, into a steady state gas flow to understand how the gas flow field behaves with the injection of melt.
- Particle-particle interaction is not considered.
- Heat transfer from particle to gas is considered, but heat transfer does not alter the state of the particle.

4.4 Mesh independency study

Following the assignment of boundary conditions, a mesh independency study was carried out to evaluate the accuracy of the results, and inspect that the results converge to a solution, and are independent of the mesh size. The mesh independency study was carried out using single phase flow (gas-only flow) with the settings mentioned in Section 4.3.1.

Four different meshes were generated with total mesh elements of 13000, 60000, 110000, and 170430, with the coarsest being 13000 and the finest being 170430. The simulations were monitored and were carried out until they completely converged. Also, monitors have been employed to determine if the gas flow-field achieved steady state, and were run until they achieved steady state. To determine the mesh independency, the gas velocity is obtained at the outlet of the domain (Figure 4.6) for each of the meshes and were compared. The velocity plots for each of the meshes are presented in Figure 4.7. From the plot it can be observed that the results obtained from meshes 110000 and 170430 remain consistent and do not change. Hence, the mesh with 110000 elements is considered to be the appropriate mesh for this study, so as to run the simulation accurately with minimum mesh elements and at minimum computational time. The total computational resource used with computer run time for each of the simulations are tabulated in Table 4-3, however, this does not include the queueing time in the HPC.

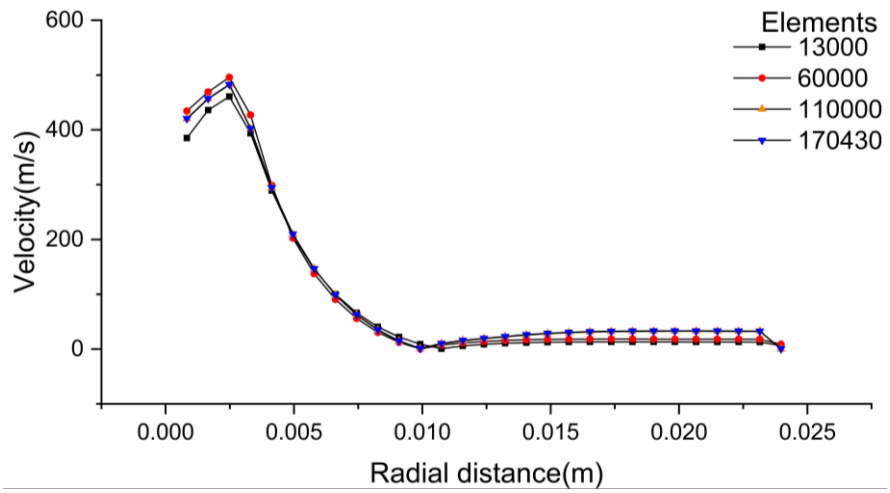

Figure 4.7 Velocity magnitude obtained at the domain outlet for the four meshes.

Table 4-3 Computational resource and CPU hours for each of the simulation carried out.

GMR / Temp	GMR - 5.5 (1 kg min^{-1})	GMR - 2.6 (2 kg min^{-1})	GMR - 1.36 (4 kg min^{-1})	GMR - 0.88 (6 kg min^{-1})	GMR - 0.44 (12 kg min^{-1})
300K	40 CPU cores; 40 Gb RAM/node 13440 CPU-hours	40 CPU cores; 40 Gb RAM/node 13440 CPU-hours	40 CPU cores; 40 Gb RAM/node 13440 CPU-hours	40 CPU cores; 40 Gb RAM/node 40320 CPU-hours	80 CPU cores; 40 Gb RAM/node 577920 CPU-hours
600K	40 CPU cores; 40 Gb RAM/node 26880 CPU-hours	40 CPU cores; 40 Gb RAM/node 15360 CPU-hours	40 CPU cores; 40 Gb RAM/node 13440 CPU-hours	40 CPU cores; 40 Gb RAM/node 73920 CPU-hours	80 CPU cores; 40 Gb RAM/node 497280 CPU-hours
1000K	40 CPU cores; 40 Gb RAM/node 33600 CPU-hours	40 CPU cores; 40 Gb RAM/node 13440 CPU-hours	40 CPU cores; 40 Gb RAM/node 40320 CPU-hours	40 CPU cores; 40 Gb RAM/node 80640 CPU-hours	80 CPU cores; 40 Gb RAM/node 456960 CPU-hours
1500K	40 CPU cores; 40 Gb RAM/node 20160 CPU-hours	40 CPU cores; 40 Gb RAM/node 13440 CPU-hours	40 CPU cores; 40 Gb RAM/node 60480 CPU-hours	40 CPU cores; 40 Gb RAM/node 80640 CPU-hours	✕
2000K	40 CPU cores; 40 Gb RAM/node 26880 CPU-hours	40 CPU cores; 40 Gb RAM/node 19280 CPU-hours	40 CPU cores; 40 Gb RAM/node 134400 CPU-hours	✕	✕

4.5 Domain independency study

To evaluate the impact of computational domain and to create a domain which do not impact the flow predictions along the radial and vertical directions, the domain independency study is carried out. The initial domain having dimensions 25 N_d x 12 N_d in the axial and radial directions, respectively is adopted from (Ashokkumar, 2020) is carried out for domain independency study. Three different axial and radial dimensions were considered for the numerical domain. For the axial direction, three dimensions: 15, 25 and 35N_d measuring from

the melt nozzle tip (Figure 4.3) were considered to examine how the boundary location affects the flow prediction. Similarly, in the radial direction, three dimensions: 6, 8 and 12N_d measuring from the atomiser's axis were considered. The domain independency study was carried out using single-phase flow (gas-only flow), and the boundary condition settings for these different axial and radial dimension are same as the conditions mentioned in Section 4.3.1.

4.5.1 Domain independency study - Axial direction

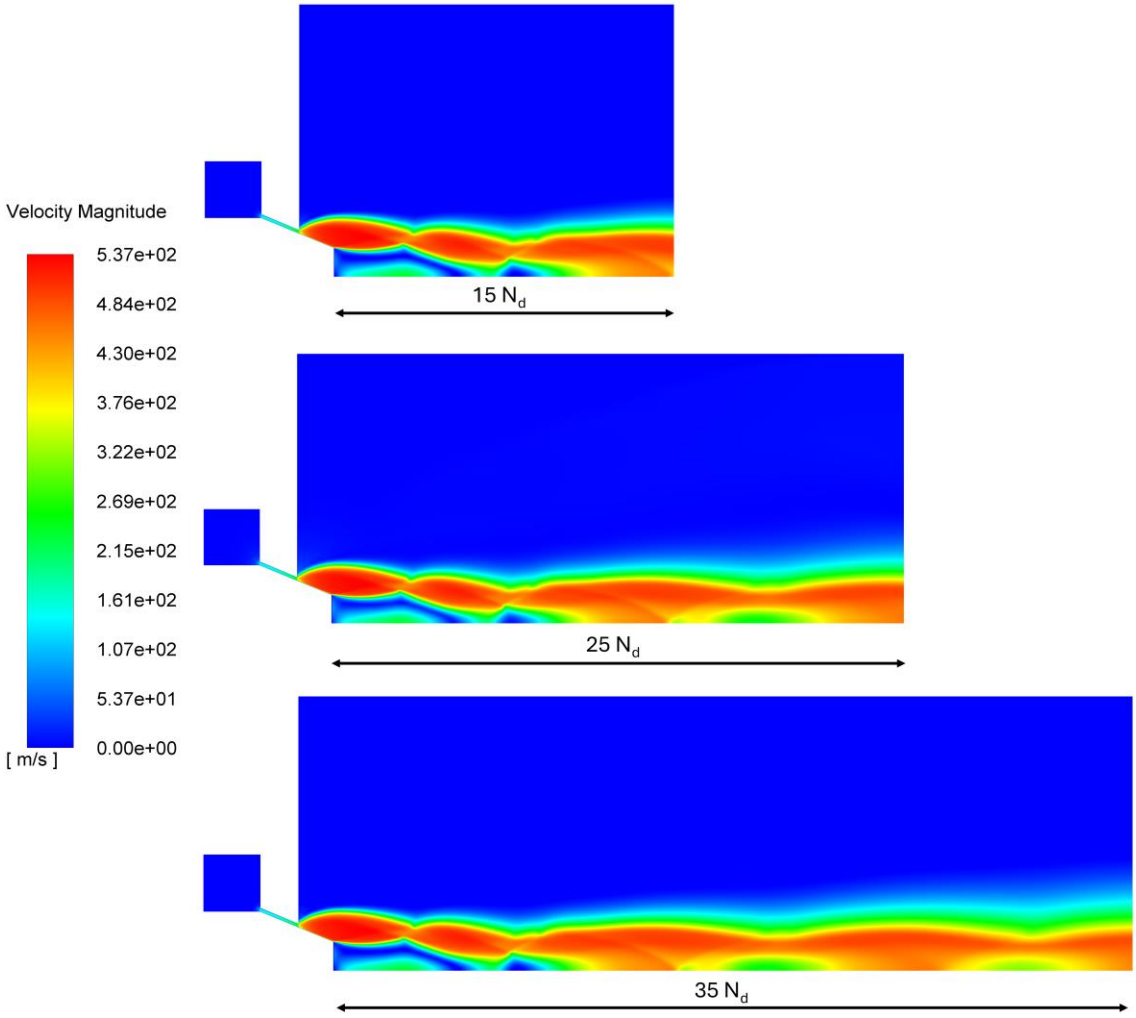

Figure 4.8 Velocity contours of domains having axial dimensions of 15, 25 and 35 N_d.

The initially considered dimension in the domain along the axial direction is 25 Nd. The domain was reduced and increased to 15 and 35 N_d, respectively. The results of the study are presented in Figure 4.8. Although the decrease in the axial dimension to 15 N_d do not exhibit any change in the flow characteristics when compared against the initial axial dimension, 25 N_d, this dimension is not considered. This is because, the principal research carried out in

this thesis, is the analysis of gas-melt interaction, and that includes the behaviour of the melt (particles) downstream. It is expected that with such a little axial dimension, important details of the gas flow fluctuation and particles' behaviour downstream beyond 15 N_d would be lost.

With the numerical domain having the axial dimension of 35 N_d, it is observed the gas flow advances further downstream, nevertheless, there are no changes to the flow profile when compared on the overlapping region between the 25 and 35 N_d domains. This is observed from Figure 4.8. This confirms the flow-field remain unchanged, and extension in the domain along the axial direction did not exhibit any changes to the flow characteristics. Hence, the initial numerical domain having axial dimension of 25 N_d is considered for the simulation runs.

4.5.2 Domain independency study - Radial direction

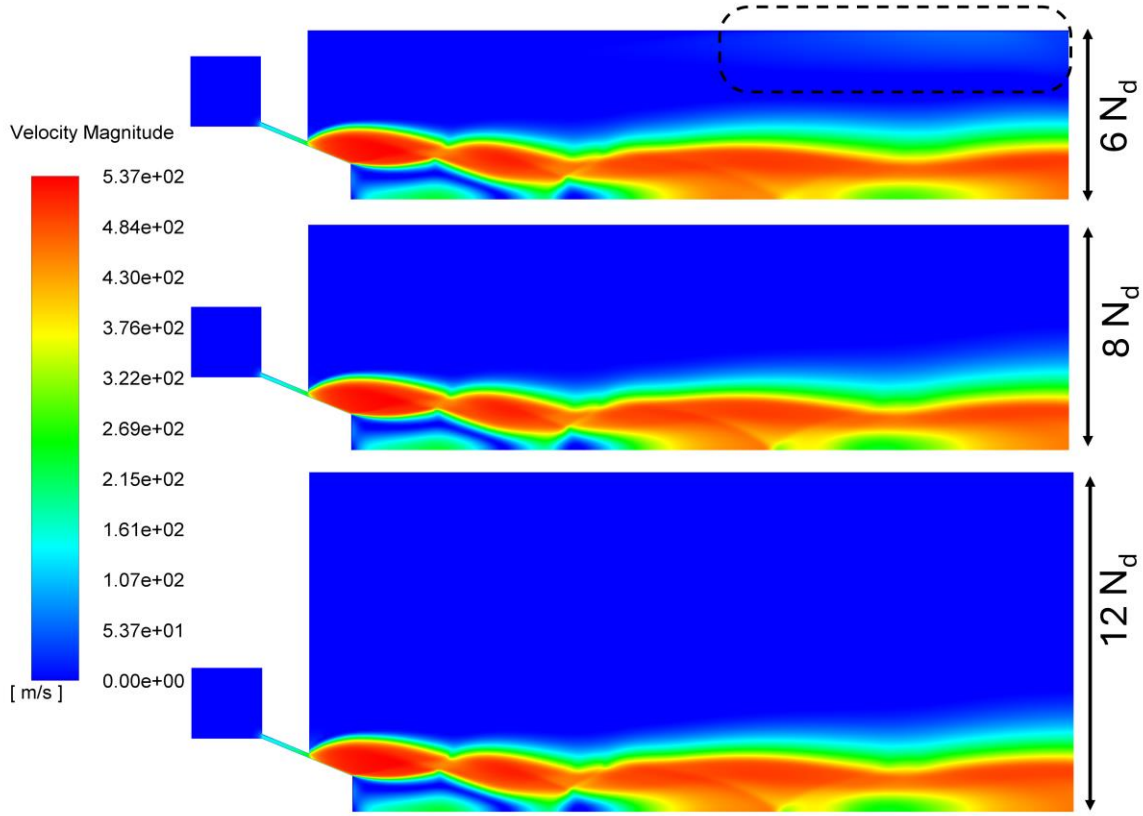

Figure 4.9 Velocity contours of domains having radial dimensions of 6, 8 and 12 N_d

The initially considered radial dimension for the domain is 12 N_d. To evaluate the impact of the radial extent in the domain, two different radial lengths, 6 and 8 N_d were employed. The results of the study are presented in Figure 4.9. For the numerical domain with radial length of 6 N_d it was observed there existed non-zero velocity in the far-field region radially away

downstream. To obtain a zero velocity in the far-field region, the radial length was further increased to 8 N_d and 12 N_d. It was observed, with the increase in the radial length to 8 N_d (Figure 4.9), the non-zero velocity is eliminated indicating the far-field is unaffected by the gas flow. However, this numerical domain is not considered because of the following reason. In the atomisation process, the strong supersonic gas-jet disintegrates the molten melt, and in the process the atomised droplets are propelled both downstream and radially away from the axis. It is expected that with a radial dimension of 8 N_d, important details of the particles' behaviour such as the extent of particle distribution radially would be lost. Hence, a radial length of 12 N_d is considered to accommodate the particle dispersion downstream, and to analyse the gas-melt interaction. Moreover, changing the radial distance of the wall or the wall conditions (Motaman, 2013) would not alter the simulation in any manner, since, the radial distance is artificial, it is adjusted to facilitate a zero-velocity far-field, and hence the assumption of no-slip stationary-wall conditions is preserved for all the considered radial dimensions to understand the flow behaviour for varying radial domain extents (Motaman, 2013).

4.6 Turbulence sensitivity study

With the gas-jet flow existing under turbulent flow regime, it is essential to use appropriate turbulence model to sensibly capture and predict the flow characteristics both near the nozzle where the gas expands, and downstream where the Mach-disk develops. For turbulence sensitivity study, four different turbulence models were investigated, and they were *k - ε, k - ε RNG, k - ω standard, and k - ω SST.* For each of the selected turbulence models, their default model constants were employed so as to not disturb the tuned values, and alter the sensitivity of the employed model in the study. These models were run for gas-only flow, and followed the boundary condition settings discussed in Section 4.3.1. The results comparing the four different turbulence models are presented in Figure 4.10.

It was observed from Figure 4.10, that *k - ε,* and *k - ω SST* models underpredicted the flow expansion compared to the experimental flow, wherein the shock-cells deteriorated quicker downstream than experimentally observed in the study carried out by Motaman (2013). This underpredicted flow is highlighted using dashed boxes in the two respective models in Figure 4.10. Likewise, *k - ε* model did not predict a Mach-disk, whereas *k - ω SST* model predicted a much weaker Mach-disk than expected. Similarly, *k - ε RNG* model overpredicted the gas flow velocity, and exhibited regions of localised increase in velocity along the axis, due

to increased numerical error, resulting in potential simulation failures. This overprediction in the velocity for the *k - ε RNG* model can be observed when comparing against velocity scales presented for each of the models in Figure 4.10, wherein all the other models predicted the velocity within a narrow tolerance, except for the *k - ε RNG* model. Moreover, this turbulence model is usually employed in internal flows.

k - ω Standard model well predicted the Mach-disk, shock-cells, and flow characteristics as observed in the experiment, unlike the other models which exhibited deteriorated shock-cells and overpredicted flow velocity. Similarly, the model predicts the flow separation better, and offers improved accuracy compared to the others. Moreover, the gas flow-field under *k - ω Standard* turbulence model was validated against the work carried out by Motaman (2013) who conducted series of gas atomisation experiments operating under gas-only flow condition, from where was also the geometry of current atomiser is acquired. Considering the two turbulence models, *k - ω standard and k - ω SST,* viable for validation, it was observed from the experimental study that the *k - ω standard* reflected the physical supersonic flow expansion including the strong second shock-cell and the downstream Prandtl-Meyer waves whereas the other model did not exhibit strong shock-cell or the Prandtl-Meyer waves downstream. This flow phenomenon is also observed and is validated against gas-only study conducted by Espina and Piomelli (1998). Hence, *k - ω standard* turbulence model is employed for the study presented in this thesis, and is applied into the Section 4.3.1.

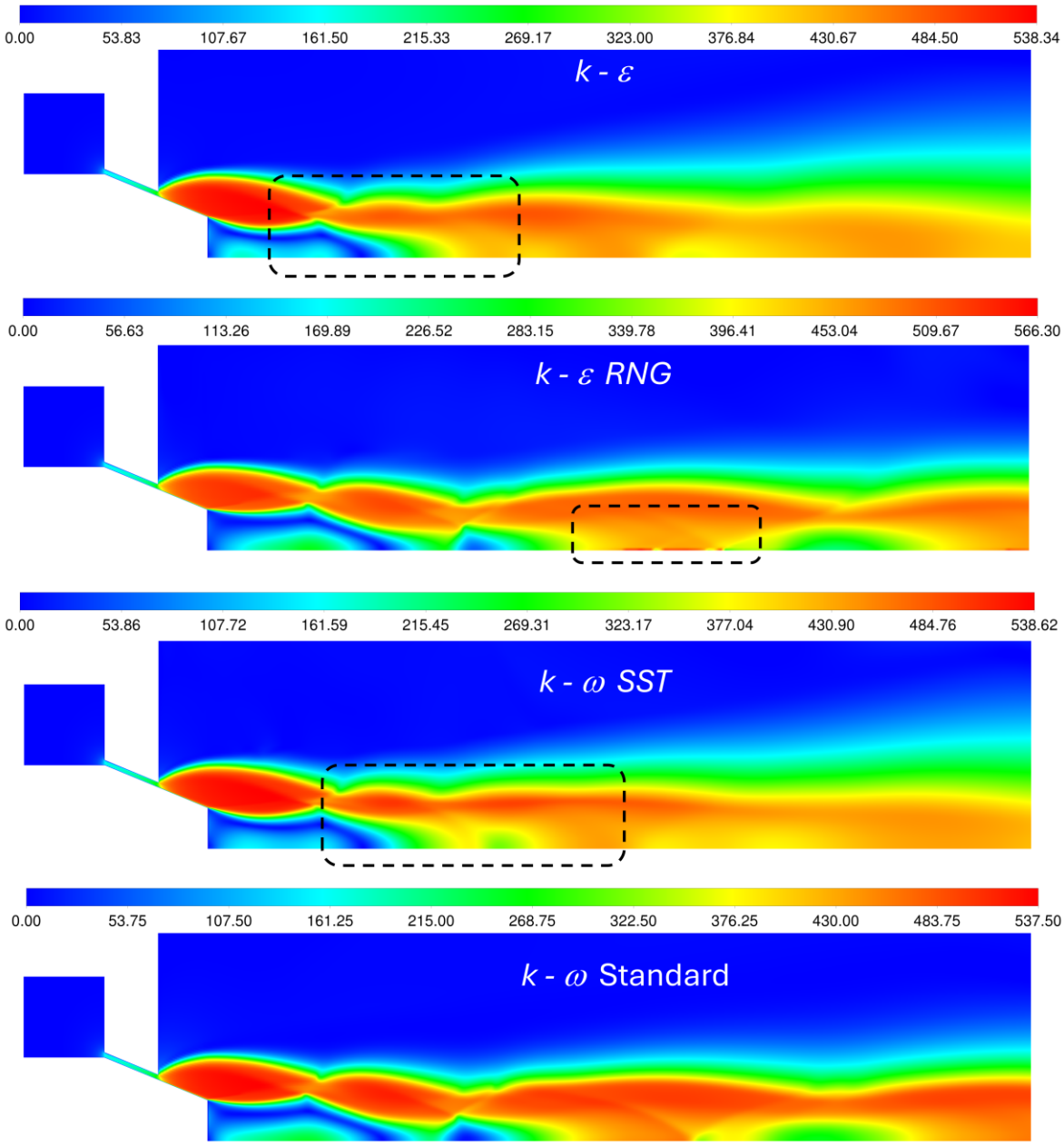

Figure 4.10 Velocity contours of four different turbulence model utilised for the sensitivity study.

4.7 DPM sensitivity study

Preliminary studies were conducted on the DPM particles to evaluate the influence of the gas flow on the DPM particles. Two different sensitivity studies were conducted: influence of stochasticity, and influence of particle size. Since, these two tests are run as two-phase flow, the boundary condition setting for primary and secondary phase is employed as discussed in Section 4.3.1 and 4.3.2, respectively. In addition to the secondary phase boundary condition mentioned in Section 4.3.2, for the DPM sensitivity studies, a constant melt mass flow rate of 0.016 kg s^{-1} (1 kg min^{-1}) is employed.

4.7.1 DPM sensitivity study - influence of stochasticity

This DPM sensitivity study is carried out to realise the influence of stochasticity in the particles in the two-phase flow. Stochastic model, also known as Discrete Random Walk (DRW) model is employed to induce random fluctuations in the flow which are filtered out by the averaging in RANS approach (Section 2.5.2). Each of the two simulations were run for 70 ms (from 30 to 100 ms) and were analysed for the influence of stochasticity. The results of the two simulations are presented in Figure 4.11. For the simulation when DRW model was absent, it is observed from Figure 4.11a that the particles injected follows the same trajectory the previous particles followed, exhibiting an orderly flow of particles downstream. This is more clearly noticed when observed at the melt nozzle front, where the particles' trajectories undergo pre-filming more or less like multiple lines coming out of the melt nozzle exit. However, with the DRW model employed, the particles seen in Figure 4.11b exhibits randomness in their particle trajectories, reflecting the nature of the physical process. Also, the melt pre-filming seen at the melt nozzle front is observed to replicate the physical process. Moreover, when the particle trajectories were examined, it was clear that the DRW model leads to more dispersion of particles as it moves downstream as shown in Figure 4.11b. Since, the observed manner of pre-filming and distribution of particles agrees better with the experimentally observed melt plume as captured by high-speed filming, DRW model is employed for the CFD study.

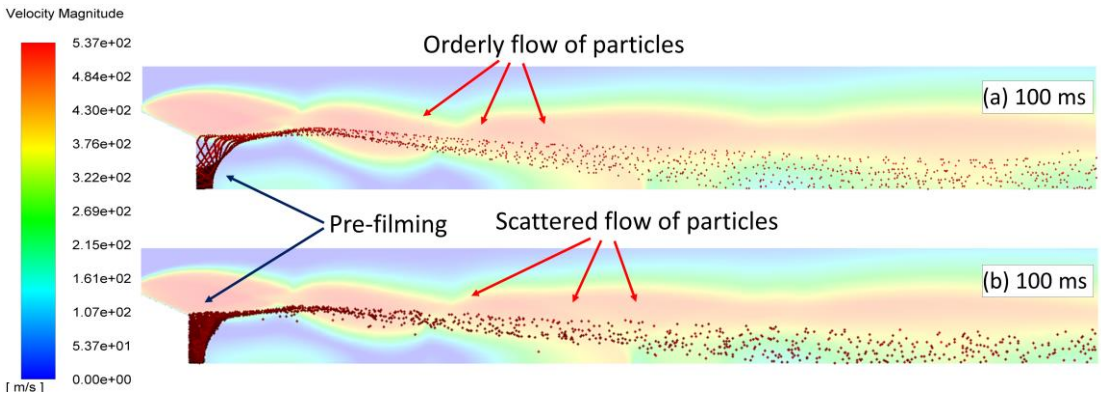

Figure 4.11 Particle trajectories shown for with and without stochastic model with velocity contour in the background.

4.7.2 DPM sensitivity study - influence of particle size

DPM sensitivity study using different particle size were investigated to analyse the effects of particle size, and in turn the effect of particle mass on the gas flow and particle trajectory. Three different particle sizes were considered for this study, and they were: 390 μm,

500 μm and 630 μm. The particle sizes were considered in such a way that the mass of the particle reduced and multiplied by a factor of two compared to that of the 500 μm particle. All the three studies were run for 20 ms (from 30 ms to 50 ms). The results of the studies are presented in Figure 4.12.

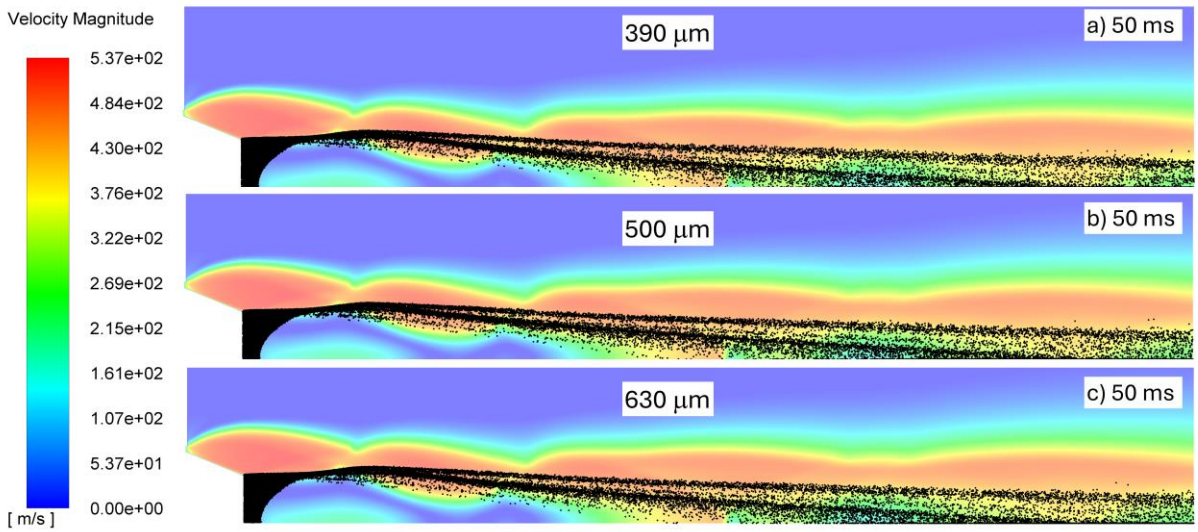

Figure 4.12 Particle trajectories with velocity contour in the background presented for three different partcle size - 390, 500, and 630 μm, all taken at 50 ms.

The flow-field and particle trajectories for each particle size were investigated for changes. It was observed from Figure 4.12 that the flow-field remains insensitive to the particle size. This is due to the strong supersonic gas-jet, developed from a 4.5 MPa inlet, exiting the plenum through a width of 0.21 mm (210 μm) gas nozzle. The strong gas-jet effectively dominates any influence the particles have on the gas flow. With flow-field being insensitive to 390 μm particle size, no further smaller size particles were simulated in the DPM sensitivity study, owing to the high computational cost it requires.

4.8 Coupling of gas and melt mass flow rates via UDF and time-averaging of pressure

As mentioned before, the primary objective of this study is to develop a CFD model of gas atomisation process to replicate the physical process, thereby to understand the instability present in the melt and the gas flow that arises due to the gas-melt interaction. The below Sections 4.8.1 and 4.8.2 details the methodology of developing such a process model using User Defined Function (UDF) – a customisation feature present in ANSYS Fluent, which allow additional physics or complexity to be programmatically included in the CFD code.

4.8.1 Implementation of UDF to couple gas and melt mass flow rates

The process modelling is carried out by coupling the melt mass flow rate ($\dot{m}$) to the gas flow variable, such that with the change in the flow variable the melt mass flow rate is also modified. The flow variable coupled to the melt mass flow rate is the aspiration pressure (A_{sp}), since in the physical atomisation, the amount of melt drawn into the atomisation chamber is controlled by the A_{sp}. A_{sp} exists at the melt nozzle front as shown in Figure 4.6 and is recorded for every timestep by setting up a monitor in the region. $\dot{m}$ is proportional to A_{sp}, and to match the experimentally observed flow rates in a physical atomiser, as carried out by Mullis et al. (2007) and McCarthy et al. (2013), a proportionality constant (K) is used, and is presented in Equation 4.1.

$$\dot{m} = K * A_{sp} \qquad 4.1$$

The proportionality constant is calculated based on the estimated A_{sp} determined in gas only flow. Usually, in the physical atomisation process an over-pressure is applied to the melt to prevent it from melt freeze-off, and to replicate the experimental process, an over-pressure of 50 kPa is considered for this model. In Equation 4.1, A_{sp} is computed by combining the estimated initial aspiration pressure and the over-pressure, which comes to be 75 kPa, giving K = 3.2 x 10^{-7} kg s^{-1} Pa^{-1}. This K is computed for $\dot{m}$ = 0.016 kg s^{-1}. As discussed in Section 4.3.2, five different nominal mass flow rates were studied in this thesis. The K value for each of the nominal mass flow rates are tabulated in the Table 4-4.

The UDF code developed to couple the mass flow rate of the secondary phase with the measured A_{sp}, based on Equation 4.1 and Table 4-4 is compiled so as to load it as a library file, thereby making it part of the ANSYS Fluent executable. The UDF code for all the five nominal melt mass flow rates are presented in Appendix.

Table 4-4 Proportionality constant (K) calculated for the five nominal mass flow rates.

S.No	Melt Flow rate (kg s^{-1})	Melt Flow rate (kg min^{-1})	Proportionality constant (K)
1	0.016	1	3.2 x 10^{-7} kg s^{-1} Pa^{-1}
2	0.033	2	6.6 x 10^{-7} kg s^{-1} Pa^{-1}
3	0.066	4	1.3 x 10^{-6} kg s^{-1} Pa^{-1}
4	0.1	6	1.9 x 10^{-6} kg s^{-1} Pa^{-1}
5	0.2	12	3.8 x 10^{-6} kg s^{-1} Pa^{-1}

4.8.2 Time-averaging of pressure in the UDF to couple with the met mass flow rate.

As discussed above, the A_{sp} is recorded for every timestep, and is coupled with the $\dot{m}$. From a practical atomisation process perspective, with a very small timestep size of $5x10^{-8}$ s as used in this study, the $\dot{m}$ of the melt will not be able to respond to this extreme high frequency changes instantaneously due to the inertia of the melt. Hence time-averaging is employed to the measured A_{sp}. This modifies the $\dot{m}$ seen in Equation 4.1 by replacing A_{sp} with *time-averaged* A_{sp}. Three different time averaging durations were run to understand the effect of time-averaging on $\dot{m}$, and they were instantaneous, 5 microseconds (µs) and 50 µs. For the three mentioned runs, an initial (nominal) mass flow rate of 0.016 kg s^{-1} was considered, and for this nominal mass flow rate, and under an aspiration pressure of 75 kPa, the constant K presented in Equation 4.1 was evaluated to be 3.2 x 10^{-7} kg s^{-1} Pa^{-1} (Table 4-4). When the simulation is in progress, the aspiration pressure continuously varies, due to the disturbance in the gas flow-field, leading to changes in the $\dot{m}$. For the instantaneous run, the A_{sp} obtained at the monitor (Figure 4.6) was updated into the A_{sp} term in Equation 4.1 without any time-averaging, whereas for time-averaged runs, the aspiration pressure obtained at the monitor (Figure 4.6) was 5 µs and 50 µs time-averaged, respectively, before being updated into the A_{sp} term of Equation 4.1 to obtain the $\dot{m}$ value.

The instantaneous, 5 µs time-averaged and 50 µs time-averaged mass flow rate plot obtained via UDF is presented in Figure 4.13, and were analysed. For the instantaneous case, an initial rapid fluctuation can be seen at the start of the injection but later smooths out. When the 5 µs time-averaging was applied, a marginal change in the initial mass flow rate is observed as seen in the Figure 4.13, but as time progresses it is evident the overall trend of the 5 µs time-averaged plot follows the same trend of the mass flow rate plot of the instantaneous model. From the above trend it was apparent the applied time-averaging period, i.e., 5 µs showed little-to-no smoothing effect on the melt flow rate oscillation. This indicated the time-averaging period should be higher than that of 5 µs. In fact, from the Figure 4.13 for most of the plot the 5 µs time-averaging plot (blue plot) exactly overlaps onto the Instantaneous (black plot). For the considered melt injection velocity of 1.38 m s^{-1}, considering the duration of the time-averaging period of 5 µs, the melt displaces only about 7µm, which would not be the same in a physical atomisation as the surface tension and viscosity tends to dampen such small amplitude oscillations. Hence, the time-averaging was increased substantially to 50 µs to make the melt respond to the pressure variations more realistically. In the 50 µs time-averaged mass

flow rate plot as seen from the Figure 4.13, a more distinct difference is observed, where the trend of the mass flow rate is different to both the instantaneous and the 5 µs mass flow rate plots. In the 50 µs time-averaging plot (Figure 4.13) it can be observed that the low frequency is preserved, eliminating only the higher frequencies. Hence, 50 µs time-averaging is employed for the CFD study.

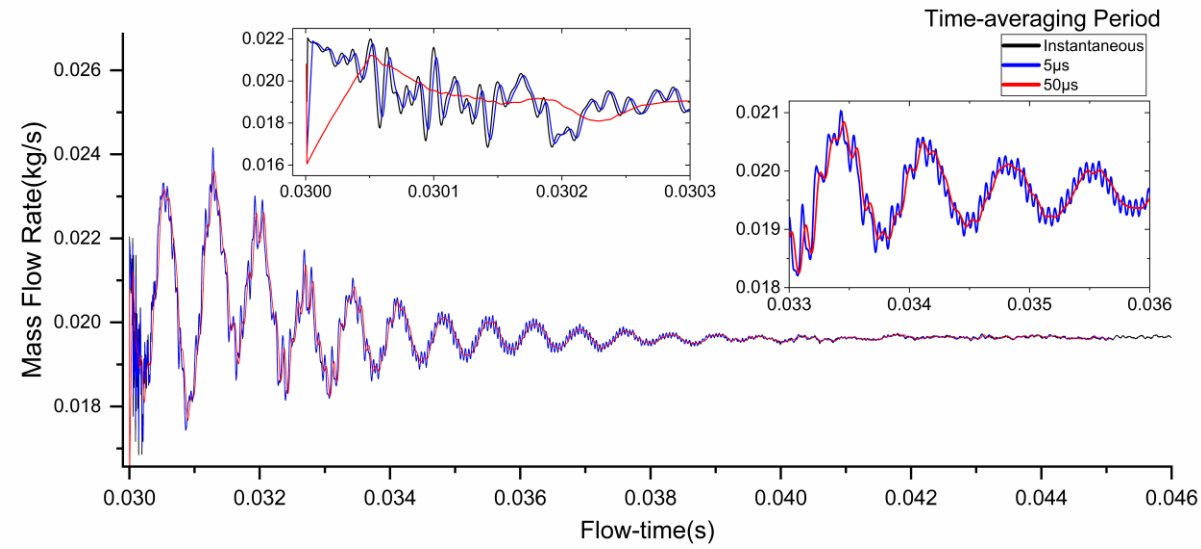

Figure 4.13 Injection mass flow rate plots showing the difference in the three time-averaging period – Instantaneous, 5 µs, and 50 µs.

4.9 Different GMRs and melt temperatures considered for this study

Following the mesh generation, assigning of boundary condition, coupling of the melt mass flow rate with aspiration pressure via UDF, the CFD model is ready to execute the simulations for the five different nominal melt mass flow rates. For all of the simulations with different melt mass flow rates carried out, the gas inlet pressure is kept constant at 4.5 MPa. This results in a range of GMRs investigated in this study. The GMR for each of the nominal melt mass flow rate is calculated and is presented in Table 4-5. However, it has be noted that these GMRs are the nominal values, and will change as the simulation progresses.

Table 4-5 Nominal melt flow rates and their respective GMRs used in the study.

Operating Pressure (MPa)	Gas Flow rate (kg s^{-1})	Melt flow rate (kg min^{-1})	Melt Flow rate (kg s^{-1})	GMR
4.5	0.088	1	0.016	5.5
4.5	0.088	2	0.033	2.6
4.5	0.088	4	0.066	1.32
4.5	0.088	6	0.1	0.88
4.5	0.088	12	0.2	0.44

Similar to the different melt mass flow rates investigated, the impact of the melt temperature is also investigated in this CFD study. For each of the nominal mass flow rates mentioned in Table 4-5, five different melt temperatures – 300K, 600K, 1000K, 1500K, and 2000K, were considered to investigate how the melt temperature influences the instability in the gas and melt flow. However, for some nominal melt mass flow rates only some melt temperatures were investigated. In total 22 simulations were conducted, and all the simulation combinations that were conducted are marked with a blue tick in Table 4-6, and those that are not carried out are marked with a red cross. The simulations which are marked with the red cross (lower GMR/higher temperature cases) aren't carried out since they were too unstable to run successfully. The lower GMR/higher temperature cases were initially run, but they seem to undergo continuous divergence even under decreased timestep size and CFL number. Even after continuous efforts they proved to be unstable, and hence considering the limited time and resource available, those runs were not carried out. Section 5 details the results of the all the 22 simulations carried out.

Table 4-6 Table of simulation run in this thesis. The blue tick indicates they are simulated, the red cross indicates they are not simulated.

GMR / **Temperature**	**GMR - 5.5 (1 kg min^{-1})**	**GMR - 2.6 (2 kg min^{-1})**	**GMR - 1.36 (4 kg min^{-1})**	**GMR - 0.88 (6 kg min^{-1})**	**GMR - 0.44 (12 kg min^{-1})**
300K	✓	✓	✓	✓	✓
600K	✓	✓	✓	✓	✓
1000K	✓	✓	✓	✓	✓
1500K	✓	✓	✓	✓	✗
2000K	✓	✓	✓	✗	✗

5 Results of the Numerical Simulations.

This section presents the results of the 22 CFD simulations (Table 4-6) carried out to understand the gas-melt instabilities in the CCGA process. It has to be noted, all the injection mass flow rates: 1, 2, 4, 6, and 12 kg min^{-1}, are nominal and initial mass flow rate values only. The values of the injection mass flow rate change as the simulation progresses, dictated by Equation 4.1.

The general results presented in this section are the injection mass flow rate plot which is the mass flow rate calculated using 50 μs time-averaged aspiration pressure, given by Equation 4.1; 50 μs time-averaged mass flow rate plot obtained at the outlet of the domain (all particles exit only via the outlet of the domain; no particles are lost/escaped through other boundaries); particle trajectories of the melt (particles) with velocity contours in the background; and velocity contours without the particles. Regarding the velocity contours without the particles, it is to be noted, throughout all 22 simulations, both the gas and melt flows are simultaneously present in the domain. The velocity contours without the particles are presented just to provide a clear understanding on the behaviour of the gas flow during the CCGA process. Moreover, particle trajectory and velocity contour figures are cropped appropriately to present their results in a compact manner to save space, although the size of their numerical domain is same as Figure 4.3. In addition to the above-mentioned results, velocity monitors recorded at seven different key sections of the domain (Figure 5.1) and FFT plots are also presented for some of the simulations.

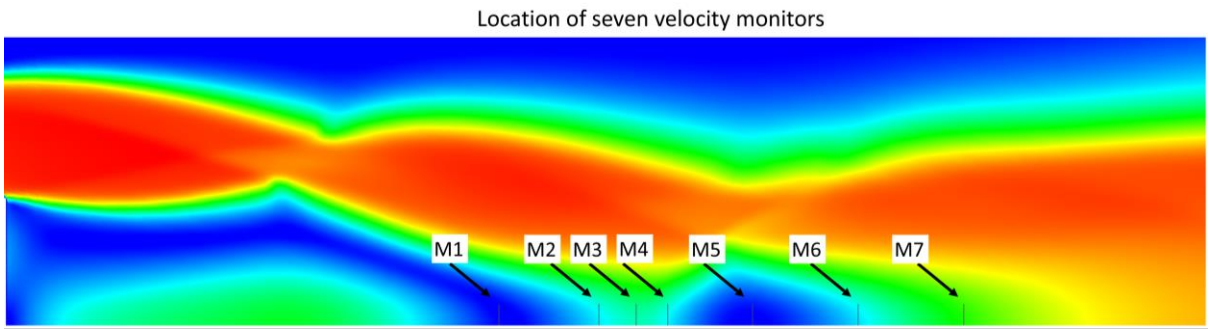

Figure 5.1 Locations of the seven velocity monitor employed in the study to record velocity of the gas flow. (Image provides monitors' location and hence velocity legend is not added.)

5.1 Results of 1 kg min^{-1} (GMR = 5.5) under increasing melt temperatures.

This section presents the results of 1 kg min^{-1} case having GMR=5.5, investigating the effect of increasing melt temperatures. The melt temperatures considered for this GMR are: 300K, 600K, 1000K, 1500K, and 2000K (Table 4-6). The section is sub-divided to present and analyse the results for each of the melt temperature individually.

5.1.1 Melt temperature: 300K.

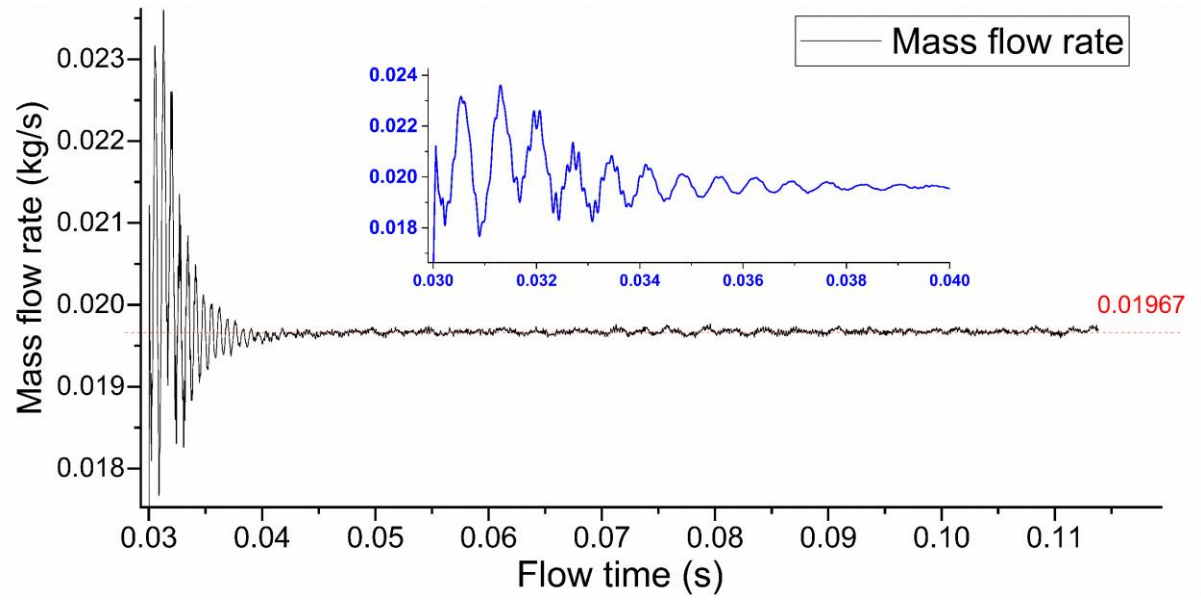

Figure 5.2 injection mass flow rate plot of 1 kg min^{-1} with melt temperature, 300K. This shows as time progresses the fluctuation attenuates to become a steady-state mass flow rate.

The 1 kg min^{-1} (0.016 kg s^{-1}) model with a GMR value of 5.5 and melt temperature of 300K was run for 84 ms (30 to 114 ms). The injection mass flow rate plot is presented in Figure 5.2. The oscillations observed in the melt injection plot are a result of the varying aspiration pressure to which they are coupled. From the zoomed section of the plot shown in Figure 5.2 there was an initial steep rise in the mass flow rate for the first 0.4 ms into the injection, and thereafter it evolved into a damped fluctuation. As seen from the Figure 5.2, starting at 30.5 ms there existed multiple high amplitude fluctuation, which damped out in the subsequent cycles. From observation, the fluctuation presented in Figure 5.2 contains high frequency fluctuations modulated into the low frequency fluctuation which eventually damped out at t > 34 ms. As the time progressed further the low frequency fluctuation also attenuated, transitioning into a steady-state having a near-steady mass flow rate of 0.01967 kg s^{-1}. The initial fluctuation observed from the mass flow rate plot (Figure 5.2) can be attributed to the onset of the melt injection into the domain which disturbs the gas flow-field, leading to the change in the

aspiration pressure. To identify different frequencies of fluctuation present in the injected mass flow rate plot, Fast Fourier Transform (FFT) analysis was conducted. From the analysis two distinct frequencies were found: a dominant low frequency of 1.4 kHz (0.71 ms), and a weaker high frequency of 9.1 kHz (0.1 ms).

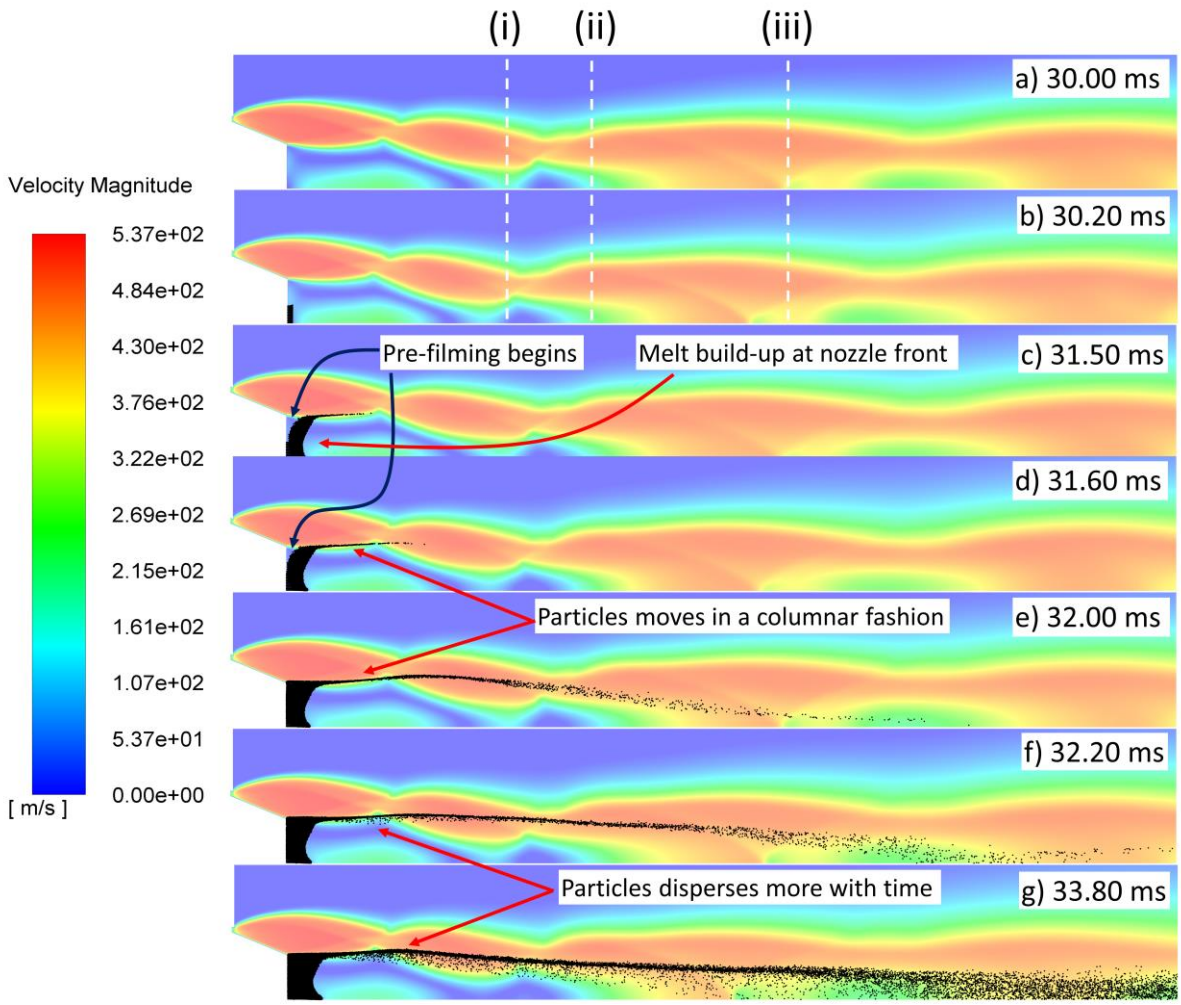

Figure 5.3 Particle trajectories with velocity contours in the background for the 1 kg min^{-1}, 300K case showing the evolvement of particles starting from onset of injection, pre-filming and movement downstream.

Considering the particle trajectories with the gas flow-field in the background, with the onset of melt injection into the domain (atomisation chamber) there was an initial significant disturbance that can be seen in the flow-field. This can be observed from Figure 5.3a&b. This can be attributed to the disruption to the steady flow, caused due to the onset of melt injection. To illustrate this disturbance three white dashed guide-lines were placed at Figure 5.3a and were compared against Figure 5.3b. Guide-lines (i), (ii), and (iii) were placed at Figure 5.3a at the first Mach-disk, stagnation point, and second Mach-disk, respectively. When compared, it

can be seen, all three mentioned key points mentioned in Figure 5.3a were shifted distinctly in Figure 5.3b. Following this, the melt underwent pre-filming at 31.5 ms with its melt pool head built-up almost perpendicular to the direction of the flow-field as observed in Figure 5.3c. This wall like melt buildup by the advancing melt, is due to the opposing force of the recirculation zone. The melt that is pulled radially out by the recirculation zone, when it comes in contact with the supersonic gas-jet, is swiftly pushed downstream owing to the kinetic energy possessed by the supersonic flow-field. Until 32.2 ms it can be observed that the particles pushed downstream from the first shock-cell were tightly collimated (Figure 5.3d&e), but later with time the particles started to disperse from and beyond the first shock-cell (Figure 5.3f). This progressive dispersion can be observed more clearly in the Figure 5.4, where initially at 37 ms (Figure 5.4a) the particles that were pushed downstream which touched the axis of the atomiser around the region of stagnation point, due to the progressive dispersion, touched the axis, at a location further upstream at 57 ms as shown in Figure 5.4e. In each frame of the Figure 5.4 the location that of the particles touching the axis is shown using arrow.

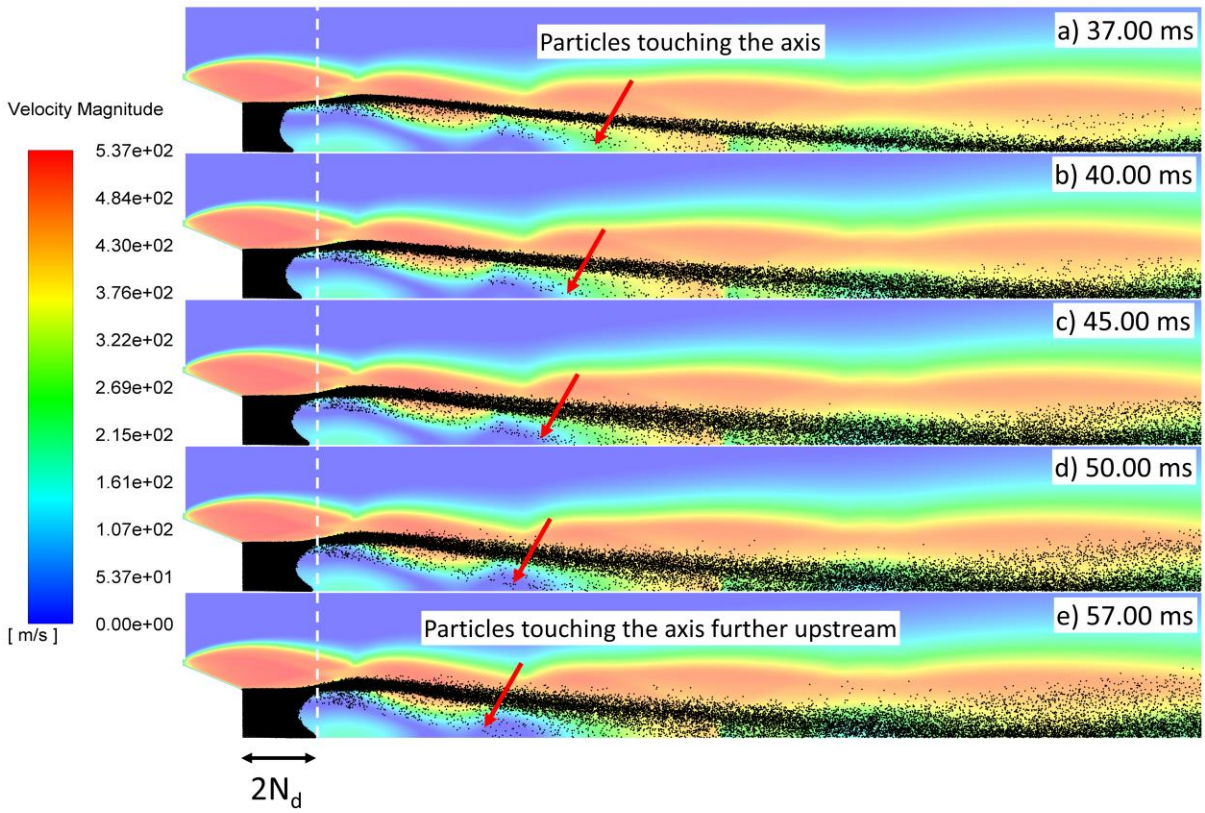

Figure 5.4 Particle trajectories with velocity contours in the background for the 1 kg min^{-1}, 300K case demonstrating how particle dispersion increases with time. The arrow shown in the frames shows how the less dispersed particles, in frame a, become more dispersed over time, as seen in frame f.

This transition from the collimated trajectories to much dispersed trajectories may be attributed to the mass build-up in the domain. Due to the mass build-up in the domain, as shown in Figure 5.4e until 57 ms the melt pool head advances $2N_d$ (nozzle-diameter) downstream before stabilising at that same location for the remainder of the simulation. This advancement of the melt pool head downstream is shown in Figure 5.4 by pinning a white dashed reference line at the melt pool head at 57 ms (frame e) which when compared against the melt pool head of other frames starting from 37 ms, displays the progressive downstream movement of the melt pool head from 37 to 57 ms. Also, the mass build-up in the domain can be noticed by comparing the particle mass flow rate plot (Figure 5.5) obtained at the outlet of the domain against the injection mass flow rate (Figure 5.2). From Figure 5.5 it is noticed, that at 64.3 ms the mass flow rate of the particles leaving the outlet becomes near steady-state having a value of 0.01964 kg s^{-1}.

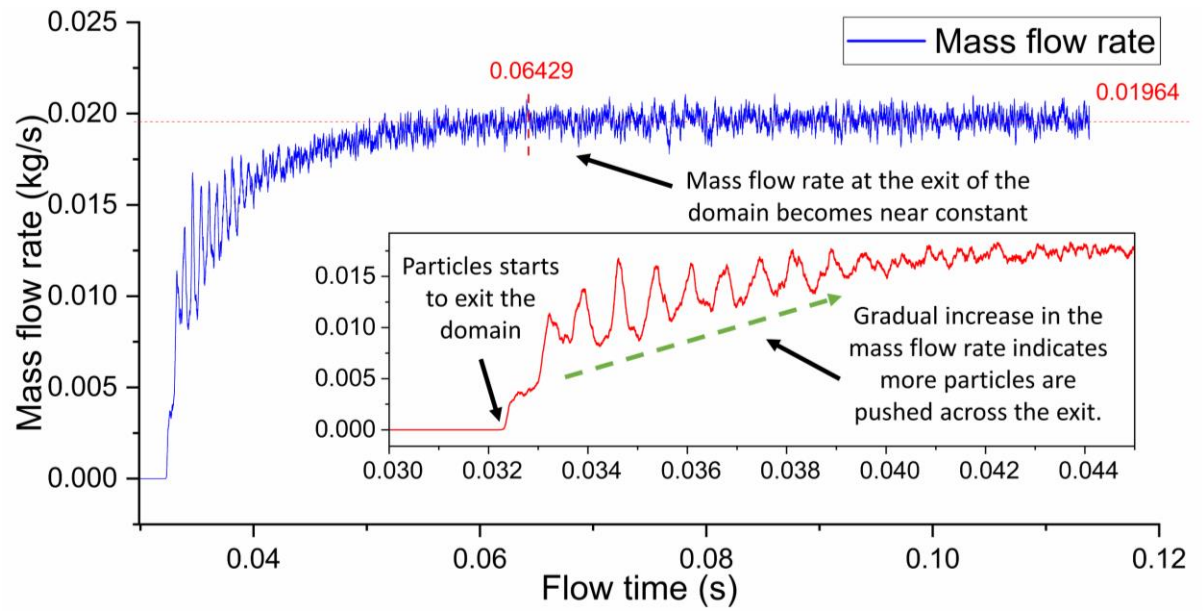

Figure 5.5 Mass flow rate of the particles obtained at the outlet of the domain for the 1 kg min^{-1}, 300K case shows the particles takes around 2.4 ms to reach to the outlet, and mass flow rate reaches an approximate steady-state mass flow rate at 64.3 ms.

Considering the gas flow-field of the 1 kg min^{-1}, 300K melt temperature case presented in Figure 5.6, it was observed, due to the injection of melt, the flow-field was disturbed from its original steady-state condition, causing flow-field oscillations. Even though the melt is present in all the frames of Figure 5.6, only the velocity contours are presented to better visualise the gas flow-field. To understand this phenomena series of velocity contours of the flow-field were obtained at close consecutive flow times and were stacked up. Changes to the flow-field were noted by using three vertical guide-lines (i), (ii), and (iii) pinned in Figure 5.6a

(30 ms) at first Mach-disk, stagnation point, and second Mach-disk, respectively, and comparing were against the other frames of the stack. It can be evidently seen when comparing Figure 5.6a against the other frames, that the flow-field oscillated by moving upstream (Figure 5.6b) and downstream (Figure 5.6c), i.e. all above-mentioned features of the flow-field moved upstream as the flow-field shrunk, and subsequently moved downstream as it expanded. It was also observed that with the flow-field undergoing fluctuation, it continued to exist in closed-wake condition (presence of first Mach-disk). The downstream movement of the melt pool head as seen in Figure 5.3 is also observed from the velocity contours (Figure 5.6b-e), and the locations of the melt pool head for each of the frame is marked using black circle.

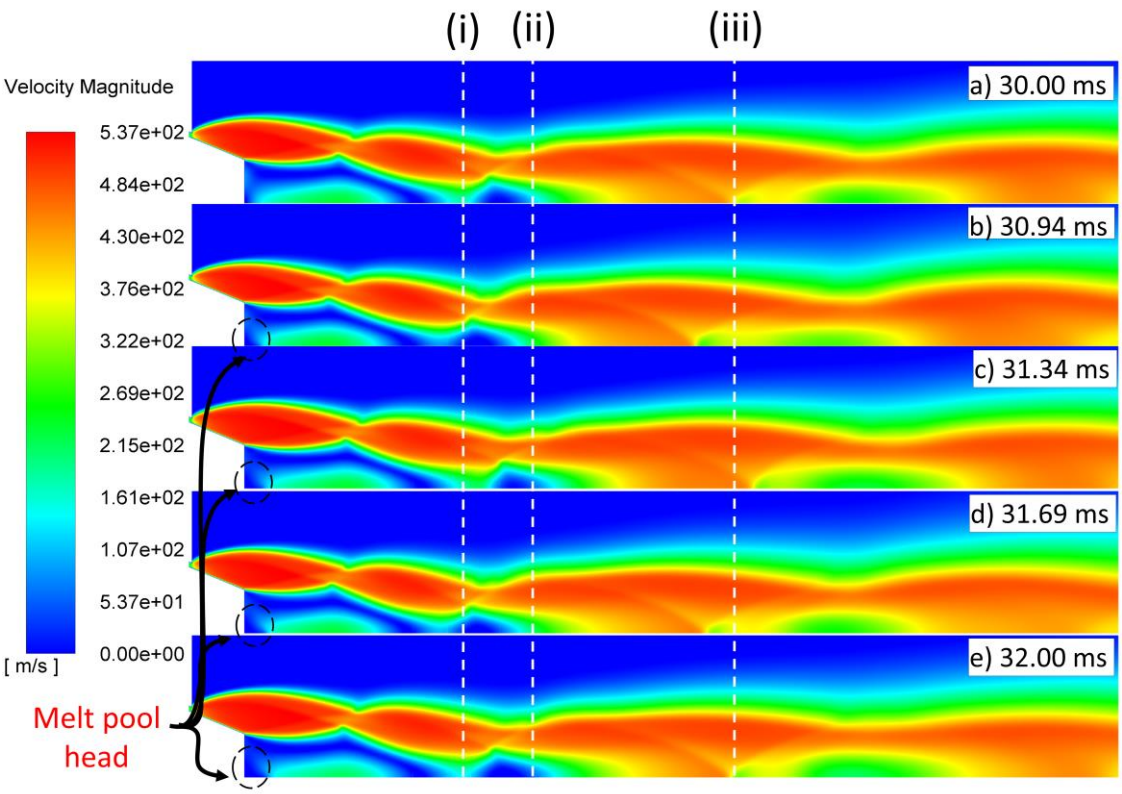

Figure 5.6 velocity contours without particles for the 1 kg min^{-1}, 300 K case showing the initial flow-field fluctuation during the onset of the melt injection, starting at 30 ms. This is illustrated using three guide-lines (i), (ii) and (iii), pinned at frame a, at first Mach-disk, stagnation point, and second Mach-disk, respectively. The melt pool heads of the frames, b-e, are marked in the circle. Using the three guide-lines the to-and-fro motion of the flow-field fluctuation is illustrated.

Following the initial fluctuation, the flow-field transitioned into open-wake condition, and remained in the same configuration for the remainder of the simulation. The flow-field fluctuation continued to damp out progressively until the flow-field became stable at t > 36 ms. However, even after the flow-field stabilised, due to the progressive downstream penetration of the melt pool head, the wake region was pushed downstream. This is shown in Figure 5.7,

where guide-lines are pinned at various key locations of the flow-field taken at 36 ms and were compared against the flow-field of subsequent flow times. Five guide-lines (i), (ii), (iii), (iv), and (v) were pinned in Figure 5.7a, at melt pool head tip, end of first shock-cell, end of second shock-cell, stagnation point, and second Mach-disk, respectively. It can be observed from all the frames, a-e, except for melt pool head tip all the other flow features remain at the same location, revealing steady flow.

Comparing the gas flow-field fluctuations with the melt fluctuation frequencies obtained from the FFT analysis, it was determined that the melt fluctuation of 1.4 kHz corresponds to the initial flow-field fluctuation. However, the melt fluctuation of 9.1 kHz, did not correspond to any flow-field fluctuations. The gas flow-fields were examined against the local maxima and local minima of the two dominant frequencies i.e. 1.4 kHz and 9.1 kHz obtained via the FFT analysis, to observe for any significant changes. It was observed, at local minima of the 1.4 kHz fluctuation, the wake region reduced in its size i.e. the configuration of the flow-field seen in Figure 5.6b&d when compared against Figure 5.6a. Similarly, at local maxima, the wake region grew in its size (Figure 5.6c&e). However, for the higher frequency, 9.1 kHz, no correlation could be observed between the flow-field and the local extrema of the melt fluctuation.

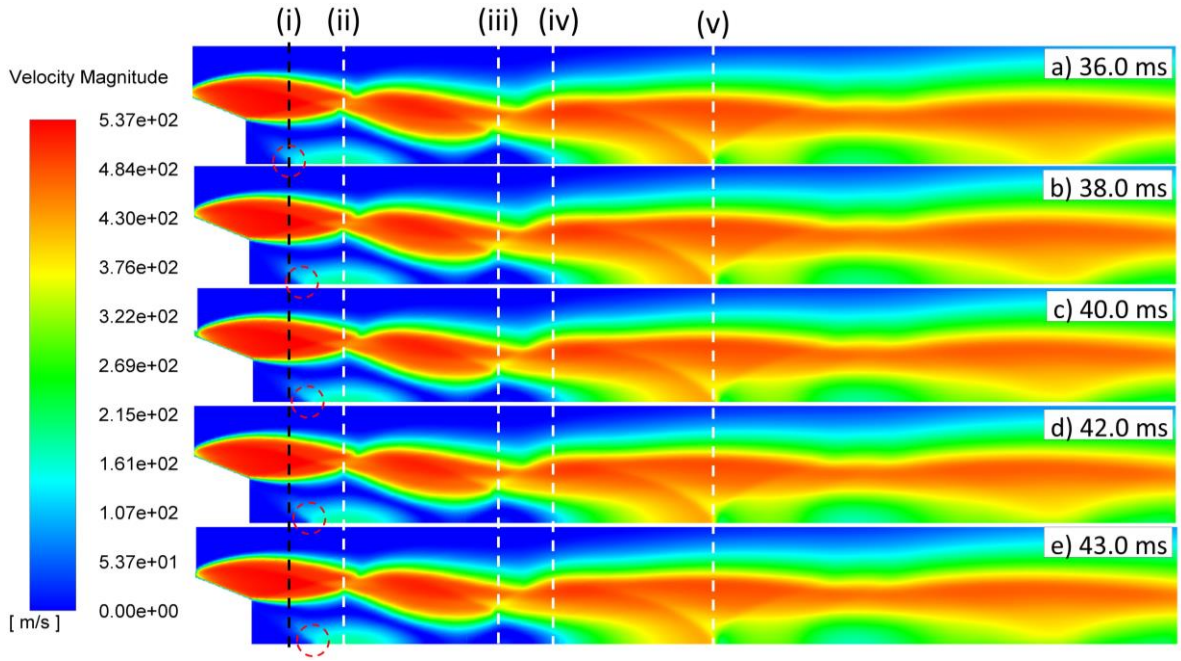

Figure 5.7 velocity contours without the particles for the 1 kg min^{-1}, 300 K case taken at different flow time are presented in sequential order showing the flow-field exist in open-wake condition once it stabilises at t > 36 ms. The melt pool heads of all the frames are marked in red circles.

5.1.2 Melt temperature: 600K

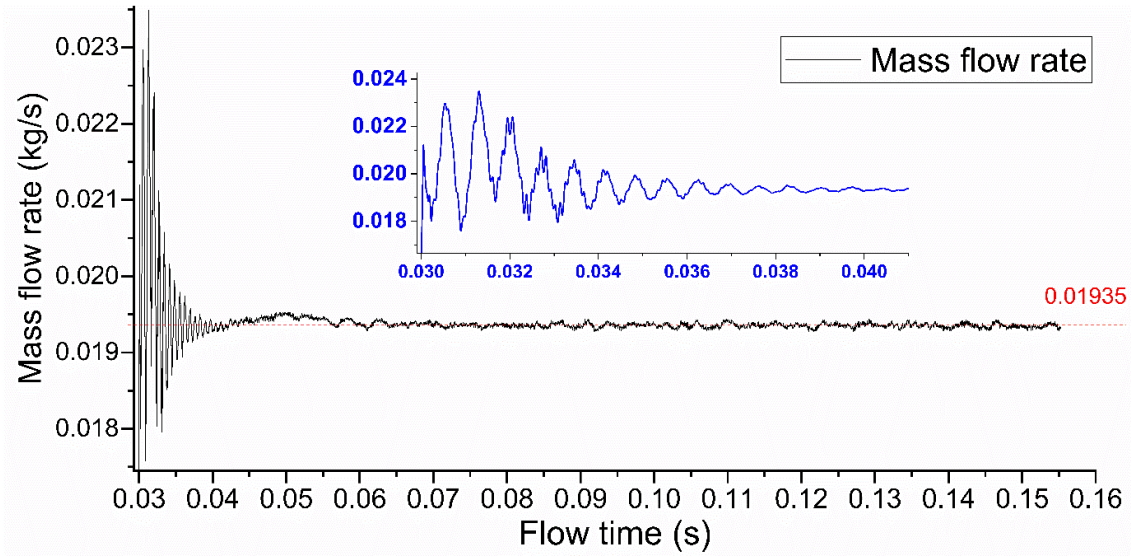

Figure 5.8 Injection mass flow rate plot of 1 kg min^{-1} case with a melt temperature of 600K. After the initial fluctuation, at 42.5 ms there is a gradual rise and fall in the mass flow rate before becoming steady-state at 63 ms.

Following the 300K case, the 1 kg min^{-1} case was run with a melt temperature of 600K for 125 ms (30 to 155 ms) to investigate the effects of elevated melt temperature. The general behaviour of this case was similar to that of the 300K case, both in the field-flow and in the particle trajectories. However, few significant differences were observed in the case which are recorded below. Unlike, the 300K case, where after the attenuation of the initial melt fluctuation the mass flow rate becomes steady-state, in the 600K case there was a gradual rise and fall in the mass flow rate from 42.5 ms to 63 ms. This is presented in Figure 5.8. Following this, the mass flow rate stabilised into a near steady-state like the 300K case, with a near-constant mass flow rate value of 0.01935 kg s^{-1}.

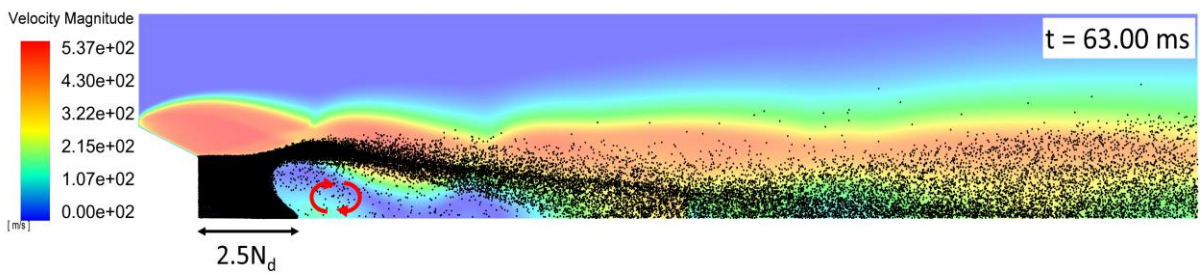

Figure 5.9 Particle trajectories taken at 63 ms exhibiting swirling of the particles in the recirculation zone. Also, at 63 ms the melt pool head penetration downstream also becomes stable.

Similarly, on observing the particle trajectories, the melt underwent pre-filming at 31.6 ms, with the particle trajectories same as observed in Figure 5.3c for the 300K case. However, there was slight delay in pre-filming time compared to that of 300K case. Also, the particle trajectories followed the same pattern of progressive dispersion. Nevertheless, a greater degree of dispersion is seen in the 600K case. This is presented in the Figure 5.9, where the particles enter the recirculation zone and circulates in the region, tracing the motion of the gas flow in the recirculation zone. Similarly, even as melt stabilisation seen in the 300K case, in the 600K case, the melt pool head downstream movement stabilised at $2.5N_d$ from t > 63 ms. This is presented in Figure 5.9.

Moreover, on examining the melt pool head movement with the mass flow rate obtained at the outlet of the domain, from Figure 5.10, it can be observed there is a steady mass build-up in the domain similar to that of the 300K case. This is inferred by comparing the injection mass flow rate plot in Figure 5.8 and the outlet mass flow rate plot in Figure 5.10. The mass flow rate reaches its near-steady state around 64 ms with a value of 0.01933 kg s^{-1}, compared to the 300K case, where mass flow rate achieves its steady state at 61.3 ms. Nevertheless, the 300K and the 600K cases were run with lower melt temperatures which might not be the same in a commerical atomisation, leading to the failure in replicating any forced instability that it is seen in the physical atomisation process. Hence, in the subsequenct runs higher melt temperatures were employed.

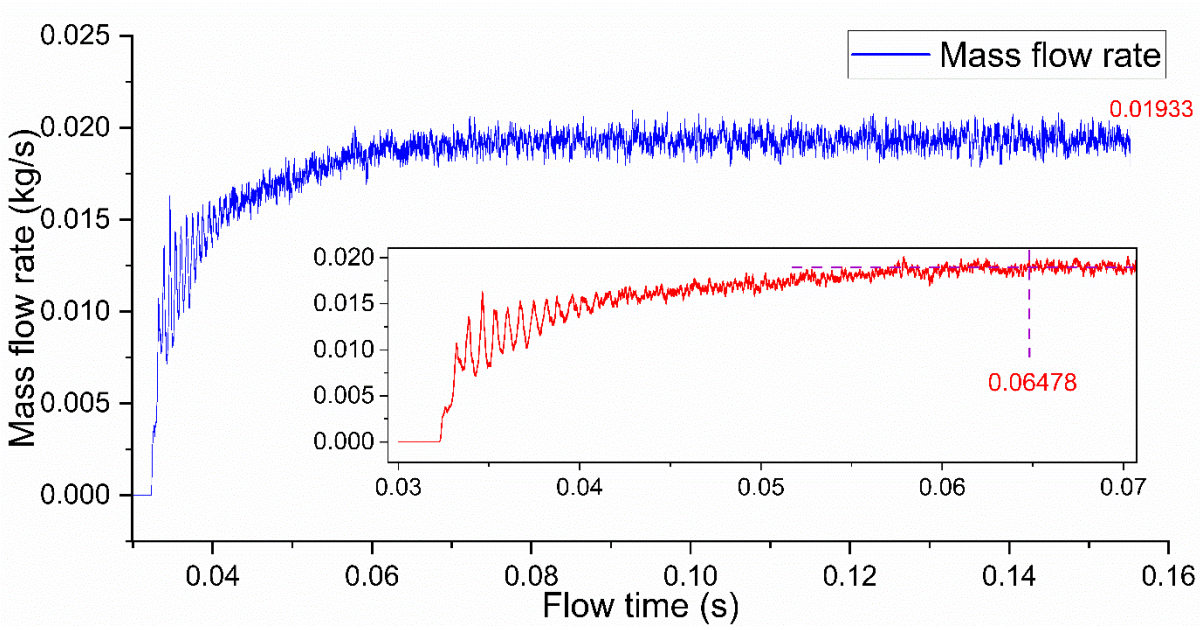

Figure 5.10 Particles' mass flow rate obtained at the outlet of the domain for 1 kg min^{-1}, 600K case, showing the flow rate reaches a near-steady state around 64 ms with a value of 0.01933 kg s^{-1}.

5.1.3 Melt temperature: 1000K

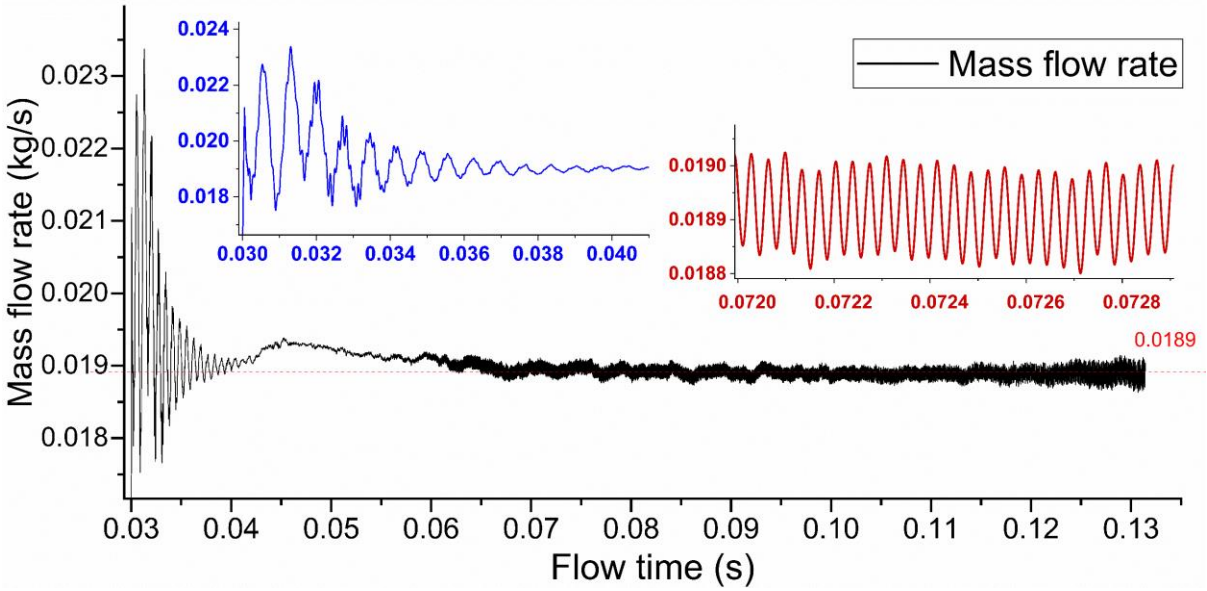

Figure 5.11 Injection mass flow rate plot for the 1 kg min^{-1}, 1000K case, showing the onset of a high frequency fluctuation at 60 ms which remains for the remainder of the simulation. The high frequency fluctuation was evaluated to be 28.5 kHz.

The 1 kg min^{-1} case with a melt temperature of 1000K run for 102 ms (30 to 132 ms), and the injection mass flow rate plot is presented in the Figure 5.11. The initial fluctuation in the mass flow rate was seen similar to that of the 300K and 600K cases. However, from 43 to 46 ms there is a sudden rise in the mass flow rate value followed by a gradual fall until 60 ms. At 60 ms there is a significant difference in the behaviour of the mass flow rate plot. A high frequency fluctuation can be observed to be coming into effect which remained for the rest of the duration. Even though, the high frequency fluctuation underwent repeated and regular fluctuation, having fixed amplitude until 110 ms, from t > 110 ms, an increase in amplitude can be observed. Evaluating the GMR of the high frequency fluctuation, it was found to be 4.59 - 4.72. Similarly, on investigating the mass flow rate plot (Figure 5.11) using FFT analysis, two frequencies were found: 1.4 kHz and 28.5 kHz, the latter of which corresponded to the high frequency fluctuation.

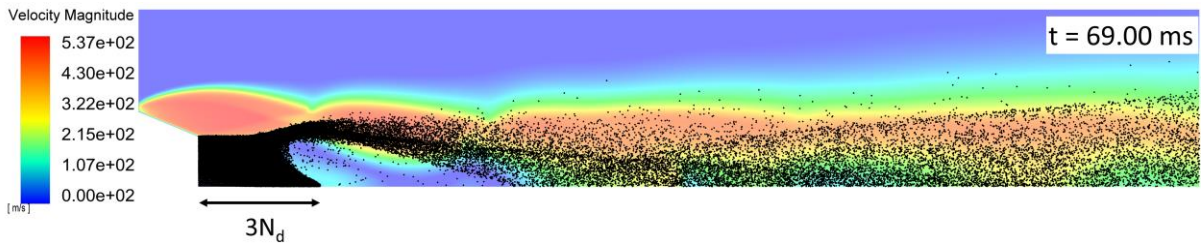

Figure 5.12 Particle trajectories obtained at 69 ms showing $3N_d$ downstream advancement of melt pool head, where it stabilises.

Similarly, the particle trajectories of the 1000K case looked very similar to that of the 300K and 600K cases. The particles underwent pre-filming at 31.7 ms (and for the 600K case it was 31.6 ms). Likewise, the particles progressively dispersed over time, and the melt pool head advanced downstream until 69 ms and stabilised at $3N_d$, as shown in Figure 5.12. The melt pool head advancing further downstream compared to that of the 600K case may be attributed to the steep mass build-up in the domain. This can be inferred by comparing the injection and outlet mass flow rate plots shown in Figure 5.11 and Figure 5.13, respectively. From the outlet mass flow rate plot seen in Figure 5.13, two stages of mass flow rate were seen: a sharp rise shown by the green arrow indicating increased rate of particles being pushed across the domain's exit, and a gradual rise shown using the violet arrow indicating much lesser rate of particles being pushed across the domain. Following this the outlet flow rate became near-constant with a value of 0.01886 kg s^{-1}.

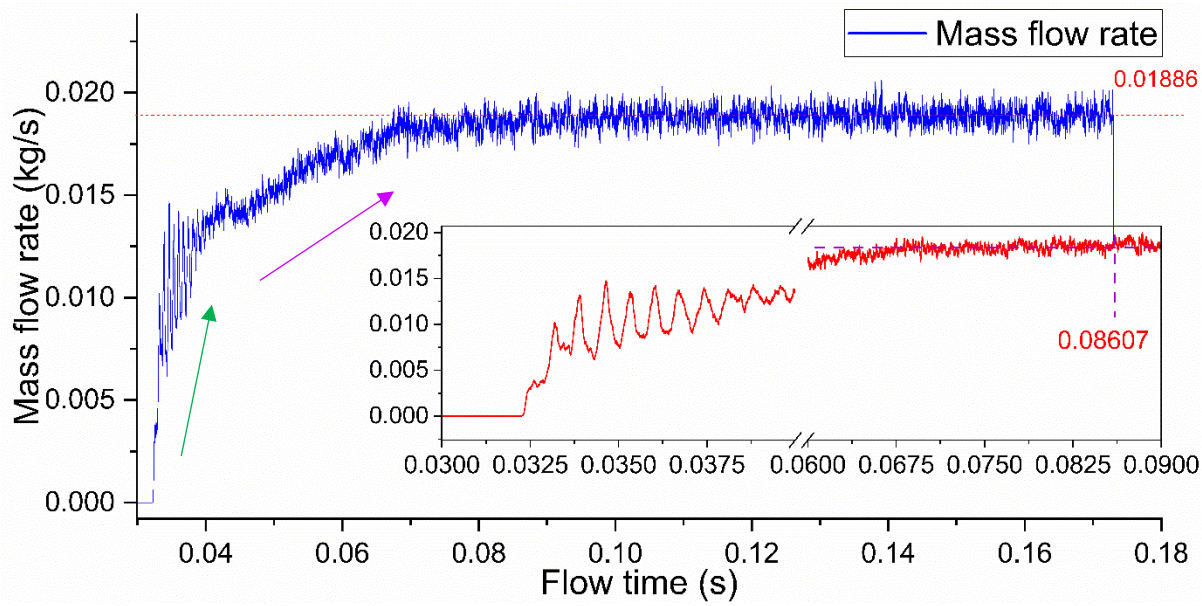

Figure 5.13 Mass flow rate of the particles obtained at the outlet of the domain for the 1 kg min^{-1}, 1000K case. There are two stages of mass flow that is observed: a steep increase as pointed by the green arrow, and a gradual rise pointed by the violet arrow.

Further to this, on examining the gas flow-field, an initial disturbance in the flow-field due to the onset of the melt injection similar to that of the previous cases (Figure 5.7) was observed. Subsequently the flow-field stabilised at 32.4 ms transitioning into open-wake condition and continued to remain in that configuration until 57 ms. At 57 ms there was an onset of instability in the flow-field which caused the flow-field to fluctuate. The fluctuation started out gradually but with time it intensified i.e. the spatial movement of the fluctuation grew with time. Moreover, at $t > 32.4$ ms the flow-field existed in open-wake condition and

continued to remain in open-wake condition during the fluctuation. To further understand the flow-field fluctuation, a series of flow-field contours were obtained in close consecutive flow time and were stacked as presented in Figure 5.14. Guide-lines were placed at key location of Figure 5.14a and were compared against with the rest of the stacks. Five vertical guide-lines (i), (ii), (iii), (iv) and (v) were placed at the end of the first shock-cell, end of the second shock-cell, stagnation point, oblique shock before the second Mach-disk, and second Mach-disk, respectively. Another secondary guide-line (white dashed line) is used to trace the ends of the second shock-cell of all the frames of the stack. Also, to understand the geometrical extent of the wake-region downstream during the fluctuation, another guide-line was used to connect the stagnation points of all the frames. Even though the melt is present in all frames of Figure 5.14, only velocity contours are presented to better the visualise the gas flow-field, especially in the wake region. During the fluctuation it was evident through guide-line (i), the first shock-cell remained fixed throughout the fluctuation. Through guide-line (ii) it was observed second shock-cell marginally increased in its geometrical extent downstream and returned back to its original configuration in Figure 5.14h, i.e., same as the configuration seen in Figure 5.14a. Contrastingly, the stagnation point moved upstream until frame e (Figure 5.14e) and returned back to its original location at the end of the fluctuation (Figure 5.14h). Likewise, the distance between the oblique shock that is present before the second Mach-disk, and the second Mach-disk gradually decreased to a very close proximity, before quicky regaining its position, as shown in Figure 5.14d and Figure 5.14g, respectively. The frequency of this flow-field fluctuation was evaluated to be 28.5 kHz, correlating to the high-frequency melt fluctuation seen in Figure 5.11.

Apart from this, a continuous wave propagation was observed beyond the second Mach-disk. This is shown in Figure 5.14 by employing ellipses to trace the wave propagation. For the duration of the flow-field fluctuation, all the above-mentioned changes in the flow-field underwent cyclic repetition. Correlations between the local extrema of the high frequency fluctuation, 28.5 kHz, seen in the mass flow rate (Figure 5.11) and the flow-field fluctuation seen in Figure 5.14 were analysed. Even though, there existed a forced continuous fluctuation in the flow-field throughout the duration, no evidence of alternation in the flow-field between open- to closed-wake were found, but rather the flow-field continued to exist in open-wake condition.

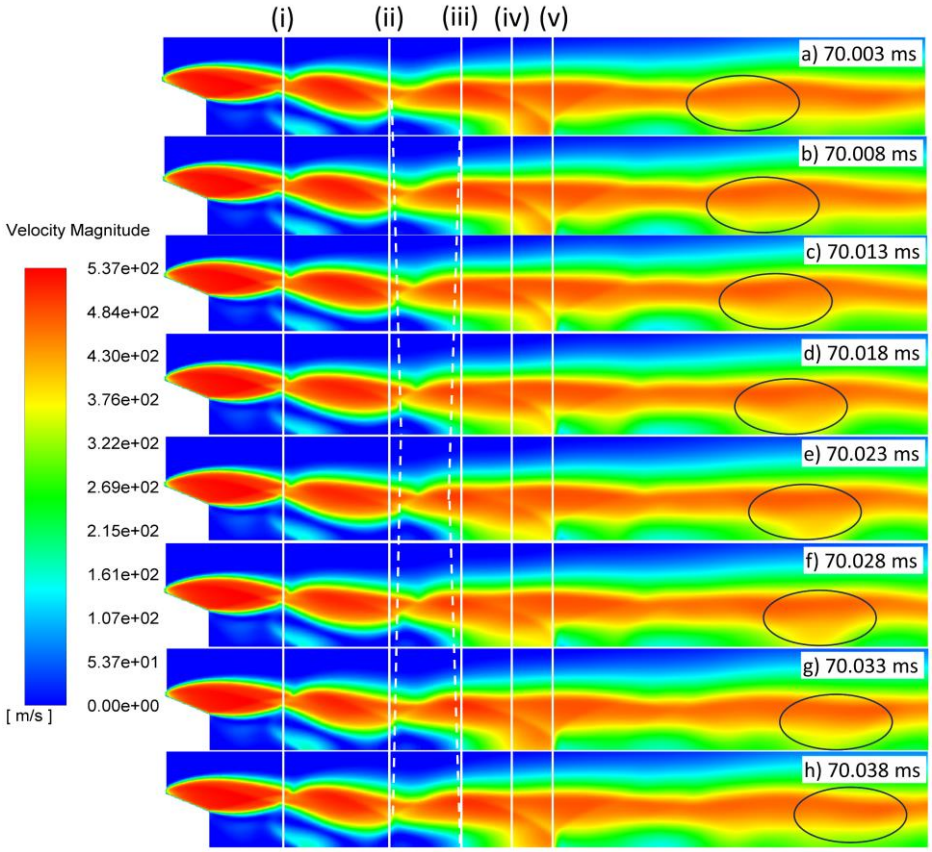

Figure 5.14 Velocity contours without particles for the 1 kg min^{-1}, 1000 K case showing flow-field fluctuation corresponding to the high frequency fluctuation seen in the injection mass flow rate. End of second shock-cell and stagnation point is seen shifting away and returning back to its original point. The wave propagation due to the flow-field oscillation is traced using ellipse.

5.1.4 Melt temperature: 1500K

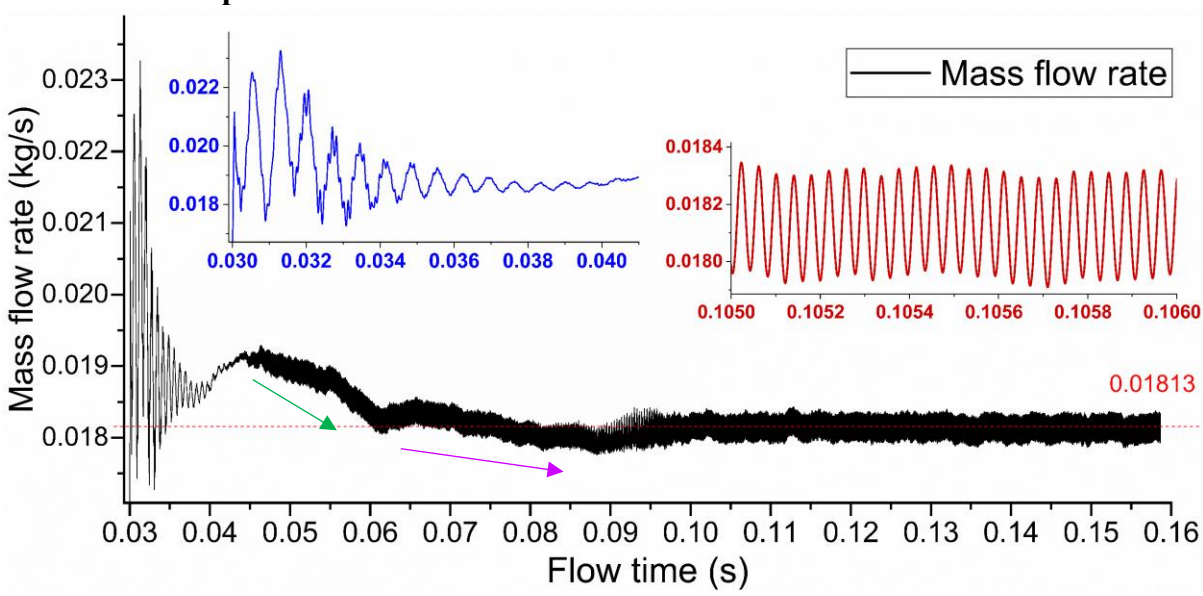

Figure 5.15 Injection mass flow rate plot of 1 kg min^{-1} case with a melt temperature of 1500K showing an initial steep rise followed by a gradual decline in two stages, shown using green and violet arrows.

The 1 kg min^{-1} case with a melt temperature of 1500K was run for 128 ms (30 to 158 ms). The Injection mass flow rate plot for the 1500K case presented in the Figure 5.15 looked similar to that of the 1000K case, however, there were few significant differences observed. After the attenuation of the initial fluctuation, at 40 ms there was a steep rise in the mass flow rate, thereafter immediately followed by a gradual and extended fall, which eventually settled into an almost-steady and near-constant amplitude flow rate. It is significant to observe from Figure 5.15, the onset of the high frequency initiated at 43 ms, well before the high frequency initiation time for the 1000K case (60 ms). After the steep rise, the decrease in the mass flow rate is seen in two stages: a steeper fall followed by a more gradual fall marked by the green and violet arrows, respectively. Thereafter, the mass flow rate stabilised to follow a repeated and orderly fluctuation from t > 100 ms, with an average mass flow rate value of 0.01813 kg s^{-1}. On evaluating, it was found the high frequency fluctuation has a varying GMR value of 4.76 – 4.93, which when compared with the 1000K case, can be evidently observed that the amplitude of the fluctuation has increased. On conducting the FFT analysis for the mass flow rate plot, two frequencies were obtained: 1.4 kHz and 25.5 kHz. The latter corresponds to the high frequency fluctuation. The same pattern of flow-field fluctuation seen in the 1000K case (Figure 5.14), corresponding to the high frequency fluctuation, was also seen in the 1500K case which corresponded to the 25.5 kHz melt fluctuation. The fluctuation possessed the same variations in the flow-field features as seen in the 1000K case (Figure 5.14).

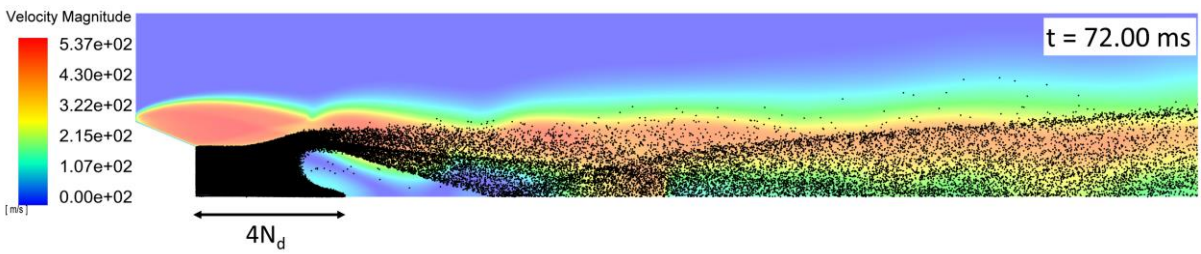

Figure 5.16 Particle trajectories of 1 kg min^{-1} case with melt temperature as 1500K obtained at 72 ms showing the extent of the melt pool head advancement downstream.

The particle trajectories followed a very similar trend as seen in the earlier cases. However, there were a few distinct differences observed in the particle trajectories. The particles underwent pre-filming at 31.9 ms (and for the 1000K case it was 31.7 ms), and from Figure 5.16 it can be observed the melt pool head advances until $4N_d$ downstream before stabilising at that location at 72 ms.

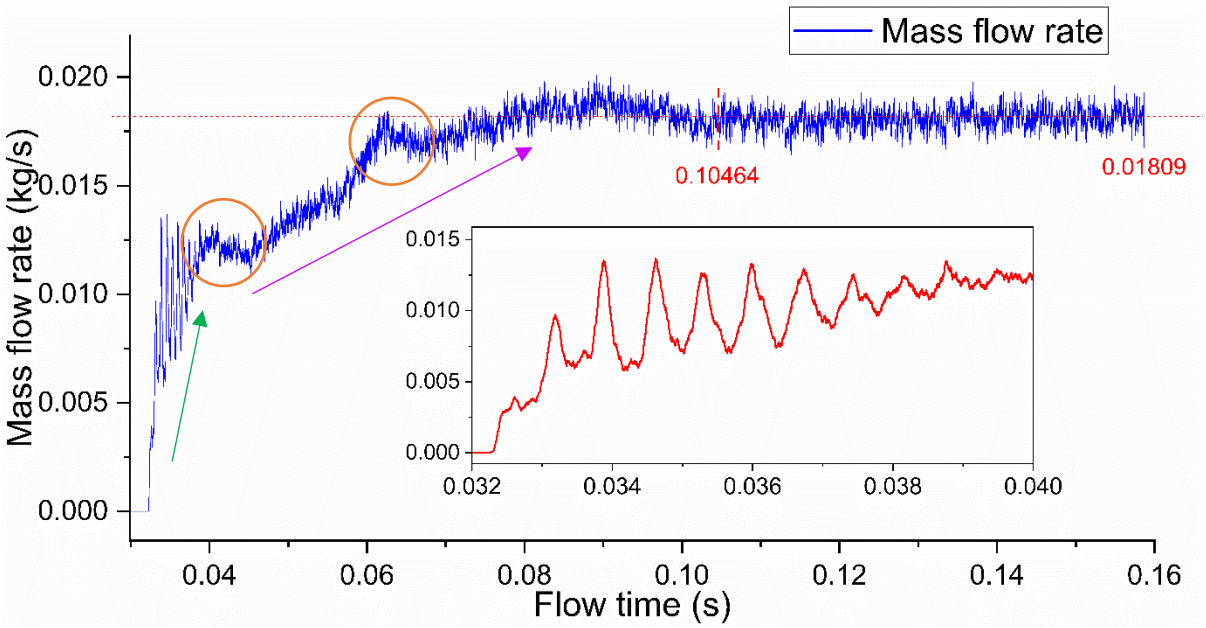

Figure 5.17 Mass flow rate of the particles recorded at the outlet of the domain for 1 kg min^{-1}, 1500K case showing two stages of continuous rise before reaching steady-state. A steeper rise followed by a gradual one, marked using the green and violet arrows, respectively. In both the stages a rise-and-fall trend is observed, shown using the orange circles. The steep rise indicates increased number of particles being pushed across the exit than the gradual rise. The rise-and-fall indicates a brief fluctuation in the rate of mass outflow.

The extended downstream movement of the melt pool head can be attributed to the increased mass build-up in the domain which can be inferred by comparing the injection mass flow rate (Figure 5.15) against the outlet mass flow rate presented in the Figure 5.17. Two stages of mass out-flow were observed in Figure 5.17: a steeper and gradual, marked by the green and violet arrows, respectively. In both the stages, there is a rise-and-fall trend, marked by the orange circles, indicated in Figure 5.17. The steep rise indicates increased number of particles being pushed across the exit than the gradual rise. The rise-and-fall (orange circles) indicates a brief fluctuation in the rate of mass out-flow, which may be attributed to the changes seen in the injection mass flow rate. The outlet mass flow rate eventually attains a relatively constant mass flow rate at 104.6 ms. Averaging the relatively constant section from t > 104 ms, the average mass flow rate was worked to be 0.01809 kg s^{-1}.

5.1.5 Melt temperature: 2000K

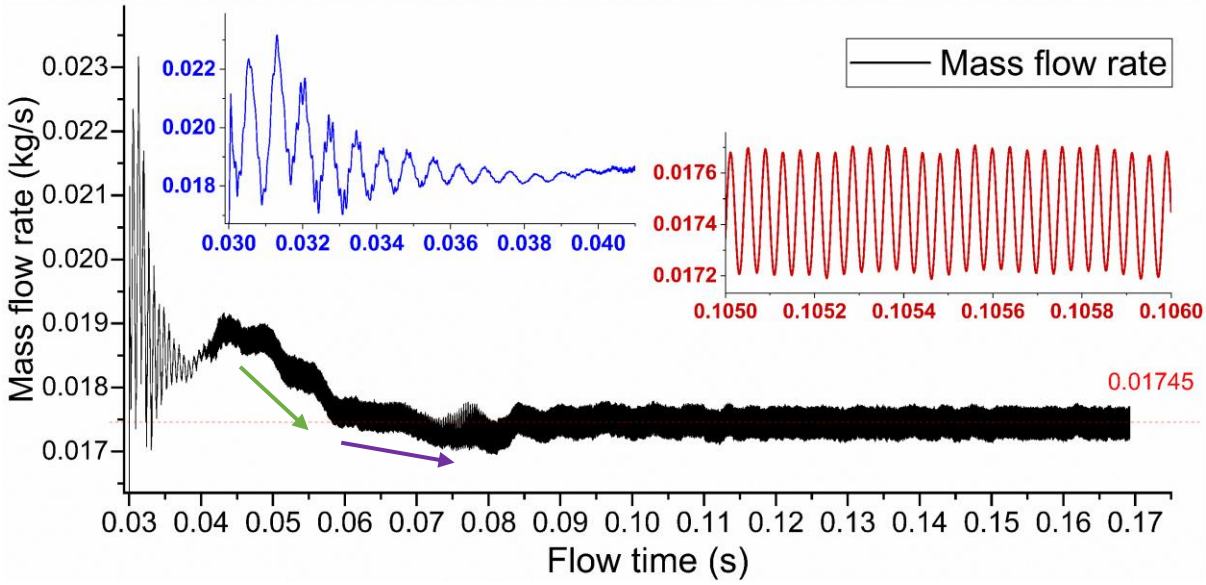

Figure 5.18 Injection mass flow rate of 1 kg min^{-1} case for a melt temperature of 2000K.

The 1 kg min^{-1} case with a melt temperature of 2000K case was run for 139 ms (30 to 169 ms). The injection mass flow rate of the 2000K case is presented in Figure 5.18. Even though the 2000K case's mass flow rate plot follows the similar trend to that of the 1500K case, there were distinct and significant developments seen in the 2000K case. After the initial fluctuation, the higher frequency fluctuation develops at 40 ms i.e. 10 ms into the melt injection. After a brief rise in the mass flow rate, from 43 to 70 ms an overall decrease in the mass flow rate was observed, however as it decreased there were multiple intermittent rise-and-fall in the flow rate present. But in general the decline could be classified into two stages: a steeper decline and another a gradual decline, marked by the green and violet arrows, respectively, as shown in Figure 5.18. Around 90ms the plot transitioned into a regular fluctuation with near-constant amplitude, fluctuating about a mean value. On averaging the plot for t > 90 ms, this mean value was calculated to be 0.01745 kg s^{-1}. Furthermore, it was found the high frequency fluctuation had a varying GMR value of 4.94 - 5.14, which when compared against the 1500K case was evident that the amplitude of the fluctuation has further increased. From the FFT analysis of the plot in Figure 5.18, two frequencies: 1.4 kHz and 25.5 kHz, same as the frequencies obtained in the 1500K case, were found. Examining the flow-field for the high frequency fluctuation, 25.5 kHz, the same flow-field fluctuation as seen in the 1000K and 1500K cases (Figure 5.14) were observed with the same characteristic changes in their flow features. However, in the 2000K case, the spatial movement of the flow-field during the

fluctuation was more pronounced compared to the 1000K and 1500K cases, and this can be attributed to the increased amplitude seen in the melt fluctuation.

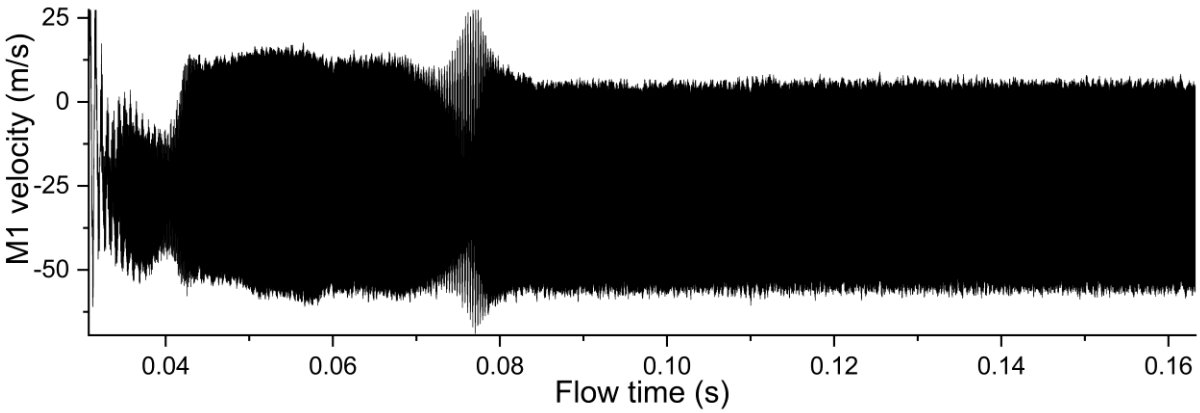

Figure 5.19 Monitor-M1 velocity obtained for the 1 kg min^{-1} , 2000K melt temperature case containing high frequency fluctuation showing the continuous and rapid oscillation of the flow-field.

The high-frequency flow-field fluctuation that corresponds to the high-frequency melt fluctuation observed in the injection mass flow rate (Figure 5.18), was further confirmed to contain the same 25.5 kHz using velocity monitors that were located at seven key locations (Figure 5.1), all on the axis of the atomiser. The first monitor, M1, is presented in Figure 5.19. The graph displays pronounced high-frequency fluctuation which is heavily condensed, rendering it difficult to examine the trends in the plot. Hence for all the seven monitors, the graphs are zoomed in at the time of melt injection and at the high frequency fluctuation segment. This is illustrated in Figure 5.20. The evaluation of the higher frequency fluctuation across all the seven monitors resulted in a consistent frequency of 25.5 kHz, validating the frequency of the observed flow-field fluctuation as visualised through the velocity contours. Also, in Figure 5.20 even though all the monitors displayed the same high frequency, there existed phase difference between the monitors. This is shown using the red dashed guide-line. This observed phase difference might be a reflection of the travel time between the spatially separated velocity monitors, and also might indicate an unsynchronised expansion and

contraction of the individual sections of the flow-field, especially between monitors M4 and M5, and M5 and M7.

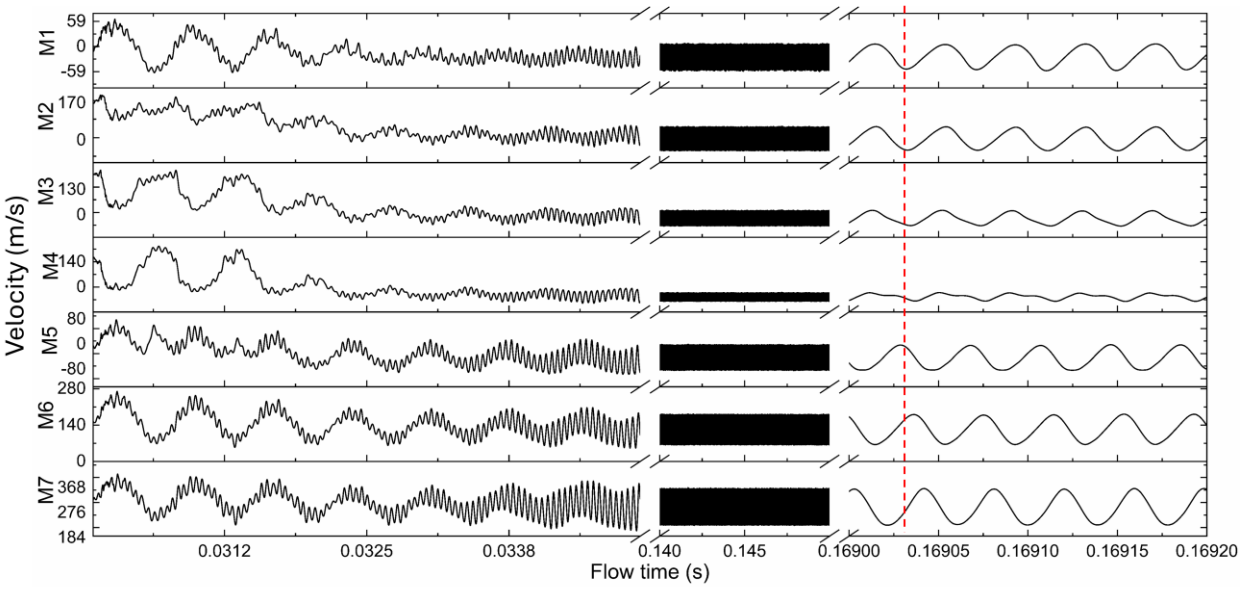

Figure 5.20 Monitors M1 to M7 for the 1 kg min^{-1} , 2000K case zoomed in at the injection of the melt and at the high frequency fluctuation. The high frequency for all the 7 monitors is same as the high frequency seen in the injection mass flow rate i.e., 25.5 kHz. The high frequency fluctuation exhibits phase difference between the monitors which is indicated by the red dashed guide-line.

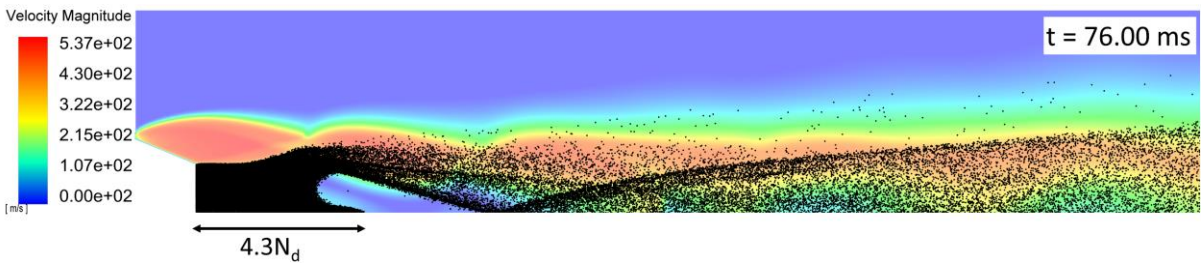

Figure 5.21 Particle trajectories obtained at 76 ms showing pointed and protracted downstream movement of the melt pool head.

The particle trajectories of the 2000K case followed a similar trend as seen in the earlier cases of 1000K and 1500K, where after the pre-filming the trajectories were more collimated, and with time they progressively dispersed. The melt underwent pre-filming at 32 ms, in the same fashion as seen in Figure 5.3c. However, the morphology of the melt pool head became sharper with time. This is shown in Figure 5.21. The melt pool head moved 4.3N_d downstream before stabilising at that location at 76 ms. This extended downstream movement of the melt pool head is due to the increased mass loading which can be observed by comparing the injection mass flow rate (Figure 5.18) against particle outlet mass flow rate presented in Figure

5.22. From the outlet mass flow rate, it was also observed that even though the rate of out-flow for the 2000K case was in two stages as seen in the 1500K case (Figure 5.17), the second stage in Figure 5.22 contained multiple fluctuation, indicating an increase in instability in the process. However, the mass out-flow steadied out around 115 ms, reaching a near-steady value of 0.01744 kg s^{-1}.

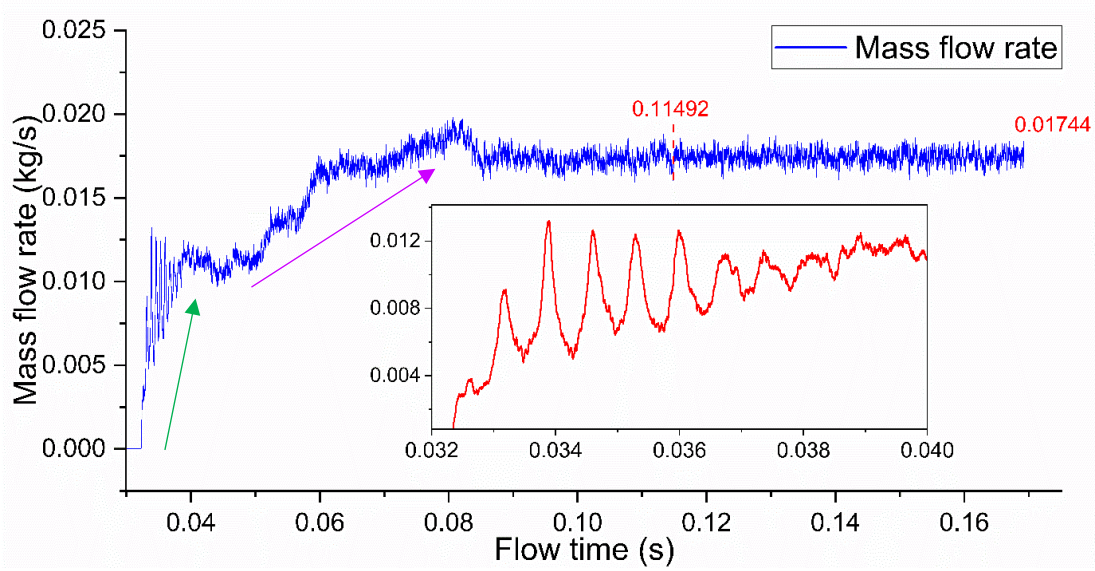

Figure 5.22 Mass flow rate of the melt obtained at the outlet of the domain for the 1 kg min^{-1} case with melt temperature as 2000K.

5.1.6 Summary

From the 1 kg min^{-1} (GMR=5.5) cases it was observed that the injection mass flow rates were stable, although increase in melt temperature induced instability into the process as evidently observed from Figure 5.18 and Figure 5.22, they were regular in nature and possessed low amplitude fluctuation. This is because, all the five cases discussed were gas dominated – GMR=5.5. However, with the increase in the melt temperature, the average injected mass flow rate decreased. Also, it was observed with the increase in the melt temperature, the pre-filming time increased and the melt pool head extended further downstream.

Likewise, the flow-field fluctuations were weak in its spatial movement and continued to exist under open-wake condition. Contrarily, in the physical atomisation, the process is far from steady-state, and the wake alternates between open- to closed-wake condition. With the observed fluctuations in the 1 kg min^{-1} cases being far from what is observed in the physical atomisation, simulation runs with lower GMR of 2.6, i.e., a higher mass flow rate of 2 kg min^{-1} were run.

5.2 Results of 2 kg min^{-1} (GMR = 2.6) under increasing melt temperatures.

This section presents the results of 2 kg min^{-1} case having GMR=2.6, investigating the effect of increasing melt temperatures. The melt temperatures considered for this GMR are: 300K, 600K, 1000K, 1500K, and 2000K (Table 4-6). The section is sub-divided to present and analyse the results for each of the melt temperature individually.

5.2.1 Melt temperature: 300K

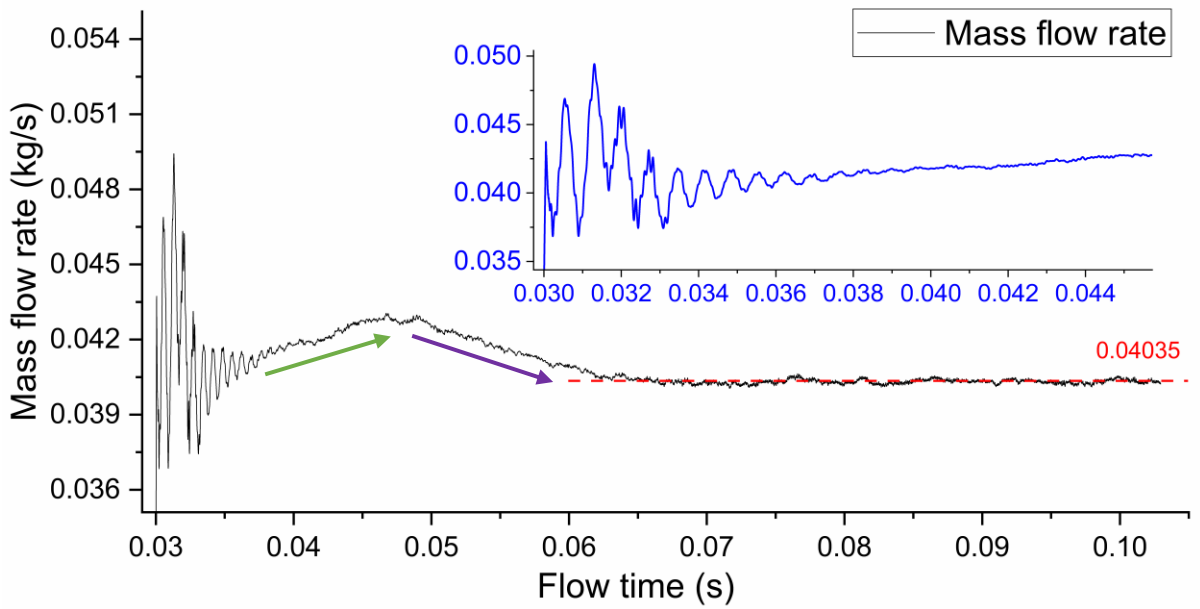

Figure 5.23 Injection mass flow rate plot of 2 kg min^{-1}, 300K melt temperature case, showing initial fluctuation followed by a gradual rise-and-fall trend, indicated using the green and violet arrows, respectively. After this brief change, it transitions into a near-constant mass flow rate.

The 2 kg min^{-1} (0.033 kg s^{-1}) case having a GMR value of 2.6 and a melt temperature of 300K was run for 74 ms (30 to 104 ms). As observed from the mass flow rate plot in Figure 5.23, there was an initial steep rise in the mass flow rate value for the first 0.5 ms into the injection, thereafter, evolving into a damped fluctuation. In the subsequent cycles, the large amplitude fluctuations seen till 33 ms reduced in its amplitude, and eventually attenuated into a fluctuation having negligible amplitude. From 39 ms i.e., 9 ms into the injection, there was a steady overall rise-and-fall trend in the mass flow rate, shown using the green and violet arrows, respectively. However, there were no high amplitude fluctuations as seen in the previous cycles. Following by the rise-and-fall, at 66.5 ms the mass flow rate becomes an approximate steady-state with a value of 0.04035 kg s^{-1}. The initial fluctuation seen until 39 ms can be attributed to the onset of the melt injection causing disturbance to the flow-field, which in turn altered the coupled mass flow rate.

Considering the particle trajectories with the gas flow-field in the background for the 2 kg min^{-1}, 300K case, due to the introduction of melt into the atomisation chamber the flow-field was disturbed from its steady-state condition. This is illustrated in Figure 5.24a, where two guide-lines were pinned at first and second Mach-disk, respectively, and were compared against Figure 5.24b to observe the changes in the flow features. The flow-field in the latter reduced in its spatial extent i.e. moved upstream, with the introduction of the melt into the atomisation chamber. The evolvement of particles seen in this case was similar to that of the 1 kg min^{-1} cases (Figure 5.3), wherein the particles initially moved downstream (Figure 5.24b), and due to the opposing force of the recirculation zone they built-up in front of the melt nozzle exit (Figure 5.24c). When the particles came in contact with the supersonic flow-field, they were pushed downstream as shown in Figure 5.24c & d. Subsequently, the particles underwent pre-filming 2 ms after the melt injection (Figure 5.24e). The particles that were pushed downstream after coming in contact with the supersonic flow-field were initially tightly collimated until the first shock-cell, but later dispersed downstream from the second shock-cell onwards. However, later as the time progressed the particles started to disperse even from the first shock-cell as evidently seen in the Figure 5.24f & g. The increase in the particle dispersion can be observed by comparing Figure 5.24 and Figure 5.25, where due to the progressive increase in dispersion, the particles which touched the axis of the atomiser beyond the second Mach-disk at 35 ms (Figure 5.24g), moves upstream and touches the axis of the atomiser midway of the second shock-cell at 70 ms (Figure 5.25c). Also, due to the mass build-up in the domain, there was a consistent downstream movement of the melt pool head until 70 ms where it stabilised at $4.3N_d$ from the nozzle exit. This is shown in Figure 5.25. To understand the melt pool head movement downstream, a guide-line is fixed at the melt pool head tip in Figure 5.25c, and is compared against with the melt pool head tips presented in Figure 5.25a & b. This enables the observation of the melt pool head's downstream movement. Another observation was, the morphology of the melt pool head transformed from being sloped at 50 ms to more pointed at 70 ms, and this may be attributed to the combined effect of melt build-up and the recirculation zone.

Comparing the particle trajectories against the mass flow rate obtained at the outlet of the domain presented in Figure 5.26, it can be observed that there is a continuous mass loading in the domain until 70ms, which might be the reason for the extended downstream movement of the melt pool head before stabilising at 70 ms. When further observed in Figure 5.26 the mass build-up happens in two stages: an initial steep build-up followed by a subsequent gradual

build-up, marked by the green and violet arrow, respectively. In-between these two stages, a brief period of declining mass flow rate was observed, indicated by the orange circle. Nevertheless, the effect of this brief decline in mass flow rate was not observed in the particle trajectories.

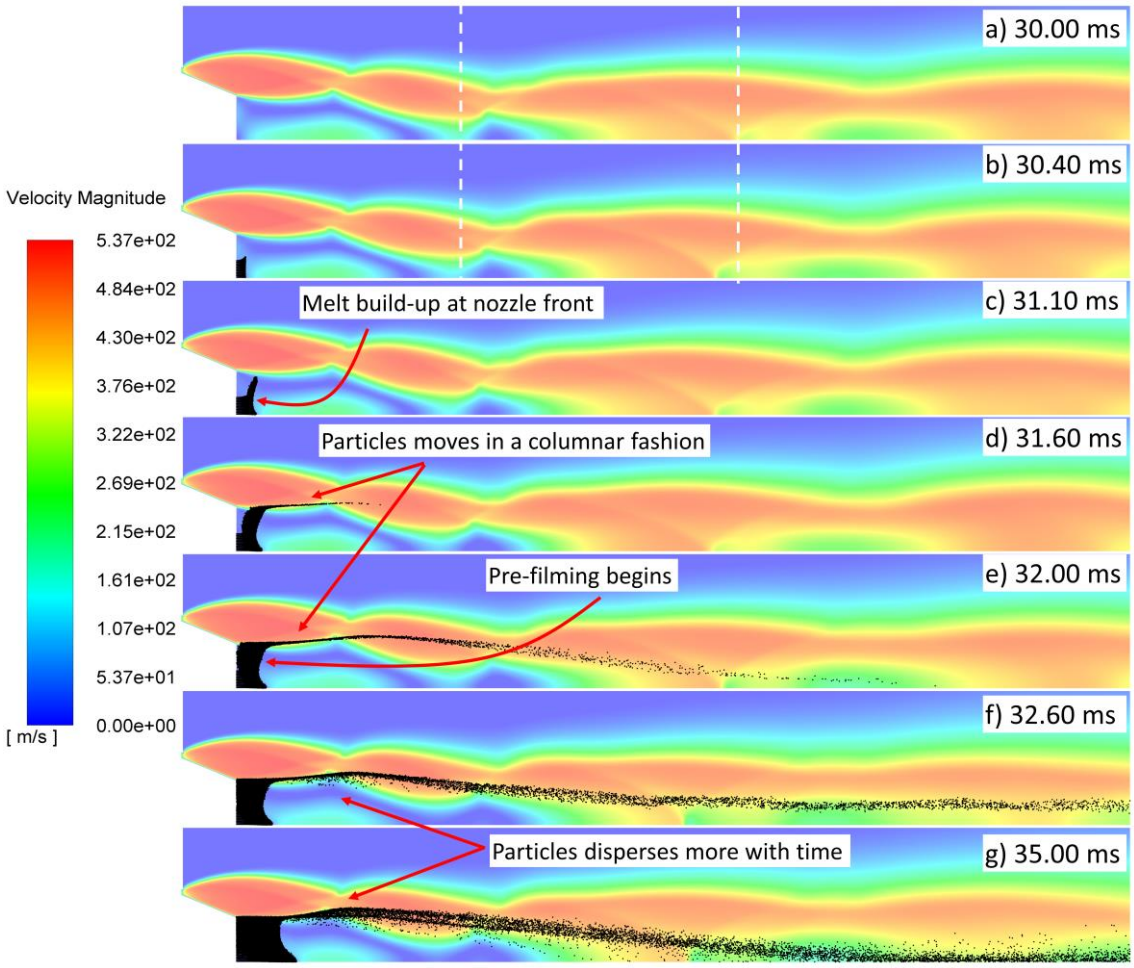

Figure 5.24 Particle trajectories with velocity contours in the background showing how the particles evolve after injection. These stacks of particle tracjectories shows the onset of injection, pre-filming, movement downstream, and increased dispersion of particles.

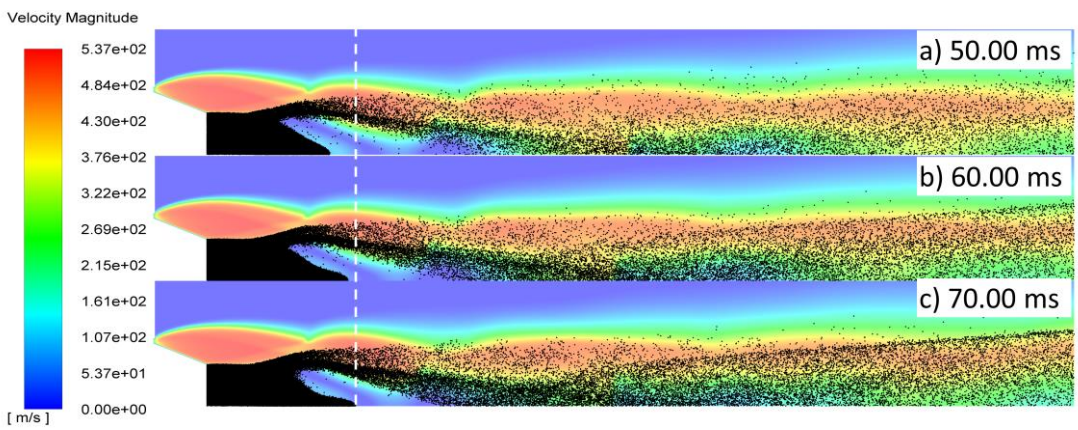

Figure 5.25 Particle trajectories with the velocity contour in the background showing melt pool head moving downstream before stabilising at 70 ms.

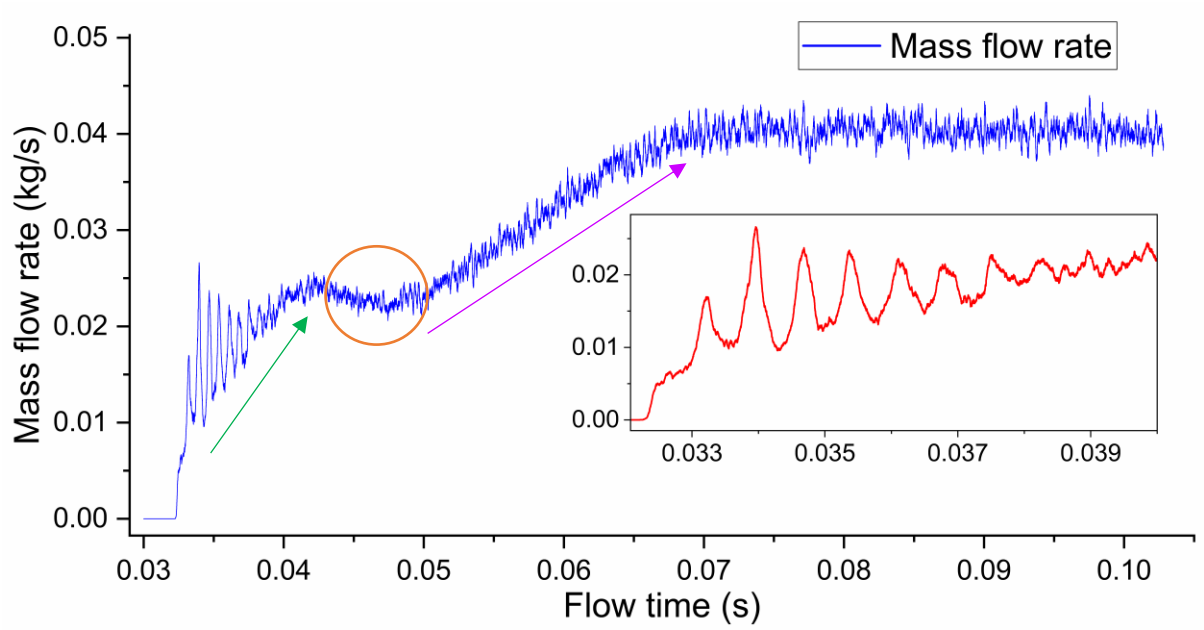

Figure 5.26 Mass flow rate of the particles obtained at the outlet of the domain for 2 kg min^{-1}, 300K case. Two stages of mass build-up is seen: an initial steep mass build-up followed by a secondary gradual build-up, marked using green and violet arrrows, respectively. Following this, around 70 ms the mass flow rate attains an approximate steady-state value.

On observing the flow-field of the 2 kg min^{-1}, 300K case, series of significant observations were noted. Upon introducing the melt into the well-established steady-state flow-field, it induced a disturbance to the steady-state condition. Due to which the flow-field underwent repeated fluctuation alternating between contracting and expanding flow-field i.e., flow features shifting upstream and downstream, repeatedly. This is illustrated in Figure 5.27 by stacking flow-field contours obtained at close consecutive flow time, recorded during the melt injection whereby detailing the upstream and downstream movements. A white dashed guide-line is fixed at the first Mach-disk in the Figure 5.27a and is compared against the other stacks to observe the movements. It is evident that the flow-field fluctuates between contracting and expanding flow-field. However, this fluctuation gradually reduced in its spatial oscillation, converging into a steady-state flow around 40 ms. With the attenuation of the fluctuation still in progress, the flow-field transitioned from closed-wake to open-wake condition at 32.5 ms and continued to exist in the same state until 65 ms. This is depicted in the Figure 5.28. Also, it was interesting to observe that the steady-state flow condition existed only for a brief period of time from 40 to 60 ms. Around 60 ms there was an onset of a fluctuation in the flow-field, which started gradually but with time grew in its spatial magnitude, and continued to exist until the remainder of the simulation. Since, the fluctuation attained its maximum spatial movement around 70 ms, series of velocity contours were recorded in close consecutive flow time at 70 ms

to understand the phenomena. This is shown in Figure 5.29, where guide-lines were pinned at key locations to analyse the movement of the flow-field features during fluctuation. Vertical guide-lines (i) and (ii) were pinned in the Figure 5.29a, at end of the first shock-cell and at the first Mach-disk, respectively and were compared against the other stacks. Similarly, another secondary guide-line in the form of a white dashed line was used to trace the end of the second shock-cell throughout the fluctuation. From the Figure 5.29 it was evident that during the fluctuation, the first shock-cell remained fixed and unchanged in its spatial extents, whereas the second shock-cell underwent fluctuation by changing its spatial extents. This is seen through the secondary white dashed guide-lines, where the line traces the ends of the second shock-cell both during expanding (Figure 5.29a-f), and contracting (Figure 5.29g-k). Through the help of guide-line (ii) it can be confirmed, that the flow-field undergoes a repeated and orderly fluctuation, with the flow-field alternating between open- to closed wake condition. The first Mach-disk which is seen in the Figure 5.29a, which indicates that the flow-field exists in closed-wake condition, gradually transitioned to open-wake condition, i.e., without the presence of any significant Mach-disk in frame f, and returned back to its original configuration of closed-wake condition having the same position as Figure 5.29a in Figure 5.29k. In addition to the above-mentioned observations, a wave propagating from the second Mach-disk and continuing to propagate until the end of domain, was also observed. In Figure 5.29 the wave propagation is marked by the blue ellipses. The flow-field fluctuation was evaluated for its frequency and was found to be 20kHz. The mass flow rate plot was examined to check for frequency corresponding to the frequency of flow-field fluctuation (20 kHz). However, when the mass flow rate plot was visually inspected for any high-frequency fluctuation as seen in the 1 kg min^{-1} cases of 1000K, 1500K and 2000K, no significant high-frequency fluctuations were seen. However, on further inspection of the plot, a high-frequency fluctuation having a negligible amplitude was found. Carrying out a FFT analysis, it was evaluated the high-frequency fluctuation had a frequency of 19.7 kHz. The reason for the difference in the flow-field fluctuation frequency (20kHz) and the mass flow rate high-frequency fluctuation (19.7kHz) is due to the lack of additional significant figures in the recorded flow times, leading to the difference of 300Hz. However, on inspecting the 19.7 kHz no relation could be drawn between the alternating flow-field fluctuation with the local extrema of the melt signal.

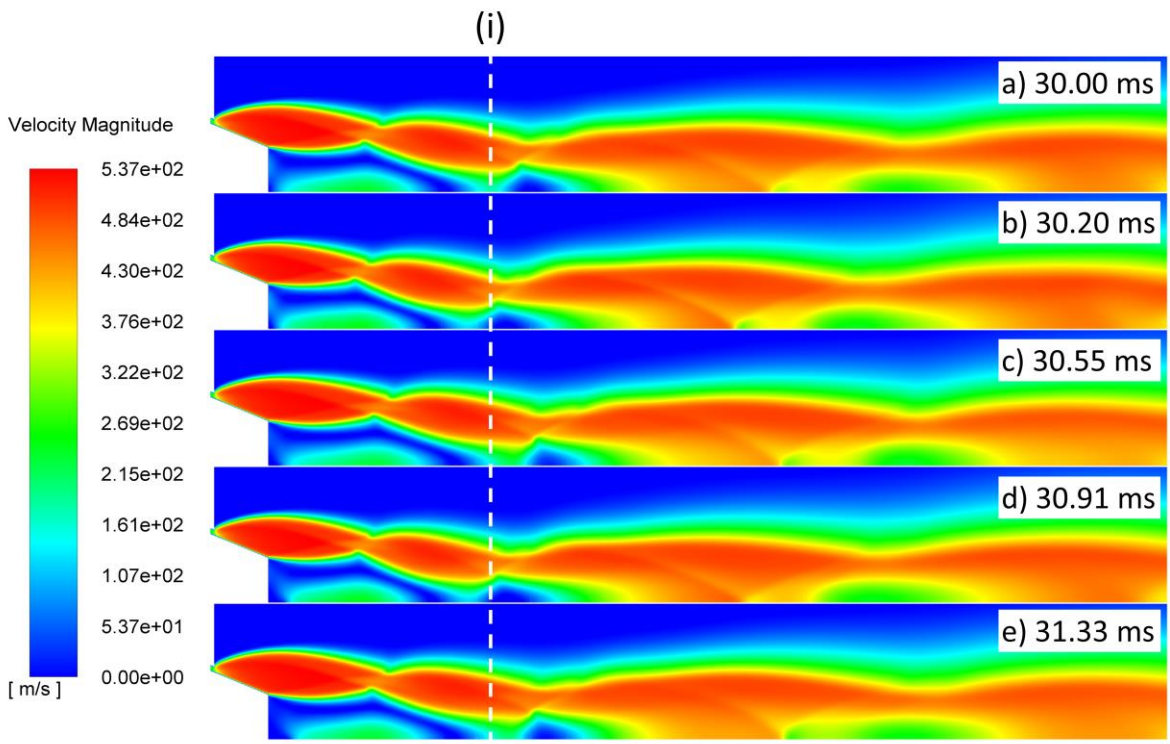

Figure 5.27 Velocity contours for the 2 kg min^{-1}, 300K case, showing the flow-field undergoing fluctuation in the first few milliseconds due to the melt injection. This is shown by the guide-line (i) fixed at the first Mach-disk of frame a) and compared against the rest of the frames.

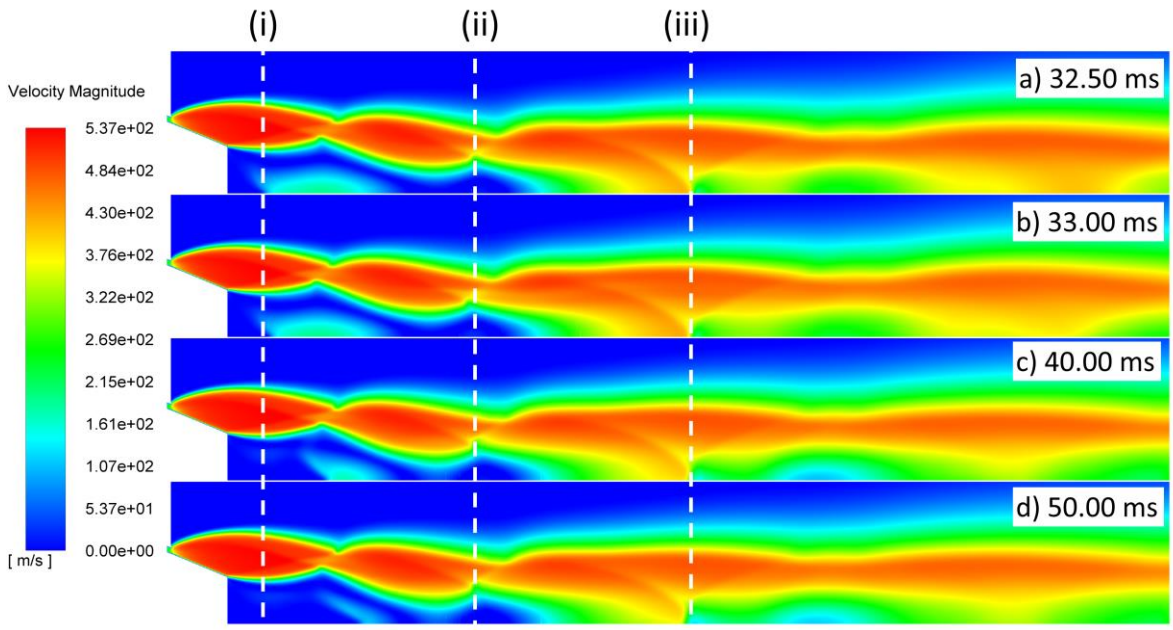

Figure 5.28 Velocity contours showing flow-field continues to exist as open wake from 32.5 ms. Three guide-lines (i), (ii), and (iii) pinned at melt pool head tip, end of second shock-cell, and second Mach-disk, respectively, in frame a. The melt pool head tip continues to move downstream even though the flow-field continues to exist in steady-state condition.

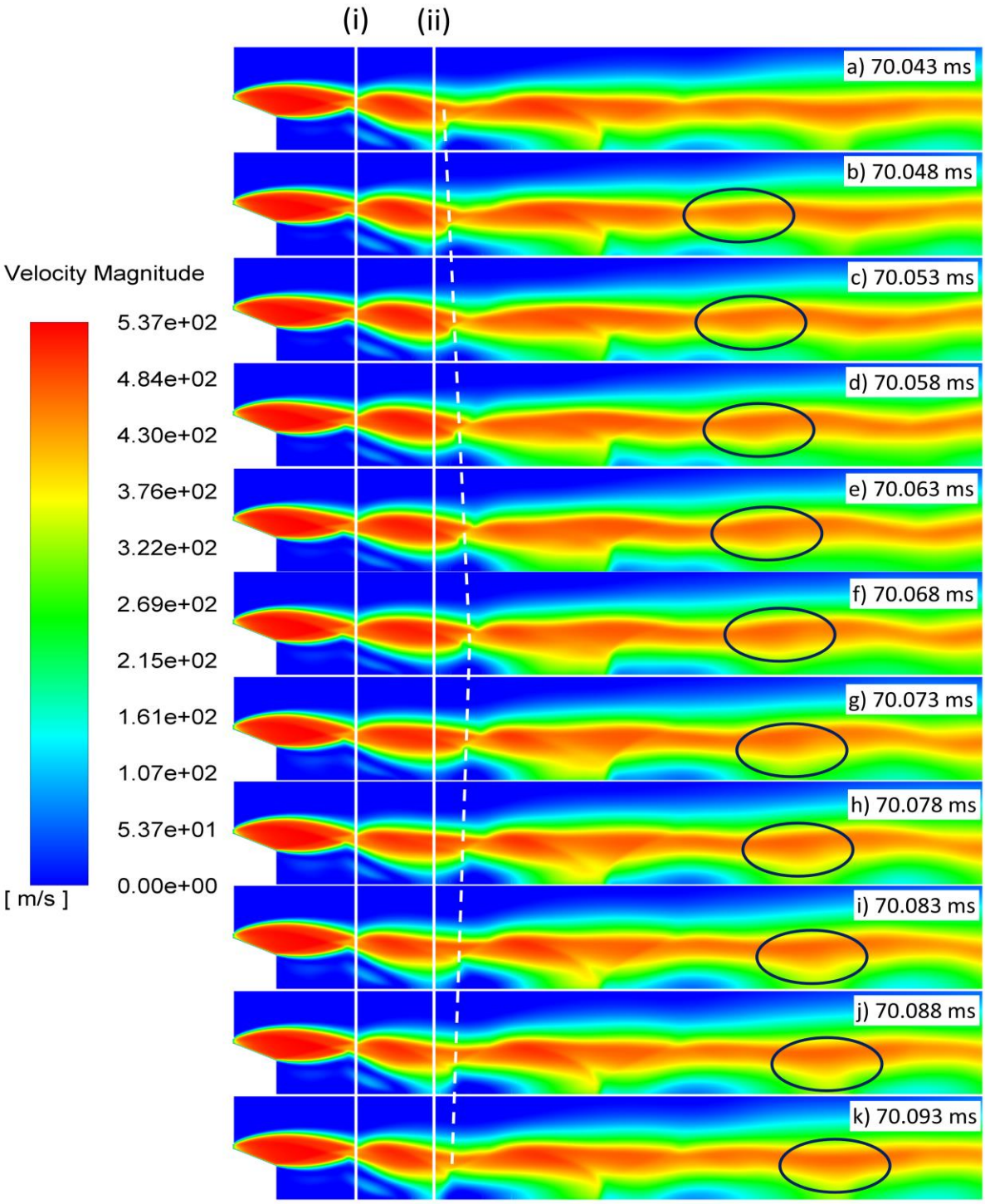

Figure 5.29 Velocity contours showing a cycle of the repeated flow-field fluctuation. Two primary guide-lines (i) and (ii) are fixed at the end of the first shock-cell and at the first Mach-disk, respectively, and are used to compare the extent of the flow-field fluctuation against the rest of the frames. Another dashed white line is used to trace the movement of the end of the second shock-cell during the fluctuation. It is seen the first shock-cell didn't change in shape or length whereas the second shock-cell, as marked with the white dashed line, changed in its spatial dimensions.

5.2.2 Melt temperature: 600K

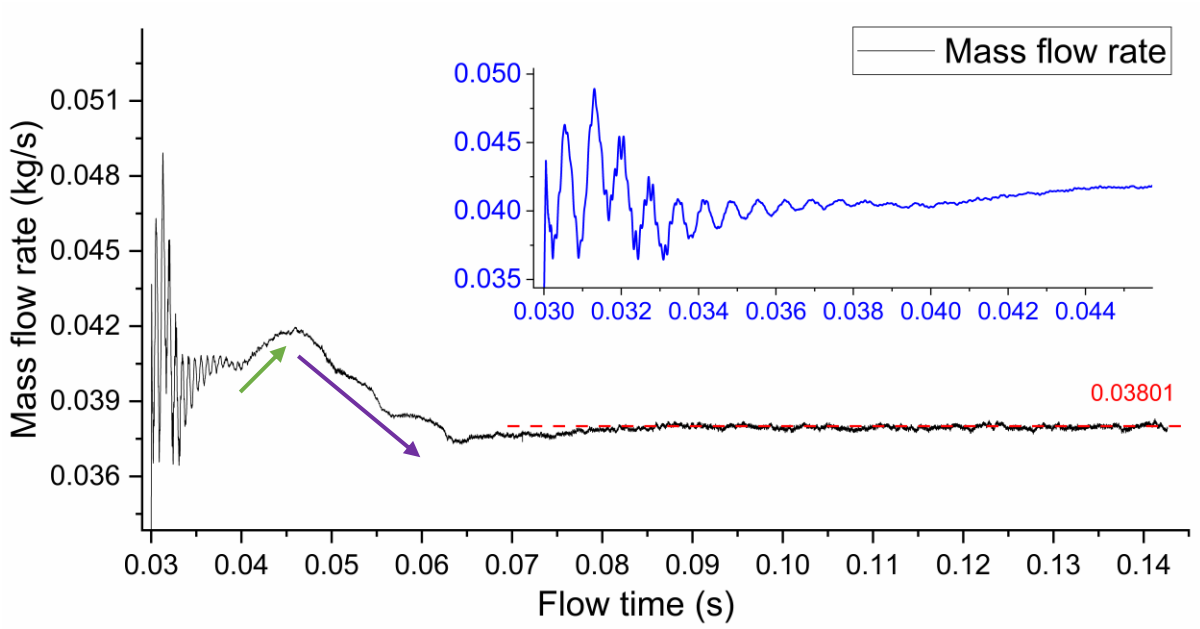

Figure 5.30 Mass flow rate plot of 2 kg min^{-1}, 600K melt temperature case, showing initial fluctuation followed by a gradual rise and steeper fall trend, indicated by the green and violet arrows, respectively. Around 85 ms, it achieves a near constant mass flow rate.

Following the 300K case, to investigate the effects of elevated melt temperature conditions, the 2 kg min^{-1} case with a melt temperature of 600K was run for 113 ms (30 to 143 ms). The mass flow rate of the melt injection is presented in Figure 5.30. The general behaviour of the 600K case was similar to that of the 300K case. However, there were few significant differences observed, as outlined below. After the attenuation of the initial fluctuation, at 40 ms there was a rise in the mass flow rate for a brief period of time, indicated by green arrow, subsequently followed by an extended fall in its value until 65 ms, indicated by violet arrow. Thereafter with a marginal increase, the mass flow rate reaches a near constant value of 0.03801 kg s^{-1} at t > 85 ms.

Considering the particle trajectories, it was observed that the 600K case followed a similar pattern to as that of the 300K case. The particle trajectories for the 600K case are presented in the Figure 5.31. The same pattern of melt been injected, melt undergoing pre-filming, progressive particles' dispersion and melt pool head movement downstream were observed in the 600K case as well. The particles underwent pre-filming at 32.10 ms, whereas for the 300K case it was 32.0 ms. In the 600K case one other significant observation was noticed: the melt pool head due to the extended movement downstream joined with the particles that were pushed downstream by the supersonic gas jet at 58 ms. This is illustrated in the Figure 5.31g. The melt pool further moves downstream plunging into the second Mach-disk, which

can be seen from the Figure 5.32. Nevertheless from 70 ms as observed from Figure 5.32, both particle trajectories and particle dispersion seem to be relatively same, without undergoing any change to its particle flow pattern.

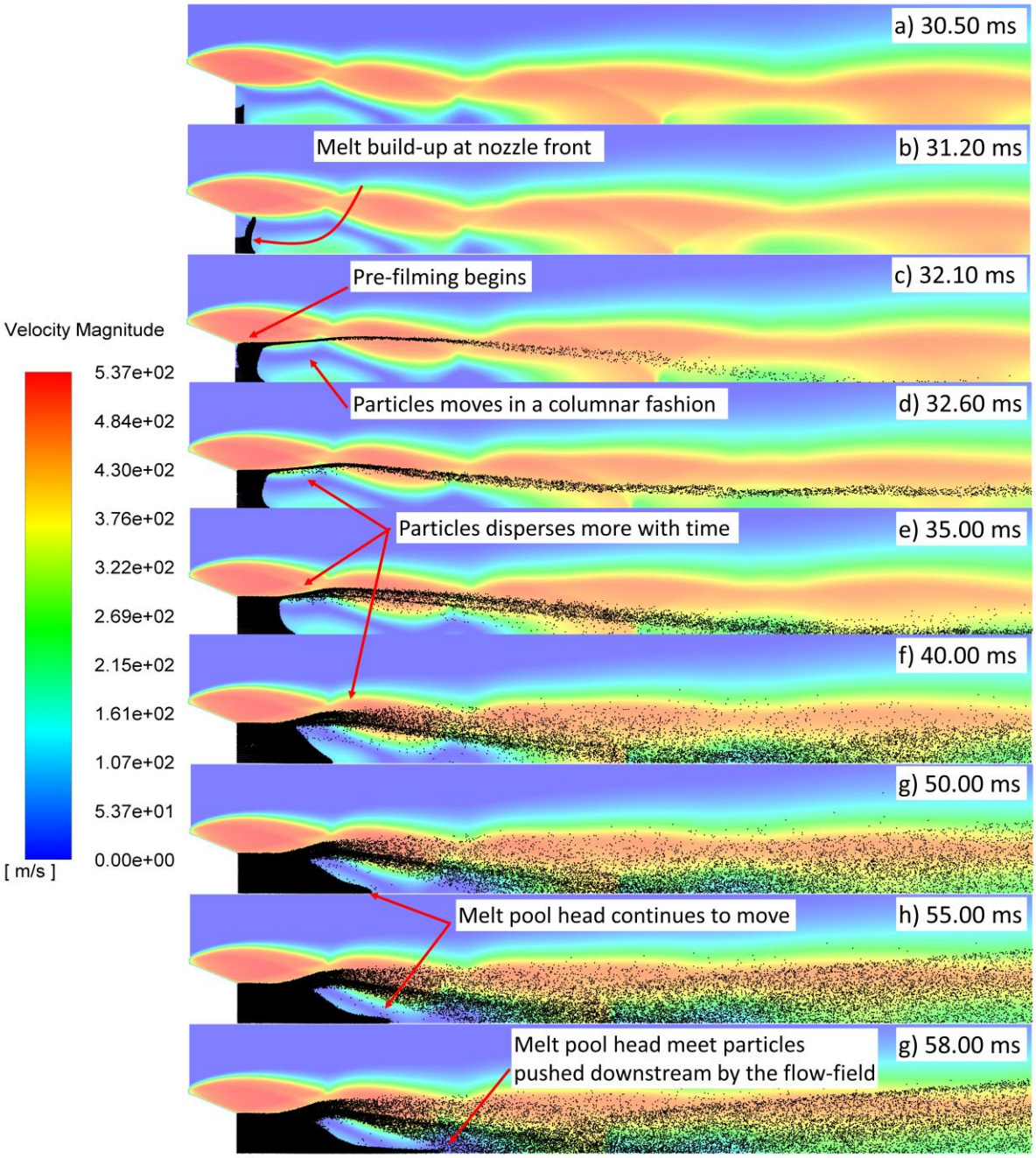

Figure 5.31 Particle trajectories with the velocity contours of the flow-field presented at the background, showing the particles evolving over time. At 58 ms the melt pool rejoins the particles that flow downstream pushed by the flow-field.

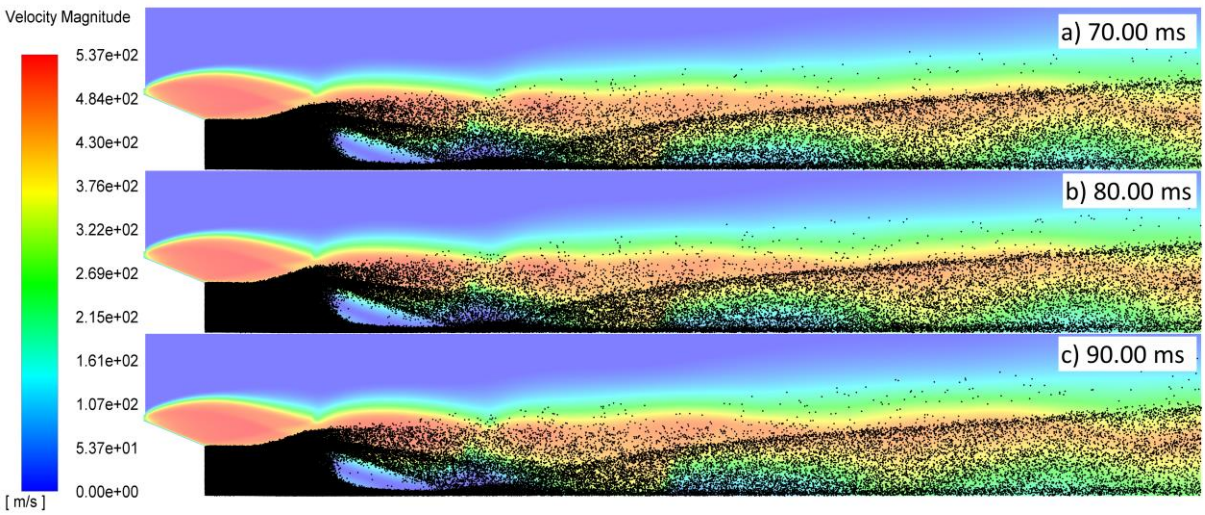

Figure 5.32 Particle trajectories with the velocity contours of the flow-field presented at the background, showing steady flow of particle trajectories.

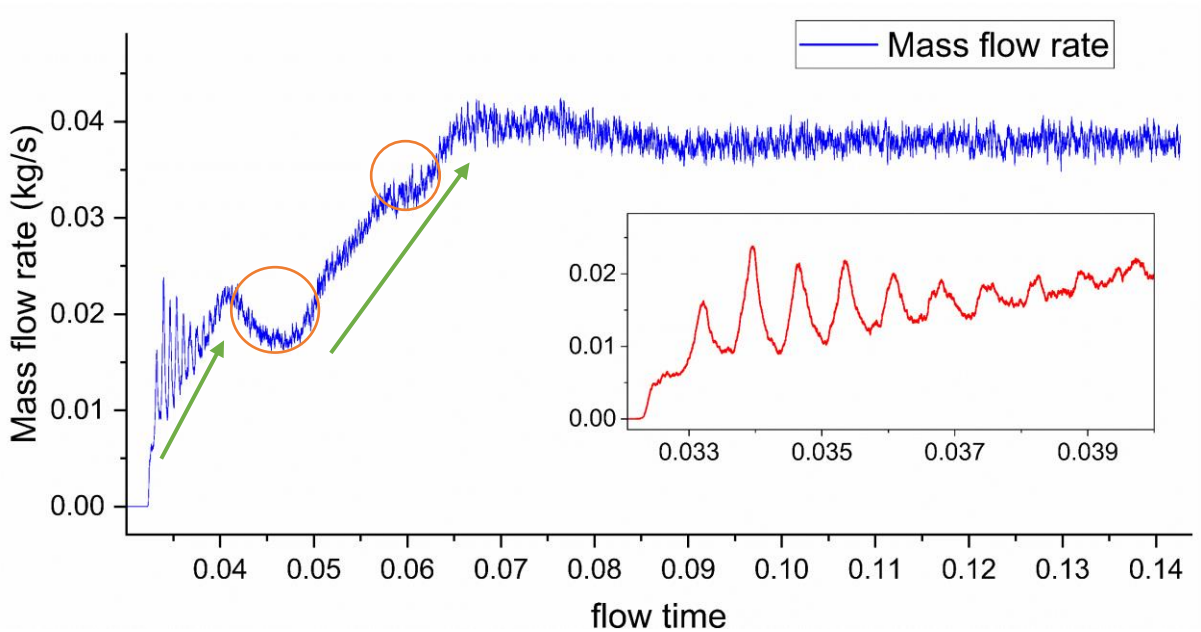

Figure 5.33 Mass flow rate of the particles obtained at the outlet of the domain for 2 kg min^{-1}, 600K case. The mass build-up takes place in two stages shown in the green arrow, continuing until 65 ms. Even though the mass build-up is interupted at two instances: 41 to 46 ms, and 59 to 61 ms having a brief period of fall in the mass flow rate, the rate of mass build-up is the same across all the two stages.

Considering the particles trajectories with the mass flow rate of the particles obtained at the outlet of the domain, presented in Figure 5.33, it can be seen that the mass build-up in the domain takes place in two stages, indicated by the green arrows. In between the mass build-up a fall in the mass flow rate is seen at two instances: between 41 to 46 ms, and between 59 to 61 ms, marked by the orange circles. Nevertheless, across both the two stages it was

observed the rate of the mass build-up was same. Similarly, on examining the flow-field of the 600K case it was observed to be same as the 300K case. However, the observed difference was that the onset of the flow-field fluctuation initiated at 58 ms, contrasting to the 300K case where it was observed to start at 60 ms. The frequency of the flow-field fluctuation remained consistent at 20 kHz, matching the 300K case. Upon conducting a FFT analysis on the injected mass flow rate plot, it was established that the flow-field fluctuation corresponded to the 19.7 kHz high-frequency fluctuation. This negligible difference in the frequencies were due to the lack of additional significant figures in the recorded flow times, leading to the difference of 300Hz. However, on inspecting the 19.7 kHz no relation could be drawn between the alternating flow-field fluctuation with the local extrema of the signal, as signal was of negligible amplitude.

5.2.3 Melt temperature: 1000K

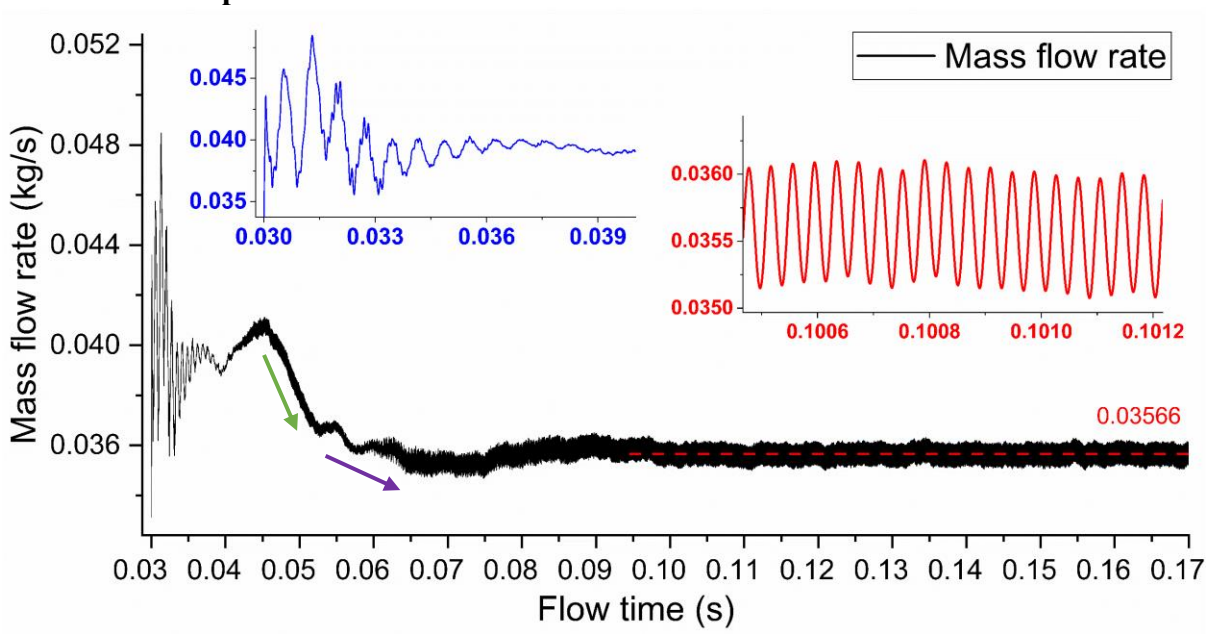

Figure 5.34 Mass flow rate plot of 2 kg min^{-1}, 1000K melt temperature case. The high-frequency fluctuation initiates at 40 ms. After the momentary rise in the mass flow rate, the fall takes place in two stages: a steep fall followed by a gradual decline, indicated by the green and the violet arrows, respectively.

The injection mass flow rate for the 2 kg min^{-1} case with melt temperature 1000K is presented in Figure 5.34 The 1000K case was similar to the earlier described 300K and 600K cases. Nevertheless, there were some significant differences observed which are detailed below. After the attenuation of the initial fluctuation, at 40 ms there was an onset of a high-frequency fluctuation that continued to exist for the rest of the simulation. Following a steep momentary rise in the mass flow rate, it decreases gradually, but in two stages: a steeper fall, followed by

a gradual decline, indicated by the green and violet arrows, respectively. Subsequently, the mass flow rate transitions into a near steady-state at a later time around 100 ms, and was observed to have a near constant amplitude about a mean value of 0.03566 kg s^{-1}, which was calculated by averaging the fluctuation having the near-constant amplitude at t > 100 ms. The high-frequency fluctuation from t > 100 ms was evaluated to possess a varying GMR of 2.43 - 2.5. From the FFT analysis two frequencies were found: 1.4 kHz and 25.4 kHz, the latter corresponded to the high-frequency fluctuation.

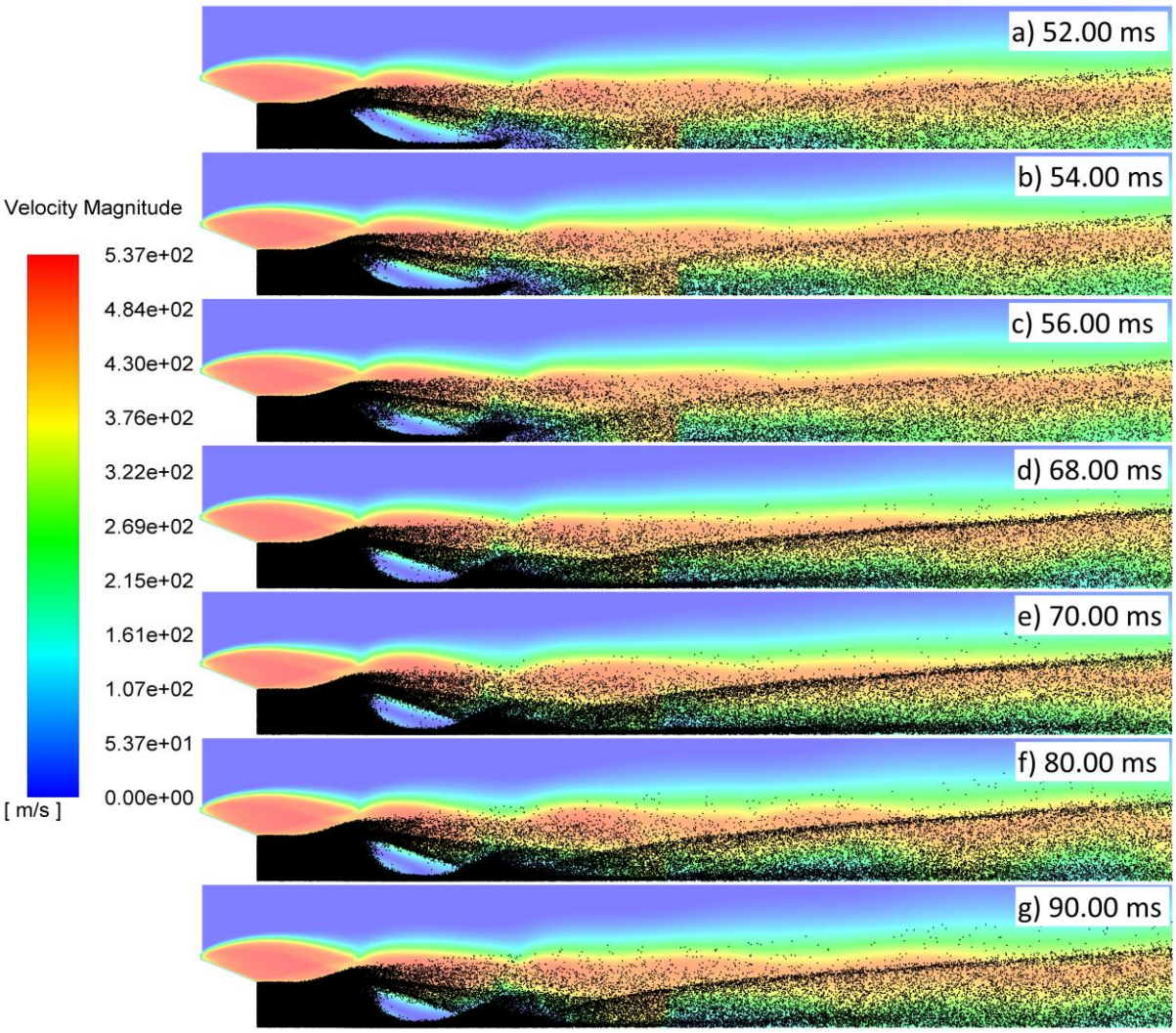

Figure 5.35 Particle trajectories with the velocity contours of the flow-field in the background showing the progressive interaction of the melt pool head with the particles that are pushed downstream. Frame b & c shows the particles following the path of the recirculation zone. From frame d particles trajectories are stabilised.

Similarly, the particle trajectories of the 1000K case looked very similar to that of the 600K case. However, there were few significant observations. The particles underwent pre-filming at 32.5 ms, whereas for the 600K case it was 32.1 ms. Moreover, as shown in Figure

5.35a, at 52 ms the melt pool head that moved downstream joined the particles that are pushed downstream by the supersonic flow-field, whereas in the 600K case it was at 58 ms. Furthermore, due to the presence of a recirculation zone before the stagnation point, the particles that entered the region followed its path, resembling a hump, as presented in Figure 5.35b & c. Later, from t > 68 ms, both particle trajectories and particle dispersion seem to be relatively same, without undergoing any change to its particle flow pattern. This is observed from Figure 5.35d-g.

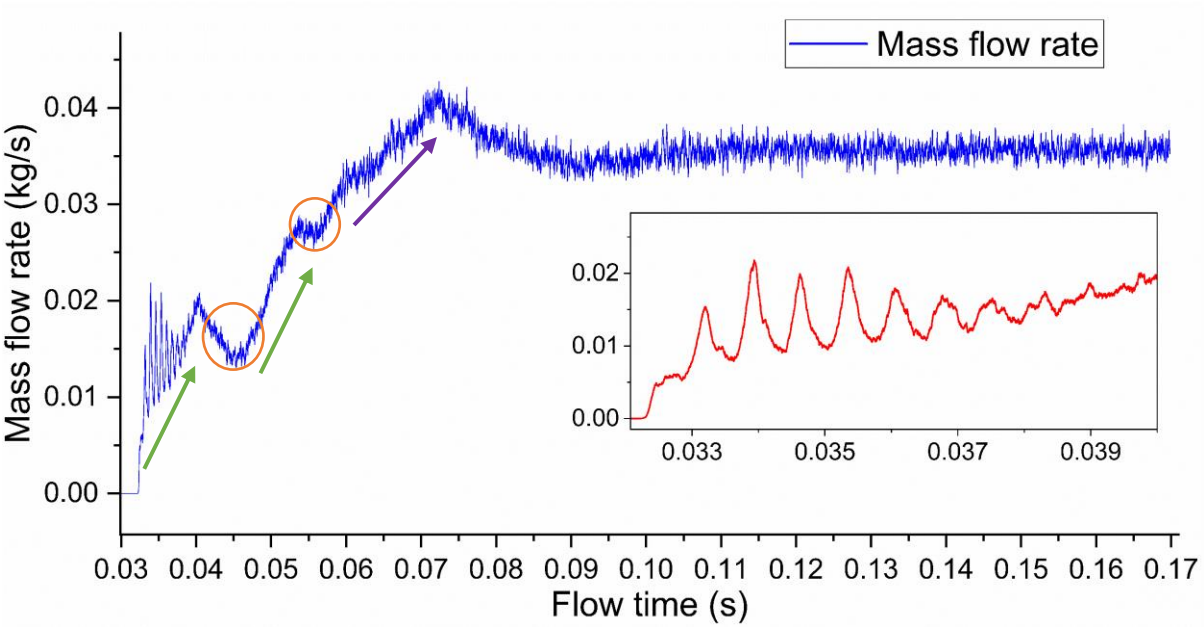

Figure 5.36 The mass flow rate of the particles obtained at the outlet of the domain for 2 kg min^{-1}, 1000K case. The mass build-up takes place in three stages: two steep build-ups followed by a much gradual build-up, indicated by green and violet arrows, respectively. In between the stages, there is brief period of decline as indicated by the orange circles. After the build-up before the mass flow rate reaches an approximate steady-state, a significant decline in the mass flow rate is observed.

By examining the particle trajectories against the mass flow rate of the particles obtained at the outlet of the domain presented in the Figure 5.36, it can be observed there are three stages of mass build-up in the domain. Two steep build-ups followed by a much gradual build-up, indicated by green and violet arrows, respectively. In between the mass build-up there was a brief period of decline in the mass flow rate, indicated using the orange circles. Unlike the 600K case, after the mass build-up there was a significant decrease in the value before it transitioned into an approximate steady-state mass flow rate at 90 ms. However, on comparing this against the particle trajectories in the Figure 5.35d-g, no significant changes were observed corresponding to the decrease in the mass flow rate.

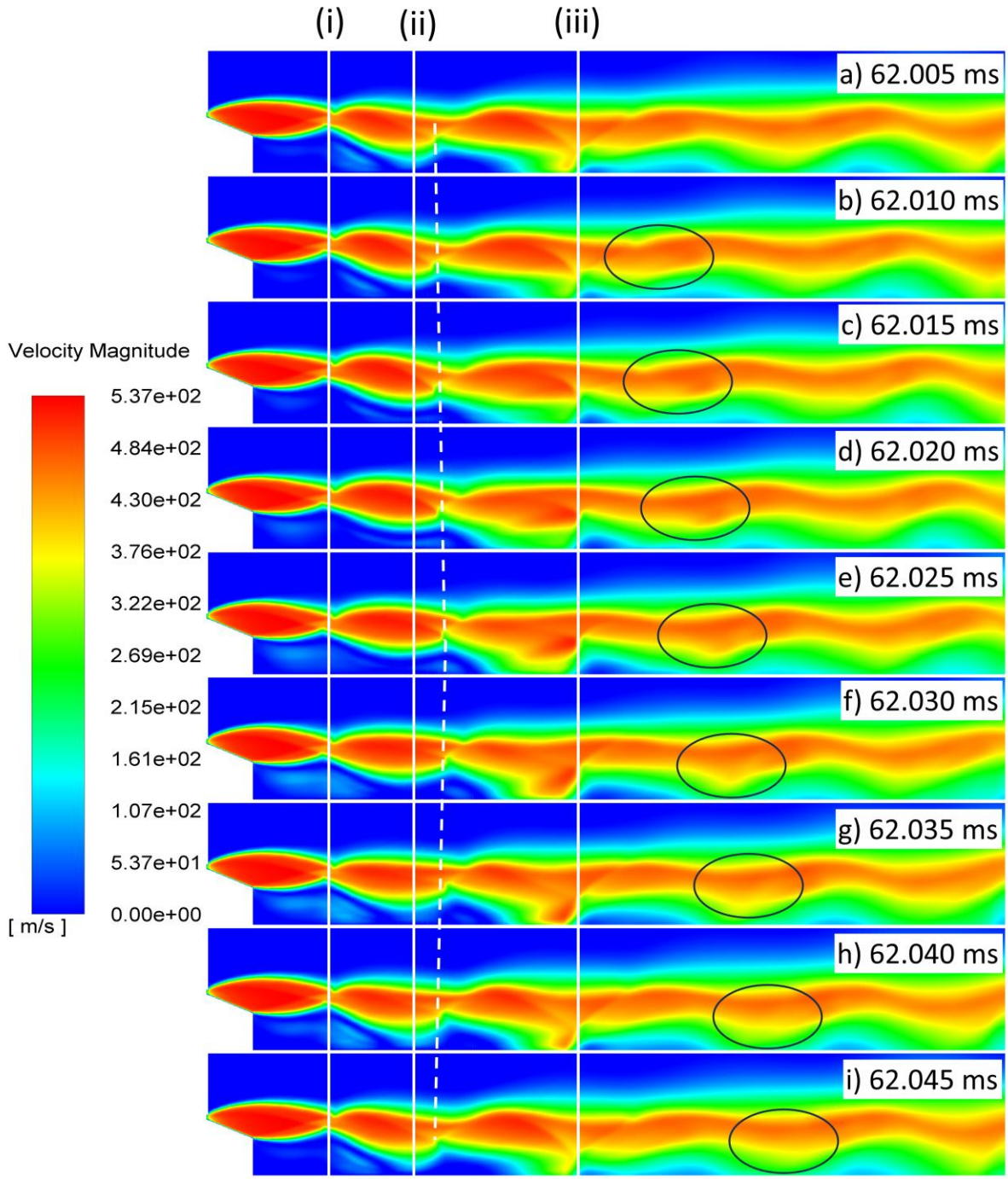

Figure 5.37 Velocity contours of the flow-field stacked in sequential order to elucidate the flow-field fluctuation and the changes in the flow features. Three white guide-lines (i), (ii), and (iii) are pinned at the end of the first shock-cell, at the first Mach-disk, and at the second Mach-disk of the first frame and are compared against the rest of the frames. Another secondary white dashed white line is used to trace the end of the second shock-cell during the fluctuation to show the spatial movement of the flow-field. The first shock-cell didn't change in shape or length whereas the second shock-cell, as marked with the white dashed line, changed in its spatial dimensions.

Upon checking the flow-field, the 1000K case underwent similar characteristics changes in its flow features as that of the 300K and 600K cases, however, the significant differences are presented below. Following after the initial fluctuation which is due to the onset of the melt injection as seen in all the above cases, the flow-field experienced damping in its spatial oscillation, nevertheless, the flow-field did not transition into a steady-state. As the flow-field continued to dampen, at 40 ms, a forced fluctuation emerged. It started gradually but progressively intensified in its spatial magnitude with time. Figure 5.37 shows the flow-field fluctuation and the flow features that changes during the fluctuation. Three white guide-lines (i), (ii), and (iii) were pinned in Figure 5.37a, at the end of the first shock-cell, at the first Mach-disk, and at the second Mach-disk, respectively. A secondary dashed white line is used to trace the end of the second shock-cell during the fluctuation. It is evident from the Figure 5.37 and guide-line (i) that the first shock-cell remains fixed and does not change in its spatial extent. From secondary guide-line it is observed that the second shock-cell undergoes spatial oscillation. It is observed that the second shock-cell which moved downstream as observed in Figure 5.37a-e, returned back to its original configuration by moving upstream, observed in Figure 5.37f-i. However, it is important to note, although a continuous fluctuation is observed, the flow-field continued to exist in open-wake condition throughout. Likewise, a wave propagation is also observed, which initiated from second Mach-disk and continued until the end of the domain. Correlation between the flow-field fluctuation and the injection mass flow rate were examined. It was found that the high-frequency fluctuation, 25.4 kHz, obtained from the FFT analysis corresponded to the flow-field fluctuation (Figure 5.37).

The high-frequency flow-field fluctuation identified from the velocity contours that corresponds to the high-frequency fluctuation present in the injection mass flow rate (Figure 5.34), were further established using velocity monitors pinned at seven key location on the axis of the atomiser (Figure 5.1) to confirm that the frequency of the fluctuation. Since, the monitors in general as seen in Figure 5.19 displayed profound high-frequency fluctuation and were highly condensed, rendering it difficult to examine the trends of the plot, the plot of the monitors were zoomed in at the time of injection and at the high frequency fluctuation. This is presented in the Figure 5.38. FFT analysis on the high-frequency fluctuation across the seven monitors resulted in a consistent frequency of 25.4 kHz, confirming the high-frequency flow-field fluctuation corresponded to the high-frequency melt fluctuation (Figure 5.34). Even though, all the monitors in Figure 5.38 resulted in the same frequency, there existed a phase difference among them as indicated by the red dashed guide-line. This might indicate an

unsynchronised upstream and downstream flow-field movement i.e., the expansion and contraction of the individual sections of the flow-field, and also might be a reflection of the travel time between the spatially separated velocity monitors. Study on this would lead to the better and detailed understanding of the flow dynamics of the process.

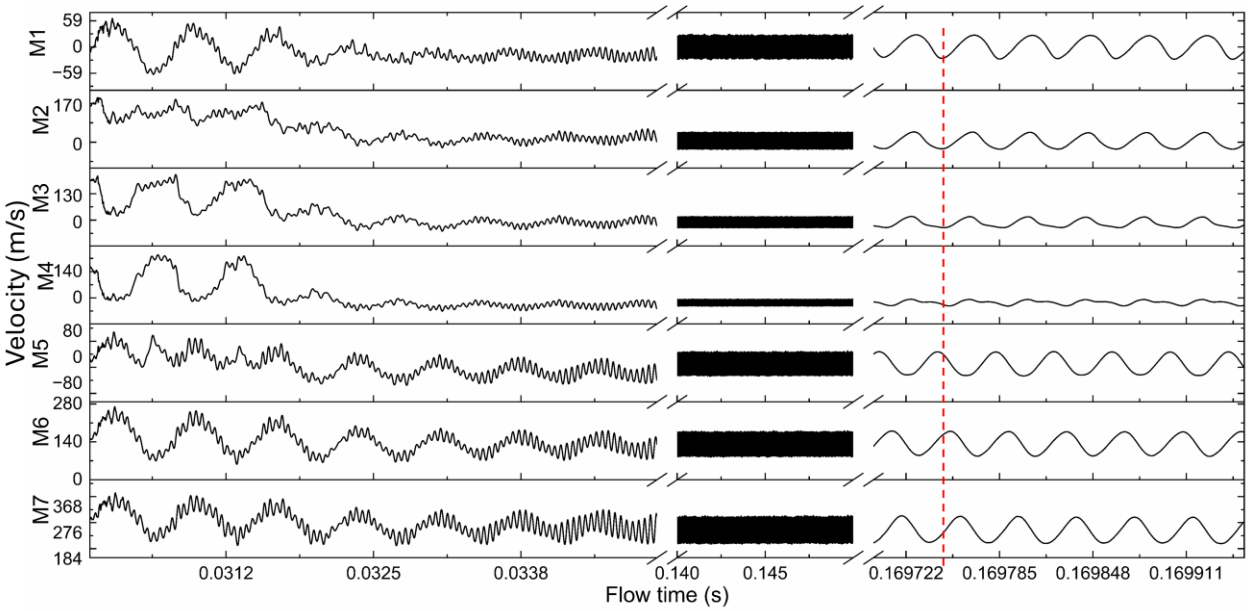

Figure 5.38 Monitors M1 to M7 zoomed in at the injection of the melt and at the high frequency fluctuation. The high frequency fluctuation for all the 7 monitors is same as the high frequency seen in the injection mass flow rate i.e., 25.4kHz. The high frequency fluctuation exhibits phase difference between the monitors indicated by the red guide-line.

5.2.4 Melt temperature: 1500K

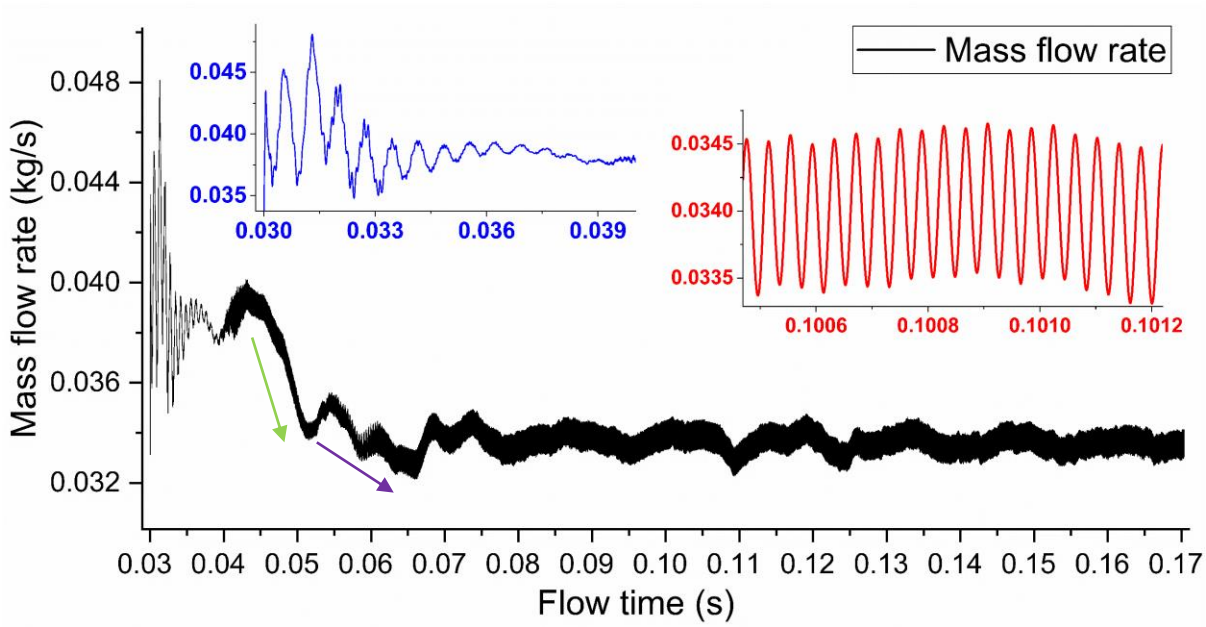

Figure 5.39 Injection mass flow rate of 2 kg min^{-1} with a melt temperature of 1500K.

Unlike the previous mentioned cases of 300K, 600K and 1000K, the 1500K case was quite different in its injection mass flow rate plot. The rest of the cases achieved an approximate steady-state condition, but from mass flow rate plot of the 1500K case presented in Figure 5.39, no evident transition into steady-state was observed. Nevertheless, the 1500K case had some similarities to that of the 1000K case. After the attenuation of initial fluctuation, at 40 ms a high-frequency fluctuation emerged which exhibited swift and pronounced growth in its amplitude, whereas in the 1000K case it took a few milliseconds to grow in its amplitude. After the brief rise in the mass flow rate value an extended fall in the mass flow rate similar to that of the 1000K case is observed. The decline occurred in two stages: a steeper decline indicated by the green arrow, and a more gradual decline indicated by the violet arrow. On carrying out a FFT analysis, two frequencies: 1.4 kHz and 25.4 kHz were found, where the latter corresponded to the high-frequency fluctuation. Even though the mass flow rate did not attenuate into a steady-state, the high-frequency fluctuation predominantly possessed a constant amplitude. Nevertheless, it did not fluctuate about a mean value as seen observed in 1000K case.

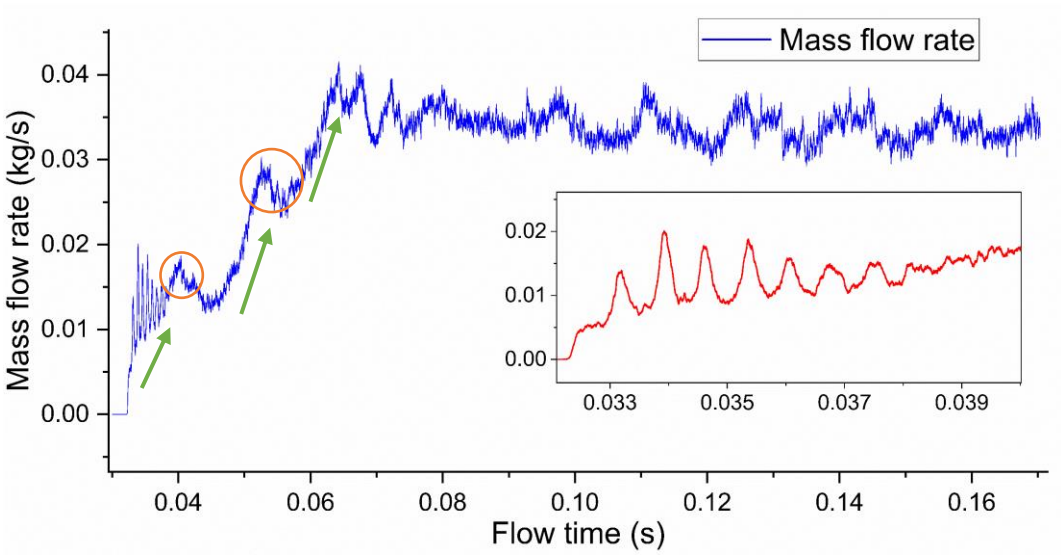

Figure 5.40 Mass flow rate of the particles obtained at the outlet of the domain for 2 kg min^{-1}, 1500K case. Three stages of mass build-up is seen and is indicated by the green arrows. The brief period of decline in between the stages are marked using the orange circles.

Similarly, the particle trajectories underwent the same pattern of particle evolvement, except for the difference that the melt underwent pre-filming at 32.7 ms, whereas for the 1000K case it is 32.5 ms. The melt pool that moves downstream without undergoing pre-filming joins with the particles that are that pushed downstream after coming in contact with the supersonic flow-field at 49 ms. The mass build-up in the domain occurs in three stages as illustrated in Figure 5.40 shown using green arrows. In between the stages a brief decline in the mass flow

rate was observed, marked using the orange circles. Nevertheless, across all the three stages, the rate of mass build-up was nearly the same. Until 65 ms a positive mass build-up trend is noticed, and was expected to transition into a steady-state. But contrarily, unlike the other cases, the outlet mass flow rate was unsteady as well. With time, due to the increased mass build-up the particle trajectories progressively dispersed until 82 ms. The particle trajectories recorded at 82 ms is presented in Figure 5.41. Since, the injection and outlet mass flow rates do not converge towards steady-state throughout the simulation, efforts were still taken to observe for any changes in the particle trajectories pattern that might correspond to the unsteady mass flow rate. However, from t > 82 ms no significant change in the particle trajectories were observed. Similarly, the flow-field fluctuations were observed and were found similar to that of the 1000K. Although it underwent continuous spatially fluctuations, it still continued to fluctuate under open-wake condition. The forced fluctuation was observed to exhibit a frequency of 25.4 kHz, but did not undergo any wake alternation, and hence couldn't be correlated with local extrema of the high-frequency melt fluctuation.

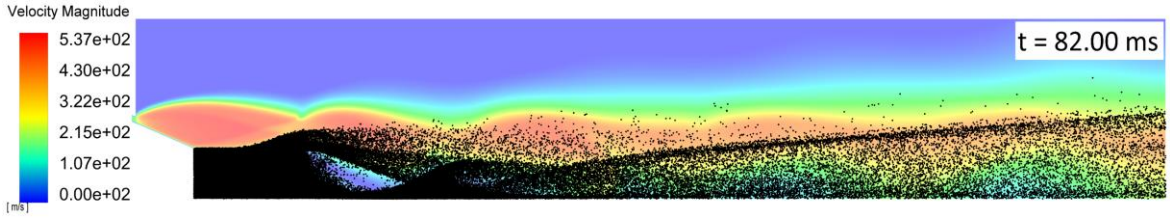

Figure 5.41 Particle trajectories with the velocity contours in the background, showing the particle dispersion recorded at 82 ms.

5.2.5 Melt temperature: 2000K

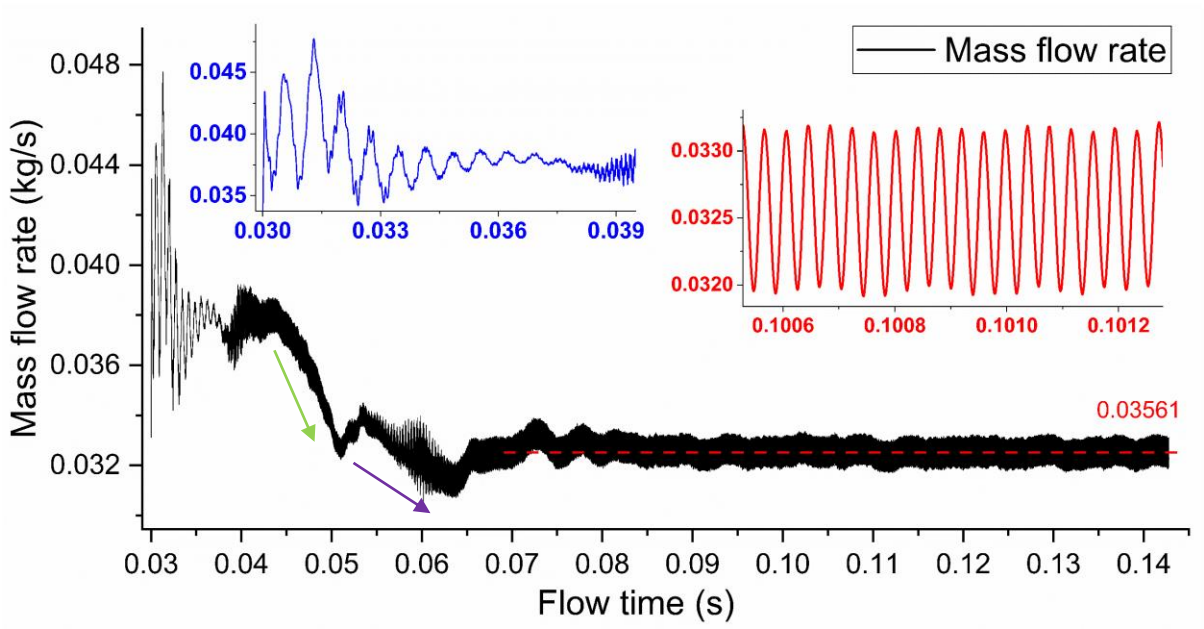

Figure 5.42 Injection mass flow rate of 2 kg min^{-1} with a melt temperature of 2000K.

The melt injection mass flow rate for 2 kg min^{-1}, 2000K is presented in the Figure 5.42. The overall mass flow rate is similar to that of the 600K, 1000K cases, and to an extent to that of the 1500K except for its observed unsteady nature. Following the attenuation of the initial fluctuation, the high-frequency fluctuation emerged at 38 ms. Upon gaining a marginal rise in the mass flow rate value, there was an extended decline until 65 ms. As observed in the previous cases, the fall in the mass flow rate took place in two stages: a steep and more gradual fall, indicated by the green and violet arrows, respectively. Subsequently after the decline, the mass flow rate stabilised into an approximate steady-state from t > 80 ms. On conducting a FFT analysis, the presence of same two frequencies as observed in the 1000K and 1500K cases – 1.4 kHz and 25.4 kHz, were found, where the latter corresponds to the high-frequency fluctuation. The high-frequency fluctuation seen from t > 80 ms i.e., the approximately steady-state mass flow rate, contained a varying GMR value of 2.63 - 2.77. The same high-frequency flow-field fluctuation as seen in Figure 5.37, is also observed wherein it corresponded to the 25.4 kHz. Also, the flow characteristics of the fluctuation were identical to the above two cases, except for the increased spatial movement of the flow-field due to the increased amplitude in mass flow rate fluctuation.

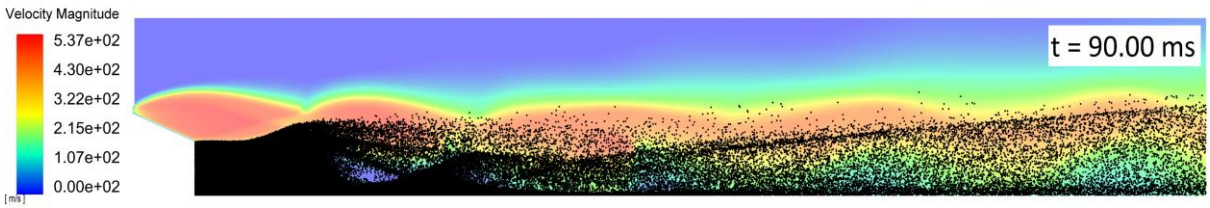

Figure 5.43 Particle trajectories with the velocity contours in the background, showing the particle dispersion obtained at 90 ms, where the trajectories stabilise.

The particle trajectories for the 2000K were observed to be similar to that of the previous described cases, except for the few timings: the particles underwent pre-filming at 32.9 ms, and around 47 ms the melt pool that moved downstream without undergoing pre-filming joined with the particles that were pushed downstream after coming in contact with the supersonic flow-field. Moreover, the particle trajectories underwent extensive dispersion, but stabilised at t > 90 ms in its flow pattern. This is presented in Figure 5.43. The mass build-up in the domain is observed from outlet mass flow rate plot presented in Figure 5.44. Similar to the 1500K case, the mass build-up was in three stages: an initial gradual rise, followed by two steeper rises, indicated by the green and violet arrows, respectively. Also, the temporary decline indicated by the orange circles, as seen in the previous cases is also seen in the 2000K case. Unlike the 1500K case, in the 2000K case the mass flow rate settles into an approximate steady-state condition from t > 80 ms, reflecting the injection mass flow rate plot.

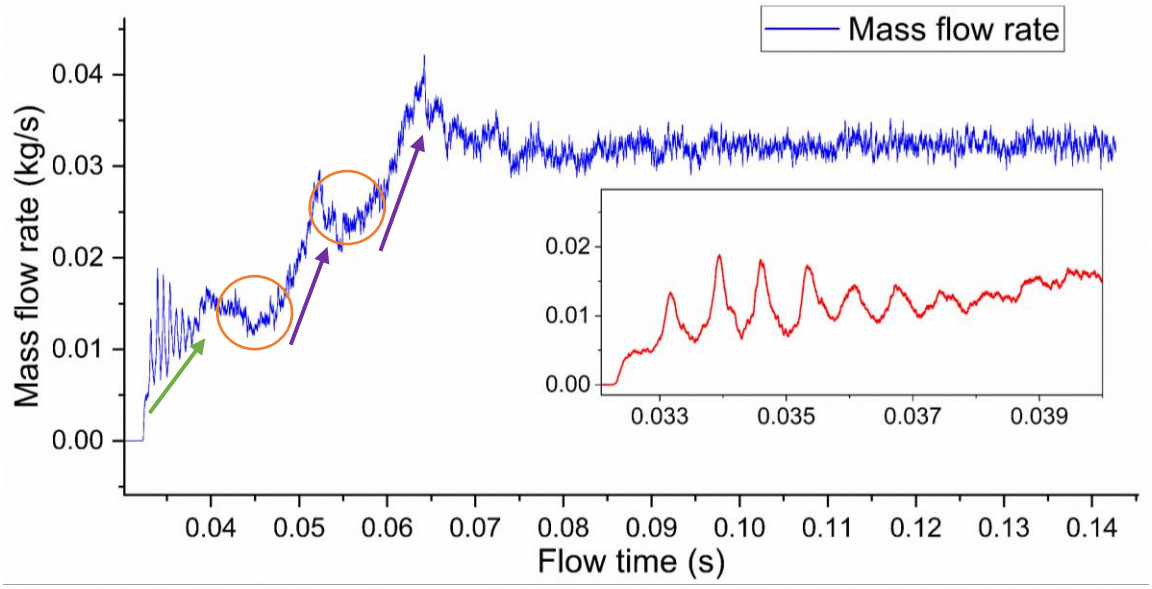

Figure 5.44 The mass flow rate of the particles obtained at the outlet of the domain for 2 kg min^{-1}, 2000K case. There are three stages of mass build-up: a gradual rise followed by two steeper rises, indicated by the green and violet arrows, respectively.

5.2.6 Summary

The 2 kg min^{-1} (GMR=2.6) cases in general were relatively stable and did not exhibit any unpredictable melt instabilities. Although increase in melt temperature initially induced a higher but transient instability in the melt injection, the instabilities were soon attenuated into near constant/ regular fluctuations, except for the 1500K case (Figure 5.39). However, with the increase in melt temperature, the amplitude of the melt fluctuation increased; the pre-filming time decreased; and the average melt flow rate decreased.

In the 300K case, the melt pool head was observed to stabilise at 4.3N_d at 70 ms, whereas in the T ≥ 600K cases, the melt pool head was observed to move continuously downstream without stabilising. Nevertheless, all the five cases were gas dominated because of the high GMR of 2.6, resulting in a predominantly steady/near-steady melt flow rate.

The 2 kg min^{-1} cases with increasing melt temperature provided insights on the forced continuous fluctuation that arises with the increased mass in-flow. For the 300K case, alternating wake condition (open- to closed-wake alternation) was observed, whereas for the higher temperature cases no wake alternation was observed, although flow-field underwent fluctuation. However, in a commercial atomiser to maximise the yield from the process, the flow rate is fixed in such a way that the GMR value is maintained at 1. Hence, the nominal mass flow rate was further increased to 4 kg min^{-1} to gain insights into the behaviour of the process and to understand significant characteristic changes, as the GMR of the process approached 1.

5.3 Results of 4 kg min^{-1} (GMR = 1.32) under increasing melt temperatures.

This section presents the results of 4 kg min^{-1} case having GMR=1.32, investigating the effect of increasing melt temperatures. The melt temperatures considered for this GMR are: 300K, 600K, 1000K, 1500K, and 2000K (Table 4-6). The section is sub-divided to present and analyse the results for each of the melt temperature individually.

5.3.1 Melt temperature: 300K

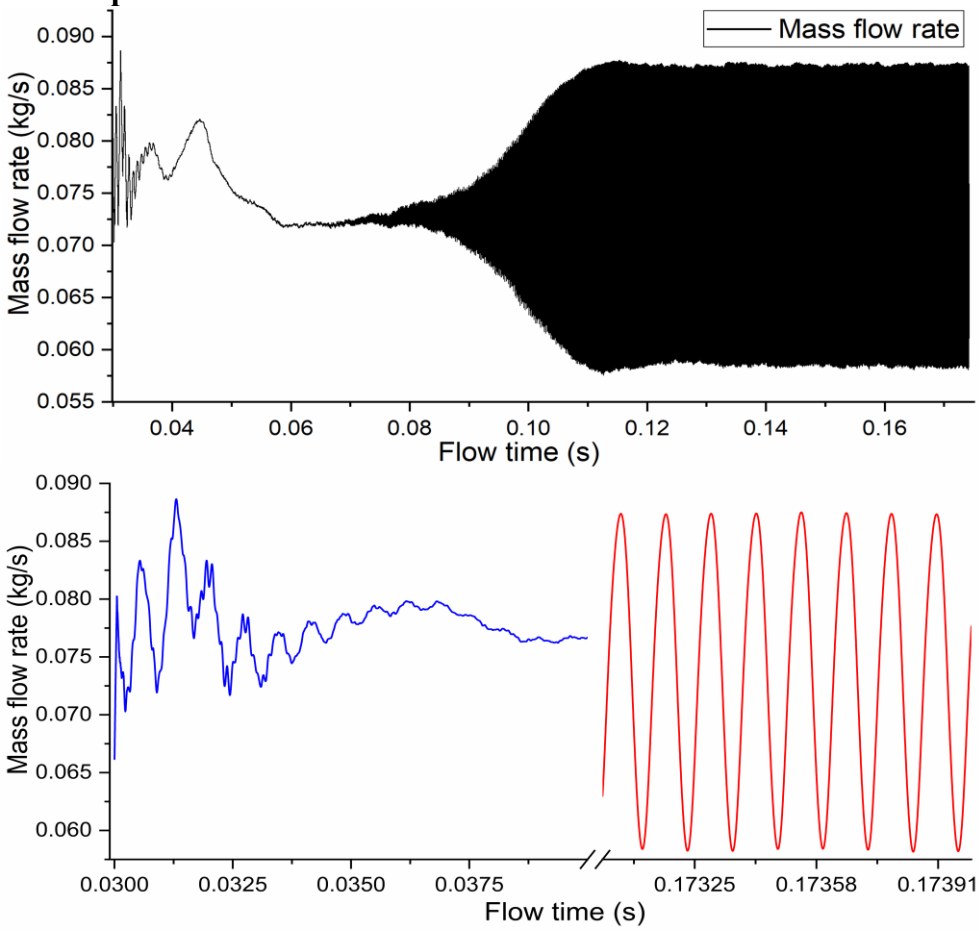

Figure 5.45 Injection mass flow rate plot of 4 kg min^{-1}, 300K case showing initial fluctuation followed by two high amplitude peaks. At t > 60 ms there is an onset of a higher frequency fluctuation that gradually increases in its amplitude and remains constant from t > 120 ms. The zoomed-in section of the initial fluctuation and the regular repeated fluctuation is also presented.

The 4 kg min^{-1} (0.066 kg s^{-1}) case having a GMR value of 1.32 and melt temperature of 300K was run for 144 ms (30 to 174 ms). Figure 5.45 shows the injection mass flow rate plot with zoomed-in section of the initial fluctuation and high frequency fluctuation shown in blue and red, respectively. With the melt being injected there were series of large amplitude fluctuations in the mass flow rate until 33 ms, and thereafter in the subsequent cycles the fluctuations attenuated to become fluctuations having negligible amplitude. This can be

observed in Figure 5.45 from 37.5 to 65 ms. Following the initial fluctuation due to the melt injection, at 60 ms there was an onset of a higher frequency fluctuation that continued for the remainder of the run-time. The high frequency fluctuation that commenced at 60 ms exhibited gradual increase in its amplitude, reaching its peak at 110 ms. After which the amplitude reduced marginally, settling at 120 ms and subsequently maintained that amplitude for the remainder of the simulation. From the FFT analysis three frequencies: low frequency of 1.4 kHz, mid frequency of 8.1 kHz, and high frequency of 16.3 kHz were found; out of which only the low and mid frequencies were observable in the plot, and the fluctuation seen at t > 60 ms corresponded to the mid frequency, 8.1 kHz. This fluctuation possessed a GMR varying between 1 to 1.5.

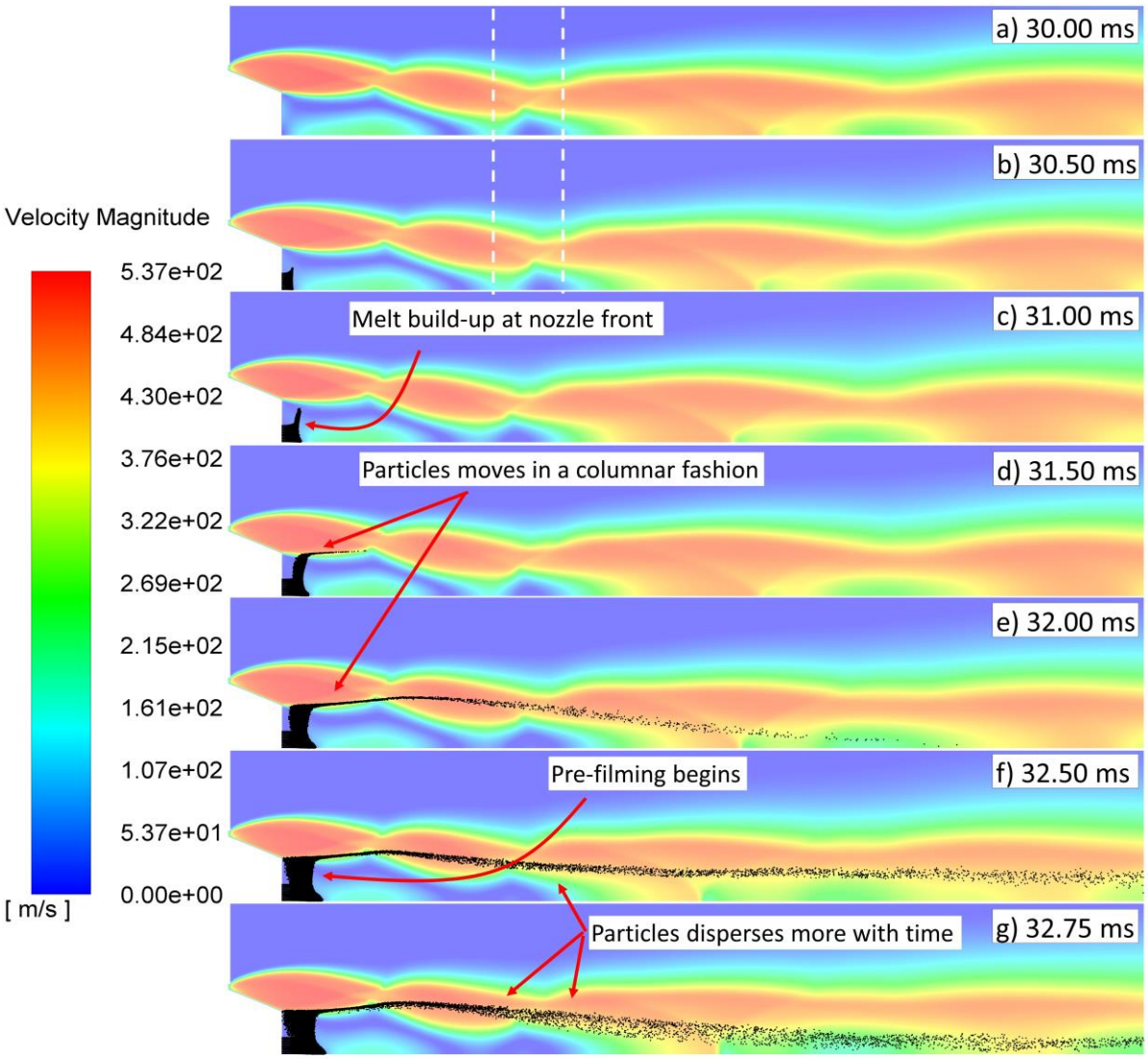

Figure 5.46 Particle trajectories with the velocity contour in the background showing the evolvement of particles after being injected into the flow stream. These stacks of particle trajectories show the onset of injection, pre-filming, melt movement downstream, and increased dispersion of particles with time.

The particles' trajectories with the velocity contours in the background, revealed that the flow-field deviated from its steady-state once the melt was injected. This is presented in Figure 5.46a where two guide-lines were fixed at the first Mach-disk and at the stagnation point, respectively, to compare against the flow-field in the Figure 5.46b. It can be observed that in the Figure 5.46b, both, the first Mach-disk and the stagnation point has shifted its position. Further to this, with the melt being injected, the melt built-up in front of the nozzle as seen in Figure 5.46c is due to the opposing force of the recirculation zone. Subsequently, when the melt comes in contact with the supersonic flow-field it was swiftly pushed downstream (Figure 5.46d&e), and thereafter at 32.5 ms the melt underwent pre-filming (Figure 5.46f). Similar to what was seen in all the above-mentioned different mass flow rates, i.e., for both 1 & 2 kg min^{-1} and its melt temperatures, the particles that were initially pushed downstream after coming into contact with supersonic flow-field were highly collimated upto the first shock-cell (Figure 5.46d&e), but beyond that they dispersed. However, as time progressed the particles started to disperse even from the first shock-cell as presented in Figure 5.46g.

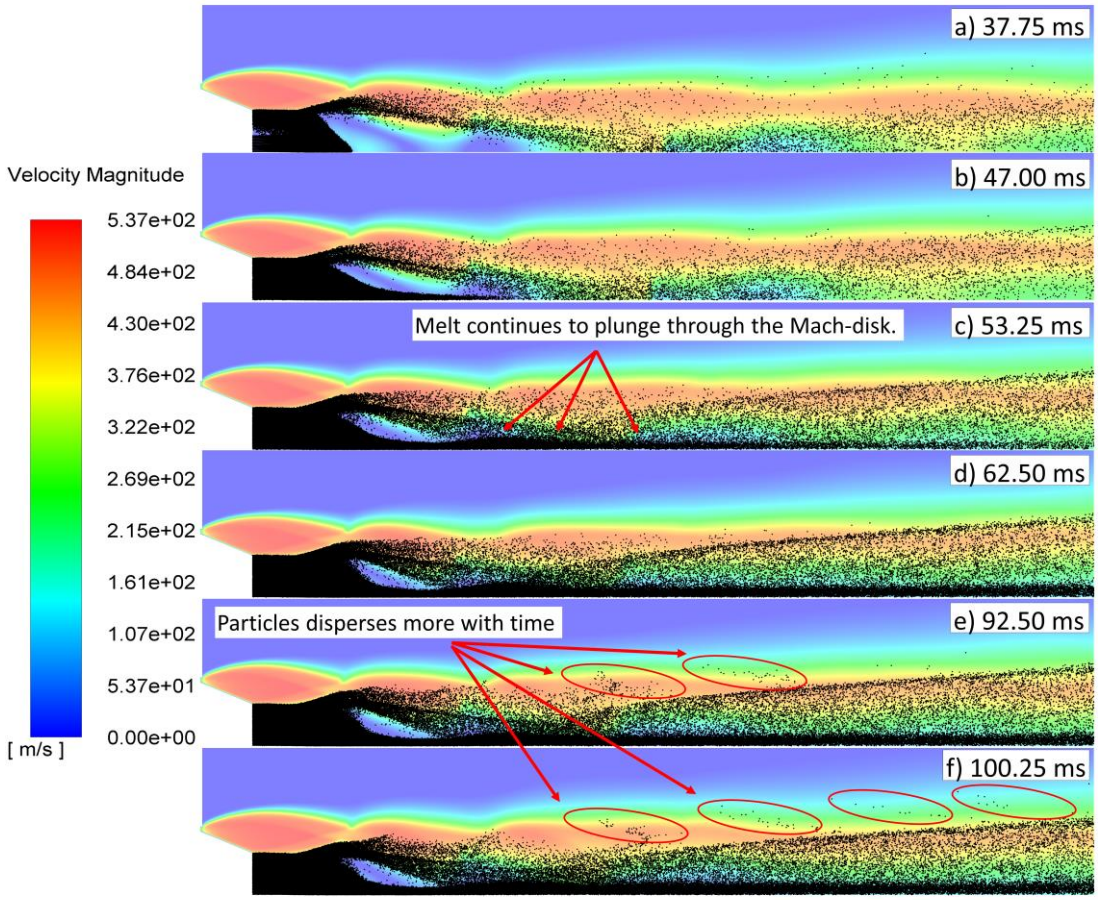

Figure 5.47 Particles trajectories with velocity contour in the background showing increasing dispersion of particles with time, and melt pool head plunging through the second Mach-disk. Frame e & f shows flares i.e. particles being propelled radially outwards from the main melt plume in small groups, marked by the red ellipses.

The effect of the dispersion is much more evidently seen in Figure 5.47. It was observed that even though the particles underwent pre-filming at 32.5 ms, the complete wetting of the melt nozzle occurs at t > 40 ms. The starting of pre-filming is shown in Figure 5.46f where the particles present radially outward i.e. melt present near the circumferential edge comes in contact with the melt nozzle tip first, progressively followed by melt present towards the atomiser axis, coming in contact with the melt nozzle tip as illustrated in Figure 5.46g and Figure 5.47a. This extended pre-filming duration and progressive wetting of the melt tip in a radially inward manner is due the increased mass loading. Also, the increased mass loading led to the continuous downstream movement of the melt pool head. Owing to which, at 47 ms, as shown in the Figure 5.47b, the melt pool head joined with the particles that were pushed downstream by the supersonic gas jet. Further, due to its continued downstream movement, the melt pool head plunges into the second Mach-disk (Figure 5.47c), and continued to move downstream along the axis of the atomiser, becoming denser with particles over time. This is shown in Figure 5.47c-f. Another interesting observation illustrated in Figure 5.47e&f using red ellipses are the flares, containing particles in groups of small number were propelled radially outwards from the main melt plume at t > 90 ms.

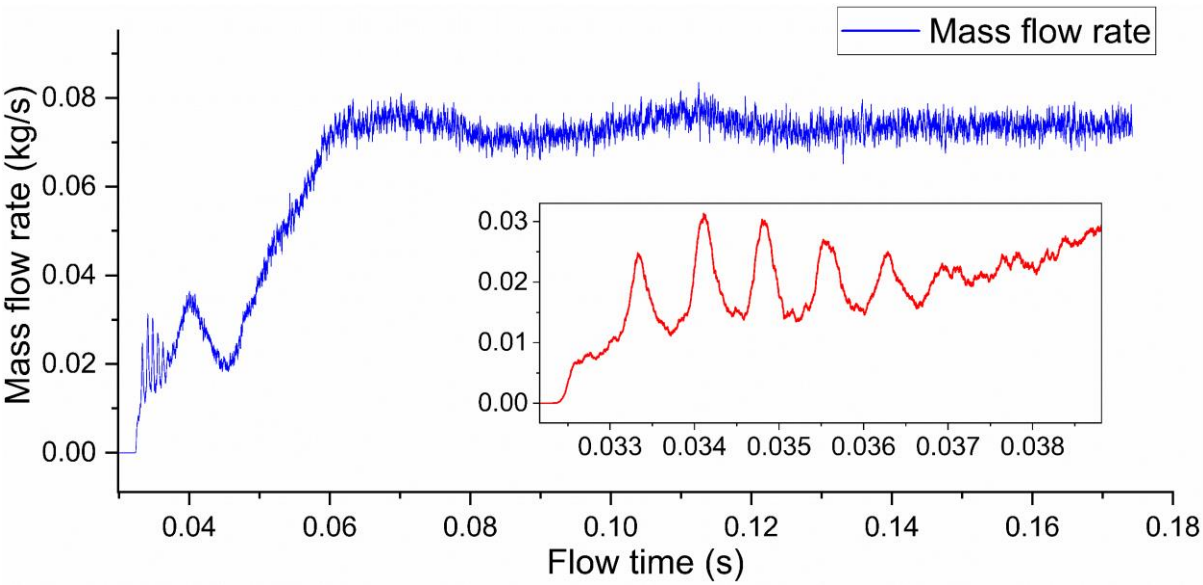

Figure 5.48 Mass flow rate of the particles obtained at the outlet of the domain for 4 kg min^{-1}, 300K case. There is an initial steady increase in the flow of particles through the outlet, but decreases briefly, but thereafter it increases rapidly. Subsequently, at t > 70 ms no significant change in the mass flow rate is seen.

The level of the increased mass loading into the domain, causing delayed pre-filming and continuous downstream of the melt pool head as seen in the Figure 5.46 and Figure 5.47

can be evaluated by comparing the injection mass flow rate and the outlet mass flow rate plot presented in the Figure 5.45 and Figure 5.48, respectively. However, at t > 80 ms, the outlet mass flow rate plot does not resemble the extent of fluctuation seen in the injection mass flow rate, rather progressed towards a near-steady mass flow rate. This is because, the injected particles, having a wide spread of particle velocities smoothed out over their course of flight downstream.

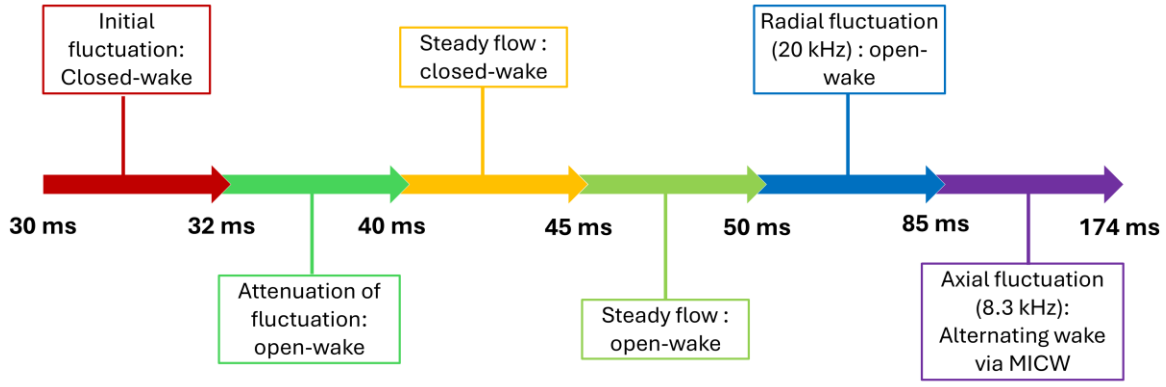

Figure 5.49 Timeline of flow-field fluctuations observed in 4 kg min^{-1}, 300K case.

Considering the velocity contours of the flow-field, the timeline of the different fluctuations observed in the flow-field are presented in Figure 5.49. It is evident that the flow-field was disturbed from its steady-state, and entered into a fluctuation. This is shown in Figure 5.50 where series of flow-field contours were obtained at close consecutive flow time, and were stacked vertically. Two guide-lines, (i) and (ii) were pinned at the first Mach-disk and second Mach-disk, respectively, of Figure 5.50a and were compared against the other frames of the stacks. With the injection of the melt into the atomisation chamber (domain), the flow-field fluctuated between moving upstream and downstream until 32 ms while continuing to exist in closed-wake condition. At 32 ms the flow-field transitioned into an open-wake, and from 32 to 40 ms the flow-field existed in open-wake condition while simultaneously attenuating in its spatial oscillation. At 40 ms the flow-field entered into a steady-state, simultaneously transitioning into a closed-wake. Shortly thereafter, at 45 ms the flow-field transitioned into an open-wake condition, and from 50 ms an onset of continuous flow-field fluctuations in the radial direction were observed. With the onset of the flow-field fluctuations, the motion of the shock-cells in the radial direction increased in its spatial extent with time, and achieved its peak at 55 ms, existing in open-wake condition. Velocity contours of the flow-field were obtained at 65 ms and were stacked sequentially to illustrate the nature of the fluctuation. This is shown in Figure 5.51.

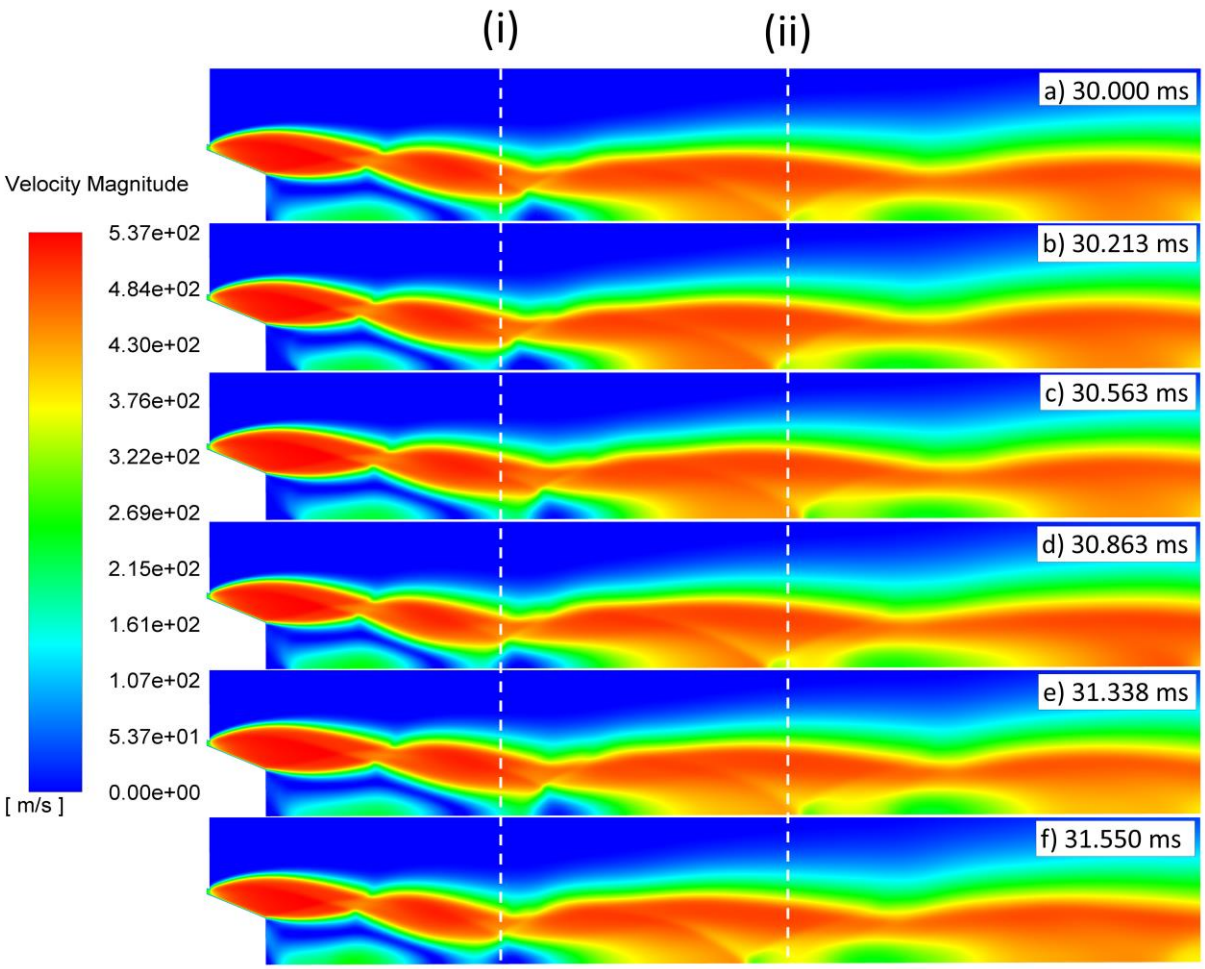

Figure 5.50 Velocity contours of 4 kg min^{-1}, 300K case showing flow-field fluctuations at the onset of the melt injection into the domain. Two guide-lines (i) and (ii) are fixed at first Mach-disk and second Mach-disk of frame a, to compare the changes with rest of the frames.

Three guide-lines, (i), (ii), and (iii), were pinned at the ends of the first, second, and third shock-cell, respectively, in Figure 5.51a, and were compared against the rest of the frames of the stack. It can be observed that the spatial extents of the first shock-cell did not change in the axial direction, whereas the extents of the second and third shock-cells changed marginally. As visualised in the Figure 5.51, the flow-field did not alternate in its wake condition, but displayed significant fluctuations which were regular in nature. In a cycle of the fluctuation, initially, the lower sonic boundary of the second shock-cell, marked by the yellow lines in Figure 5.51a lies in close proximity to the atomiser's axis. As the fluctuation progressed, the sonic boundary gradually moved further away from the atomiser's axis, shown using the curved red line in Figure 5.51c. Subsequently, in Figure 5.51e the sonic boundary returned back to the same configuration seen in Figure 5.51a. Similarly, during a cycle of the fluctuation it was observed that the third-shock cell engulfed the axis to a certain extent as shown in Figure 5.51a

using the yellow lines, but later it advances further to engulf the axis to a much larger extent, as pointed out in Figure 5.51c using the red lines. Subsequently, in Figure 5.51e it returned back to its original configuration as seen in Figure 5.51a. Because of the fluctuation, a wave propagation was observed starting from the end of the third shock-cell and continued to propagate until the end of domain, marked by the ellipses. The frequency of this regular fluctuation was evaluated to be 20 kHz.

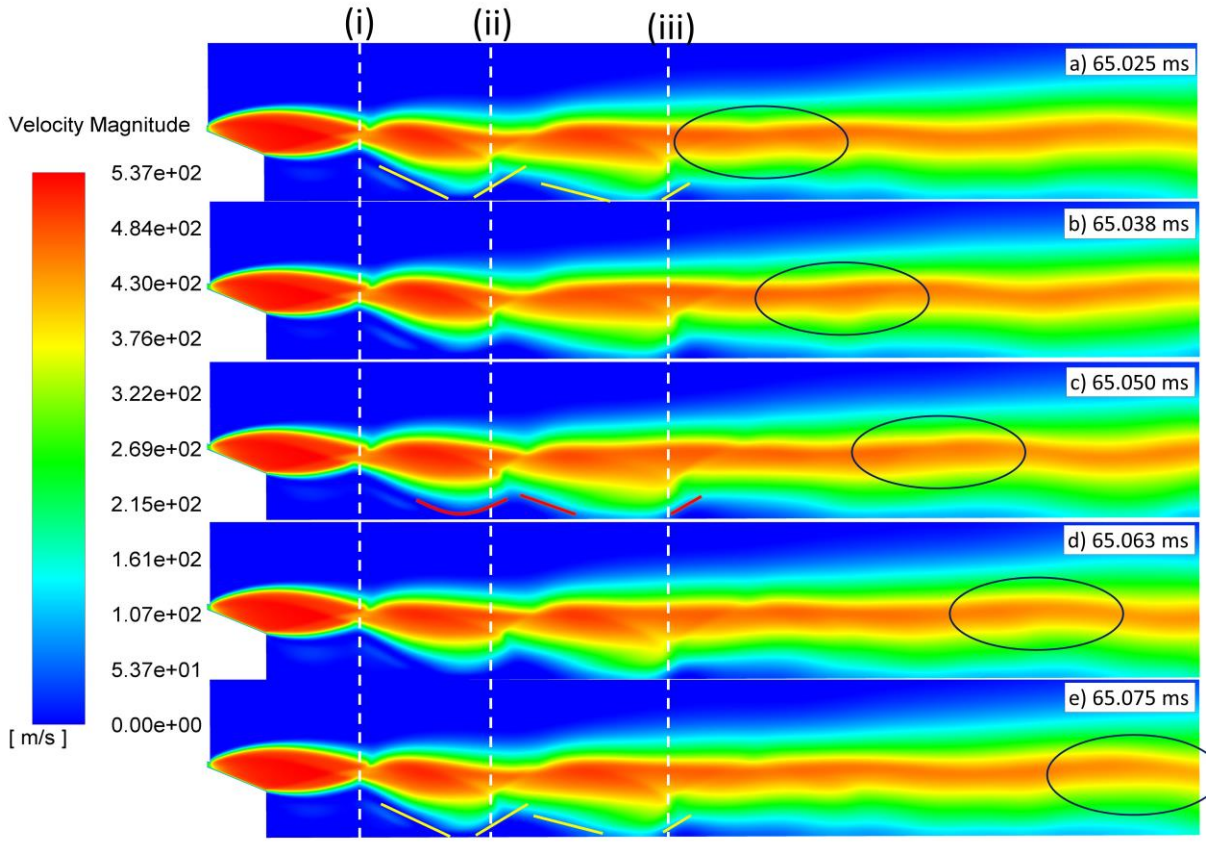

Figure 5.51 Velocity contours showing a cycle of the continuous flow-field fluctuation. Three guide-lines (i), (ii), and (iii) are fixed at the end of the first, second and third shock-cell, respectively. The lower sonic boundary of the second shock-cell of frames a & e lies close to the atomiser's axis, as marked by the yellow lines, whereas the sonic boundary seen in frame c is far from the axis as shown using the curved red line. Similarly, the third shock-cell seen in frames a & e sparingly touches the axis, whereas, in frame c it seems to engulf the axis to a much larger extent than seen in frame a & e. A wave propagation from the end of third shock-cell is observed, marked using blue ellipses. The frequency of the fluctuation was evaluated to be 20 kHz.

Around 85 ms, the fluctuation seen in Figure 5.51 evolved into a fluctuation where the spatial extent of the shock-cells varied along the axial direction. This is presented in Figure 5.52. The fluctuation grew with time, achieving its maximum spatial oscillation at 100 ms. To understand the fluctuation, at 100 ms, series of velocity contours were obtained in close

consecutive flow times and were stacked sequentially. Two vertical guide-lines, (i) and (ii) were pinned at the downstream end of the first and second shock-cells, respectively. Another two sets of guide-lines were used to trace the extent of movement of the ends of the first and second shock-cells. It was observed that the second shock-cell underwent a significantly larger fluctuation along the axial direction, compared to the first shock-cell. During the fluctuation it was evident through the vertical guide-lines, (i) and (ii), that the closed-wake condition, seen in the Figure 5.52a, indicated using the Mach-disk, gradually transitioned into open-wake condition as seen in the Figure 5.52f, and returned back to its original configuration i.e. closed-wake condition, in Figure 5.52k. Even though the wake appears to be in open-wake condition in Figure 5.52a&k, it exists in closed-wake condition. This is because the first Mach-disk isolates the wake region by immersing into the melt plume, resulting in the same type of wake seen during closed-wake condition, presented in Figure 5.50. In section 6.7 this is explained in detail. The closed-wake type as observed in Figure 5.52a will be henceforth called as Melt-isolated Closed-wake (MICW) condition. It was observed during the fluctuation, that the same wave propagation pattern seen in Figure 5.51 starting from the end of the third shock-cell, was also seen in Figure 5.52. The frequency of this flow-field fluctuation was evaluated to be 8.3 kHz. Correlation between the gas flow-field fluctuation (Figure 5.52) and the fluctuation present in the injection mass flow rates (Figure 5.45) were examined, and it was found that the melt fluctuation of 8.1 kHz, seen in Figure 5.45 corresponded to the flow-field fluctuation having frequency of 8.3 kHz (Figure 5.52). Also, the melt fluctuation signal (8.1 kHz,) and the flow-field fluctuation seen in Figure 5.52 transitioning between open- to closed-wake were examined, and it was found that at the local minima of the melt fluctuation, the flow-field existed in closed-wake condition (Figure 5.52a&k), and at the local maxima of the melt fluctuation, the flow-field existed in open-wake condition (Figure 5.52f). However, no correlation could be drawn from the mass flow rate fluctuation for the higher order flow-field fluctuation of 20 kHz, seen in Figure 5.51.

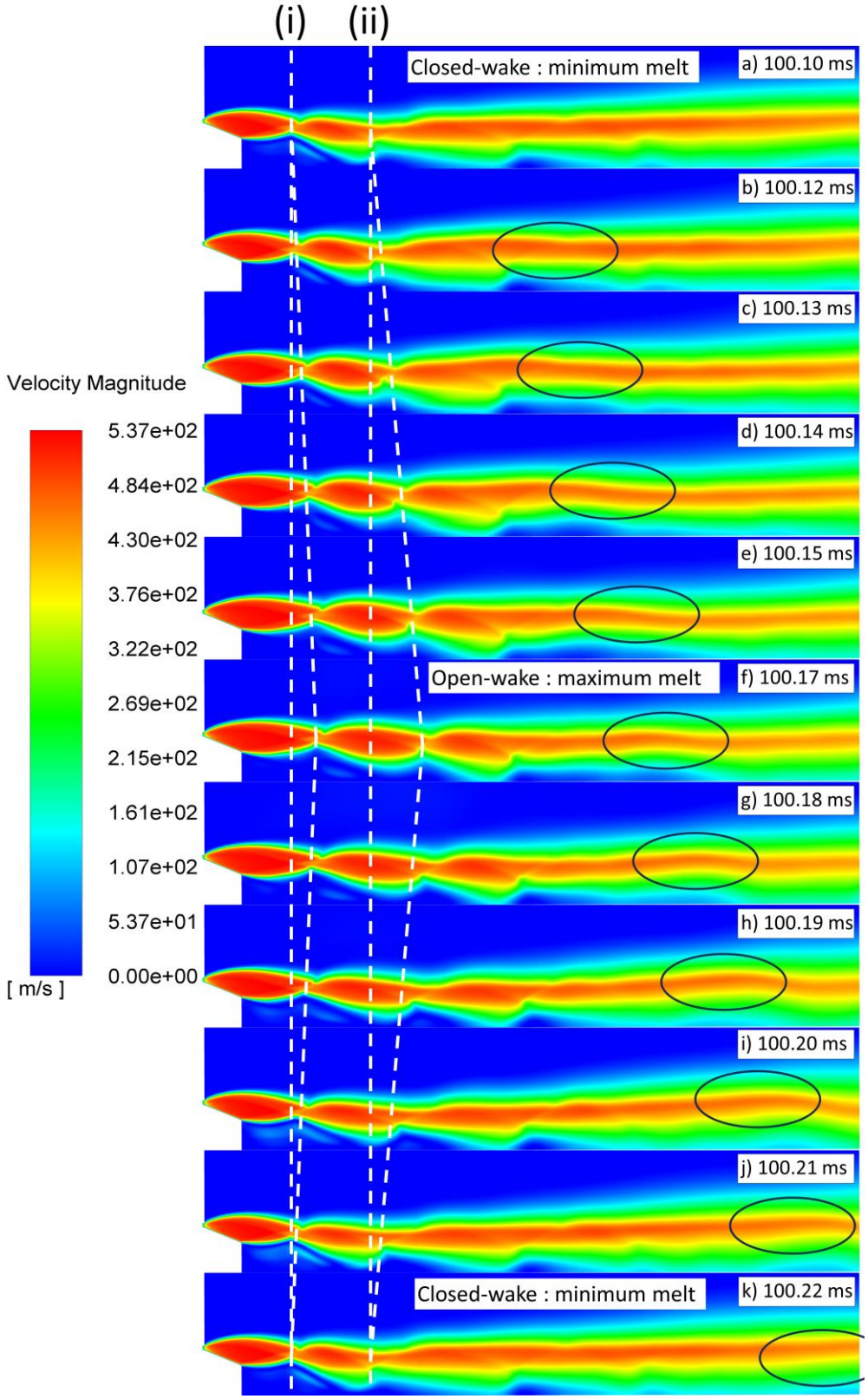

Figure 5.52 velocity contours of the flow-field showing a cycle of the repeated fluctuation seen at t > 100 ms. Two vertical guide-lines (i) & (ii) are fixed at frame 'a' at the end of first shock-cell and end of second shock-cell, respectively to compare the extent of fluctuation against other frames. Another two sets of guide-lines are used to trace the movement of the first and second shock-cell ends. The frequency of this fluctuation was found to be 8.3 kHz.

The above seen flow-field fluctuation of 8.3 kHz (Figure 5.52) that corresponded to the melt frequency fluctuation of 8.1 kHz, seen in the mass flow rate plot from 60 ms, was validated using velocity monitors pinned at seven different locations on the atomiser's axis (Figure 5.1). The velocity monitors taken at seven different locations are presented in Figure 5.53. The FFT analysis revealed that all seven monitors consistently exhibited a frequency of 8.1 kHz from t > 95 ms, validating with the frequency obtained for the flow-field fluctuation. The discrepancy between the frequency seen in the mass flow rate and velocity monitors (8.1 kHz), and the flow-field fluctuation (8.3 kHz), is due to the lack of additional significant figures in the recorded flow times, leading to this difference of 200 Hz. In addition to this consistent frequency, two other higher frequencies were obtained from the FFT analysis. They were, 16.3 and 19.7 kHz. The latter can be correlated to the flow-field fluctuation having a frequency of 20 kHz, but no significant flow-field fluctuation having a frequency of 16.3 kHz was observed. Additionally, in Figure 5.53 even though all the monitors displayed the same frequency in a given duration, there existed a phase difference between the monitors as illustrated using the red dashed line. This might indicate any unsynchronised expansion or contraction of the individual sections of the flow-field. This might also be a reflection of the travel time between monitors of different distances downstream.

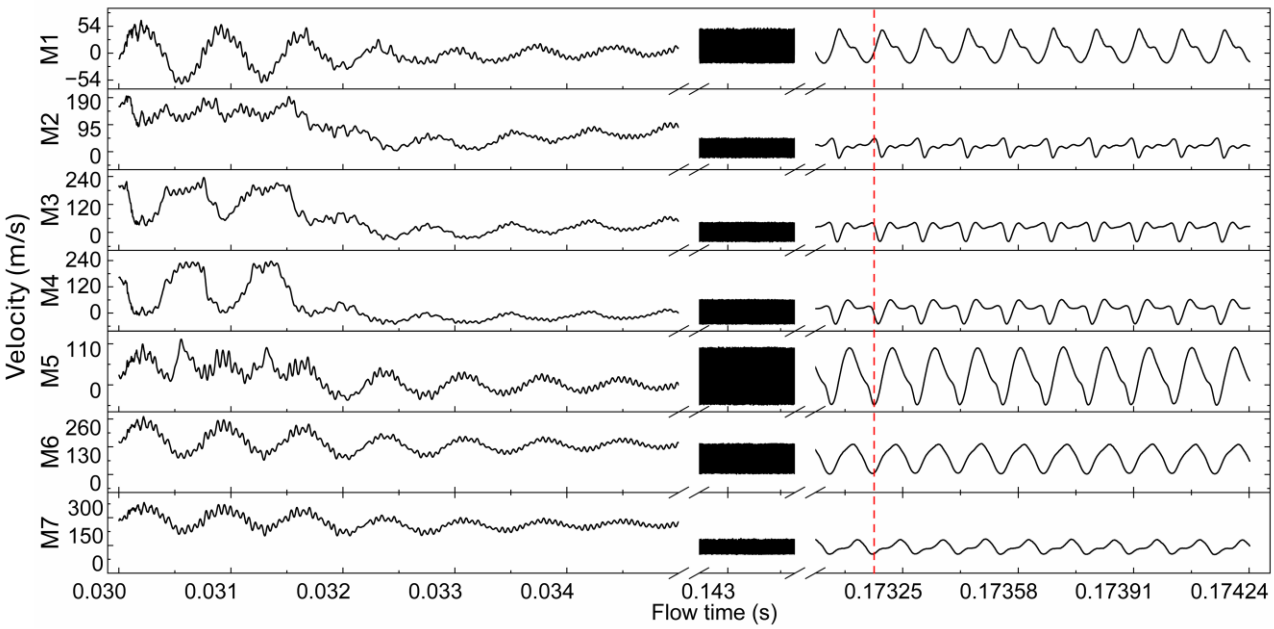

Figure 5.53 Monitors M1 to M7 zoomed in at the injection of the melt and at the mid frequency fluctuation. The frequency for all the seven monitors is same as the mid frequency seen in the injection mass flow rate i.e. 8.1 kHz. Existence of phase difference between the monitors is indicated using the red dashed line.

5.3.2 Melt temperature: 600K

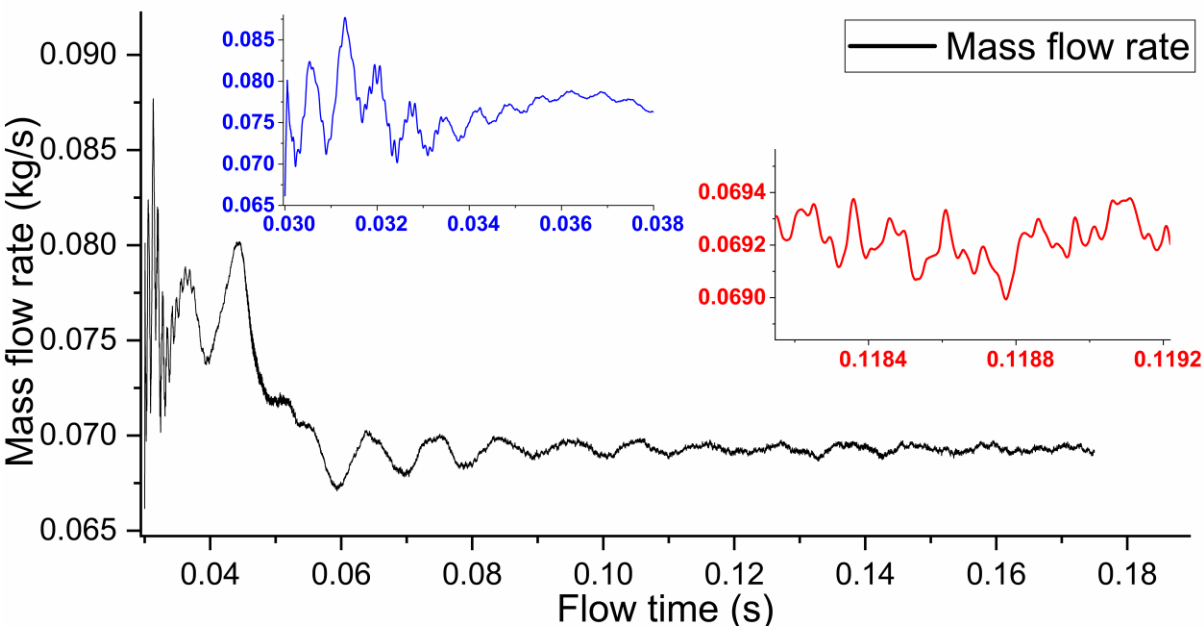

Figure 5.54 Injection mass flow rate plot of 4 kg min^{-1}, 600K case showing zoomed-in part of the initial fluctuation in blue and irregular fluctuation around 110 ms in red. There is a rapid decline in the mass flow rate from 50 to 60 ms. Subsequently, the fluctuation continuously attenuates to become a near-constant steady-state mass flow rate with negligible amplitude.

The investigation on 4 kg min^{-1} cases was further extended to explore the effects of higher melt temperatures on the gas-melt interactions. The 4 kg min^{-1} case, with a melt temperature of 600K was run for 145 ms (30 to 175 ms). The injection mass flow rate plot is presented in Figure 5.54. With the melt injected into the domain, the mass flow rate undergoes the same initial fluctuation seen in the 300K case. After the attenuation of the initial fluctuation, there was an onset of a higher frequency fluctuation at 45 ms which existed for the remainder of the run-time, although it was of negligible amplitude. However, after the initial fluctuation, a fall in the mass flow rate was observed from 50 to 60 ms. Thereafter, it transitioned into a fluctuation having a time period of ~10 ms but underwent continuous attenuation before becoming a near-constant mass flow rate having negligible amplitude. Through the FFT analysis, three frequency levels were obtained: low-frequencies of 96 Hz,158 Hz, and 1.4 kHz; a mid-frequency of 8.1 kHz; and a high-frequency of 19.8 kHz. On observing the injection mass flow rate for a consistent fluctuation frequency as seen in the 300K case, no such frequency was observed due to the irregular nature of the fluctuations. The GMR of the plot after it achieved near-constant flow rate was evaluated to be 1.26 i.e., only ~5% lower than the nominal GMR. The mass flow rate of the particles obtained at the outlet of the domain, as shown in Figure 5.55, reflected the low frequency fluctuation (time period of ~10 ms) seen in

the injection mass flow rate (Figure 5.54). The steep rise observed between 47 to 60 ms in Figure 5.55 can be correlated to an increased mass outflow, but when the injection mass flow rate is observed a steep fall in the mass flow rate noted.

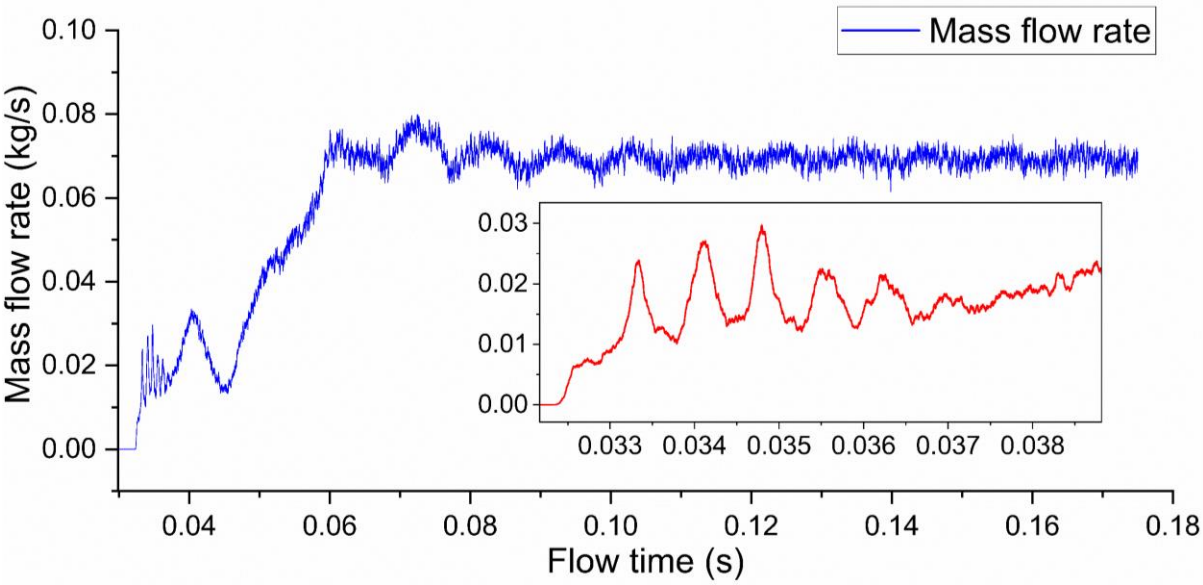

Figure 5.55 Mass flow rate of the particles obtained at the outlet of the domain for 4 kg min^{-1}, 600K case. The flow of particles through the outlet rises steadily at first, then decreases briefly, before rapidly increasing till 60 ms. Thereafter, the plot exhibits a low frequency fluctuation and simultaneously dampens out its fluctuations.

The particles' trajectories of the 600K case were very much similar to that of the 300K. However, there were two distinct differences that were observed. The melt underwent pre-filming at 33.1 ms (whereas for 300K case it is 32.5 ms) and the melt pool head that moved downstream due to the increased mass loading, joined with the particles that were pushed downstream by the supersonic gas jet, at 45 ms.

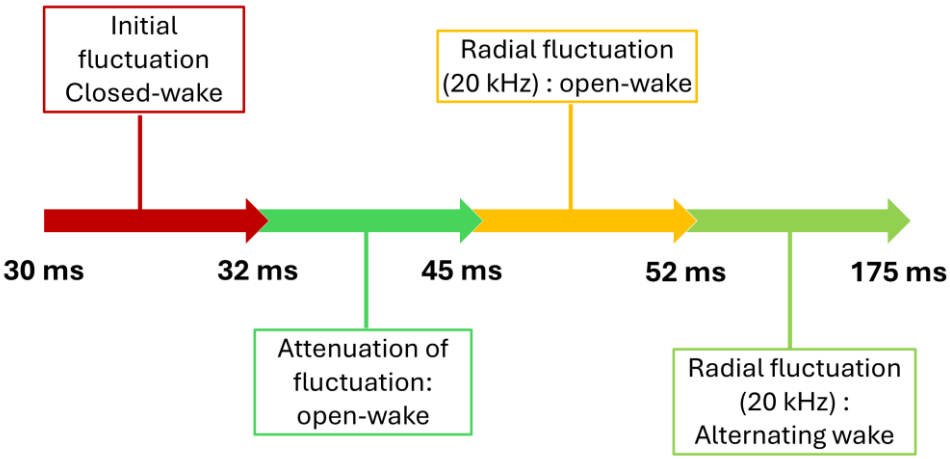

Figure 5.56 Timeline of flow-field fluctuations observed in 4 kg min^{-1}, 600K case.

Similarly, the flow-field observed in the 600K was similar to that of the 300K case to a certain extent, and the timeline of different flow-field fluctuations observed in 600K case is presented Figure 5.56. The flow-field underwent the same initial fluctuation due to the onset of melt injection as seen in Figure 5.50, existing in closed-wake condition, but quickly transitioned into open-wake condition from 32 ms and continued to exist in open-wake condition until 52 ms while simultaneously undergoing dampening in its flow-field fluctuations. At 45 ms, an onset of a continuous flow-field fluctuation emerged in the flow-field and remained for remainder of the run-time. The flow-field underwent a similar fluctuation as seen in Figure 5.51 of 300K case. Albeit, from 45 to 52 ms the fluctuation continued to exist in open-wake condition, but thereafter alternated between open- to closed-wake conditions. The frequency of the flow-field fluctuation was evaluated to be 20 kHz. Correlating the frequency of the flow-field fluctuation with that of the frequency obtained from the FFT analysis from injection mass flow rate plot, it can be seen that only the high frequency, 19.8 kHz, corresponded to the flow-field fluctuations. Moreover, in the 600K case, the axial flow-field fluctuation observed in the 300K case (Figure 5.52) was absent.

5.3.3 Melt temperature: 1000K

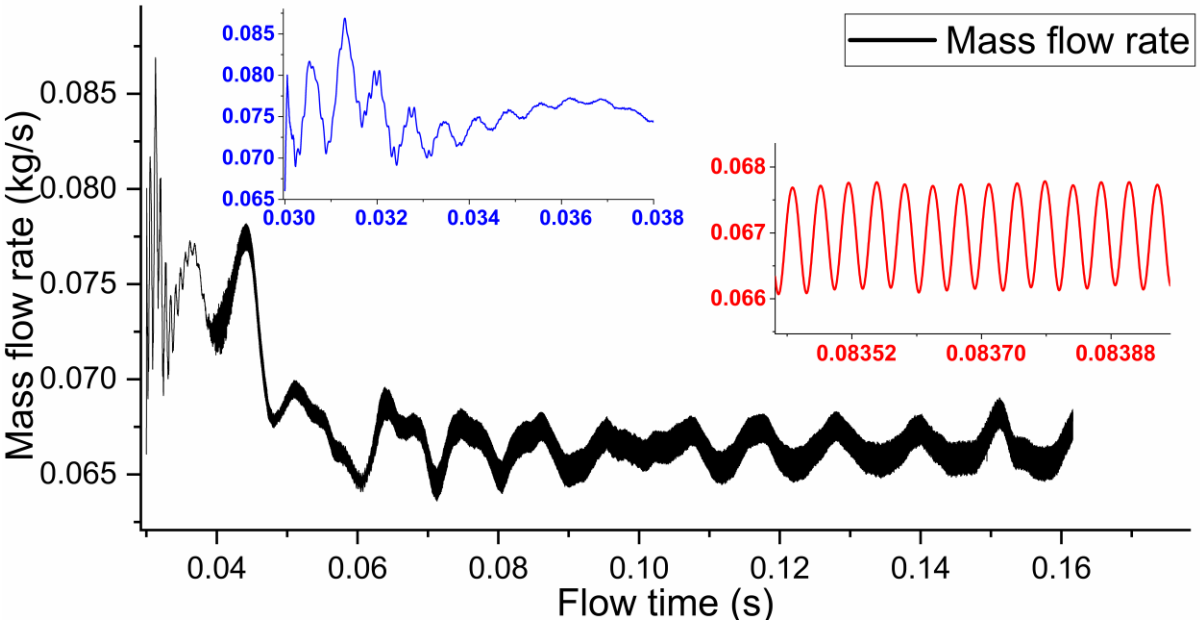

Figure 5.57 Injection mass flow rate plot of 4 kg min^{-1}, 1000K case showing the initial fluctuation and the high frequency fluctuation. From t > 39 ms the presence of a higher frequency fluctuation is seen. The high frequency fluctuation is of constant amplitude as seen in the zoomed plot. At t > 60 ms the mass flow rate fluctuation undergoes periodic fluctuation with a time period of ~9 ms.

The 4 kg min^{-1} case with a melt temperature of 1000K was run for 131 ms (30 to 161 ms), and its injection mass flow rate plot is presented in Figure 5.57. The 1000K case was similar to that of the 600K case with few differences. After the attenuation of the initial fluctuation, at 39 ms there was an onset of a higher frequency fluctuation that continues to exist for the rest of the simulation. Unlike the injection mass flow rate of 600K which attenuated to become a near-constant flow rate, in the 1000K case there existed a regular pattern to the fluctuation. It was observed that the mass flow rate fell sharply from 43 to 60 ms before evolving into fluctuation having a time period of ~9 ms. (This sharp drop in the mass flow rate is also observed in the 600K case). From the FFT analysis two levels of frequency were observed: low-frequencies of 91 Hz, 159 Hz, and 1.45 kHz; and a high-frequency of 25.6 kHz. The latter corresponded to the high-frequency fluctuation seen in the injection mass flow rate from t > 39 ms (Figure 5.57). The GMR for the 1000K case was evaluated to be 1 - 1.38.

The particles' trajectories of the 1000K case were also similar to that of the 300K and 600K case. Nevertheless, there were a few differences that were observed. The melt underwent delayed pre-filming at 34 ms (whereas for 600K it was at 33.1 ms), and the melt pool head that moved downstream due to the increased mass loading, joined with the particles that were pushed downstream by the sonic gas jet, at 44.3 ms, and shortly thereafter plunged into the second Mach-disk.

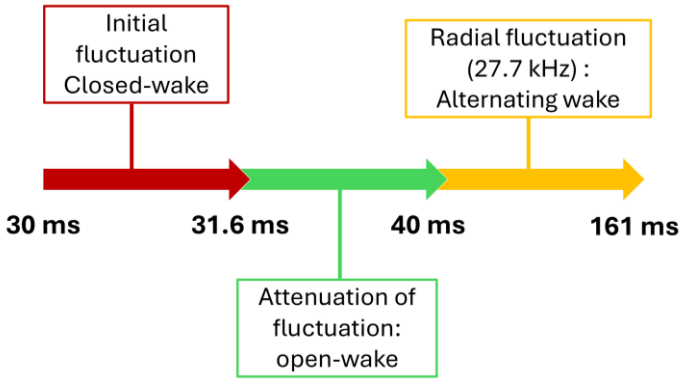

Figure 5.58 Timeline of flow-field fluctuations observed in 4 kg min^{-1}, 1000K case.

Likewise, the flow-field for the 1000K case looked very similar to that of the 600K case. The flow-field underwent the same initial fluctuation as seen in 300K case (Figure 5.50). Initial the fluctuation existed in closed-wake condition until 31.6 ms and thereafter transitioned into open-wake condition while simultaneously continuing to attenuate until 40 ms. At 40 ms the fluctuation grew in its spatial oscillation along the radial direction indicating the onset of a high frequency flow-field fluctuation. This fluctuation existed for the remainder of the

simulation alternating between open- to closed-wake condition as illustrated in Figure 5.51. The frequency of this fluctuation which alternated between open- to closed-wake condition was evaluated to be 27.7 kHz, and it corresponded to the 25.6 kHz seen in the mass flow rate (Figure 5.57). The discrepancy in the difference in two frequencies might be due to the lack of additional significant numbers in the flow times recorded for the flow-field. Apart from the 25.6 kHz frequency, other frequencies seen in the injection mass flow rate were not able to be observed in the flow-field fluctuation.

5.3.4 Melt temperature: 1500K

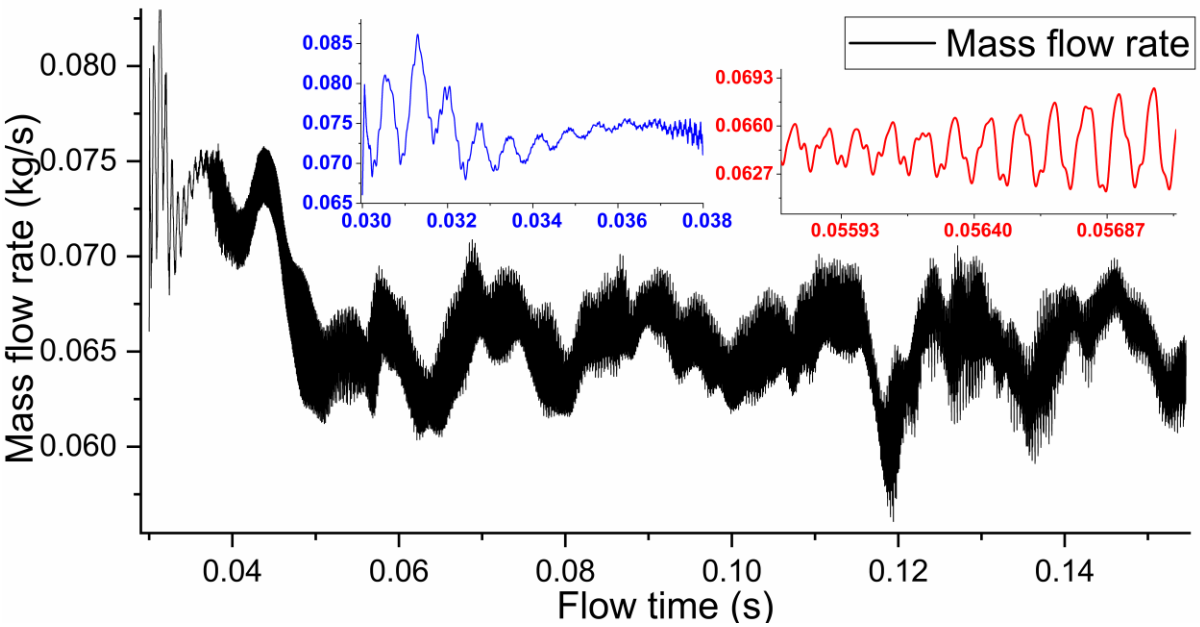

Figure 5.59 Injection mass flow rate plot of 4 kg min^{-1}, 1500K case showing the onset of high frequency at 36 ms. There is a considerable decline in the mass flow rate at 44 ms. The mass flow rate plot from 50 ms is irregular both in its amplitude and in its frequency of fluctuation.

The 4 kg min^{-1} case with melt temperature 1500K was run for 124 ms (30 to 154 ms). The injection mass flow rate plot is presented in Figure 5.59. The initial fluctuation seen in the 1500K case was similar to that of the earlier cases. After the initial fluctuation due to the melt injection, even as the fluctuation continued to attenuate, at 36 ms there was an onset of a higher frequency, remaining for the rest of the simulation. Following this, as observed in the earlier cases, there was a considerable fall in the mass flow rate until 50 ms. Thereafter at t > 50 ms the fluctuation was highly irregular with varying frequency and amplitude, observed from Figure 5.59. GMR for the 1500K case was evaluated to be 1 - 1.56. FFT analysis on the mass flow rate (Figure 5.59) revealed broad range of frequencies being present in the fluctuation. They were classified as low, mid and high-frequencies. Low-frequencies of 56-88 Hz, and 1.4

kHz; mid-frequencies of 8.6 kHz, 11.4 kHz, and 14.3 kHz; and high-frequencies of 22.8 kHz, 25.6 kHz, 28.6 kHz and 31.4 kHz, were found.

No particular frequency obtained from the FFT analysis were been able to consistently correlate to the fluctuation seen in the mass flow rate. However, in many sections of the mass flow rate plot it was observed, there existed a dominant base (modulating) wave of 8.6 kHz, and upon it, various high-frequency fluctuations were modulated in frequency modulation. Unlike the changes seen in the injection mass flow rate, the particles' trajectories were similar to that of the earlier cases (Figure 5.47), except for the time of pre-filming which occurred at 36 ms and melt pool head plunging into the second Mach-disk taking place at 45 ms.

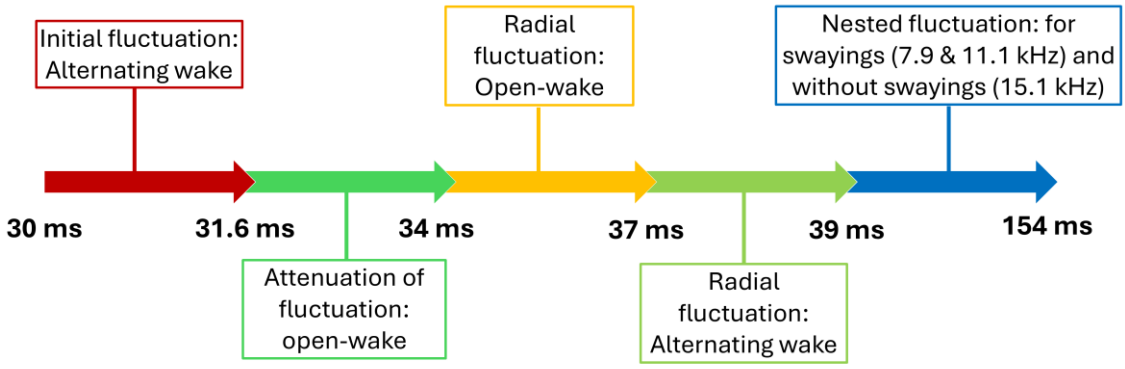

Figure 5.60 Timeline of flow-field fluctuations observed in 4 kg min^{-1}, 1500K case.

The flow-field displayed significant changes in its fluctuation characteristics. The initial flow-field fluctuation due to the melt injection alternated between open- to closed-wake condition, but at 31.6 ms it transitioned into open-wake condition while continuing to attenuate in its fluctuation. Even though the flow-field attenuated in its spatial oscillations until 34 ms, it did not transition into a steady- or near-steady state flow-field. At 34 ms, the already existed fluctuation significantly increased in its spatial movement along the radial direction from the second Mach-disk and beyond, indicating the onset of a higher frequency flow-field fluctuation. At 37 ms the flow-field fluctuation transitioned into an alternating wake, simultaneously continuing to intensify in its fluctuation over time. The alternating flow-field existed until 39 ms, and thereafter transitioned into a different type of fluctuation as presented in Figure 5.61. It was observed, the closed-wake (MICW) seen in Figure 5.61a transitioned into open-wake, seen in Figure 5.61b&c. While continuing to exist in open-wake, the lower sonic boundary of the second shock-cell was observed to come in close proximity to the atomiser's axis as seen in Figure 5.61e, but did not touch the axis to transition into a closed-wake. The movement of the lower sonic boundary approaching the axis can observed when

Figure 5.61c&e are compared. In the ensuing frames, Figure 5.61f-h, it is evident that the sonic boundary again moved further radially away from the axis, before returning back to its original configuration, i.e., closed-wake. In other words, this fluctuation can also be divided into four stages. First stage – the closed-wake transitions into open-wake (Figure 5.61a&b); second stage – the lower sonic boundary approaches the atomiser's axis to close proximity (Figure 5.61c-e); third stage – the sonic boundary recedes back from the axis (Figure 5.61f); fourth stage – the sonic boundary immerses into the melt layer to fully re-establish as a closed-wake (Figure 5.61h). Henceforth, such fluctuations seen in Figure 5.61 will be called as Nested fluctuations. In such nested fluctuations, the radial motion of the lower sonic boundary approaching and receding the atomiser's axis without touching it, as observed in Figure 5.61d-f will be henceforth called as swaying.

In nested fluctuation seen in Figure 5.61, the first and second shock-cell did not undergo any change in its spatial extent along the axial direction. This is shown using three guide-lines, (i), (ii), (iii), pinned in Figure 5.61a at the downstream ends of the first, second and third shock-cells, respectively, and were compared against the flow-fields of the other frames. It is evident that the first and the second shock-cell remain fixed throughout the fluctuation, whereas the third shock-cell underwent marginal change in its size along the axial direction. In addition to this, although the number of swayings in the nested fluctuation presented in Figure 5.61 were only one, in other sections of the flow-field fluctuation the number of swaying varied irregularly over time, resulting in irregular flow-field fluctuation. However, out of the irregular fluctuations, two prominent frequencies of fluctuation were observed. They were 7.9 and 11.1 kHz. The former corresponded to nested fluctuation containing two swayings, whereas the later corresponded to nested fluctuation containing one swaying. Another frequency of flow-field fluctuation was also observed – 15.1 kHz although it was insignificant. The 15.1 kHz fluctuation was observed when the flow-field alternated between open- and closed-wake without any swaying.

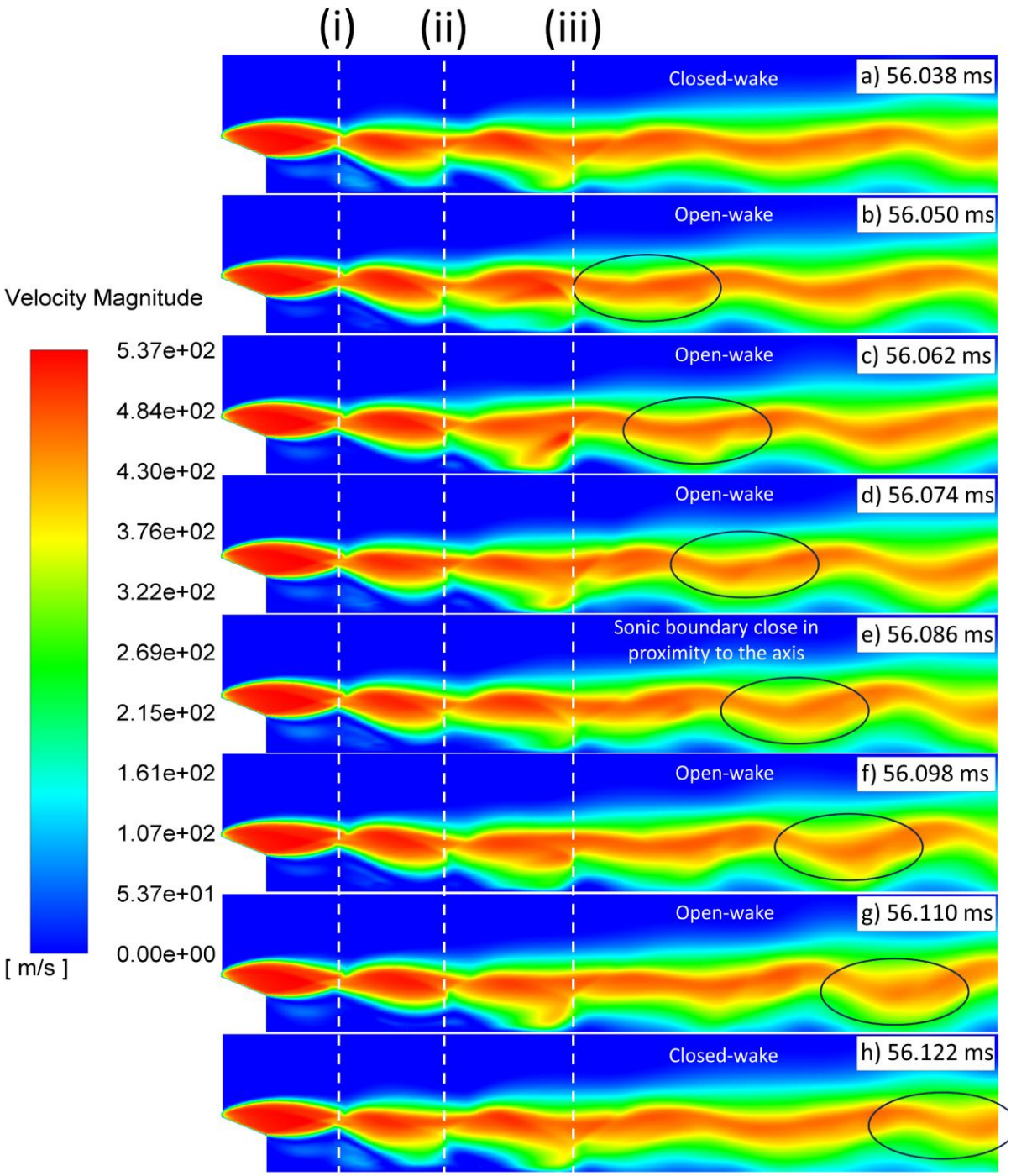

Figure 5.61 Velocity contours of 4 kg min^{-1}, 1500K case showing flow-field fluctuations. Three guide-lines (i), (ii), and (iii) are pinned in frame a, at the ends of the first, second and third shock-cell, respectively, and are compared against the other frames. It is observed the first and second shock-cells remain fixed throughout the fluctuation, whereas third shock-cell exhibit marginal change in its spatial extent. In frame a, the flow-field exists in closed-wake condition. In the consecutive frames, from frames b till e it is seen the flow-field enters into open-wake condition, and tends to return back to closed-wake condition. However, as seen in frame e, even though the lower sonic boundary is near to the atomiser's axis, still it continues to exist in open-wake condition. Consequently, the sonic boundary moves away from the atomiser's axis before returning to closed-wake condition in frame h. A significant wave propagation from the second Mach-disk is observed which is marked using ellipses.

The flow-field fluctuation seen in Figure 5.61 was examined against the melt fluctuation seen in Figure 5.59. It was observed that at the local minima of the melt fluctuation, the flow-field existed as closed-wake, and at the local maxima of the melt fluctuation the flow-field existed as open-wake with its lower sonic boundary being furthest radially away from the atomiser's axis, and it is usually the one that occurs after the swaying. During swaying, where sonic boundary approaches and recedes the atomiser's axis, the melt flow rate continued to rise. Although efforts were taken to analyse to observe for further correlation between the flow-field fluctuation and the melt fluctuation, apart from the local minima and local maxima corresponding to closed-wake and open-wake condition, respectively, no other characteristics part of the flow-field fluctuation were been able to consistently associate with the melt fluctuation, as they were highly irregular in nature.

5.3.5 Melt temperature: 2000K

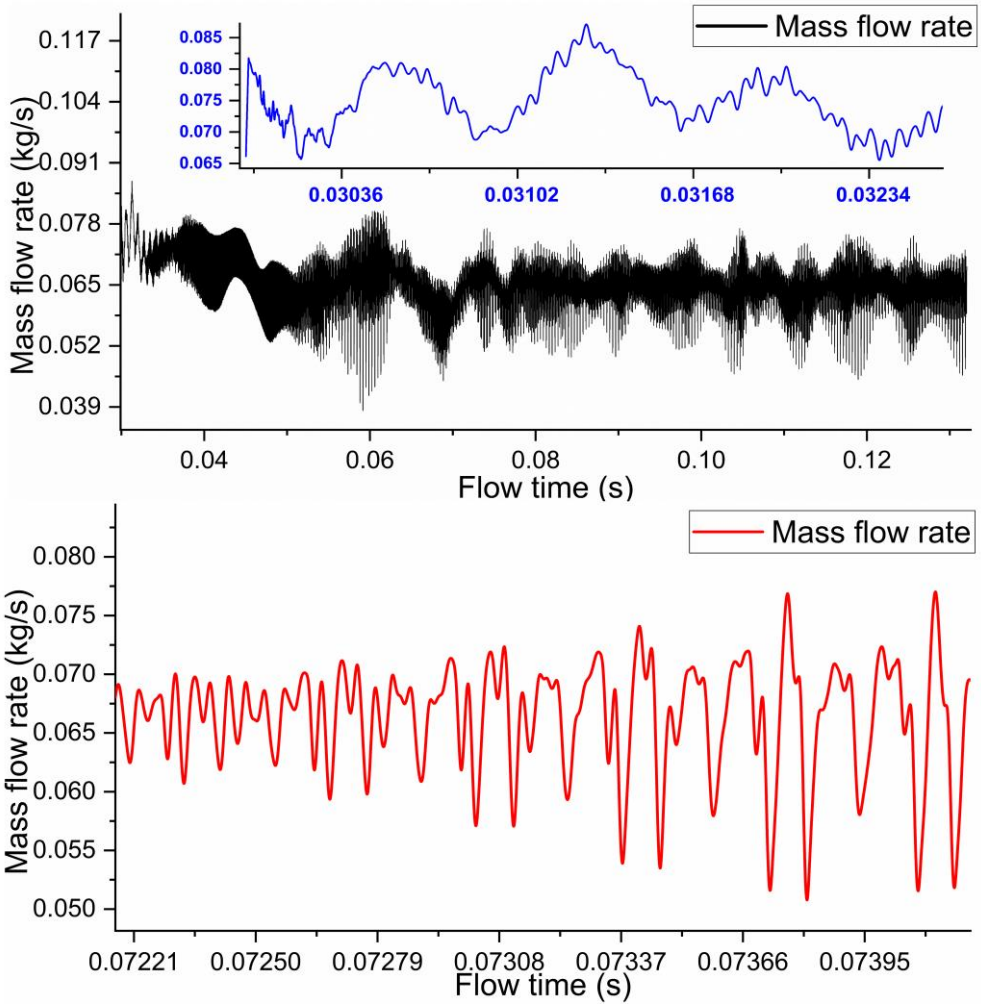

Figure 5.62 Injection mass flow rate plot of 4 kg min^{-1}, 2000K case showing the onset of high frequency around 32.6 ms, and highly irregular fluctuation thereafter. The mass flow rate plot is extremely irregular both in the amplitude and the frequency of the fluctuation. The zoomed section of the high-frequency fluctuation shows the extent of the variation in amplitude and frequency.

The 4 kg min^{-1} case with melt temperature 2000K was run for 102 ms (30 to 132 ms). The injection mass flow rate plot is shown in Figure 5.62 along with its zoomed-in section showing the irregular frequency and amplitude of the fluctuation. The 2000K case is similar to that of the 1500K case with few differences. The initial fluctuation due to the melt injection can be distinctly observed. Subsequently, just 2.6 ms into the melt injection, with the fluctuation attenuating but still significant, the onset of higher frequency fluctuations was observed. In general, over the entire period of simulation, the melt fluctuations were highly irregular, however after the onset of the higher frequency fluctuation at 32.6 ms, for a short period of time until 50 ms, regular fluctuations were observed, but with the exception that it was irregular from 36 to 39 ms. After this, for the rest of the simulation, the fluctuation was highly irregular without corresponding to any particular frequency.

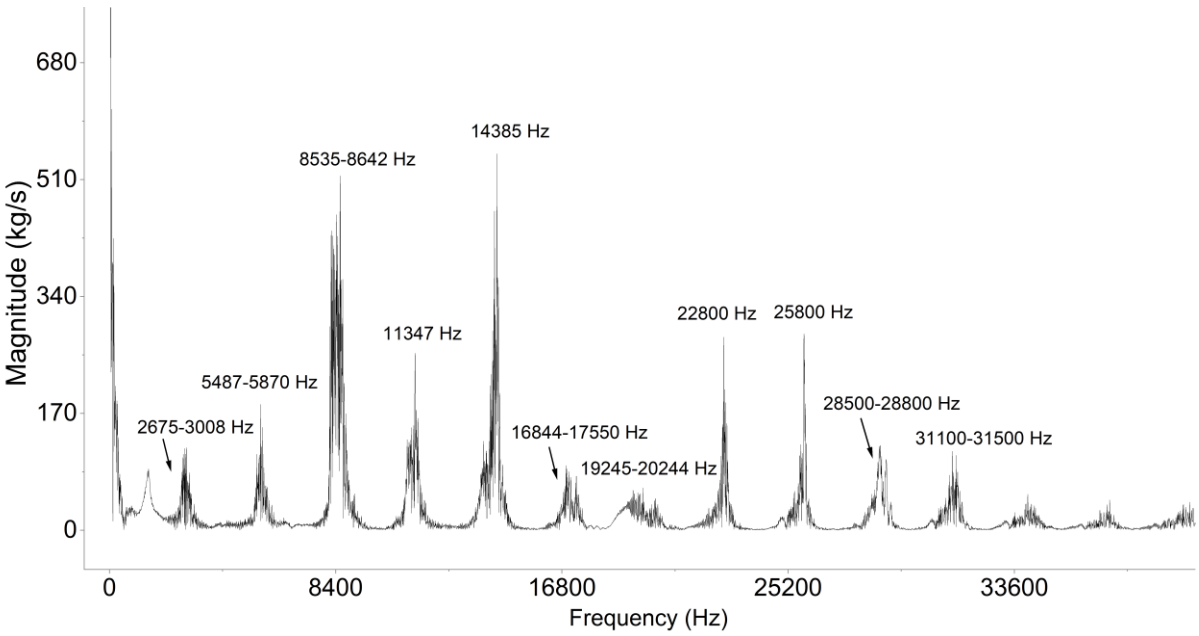

Figure 5.63 FFT analysis of the injection mass flow rate for the 4 kgmin^{-1}, 2000K case shows multiple frequencies reflecting the instability in the mass flow rate.

From the FFT analysis, it was revealed there were numerous frequencies of fluctuations present, and their FFT peaks are presented in Figure 5.63. It is clear from Figure 5.63 that some of the higher frequencies, such as 16.8 - 17.5 kHz, 22.8 kHz and 28.5 - 28.8 kHz are harmonics of the lower frequencies, 8.5 - 8.6 kHz, 11.3 kHz, and 14.3 kHz, respectively. The GMR for the 2000K case varied between 1 - 2.3. Also, similar to the 1500K case, it was observed that in many sections of the mass flow rate plot there was a base fluctuation i.e. a modulating wave, upon which there were fluctuations of different frequencies modulated in frequency modulation. Few such modulating wave frequencies seen in the mass flow rate were: 2.7 kHz,

8.5 kHz, and 11.3 kHz, and all these frequencies corresponded to FFT peaks as observed in Figure 5.63. Moreover, considering the particles trajectories of the 2000K case, they were similar to those seen previous cases, except for the melt pre-filming occurring at 37 ms, and the melt pool head plunging into the second Mach-disk at 47 ms.

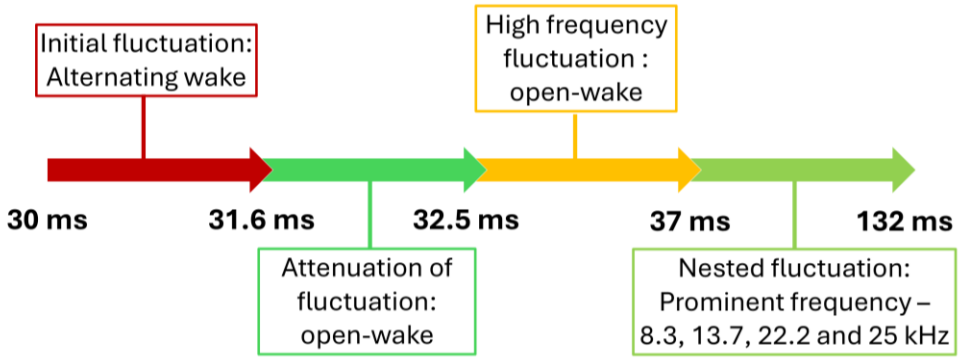

Figure 5.64 Timeline of flow-field fluctuations observed in 4 kg min^{-1}, 2000K case.

The flow-field of the 2000K case looked very similar to that of the 1500K case with the exception there were deviation in the times of certain flow-field characteristics. The timeline of the different flow-field fluctuation observed in the 2000K case is presented in Figure 5.64. The initial flow-field fluctuation due to the onset of melt injection was observed to undergo wake alternation, but subsequently transitioned into open-wake condition at 31.6 ms. While continuing to fluctuate, at 32.5 ms the onset of a higher frequency fluctuation was observed, and it intensified over time. As the fluctuation intensified, the second Mach-disk (see Figure 5.50 to refer second Mach-disk) underwent continuous alternation between retracting and re-establishing, even though the wake existed under open-wake condition (absence of first Mach-disk) until 37 ms. Nevertheless, even though the flow-field did not undergo wake alternation i.e., open- to closed-wake condition, until 37 ms, it still did possess significant fluctuation as seen in Figure 5.51. Subsequently, at t > 37 ms, it transitioned into nested fluctuation as presented in Figure 5.61. The flow-field fluctuations were highly irregular to associate the fluctuations to one frequency. However, the frequencies of flow-field fluctuation, 8.3 kHz, 13.7 kHz, 22.2 kHz, and 25 kHz were found to be prominent but spread out across different timelines of the simulation. Observation comparing the flow-field fluctuation against the melt fluctuations identified via FFT analysis (Figure 5.63) indicated that lower frequencies of melt fluctuation corresponded to nested fluctuation with increased number of swayings, whereas higher frequencies of the melt fluctuation corresponded to nested fluctuation with decreased number of swayings. In addition to the two above seen observations, it was also

observed, in some instances that flow-field fluctuation having frequencies towards the lower end of FFT frequency spectrum underwent wake alternation with nested fluctuations as seen in Figure 5.61, and in other instances, without nested fluctuations as observed in Figure 5.52 (regular open- to closed-wake alternation).

5.3.6 Summary

The 4 kg min^{-1} (GMR=1.32) cases with increasing melt temperature exhibited unexpected trends. The melt flow rate in 300K case was highly regular in nature with large amplitude, whereas T > 600K cases exhibited no regular fluctuation and took the form of a completely different mode of fluctuation. At lower temperatures (600K), the melt flow rate reached near-steady state, but with further increase in melt temperature, randomness in the process started building up. The 1500K and 2000K cases revealed the extend of randomness in the melt injection reflecting the physical atomisation process.

It is observed that only the 300K case undergoes axial flow-field fluctuation, whereas the higher temperature cases undergo radial fluctuation. Nevertheless, all the cases exhibited continuous melt movement downstream, and also demonstrated delayed pre-filming with increase in temperature.

The simulations with increasing melt temperatures (T ≥ 1500K) also revealed the existence of a new higher order flow-field fluctuation known as Nested fluctuation coming into effect. The growing instability in the process with the increasing melt temperature is also measured by the increasing number of frequencies in the melt injection, and by their randomness in distribution across the flow-time.

The trend in the melt injection behaviour and their associated flow-field characteristics were further investigated for a higher nominal mass flow rate of 6 kg min^{-1} under increasing melt temperatures.

5.4 Results of 6 kg min^{-1} (GMR = 0.88) under increasing melt temperatures.

This section presents the results of 6 kg min^{-1} case having GMR=0.88, investigating the effect of increasing melt temperatures. The melt temperatures considered for this GMR are: 300K, 600K, 1000K, and 1500K (Table 4-6). Melt temperature case with 2000K was not carried out since the simulation was extremely unstable to run. The section is sub-divided to present and analyse the results for each of the melt temperatures individually.

5.4.1 Melt temperature: 300K

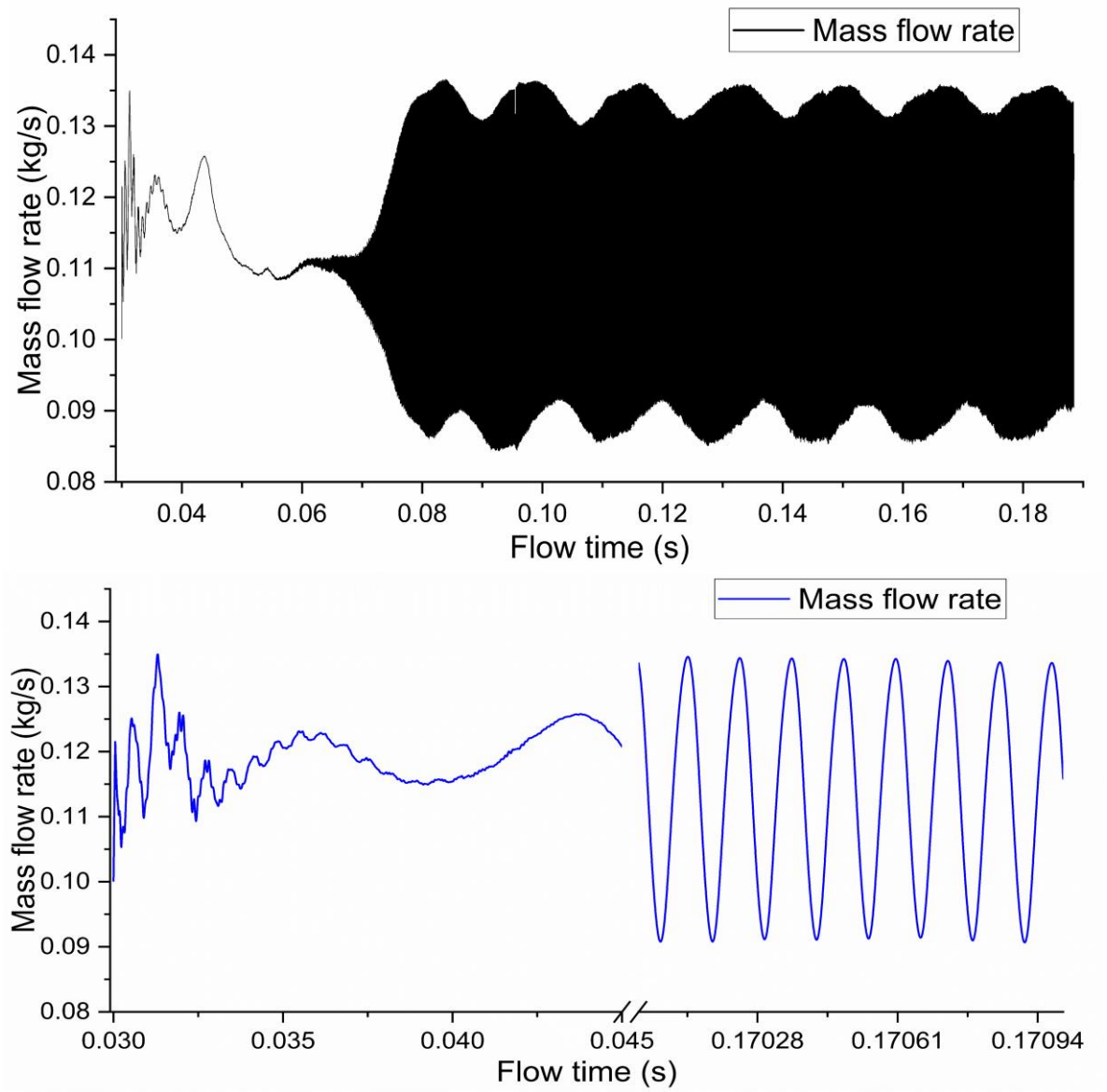

Figure 5.65 Injection mass flow rate plot of 6 kg min^{-1}, 300K case shows the initial fluctuation followed by two high amplitude peaks. At t > 58 ms there is an onset of a higher frequency fluctuation that gradually increases in its amplitude and remains constant from t > 80 ms. The zoomed section of the initial fluctuation and the regular repeated fluctuation is also presented.

The 6 kg min^{-1} case with a melt temperature of 300K having a GMR = 0.88 was run for 158 ms (30 to 188 ms). The injection mass flow rate is presented in Figure 5.65, with the zoomed sections of the plot at the bottom showing the onset of the injection and the periodic higher frequency fluctuation. From the plot it was observed at 30 ms the mass flow rate increased rapidly, and subsequently evolved into high-amplitude peaks until 32.4 ms. Following this, the fluctuation continued to damp, and from 40 till 58 ms no significant fluctuations were seen except for rise and fall in the mass flow rate seen between 40 and 50 ms (Figure 5.65). At 58 ms there was an onset of a higher frequency fluctuation, and it continued to exist for the remainder of the simulation. It started out gradually but grew over time in its amplitude. At 80 ms the fluctuation attained its peak amplitude, undergoing repeated and regular fluctuation as seen in Figure 5.65. Also, from Figure 5.65 it is seen at t > 80 ms, the mass flow rate evolves into a plot possessing two frequencies present in amplitude modulation.

Table 5-1 The frequencies obtained from the FFT analysis of 6 kg min^{-1}, 300K case, and their correlation to the flow-field fluctations.

Flow-time	**Frequency obtained from the FFT analysis**	**Fluctuation observed in the flow field**
30 - 40 ms	1.4 kHz	• Initial fluctuation until 31.7 ms • Attenuation of initial fluctuation observed 31.7 - 42 ms
40 - 50 ms	~77 Hz	• ~77 Hz was not observed. • 42 - 50 ms the flow field existed in steady-state.
50 - 58 ms	8.1 kHz	• 8.1 kHz flow-field fluctuation was not observed. • 50 - 58 ms, flow-field fluctuated at 20 kHz, but in open-wake.
58 - 188 ms	8.1 kHz (superimposed on 56 Hz)	• From 58 - 71 ms, flow-field fluctuated at 20 kHz, but in open-wake. • From 71 - 74.5, flow-field underwent transition fluctuation: adial to axial. • t > 74.5 ms, 8.3 kHz flow-field fluctuation undergoing wake alternation between open- to closed-wake via MICW was observed.
Not obviously observable	16.3 kHz	Nil

Low frequency Mid frequency High frequency

From FFT analysis of the injection mass flow rate plot (Figure 5.65) three levels of frequency were found: a low-frequency of 56 Hz; mid-frequency of 1.4 kHz; and a high frequency of 8.1 kHz. For the regular fluctuation in amplitude modulation seen at t > 80 ms, low-frequency 56 Hz corresponded to the modulating wave, while high-frequency, 8.1 kHz corresponded to the carrier signal. From the FFT analysis, in addition to the three above mentioned frequencies, another less significant high-frequency fluctuation at 16.3 kHz was also observed. The variation in GMR for the high-frequency melt fluctuation seen at t > 80 ms was evaluated to be 0.64-1. The frequencies obtained via the FFT analysis, and its corresponding flow-field fluctuations are tabulated in Table 5-1.

Considering the particles' trajectories with the velocity contours in the background, it was observed that the gas flow-field was disturbed from its steady-state due to the onset of melt injection. This is explained by comparing Figure 5.66a against Figure 5.66b. In Figure 5.66a, the flow was at steady-state, and two guide-lines were pinned at the first and second Mach-disks of Figure 5.66a, and were compared against Figure 5.66b. The velocity contours in Figure 5.66b revealed displacement of the first and second Mach-disk upstream when compared against Figure 5.66a, clearly indicating that the flow-field was disturbed as a result of the melt injection. Following this, due to the opposing force of the recirculation zone, the melt that was injected was prevented from moving downstream, leading to melt build-up at the melt nozzle front, as shown in Figure 5.66c&d. The recirculation zone also induces a radial pull on the melt, causing the melt to move radially away from the atomiser's axis i.e. towards the supersonic gas-jet as shown in Figure 5.66d. Thereafter, when the melt comes in contact with the gas-jet, it was swiftly pushed downstream as illustrated in Figure 5.66e&f. The particles that were initially pushed downstream after coming in contact with the gas-jet were highly collimated until the end of the first shock-cell but dispersed beyond that. This is shown in Figure 5.66f. However, as time progressed the particles started to disperse even from the first shock-cell. This is observed in Figure 5.66h. Subsequently, the melt underwent pre-filming at 33.8 ms. The earlier seen dispersion in the particles in Figure 5.66h, continued to further increase with time, evolving into Figure 5.66i. It was also noted from Figure 5.66i that the melt pool head significantly moved downstream, and has morphologically transformed into a sharper and more pointed melt pool head. With the melt pool head further moving downstream, at 43.5 ms, the melt re-joined the particles that were pushed downstream by the gas-jet (Figure 5.66j). The melt pool head moved further downstream and plunged into the second Mach-disk, and continued to move downstream as presented in Figure 5.67a.

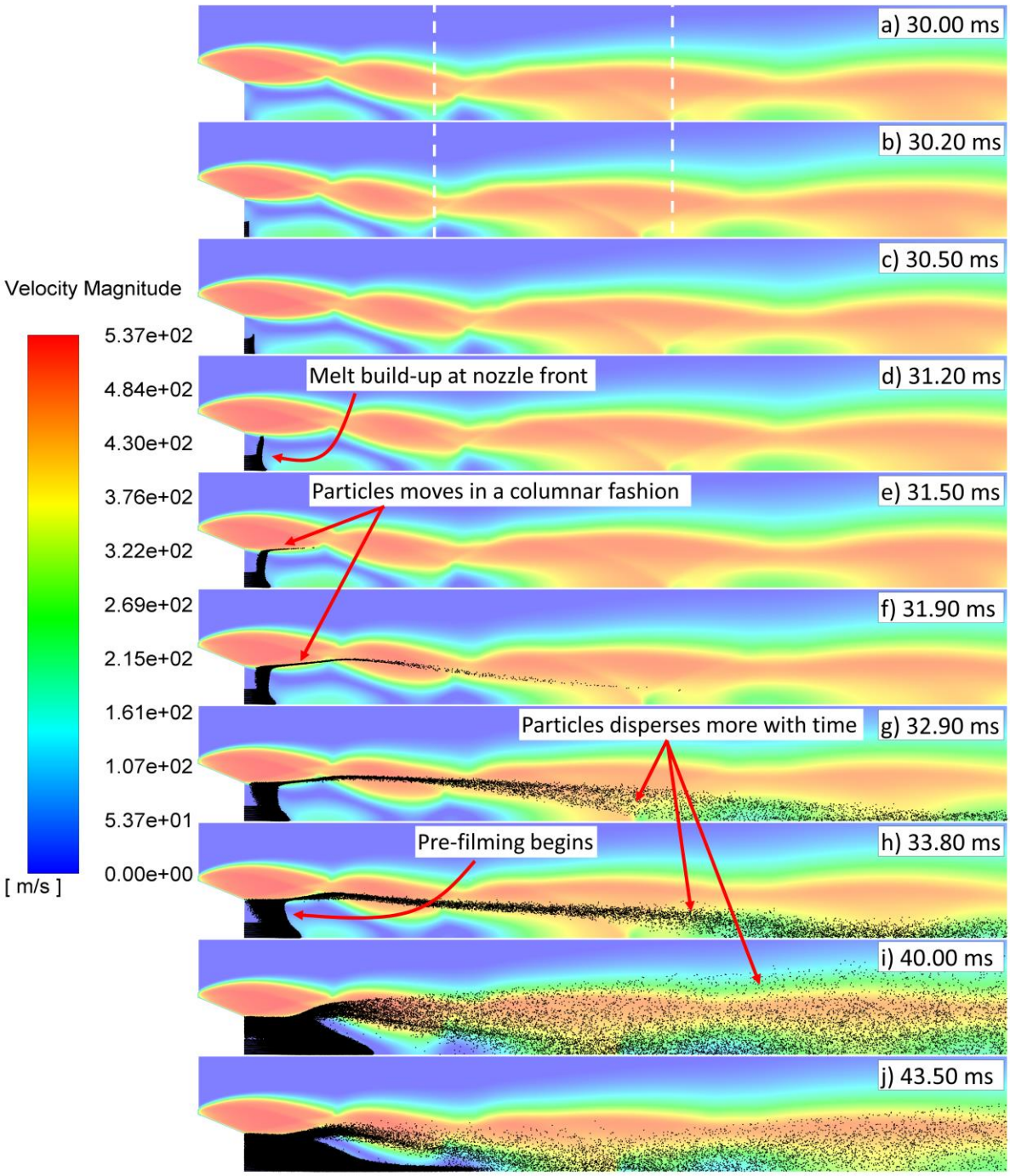

Figure 5.66 Particle trajectories of the 6 kg min^{-1}, 300K case, with the velocity contour in the background showing the evolvement of particles after being injected into the flow stream. These stacks of particle trajectories show the onset of injection, pre-filming, melt movement downstream, and increased dispersion of particles with time.

On top of the particle dispersion seen in Figure 5.66, the extent of increase in particle dispersion can also be understood from Figure 5.67. Due to the increased particle dispersion, starting at t > 75 ms, flares, i.e., particles in groups of small numbers, were propelled radially outwards from the main melt plume by the flow-field. This is illustrated in Figure 5.67b-g using

ellipses. Moreover, on comparing all the frames of Figure 5.67a-g, it was also evident that due to the increased mass loading, the melt which moved downstream along the axis after plunging into the second Mach-disk increases in its thickness over time. Increase in mass loading in the domain can be confirmed by comparing injection mass flow rate (Figure 5.65) against the mass flow rate of the particles obtained at the outlet of the domain (Figure 5.68). Nevertheless, commencing at t > 80 ms the outlet mass flow rate plot does not resemble the extent of fluctuation seen in the injection mass flow rate plot; instead, the plot possesses a fluctuation having a small amplitude. This can be due to the damping effect experienced by the injected particles as they travel downstream through the supersonic flow-field, effectively removing all high-frequency fluctuations.

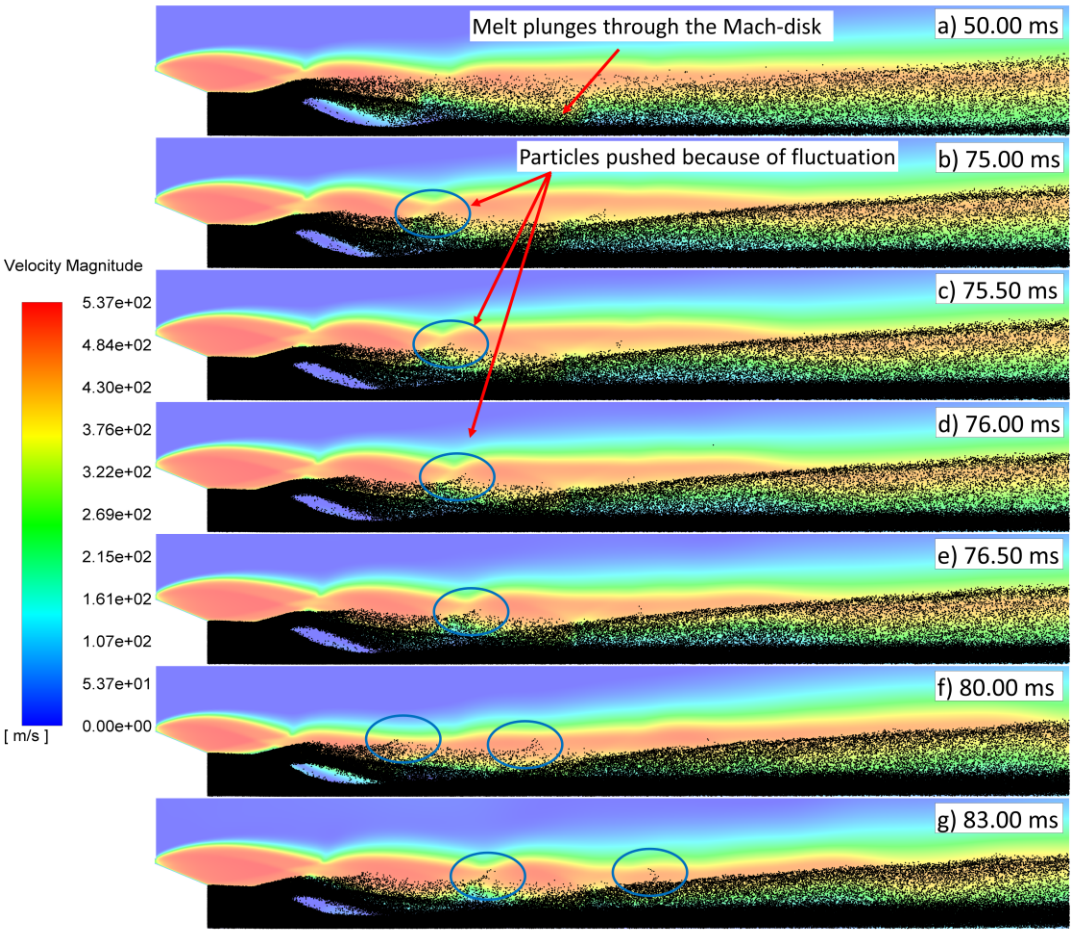

Figure 5.67 Particles trajectories 6 kg min^{-1}, 300K case with velocity contour in the background showing increasing dispersion of particles with time, and melt pool head plunging through the second Mach-disk. Frame b - g shows flares i.e. particles being propelled radially outwards from the main melt plume in small groups, marked by ellipses.

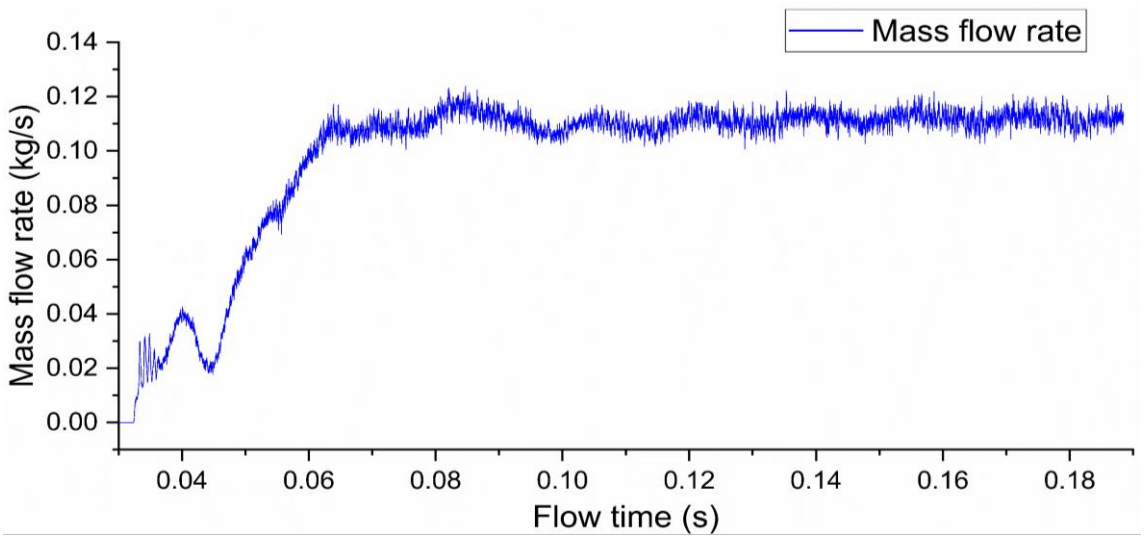

Figure 5.68 Mass flow rate of the particles obtained at the outlet of the domain for 6 kg min^{-1}, 300K case. There is an initial steady increase in the flow of particles through the outlet, but decreases briefly at 40 ms, but thereafter increases rapidly. Subsequently, at t > 65 ms no significant change in the mass flow rate is seen.

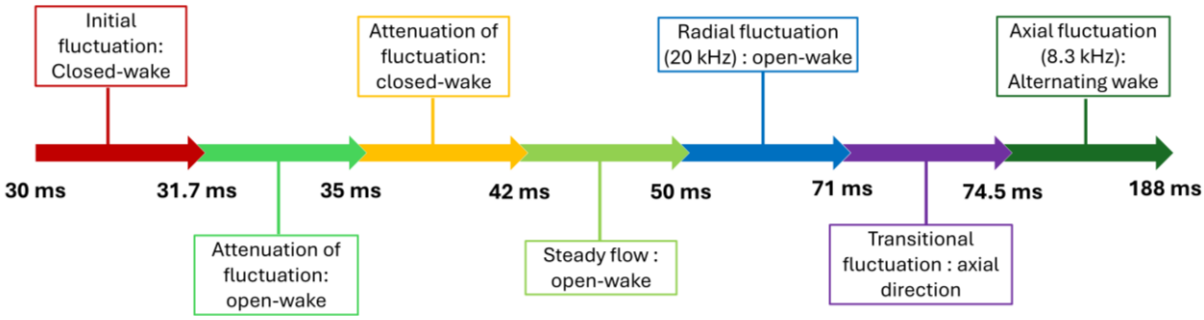

Figure 5.69 Timeline of flow-field fluctuations observed in 6 kg min^{-1}, 300K case.

Considering the flow-field contours of the fluctuation, the different types of fluctuation observed in the 300K case during the flow-time are presented in Figure 5.69. From the velocity contours of the flow-field, presented in Figure 5.70, it was again confirmed, the flow-field that was disturbed from its steady-state due to the introduction of melt into the domain, as seen in Figure 5.66b, underwent repeated fluctuation by shifting upstream and downstream along the axial direction. Even though in all the cases discussed in the 6 kg min^{-1} model, both the particles (melt) and gas flow-field co-exist, to have to have better understanding of the flow-field, only velocity contours are presented. The above-mentioned disturbance to the flow-field is illustrated using Figure 5.70 where series of velocity contours of the flow-field were obtained in close consecutive flow times, and were stacked. Two guide-lines, (i) and (ii) were pinned in Figure 5.70a, at the first and the second Mach-disk, respectively, and were compared against the rest of the frames of Figure 5.70. On comparing, it was observed the flow-field alternated

upstream and downstream continuously i.e. the flow-field features, including the first and second Mach-disk moved upstream in Figure 5.70b, and subsequently moved downstream in Figure 5.70c. It was also observed, while the flow-field displaced upstream and downstream, the wake continued to remain in closed-wake condition until 31.7 ms while simultaneously attenuating in its spatial oscillations along the axial direction. In addition to the flow-field fluctuations, the continuous downstream movement of the melt pool head observed in Figure 5.66, is also seen in Figure 5.70. This is indicated using black circles. At 31.7 ms the flow-field transitioned into an open-wake, and continued to exist in the same configuration until 35 ms.

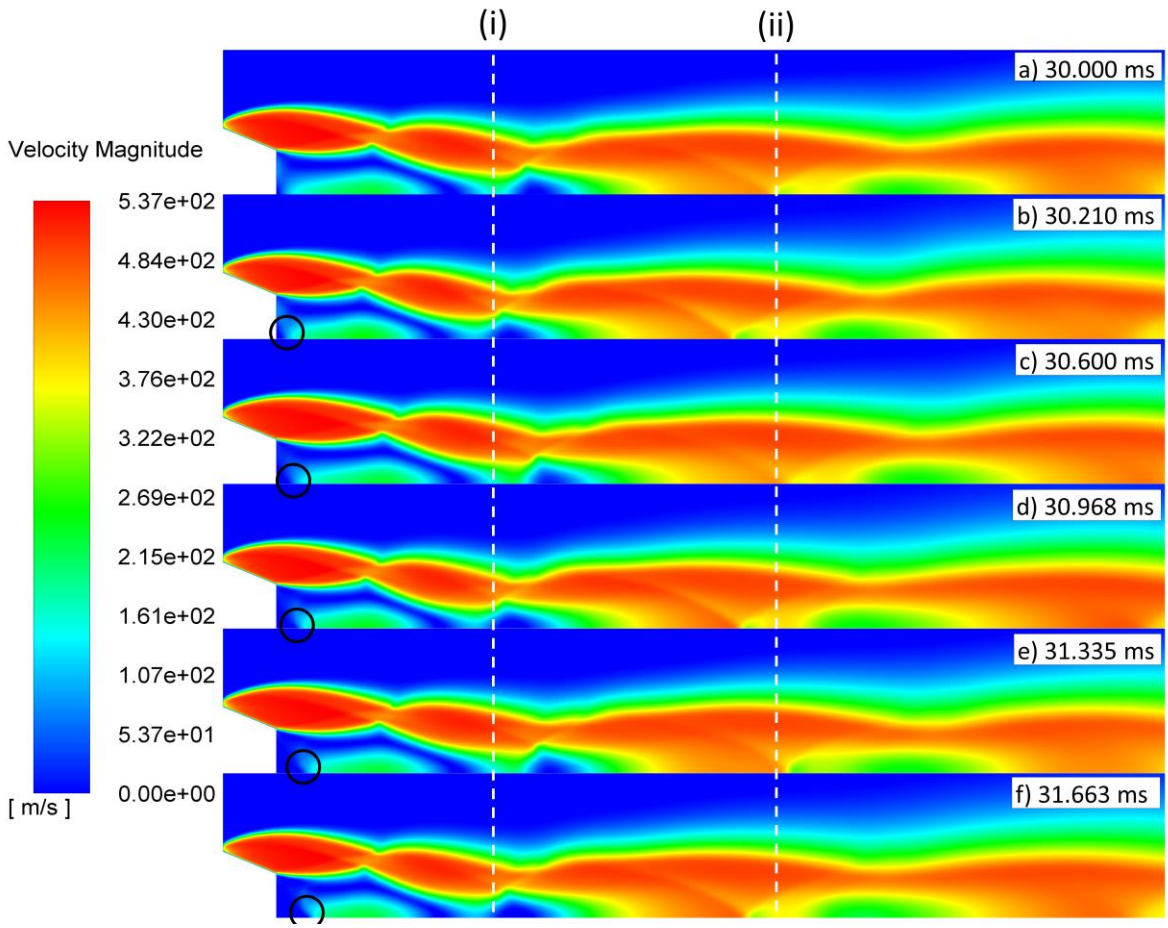

Figure 5.70 Velocity contours of 6 kg min^{-1}, 300K case, is presented without particles, showing flow-field fluctuations at the onset of the melt injection into the domain. Two guide-lines (i) and (ii) are fixed at first and second Mach-disk of frame a, to compare the changes with rest of the frames.

Following this the flow-field transitioned into a closed-wake and continued to exist in the same configuration until 42 ms before transitioning back into open-wake. Nevertheless, irrespective of the wake configuration the spatial oscillations in the flow-field continued to attenuate from 31.7 ms to 42 ms. At 42 ms the flow-field transitioned into an open-wake

condition and simultaneously achieved steady-state, operating in the same state until 50 ms. At 50 ms there was an onset of continuous flow-field fluctuations which started gradually but intensified in its spatial oscillations over time, continuing to operate under open-wake condition.

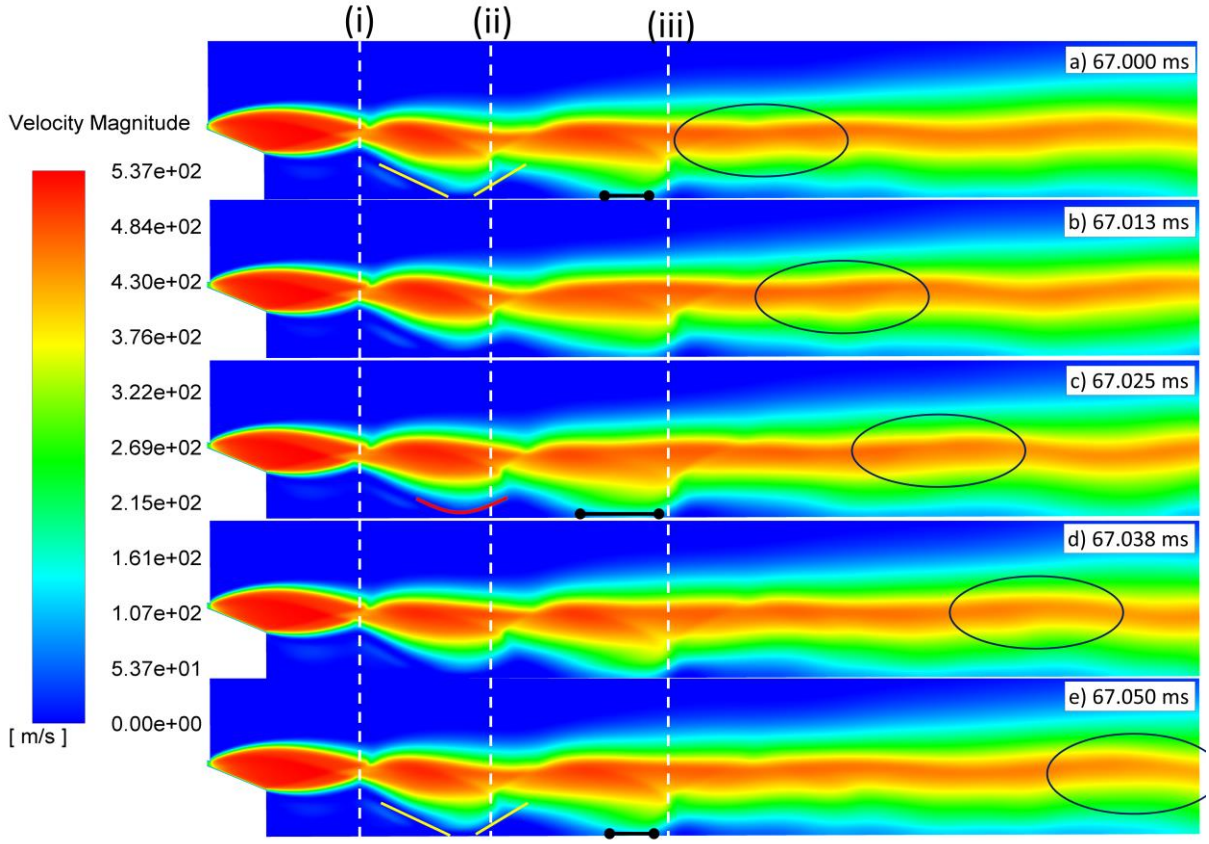

Figure 5.71 Velocity contours showing a cycle of the continuous flow-field fluctuation. Three guide-lines (i), (ii), and (iii) are fixed at the ends of the first, second and third shock-cell, respectively. The lower sonic boundary of the second shock-cell of frames a & e lies in close proximity to the atomiser's axis, marked using the yellow lines, whereas the sonic boundary seen in frame c is furthest away from the axis, shown using the curved red line. Similarly, the third shock-cell seen in frames a & e sparingly touches the axis, whereas, in frame c seems to engulf the axis to a much larger extent than seen in frame a & e. A wave propagation from the end of third shock-cell is observed and marked using ellipses. The frequency of the fluctuation was evaluated to be 20 kHz.

At 67 ms the above flow-field fluctuations attained its peak spatial oscillation, and hence, series of velocity contours of the flow-field were recorded at close consecutive times and were stacked-up sequentially in Figure 5.71 to illustrate the nature of the fluctuation. Three guide-lines, (i), (ii), and (iii), were pinned in Figure 5.71a, at the downstream ends of the first, second, and third shock-cell, respectively, and were compared against the rest of the frames, Figure 5.71b-e. It can be observed that the spatial extent of the first shock-cell did not change, whereas the extent of the second and third shock-cells displayed marginal changes along the

axial direction. The flow-field fluctuations presented in Figure 5.71 were significant but regular in nature. Nevertheless, the flow-field did not undergo wake alternation i.e., transition from open- to closed-wake condition. In a cycle of the fluctuation, initially, the lower sonic boundary of the second shock-cell lies in close proximity to the atomiser's axis, marked by the yellow lines, shown in Figure 5.71a. As the fluctuation progressed, the sonic boundary gradually moved further away from the atomiser's axis, shown in Figure 5.71c using the curved red line. Subsequently, in Figure 5.71e the sonic boundary returned back to the same configuration seen in Figure 5.71a. Similarly, during a cycle of the fluctuation, the third shock-cell, observed in Figure 5.71a initially made narrow contact with the atomiser's axis due to the sparingly crossing oblique shocks, as pointed out by the black line. Subsequently, the contact area increased to engulf the axis to a much larger extent, pointed out using the black line in Figure 5.71c. Later, in Figure 5.71e, it returned back to its original configuration as observed in Figure 5.71a. Because of the fluctuation, a wave propagation was observed starting from the end of third shock-cell, continuing to propagate until the end of the domain, marked by the ellipses. The frequency of this regular fluctuation was evaluated to be 20 kHz.

Around 71 ms, the fluctuation seen in Figure 5.71 started to transition into a fluctuation whose flow-field oscillated along the axial direction. At 74.5 ms the fluctuation completely transitioned into the latter mentioned type of oscillation. The fluctuation grew with time, achieving its maximum spatial movements at 80 ms. To understand the fluctuation, series of velocity contours of the flow-field were obtained in close consecutive flow time, and were stacked sequentially. This is presented in Figure 5.72, where two vertical guidelines (i) and (ii) were pinned in Figure 5.72a, at the ends of the first and second shock-cell, respectively. Another two sets of guide-lines were used to trace the extent of movement of the first and second shock-cells. It was observed from Figure 5.72 that the second shock-cell underwent a significantly larger fluctuation i.e. change in the shock-cell's spatial dimension along the axial direction, compared to the first shock-cell. During the fluctuation it was evident through the vertical guide-lines, (i) and (ii), that the closed-wake condition i.e. well established first Mach-disk seen in the Figure 5.72a, gradually transitioned into an open-wake condition as found in the Figure 5.72g, and subsequently returned back to its original configuration i.e., closed-wake condition, at the end of the fluctuation as found in Figure 5.72m. Even though the wake appears to be in open-wake condition in Figure 5.72a&m, it exists in closed-wake condition via MICW. In Section 6.7 this is explained in detail. This is because the first Mach-disk isolates the wake region by immersing into the melt plume, resulting in the same type of wake seen during

closed-wake condition seen in Figure 5.70. Since, the first Mach-disk is no longer touching the axis, but rather immersed into the melt (particles) flow present along the axis, the determination of the wake whether present in open/closed-wake condition from gas flow-field alone is challenging. To aid in addressing this challenge, particle trajectories corresponding to the flow-field velocity contours seen in Figure 5.72a&g, were inspected to determine the extent of melt built-up along the axis. This is presented in Figure 5.73. From Figure 5.73a, it was evident that the first Mach-disk was immersed into the 0.8 mm thick layer of melt (particles) confirming the wake existed in closed-wake condition, whereas, in Figure 5.73b, the wake existed in open-wake condition since there prevailed considerable space between the lower sonic boundary (1.37 mm) and the melt layer (1.0 mm). This confirmed that the wake existed as closed-wake condition in Figure 5.72a&m, and as open-wake condition in Figure 5.72g. Apart from these observations in Figure 5.72, a wave propagation was also observed in the flow-field, starting from the end of third shock-cell and continued to propagate until the end of the domain. The wave propagation is traced using ellipses, illustrated in Figure 5.72. The frequency of this flow-field was evaluated to be 8.3 kHz. Correlation between alternating flow-field, transitioning from open- to closed-wake condition observed in Figure 5.72, and the melt fluctuation observed in Figure 5.65 were examined. It was found that the frequency of melt fluctuation, 8.1 kHz, obtained from the FFT analysis corresponded to the flow-field fluctuation having frequency of 8.3 kHz. Furthermore, it was found that at local maximum of the melt fluctuation frequency, 8.1 kHz (Figure 5.65), the flow-field corresponded to an open-wake condition (Figure 5.72g), and at local minima, the flow-field corresponded to a closed-wake condition (Figure 5.72a&m). However, no correlation could be observed from the melt fluctuation for the high order flow-field fluctuation of 20 kHz seen in Figure 5.71.

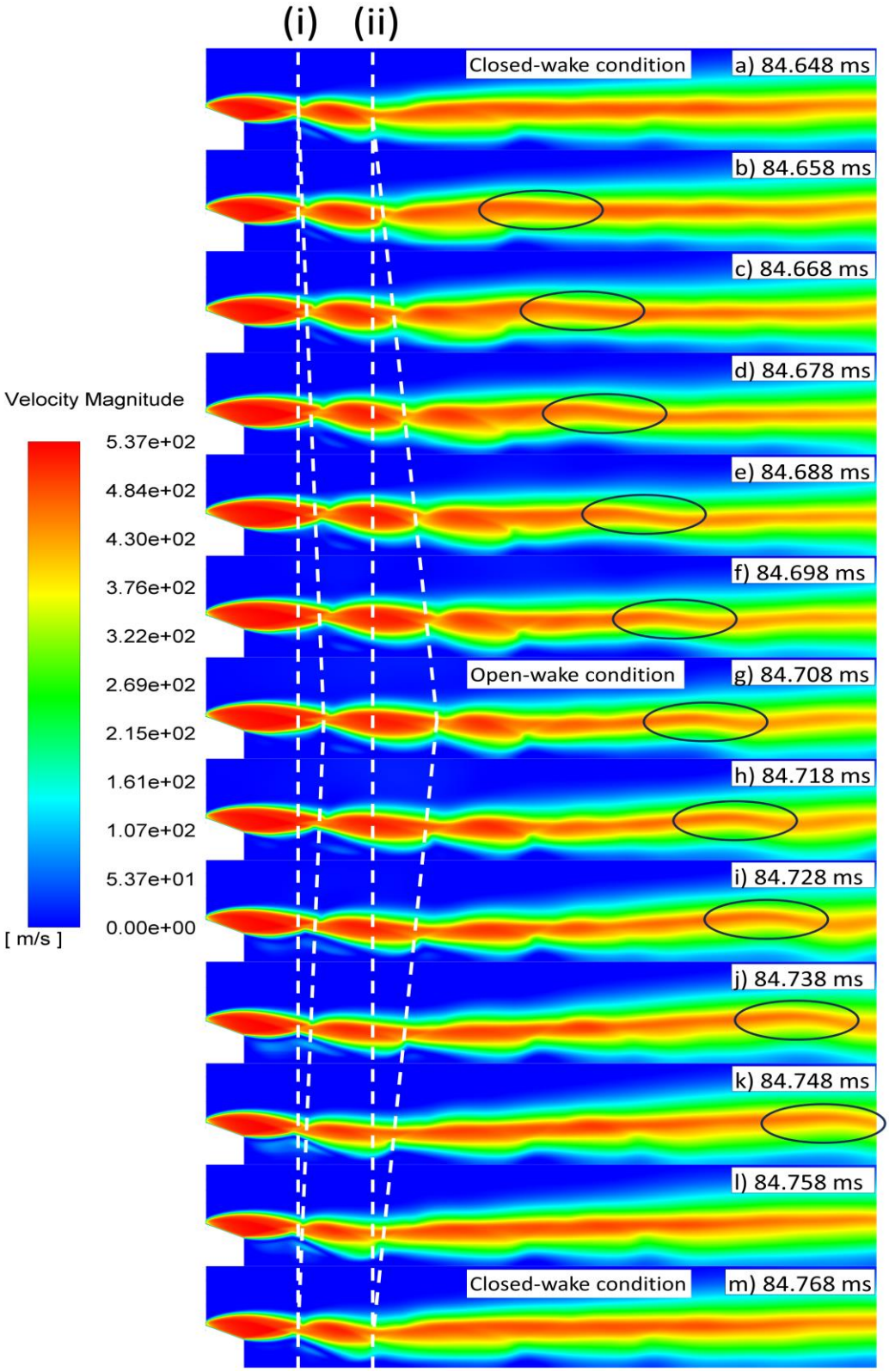

Figure 5.72 velocity contours of the flow-field without particles showing a cycle of the repeated fluctuation that is seen from t > 80 ms. Two vertical guide-lines (i) & (ii) are fixed at the ends of the first and second shock-cell, respectively, of frame a to compare the extent of fluctuation against other frames. Another two sets of guide-lines are used to trace the movement of the first and second shock-cell ends. The frequency of the fluctuation was found to be 8.3 kHz.

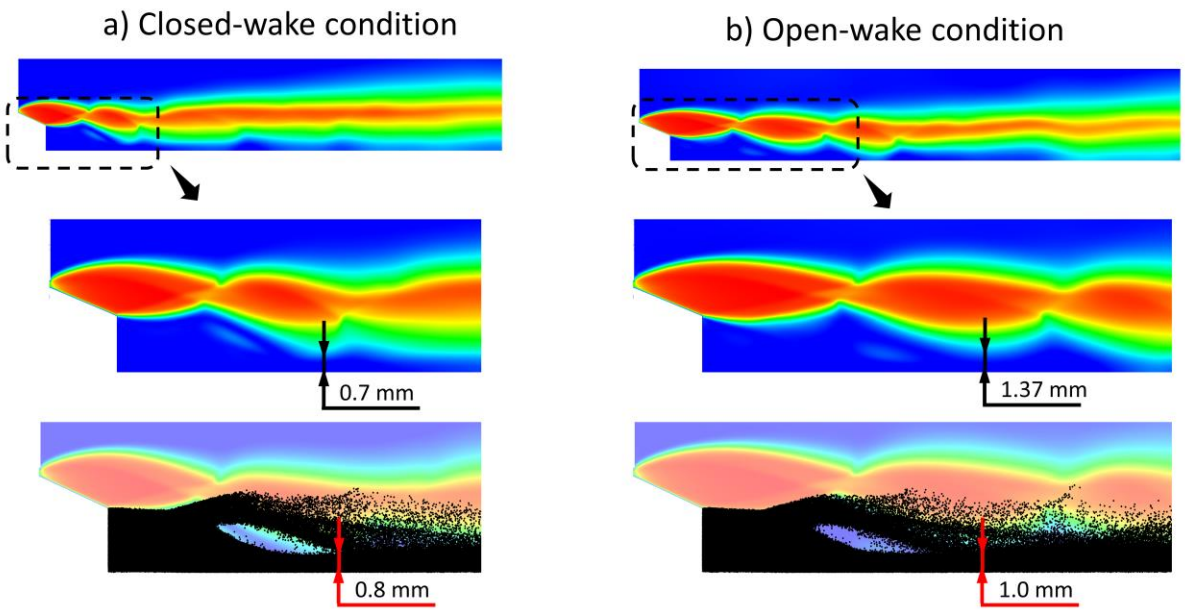

Figure 5.73 Determination of open- and closed-wake by comparing velocity contours against particle trajectories. (a) the lower sonic boundary of the second shock-cell lies 0.7 mm radially away from the axis, while, the thickness of the melt layer is 0.8 mm indicating the first Mach-disk is immersed in the melt layer, resulting in closed-wake. (b) the lower sonic boundary of the second shock-cell lies 1.37 mm radially away from the axis, while, the thickness of the melt layer is 1.0 mm, resulting in considerable space between the sonic boundary and the melt layer, indicating wake exists in open-wake condition.

To confirm the high-frequency flow-field fluctuation – 8.3 kHz (Figure 5.72), velocity monitors were pinned at seven key locations on the axis of the atomiser (Figure 5.1) and were analysed for their frequency of the fluctuation. The FFT analysis of the high-frequency fluctuation at t > 80 ms across all the seven monitors resulted in two consistently dominant frequencies: 8.1 kHz and 16.3 kHz. Through the 8.1 kHz fluctuation observed from the monitors, it can be confirmed the high-frequency flow-field fluctuation, 8.3 kHz (Figure 5.72), corresponded to the high-frequency melt fluctuation, 8.1 kHz (Figure 5.65). Efforts were taken to observe for the other frequency, 16.3 kHz, in the flow-field fluctuation, however, no corresponding fluctuation could be correlated, and possibly might be the harmonics of the 8.1 kHz frequency. Even though the 16.3 kHz fluctuation could be observed from the FFT analysis of the mass flow rate plot (Figure 5.65), it was a non-significant peak compared to the other three dominant frequencies. Similarly, from the FFT analysis of the velocity monitors, a negligible and non-significant peak at 56 Hz was observed, although no flow-field fluctuation with that frequency were observable. In addition to this, even though all the monitors in Figure 5.74 resulted in the same two frequency, there existed phase difference among them as shown by the red dashed guide-line. This might possibly reflect the travel time between different

locations of the monitors downstream; also, it might indicate an unsynchronised upstream and downstream flow-field movement i.e., unsynchronised expansion and contraction of the individual sections of the flow-field.

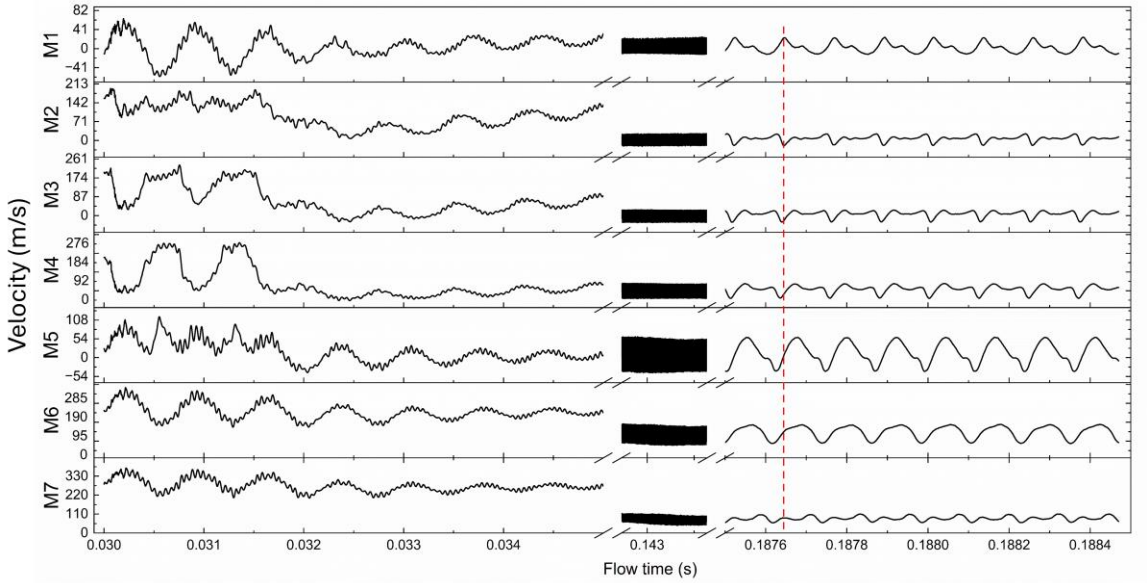

Figure 5.74 Monitors M1 to M7 zoomed in at the injection of the melt and at the high frequency fluctuation. FFT analysis of the monitors resulted in two dominant frequencies: 8.1 kHz and 16.3 kHz. The high frequency, 8.1 kHz observed in the monitors, corresponded to the high frequency 8.1 kHz, obtained from the injection mass flow rate, confirming the frequency of the flow-field fluctuation. Existence of phase difference between the monitors is indicated using the red dashed line.

5.4.2 Melt temperature: 600K

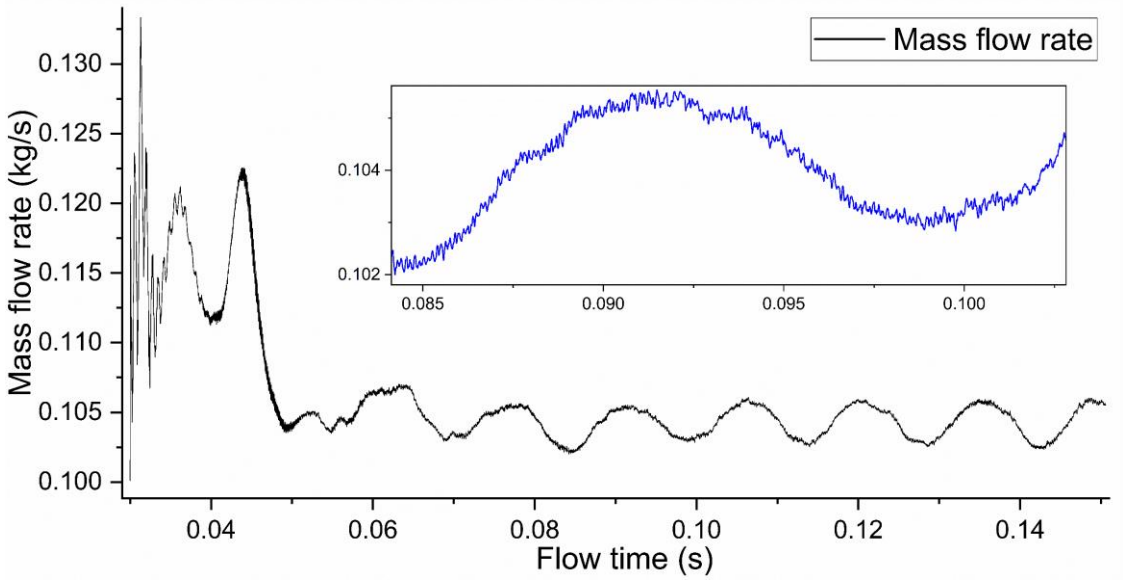

Figure 5.75 Injection mass flow rate plot of 6 kg min^{-1}, 600K case showing the initial fluctuation followed by two high amplitude peaks between 35-50 ms. At 39 ms there is an onset of a higher frequency fluctuation that exists for the remainder of the simulation. The zoomed section of the high frequency fluctuation is presented in the blue plot.

The 6 kg min^{-1} case with a melt temperature of 600K was run 120 ms (30 to 150 ms). The injection mass flow rate plot for the 600K case is presented in Figure 5.75 along with its zoomed section in blue plot. The initial fluctuation seen in the 600K case is similar to that of the 300K case. With the onset of melt injection, multiple high amplitude fluctuations were observed, but after 35 ms they were seen to attenuate. At 39 ms there was an onset of a higher frequency fluctuation having negligible amplitude existing for the remainder of the simulation. The negligible magnitude of the amplitude present in the higher frequency fluctuation can be observed from the blue plot presented in the zoomed section of the Figure 5.75. With the onset of the higher frequency fluctuation, there was a rise and fall in the mass flow rate, whose peak value was 0.1225 kg s^{-1}. Following the fall at 49 ms, in addition to the observed high frequency fluctuation, there emerged another secondary fluctuation in mass flow rate having a much lower frequency of fluctuation.

Table 5-2 The frequencies obtained from the FFT analysis of 6 kg min^{-1}, 600K case, and their correlation to the flow-field fluctations.

Flow-time	**Frequency obtained from the FFT analysis**	**Fluctuation observed in the flow field**
30 - 40 ms	1.4 kHz	• Initial fluctuation until 32 ms • Attenuation of initial fluctuation in open-wake: 32 - 39 ms.
40 - 50 ms	A single cycle of 109 Hz observed.	• 109 Hz, 8.6, 9.1 and 28.5 kHz were not observed in flow-field. • From 39 - 41 ms the flow field attenuated in its oscillation but underwent alternating wake • From 41 - 47 ms flow field underwent axial fluctuation in open-wake condition. • From 47 - 52 ms, flow-field underwent radial fluctuation in open-wake condition at 15 kHz.
	28.5 kHz	
	8.6 and 9.1 kHz (superimposed on 28.5 kHz)	
t > 55 ms	~66 kHz (Superimposed on varying high frequency 6.3 - 18.2 kHz)	• ~66 Hz was not observed in the flow-field. • From t > 52 ms flow-field underwent axial fluctuation at 20.8 kHz, undergoing alternating wake via MICW.
	varying frequency 6.3 - 18.2 kHz	
Not obviously observable	91 Hz	Nil
	149 Hz	
	232 kHz	

Low frequency Mid frequency High frequency

From FFT analysis it was found that there existed multiple levels of frequencies, with each level encompassing range of frequencies. Low frequencies of 66 Hz, 91 Hz, 109 Hz, 149 Hz, 232 Hz and 1.4 kHz; mid-frequencies of 8.6 kHz and 9.1 kHz; and a high frequency of 28.5 kHz, were obtained from the analysis. Out of the obtained frequencies, only a few frequencies could be evidently observed in the mass flow rate fluctuations seen in Figure 5.75, and they were, 66 Hz, 109 Hz, 1.4 Hz, 8.6 kHz, 9.1 kHz, and 28.5 kHz, and the rest not identifiable. The frequencies obtained via the FFT analysis, and its corresponding flow-field fluctuations are tabulated in Table 5-2. The GMR for the 600K case was evaluated to be 0.66-0.86. Similarly, the GMR for the mass flow rate were the regular fluctuation having 66 Hz seen at t > 55 ms was evaluated to be 0.82-0.86, possessing a narrow GMR interval.

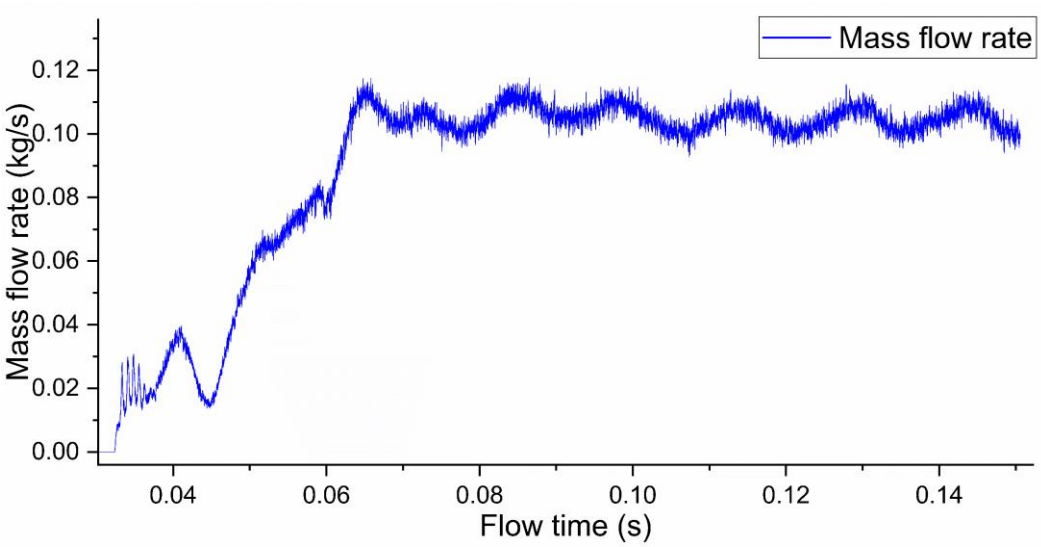

Figure 5.76 Mass flow rate of the particles obtained at the outlet of the domain for 6 kg min^{-1}, 600K case. The rise in the outlet flow from 45 to 65 ms is observed in three stages; a steep rise, followed by a stalled rise, and again through a steep rise. Subsequently, at t > 80 ms the plot undergoes a regular fluctuation reflecting the injection mass flow rate at t > 55 ms.

It was also observed from the mass flow rate plot obtained at the outlet of the domain at t > 80 ms presented in Figure 5.76, that it resembled the same trend of the injection mass flow rate plot seen at t > 55 ms (Figure 5.75). However, before the outlet mass flow rate attained such a trend, there were three stages of flow of particles through the outlet. Between 45 and 51 ms, a rapid increase in the flow of particles, followed by a stall in the flow of particles from 51 to 60 ms, before encountering another steep rise in the flow of particles until 65 ms. Unlike the changes noticed in the injection mass flow rate plots between 300K to 600K cases, the particles' trajectories of the two cases were observed to be very similar, except for the deviations in the timing. The melt underwent pre-filming at 35.7 ms, whereas for the 300K

case it was 33.8 ms. Similarly, the melt pool head that moved downstream due to the increased mass loading rejoined with the particles that were pushed downstream by the gas-jet, at 43 ms, (and 43.5 ms for the 300K case). Subsequently, at 44.5 ms the melt pool head plunged into the second Mach-disk.

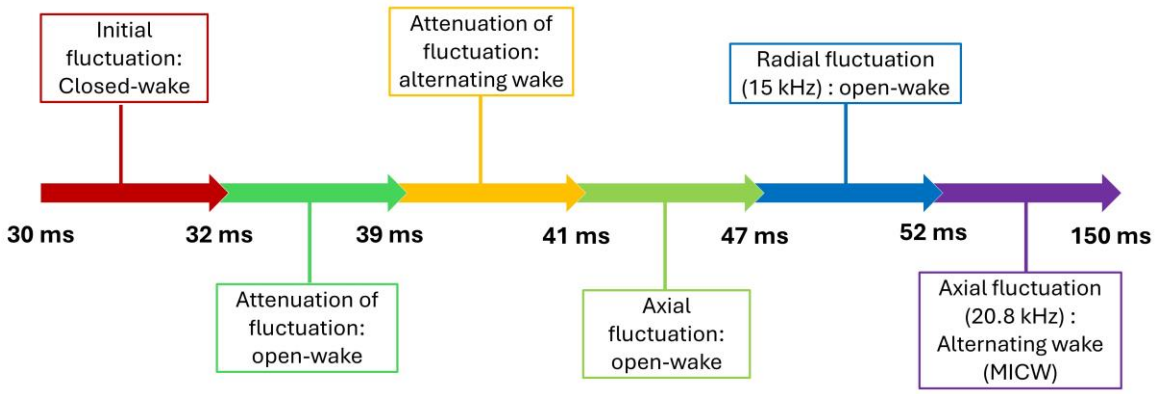

Figure 5.77 Timeline of flow-field fluctuations observed in 6 kg min^{-1}, 600K case.

Considering the velocity contours of the flow-field, the initial fluctuation due to the melt introduction looked same as the fluctuation seen in the 300K case, presented in Figure 5.70. The different flow-field fluctuations observed in the timeline of the 600K case is presented in Figure 5.77. Following the initial fluctuation, at 32 ms the flow-field transitioned into open-wake while still continuing to attenuate in its spatial oscillations along the axial direction. Subsequently at 39 ms the wake engaged to become closed-wake and briefly alternated between open- to closed-wake condition until 41 ms. Subsequently, at 41 ms the wake transitioned into open-wake and simultaneously underwent increased magnitude of spatial oscillation along the axial direction. At 47 ms the flow-field transformed into the fluctuation as observed in Figure 5.71 of 300K case, and it remained until 52 ms. The frequency of this fluctuation was evaluated to be 15 kHz. From t > 52 ms the flow-field fluctuation intensified in its spatial oscillation along the axial direction and also transformed into an alternating wake. The closed-wake observed here was in the MICW type (Figure 5.73a). In Section 6.7 MICW is explained in detail. To understand the fluctuation, series of velocity contours of the flow-field were obtained in close consecutive flow time and were stacked sequentially. This is presented in Figure 5.78. Three guide-lines, (i), (ii), and (iii) were pinned in the Figure 5.78a at the ends of the first, second and third shock-cell, respectively, and were compared against the rest of the stacks. A secondary guide-line was employed to trace the extent of the movement of the second shock-cell while it fluctuates. It was observed from guide-lines (i) and (iii), the first and third shock-cell remained fixed without undergoing any

movement throughout the fluctuation, whereas the second shock-cell underwent marginal changes in its spatial extent along the axial direction. The change in the second shock-cell's spatial extent along the axial direction can be evidently seen when comparing the guide-line (ii) against the secondary guide-line. It can be observed from Figure 5.78 that the flow-field transitioned from close-wake condition present in Figure 5.78a to open-wake condition seen Figure 5.78e, and thereafter returned back to the original configuration i.e., closed-wake condition in Figure 5.78i. In addition to this, a wave propagation was observed in Figure 5.78, starting from the end of third shock-cell and continuing to propagate until the end of the domain. The wave propagation is traced using ellipses. The frequency of the flow-field fluctuation was evaluated to be 20.8 kHz. Correlation between the flow-field alternating between open- to closed-wake, seen in Figure 5.78, and the melt fluctuation seen in Figure 5.75 were examined. However, no corresponding melt fluctuation frequency could be associated for the alternating flow-field fluctuation of 20.8 kHz seen in Figure 5.78. It is interesting to note that at t > 60 ms, the frequency of the fluctuation seen in the flow-field (Figure 5.78) is 20.8 kHz, whereas, the frequency of the fluctuation seen in the mass flow rate (Figure 5.75) varied from 6.3 to 18.2 kHz. It is not found what could be the reason for such a drastic mismatch between the flow-field and melt fluctuations. Similarly, efforts were taken to correlate the flow-field fluctuation of 15 kHz seen between 47 and 52 ms, with the melt fluctuation seen in Figure 5.75. However, no potential correlation could be drawn between the fluctuations. Another frequency of interest found from the FFT analysis of melt flow rate was the 66 Hz, i.e., melt fluctuation seen at t > 55 ms. Efforts were taken to observe this low frequency fluctuation in the flow-field, however no potential correlation could also be drawn.

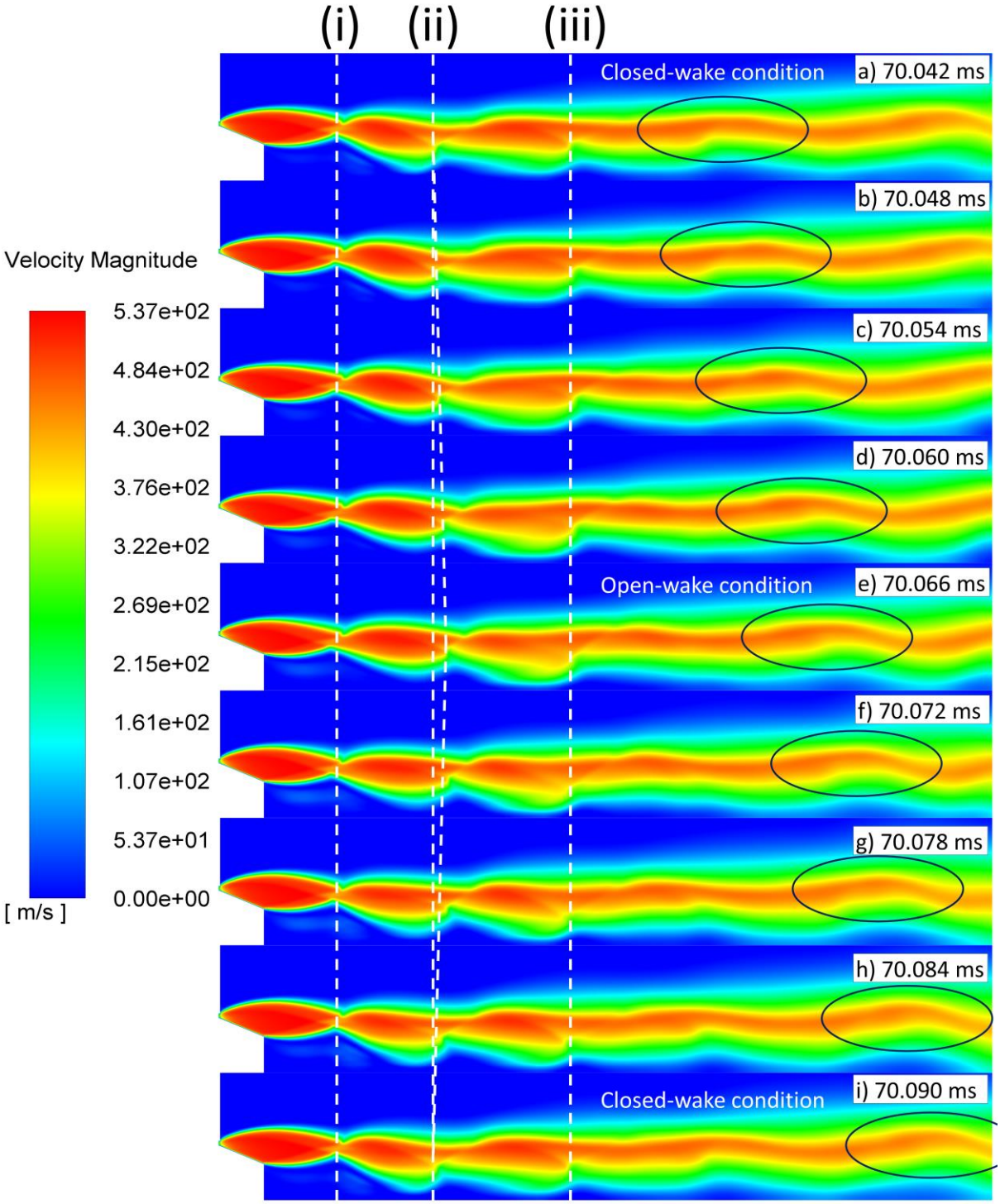

Figure 5.78 Velocity contours of the flow-field without particles showing a cycle of the repeated fluctuation that is seen at t > 52 ms. Three vertical guide-lines (i), (ii) and (iii) are fixed at the ends of the first, second and third shock-cell, respectively, of frame a to compare the extent of fluctuation against other frames. Another two sets of guide-lines are used to trace the movement of the second shock-cell end. First and third shock-cells remain fixed, whereas the second shock-cell marginally varies in its spatial extent. The frequency of the fluctuation was found to be 20.8 kHz.

5.4.3 Melt temperature: 1000K

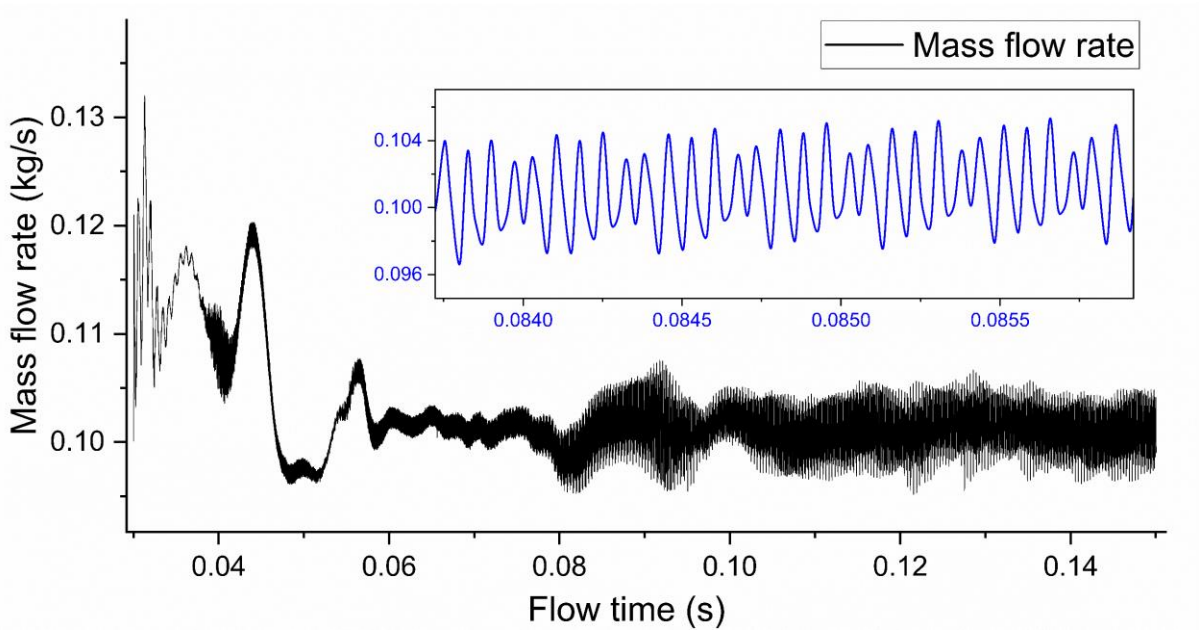

Figure 5.79 Injection mass flow rate plot of 6 kg min^{-1}, 1000K case showing the initial fluctuation followed by two high amplitude peaks seen between 35-50 ms. At 38 ms there is an onset of a higher frequency fluctuation that exists for the remainder of the simulation. The zoomed section in the blue plot shows one of the many high-frequency fluctations observed in the case.

The 6 kg min^{-1} case with a melt temperature of 1000K was run for 120 ms (30 to 150 ms). The injection mass flow rate is presented in Figure 5.79. The initial fluctuation seen in the 1000K case was similar to that of the 300K and 600K cases. Following the initial fluctuation, at 38 ms there was an onset of a higher frequency fluctuation which existed for the remainder of the simulation. However, the observed high frequency fluctuation did not possess a constant frequency like the fluctuation seen in 300K case (Figure 5.65), instead it continuously varied throughout the flow-time. Following the onset of the higher frequency fluctuation, two consecutive rise-and-falls in the mass flow rate were observed between 35 and 50 ms. In addition to this, another peak is also observed between 51-58 ms, with its peak at 0.107 kg s^{-1}. From the FFT analysis conducted on the injection mass flow rate (Figure 5.79) a wide range of frequencies of fluctuation existing in multiple levels were found. Low-frequencies of 91.6 Hz, 158.2 Hz, 233 Hz, 274 Hz, 316 Hz, 358 Hz, and 1.4 kHz; mid-frequencies of 8.6 kHz, 11.3 kHz, and 13.2 kHz; and high frequencies of 25.6 kHz and 28.6 kHz, were found. Out of the obtained frequencies, only some frequencies could be evidently observed in the mass flow rate fluctuation (Figure 5.79), and they were, 91.6 Hz, 158.2 Hz, 1.4 kHz, 8.6 kHz, 13.2 kHz, 25.6 kHz, and 28.6 kHz, and the rest were not identifiable. The frequencies obtained via the FFT analysis, and its corresponding flow-field fluctuations are tabulated in Table 5-3. It can be

drawn from the various frequencies mentioned in Table 5-3, that the melt injection in the 1000K case is far from being a regular fluctuation. In addition to the irregular frequencies seen in Figure 5.79, the amplitude of these fluctuations also varied throughout the flow time. The GMR for the 1000K case was evaluated to be 0.66 - 0.92, and the GMR for the case seen at t > 80 ms was evaluated to be 0.81 - 0.92.

Table 5-3 The frequencies obtained from the FFT analysis of 6 kg min^{-1}, 1000K case, and their correlation to the flow-field fluctations.

Flow-time	**Frequency obtained from the FFT analysis**	**Fluctuation observed in the flow field**
30 - 40 ms	1.4 kHz	• Initial fluctuation until 31.7 ms • 8.6 kHz is not observed • Attenuation of initial fluctuation in open-wake: 31.7 - 34.5 ms. • Axial fluctuation in open-wake: 34.5 - 38 ms
	8.6 kHz (from 38 - 42.5 ms)	
40 - 49 ms	A single cycle of 91.6 Hz observed.	• 91.6 kHz was not observed in flow-field • 38 - 46 ms: axial flow-field underwent alternating wake at 9.5 kHz. From 41 ms, it underwent MICW. • 46 - 54 ms: attenuation in axial fluctuation in open-wake exhibiting 25.6 & 28 kHz
	8.6 kHz (from 38 - 42.5 ms)	
	28.6 kHz was observed from 38 - 52 ms. It was superimposed on 8.6 kHz between 38 - 42.5 ms	
51 - 58 ms	A single cycle of 158.2 Hz observed.	• 158.2 Hz was not observed in the flow-field
55 - 77 ms	158.2 Hz (from 55 - 58 ms)	• 158.2 Hz was not observed in the flow-field • 54 - 77.5 ms: Axial fluctuation undergoing alternating wake via MICW was observed to exhibit 25.6 kHz
	25.6 kHz	
t > 80 ms	13.2 kHz observed to be distributed irregularly	• t > 77.5 ms: Nested fluctuation at 12.8 kHz was observed. • Swayings within nested fluctuation exhibited at 25.6 kHz
	25.6 kHz found at different sections modulated on 13.2 kHz	
Not obviously observable	233 Hz	Nil
	274 Hz	
	316 Hz	
	358 Hz	
	11.3 kHz	

Low frequency Mid frequency High frequency

Unlike the changes noticed in the injection mass flow rate in the 1000K when compared to the previous cases, the particle trajectories were observed to be similar to that of the 300K and 600K cases with the exception of deviations in timing of pre-filming and melt movement downstream. The melt underwent pre-filming at 36.1 ms, whereas for the 600K case it is 35.7 ms. Similarly, the melt pool head that moved downstream due to the increased mass loading rejoined with the particles that were pushed downstream by the sonic jet, at 42.5 ms, (and 43 ms for 600K case). Subsequently, at 44 ms the melt pool head plunged into the second Mach-disk.

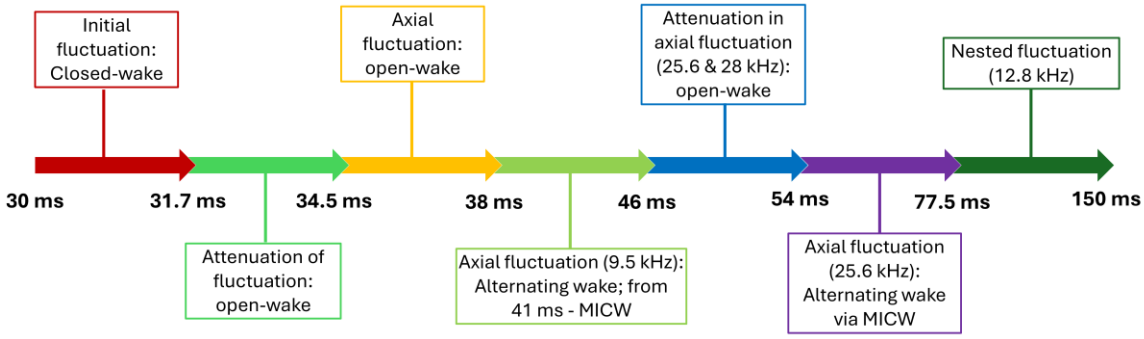

Figure 5.80 Timeline of flow-field fluctuations observed in 6 kg min^{-1}, 1000K case.

Considering the velocity contours of the flow-field, the initial fluctuation due to the melt introduction looked same as the fluctuation in the previous cases, 300K and 600K, as presented in Figure 5.70. The different flow-field fluctuations observed in the timeline of the 1000K case is presented in Figure 5.80. Following the initial fluctuation, as the fluctuation continued to attenuate, at 31.7 ms the flow-field transitioned into an open-wake condition and continued to exist in the same configuration until 38 ms. While the wake continued to exist in open-condition, at 34.5 there was an onset of a high frequency flow-field fluctuation which increased in its spatial oscillation along the axial direction. At 38 ms the flow-field transitioned into an alternating wake i.e., open- to closed-wake condition, and this flow-field configuration continued until 46 ms, and simultaneously, the high frequency fluctuation observed at 34.5 ms continued to increase in its spatial oscillations along the axial direction until 46 ms. However, from 41 to 46 ms, the wake alternation was subjected to the MICW type of closed-wake, as observed in Figure 5.73a. In Section 6.7 MICW is explained in detail. Subsequently, the flow-field transitioned into the open-wake condition at 46 ms and remained thereafter in the same configuration until 54 ms as observed in Figure 5.71. Also, from 46 to 54 ms, the flow-field fluctuation began to progressively attenuate in its spatial oscillation. At 54 ms, onset of another high frequency fluctuation into the flow-field was observed, and at the same time, the wake

transitioned from open-wake to alternating wake as seen in Figure 5.78, with the closed-wake being present in MICW type. Subsequently at t > 77.5 ms the flow-field fluctuation transitioned into nested fluctuation. (Refer Section 5.3.4 and Figure 5.61 for nested fluctuation). To observe the nature of the nested fluctuation, series of the velocity contours obtained in close intervals of flow-time were sequentially stacked and were analysed. This is presented in Figure 5.81. Three guide-lines, (i), (ii), and (iii) were pinned in the Figure 5.81a at the ends of the first, second and third shock-cell, respectively, and were compared against the rest of the stacks to observe for changes in the flow-field. It was observed from guide-line (i), that the first shock-cell remained fixed without undergoing any changes to its spatial extent throughout the fluctuation. Similarly, it was observed from guide-line, (ii) and (iii), that the second and three shock-cells remain almost fixed during the fluctuation with little-to-no change in its spatial extent. It can also be observed from Figure 5.81a that the MICW type of closed-wake transitions into open-wake in Figure 5.81b. Subsequently, while existing as open-wake, the lower sonic boundary of the second shock-cell comes in close proximity to the atomiser's axis (Figure 5.81d), but later moves further radially away from the axis (Figure 5.81e&f). Thereafter the wake transitions back into MICW type of closed-wake (Figure 5.81h). In addition to this, a wave propagation was observed in Figure 5.81, starting from the end of third shock-cell and continuing to propagate until the end of the domain. The generation of the wave can be observed at two instances, once at closed-wake condition (Figure 5.81a), and another at open-wake condition when the sonic boundary is in close proximity to the atomiser's axis (Figure 5.81d). The wave propagation is traced using ellipses. The frequency of the flow-field fluctuation was evaluated to be 12.8 kHz. Similarly, a frequency of 25.6 kHz was evaluated for part of the fluctuation seen in Figure 5.81a-d, i.e., from closed-wake to the open-wake, where the sonic boundary lies closest to the axis. The nested flow-field fluctuation presented in Figure 5.81 undergoes only one swaying. (Refer Section 5.3.4 and Figure 5.61 for swaying in nested fluctuation). Whereas, at other instances of the flow-time (t > 77.5), it was found, fluctuations with the same frequency of fluctuation, 12.8 kHz, underwent regular wake alternation, without undergoing any swayings. This revealed the flow-field possessed fluctuations of 12.8 kHz both as regular and nested fluctuations.

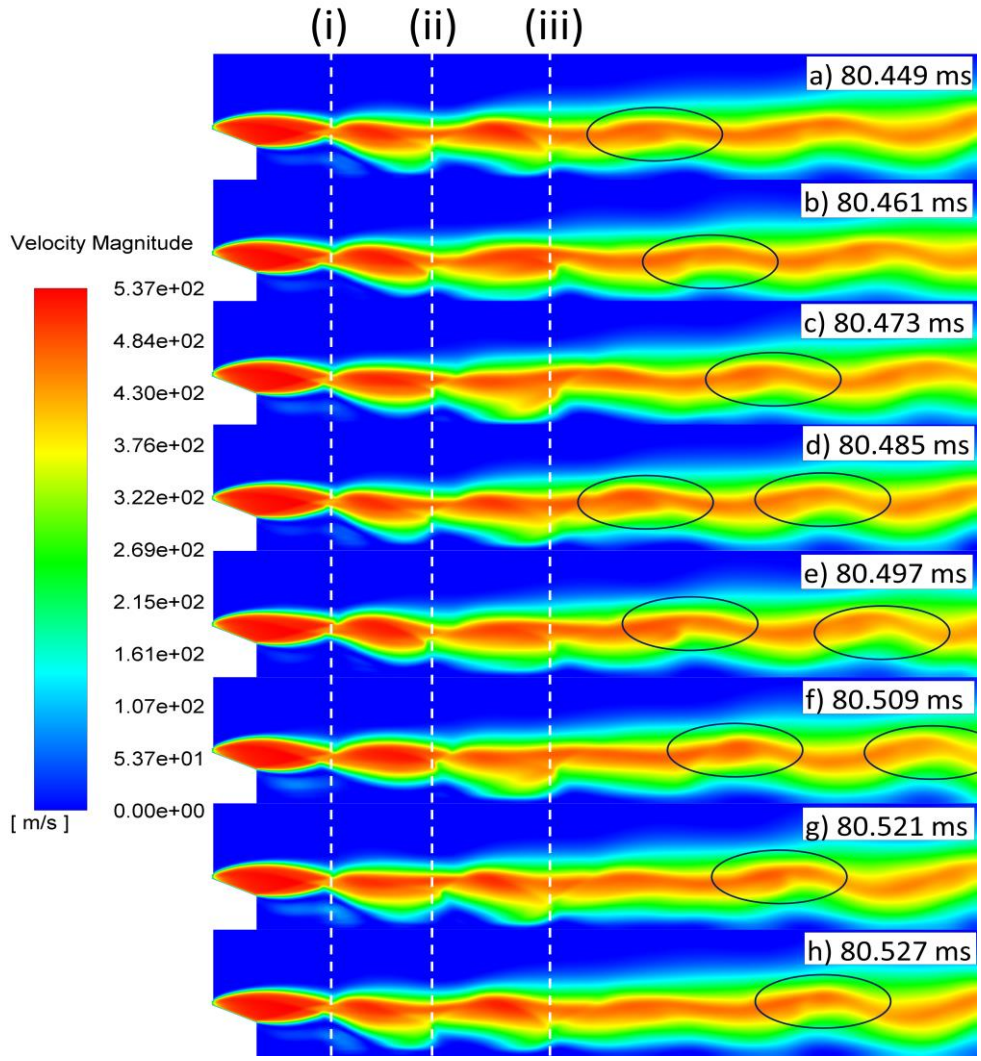

Figure 5.81 Velocity contours of the flow-field without particles showing a cycle of the nested fluctuation that is seen at t > 77.5 ms. Three vertical guide-lines (i), (ii) and (iii) are fixed at the ends of the first, second and third shock-cell, respectively, of frame a to compare the extent of fluctuation against other frames. All the three shock-cells remain fixed. The frequency of the fluctuation was found to be 12.8 kHz.

Similar to the irregular frequencies of fluctuation seen in the mass flow rate, irregular frequencies of the fluctuation were observed in the flow-field fluctuation as well. However, at different durations of the flow time, few frequencies were well observable. The alternating flow-field fluctuation seen at 38 - 46 ms was evaluated to have frequency of 9.5 kHz. The flow-field seen at 46 - 54 ms, existing in open-wake while continuing to fluctuate, was observed to contain to two significant frequencies, 25.6 kHz and 28 kHz. The flow-field fluctuation with alternating wake seen at 54 - 77.5 ms, was observed to contain a frequency of 25.6 kHz. Correlation between the flow-field fluctuation and the melt fluctuation were examined. It was observed that the 25.6 kHz flow-field fluctuation undergoing wake alternation at 54 - 77.5 ms

corresponded to the 25.6 kHz seen in the melt fluctuation in Figure 5.79. On examining this melt fluctuation, it was observed that the local maxima of the melt fluctuation corresponded to the open-wake condition, and the local minima of the melt fluctuation corresponded to the closed-wake condition seen in MICW.

Similarly, the nested fluctuation (Figure 5.81) seen at t > 77.5 ms having a frequency of 12.8 kHz, corresponded to the melt fluctuation frequency, 13.2 kHz. On examining the nested flow-field fluctuation from t > 77.5 ms (Figure 5.81) against the melt fluctuation (Figure 5.79), it was observed that at the local minima of the melt fluctuation, the flow-field existed as closed-wake, and at the local maxima of the melt fluctuation the flow-field existed as open-wake with its lower sonic boundary being furthest radially away from the atomiser's axis, usually the open-wake that is observed at the end of the swaying. The open-wake at the beginning of the swaying is observed to be associated with a inflection point in the melt fluctuation. During swaying, where sonic boundary approaches and recedes the atomiser's axis, the melt flow rate continued to rise. However, apart from the local minima of the melt fluctuation corresponding to the closed-wake condition, and the local maxima corresponding to the open-wake condition at the end of swaying, no other characteristics part of the flow-field fluctuation were been able to consistently associate with the melt fluctuation, as they were highly irregular in nature. The fluctuation which was observed at t > 77.5 ms having the same frequency of 12.8 kHz, but which did not exhibit the nested fluctuation (no swaying) also corresponded to the 13.2 kHz melt fluctuation seen at t > 80. The difference in 13.2 kHz melt fluctuation that corresponds to with and without nested flow-field fluctuation were found using the shape of the wave-form. The 13.2 kHz wave-form which possessed superimposed waves on it, reflected the nested fluctuation, whereas 13.2 kHz wave-form without any superimposed wave-forms corresponded to the regular flow-field fluctuations. On examining the melt fluctuation in Figure 5.79 for the regular wave-form fluctuation, it was observed that the local maxima of the melt fluctuation corresponded to the open-wake condition, and the local minima of the melt fluctuation corresponded to the closed-wake condition, seen in MICW.

5.4.4 Melt temperature: 1500K

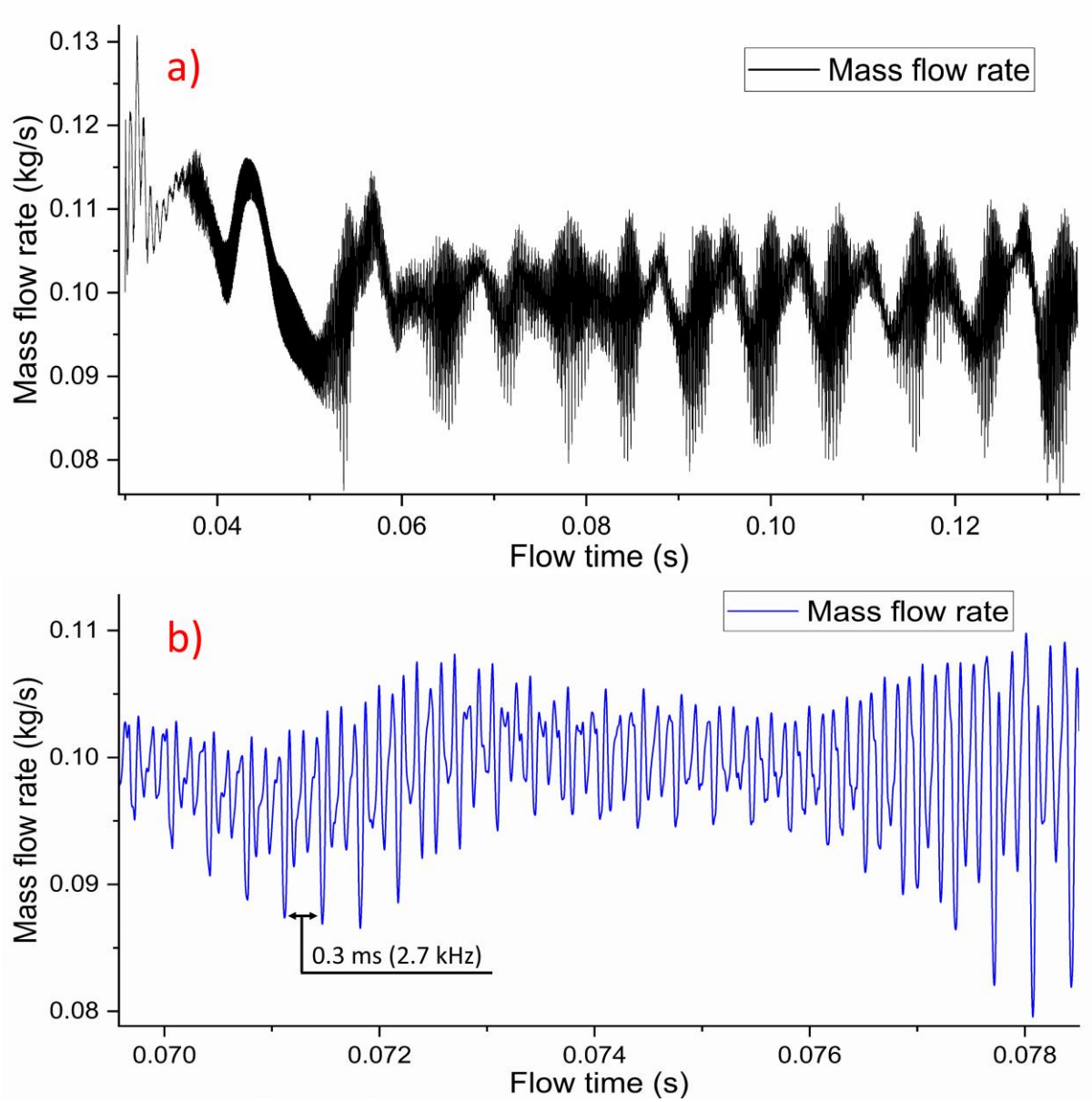

Figure 5.82 Injection mass flow rate plot of 6 kg min^{-1}, 1500K case showing the initial fluctuation and the irregular fluctuation that ensues after it. a) at 36 ms there is an onset of a higher frequency fluctuation that exists for the remainder of the simulation. b) the zoomed section in the blue plot showing the high-frequency fluctation.

The 6 kg min^{-1} case with a melt temperature of 1500K was run for 103 ms (30 to 133 ms). The injection mass flow rate is presented in Figure 5.82. The initial fluctuation observed in all the previous cases, is also observed in the 1500K case. Following the initial fluctuation, at 36 ms there was an onset of a higher frequency fluctuation which continued for the remainder of the flow-time. However, the observed high-frequency fluctuation was highly irregular, continuously varyinh in its frequency and amplitude. Following the onset of the high-frequency fluctuation, two rise-and-falls in the mass flow rate were observed: once between 41 - 51.5 ms,

attaining its peak at 0.116 kg s^{-1}, and another between 51.5 - 59.5 ms, attaining its peak at 0.114 kg s^{-1}. Thereafter, at t > 60 ms the mass flow rate plot evolved into a fluctuation having an observable generic pattern but overlaid with high-frequency in amplitude modulation. From the FFT analysis of injection mass flow rate in Figure 5.82, a wide range of frequencies in multiple levels were found. Low frequencies of 87 Hz, 125 Hz, 154 Hz, 261 Hz, and 1.4 kHz; mid-frequencies of 2.7 - 2.9 kHz, 5.6 - 5.8 kHz, 8.2 - 8.5 kHz, and 11.2 kHz, 14.1 - 14.3 kHz; and high-frequencies of 22.7 kHz, 25.6 kHz and 28.5 kHz, were found. Among these frequencies, except for the three mentioned high-frequencies, rest all were dominant and were identifiable in the mass flow rate plot (Figure 5.82).

Table 5-4 The frequencies obtained from the FFT analysis of 6 kg min^{-1}, 1500K case, and their correlation to the flow-field fluctations.

Flow-time	**Frequency obtained from the FFT analysis**	**Fluctuation observed in the flow field**
30 - 40 ms	1.4 kHz	• Initial fluctuation until 36 ms • 36 - 37 ms: Axial fluctuation in open-wake
37 - 51.5 ms	Varying frequency of 14.1 - 14.3 kHz	• 87 Hz was not observed in flow-field • 37 - 41 ms: Nested fluctuation at 14.4 kHz observed in flow-field • 41 - 52.5 ms: Radial flow-field undergoing alternating wake at 13.5 kHz via MICW.
	A single cycle of 87 Hz seen between 41 - 51.5 ms	
51.5 - 59.5 ms	A single cycle of 125 Hz observed.	• 125 Hz was not observed in the flow-field • 52.5 - 55 ms: Transitional fluctuation observed in flow-field without corresponding to one frequency
	8.6 kHz superimposed on 125 Hz	
t > 60 ms	2.7 - 2.9 kHz	• t > 55 ms: Nested fluctuation observed in the flow-field at 7.2 - 7.4 and 8.1 - 8.3 kHz. But swayings were irregulat and were observed to be in different frequencies. • 2.7 - 2.9 kHz was not observed in the flow-field. • 154 and 261 Hz was not observed in the flow-field.
	5.6 - 5.8 kHz, 8.2 - 8.5 kHz, and 11.2 kHz, superimposed on 2.7 - 2.9 kHz, but were distributed in an irregular manner	
	154 and 261 Hz observed at t > 63 ms	
Not obviously observable	22.7 kHz	Nil
	25.6 kHz	
	28.5 kHz	

Low frequency Mid frequency High frequency

The frequencies obtained via the FFT analysis, and its corresponding flow-field fluctuations are tabulated in Table 5-4. In addition to the wide spread and irregular frequency distribution across the flow time, it can be observed from Figure 5.82 that the amplitude of the fluctuation has also become substantially large. The GMR for the 1500K case was evaluated to be 0.67 - 1.14, and the GMR for the case seen at t > 60 ms was evaluated to be 0.79 - 1.14. On comparing the melt fluctuation of the 1000K and 1500K case, it can be deduced that the 1500K case is more chaotic than the 1000K.

Unlike the changes in the injection mass flow rate in the 1500K case, when compared to the previous cases, the particle trajectories were observed to be similar to that of the previous cases with the exception of deviations in the timing of pre-filming and melt movement downstream. The melt underwent pre-filming at 36.6 ms, whereas for 1000K case it was 36.1 ms. Similarly, the melt pool head that moved downstream due to the increased mass loading rejoined with the particles that were pushed downstream by the sonic jet, at 42.5 ms, (same as the 1000K case). Subsequently, at 44 ms the melt pool head plunged into the second Mach-disk.

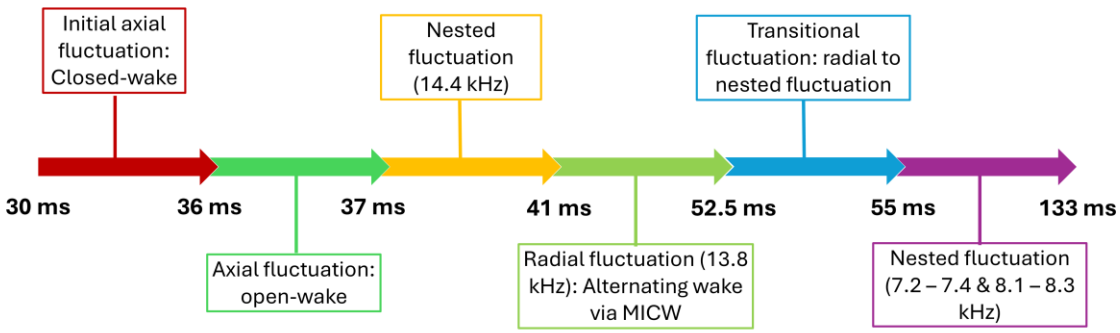

Figure 5.83 Timeline of flow-field fluctuations observed in 6 kg min^{-1}, 1500K case.

Considering the velocity contours of the flow-field, the initial fluctuation due to the melt introduction and the general flow-field fluctuation were observed to be similar to that of the 1000K case. The different flow-field fluctuations observed in the timeline of the 1500K case is presented in Figure 5.83. Following the initial fluctuation as observed in Figure 5.70, while the flow-field continued to attenuate in its spatial oscillations along the axial direction, at 36 ms there was an onset of a high frequency flow-field fluctuation that remained for the remainder of the simulation. The high-frequency fluctuation increased in its spatial oscillation along the axial direction, following which at 37 ms the flow-field transitioned into a nested

fluctuation as presented in Figure 5.81. (Refer Section 5.3.4 and Figure 5.61 for nested fluctuations). The frequency of this fluctuation was evaluated to be 14.4 kHz. Subsequently at 41 ms the flow-field transitioned into an alternating wake, i.e., open- to closed-wake condition, with the closed-wake type being MICW (Figure 5.73a). (In Section 6.7 MICW is explained in detail). While continuing to alternate, the fluctuation attenuated in its spatial oscillation until 52.5 ms. The frequency of the fluctuation was evaluated to be 13.8 kHz. At 52.5 ms the fluctuation increased in its spatial extent, and simultaneously the flow-field started to transition into nested fluctuation, and subsequently at t > 55 ms the flow-field transitioned into nested fluctuation and continued to exist in the same configuration for the remainder of the flow time. Since, the frequency of the nested fluctuation, and the number of swayings present within the fluctuation varied, no single frequency of fluctuation could be observed. (Refer Section 5.3.4 and Figure 5.61 for swayings in nested fluctuations). However, on observing at different instances along the flow time, few frequencies of fluctuation were evident than the others. At t > 55 ms, the nested fluctuation having a frequencies, 7.2 - 7.4 kHz and 8.1 - 8.3 kHz, were observed with two swayings. Similarly, another frequency, 6.8 kHz, was observed with one swaying. Moreover, owing to the irregularity in the fluctuation spread across the flow time, on inspecting the flow-field fluctuations, nested fluctuation randomly varying in number of swayings between 1-3 were observed. In addition to this irregular and chaotic fluctuations, alternating flow-field fluctuation i.e., regular open- to closed-wake fluctuation, was also observed randomly among the nested fluctuations.

Correlation between the flow-field fluctuations and the melt fluctuations (Figure 5.82) were examined. Nested fluctuation having a frequency, 14.4 kHz, seen at the 37 - 41 ms, and the alternating flow-field fluctuation having a frequency, 13.8 kHz, observed at 41 - 52.5 ms, corresponded to the 14.1 -14.3 kHz melt fluctuation observed at 37 - 51 ms. On examining the alternating flow-field fluctuation having frequency, 13.8 kHz, against the melt fluctuation of 14.1 - 14.3 kHz, it was found that the local maxima of the melt fluctuation corresponded to the open-wake condition, and the local minima of the melt fluctuation corresponded to the closed-wake condition, with the closed-wake seen in MICW. Efforts were taken to compare the flow-field fluctuation at t > 55 ms against the melt fluctuation. However, owing to the irregular nature of the fluctuation spread across the flow-time, no single melt fluctuation could be potentially associated with the flow-field fluctuation.

5.4.5 Summary

The 6 kg min^{-1} (GMR=0.88) cases with increasing melt temperature exhibited similar trend to that of the 4 kg min^{-1} cases. The cases can be divided into two categories: a) T=300K, and b) T ≥ 600K cases. The 300K cases exhibited highly regular, large amplitude fluctuations, whereas T ≥ 600K cases did not exhibit one consistent mode of fluctuation. However, T=600K case displayed a regular low frequency fluctuation although the high frequency observed in the fluctuation was highly irregular. But with the increase in melt temperature to T ≥ 1000K, irregular instability was induced in the melt flow rate both in its amplitude as well as in its frequency. The sharp rise in the level of randomness in the melt injection can be observed by comparing the melt injections of 1000K and 1500K cases.

It is observed that only the 300K case undergoes consistent axial flow-field fluctuation, whereas the higher temperature cases can be observed to undergo both axial and radial fluctuations, spread out irregularly across the flow-time. Moreover, all the cases exhibited continuous melt movement downstream, and also demonstrated delayed pre-filming with increase in temperature.

In addition to the unevenly spread irregular pattern in the flow-field fluctuations across the flow-time, to add to the existing irregularity, higher melt temperatures cases introduced nested fluctuations to the existing fluctuation, making the fluctuations all the more complex and unpredictable. Furthermore, the fluctuations became even more complex when the number of swayings within the nested fluctuations randomly varied.

The trend in the melt injection behaviour and their associated flow-field characteristics were further investigated for a higher nominal mass flow rate of 12 kg min^{-1} under increasing melt temperature.

5.5 Results of 12 kg min^{-1} (GMR = 0.44) under increasing melt temperatures.

This section presents the results of 12 kg min^{-1} case having GMR=0.44, investigating the effect of increasing melt temperatures. The melt temperatures considered for this GMR are: 300K, 600K, and 1000K (Table 4-6). Melt temperature cases of 1500K and 2000K were not carried out since the simulations were extremely unstable to run. The section is sub-divided to present and analyse the results for each of the melt temperature individually.

5.5.1 Melt temperature: 300K

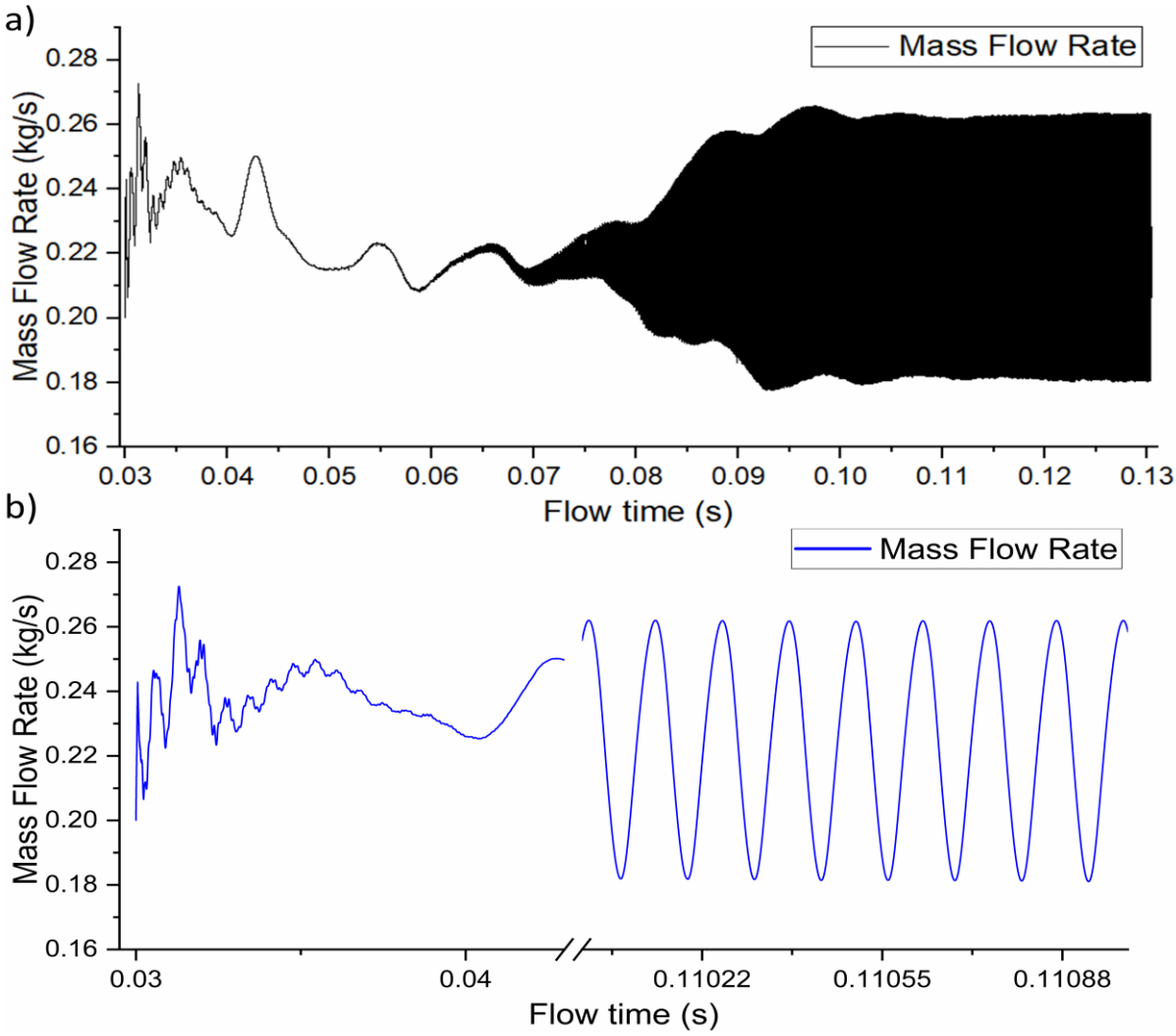

Figure 5.84 Injection mass flow rate plot of 12 kg min^{-1}, 300K case showing: a) the initial fluctuation followed by multiple peaks between 40 - 70 ms that continue to attenuate. At t > 60 ms an onset of a higher frequency fluctuation is observed that gradually increases in its amplitude and remains constant from t > 110 ms; b) the zoomed section of the initial fluctuation and the regular repeated fluctuation seen at t > 110 ms.

The 12 kg min^{-1} case with a melt temperature of 300K having a GMR = 0.44 was run for 100 ms (30 to 130 ms). The injection mass flow rate is presented in Figure 5.84a, while the

zoomed sections of the plot showing the onset of the injection and the high frequency fluctuation is shown in Figure 5.84b. From Figure 5.84a, it was observed, at 30 ms with the onset of the melt injection, the mass flow rate increased to evolve into high-amplitude peaks until 32.4 ms, following which it underwent damped fluctuation. After the initial fluctuation, from 40 to 60 ms, as observed in Figure 5.84a no significant large amplitude fluctuations were seen, except for the two peaks: a large peak, starting at 40 ms, followed by a comparatively smaller peak at 50 ms, exhibiting two consecutive rise and falls in the mass flow rate. At 60 ms there was an onset of a higher frequency fluctuation that continued to exist for the rest of the simulation. Similar to what observed in the previous mass flow rate cases (300K cases of 4 and 6 kg min^{-1}), the fluctuation commenced with a negligible amplitude, but grew in its amplitude over time. The fluctuation attained its maximum amplitude of 0.083 kg s^{-1} at 97 ms, but reduced slightly thereafter until 110 ms and remained almost constant for the remainder of the simulation, only allowing for a marginal increase at t > 110 ms. Moreover, the fluctuation was observed to be repeated and regular in nature at t > 80 ms.

Table 5-5 The frequencies obtained from FFT analysis of 12 kg min^{-1}, 300K case, and their correlation to the flow-field fluctuations.

Flow-time	**Frequency obtained from the FFT analysis**	**Fluctuation observed in the flow field**
30 - 40 ms	1.4 kHz	• Initial fluctuation until 34.2 ms • Steady state observed 34.2 - 42.5 ms
40 - 112 ms	90 Hz	• 90 Hz was not observed. • 42.5 - 68.5 ms the flow field fluctuated at 20 kHz. • From 79 ms flow field fluctuated at 8.1 kHz.
t > 60 ms	8.1 kHz (Superimposed on 90 Hz)	• 68.5 - 79 ms, continuously varying fluctuation. • 8.1 kHz observed at t > 79ms.
Not obviously observable	169.3 Hz	Nil
	249 Hz	
	16.3 kHz	
	24.5 kHz	

Low frequency Mid frequency High frequency

On examination, the injection mass flow rate plot seen in Figure 5.84a, was observed to contain fluctuations of multiple frequencies, and to understand the frequencies present in the melt fluctuations, an FFT analysis was conducted. The FFT analysis revealed there existed three levels of frequency: low-frequencies of 90 Hz, 169.3 Hz, and 249 Hz; mid-frequencies

of 1.4 kHz and 8.1 kHz; and high-frequencies of 16.3 kHz and 24.5 kHz. Out of these frequencies, only 90 Hz, 1.4 kHz and 8.1 kHz were visibly observable in the melt fluctuation plot, Figure 5.84a, while the rest could not be distinctly observable. The frequencies obtained from the FFT analysis and their corresponding flow-time during which they are observed are presented in Table 5-5. The GMR of the 300K case was evaluated to be 0.32 - 0.50, and the GMR of the high-frequency melt fluctuation at t > 60 ms was evaluated to be 0.33 - 0.5.

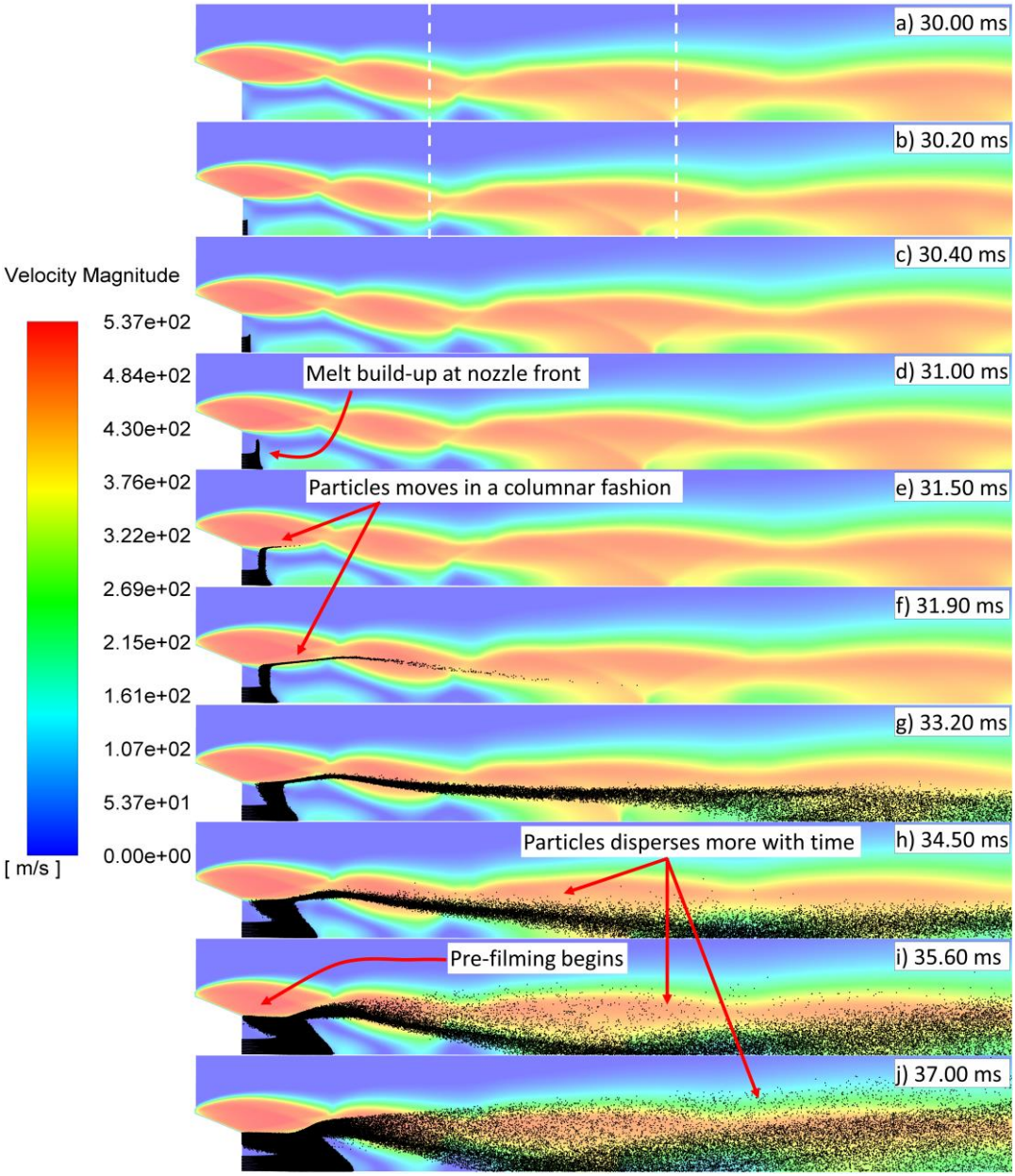

Figure 5.85 Particle trajectories of the 12 kg min^{-1}, 300K case, seen with the velocity contours in the background displaying the evolvement of particles after being injected into the flow stream. The particle trajectories show the onset of injection, pre-filming, melt movement downstream, and increased dispersion of particles with time. The pre-filming starts from the circumferential edge of the nozzle and continues to wet the entire nozzle by moving radially inward.

Considering the particles' trajectories with the velocity contours in the background, it was observed that with the onset of melt injection, the gas flow-field was disturbed from its steady-state condition. This is illustrated by comparing Figure 5.85a against Figure 5.85b. Two guide-lines were pinned at the first and second Mach-disk, respectively, in Figure 5.85a, and were compared against Figure 5.85b. With the onset of injection, the steady-state seen in Figure 5.85a was disturbed and the gas flow-field displaced upstream as observed through the guide-lines, (i) and (ii) in the Figure 5.85b. Following this, with the melt continuing to be injected, an opposing force from the recirculation zone, prevented the melt from moving downstream, leading to melt build-up at the melt nozzle front, as shown in Figure 5.85c&d. The recirculation zone also induces a radial pull on the melt, causing it to move radially away from the atomiser's axis i.e. towards the supersonic gas-jet as shown in Figure 5.85d. When the melt comes in contact with the gas-jet, it was swiftly pushed downstream (Figure 5.85e&f). The particles that were initially pushed downstream after coming in contact with the gas-jet were highly collimated until the end of the first shock-cell but dispersed beyond that. This is shown in Figure 5.85f. However, as time progressed the particles began to disperse even from the first shock-cell, as observed from Figure 5.85g&h. Following this, the melt underwent pre-filming at 35.6 ms, and it can be noticed that the pre-filming started with the melt wetting the circumferential edge of the nozzle first and continues to wet the entire nozzle by gradually moving towards atomiser's axis, i.e., radially inward. This radially inward wetting can be observed in Figure 5.85i&j. Contrastingly, the lower mass flow rates cases of 1 and 2 kg min^{-1} exhibited pre-filming via continuous outward radial movement, seen in Figure 5.3 and Figure 5.24. The earlier seen dispersion in the particles in Figure 5.85h, continued to further increase with time, evolving into Figure 5.85i. It was also observed from Figure 5.85i that the melt pool head significantly moved downstream and has morphologically transformed into a sharper and more pointed melt pool head. With the melt pool head further moving downstream, at 39.8 ms, it plunged into the first Mach-disk (Figure 5.86a), and simultaneously, the melt pool head re-joined with the particles that were pushed downstream by the gas-jet. The melt pool head moved further downstream, plunging into the second Mach-disk, and continued to move downstream as observed in Figure 5.86b&c. Moreover, a greater extent of particle dispersion is observed in Figure 5.86 compared to that in Figure 5.85i&j. Due to the increased particle dispersion, starting at $t > 100$ ms, flares, i.e., particles in groups of small numbers, were propelled radially outwards from the main melt plume by the flow-field. This is shown in Figure 5.86e&f, marked using ellipses. Over time, the melt which moved downstream after plunging into the second Mach-disk accumulates along the atomiser's axis and forms a thick

melt layer. This is observed in Figure 5.86d-f. This thick melt layer is due to the increased mass loading into the domain which can be confirmed by comparing the injection mass flow rate (Figure 5.84) against the mass flow rate of the particles obtained at the outlet of the domain (Figure 5.87). Nevertheless, when observing both in the injection and outlet mass flow rate plots at t > 60 ms, the latter did not resemble the extent of fluctuations seen in the injection mass flow rate, instead, the plot possessed a fluctuation having a small amplitude. This can be due to the damping effect experienced by the injected particles as they travel downstream through the supersonic flow-field.

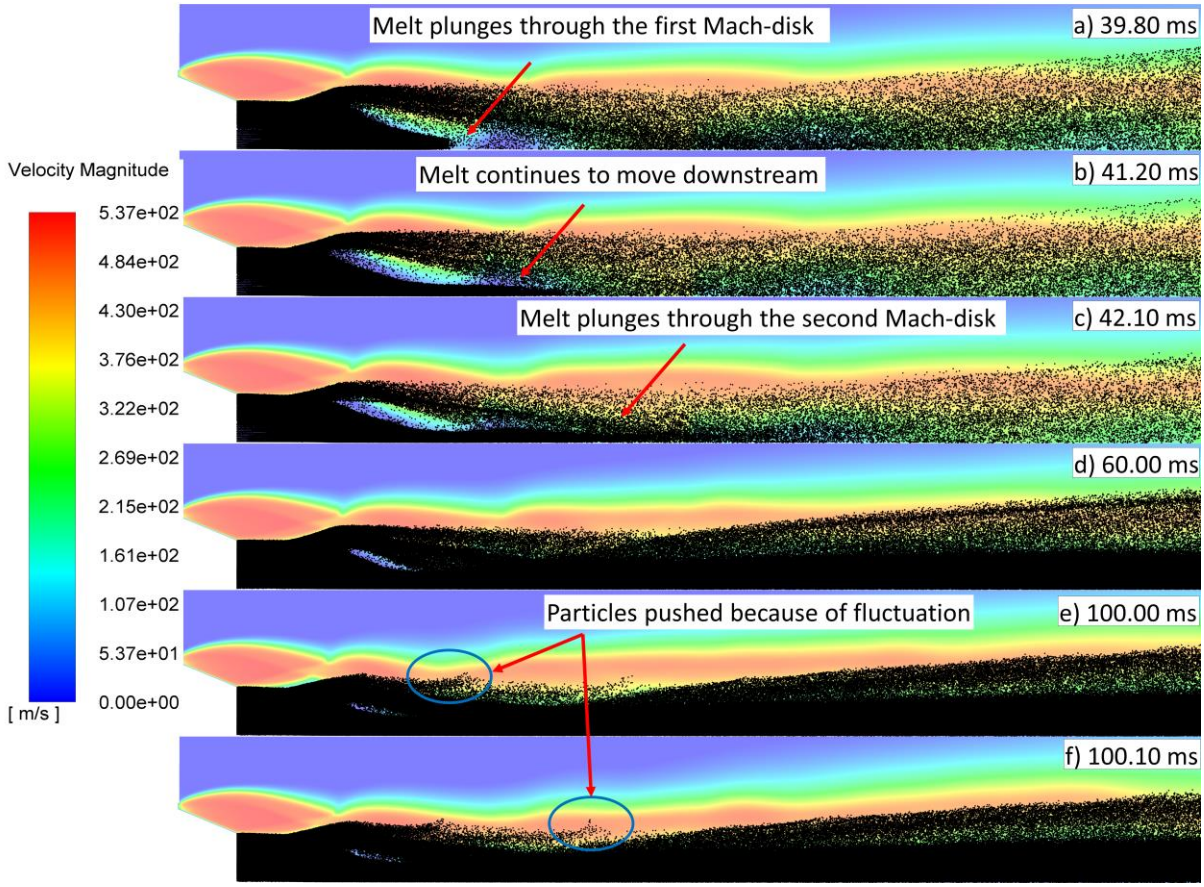

Figure 5.86 Particles trajectories 12 kg min^{-1}, 300K case with velocity contours in the background showing increasing dispersion of particles with time and melt pool head plunging through the first and second Mach-disks. Frames e&f shows flares, i.e., particles in small group being propelled radially outwards from the main melt plume, marked by ellipses.

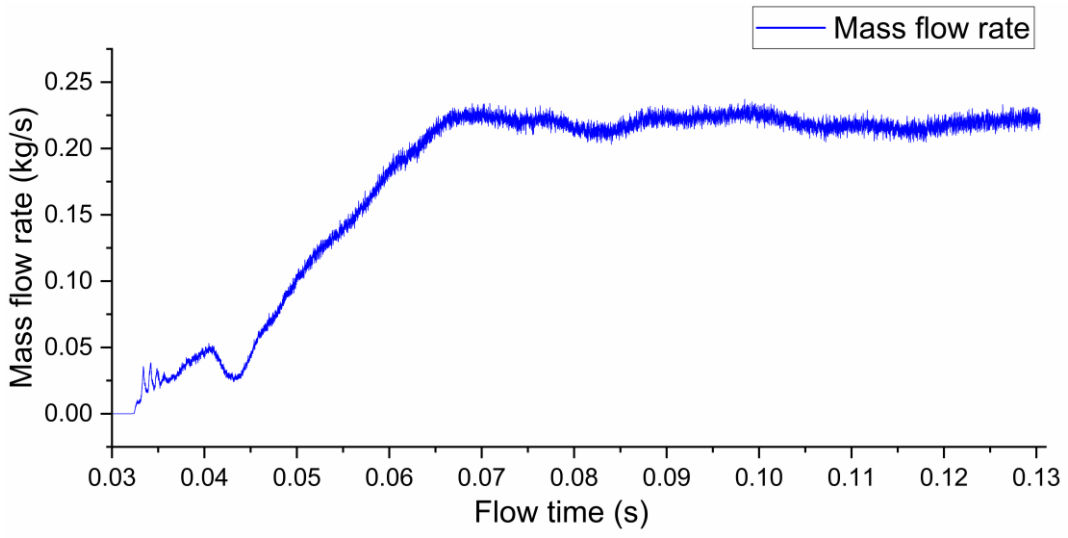

Figure 5.87 Mass flow rate of the particles for the 12 kg min^{-1}, 300K case obtained at the outlet of the domain. There is an initial steady increase in the flow of particles through the outlet till 40 ms, but decreases briefly, and thereafter rapidly increases. Subsequently, at t > 67 ms no significant change in the mass flow rate is seen.

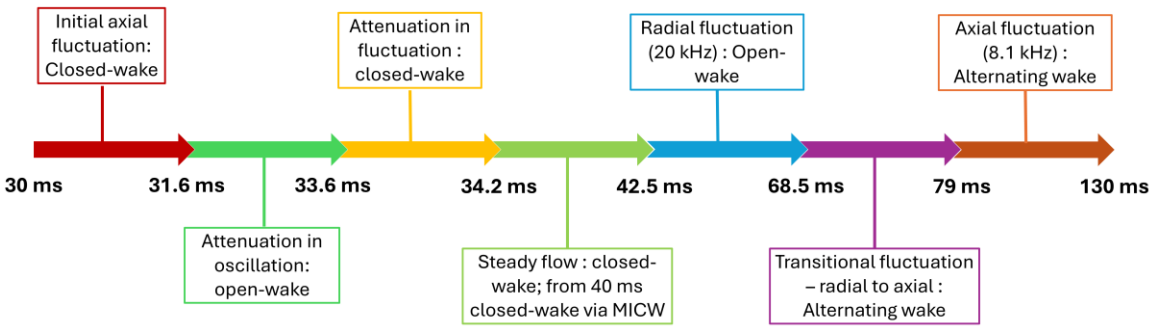

Figure 5.88 Timeline of flow-field fluctuations observed in 12 kg min^{-1}, 300K case.

Considering the flow-field fluctuation, the different fluctuations observed during the flow-time are presented in Figure 5.88. From the velocity contours of the gas flow-field presented in Figure 5.89, it was confirmed the flow-field that was disturbed from its steady-state due to the introduction of melt (Figure 5.85b), undergoing repeated fluctuation by displacing upstream and downstream along the axial direction. Even though, both the particles (melt) and flow-field co-exist in all the cases of 12 kg min^{-1} model, to have to have a better understanding how the flow-field changes, only velocity contours are presented. The above-mentioned disturbance to the flow-field is understood through Figure 5.89 where series of velocity contours of the flow-field were obtained in closed spaced flow intervals, and were stacked sequentially. Two guide-lines, (i) and (ii) were pinned in Figure 5.89a, at the first and second Mach-disk, respectively, and were compared against the rest of the frames of Figure

5.89. On comparing, it was observed the flow-field continuously fluctuated by displacing upstream and downstream, i.e., the flow-field features including the first and second Mach-disk moved upstream in Figure 5.89b, and subsequently moved downstream in Figure 5.89c. While the flow-field continued to fluctuate, upstream and downstream, it was observed the wake remained in closed-wake condition until 31.6 ms. Thereafter the ongoing flow-field fluctuation in Figure 5.89, simultaneously attenuated in its spatial oscillation along the axial direction. Furthermore, the continuous downstream movement of the melt pool head seen in Figure 5.85 is also observed in Figure 5.89, and its movement is marked by the black circles.

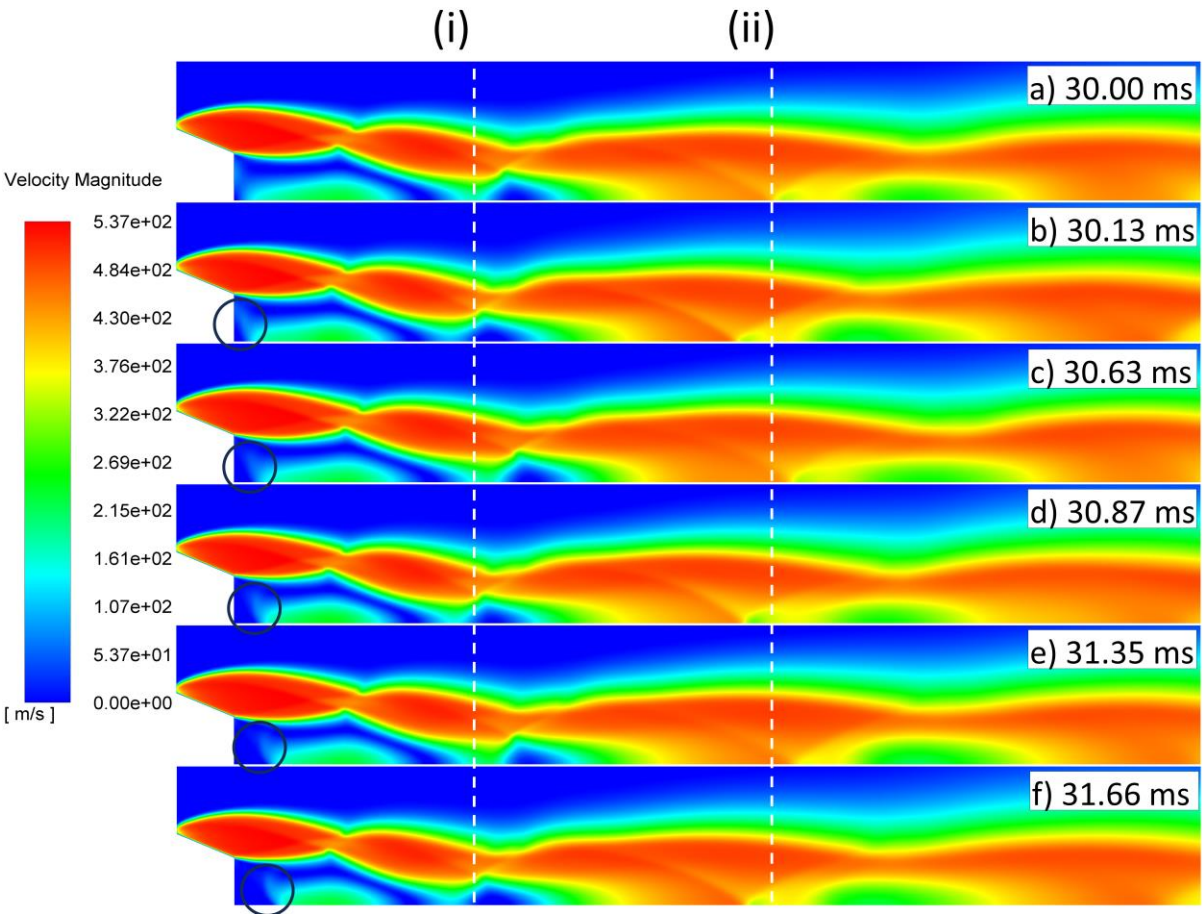

Figure 5.89 Velocity contours of 12 kg min^{-1}, 300K case, is presented without particles, showing flow-field fluctuations at the onset of the melt injection into the domain. Two guide-lines (i) and (ii) are fixed at first and second Mach-disk of frame a, to compare the changes with rest of the frames.

Following the closed-wake fluctuation, at 31.6 ms the fluctuating flow-field transitioned into open-wake condition while simultaneously reducing its amplitude of lateral oscillation. The flow-field continued to exist in the open-wake configuration until 33.6 ms and

is presented in Figure 5.90. The further downstream advancement of the melt pool head is evidently seen in Figure 5.90, marked by the black eclipses.

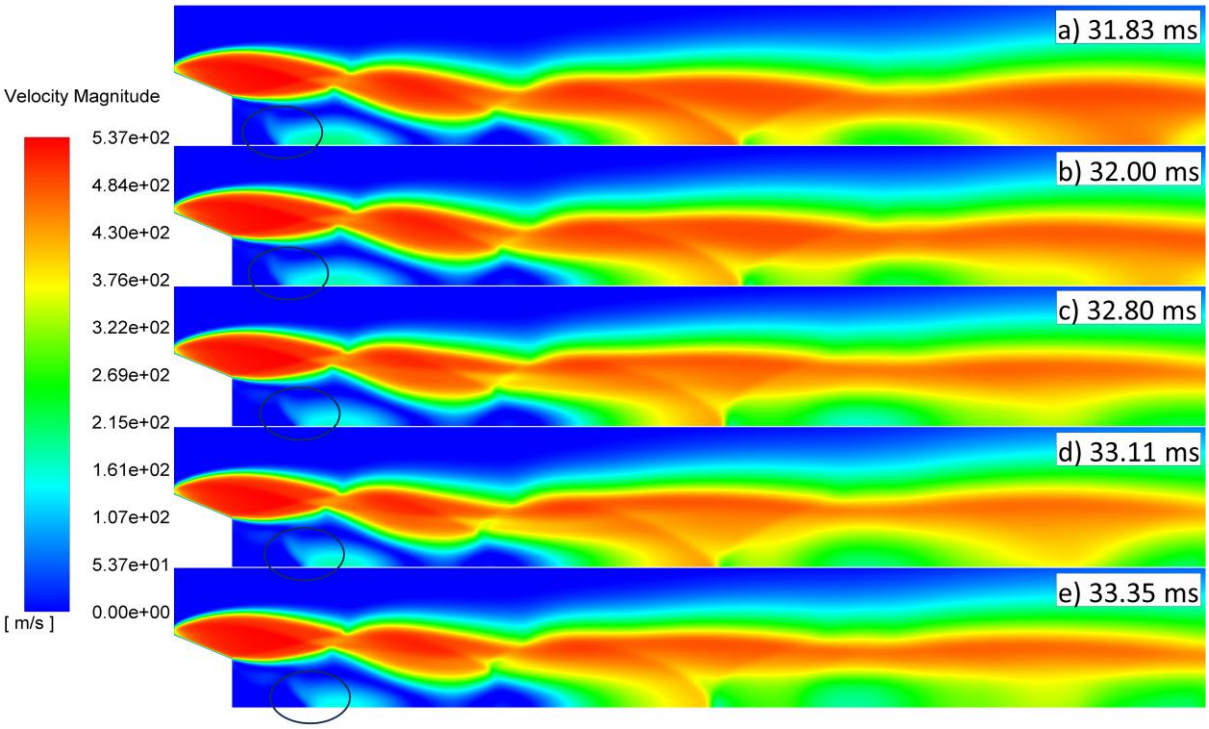

Figure 5.90 Velocity contours of 12 kg min^{-1}, 300K case, is presented without particles, showing flow-field fluctuations existing in open-wake configuration. The downstream movement of the melt pool head is observed, marked using the ellipses.

At 33.6 ms the flow-field transitioned back into closed-wake condition while still continuing to attenuate in its spatial oscillations, i.e., reducing its amplitude of lateral oscillation. Shortly thereafter at 34.2 ms, the flow-field entered into steady-state and continued to remain in that state until 42.5 ms, while existing in closed-wake condition. This is shown in Figure 5.91 were velocity contours obtained at closely spaced flow intervals and were stacked-up to illustrate the achieved steady gas flow-field. Two primary guide-lines, (i) and (ii) were pinned in Figure 5.91a, at the ends of the first and second shock-cell, respectively, and were compared against the rest of the frames. It can be observed from guide-lines, (i) and (ii) that the spatial extent of the first and second shock-cells did not change from 34.2 ms to 41 ms (Figure 5.91a-h), indicating steady gas flow. Nevertheless, with the downstream advancement the melt pool head, the spatial extent of the third shock-cell steadily reduced in its size along the axial direction (Figure 5.91a-j). Moreover, the downstream movement of the melt pool head is also observed in Figure 5.91, marked using the black ellipses. The melt pool head continued to advance further and plunged into the first Mach-disk at 40 ms, shown using the white arrows (Figure 5.91f-h). With the melt pool head plunging into first Mach-disk, the closed-wake seen

earlier transitions into MICW type closed-wake, since the wake remains isolated between the melt pool head and the lower sonic boundary layer that is immersed into the melt pool. In Section 6.7 MICW is explained in detail. The melt pool further advanced downstream to plunge into the second Mach-disk at 45 ms. This is shown using a secondary guide-line pinned at the stagnation point in Figure 5.91g and comparing against stagnation points of the rest of the frames, Figure 5.91h-j. The stagnation points seen in Figure 5.91g&h remained fixed, whereas due to the downstream movement of the melt it is pushed downstream in Figure 5.91i&j. This downstream movement is shown using black arrows.

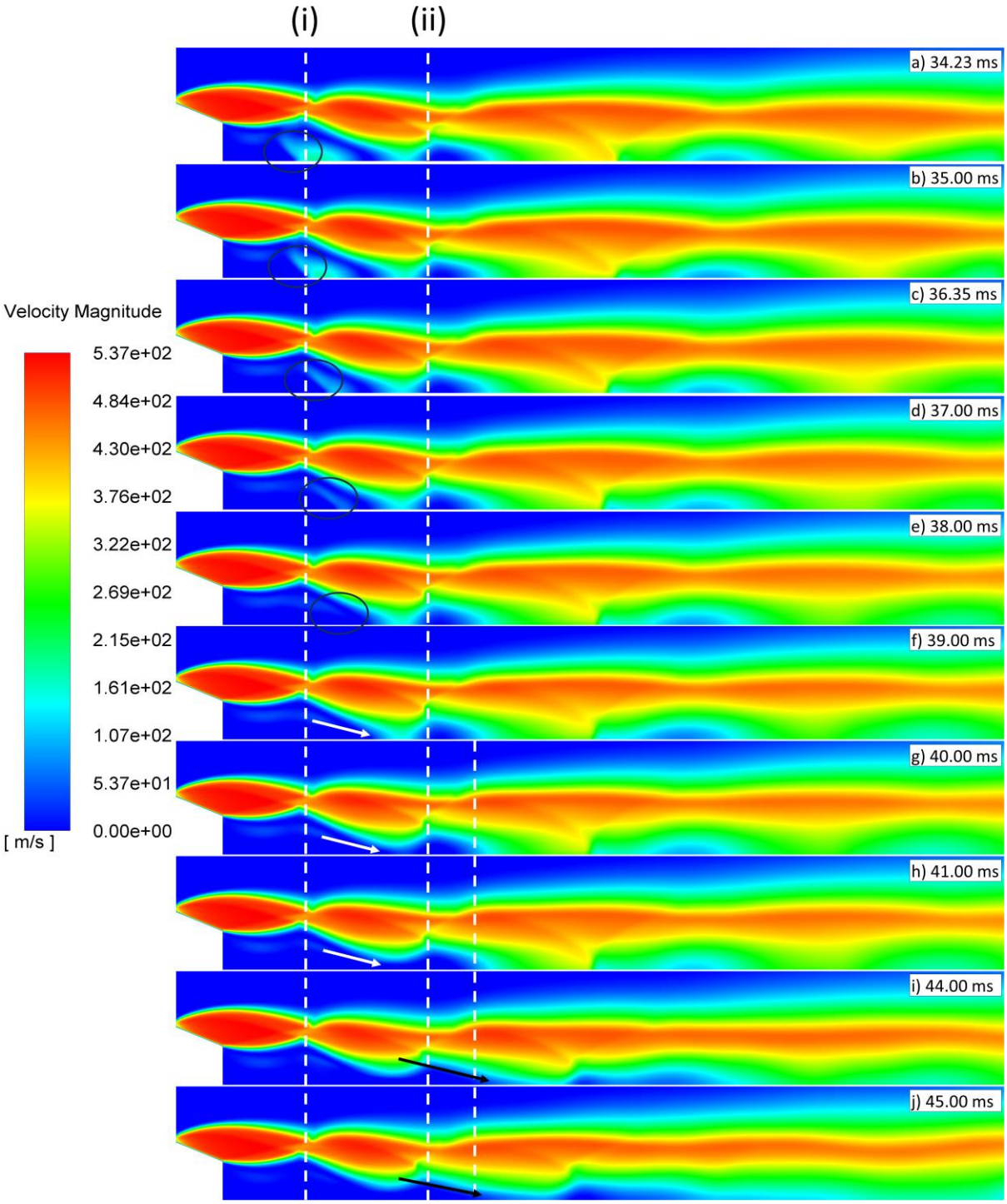

Figure 5.91 Velocity contours of 12 kg min^{-1}, 300K case, is presented without particles, showing the steady gas flow, from 34.2 - 42.5 ms. The two primary guide-lines (i) and (ii), pinned at the first and second Mach-disk, respectively, indicate the flow-field continues as steady state. The downstream movemnt of the melt pool head is marked using the ellipses. White arrows indicate the melt pool head plunging into the first Mach-disk, transforming the flow-field into MICW configuration. The secondary guide-line in frame g pinned at the stagnation point shows the downstream displacement of the stagnation points in frame i&j. This is due to the downstream movemnt of the melt. Melt beginning to plunge into the second Mach-disk is shown using the black arrows.

Following the steady-state flow, at 42.5 ms an onset of a continuous flow-field fluctuation that started out gradually was observed and with time it grew in its spatial oscillation along the radial direction. Nevertheless, the observed fluctuation was small although it was noticeable. For a brief period of time the fluctuation reduced in its spatial oscillation at 51 ms, before quickly regaining its original oscillation. The frequency of this fluctuation was evaluated to be 20 kHz, and it existed in open-wake configuration. However, on comparing this frequency with the melt fluctuation, no correlation could be drawn, indicating the melt flow rate had no impact on the flow-field fluctuation. Subsequently, the 20 kHz fluctuation operating under open-wake configuration, transitioned into transient fluctuation at 68.5 ms, continuously evolving without exhibiting one single mode of fluctuation. This is because the radial fluctuation gradually transitioned into axial fluctuation, and hence two modes of fluctuation were simultaneously observed. The flow-field fluctuation completely transitioned into axial mode of fluctuation at 79ms. This is presented in Figure 5.92. The fluctuation grew with time, i.e., the spatial extent of the oscillation increased with time along the axial direction, and achieved its maximum spatial oscillation at 93 ms. To understand the nature of the fluctuation, series of velocity contours of the flow-field were obtained in closely space time intervals, and were stacked sequentially. This is presented in Figure 5.92, where two vertical guide-lines, (i) and (ii) were pinned in Figure 5.92a, at the ends of the first and second shock-cell, respectively, and were compared against other frames of the stack. Another two sets of guide-lines were used to trace the extent of movement of the first and second shock-cells. It was observed from Figure 5.92 that the second shock-cell underwent a significantly larger fluctuation i.e. change in the shock-cell's spatial dimension along the axial direction, compared to the first shock-cell. During the fluctuation it was evident through the vertical guide-lines, (i) and (ii), that the first and second shock-cell increased in its spatial dimension along the axial direction, and reached its maximum size in Figure 5.92f but eventually returned back to its original size in Figure 5.92k, even as observed in Figure 5.92a. On comparing Figure 5.92a with Figure 5.92f, it is observed that in the latter, the first and second shock-cells attained their maximum spatial extent at 1.25 and 1.5 times the shock-cell size seen in Figure 5.92a, respectively. It was also noted that the maximum spatial extent of the first and second shock-cells observed in Figure 5.92f, was measured to be identical to that of the shock-cells observed during gas-only flow (no melt), as seen in Figure 5.89a.

Similarly, it was observed, the closed-wake present as MICW, seen in Figure 5.92a, gradually transitioned into an open-wake, as observed in Figure 5.92f, and subsequently

returned back to its original configuration i.e., closed-wake condition, at the end of the fluctuation (Figure 5.92k). In Section 6.7 MICW is explained in detail. To further check and confirm the state of the wake, lower sonic boundary distance from the atomiser's axis and the melt layer thickness were measured for both the closed-wake and open-wake conditions seen in Figure 5.92a and Figure 5.92f. In Figure 5.92a, with the lower sonic boundary situated at 0.8 mm away from the axis, and melt layer thickness being 0.85 mm, the wake existed as MICW. Whereas, in Figure 5.92f, the lower sonic boundary was measured at a distance of 0.95 mm, whereas the melt layer thickness remained being 0.85 mm, indicating the wake exist in open-wake condition. In addition to this, a wave propagation was observed in Figure 5.92, starting from the end of third shock-cell and continued to propagate until the end of the domain. The wave propagation is traced using the ellipses. The frequency of this flow-field was evaluated to be 8.1 kHz. Correlation between alternating flow-field fluctuation, i.e., open- to closed-wake fluctuation observed in Figure 5.92, and the melt fluctuation observed in Figure 5.84 were conducted. It was found that the frequency of melt fluctuation, 8.1 kHz, obtained from the FFT analysis corresponded to the flow-field fluctuation. This correlation is also tabulated in Table 5-5. Furthermore, it was discovered in the correlation that at the local maximum of the melt fluctuation, seen in Figure 5.84, the flow-field corresponded to an open-wake condition (Figure 5.92f), and at the local minima, the flow-field corresponded to a closed-wake condition (Figure 5.92a&k).

As carried out in the previous cases of 1, 2, 4 and 6 kg min^{-1} models (Figure 5.74), the flow-field fluctuations were compared against the velocity monitors to validate its frequency of fluctuation. The velocity monitors were recorded at seven key locations and were examined. The FFT analysis of the high-frequency fluctuation at $t > 79$ ms across all seven monitors resulted in two consistently dominant frequencies: 8.1 kHz and 16.3 kHz. The 8.1 kHz fluctuation observed from the monitors, validated the flow-field fluctuation with 8.1 kHz as observed in Figure 5.92. Efforts were taken to observe the other frequency (16.3 kHz) obtained from the FFT analysis in the flow-field fluctuation, however, no corresponding fluctuation could be correlated. Nevertheless, the frequency, 16.3 kHz, was observed in the FFT analysis of melt fluctuation (Table 5-5), probably indicating it might be a harmonic of 8.1 kHz.

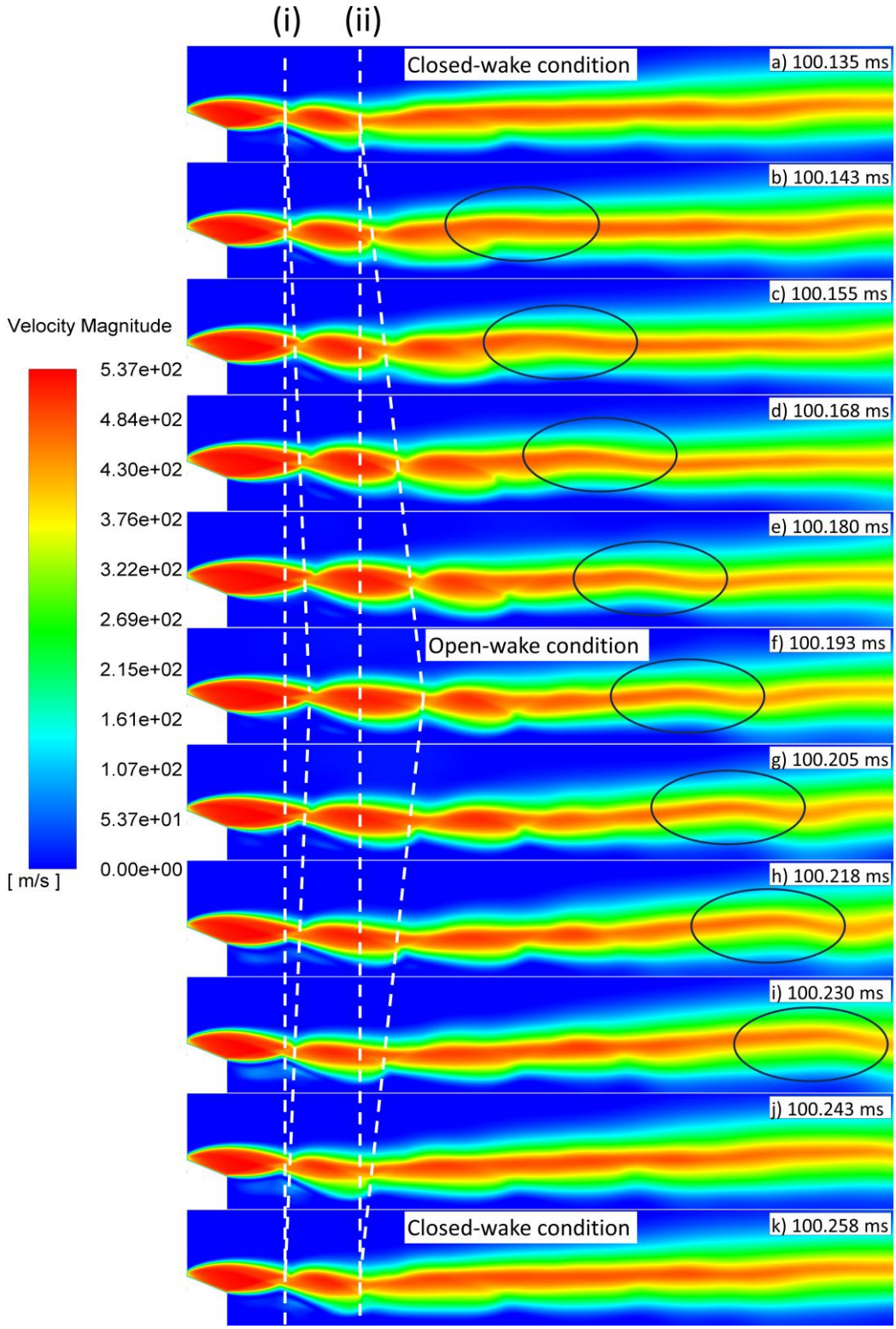

Figure 5.92 Velocity contours of the flow-field without particles for the 12 kg min^{-1}, 300K case, showing a cycle of the repeated fluctuation that is seen at t > 79 ms. Two vertical guide-lines, (i) and (ii) are fixed at the ends of the first and second shock-cell, respectively, of frame a to compare the extent of fluctuation against other frames. Another two sets of guide-lines are used to trace the movement of the first and second shock-cell ends. The second shock-cell undergoes significant spatial fluctuation compared to the first shock-cell. The frequency of the fluctuation was found to be 8.1 kHz.

5.5.2 Melt temperature: 600K

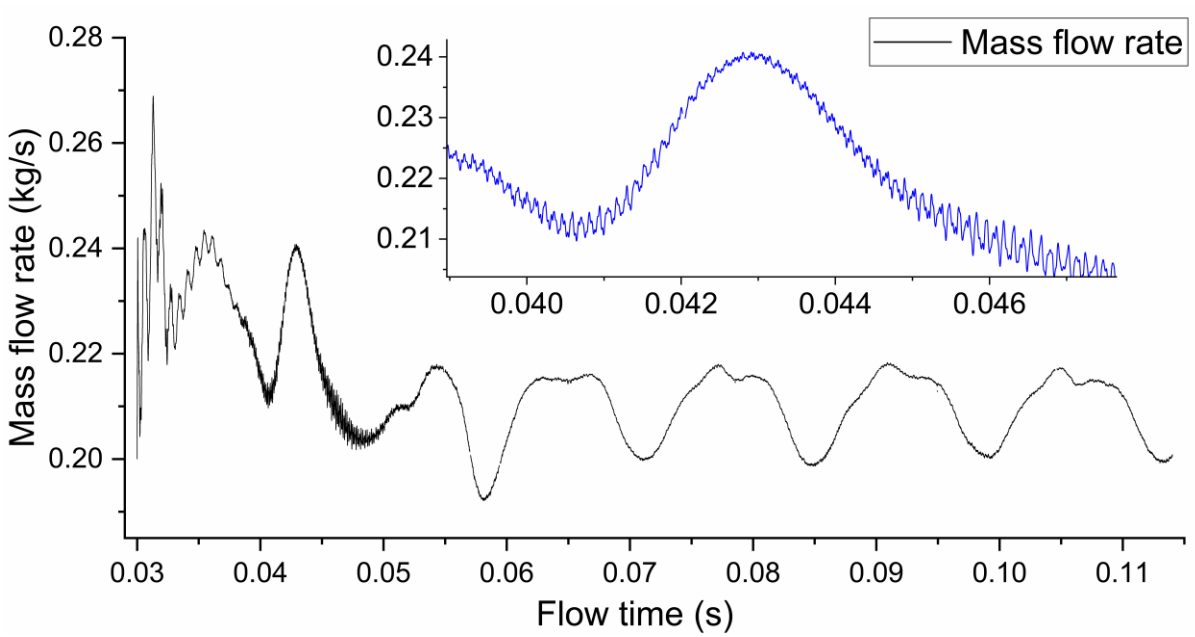

Figure 5.93 Injection mass flow rate plot of 12 kg min^{-1}, 600K case showing the initial fluctuation followed by a rise and fall in the mass flow rate between 40 - 48 ms. A higher frequency fluctuation is observed between 38.4 - 52 ms. At t > 55 ms no significant large amplitude fluctuations are observed. At t > 58 ms, a lower frequency fluctuation is observed.

The 12 kg min^{-1} case with a melt temperature of 600K having a GMR = 0.44 was run for 84 ms (30 to 114 ms). The injection mass flow rate is presented in Figure 5.93, with the zoomed-in section of the plot showing the high frequency fluctuation. The initial fluctuation seen in the 600K case is similar to that of the 300K case. With the initial fluctuation continuing to attenuate, i.e., reducing in its amplitude, at 38 ms an onset of a higher frequency fluctuation was observed, which lasted until 52 ms. This is seen in Figure 5.93 presented in the zoomed-in section. Simultaneously, between 40 - 48 ms, a rise-and-fall in the mass flow rate was observed in Figure 5.93. Subsequently, at 58 ms, the melt fluctuation evolved into a lower frequency fluctuation of 71 Hz (time-period of ~14 ms). Although no significant higher frequency fluctuation could be observed on the first glance, a closer inspection and zooming in to the plot revealed a higher frequency fluctuation, irregular in nature and insubstantial in amplitude. From FFT analysis it was found that there existed multiple levels of frequency, with each level encompassing multiple frequencies. Low-frequencies of 71 Hz, 166.6 Hz, 249 Hz, and 375 Hz; mid-frequencies of 1.4 kHz and 8.4 - 9.1 kHz; and a high-frequency of 13.9 kHz, were revealed in the FFT analysis. Out of the obtained frequencies, only a few were visibly observable in the melt fluctuation plot (Figure 5.93), and the rest were not obviously

observable. The frequencies identified from the FFT analysis, along with their associated durations in the flow-time, are tabulated in Table 5-6. The GMR for the 600K case was evaluated to be 0.32 - 0.45. For the relatively consistent lower-frequency fluctuations (71 Hz) observed at t > 58ms, the GMR was evaluated to be 0.4 - 0.45.

Table 5-6 The frequencies obtained from FFT analysis of 12 kg min^{-1}, 600K case and their correlation to the flow-field fluctuations.

Flow time	**Frequency obtained from the FFT analysis.**	**Fluctuation observed in the flow field**
30 - 40 ms	1.4 kHz	• Initial fluctuation
38 - 52 ms	Irregular fluctuation continuously varying between 8.4 - 9.1 kHz.	• For t > 37 ms, 20 kHz is observed. • 9.8 kHz observed between 42.5 - 47 ms in nested fluctuation, wherein 9.8 kHz is observed in fundamental oscillations, and within it 20 kHz, present as swayings. • However, the frequency, 9.8 kHz continued to vary slightly between 42 - 47 ms.
	Irregular fluctuation 28.3 - 28.6 kHz.	
t > 58 ms	71 Hz	• 71 Hz is not observed, rather 20 kHz is observed at t > 58 ms.
Not obviously observable	166.6 Hz	Nil
	249 Hz	
	375 Hz	
	13.9 kHz	

Low frequency Mid frequency High frequency

In the 600K case it was noted that from t > 72 ms the mass flow rate of the particles obtained at the outlet of the domain, presented in Figure 5.94, followed a similar fluctuation trend observed in the injection mass flow rate (Figure 5.93). The frequency of the fluctuation observed at t > 72 ms in the mass outflow plot (Figure 5.94) was evaluated to be 71 Hz, reflecting the same frequency obtained via FFT analysis (Table 5-6). This however was not the same in the 300K case, where the mass outflow rate plot (Figure 5.87) contained a negligible amplitude fluctuation at t > 67 ms, although a significant higher frequency fluctuation with large amplitude was observed at t > 60 ms in the injection mas flow rate plot (Figure 5.84). This consistently indicates that the gas flow efficiently damps out only the high frequency, but is unable to damp the lower frequencies.

Even though significant changes were observed between the 300K and 600K both in the melt injection and outflow plots, no significant changes were observed in the particles' trajectories, except for the deviations in the time for a few melt flow characteristics. The deviations are: the melt underwent pre-filming at 36 ms (for the 300K case it is 35.6 ms), and the melt pool head that moved downstream due to the increased mass loading rejoined with the particles that were pushed downstream by the sonic jet, at 39.5 ms. Shortly thereafter at 42.5 ms the melt pool head plunges into the second Mach-disk.

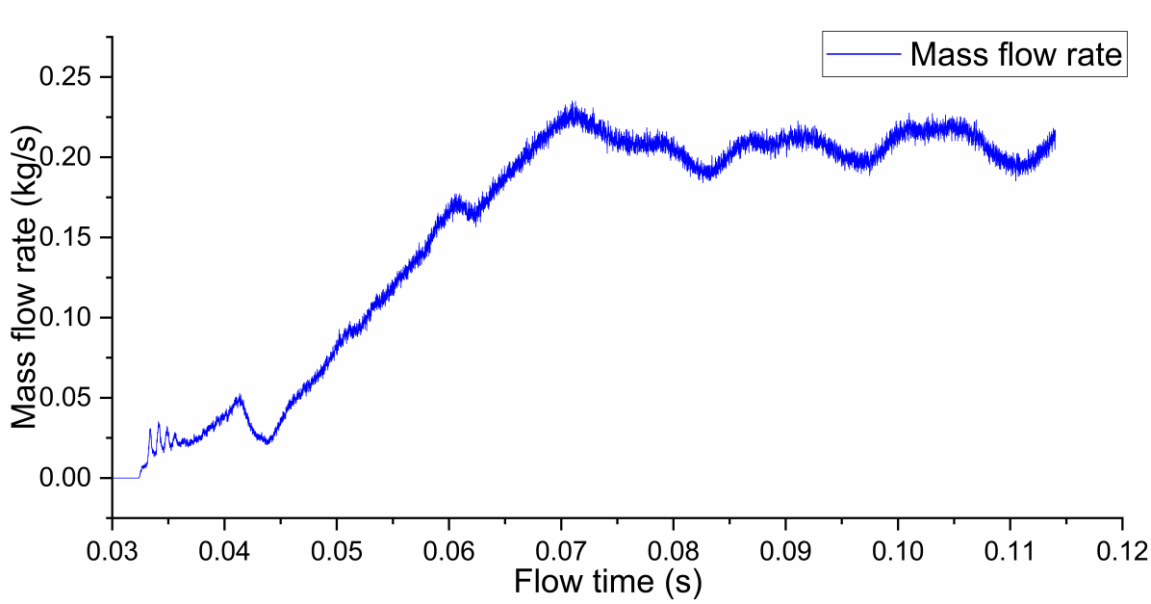

Figure 5.94 Mass flow rate of the particles for the 12 kg min^{-1}, 600K case, obtained at the outlet of the domain. There is an initial steady increase in the flow of particles through the outlet. Following a brief decrease at 41 ms, a sharp rise is observed until 72 ms, after which the plot transforms into a fluctuation similar to the fluctuation seen in injection mass flow rate, at t > 55 ms.

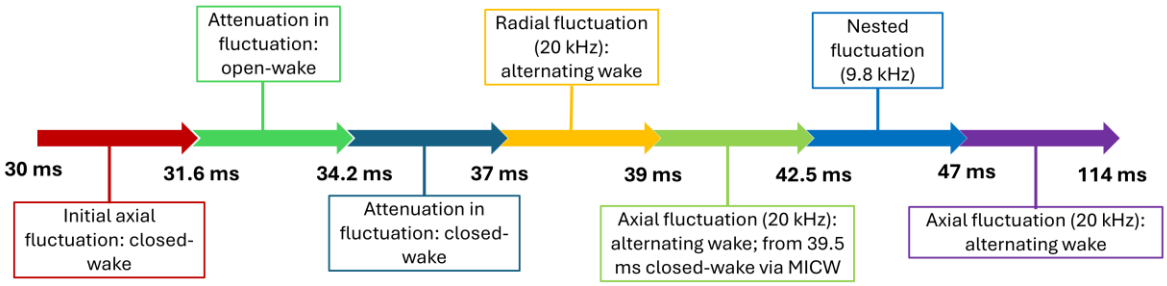

Figure 5.95 Timeline of flow-field fluctuations observed in 12 kg min^{-1}, 600K case.

Considering the velocity contours of the flow-field, the different flow-field fluctuation observed during the flow-time of the simulation is presented in Figure 5.95. The initial fluctuations due to the melt introduction looked same as that of the 300K case, presented in Figure 5.89. Following this at 31.6 ms the flow-field transitioned into an open-wake as seen in

Figure 5.90 while still continuing to reduce its amplitude of spatial oscillation along the axial direction. Subsequently at 34.2 ms the wake re-established to be become a closed-wake while yet continuing to attenuate in its spatial oscillations along the axial direction. At 37 ms, there was an onset of a higher frequency fluctuation in the flow-field, which transformed the closed-wake fluctuation into an alternating flow-field fluctuation, i.e., open- to closed-wake fluctuation. To understand this fluctuation, series of velocity contours were obtained in closely spaced time intervals and were stacked sequentially. This is presented in Figure 5.96. Two guide-lines, (i) and (ii) were pinned in Figure 5.96a, at the downstream ends of the first and second shock-cell, and were compared against the rest of the frames. It could be observed from the two guide-lines that the first and second shock-cells remain fixed throughout the fluctuation without undergoing any changes to their spatial extent. Also, it can be observed that the flow-field gradually transitioned from closed-wake condition seen in Figure 5.96a to open-wake condition (Figure 5.96f), and thereafter returned back to its original configuration, i.e., closed-wake condition (Figure 5.96k). In addition to this, a wave propagation was observed, originating from the end of third shock-cell and continuing to propagate until the end of the domain, whose propagation is traced using ellipses. The frequency of this flow-field fluctuation was evaluated to be 20 kHz. On comparing the flow-field fluctuations seen in Figure 5.96, against the melt fluctuation seen in the injection mass flow rate plot (Figure 5.93), it became apparent that the neither of the wake conditions, open-wake or closed-wake conditions, were associated with local extrema of the melt fluctuation.

Subsequently at 39 ms the flow-field began to gain spatial oscillation in the axial direction while continuing to undergo alternating flow-field fluctuation. Shortly thereafter at 39.5 ms, with the melt pool head plunging into the first Mach-disk, the closed-wake transformed into MICW. A typical transformation of closed-wake into MICW is presented in Figure 5.91f-h. Following the transformation, the alternating flow-field fluctuation continued for the remainder for the flow-time, with exception between 42.5 - 47 ms, where the flow-field underwent nested fluctuation. (Refer Section 5.3.4 and Figure 5.61 for nested fluctuations and swayings present within nested fluctuations). During nested fluctuation, a single cycle of the fluctuation, i.e., a closed- to closed-wake cycle fluctuated at 9.8 kHz, and the swayings present within the nested fluctuations fluctuated at 20 kHz. Nevertheless, it was also observed that the 9.8 kHz frequency, seen in the nested fluctuations, varied marginally in its frequency at other instances.

The above-mentioned alternating flow-field fluctuation that underwent axial spatial oscillations at 39 ms, attained its maximum spatial oscillation at 40 ms and thereafter it remained the same for the remainder of the flow-time. Although there was an increase in the spatial oscillation with the melt pool head plunging into the first Mach-disk at 39.5 ms, the fluctuation continued to fluctuate at 20 kHz. Efforts were taken to observe correlation between the alternating flow-field fluctuation seen at $t > 39$ ms and the melt fluctuation. However, with the melt fluctuation (Figure 5.93) being irregular in nature, no meaningful correlation could be established with the flow-field fluctuations. Efforts were similarly made to analyse and correlate the nested fluctuations observed between $42.5 < t < 47$ ms. Since the melt fluctuations were well-defined 42.5 - 44.5 ms, obvious correlations could be extracted. The local-minima of the melt fluctuation seen between 42.5 - 44.5 ms corresponded to closed-wake condition. However, ambiguity prevailed in correlating the local-maxima against open-wake or the swayings present. The melt fluctuations seen between 44.5 - 47 ms were irregular, hindering the ability to correlate with the flow-field fluctuation further adding complexity to the analysis. Moreover, efforts were taken to correlate the 20 kHz flow-field fluctuation against low frequency melt fluctuation, ~71 Hz (Table 5-6), to identify flow features of interest such as open- and closed-wake against local maximum and minimum of the ~71 Hz melt fluctuation. However, no potential correlation could be drawn. Nevertheless, it is interesting to observe ~71 Hz melt fluctuation from the simulation, since it is of physical relevance and is observed in atomisation process.

It is clearly evident from the above sequence of correlation analysis that in the 600K case, the atomisation process became significantly more complex compared to the 300K case, resulting in notable mismatch between the melt and flow-field fluctuations. This might indicate that with the increase in the melt temperature, the coupling between the melt and the flow-field fluctuations may not be directly related, and perhaps linked via unknown factors which are yet to be explored. Another case with a melt temperature of 1000K is run to better understand the level of complexity and uncertainty present in the model.

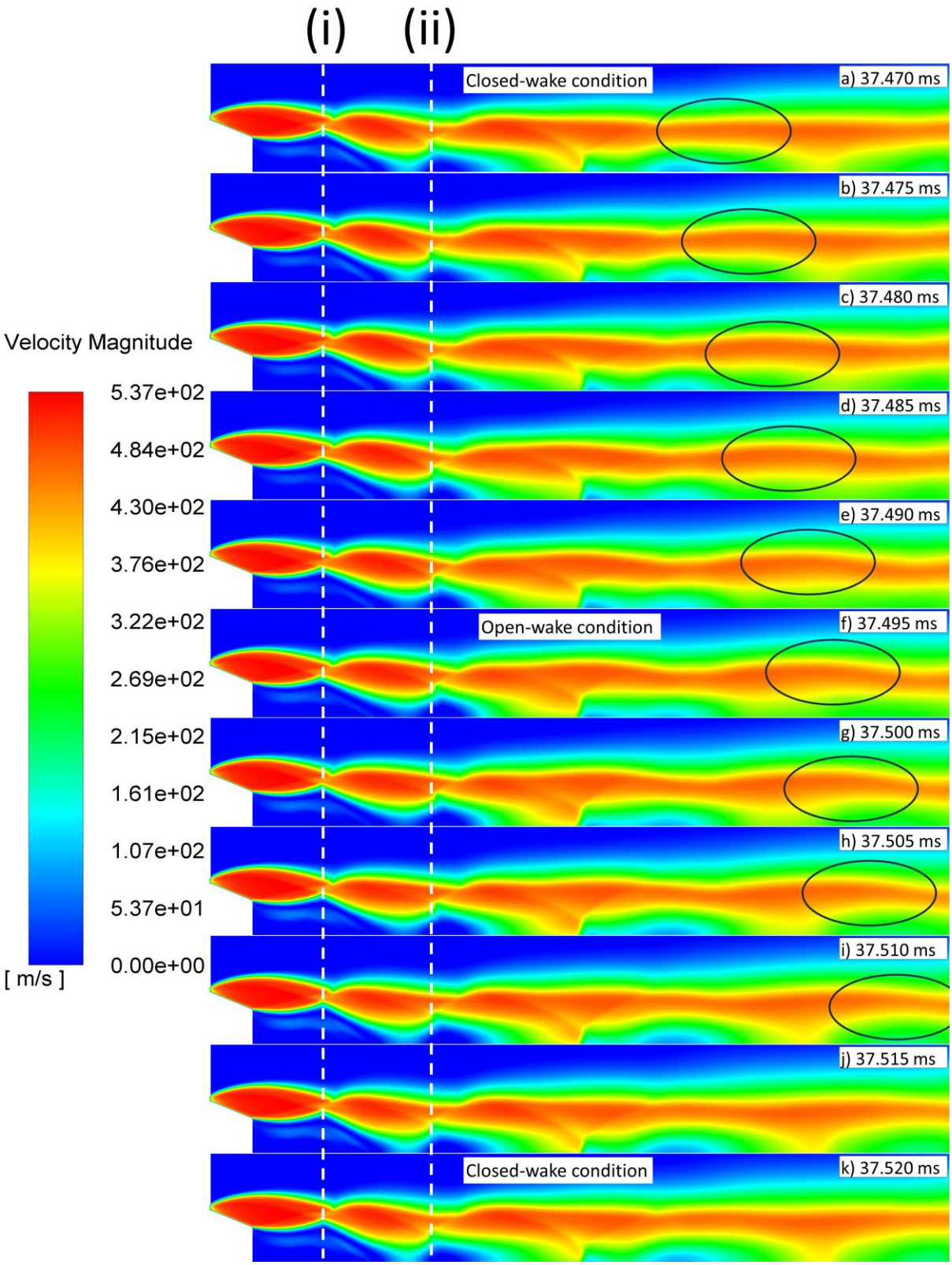

Figure 5.96 Velocity contours of the flow-field without particles for the 12 kg min^{-1}, 600K case, showing a cycle of the alternating flow-field fluctuation. Two guide-lines, (i) and (ii) were pinned in frame a, at the ends of the first and second shock-cell, and were compared against the rest of the frames. The first and second shock-cell remains fixed throughout the fluctuation without undergoing any changes to their spatial extent. A wave propagation is observed starting at the end of the third shock-cell, and is marked using ellipses.

5.5.3 Melt temperature: 1000K

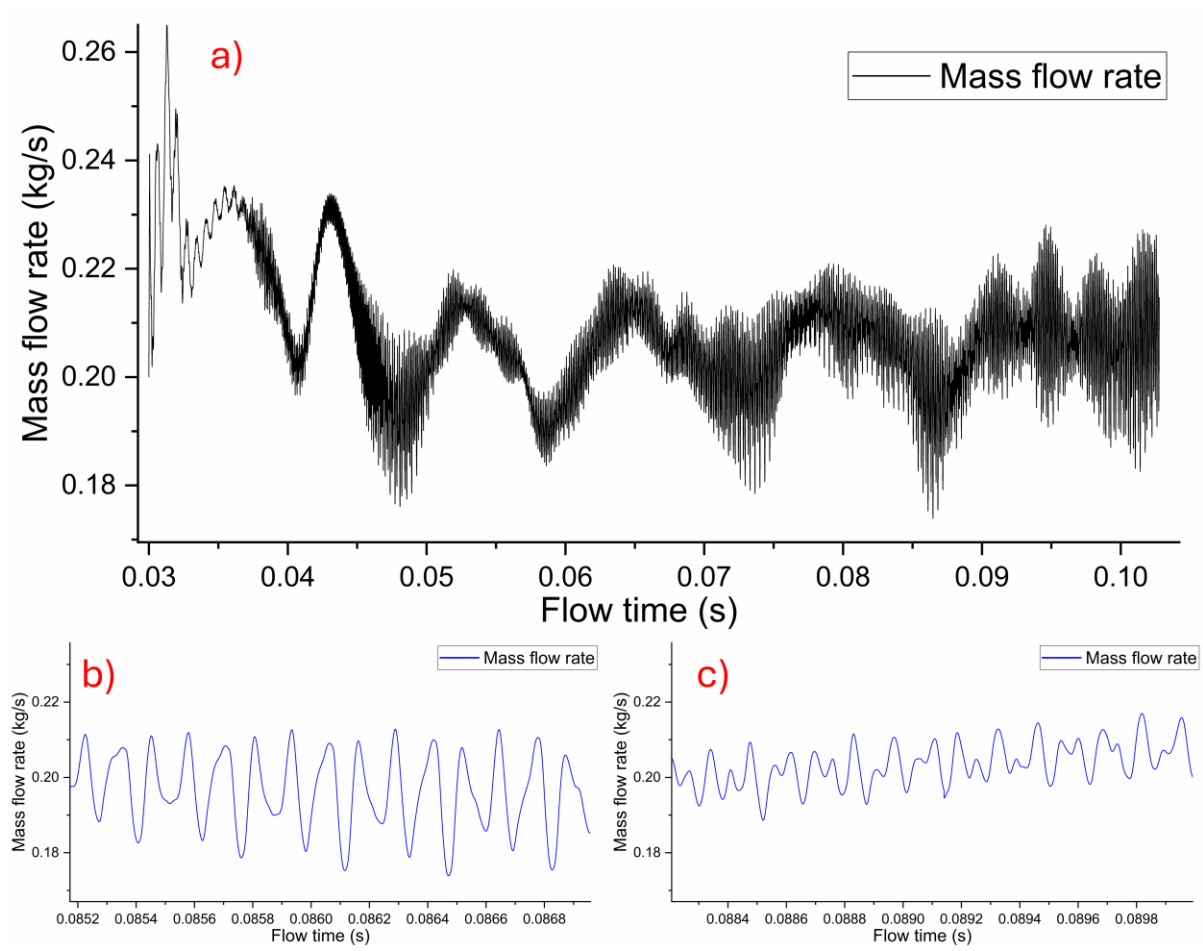

Figure 5.97 Injection mass flow rate plot of 12 kg min^{-1}, 1000K case. a) The initial and higher frequency fluctuation are shown, with latter becoming prominent at t > 36.5 ms and persisting for the remainder of the simulation. Zoomed section of the plot highlights the repetitive pattern in the melt, b) single frquency of 8.5 kHz followed by, c) varying frequencies in ampplitude modulation.

The 12 kg min^{-1} case with a melt temperature of 1000K having a GMR = 0.44 was run for 73 ms (30 to 103 ms). The injection mass flow rate plot is presented in Figure 5.97, with the zoomed section of the plot showing the high frequency fluctuations. The initial fluctuation observed in the 1000K case is very similar to the 300K and 600K cases. Even as the initial fluctuation continued to attenuate, an onset of a higher frequency fluctuation was observed at 36.5 ms, persisting for the remainder of the simulation. The rise-and-fall in the mass flow rate that ensued the initial fluctuation in the 300K and 600K cases, is also noted in the 1000K case. On examining the higher frequency fluctuations, it became apparent that there were numerous irregular fluctuations present. An FFT analysis of the injection melt fluctuation (Figure 5.97) revealed frequencies of multiple levels in existence. The obtained frequencies were categorised

into three levels: low, mid, and high-frequencies and are listed in the Table 5-7. Out of the obtained frequencies, some of them were distinctly observable in the melt fluctuation plot (Figure 5.97), whereas the rest were not evidently observable. It was observed at t > 47 ms, the melt fluctuation exhibited a non-definite and varying low-frequency cycles displaying ~95 Hz, ~66 Hz, and ~77 Hz frequencies, sequentially. Similarly, at t > 47 ms the higher frequency fluctuations exhibited a repetitive pattern in its frequency. The pattern contained a single frequency fluctuation followed by a varying frequency fluctuation present in amplitude modulation. The observed repetitive single and varying frequency pattern is presented in Figure 5.97b&c, respectively. The single frequency was evaluated to be 8.5 kHz, whereas the varying frequency in amplitude modulation contained three frequencies - 8.5 kHz, 14.1 kHz, and 22.7 kHz, where 8.5 kHz was the modulating frequency, and 14.1 kHz, and 22.7 kHz were the carrier frequencies. Nevertheless, irrespective of the cyclic nature of the fluctuations, at t > 47 ms the amplitude of the fluctuations varied significantly throughout the flow-time.

Similar to the 300K and 600K cases, the 1000K case also consistently demonstrated that during the particles' flight downstream, higher frequency fluctuations are damped out, leaving only lower frequency fluctuations persisting. This is evident from the mass flow rate plot of the particles obtained at the outlet of the domain presented in Figure 5.98 at t > 75 ms. However, the reason for the continuous rise in the mass flow rate until 75 ms is unknown. In addition to this, the GMR for the 1000K case was evaluated to be 0.33 - 0.5, whereas for t > 47 ms the GMR ranged between 0.38 - 0.5.

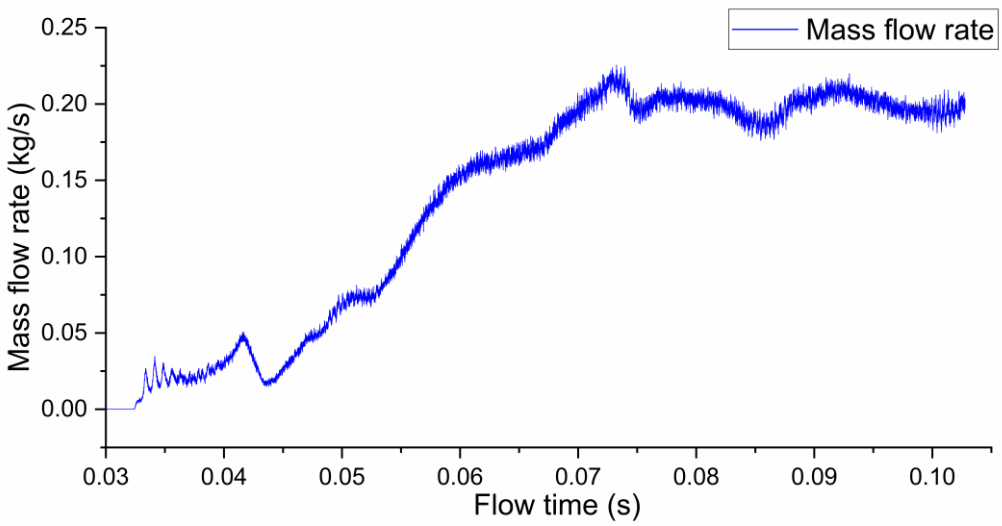

Figure 5.98 Mass flow rate of the particles for the 12 kg min^{-1}, 1000K case, obtained at the outlet of the domain. There is an initial steady increase in the flow of particles through the outlet. Following a brief decrease at 41 ms, a rapid rise is observed until 75 ms, after which the plot transforms into a much lower frequency fluctuation.

Unlike the changes noticed in the injection mass flow rate of the 1000K when compared to the previous cases, the particle trajectories were observed to be similar to that of the 300K and 600K cases with the exception of deviations in timing of pre-filming and melt movement downstream. The melt underwent pre-filming at 36.7 ms whereas for 600K case it is 36 ms. Similarly, the melt pool head that moved downstream due to the increased mass loading rejoined with the particles that were pushed downstream by the gas-jet, at 39.5 ms, and simultaneously it plunged into the first Mach-disk. Subsequently, at 44 ms the melt pool head plunged into the second Mach-disk.

Table 5-7 The frequencies obtained from FFT analysis of of 12 kg min^{-1}, 1000K case and their correlation to the flow-field fluctuations.

Flow time	**Frequency obtained from the FFT analysis.**	**Fluctuation observed in the flow field**
30 - 37 ms	1.4 kHz	• Initial fluctuation
37 - 44.5 ms	8.5 kHz	• 20 kHz observed between 34.7 - 36.3 ms • Irregular nested fluctuation that does not correspond any single frequency observed between 36.3 - 40 ms • Between 40 - 44.5 ms, nested fluctuation having 8.5 kHz and 14.3 kHz is observed. But the swaying is observed to fluctuate at 28.5 kHz.
	14.1 kHz 28.3 kHz	
44.5 - 47 ms	14.1 kHz	• 44.5 - 47 ms open- to closed-wake fluctuation (MICW) at 14.1 kHz.
t > 47 ms	8.5 kHz	• t > 47 ms, 8.5 kHz flow-field is not observed. • t > 47 ms the fluctuations were alternating between open- to closed-wake fluctuation and nested fluctuation, but they were not cyclic or regular in nature. • Irrespective of the nature of the fluctuation, whether the fluctuation underwent nested fluctuation or open- to closed-wake alternation, a single oscillation contained a frequency of fluctuation of 22 - 25 kHz.
	14.1 kHz (Superimposed on 8.5 kHz)	
	22.7 kHz (Superimposed on 14.1 kHz)	
Not obviously observable	82.4 Hz	Nil
	151.1 Hz	
	233.6 Hz	
	274 Hz	
	357.2 Hz	
	5.5 - 5.7 kHz	
	11.2 kHz	

Low frequency Mid frequency High frequency

Considering the velocity contours of the flow-field, the different flow-field fluctuation observed during the flow-time of the simulation is presented in Figure 5.99. The frequencies obtained via the FFT analysis, and its corresponding flow-field fluctuation are tabulated in Table 5-7. The initial fluctuation due to the melt introduction looked same as the fluctuation seen in the previous cases (300K and 600K cases), presented in Figure 5.89. Following the initial fluctuation at 31.6 ms, as the fluctuation continued to reduce in the amplitude of its spatial oscillation the flow-field transitioned into an open-wake condition as presented in Figure 5.90, and continued to exist in the same configuration until 34.7 ms.

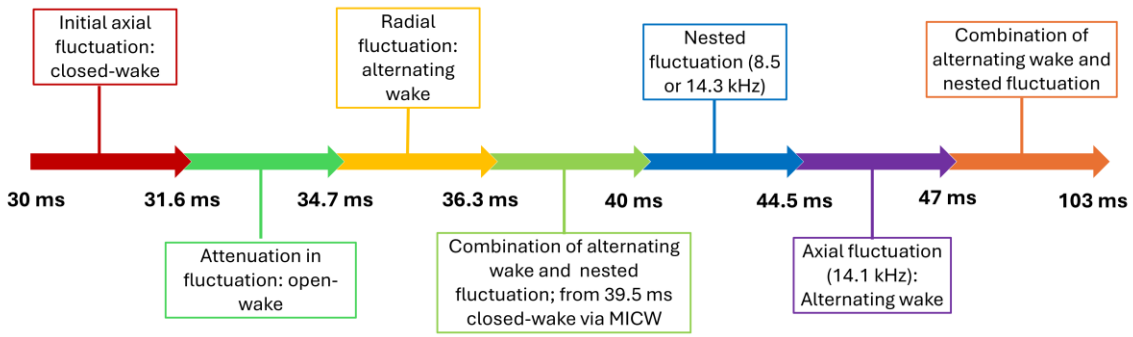

Figure 5.99 Timeline of flow-field fluctuations observed in 12 kg min^{-1}, 1000K case.

At 34.7 ms, the flow-field transitioned into an alternating wake, i.e., open- to closed-wake condition, but shortly thereafter, from 36.3 to 40 ms, the alternating flow-field fluctuation transitioned into a combination of alternating flow-field fluctuation and nested fluctuation. (Refer Section 5.3.4 and Figure 5.61 for nested fluctuations and swayings present within nested fluctuations). It is to be noted that the closed-wake condition observed in the flow-field from 39.5 ms onwards operated as MICW, since at 39.5 ms the melt pool head plunged into the first Mach-disk. (In Section 6.7 MICW is explained in detail). Subsequently, at 40 ms, the fluctuation transitioned into fluctuation having nested fluctuations only, as observed in Figure 5.81. The fundamental fluctuation (a single cycle of the fluctuation), i.e., from closed- to closed-wake condition fluctuated at either 8.5 kHz or 14.3 kHz, but the swayings within them always fluctuated at 28.5 kHz. On comparing the flow-field condition of the fluctuation against the melt fluctuation, it was observed the closed-wake condition corresponded to the local-minima of the melt fluctuation. However, for the swayings (which makes open-wake a part of it) no definitive correlation could be associated with the melt fluctuation.

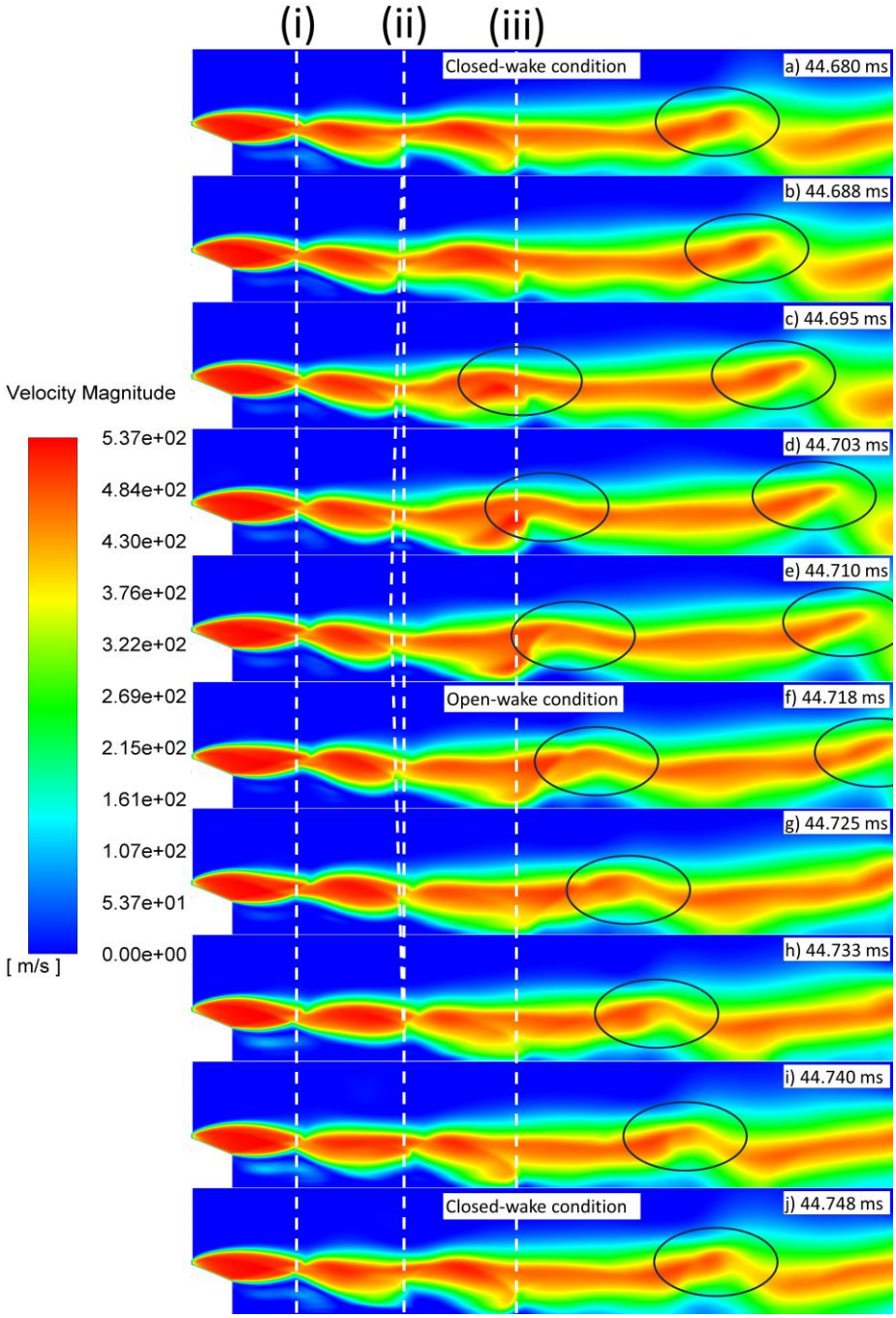

Figure 5.100 Velocity contours of the flow-field without particles for the 12 kg min^{-1}, 1000K case, showing a cycle of the alternating flow-field fluctuation. Three guide-lines, (i), (ii), and (iii), were pinned in frame a, at the downstream ends of the first, second and third shock-cell, respectively, and were compared against the rest of the frames. The first shock-cell remained fixed throughout the fluctuation, whereas the second shock-cell reduced in its spatial extent, and the third shock-cell underwent significant spatial movement downstream. The wave propagation is marked using ellipses.

Following this, the nested fluctuation transitioned into alternating flow-field fluctuation at 44.5 ms and continued to exist in this configuration until 47 ms. Unlike the other alternating flow-field fluctuations where the spatial extent of the shock-cell extended downstream, as seen in Figure 5.29, Figure 5.52, Figure 5.72, or remained in the same position, as shown in Figure 5.96, in this particular fluctuation it was observed that the spatial extent of the shock-cell reduced in its size during the fluctuation, making it unique and different to others. To better understand the fluctuation, series of the velocity contours obtained in closely spaced time intervals and were sequentially stacked and analysed. This is presented in Figure 5.100. Three guide-lines, (i), (ii) and (iii) were pinned in Figure 5.100a, at the downstream ends of the first, second and third shock-cell, respectively, and were compared against the rest of the frames. Another secondary guide-line was used to trace the extent of the second shock-cell's spatial oscillation. It was observed that the first shock-cell remained fixed and did not undergo any change in its spatial extent. Contrastingly, through the secondary guide-line, it is evident that during the fluctuation, the spatial extent of the second shock-cell reduced from its original spatial size. Furthermore, through guide-line (ii), it is seen the closed-wake present as MICW, seen in Figure 5.100a, gradually transitioned into an open-wake as found in Figure 5.100f, and subsequently returned back to its original configuration i.e., closed-wake condition, at the end of the fluctuation (Figure 5.100k). Also, through guide-line (iii), it is evident that the third shock-cell undergoes significant spatial oscillation downstream. In addition to the observed changes, a wave propagation can be also seen, starting from the end of the third shock-cell and continuing to propagate until the end of the domain, marked using ellipses. On examining this flow-field fluctuations against the melt fluctuations, it was evident that the closed-wake condition corresponded to the local-minima, and the open-wake condition corresponded to the local-maxima. The frequency of the fluctuation was evaluated to be 14.1 kHz.

At t > 47 ms the alternating flow-field fluctuation transitioned into a combination of alternating flow-field fluctuation and nested fluctuation, same as the fluctuation type observed between 36.3 - 40 ms. However, no specific cyclic pattern of fluctuation was discernible between the alternating and nested fluctuations. Furthermore, the nested fluctuation displayed an irregular number of swayings, complicating the observation of the flow-field fluctuations. Despite efforts to observe the flow-field fluctuations, it was evident that only the alternating flow-field fluctuations possessed a frequency of 23 kHz, whereas the nested fluctuations were irregular and lacked any single frequency that it could be associated with. Nevertheless, regardless of the nature of the fluctuations, whether open- to closed-wake alternation or

swayings present within the nested fluctuations, every single flow-field oscillation had a frequency of 23 kHz. Moreover, associating the flow-field fluctuation with the melt fluctuation further became increasingly challenging. Only to a certain extent, the closed-wake conditions in the flow-field fluctuation corresponded to the local-minima of the melt fluctuation. This is because, when the melt fluctuations seen in the injection mass flow rate plot that do not have any superimposed frequencies, i.e., without modulation, are compared to their respective flow-field fluctuations, they exhibit nested fluctuation, rather than the expected alternating flow-field fluctuation, thus complicating the task of associating the open-wake condition to the melt fluctuations.

5.5.4 Summary

The 12 kg min^{-1} (GMR=0.44) cases with increasing melt temperature exhibited similar trends to that of the 4 kg min^{-1} and 6 kg min^{-1} cases. However, in the 12 kg min^{-1} model, the melt instability accelerated more rapidly with rising melt temperature compared to the lower mass flow rates. The cases can be divided into two categories: a) T=300K, and b) T ≥ 600K cases. The 300K cases exhibited highly regular and large amplitude fluctuations, whereas T ≥ 600K cases did not exhibit one consistent mode of fluctuation. However, T=600K case displayed a regular low frequency fluctuation although the high frequency observed was highly irregular. But with the increase in melt temperature to T = 1000K, sharp rise in irregular instability was induced in the melt flow rate, both in its amplitude and in its frequency. This increased randomness was also reflected on to the flow-field fluctuations.

The flow-field fluctuations for the 12 kg min^{-1} cases were generally irregular and inconsistent in nature, unevenly spread across the flow-time, albeit the 300K case exhibited a definitive pattern in its flow-fluctuation. In the higher melt temperature cases, especially in the 1000K case, the flow-field fluctuations were extremely random and unpredictable. The fluctuations were observed to undergo both axial and radial mode of fluctuations, and at the same time it possessed both nested fluctuation and alternating wake fluctuation. The fluctuations were so random, no specific cyclic pattern of fluctuation was discernible between the alternating and nested fluctuations. The complexity in the process further increased due to the irregular number of swayings within the nested fluctuations. Thus, the simulation runs of 12 kg min^{-1} provided deep insights into the CCGA operation, reflecting the physical gas atomisation process, and its random and chaotic environment present within it.

6 Discussion

In this section, the various key characteristics of the simulation developed due to the gas-melt interactions are discussed based on the analysis from the 22 simulation runs (Table 4-6).

6.1 Melt fluctuation behaviour over increasing mass flow rates.

Melt fluctuation behaviour was observed over decreasing GMRs for a fixed melt temperature. It was observed that the melt fluctuation behaviour could be broadly classified into two categories: a) GMRs with 300K in one group, and b) GMRs with rest of the melt temperatures (600K, 1000K, 1500K and 2000K) as the other group. In category a), it was observed for cases having GMR=5.5 (Figure 5.2) and GMR=2.6 (Figure 5.23), the melt initially fluctuates, but subsequently reaches a steady mass flow rate. This is due to the high GMR, that the gas dominates and attenuates the melt fluctuations in the due course of time. However, for lower GMRs of 1.32 and below, the melt fluctuations display regular and well-defined fluctuations. This is observed in Figure 6.1, where all the three melt flow rates display same frequency of oscillation after the initial fluctuation. It is observed, with the decrease in the GMR from 1.32, there is a corresponding increase in the amplitude of their fluctuation, i.e., with the increasing melt flow rate, the amplitude of the fluctuation also increases. Although the increase in the amplitude of the melt fluctuation is reflected in their gas flow-field fluctuations, wherein the amplitude of the spatial oscillation increase, they were not as proportional to the increase in their amplitudes seen in the Figure 6.1.

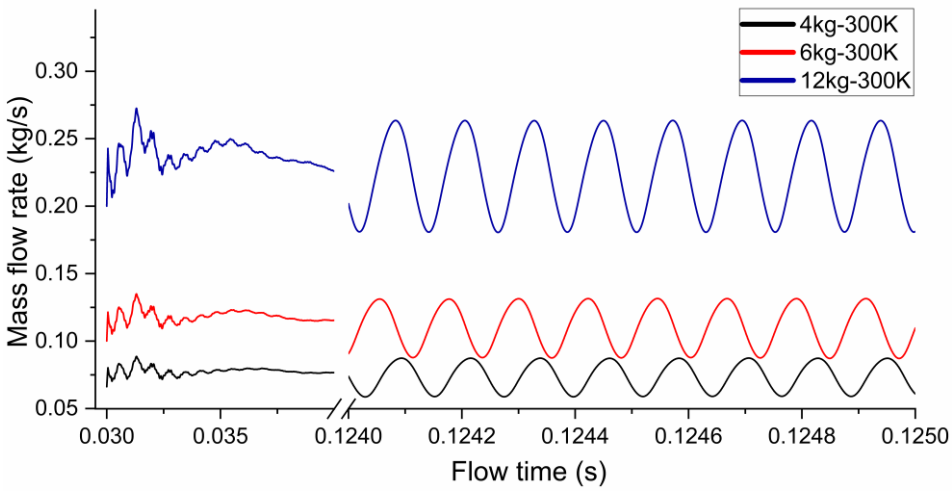

Figure 6.1 Mass flow rate plot of the melt injection for cases 4 kg min^{-1} (GMR=1.32), 6 kg min^{-1} (GMR=0.88), and 12 kg min^{-1} (GMR=0.44) all having a melt temperature of 300K; the plots exhibits a constant frequency but increasing amplitude with increasing mass flow rates.

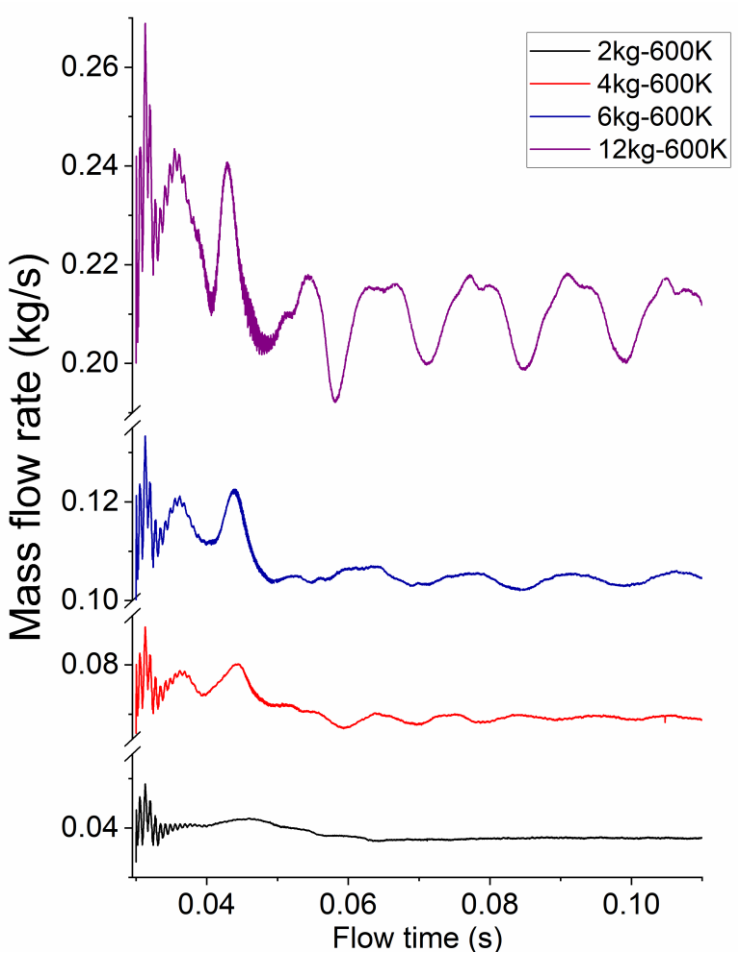

Figure 6.2 Stacked melt injection plot of 2 kg min^{-1} (GMR=2.6), 4 kg min^{-1} (GMR=1.32), 6 kg min^{-1} (GMR=0.88), and 12 kg min^{-1} (GMR=0.44) cases, all obtained at 600K, displaying varying frequency and amplitude with decreasing GMR.

Unlike, category a), a different set of observations were noted in category b). With the decrease in the GMR, the melt injection evolves to develop into a fluctuation having a varying frequency and amplitude as observed in Figure 6.2, shown for the melt injection of 2 kg min^{-1} (GMR=2.6), 4 kg min^{-1} (GMR=1.32), 6 kg min^{-1} (GMR=0.88), and 12 kg min^{-1} (GMR=0.44) cases all having a melt temperature of 600K. Moreover, for the lower GMRs of 0.44 (12 kg min^{-1}) and to a certain extent in 0.88 (6 kg min^{-1}), the melt fluctuations are not regular or well-defined compared to what is observed in Figure 6.1, but rather display a fluctuation containing multiple frequencies superimposed. This trend of frequencies and amplitude varying with decreasing GMR can be more distinctly observed for melt temperatures of 1000K, 1500K and 2000K. In addition to the above trend, the decrease in GMR induces multiple levels of frequencies into the melt fluctuation, adding complexity and chaotic behaviour to the process.

It is also interesting to observe from Lubanska relation, $D_{50} = \varphi/\sqrt{GMR}$ (McCarthy et al., 2013), which gives an empirical relation between the D_{50} and GMR (where φ is the constant dependent on the atomiser), that with decreasing GMR bigger particle size is obtained which directly infers to the increasing instability in the process. Considering three values of φ – 40, 60 and 80, out of the range of 40-80 as mentioned by Lubanska (1970), predicted values of D_{50} are calculated and are tabulated in Table 6-1. Although this calculation is a predictive analysis, this trend in increasing particle size endeavours to help in the understanding how significantly GMR can affect the process instability.

Table 6-1 Predictive calculation of D_{50} based on different GMRs and model constants.

GMR	**D_{50} (µm)**		
	φ = 40	**φ = 60**	**φ = 80**
5.50	17.056057	25.584086	34.112115
2.60	24.806947	37.210420	49.613894
1.32	34.815531	52.223297	69.631062
0.88	42.640143	63.960215	85.280287
0.44	60.302269	90.453403	120.604538

6.2 Melt fluctuation behaviour over increasing melt temperatures.

Across a given GMR, on comparing the melt injection plots for increasing melt temperatures it was confirmed that the melt injection displayed incremental increase in its instability. And this increasing instability, continued to intensify across lower GMRs. The melt fluctuation can be classified into two categories based on the GMR: a) 5.5 and 2.6 (1 and 2 kg min^{-1}, respectively), and b) 1.32, 0.88 and 0.44 (4, 6, and 12 kg min^{-1}, respectively). In category a) the generally observed trends were: melt fluctuation for the 300K and 600K cases attained steady-state over time, whereas higher melt temperatures 1000K, 1500K and 2000K possessed a sustained higher frequency throughout the process. Nevertheless, the higher temperature cases exhibited almost constant amplitude, indicating they are relatively stable, except for the 2 kg min^{-1}, 1500K case which exhibited a low frequency modulation. The above-mentioned characteristics can be seen in Figure 6.3 and Figure 6.4, shown for cases having GMRs of 5.5 and 2.6, respectively.

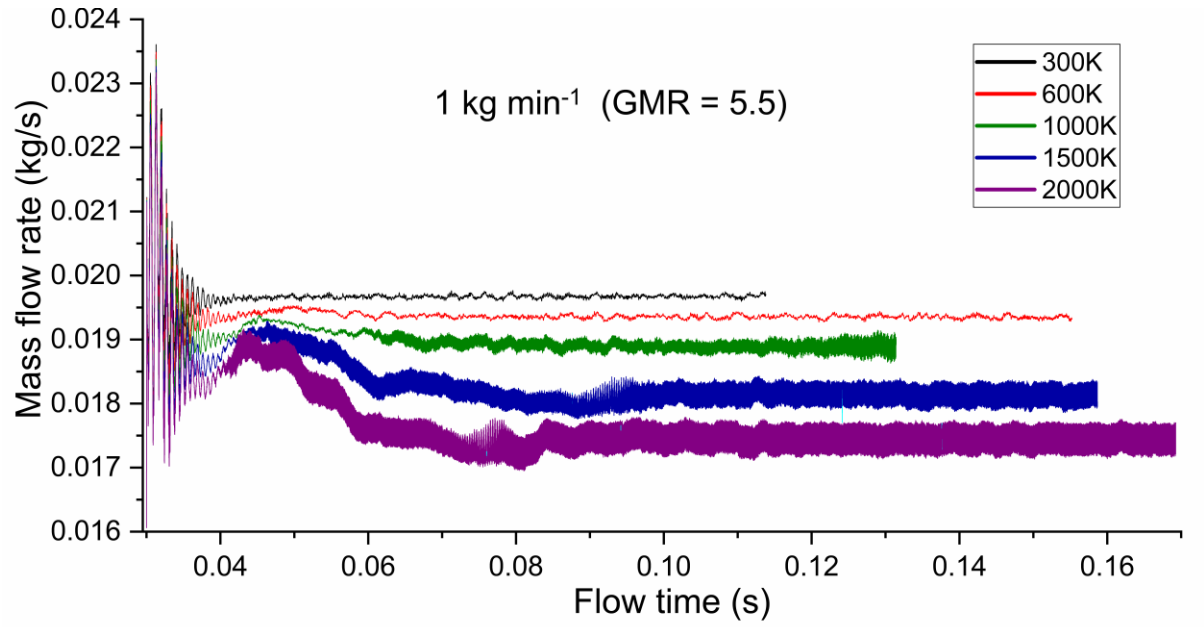

Figure 6.3 GMR=5.5 (1 kg min^{-1}) case showing all the five different melt injection plots corresponding to melt temperatures, 300K, 600K, 1000K, 1500K, and 2000K.

In addition to this, in category a) it was observed in Figure 6.3 and Figure 6.4 that with the increase in melt temperature the average injected mass flow rate reduces. This is because, with the increase in melt temperature, due to the heat transfer, the wake region gains thermal energy leading to higher (positive) aspiration pressure, effectively reducing the amount of melt that could be drawn into the atomiser.

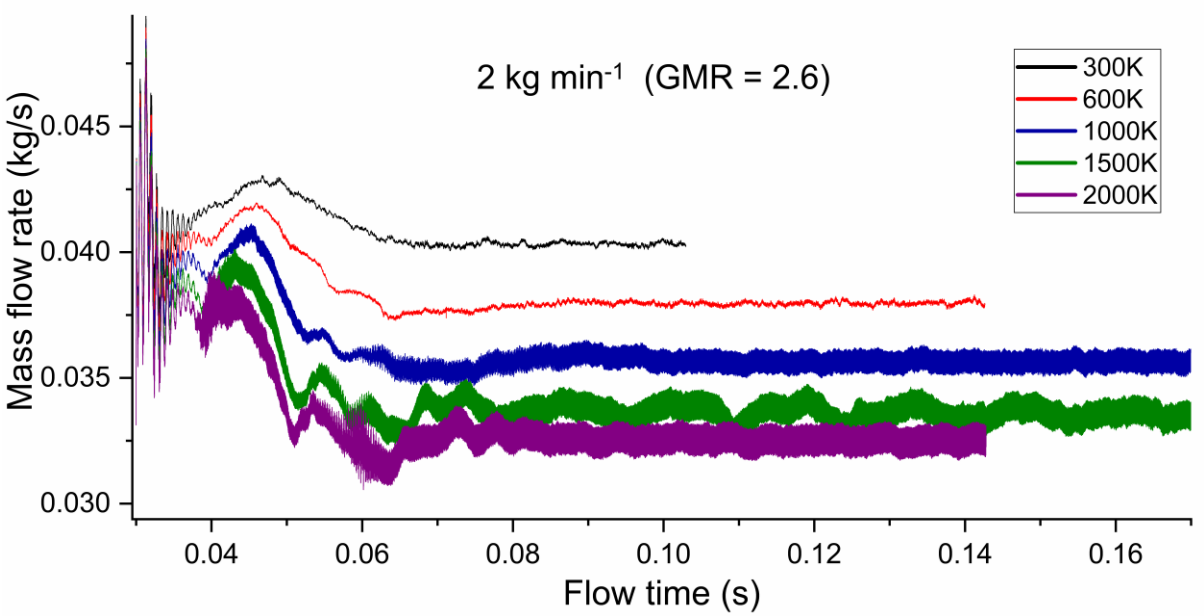

Figure 6.4 GMR=2.6 (2 kg min^{-1}) case showing all the five different melt injection plots corresponding to melt temperatures, 300K, 600K, 1000K, 1500K, and 2000K.

In category b), i.e., GMR cases of 1.32, 0.88 and 0.44, the melt injection for the 300K cases were well-defined and regular in nature, whereas for higher melt temperatures, the melt injection exhibited progressive growth in its instability over increasing temperature. Nevertheless, a paradigm shift in the nature of the melt injection is observed between 300K and 600K. The high amplitude and regular fluctuation seen in the 300K case transitions into a low amplitude but irregular fluctuation in 600K. This is observed in the injection plots shown in Figure 6.5 for the GMR=1.32 (4 kg min^{-1}) case, containing all the five melt temperatures cases, 300K, 600K, 1000K, 1500K, and 2000K. This instability seen in the 600K case continues to further increase progressively in the 1000K and 1500K cases, wherein both the frequency and amplitude of the fluctuation varies continuously. Subsequently, in the 2000K case, it evolves into a melt fluctuation chaotic and unpredictable in nature.

Even as the trend seen in category a), wherein the average injected mass flow rate decreased with increase in the melt's temperature, the same trends is also observed in category b) as presented in Figure 6.5, but comparatively less than that shown in Figure 6.4. This progressive growth in instability seen across increase melt temperature of GMR=1.32, further increases in the lower GMRs. Only results of GMR=1.32 case is presented in Figure 6.5. Results of GMR=0.88 and 0.44 cases are present in sections 5.4 and 5.5, respectively. Comparing this with physical atomisation process, it can be implied that for alloys having higher melting temperature, the process can be expected to be more chaotic and unsteady compared to that of alloys with lower melting temperatures. It is understood that thermal energy plays an important role in inducing and maintaining the instability in the process, however, the origin of its instability is yet not clearly understood.

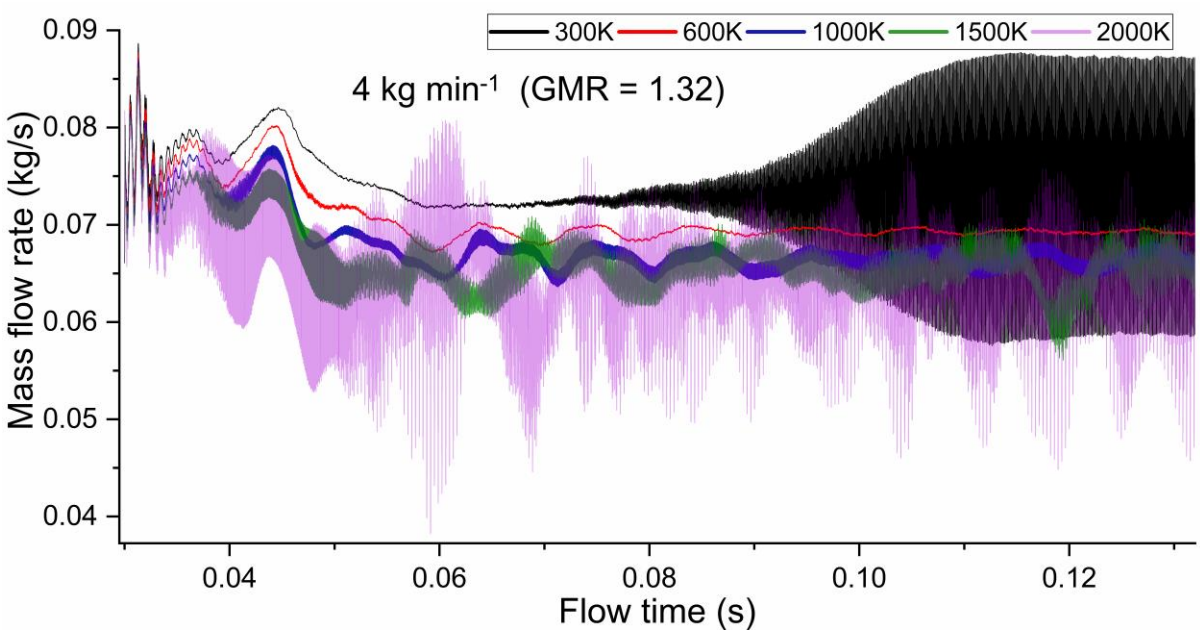

Figure 6.5 GMR=1.32 (4 kg min^{-1}) case showing all the five different melt injection plots corresponding to melt temperatures, 300K, 600K, 1000K, 1500K, and 2000K.

6.3 The exhibited frequencies of melt fluctuation and its trends and similarities

From sections 6.1, and 6.2, it is now established that with either decrease in GMR or increase in melt temperature or both results in increased instability in the melt injection. These comparisons are made with GMR=5.5 (1 kg min^{-1}), 300K case as the reference case. In order to understand how the above two parameters (GMR and melt temperature) contribute to the melt instability, the flow time at which the melt instability onsets is recorded, and tabulated. This is presented in Table 6-2. As observed from Table 6-2, the 300K and 600K cases of GMR=5.5, and GMR=2.6 achieve steady melt flow, whereas all the other temperatures and GMRs possess melt fluctuation. Overall observations indicate that across a given GMR, for increasing melt temperatures the melt instability develops into the process quicker than its predecessor. However, for decreasing GMRs, the melt instability can grouped into two temperatures: a) 300K and b) rest of the temperatures. In the 300K cases, all GMRs have a very similar onset of melt instability, ~60 ms, whereas for the rest of the melt temperatures, the instability develops much quicker than its predecessor GMR. The onset of the melt instability seen in Table 6-2 is plotted on graph presented in Figure 6.6 for better understanding. From Figure 6.6, it is evident majority of the melt instability appears to develop between a narrow time frame as observed in the shaded grey region, indicating a critical relationship exists between the thermal parameters of the gas flow-field and the melt in the wake region. However, the mechanism of the onset of melt instability and its accelerated onset with decreasing GMRs

and increasing melt temperatures is not yet understood. Nevertheless, it is clear that there exists an underlying relationship between thermal conditions and the onset kinetics of the melt instability in the process.

Table 6-2 Onset of melt instability recorded in ms.

Cases	GMR - 5.5 (1 kg min^{-1})	GMR - 2.6 (2 kg min^{-1})	GMR - 1.32 (4 kg min^{-1})	GMR - 0.88 (6 kg min^{-1})	GMR - 0.44 (12 kg min^{-1})
300K	Steady	Steady	60 ms	58 ms	60 ms
600K	Steady	Steady	45 ms	39 ms	38 ms
1000K	60 ms	40 ms	39 ms	38 ms	36.5 ms
1500K	43 ms	40 ms	36 ms	36 ms	-
2000K	40 ms	38 ms	32.6 ms	-	-

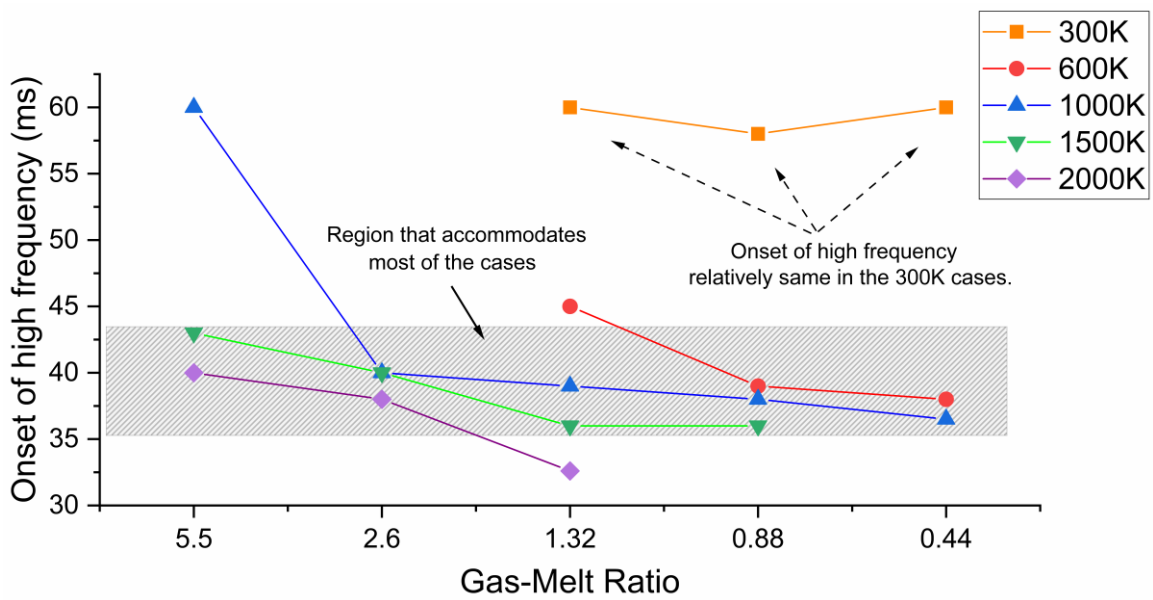

Figure 6.6 Onset of melt instability in ms observed for different GMRs and melt temperatures. 300K cases exhbited very similar times of onset of melt instability.

From Figure 6.2 and Figure 6.5 and Table 6-2 it is observed that either decrease in GMR (section 6.1) or increase in melt temperature (section 6.2), not only accelerates the onset of melt instability, but also increases its complexity. To further understand the instabilities and their relationships, all the melt frequencies obtained via the FFT analysis are tabulated for each of the case. This is presented in Table 6-3, where the frequencies are divided into low-frequency (L.F), mid-frequency (M.F) and high-frequency (H.F). Upon analysis of Table 6-3 it is observed that certain frequencies were consistent across all the cases irrespective of their GMR or melt temperature, and they are 1.4 kHz, ~8.1 kHz, and ~25.6 kHz. The 1.4 kHz is the melt frequency of the initial fluctuation, whereas the ~8.1 kHz, and ~25.6 kHz are part of the melt instability, and they are highlighted in Table 6-3 in green and pink, respectively. The ~8.1 kHz

is consistently seen for cases having GMR = 1.32 and smaller, indicating an existance of an underlying critical GMR that induces this low frequency in the process. Similarly, ~25.6 kHz is consistently seen for cases having melt temperatures 1000K and above, indicating, high temperatures induce higher instabilities, resulting in high frequencies, although few exceptions to this are seen in 300K case of GMR=0.44, and 600K cases of GMR=0.88 and 0.44. On comparing the two consistent melt fluctuation frequencies (~8.1 kHz, and ~25.6 kHz) in Table 6-3 against the flow-field fluctuations, it is noted only the lower melt temperature cases exhibit the ~8.1 kHz frequency consistently in their flow-field fluctuations, whereas the flow-field fluctuations of the higher melt temperatures exhibits only higher frequencies, albeit ~25.6 kHz is inconsistently observed, indicating irrespective of the GMR, at higher melt temperatures the process is affected by the melt temperature to much higher degree than the GMR.

Table 6-3 Various frequencies obtained via FFT analysis

Cases	GMR - 5.5 (1 kg min^{-1})			GMR - 2.6 (2 kg min^{-1})			GMR - 1.32 (4 kg min^{-1})			GMR - 0.88 (6 kg min^{-1})			GMR - 0.44 (12 kg min^{-1})		
	L.F	M.F	H.F	L.F	M.F	H.F	L.F	M.F	H.F	L.F	M.F	H.F	L.F	M.F	H.F
300K	1.4 kHz	-	9.1 kHz	1.4 kHz	-	19.7 kHz	1.4 kHz	8.1 kHz	16.3 kHz	56 Hz	1.4 kHz	8.1 kHz	90 Hz 169.3 Hz 249 Hz	1.4 kHz 8.1 kHz	16.3 kHz 24.5 kHz
600K	1.4 kHz	-	9.1 kHz	1.4 kHz	-	19.7 kHz	96 Hz 158 Hz 1.4 kHz	8.1 kHz	19.8 kHz	66 Hz 91 Hz 149 Hz 232 Hz 1.4 kHz	8.6 kHz 9.1 kHz	28.5 kHz	71 Hz 166.6 Hz 249 Hz 375 Hz	1.4 kHz 8.4-9.1 kHz	13.9 kHz 28.3-28.6 kHz
1000K	1.4 kHz	-	28.5 kHz	1.4 kHz	-	25.4 kHz	91 Hz 159 Hz 1.4 kHz	8.5-9.1 kHz	25.6 kHz	91.6 Hz 158.2 Hz 233 Hz 274 Hz 316 Hz 358 Hz 1.4 kHz	8.6 kHz 11.3 kHz 13.2 kHz	25.6 kHz 28.6 kHz	82.4 Hz 151.1 Hz 233.6 Hz 274 Hz 357.2 Hz	1.4 kHz 5.5-5.7 kHz 8.5 kHz	11.2 kHz 14.1 kHz 22.7 kHz 28.3 kHz
1500K	1.4 kHz	-	25.5 kHz	1.4 kHz	-	25.4 kHz	56-88 Hz 1.4 kHz	8.6 kHz 11.4 kHz 14.3 kHz	22.8 kHz 25.6 kHz 28.6 kHz 31.4 kHz	87 Hz 125 Hz 154 Hz 261 Hz 1.4 kHz	2.7-2.9 kHz 5.6-5.8 kHz 8.2-8.5 kHz 11.2 kHz 14.1-14.3 kHz	22.7 kHz 25.6 kHz 28.5 kHz	–	–	–
2000K	1.4 kHz	-	25.5 kHz	1.4 kHz	-	25.4 kHz	2.6-3.0 kHz 5.4-5.8 KHz	8.5-8.6 kHz 11.3 kHz 14.3 kHz 16.8-17.5 kHz	19.2-20.2 kHz 22.8-25.8 kHz 28.5-28.8 kHz 31.1-31.5 kHz	–	–	–	–	–	–

Similar to the two consistent frequencies that has been obtained via FFT analysis seen in Table 6-3, there also exist pattern in the melt instabilities observed between cases. Hence the nature of the melt injection plot for each of the cases is analysed and are categorised into their melt fluctuation modes. The instability-map, indicating the mode of melt fluctuation for each

of the 22 simulations is presented in Table 6-4, and their characteristics for each of the modes are explained in Table 6-5. The higher GMRs of 5.5 and 2.6 exhibit consistency in their mode of fluctuation, with an exception to 1500K case of GMR = 2.6. The 300K and 600K cases achieves steady-state, whereas the 1000K and above cases exhibits 'H.F Near-regular' mode of fluctuation. As discussed in section 6.1 via Figure 6.1, and through Figure 6.6, it is more evident that the 300K cases, for all the GMRs are either steady or regular in nature, even holding similar timing in the onset of melt instability. Similarly, the 600K cases for the lower GMRs of 1.32 and below do not possess any significant melt instability, reflecting the above-mentioned processes far from actual physical atomisation. However, the 1000K, 1500K and 2000K cases for GMR=1.32 and below, reflects the physical atomisation process, wherein the irregularity and randomness observed in the physical process becomes more evident, indicating the higher complexity present in the process. The cases having higher melt temperatures and lower GMRs, such as the 1000K cases of the GMR=0.88 and 0.44, and the 1500K and 2000K cases of the GMR=1.32 follow the 'H.F Highly Irregular' mode of melt fluctuation which in essence, is unpredictable and chaotic in nature as seen in the physical atomisation process. Hence to outline this region where the process becomes increasingly random, unpredictable and complex, a box with darker outline is drawn in Table 6-4. Table 6-3 and Table 6-4 evidently reveal that the melt temperature is of far more great significance than the GMR. The higher melt temperatures not only induce melt instability in the form of multiple melt fluctuation frequencies, but also introduces irregularity and uncertainty into the process.

Table 6-4 Melt instability-map, showing the mode of melt fluctuation.

Cases	**GMR - 5.5 (1 kg min^{-1})**	**GMR - 2.6 (2 kg min^{-1})**	**GMR - 1.32 (4 kg min^{-1})**	**GMR - 0.88 (6 kg min^{-1})**	**GMR - 0.44 (12 kg min^{-1})**
300K	Steady-state	Steady-state	H.F Very Regular	H.F Very Regular	H.F Very Regular
600K	Steady-state	Steady-state	No H.F but irregular	No H.F but Regular	No H.F but Regular
1000K	H.F Near-regular	H.F Near-regular	H.F Moderately irregular	H.F Highly Irregular	H.F Highly Irregular
1500K	H.F Near-regular	H.F Moderately irregular	H.F Highly Irregular	H.F Highly Irregular and complex pattern	-
2000K	H.F Near-regular	H.F Near-regular	H.F Highly Irregular	-	-

Table 6-5 Different modes of melt fluctuation and their characteristcs observed during the melt injection.

Steady-state	The melt achieves steady-state reaching a constant mass flow rate.
H.F Near-regular	The melt undergoes high frequency fluctuation; possess a near-constant baseline with minor instabilities.
H.F Moderately irregular	The melt undergoes high frequency fluctuation; do not possess a constant baseline and possess varying amplitude.
H.F Very Regular	The melt undergoes high frequency fluctuation; possesses a constant baseline; and its amplitude follows a regular or well-defined pattern.
H.F Highly Irregular	The high-frequency melt fluctuation is extremely irregular, without containing fixed frequency and amplitude; the changes in its frequency and amplitude are unpredictable and do not follow any pattern.
No H.F but irregular	The melt fluctuation does not possess any high-frequency fluctuation; does not possess a fixed amplitude.
No H.F but Regular	The melt fluctuation does not possess any high-frequency fluctuation; does possess a fixed amplitude, and a constant baseline.
H.F Highly Irregular and complex pattern	The melt undergoes high frequency fluctuation; possess varying frequency and amplitude, however, the overall trend appears to exhibit a complex pattern in its fluctuation.

6.4 Trends in melt fluctuation both across increasing mass flow rates and its melt temperatures.

Although a few cases, having higher GMRs, and lower melt temperatures can be said to be highly stable (Table 6-4), where it achieves steady state, yet the progressive instability can be observed even in these models when compared against the reference case – 300K case of GMR = 5.5 (1 kg min^{-1}). This can be explained using 1 kg min^{-1}, 600K case (Figure 6.3) and 2 kg min^{-1}, 300K case (Figure 6.4), which are the immediate next increments to the reference case. In the former case, a marginal but evident rise and fall in the mass flow rate is observed after the initial melt fluctuation (Figure 5.8), demonstrating deviation in the mass flow rate from the reference case. Similarly, in the latter, a significant and extended rise and fall in the mass flow rate is observed after the initial melt fluctuation (Figure 5.23). Likewise, with further increments in GMR or melt temperatures, the melt instability is increasingly profound, leading to the conclusion that both increasing GMR and melt temperatures contributes to the melt

instability, nevertheless, the dominant parameter is melt temperature compared to the GMR, corroborating with section 6.3.

6.5 Behaviour of the melt in the wake region during decreasing GMR and increasing melt temperatures.

With the melt temperature increasing across a given GMR, the time taken for the melt to undergo pre-filming also increases. Table 6-6 presents the different time at which the melt undergoes pre-filming. From Table 6-6, considering GMR = 5.5 as an example, the delay in the pre-filming is evident wherein the 300K case undergoes pre-filming at 31.5 ms, but 2000K undergoes pre-filming at a later time – 32.0 ms. The delay in the pre-filming time in the higher melt temperature cases is the due to the following reason: melt entering into the atomiser alters the recirculation zone, and with the heat being transferred from the melt to the gas in the recirculation zone, it gains thermal energy, subsequently increasing its velocity locally as presented in Figure 6.7. The higher velocity flow travels radially outward, swiftly pulling the melt radially away. Hence, compared to the 300K case, in the 2000K case, due to the increased radially velocity, a significantly higher proportion of the melt that entrains into the atomisation chamber, swiftly travels radially away, subsequently, comes in contact with supersonic gas-jet and thereafter moves downstream. With lesser melt available in the melt nozzle front, the melt touches the melt nozzle tip at a later time, leading to the delayed pre-filming time. In addition to the melt temperature, the GMR also affects the pre-filming. With decreasing GMR, increasing pre-filming time is observed (Table 6-6). This is due to the increased momentum possessed by the melt at higher mass flow rates, the melt travels downstream a considerable distance before getting advected and subsequently travels upstream to undergo pre-filming. It is also evident with decreasing GMR, the gap in the pre-filming time increases across any given melt temperature. For the cases of GMR=5.5 it ranged between 31.5 to 32.0 ms, containing a gap of 0.5 ms, whereas for the cases of GMR=2.6, the gap increased to 0.9 ms and further for GMR=1.32 cases to 4.5 ms. However, between GMR = 0.88 and 0.44, the trend is reversed. The gap between 300K and 1000K cases for GMR = 1.32 was calculated be 1.5 ms; for GMR = 0.88 it is 2.3 ms; but for GMR = 0.44 the gap in the pre-filming time reduced to 1.1 ms. This reversal in the pre-filming time might be a direct result of the momentum possessed by the melt, wherein at significantly high mass flow rates, the momentum of the melt dominates the influence of melt temperature for pre-filming.

In the physical atomisation, the pre-filming process is affected by various factors, both influenced by the melt properties and atomiser's operating parameters. Melt with increased surface tension tend to stay cohered, resulting in poor primary and secondary atomisation (Gepperth et al., 2010). However, with increase in temperature, the surface tension of the melt reduces, which is one of reason why melt with higher melt temperatures undergo finer atomisation compared to that of lower melting temperatures. Similarly, wetting angle of the melt on the melt nozzle tip proves to be a very vital parameter for executing better atomisation. Wetting angle is affected by both surface tension and by nozzle's material. Increased surface tension results in poor wetting angle, and likewise nozzle materials such as ceramics also result in poor wetting. Apart from these, melt with higher viscosity prevents the deformation of the melt layers, leading to poor pre-filming and poor atomisation (Liu et al., 2007).

Table 6-6 Time taken in ms to undergo pre-filming for different simulations.

Cases	**GMR - 5.5 (1 kg min^{-1})**	**GMR - 2.6 (2 kg min^{-1})**	**GMR - 1.32 (4 kg min^{-1})**	**GMR - 0.88 (6 kg min^{-1})**	**GMR - 0.44 (12 kg min^{-1})**
300K	31.5	32.0	32.5	33.8	35.6
600K	31.6	32.1	33.1	35.7	36.0
1000K	31.7	32.5	34.0	36.1	36.7
1500K	31.9	32.7	36	36.6	-
2000K	32.0	32.9	37	-	-

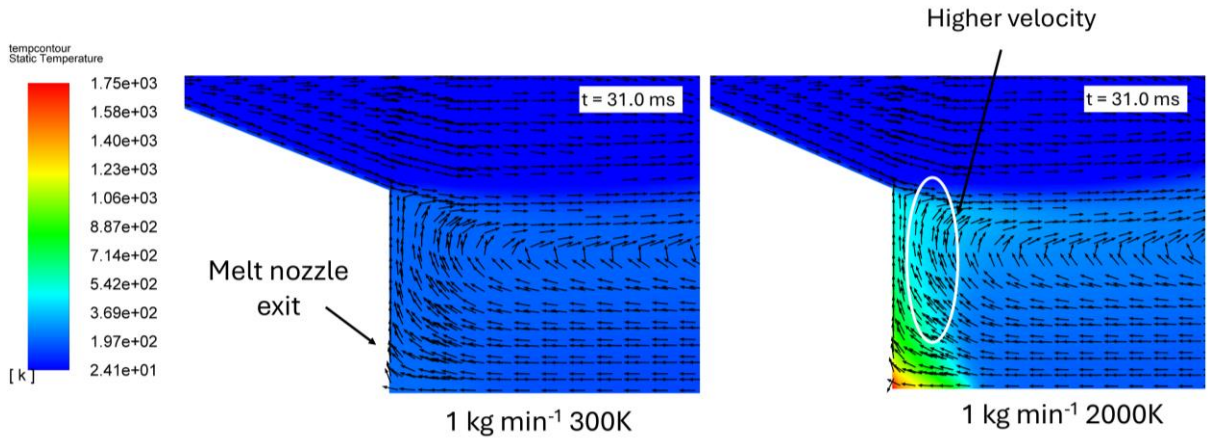

Figure 6.7 Temperature contours with flow vectors showing the flow direction for the 1 kg min^{-1} 300K and 2000K cases taken at 31 ms. Temperature contour of the 2000K indicates the region of elevated temperature reflecting the higher velocity in that region.

The delay in the pre-filming time due to the increased momentum for the lower GMR cases, seen in the Table 6-6 is corroborated by Table 6-7. Table 6-7 presents the time taken by the melt pool head to rejoin with the particles that are pushed downstream following the pre-filming process, recorded across decreasing GMR and their respective melt temperatures,

except for all cases of 1 kg min^{-1} and 300K case of 2 kg min^{-1}. In all the five cases of GMR=5.5, and 300K case of GMR=2.6, the melt pool head do not rejoin with the particles downstream, as they stabilise in their movement downstream at different locations, measured in nozzle-diameters (N_d). Hence the flow time when the melt pool head stabilises and its corresponding distance downstream where they stabilise are recorded and tabulated in Table 6-7. It is evident, in decreasing GMR cases, due to the higher momentum possessed by the melt, the rejoining time decreases. Moreover, the decrease in rejoining time is also observed for increasing melt temperatures as well. This is because, at higher melt temperatures, the gas in the wake region heats up, resulting in lower pressure than its predecessor's melt temperature. As a consequence, there is a reduced opposing force acting against the downstream movement of the melt pool head, allowing for melt pool head to rejoin with the particles downstream quicker than its predecessor's melt temperature. Although it may be expected for the pressure to rise with increase in temperature, it is observed otherwise in the higher melt temperature cases. This is also discussed in section 6.8 which presents the pressure fluctuation in the wake region for two different melt temperatures, 300K and 1000K cases, of GMR=1.32 (4 kg min^{-1}), demonstrating the 300K case possess higher pressure than the 1000K case. Even though section 6.8 discusses the pressure fluctuation for GMR=1.32 cases, the same is applicable to GMR=5.5 cases.

Similar to the decreasing rejoining time observed across decreasing GMR and across increasing melt temperatures, it also seen that the gap in the rejoining time decreases across decreasing GMR cases. Comparing the 300K and 1000K cases of GMR=1.32, the rejoining gap is 2.7 ms; for GMR=0.88 the gap is 1 ms; and for GMR=0.44 it's only a mere 0.3 ms. This is because at lower GMRs the momentum of the melt dominates.

Table 6-7 Table showing the time taken for melt pool head to rejoin with the particles that are pushed after pre-filming for different simulations.

Cases	**GMR - 5.5 (1 kg min^{-1})**	**GMR - 2.6 (2 kg min^{-1})**	**GMR - 1.32 (4 kg min^{-1})**	**GMR - 0.88 (6 kg min^{-1})**	**GMR - 0.44 (12 kg min^{-1})**
300K	2 N_d (57 ms)	4.3 N_d (70 ms)	47 ms	43.5 ms	39.8 ms
600K	2.5 N_d (63 ms)	58 ms	45 ms	43 ms	39.5 ms
1000K	3 N_d (69 ms)	52 ms	44.3 ms	42.5 ms	39.5 ms
1500K	4 N_d (72 ms)	49 ms	43.8 ms	42.5 ms	-
2000K	4.3 N_d (76 ms)	47 ms	43.5 ms	-	-

In all the five cases of 1 kg min^{-1} , and 300K case of 2 kg min^{-1}, the melt pool head do not rejoin with particles downstream, as they stabilise at different N_d. Hence their N_d and corresponding ms where stabilise are mentioned

A notable contrast observed between the steady cases recorded in Table 6-2 and those in Table 6-7 is that, the 600K case of GMR=2.6, is steady in its melt injection (Figure 5.30) but

contrastingly the melt pool head continues to move downstream without stabilising (Figure 5.32). The dynamics of the melt moving downstream overcoming the counteracting flow in the recirculation zone, and gas flow-field effectively attenuating the melt fluctuation (Figure 5.30) is not yet understood. In addition to this, a reverse phenomenon is also observed on comparing Table 6-2 and Table 6-7, where the melt pool head stabilises at different N_d without moving downstream (Table 6-7), but exhibits continuous melt fluctuation (Table 6-2). This is seen in GMR=5.5 cases having melt temperatures 1000K and above. The dynamics of melt stabilising due to the strong gas jet but exhibiting continuous melt fluctuation is also not yet understood.

6.6 Effect of GMR with increasing melt temperatures beyond the wake region, and gas - melt interaction far downstream.

With the melt behaviour observed and discussed in section 6.5, sequences of events that happen beyond the wake region is also useful to understand the process from a holistic point of view, since the particles traverse the entire length of the atomiser. As observed in Section 5.2.2 and later (higher mass loading), the melt pool head that continues to move downstream to rejoin with particles following pre-filming, continues further downstream to plunge into the Mach-disk, and eventually reaches the end of the domain. This phenomenon is observed in Figure 5.32 and Figure 5.35. This observed layer of melt that moves downstream until the end of the domain is not a continuous layer, but a region in which the density of particles are high. The thickness of the melt layer is quantified and is presented in Table 6-8. The melt layer thickness within the wake region varies due to the continuous and direct action of the gas-jet impinging on the melt layer. However, beyond the third shock-cell and far field downstream, the energy of gas-jet attenuates to become insignificant and hence, the melt layer thickness was recorded far downstream. In all the cases of GMR=2.6, except for 300K case, the melt traverses far downstream (Figure 5.32), however with melt present in lesser quantity no significant layer build up is observed. Hence in the Table 6-8 they are marked as cases with Non-Realisable Thickness (NRT). For lower GMR cases, a distinct layer of melt is formed affecting wake condition to transform a standard closed-wake into a MICW (Figure 6.9). The melt layer thickness across decreasing GMR tends to increase. This melt that traverses downstream without participating in pre-filming, involving in reduced gas-melt interaction might be one of the reasons why a wider PSD is observed in gas-atomised powders. This might also indicate that if substantially lower GMRs are run, the process might turn out to be highly inefficient, resulting in a bigger median particle size. However, contrasting to the changes observed in the

melt layer thickness across decreasing GMR, no significant changes could be observed across increasing melt temperatures for a given GMR.

Table 6-8 Melt layer thickness measured in millimetres (mm) at 100 ms.

Cases	GMR - 5.5 (1 kg min^{-1})	GMR - 2.6 (2 kg min^{-1})	GMR - 1.32 (4 kg min^{-1})	GMR - 0.88 (6 kg min^{-1})	GMR - 0.44 (12 kg min^{-1})
300K	AML	AML	0.38	0.75	1.2
600K	AML	NRT	0.5	0.6	1.2
1000K	AML	NRT	0.5	0.6	1.1
1500K	AML	NRT	0.5	0.7	-
2000K	AML	NRT	0.5	-	-

AML - Absence of melt layer; NRT - Non-realisable thickness

In the far downstream region, alongside the presence of the melt layer, there is also observable movement of particles in flight. These swiftly moving particles predominantly comprise those that have undergone pre-filming process, subsequently interacting with the supersonic gas-jet before being propelled downstream, resulting in substantial dispersion of particles as they arrive downstream. The maximum extent of particle dispersion is measured at the exit of domain along the radial direction to evaluate the impact of the gas-melt interactions in the far downstream region. The radial measurements recorded in terms of N_d are presented in Table 6-9. It is observed that except for the 1 kg min^{-1}, 300K case, all the cases exhibit very similar values of particle dispersion. This confirms that irrespective of the influences of the GMR or the melt temperature, the strong supersonic gas-jet effectively attenuates the melt fluctuations in the far downstream to result in a very similar particle dispersion. The effect of supersonic gas on melt is also evident for each case, that through the mass flow rate plots obtained at the outlet of the domain, all high-frequency melt fluctuations observed in the injection melt flow rate plots were entirely eliminated, and only lower frequency melt fluctuations were retained.

Table 6-9 Maximum extent of particles scattering in the radial direction recorded at the domain's outlet, measured in N_d.

Cases	GMR - 5.5 (1 kg min^{-1})	GMR - 2.6 (2 kg min^{-1})	GMR - 1.32 (4 kg min^{-1})	GMR - 0.88 (6 kg min^{-1})	GMR - 0.44 (12 kg min^{-1})
300K	1.9	2.4	2.3	2.2	2.5
600K	2.35	2.5	2.6	2.6	2.6
1000K	2.40	2.5	2.5	2.5	2.4
1500K	2.45	2.3	2.5	2.3	-
2000K	2.40	2.3	2.35	-	-

6.7 Formation of melt-isolated closed-wake (MICW) condition due to increasing mass loading.

From Table 6-8 it is observed that with the decrease in GMR (or increase in melt flow rate), due to the higher mass loading, the melt pool head continues to move downstream alongside the axis of the atomiser, and plunges into the Mach-disk. This radially displaces the Mach-disk from the axis. Although, the radial movement of the Mach-disk away from the axis might seem the wake continues to exist in open-wake for the remainder of the process, it actually undergoes wake alternation. The gas flow-field immerses into the melt layer to isolate the wake just as observed in the regular closed-wake condition. This type of closed-wake condition formed because of the presence of melt layer is called Melt-isolated closed-wake (MICW) condition. MICW condition is illustrated using Figure 6.8 for the different GMRs, except GMR = 5.5, since melt pool head stabilises with time, and no melt layer is developed (Table 6-8). The results produced in Figure 6.8 are taken when the wake undergoes MICW, and they are recorded around 100 ms, same as that of Table 6-8.

For GMR = 2.6, although a melt layer is present, the melt layer thickness (MLT) is of non-realisable thickness (NRT), hence the traditional or regular closed-wake condition is observed (Figure 6.8a). For cases with GMR ≤ 1.32, a significant MLT is observed resulting in MICW. This is illustrated in Figure 6.8b-d, where the MLTs were consistently larger compared to the gaps between the lower sonic boundary of the second shock-cell and the atomiser's axis of their respective cases. For GMR = 1.32 (Figure 6.8b), the MLT is 0.5 mm from the atomiser' axis, whereas the gap between the lower sonic boundary of the second shock-cell and the atomiser's axis seen in the velocity contour is only 0.2 mm, distinctly indicating the gas flow-field being immersed into the melt layer, resulting in MICW. Similar phenomena are observed for GMRs of 0.88 and 0.44, presented in Figure 6.8c&d, respectively. The difference between a regular closed-wake and MICW is presented in Figure 6.9 using schematic illustration.

MICW phenomena is the outcome of higher mass loading, and from these series of simulations it is consistently observed that the melt layer effectuating MICW is not affected by the supersonic gas jet nor does it undergo effective atomisation, leading to the conclusion higher mass loading beyond a critical flow rate results in poor atomisation. However, industries usually operate at higher mass flow rates to improve economic efficiency.

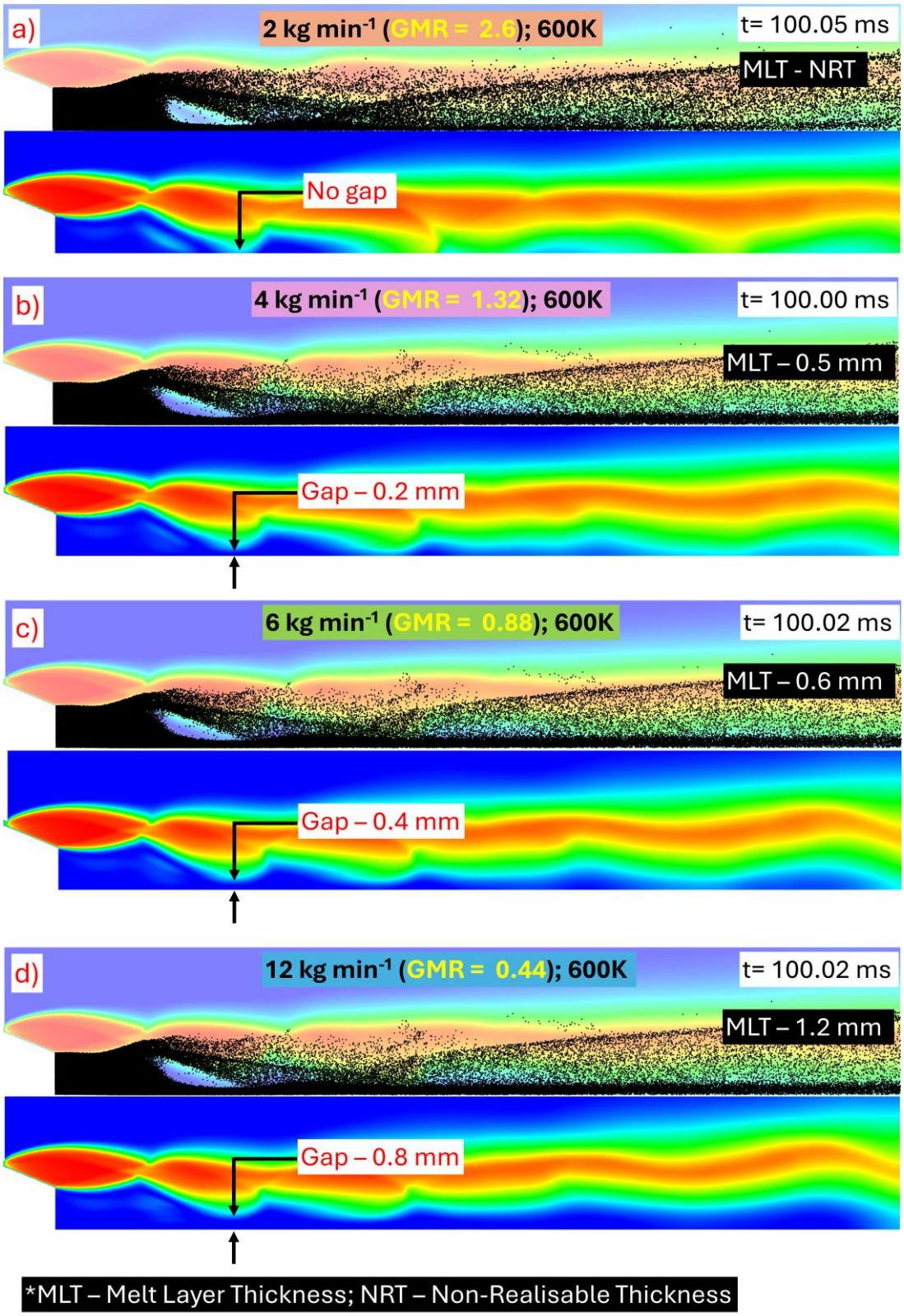

Figure 6.8 Illustration of melt-isolated closed-wake (MICW) condition seen for different GMR cases, except GMR=5.5. The flow-field immerses into the melt layer, leading to the same condition as observed in regular closed-wake condition. The melt layer thicknes and the gap between lower sonic boundary and aomiser's axis is presented for all the four cases.

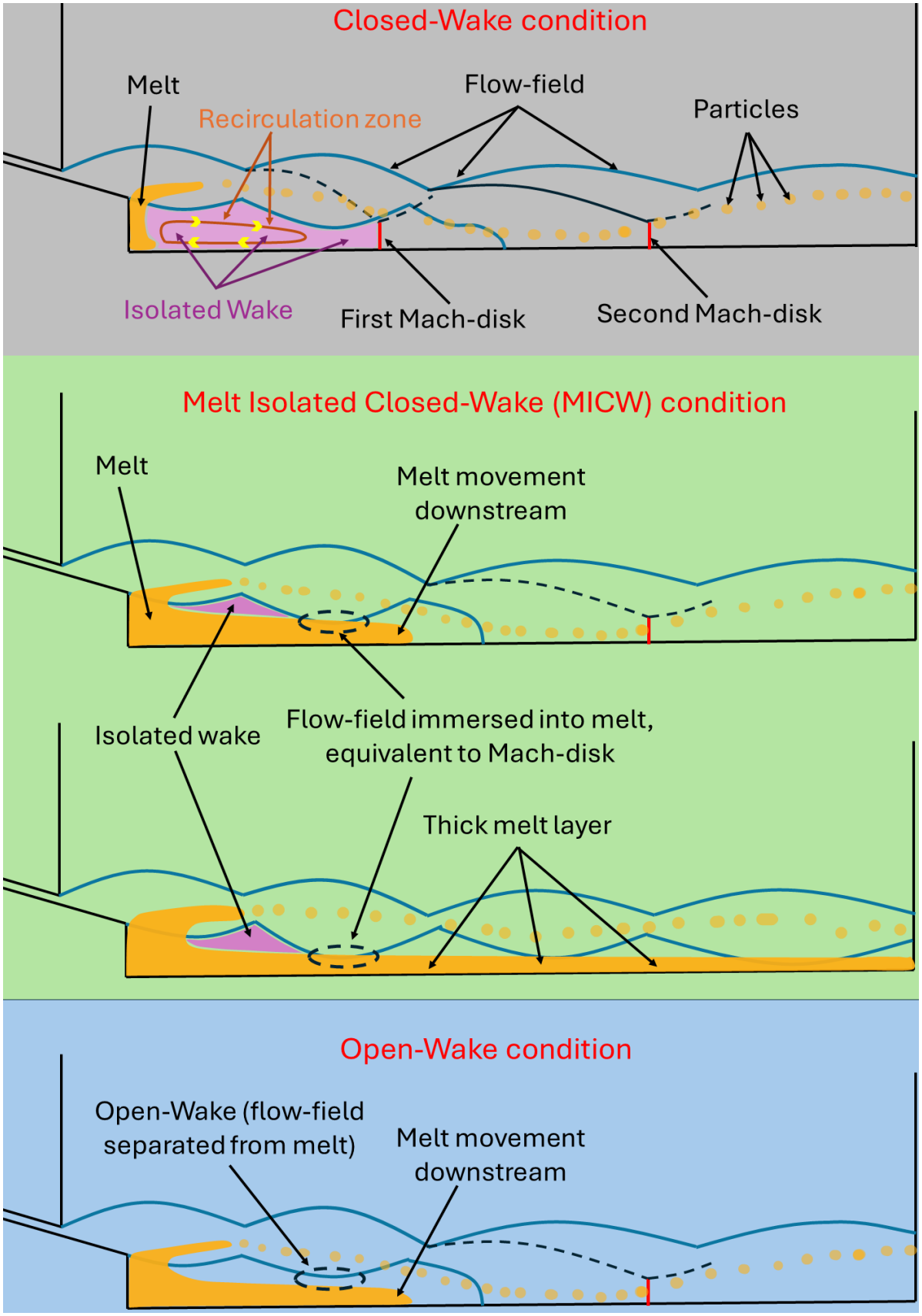

Figure 6.9 A schematic diagram illustrating the difference between regular closed-wake and melt isolated closed-wake (MICW). It also illustrates the nature of open-wake condition formed during the presence of melt layer.

6.8 Flow-field fluctuation and its mechanism behaviour over increasing melt temperatures.

Further investigation from section 6.1 led to the observations, that just as the melt fluctuations can be categorised into distinct types based on their pattern, the gas flow-field fluctuations that are observed in process can be categorised. They are categorised into two types: a) axial mode of fluctuation, for melt temperature of 300K, wherein the flow-field fluctuation underwent spatial oscillations along the axial direction as observed in Figure 5.52, Figure 5.72, and Figure 5.92, and b) radial mode of fluctuation, for melt temperatures of 600K and above, wherein the flow-field underwent fluctuations only along the radial direction as observed in Figure 5.71, and Figure 5.81. This change in the mode of fluctuation in the flow-field is due to the change in their melt temperatures which affects the pressure in the wake region, leading to two different mechanisms of fluctuations. Since, cases of higher GMRs of 5.5 and 2.6 seen in section 6.2 were relatively stable, especially their 300K cases, flow-field fluctuations seen in 300K and 1000K cases of a lower GMR, 1.32 (4 kg min^{-1}) were considered to illustrate the two mechanisms.

The flow-field oscillation of GMR = 1.32, 300K case is shown in Figure 6.10 and Figure 6.11. To illustrate the mechanism of the fluctuation, velocity contours overlaid with pathlines[2] were obtained at close time frames and were stacked sequentially. The pathlines of the gas flow are coloured using gas temperature, to show how temperatures changes in that region during the oscillation. To ensure high-resolution for optimal clarity, a zoomed in version of the images focussing the wake region are presented. Hence, due to the constraints of space, a single flow-field oscillation is spilt into two images: Figure 6.10 from frame a till f, and Figure 6.11 from frame g till k. Two regions of interest, zone-1 and zone-2 were identified in the flow-field involving in the effectuation of the mechanism. Zone-1 is the region in the wake under the second shock-cell, and zone-2 is the second recirculation zone, present in-between second and third shock-cell. This is shown in Figure 6.10a. Also, for further understanding the pressures at zone-1 and zone-2 are recorded. The oscillation starts with the closed-wake condition (Figure 6.10a), and ends with closed-wake condition (Figure 6.11k). Since, it was found that the number of recirculation zones varied throughout the fluctuation, the recirculation zones are named 'R.Z'.

[2] Pathlines helps in understanding the path of the fluid motion.

The sequence of changes observed during a cycle of flow-field fluctuation for the 300K case are as follows:

- In Figure 6.10a, the flow-field exists in closed-wake condition, where the flow-field is in its retracted position, and the volume of the wake is at its minimum. Two recirculation zones are present in the wake region, R.Z - 1 and R.Z - 2. The R.Z - 1 possesses a counter-clockwise vorticity, whereas R.Z - 2 possesses clockwise vorticity.
- Following the closed-wake condition seen in Figure 6.10a, it is observed the shock-cells stretch downstream increasing the volume of wake (Figure 6.10b). R.Z - 1 underwent vortex dissociation, resulting in a smaller vortex. Simultaneously, the dissociated vortex from R.Z - 1 started merging into R.Z - 2. Moreover, an incremental decrease in the temperature is observed in zone-1 which might be due to the increase in wake volume.
- The volume of the wake region continued to increase, and the temperature in zone-1 was observed to decrease (Figure 6.10c). The recirculation zone at the nozzle front possessing counter-clockwise vorticity transitions into clockwise vorticity (Figure 6.10c), and converges to form a well-defined recirculation zone. Also, the dissociated vortex from R.Z - 1 still continued to merge into R.Z - 2.
- Subsequently, volume of the wake region further increases, and R.Z - 1 and R.Z - 2 grows in its spatial size (Figure 6.10d).
- Following this the wake attained its maximum extension spatially downstream, containing the maximum wake volume, i.e., open-wake condition (Figure 6.10e). It was observed, a new recirculation zone, R.Z -3 was established in zone-2; R.Z - 1 grew in its size; and R.Z - 2 split up into R.Z - 2a and R.Z - 2b. Nevertheless, the dissociated recirculation zones, R.Z - 1 and R.Z - 2 seen in Figure 6.10d, began to merge. Moreover, it is also observed the temperature in R.Z - 2 seen in Figure 6.10e, appears to vary significantly in different parts of the recirculation zone, indicating R.Z - 2 undergoes complex changes.
- Subsequently, the wake undergoes progressive decrement in its wake volume (Figure 6.10f), and this might be due to the higher pressure in zone-2 compared to zone-1. The pressure plot containing the pressures for zone-1 and zone-2, recorded throughout the fluctuation are presented in Figure 6.12. With the reduction in the volume of the wake, the temperature in zone-1 increases. R.Z - 2a and R.Z - 2b seen in Figure 6.10e merged in to one recirculation zone, R.Z - 2, in Figure 6.10f. Also, R.Z - 3 grows in its spatial

size, increasing in its pressure and temperature. Similarly, R.Z -1 is also observed to grow in its spatial size.

- The flow-field continues to move upstream, reducing in its wake volume as observed in Figure 6.11g. It is observed the temperature rises in both zone-1 and zone-2, and might be the potential cause for the rise in the pressure in zone-1 and zone-2, but higher pressure in zone-2. Likewise, the spatial size of R.Z - 3 further increases (Figure 6.11g). It is also observed that with the melt entrainment, the flow direction at the nozzle front is changed. This is marked in Figure 6.11g using the black circle.
- The melt entrainment observed in Figure 6.11g induces a new recirculation zone at the melt nozzle front in Figure 6.11h. The recirculation zones, R.Z - 1 and R.Z - 2 seen in Figure 6.11h completely merged into one recirculation zone, R.Z - 2. The spatial size of R.Z - 3 reduced, but it was observed its temperature increased, and likewise its pressure attained its maximum pressure (Figure 6.12). Similarly, with the flow-field continuing to move upstream, the spatial size of R.Z - 2 decreased, but its temperature increased (Figure 6.11h).
- The formation of recirculation zone at the melt nozzle front having a counter-clockwise vorticity is well observed in Figure 6.11i. Simultaneously, R.Z - 3 progressively dissipates, i.e., decreasing in its spatial size (Figure 6.11i). Although, the temperature in zone-2 is observed to remain the same, the pressure is observed to reduce (Figure 6.12).
- Subsequently, the flow-field moves further upstream (Figure 6.11j). The recirculation zone at the nozzle front develops more distinctly and possesses a counter-clockwise vorticity. The temperature and pressure in both zone-1 and zone-2 reduces. Simultaneously, R.Z - 3 continues to undergo further dissipation and is observed to be highly diminished.
- Eventually the flow-field attains its retracted position, returning back to its original configuration of closed-wake condition (Figure 6.11k). The recirculation zone at the nozzle front grows notably in its spatial size by expanding downstream to form R.Z - 1. The temperature in zone-1 significantly reduces. Also, R.Z -3 seen in Figure 6.11j completely dissipates.

The above seen sequence of changes in the flow-field, oscillating between upstream and downstream is due to the complex combination of multiple parameters such as pressure, temperature and action of recirculation zones in zone-1 and zone-2. However, the downstream,

and its following upstream movement of the flow-field is expected to occur on the following mechanism: the flow-field movement downstream might be attributed to the lower pressure in zone-1 and zone-2 (Figure 6.12) resulting in the gas-jet to attain its full extension downstream, as it would be in a gas-only flow without the injection of melt. The upstream movement of the flow-field might be attributed to the higher pressure in zone-2, pushing the flow-field along with its shock-cells towards the melt nozzle. However, it is observed, that the peak pressure within the wake is prior to re-closure of the wake (Figure 6.11k), although the closed-wake condition corresponds to the minimal wake volume.

As mentioned earlier the recorded pressures at zone-1 and zone-2, and the aspiration pressure are plotted Figure 6.12 against the flow time to illustrate the nature of the pressure fluctuation. It is evident that the aspiration pressure reaches its minimum value (26.7 kPa) at open-wake (Figure 6.10e), resulting in the maximum melt drawn in the atomiser. However, at closed-wake condition (Figure 6.11k) it is seen that the aspiration pressure attained a value, lower than the maximum aspiration pressure. Nevertheless, from the plot it is also observed that the maximum aspiration pressure occurred at a momentary instance just prior to the closure of the wake. This might be attributed to the delayed realisation of pressure changes between zone-1 and melt nozzle front where aspiration pressure is recorded, due to the time lag. Hence, with the zone-1 gaining its highest pressure at an instance prior to the highest aspiration pressure, this time lag indicates the time taken for the pressure from zone-1 to reflect at the nozzle front, i.e., aspiration pressure. With a time difference of 13 μs between Figure 6.11j and Figure 6.11k; the distance measuring from the melt nozzle tip to the farthest extend of the wake downstream to be 8.4 mm; assuming a uniform temperature of 360K in the wake region, it is calculated pressure wave travels a distance of 5.3 mm. This corroborates the delayed pressure realisation between zone-1 and melt nozzle front.

The flow-field fluctuation mechanism shown using velocity contours and pathlines also captures the melt entrainment into the atomiser. This is observed in Figure 6.11g, where due to the melt entrainment, a recirculation zone is induced in front of the melt nozzle. This is in contrast, that even though the recirculation zone draws the melt radially outward starting from Figure 6.10d, the melt is able to respond only at a later time, i.e., Figure 6.11g, reflecting the physical atomisation process. Moreover, the characteristic path traced by the melt while undergoing pre-filming is observed from the pathlines in Figure 6.11j-k and Figure 6.10a-b.

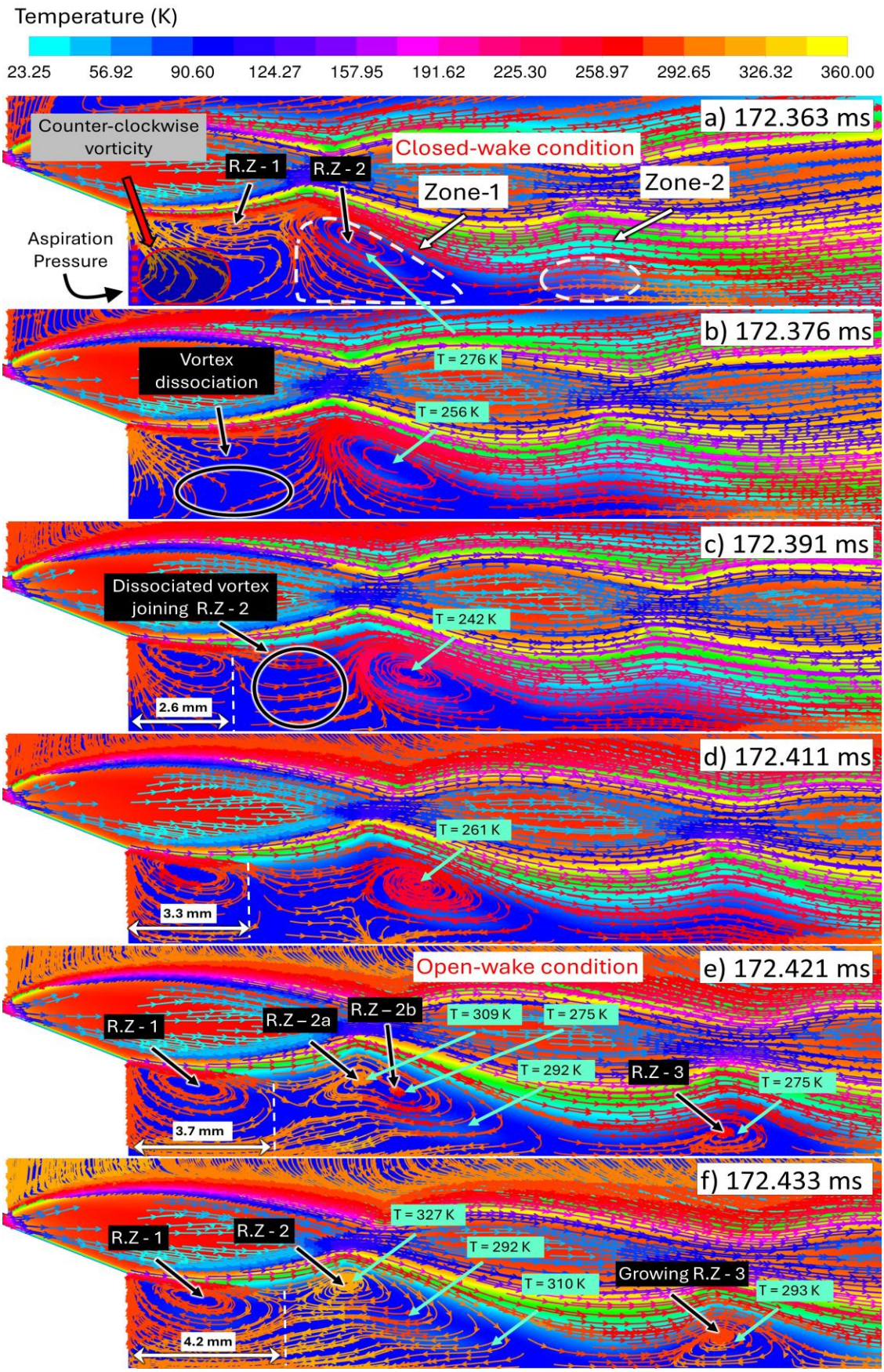

Figure 6.10 The mechanism of flow-field fluctuation for 300K cases shown using velocity contour in the background and pathlines in the foreground, containing frames a till f.

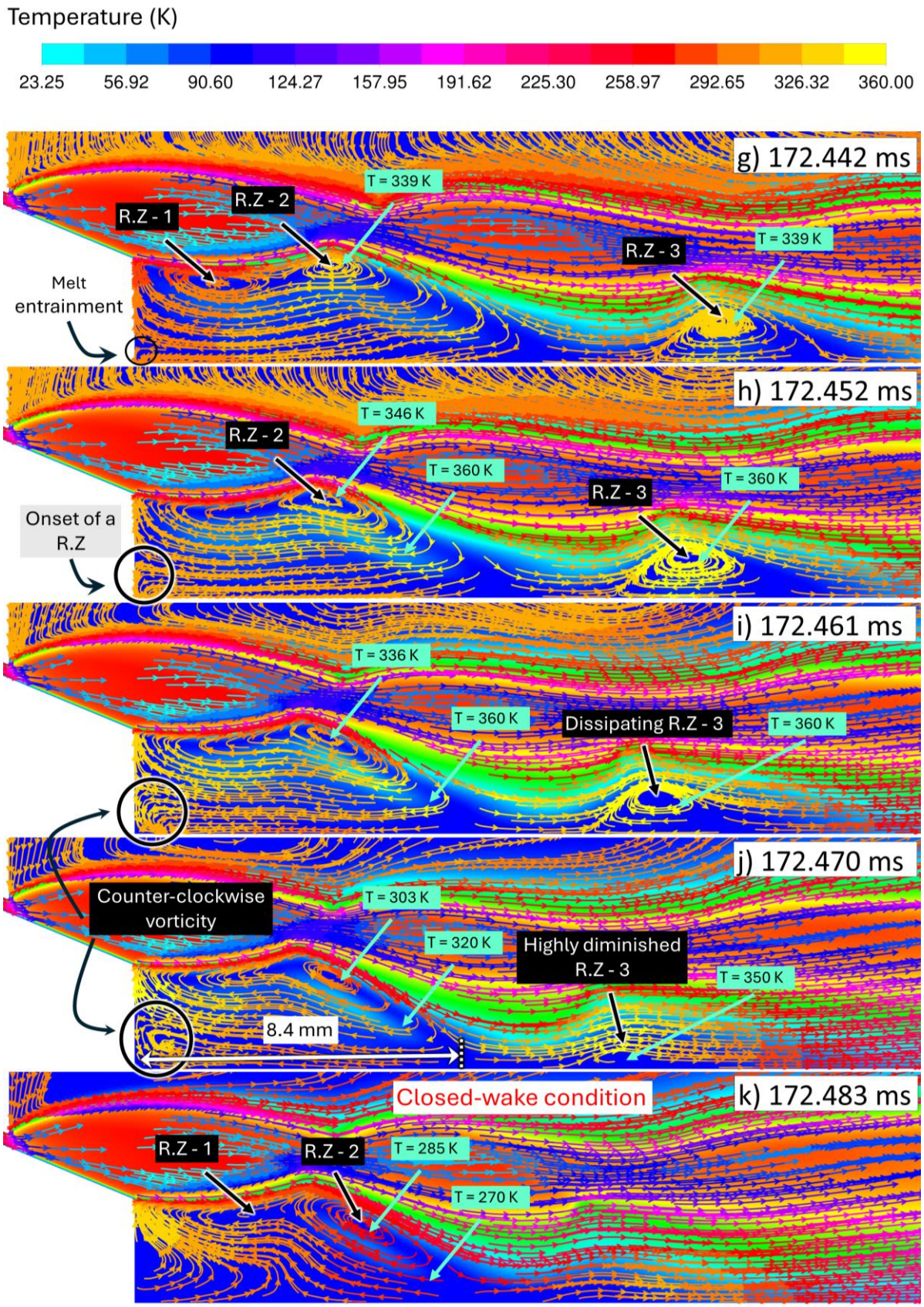

Figure 6.11 The mechanism of flow-field fluctuation for 300K cases shown using velocity contour in the background and pathlines in the foreground, containing frames g till k.

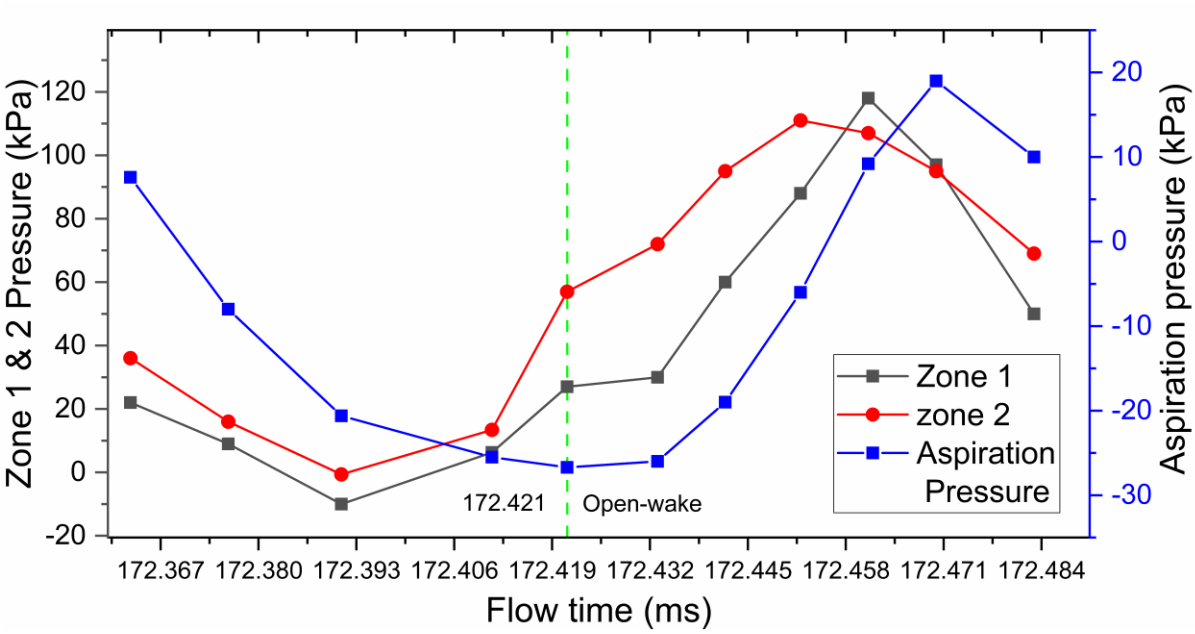

Figure 6.12 Pressure plot showing the aspiration pressure and pressures recorded at zone-1 and zone-2.

Similar to the sequence of changes in the above illustrated 300K case, the flow-field oscillation of the 4 kg min^{-1}, 1000K case is also discussed below. The velocity contours layered with pathlines of gas flow for the flow-field fluctuation are shown in Figure 6.13 and Figure 6.14. The pathlines of the gas flow are coloured using gas temperature, to show how temperatures changes during the oscillation. Similar to 300K cases, considering the clarity, so as to assist the understanding of the behaviour of the changes occurring at the wake region and in its closed proximity, the zoomed-in section of the flow-field focussing the first three shock-cells are considered for analysis. Due to the constraints for space, a single oscillation is spilt into two images: Figure 6.13 from frame a till e, and Figure 6.14 from frame f till i. The same two zones of interest, identified in the 300K case are considered in the 1000K case as well (Figure 6.13a). Likewise, the pressures of zone-1 and zone-2 are also recorded. The oscillation starts with closed-wake condition (Figure 6.13a) and ends with closed-wake condition (Figure 6.14i).

The sequence of changes observed during a cycle of flow-field fluctuation for the 1000K case are as follows:

- In Figure 6.13a, the flow-field exists in its closed-wake condition. Three distinct recirculation zones, R.Z - 1, R.Z - 2, and R.Z - 3 were observed in the wake region. The recirculation zone, R.Z - 1 at nozzle front possesses a counter-clockwise vorticity

whereas the other two recirculation zones possess a clockwise vorticity. Simultaneously in zone-2 another recirculation zone is observed to be actively forming.

- Subsequently, the second shock-cell is displaced radially away (Figure 6.13b). This radial displacement of the shock-cell might be to the complex action of the recirculation zones, R.Z - 2 and R.Z - 3 pushing the shock-cell downstream, but the significantly higher pressure at zone-2 opposing the downstream movement resulting in the radial displacement. The pressures recorded at zone-1 and zone-2 are plotted in Figure 6.15. Simultaneously, R.Z - 1 undergoes dissociation, by elongating downstream to part into two recirculation zones, and R.Z - 4 continues to develop to evolve into a recirculation zone.
- The second shock-cell further displaces radially outward (Figure 6.13c) due to the increasing pressure in zone-2 (Figure 6.15). The recirculation zone, R.Z - 1 dissociates into two recirculation zone, R.Z - 1a and R.Z - 1b, with the newly formed recirculation zone, R.Z - 1b possessing a clockwise vorticity, whereas the parent recirculation zone R.Z - 1a possessed a counter-clockwise vorticity. Similarly, R.Z - 4 recirculation zone in zone-2 also becomes fully developed and well-defined (Figure 6.13c), and is observed to extend towards zone-1.
- Following this R.Z - 1a is observed to diminish in its spatial size while continuing to move upstream (Figure 6.13d). Similarly, R.Z - 1b is also observed to dissipate, but moves downstream (Figure 6.13d). With the second shock-cell displaced radially outward, wake opens up allowing for the back flow from zone-2 into zone-1, i.e., flow from high pressure region (zone-2) to low pressure region (zone-1). A schematic diagram of Figure 6.13d showing the back-flow into the wake region is presented in Figure 6.16.
- Subsequently, the pressures in zone-1 and zone-2 reach their respective extremes, with zone-1 reaching its lowest pressure and zone-2 reaching its highest pressure (Figure 6.15). Both R.Z - 1a and R.Z - 1b were observed to be completely dissipated (Figure 6.13e). Also, R.Z - 2 and R.Z - 4 increases in its spatial size, whereas R.Z - 3 was observed to diminish in its spatial size. Moreover, the back flow observed in Figure 6.13d continues to prevail in the Figure 6.13e.
- Following this, the wake enters into open-wake condition (Figure 6.14f), where the lowest point of the inner sonic boundary is at its furthest distance radially from the atomiser's axis. Owing to this R.Z - 4 extends upstream, but reduces in it spatial size

(Figure 6.14f). Also, the dissipating R.Z - 3 observed in Figure 6.13e, completely dissipates in Figure 6.14f, resulting R.Z - 2 and R.Z - 3 into merge into one larger recirculation zone, R.Z - 2. Moreover, an onset of a recirculation zone is observed at the melt nozzle front. This is marked using a red circle in Figure 6.14f. It was also observed, the pressure in zone-1 increased, whereas the pressure in zone-2 decreased (Figure 6.15).

- With further increase in pressure in zone-1, and continued decline in pressure in zone-2, the pressure within zone-1 surpassed that of zone-2, resulting in a shift in the pressure gradient between the zones (Figure 6.15). It was observed, the lower sonic boundary moves radially inward closing the gap, decreasing the spatial size of R.Z - 4, and also pushes it downstream (Figure 6.14g). Due to the radially inward movement of the second shock-cell, the back flow from zone-2 to zone-1 stopped. In addition to this, it was observed R.Z - 1 and R.Z - 3 re-established in Figure 6.14g, however R.Z - 1 possessed a counter-clockwise vorticity, whereas R.Z - 3 possessed clockwise vorticity.
- Subsequently, R.Z - 1 enlarges in the downstream direction, and R.Z - 3 grows in its spatial size (Figure 6.14h). The lower sonic boundary further advances towards the atomiser's axis while R.Z - 4 is observed to dissipate.
- Eventually the wake enters into closed-wake condition (Figure 6.14i), wherein the recirculation zone at nozzle front further expands downstream, reflecting the same configuration of wake condition observed in Figure 6.13a.

In the above sequence of changes in the flow-field fluctuation, it is observed that the mechanism of fluctuation is increasingly complex due to the interplay of the multiple parameters such as the presence of multiple recirculation zones – up to five recirculation zones observed in Figure 6.13c, formation and dissipation of recirculation zones, high thermal gradient within a small spatial region (zone-1), back flow from zone-2 to zone-1, and inversely varying pressure between zone-1 and zone-2.

The above seen sequence of changes in the flow-field might be thus summarised. The opening of the wake by displacing the second shock-cell radially outward might be attributed to the increasing pressure within zone-2 and simultaneously dissipation of R.Z - 3 in zone-1. Similarly, the radially inward movement of the shock-cell and the closure of the wake might be attributed to the re-establishment of R.Z - 3 in zone-1 and the decreasing pressure in zone-2 (Figure 6.15). Even as the trend observed in 300K mechanism, the peak wake pressure was at a time prior to the closure of the wake (Figure 6.14i), although closed-wake condition

corresponds to minimal wake volume. Similarly, the least wake pressure in zone-1 was not at the open-wake condition (Figure 6.15), but rather occurred at a time earlier to this, despite open-wake condition corresponds the maximum wake volume.

In addition to the pressures at zone-1 and zone-2, the aspiration pressure is also recorded and is plotted against flow time in Figure 6.15, to illustrate the nature of the pressure fluctuation. The aspiration pressure mirrors the trend in pressure within zone-1. The aspiration pressure recorded at open-wake condition (-0.5 kPa) is observed to be greater than the lowest aspiration pressure (-4.4 kPa). This phenomenon might thus explained: following the closed-wake condition, high pressure in zone-2 radially pushes the atomising gas-jet (Figure 6.13b), onsetting the wake opening process. As the pressure in zone-2 increases, the wake volume increases, leading to decreased pressure (Figure 6.15). With further radial displacement of the gas-jet, the wake opens in Figure 6.13d, and it is observed from Figure 6.15 that the aspiration pressure is at its lowest at the opening of the wake. With the wake opening in Figure 6.13d a back flow is observed from zone-2 into zone-1, i.e., flow from higher pressure to lower pressure region. When observed from Figure 6.15 and Figure 6.13e, it is clear, when the back flow occurs, the pressure in zone-1 increases, reflecting in higher aspiration pressure as observed in Figure 6.15. Hence, at open wake condition were the inner sonic boundary of the second shock-cell is at its furthest distance from the atomiser's axis radially, it is observed the aspiration pressure is higher compared to that seen in Figure 6.13d.

The flow-field fluctuation mechanism shown using velocity contours and pathlines also captures the melt entrainment into the atomiser. This is shown in Figure 6.14f, where due to the melt entrainment a recirculation zone is induced in front of the melt nozzle. Moreover, the characteristic path traced by the melt while undergoing pre-filming is also observed from the pathlines starting from Figure 6.14g continuing into the next fluctuation cycle, till Figure 6.13d.

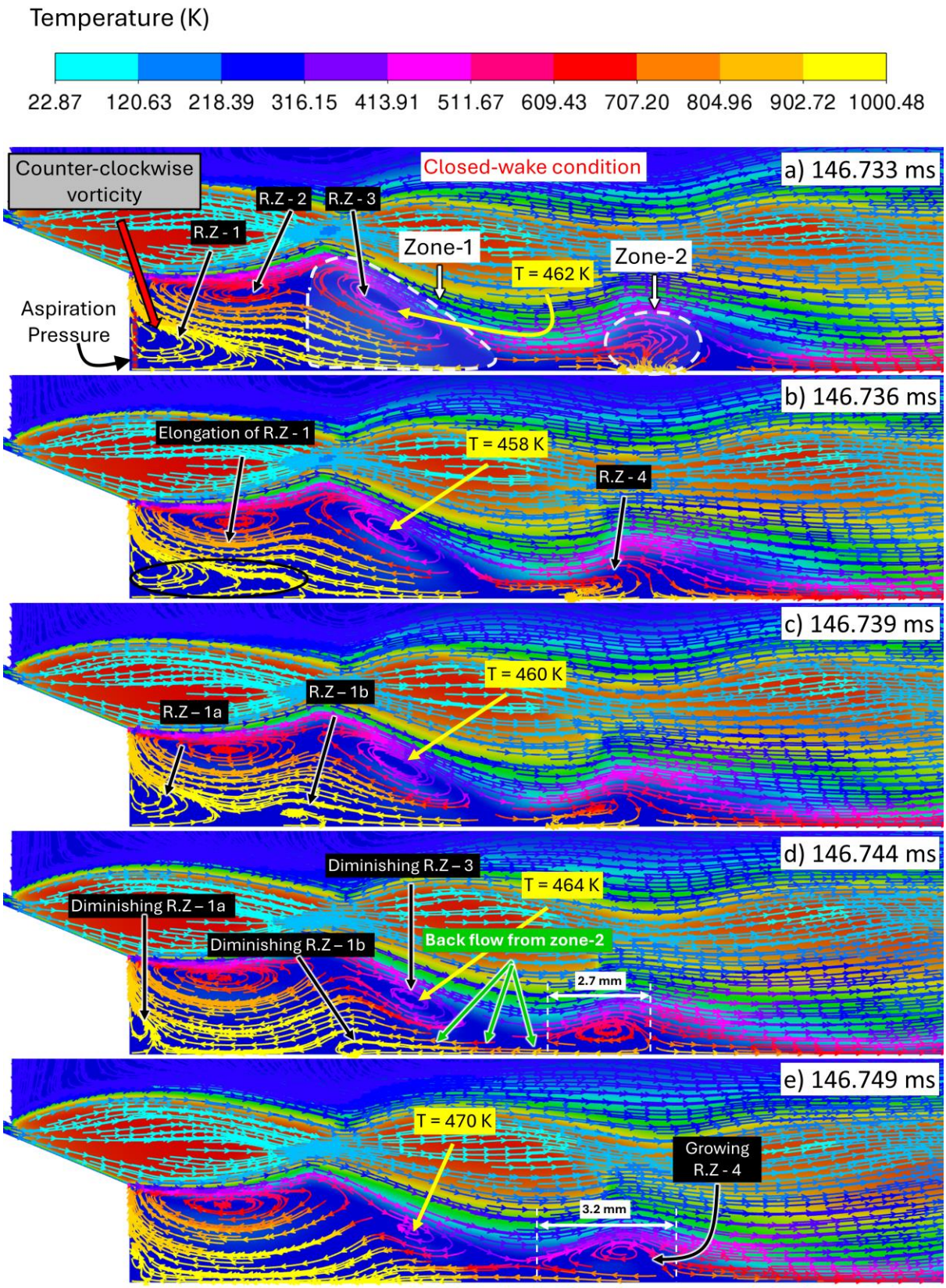

Figure 6.13 The mechanism of flow-field fluctuation for 1000K cases shown using velocity contour in the background and pathlines in the foreground, containing frames a till e.

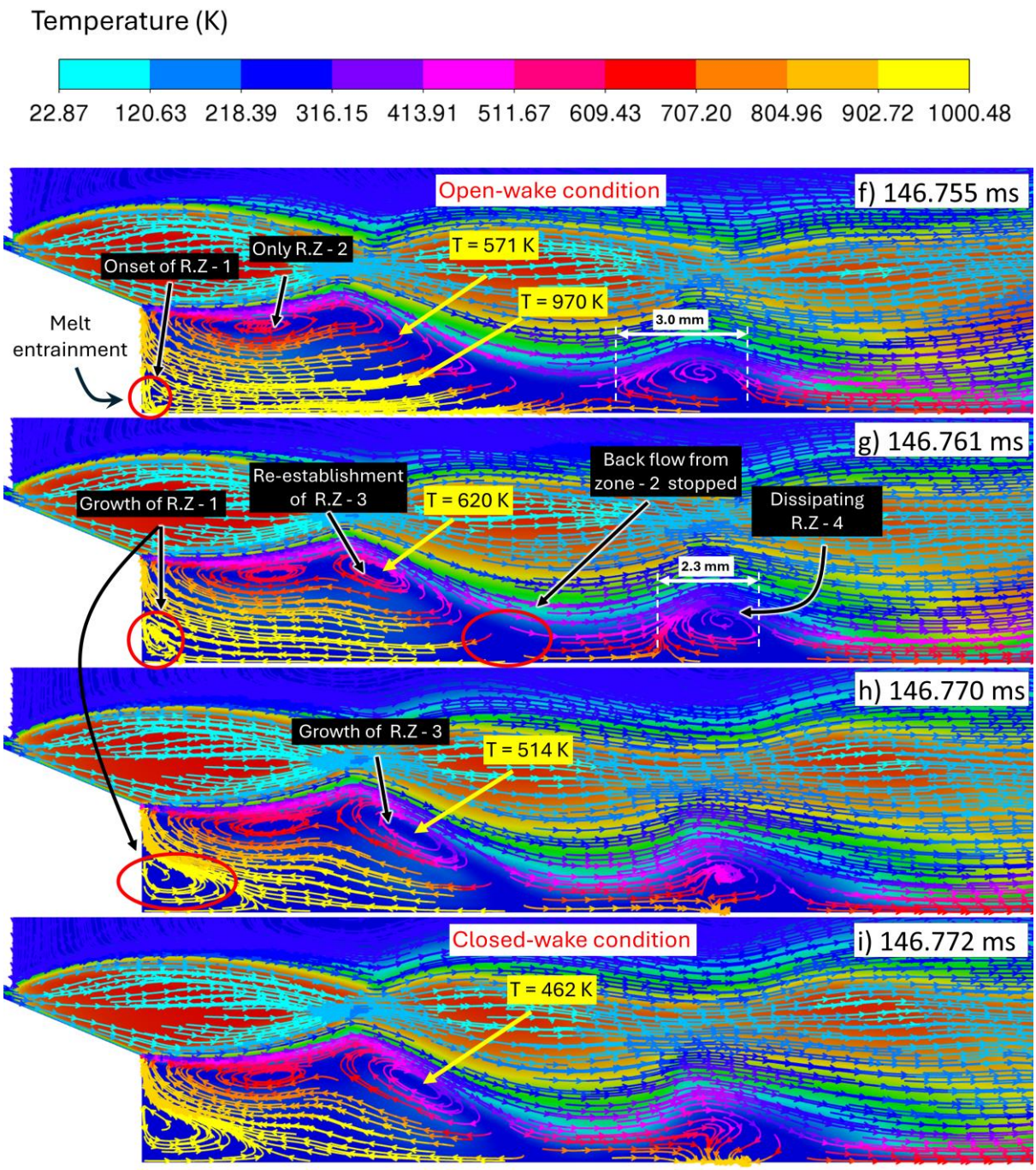

Figure 6.14 The mechanism of flow-field fluctuation for 1000K cases shown using velocity contour in the background and pathlines in the foreground, containing frames f till i.

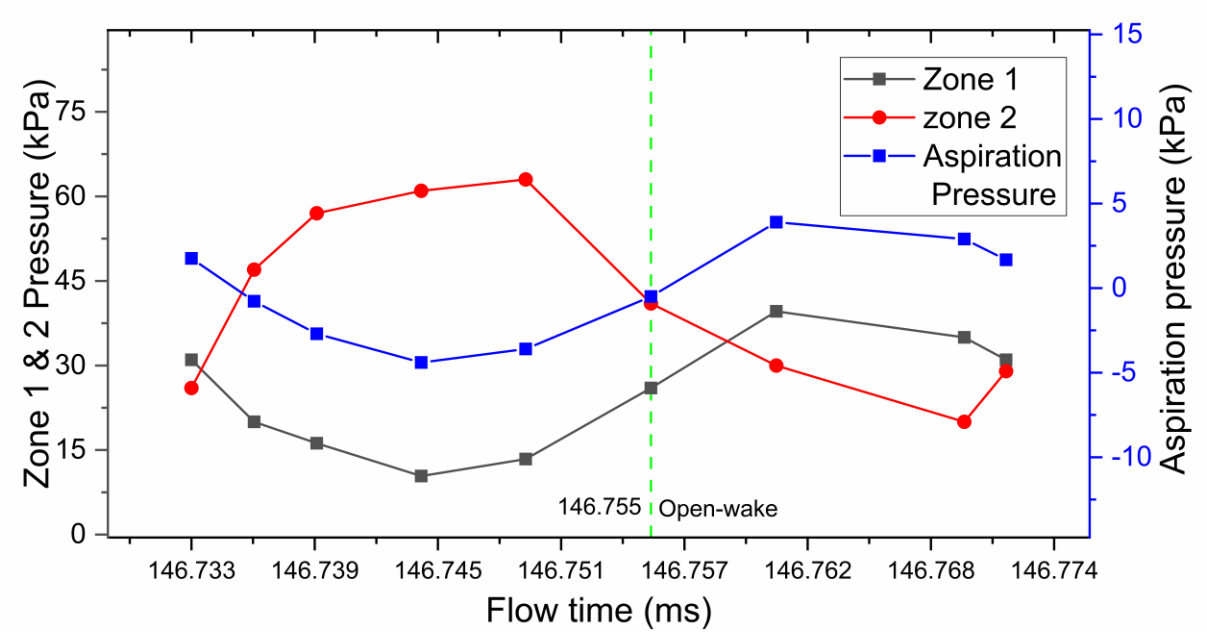

Figure 6.15 Pressure plot showing the aspiration pressure and pressures recorded at zone-1 and zone-2. Zone-1 and aspiration pressure follows the same trend of pressure fluctuaiton.

From the mechanism of 300K and 1000K cases' flow-field fluctuations, it is noted that there exist several similarities and differences.

- The mechanism of the gas flow-field fluctuation for the higher melt temperature case, T = 1000K is much more complex in nature than compared to lower temperature case, T = 300K. The higher temperature case is observed to involve high thermal gradient flow in the wake region, and the contains up to five recirculation zones (Figure 6.13c).
- In the 300K case, the pressures in zone-1 and zone-2 undergoes simultaneous rises or falls, with zone-2 having higher pressure for the majority of the fluctuation period (Figure 6.12). However, for the 1000K case an inverse relationship in pressures between zone-1 and zone-2 is observed (Figure 6.15).
- In the 300K case, lowest aspiration pressure is recorded at the open-wake condition, whereas in the 1000K case, lowest the aspiration pressure is recorded at an instance earlier to the open-wake condition.
- In both the 300K and 1000K cases, the highest aspiration pressure did not correspond to the closed-wake condition, but to a time prior to it.
- In the 300K case, the recirculation zone at the melt nozzle front induced due to the melt entrainment evolves into a well-defined circular vortex, whereas in the 1000K case, the recirculation zone, R.Z - 1, is an elongated vortex.

- In both the 300K and 1000K cases, it is observed that the melt entrainment into the atomisation chamber and the opening of the wake is not simultaneous, but rather the melt entrains after a brief period of time following the opening of wake.
- The aspiration pressure is stronger in the 300K, wherein it varies from -26.7 to +19 kPa, whereas for the 1000K case, it is much weaker, varying from -4.4 to +3.9 kPa.
- In the 300K case, the pressure in zone-1 varies between 27 to 97 kPa, and the pressure in zone-2 varies from -0.63 to 111 kPa.
- Likewise, in the 1000K case, the pressure in zone-1 varies from 10.4 to 39.6 kPa, and the pressure in the zone-2 varies from 20 to 63 kPa.
- Overall, for the 4 kg min^{-1} case, the 300K case undergoes a larger amplitude pressure fluctuation, resulting in larger amplitude melt fluctuations, whereas 1000K case undergoes smaller amplitude pressure fluctuation, resulting in smaller amplitude melt fluctuations.
- In the 300K case, no back flow is observed throughout the fluctuation whereas in 1000K case back flow from zone-2 to zone-1 is observed when the wake opens (Figure 6.13d).

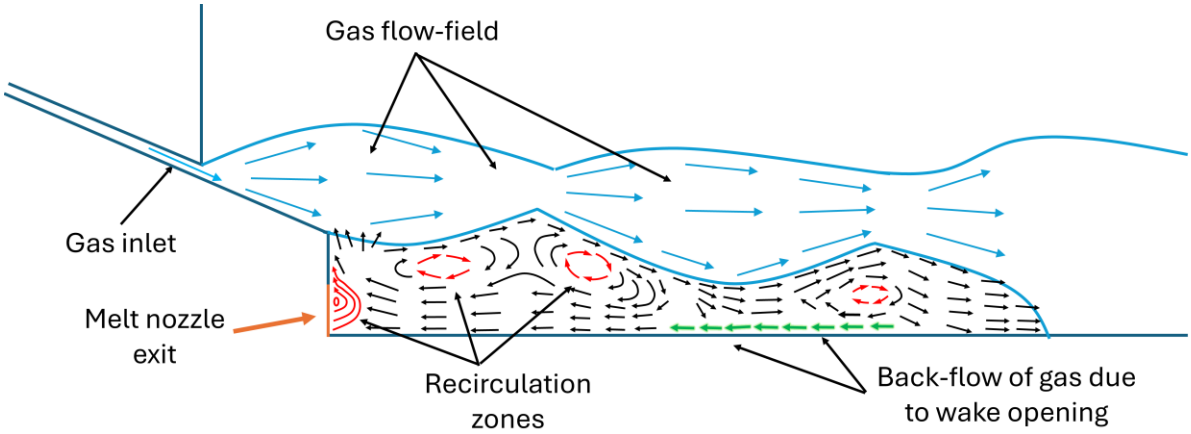

Figure 6.16 Schematic diagram showing the back flow of gas seen in the 1000K case of GMR = 1.32 (4 kg min^{-1}).

6.9 Summary

From the above 22 simulations conducted with decreasing GMR and increasing melt temperatures, it is evident that the melt instability is induced and controlled by the melt temperature to a greater extent than the GMR, wherein it is observed higher melt temperatures corresponds to increased melt instability. This study also reveals the underlying complexity in

the process for increasing melt temperatures. From Table 6-3, the intensifying complexity with the increase in the melt temperature is seen by the manifold frequencies recorded.

Moreover, the mode of melt instability is twofold; a regular and well-defined mode observed during the 300K cases, and an irregular mode observed in the 600K and above cases. Nevertheless, the transition from regular mode (300K) to irregular mode (600K and above) is abrupt but noteworthy. Similarly, the gas flow-field fluctuations associated with the above two modes of melt instability are also classified into two types: axial and radial fluctuation. Axial fluctuation is seen during the 300K cases having regular mode of melt instability, whereas radial fluctuation is observed during the 600K and higher melt temperature cases having irregular mode of melt instability. The melt temperature controls the mechanism of the flow-field fluctuation wherein the pressure in the wake and the second recirculation zone varies in two distinct and different ways. Similar to the complexity observed in the melt instability, this study unveils the complexity present in the gas flow-field, especially in the wake region. In Figure 6.17, the pathlines of the gas flow-field in the wake region is compared to the common considered textbook schematic (Motaman et al., 2015, Anderson et al., 2010, Anderson et al., 2005). From Figure 6.17, it can be understood the process is extremely complex and chaotic. And combining the complexity and uncertainties of the gas and melt flow at high temperature, one can imagine how inter-twined the complexities are, resulting in such unpredictable nature of the process.

Additionally, this study reveals two consistent melt fluctuation frequencies, ~8.1 kHz and ~25.6 kHz, in all the cases despite the increased melt instability observed at higher melt temperatures. However, these consistent melt fluctuation frequencies are not always observed in their corresponding gas flow-field fluctuations. At a melt temperature of 300K, the flow-field fluctuations exhibit ~8.1 kHz, whereas at higher melt temperatures, they transition to higher frequency fluctuations, but not ~25.6 kHz always, thus revealing a disjoint between the melt and gas flow-field fluctuation frequency.

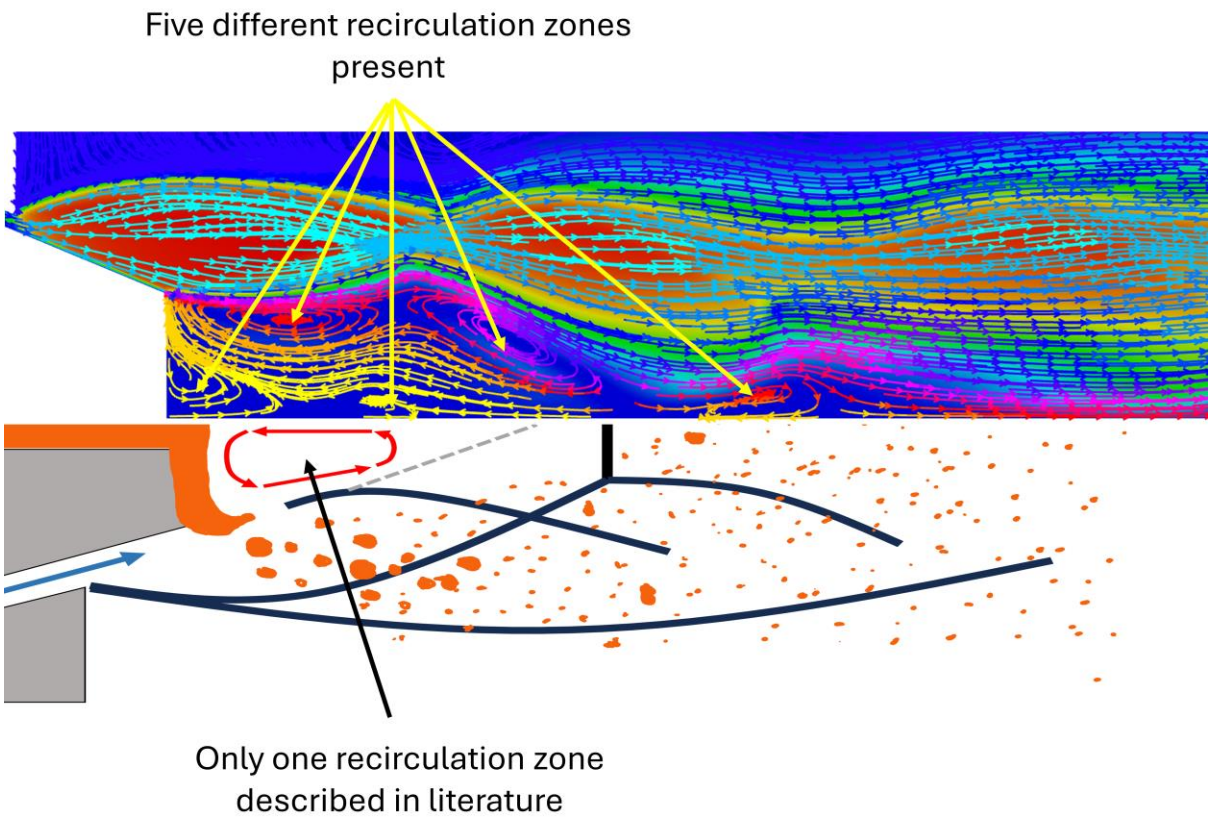

Figure 6.17 Comparison between the pathlines obtained from the simulation results and standard textbook schematic highlighting the complexity in the atomisation process, present in the wake region. The simulation results presents five complex recirculation zones whereas the schematic presents a simple single recirculation zone present at the melt nozzle front.

7 Conclusion

This thesis through a series of 22 simulations investigated the effect of gas-melt interactions and their instabilities. The investigation was carried out on two determinant parameters: gas-to-melt ratio (GMR) and melt temperature. The computationally intensive simulations revealed that both GMR and melt temperature plays a vital role in inducing melt instability. The melt instability induced by the effect of temperature across a given GMR can be classified into sub-groups: a) melt temperature of 300K, and b) rest of the melt temperatures. A transitional instability comes into effect between 300K to 600K which transitions the very regular and predictable process into irregular and random, and amplifies it with increase in temperature. Similarly, the melt instability induced in the process due to GMR across a given temperature can be divided into two groups: a) GMRs of 5.5 and 2.6, and b) GMRs of 1.32, 0.88, and 0.44. The former revealed a very regular instability, whereas the latter induced an irregular and unpredictable melt instability. Nevertheless, it is evident the effect of melt temperature on the melt instability is far greater and substantial compared to the effect of GMR on the melt instability.

The study also revealed that the gas flow-field fluctuations were associated with the melt instability. For lower melt temperature of 300K, the gas flow-field underwent axial fluctuation, and for 600K and above melt temperatures, it underwent radial fluctuation. The gas flow-field fluctuation mechanism and the pressure fluctuations for the 300K melt temperature exhibited a very different and contrasting flow characteristics to that of the higher melt temperatures. Moreover, the flow characteristics within the wake and at near vicinity of the melt nozzle, are far from what is presented in the literature. Only one recirculation zone is presented in the wake region in the textbook literature, whereas from this study three recirculation zones for 300K, and four recirculation zones for 1000K, were observed in their respective wake regions. This highlights the extent of complexity and chaos inherent in the process, deeming it unpredictable in nature. This unpredictable in the process leads to the poor understanding of the process, and also to the wider PSD.

The study also revealed that there exist a disjoint between melt instabilities and the gas fluctuation frequencies. Two consistent melt fluctuation frequencies, ~8.1 kHz and ~25.6 kHz, were observed in all the cases. However, only for cases with melt temperature of 300K, the gas flow-field possessed a fluctuation frequency of ~8.1 kHz, and for cases with melt temperatures of 600K and above, the gas flow-field exhibited a higher frequency of fluctuation, albeit only

few cases exhibited the ~25.6 kHz frequency. This reveals the deepening complexity in the CCGA process when melt temperatures equivalent to physical process are applied.

The study also offers a comprehensive insight into the growing complexity in melt instabilities observed under typical commercial GMR operating conductions, and also for extreme cases of very low GMR=0.44. At GMR ≤ 1.32, the model predicts the presence of melt flow without participating in the pre-filming process, and this is particularly profound for cases with GMR=0.88 and 0.44. This increasing non-participating melt flow with decreasing GMR might be one of the important factors for increasing particle size.

Thus, the study in this thesis, through a series of 22 simulations, has successfully met all the aims and objectives of the study, and has captured the melt instability in the CCGA process under varying GMRs and melt temperatures, revealing multi-level complexity in the gas and melt flow, and their interactions with each other leading to such a complex and chaotic process.

8 Research gaps to explore and future work.

Even though the simulations helped in the understanding the gas-melt interactions and flow-field fluctuations across decreasing GMR and melt temperature, yet further important research gaps were identified which would supplement in understanding of the process.

- With the mode of melt instability established - 300K follows a mode of melt fluctuation, and the rest follows differently, the origin of melt instability is not yet understood.
- The critical temperature at which the flow-field fluctuation transitions from axial to radial is yet to found.
- It is evident higher melt temperature increases randomness to the process, however, how the higher melt temperature induces such randomness, and apart from the temperature what parameter or underlying relationship in the process aids in sustaining the randomness is yet to be explored.
- Similarly, at higher GMRs and melt temperatures, the flow-field fluctuations become unpredictable and random, even though they exhibit the radial mode of fluctuation. The sequence of changes resulting from the gas-melt interaction and the cause-correlation that triggers this phenomenon is yet to be studied.
- Even though 4kg 600K case and 1000K case follows the same pattern of flow field fluctuation their melt fluctuations have contrasting characteristics, wherein 600K case doesn't have any significant amplitudes to melt fluctuations, whereas the 1000K case do exhibit and display very significant and distinct amplitude into melt fluctuations. The underlying reasons and the sequence of changes that causes such melt instability with the flow field fluctuations still existing in the same mode of fluctuations, is not yet understood.
- Although the conducted work might be the first of the realistic process model for atomisation, the model is yet to be extended towards industrial-scale operation. This involves the challenge of introducing higher melt flow rates, but cutting down the number of the particles, so as to reduce the computational cost, and carrying out longer simulations.
- Extending the current model from cylindrical nozzle (choked-nozzle) to convergent-divergent nozzle to understand the atomisation process.
- Extending the model to VOF-to-DPM model with Four-way coupling, and including temperature dependent surface tension and viscosity, would improve the model set-up

to help in the development a more realistic atomisation model. However, this is extremely challenging as it requires very high computational resources.

- Expanding this model from 2D to 3D would render a more accurate depiction of the process. This enhancement is particularly crucial for understanding the gas flow-field fluctuations from a 3D perspective, as in 2D simulations only the axial and radial components are observed, while the z-component remains unaccounted for. This also applies for the flow of the gas with the recirculation zone. Moreover, transitioning to a 3D approach would supplement the understanding of discrete-jet gas atomisers.

9 Appendix

9.1 Melt-aspiration pressure coupling UDF for 1 kg min^{-1} (0.0166 kg s^{-1}) model

```
#include "udf.h"
real sum, ttp, ftp, p_avg, avg, fr, dpm, atp[100];
int i, size, t, s, icount;

// Function to calculate the average pressure at each timestep
DEFINE_EXECUTE_AT_END(average_pressure)
{
   Domain *d;
   real *array;
   face_t f;
   cell_t c0;
   int ID = 23;
   Thread *thread, *t0;
   FILE *fp1, *fp2, *fp3;
   // Get the domain and thread
   d = Get_Domain(1);
   thread = Lookup_Thread(d, ID);
   // Get the number of elements in the thread
   size = THREAD_N_ELEMENTS_INT(thread);
   array = (real *)malloc(size * sizeof(real));
   // Open files for writing data
   fp1 = fopen("instpressure.txt", "a+");
   fp2 = fopen("timestpres.txt", "a+");
   fp3 = fopen("movingavg.txt", "a+");
   t = N_TIME;
   real l = CURRENT_TIME;
   Message("the time is \n%d\n", N_TIME);

   // Loop through faces to get pressure data
   begin_f_loop(f, thread)
   {
      c0 = F_C0(f, thread);
      t0 = THREAD_T0(thread);
      array[f] = F_P(c0, t0);
   }
   end_f_loop(f, thread)
   // Calculate sum and write instant pressure to file
   sum = 0.0;
   for (i = 0; i < size; i++)
   {
      fprintf(fp1, "%g\n", array[i]);
      sum += array[i];
   }
  // Calculate the timestep average pressure
   ttp = sum / 14;
   icount = N_TIME % 100;
   // Update the moving average array and calculate the moving average
   ftp -= atp[icount] / 100;
```

```
    atp[icount] = ttp;
    ftp += atp[icount] / 100;

    Message("the timestep average is \n%g\n", ttp);
    fprintf(fp2, "%g\t\t%d\t\t%0.8g\t\n", ttp, N_TIME, CURRENT_TIME);
    Message("the totalsum for 10 timestep is \n%g\n", ftp);
    fprintf(fp3, "%g\t\t%d\t\t%0.8g\t\n", ftp, N_TIME, CURRENT_TIME);
    // Free allocated memory and close files
    free(array);
    fclose(fp1);
    fclose(fp2);
    fclose(fp3);
}
// Function to initialize the discrete phase model (DPM) injection
DEFINE_DPM_INJECTION_INIT(initdpm, I)
{
    FILE *fp4, *fp5;
    Particle *p;
    // Open files for writing data
    fp4 = fopen("instdpm.txt", "a+");
    fp5 = fopen("movingdpm.txt", "a+");
    s = N_TIME;
    real l = CURRENT_TIME;
    Message("the PHYSICAL TIME is \n%g\n", CURRENT_TIME);
    // Loop through particles to set flow rate based on pressure
    loop(p, I->p_init)
    {
        PP_FLOW_RATE(p) = (0.00000032 * (-ftp) + 0.016) / 12;
        dpm = 0.00000032 * (-ftp) + 0.016;
        fprintf(fp5, "%g\t\t%d\t\t%0.8g\t\n", dpm, N_TIME, CURRENT_TIME);
        fr = 0.00000032 * (-ftp) + 0.016;
        fprintf(fp4, "%g\t\t%d\t\t%0.8g\t\n", fr, N_TIME, CURRENT_TIME);
    }
    // Close files
    fclose(fp4);
    fclose(fp5);
}
```

9.2 Melt-aspiration pressure coupling UDF for 2 kg min^{-1} (0.033 kg s^{-1}) model

```
#include "udf.h"
real sum, ttp, ftp, p_avg, avg, fr, dpm, atp[100];
int i, size, t, s, icount;

// Function to calculate the average pressure at each timestep
DEFINE_EXECUTE_AT_END(average_pressure)
{
    Domain *d;
    real *array;
    face_t f;
    cell_t c0;
    int ID = 23;
    Thread *thread, *t0;
    FILE *fp1, *fp2, *fp3;
```

```
    // Get the domain and thread
    d = Get_Domain(1);
    thread = Lookup_Thread(d, ID);
    // Get the number of elements in the thread
    size = THREAD_N_ELEMENTS_INT(thread);
    array = (real *)malloc(size * sizeof(real));
    // Open files for writing data
    fp1 = fopen("instpressure.txt", "a+");
    fp2 = fopen("timestpres.txt", "a+");
    fp3 = fopen("movingavg.txt", "a+");
    t = N_TIME;
    real l = CURRENT_TIME;
    Message("the time is \n%d\n", N_TIME);

    // Loop through faces to get pressure data
    begin_f_loop(f, thread)
    {
      c0 = F_C0(f, thread);
      t0 = THREAD_T0(thread);
      array[f] = F_P(c0, t0);
    }
    end_f_loop(f, thread)
    // Calculate sum and write instant pressure to file
    sum = 0.0;
    for (i = 0; i < size; i++)
    {
      fprintf(fp1, "%g\n", array[i]);
      sum += array[i];
    }
   // Calculate the timestep average pressure
    ttp = sum / 14;
    icount = N_TIME % 100;
    // Update the moving average array and calculate the moving average
    ftp -= atp[icount] / 100;
    atp[icount] = ttp;
    ftp += atp[icount] / 100;

    Message("the timestep average is \n%g\n", ttp);
    fprintf(fp2, "%g\t\t%d\t\t%0.8g\t\n", ttp, N_TIME, CURRENT_TIME);
    Message("the totalsum for 10 timestep is \n%g\n", ftp);
    fprintf(fp3, "%g\t\t%d\t\t%0.8g\t\n", ftp, N_TIME, CURRENT_TIME);
    // Free allocated memory and close files
    free(array);
    fclose(fp1);
    fclose(fp2);
    fclose(fp3);
}
// Function to initialize the discrete phase model (DPM) injection
DEFINE_DPM_INJECTION_INIT(initdpm, I)
{
    FILE *fp4, *fp5;
    Particle *p;
    // Open files for writing data
    fp4 = fopen("instdpm.txt", "a+");
    fp5 = fopen("movingdpm.txt", "a+");
```

```
    s = N_TIME;
    real l = CURRENT_TIME;
    Message("the PHYSICAL TIME is \n%g\n", CURRENT_TIME);
    // Loop through particles to set flow rate based on pressure
    loop(p, I->p_init)
    {
        PP_FLOW_RATE(p) = (0.00000066 * (-ftp) + 0.033) / 12;
        dpm = 0.00000066 * (-ftp) + 0.033;
        fprintf(fp5, "%g\t\t%d\t\t%0.8g\t\n", dpm, N_TIME, CURRENT_TIME);
        fr = 0.00000066 * (-ftp) + 0.033;
        fprintf(fp4, "%g\t\t%d\t\t%0.8g\t\n", fr, N_TIME, CURRENT_TIME);
    }
    // Close files
    fclose(fp4);
    fclose(fp5);
}
```

9.3 Melt-aspiration pressure coupling UDF for 4 kg min^{-1} (0.066 kg s^{-1}) model

```
#include "udf.h"
real sum, ttp, ftp, p_avg, avg, fr, dpm, atp[100];
int i, size, t, s, icount;

// Function to calculate the average pressure at each timestep
DEFINE_EXECUTE_AT_END(average_pressure)
{
    Domain *d;
    real *array;
    face_t f;
    cell_t c0;
    int ID = 23;
    Thread *thread, *t0;
    FILE *fp1, *fp2, *fp3;
    // Get the domain and thread
    d = Get_Domain(1);
    thread = Lookup_Thread(d, ID);
    // Get the number of elements in the thread
    size = THREAD_N_ELEMENTS_INT(thread);
    array = (real *)malloc(size * sizeof(real));
    // Open files for writing data
    fp1 = fopen("instpressure.txt", "a+");
    fp2 = fopen("timestpres.txt", "a+");
    fp3 = fopen("movingavg.txt", "a+");
    t = N_TIME;
    real l = CURRENT_TIME;
    Message("the time is \n%d\n", N_TIME);

    // Loop through faces to get pressure data
    begin_f_loop(f, thread)
    {
        c0 = F_C0(f, thread);
        t0 = THREAD_T0(thread);
        array[f] = F_P(c0, t0);
```

```
    }
    end_f_loop(f, thread)
    // Calculate sum and write instant pressure to file
    sum = 0.0;
    for (i = 0; i < size; i++)
    {
        fprintf(fp1, "%g\n", array[i]);
        sum += array[i];
    }
   // Calculate the timestep average pressure
    ttp = sum / 14;
    icount = N_TIME % 100;
    // Update the moving average array and calculate the moving average
    ftp -= atp[icount] / 100;
    atp[icount] = ttp;
    ftp += atp[icount] / 100;

    Message("the timestep average is \n%g\n", ttp);
    fprintf(fp2, "%g\t\t%d\t\t%0.8g\t\n", ttp, N_TIME, CURRENT_TIME);
    Message("the totalsum for 10 timestep is \n%g\n", ftp);
    fprintf(fp3, "%g\t\t%d\t\t%0.8g\t\n", ftp, N_TIME, CURRENT_TIME);
    // Free allocated memory and close files
    free(array);
    fclose(fp1);
    fclose(fp2);
    fclose(fp3);
}
// Function to initialize the discrete phase model (DPM) injection
DEFINE_DPM_INJECTION_INIT(initdpm, I)
{
    FILE *fp4, *fp5;
    Particle *p;
    // Open files for writing data
    fp4 = fopen("instdpm.txt", "a+");
    fp5 = fopen("movingdpm.txt", "a+");
    s = N_TIME;
    real l = CURRENT_TIME;
    Message("the PHYSICAL TIME is \n%g\n", CURRENT_TIME);
    // Loop through particles to set flow rate based on pressure
    loop(p, I->p_init)
    {
        PP_FLOW_RATE(p) = (0.00000088 * (-ftp) + 0.066) / 12;
        dpm = 0.00000088 * (-ftp) + 0.066;
        fprintf(fp5, "%g\t\t%d\t\t%0.8g\t\n", dpm, N_TIME, CURRENT_TIME);
        fr = 0.00000088 * (-ftp) + 0.066;
        fprintf(fp4, "%g\t\t%d\t\t%0.8g\t\n", fr, N_TIME, CURRENT_TIME);
    }
    // Close files
    fclose(fp4);
    fclose(fp5);
}
```

9.4 Melt-aspiration pressure coupling UDF for 6 kg min^{-1} (0.1 kg s^{-1}) model

```
#include "udf.h"
real sum, ttp, ftp, p_avg, avg, fr, dpm, atp[100];
int i, size, t, s, icount;

// Function to calculate the average pressure at each timestep
DEFINE_EXECUTE_AT_END(average_pressure)
{
   Domain *d;
   real *array;
   face_t f;
   cell_t c0;
   int ID = 23;
   Thread *thread, *t0;
   FILE *fp1, *fp2, *fp3;
   // Get the domain and thread
   d = Get_Domain(1);
   thread = Lookup_Thread(d, ID);
   // Get the number of elements in the thread
   size = THREAD_N_ELEMENTS_INT(thread);
   array = (real *)malloc(size * sizeof(real));
   // Open files for writing data
   fp1 = fopen("instpressure.txt", "a+");
   fp2 = fopen("timestpres.txt", "a+");
   fp3 = fopen("movingavg.txt", "a+");
   t = N_TIME;
   real l = CURRENT_TIME;
   Message("the time is \n%d\n", N_TIME);

   // Loop through faces to get pressure data
   begin_f_loop(f, thread)
   {
      c0 = F_C0(f, thread);
      t0 = THREAD_T0(thread);
      array[f] = F_P(c0, t0);
   }
   end_f_loop(f, thread)
   // Calculate sum and write instant pressure to file
   sum = 0.0;
   for (i = 0; i < size; i++)
   {
      fprintf(fp1, "%g\n", array[i]);
      sum += array[i];
   }
  // Calculate the timestep average pressure
   ttp = sum / 14;
   icount = N_TIME % 100;
   // Update the moving average array and calculate the moving average
   ftp -= atp[icount] / 100;
   atp[icount] = ttp;
   ftp += atp[icount] / 100;

   Message("the timestep average is \n%g\n", ttp);
   fprintf(fp2, "%g\t\t%d\t\t%0.8g\t\n", ttp, N_TIME, CURRENT_TIME);
   Message("the totalsum for 10 timestep is \n%g\n", ftp);
   fprintf(fp3, "%g\t\t%d\t\t%0.8g\t\n", ftp, N_TIME, CURRENT_TIME);
```

```
    // Free allocated memory and close files
    free(array);
    fclose(fp1);
    fclose(fp2);
    fclose(fp3);
}
// Function to initialize the discrete phase model (DPM) injection
DEFINE_DPM_INJECTION_INIT(initdpm, I)
{
    FILE *fp4, *fp5;
    Particle *p;
    // Open files for writing data
    fp4 = fopen("instdpm.txt", "a+");
    fp5 = fopen("movingdpm.txt", "a+");
    s = N_TIME;
    real l = CURRENT_TIME;
    Message("the PHYSICAL TIME is \n%g\n", CURRENT_TIME);
    // Loop through particles to set flow rate based on pressure
    loop(p, I->p_init)
    {
        PP_FLOW_RATE(p) = (0.00000133 * (-ftp) + 0.1) / 12;
        dpm = 0.00000133 * (-ftp) + 0.1;
        fprintf(fp5, "%g\t\t%d\t\t%0.8g\t\n", dpm, N_TIME, CURRENT_TIME);
        fr = 0.00000133 * (-ftp) + 0.1;
        fprintf(fp4, "%g\t\t%d\t\t%0.8g\t\n", fr, N_TIME, CURRENT_TIME);
    }
    // Close files
    fclose(fp4);
    fclose(fp5);
}
```

9.5 Melt-aspiration pressure coupling UDF for 12 kg min^{-1} (0.2 kg s^{-1}) model

```
#include "udf.h"
real sum, ttp, ftp, p_avg, avg, fr, dpm, atp[1000];
int i, size, t, s, icount;

// Function to calculate the average pressure at each timestep
DEFINE_EXECUTE_AT_END(average_pressure)
{
    Domain *d;
    real *array;
    face_t f;
    cell_t c0;
    int ID = 23;
    Thread *thread, *t0;
    FILE *fp1, *fp2, *fp3;
    // Get the domain and thread
    d = Get_Domain(1);
    thread = Lookup_Thread(d, ID);
    // Get the number of elements in the thread
    size = THREAD_N_ELEMENTS_INT(thread);
    array = (real *)malloc(size * sizeof(real));
```

```
    // Open files for writing data
    fp1 = fopen("instpressure.txt", "a+");
    fp2 = fopen("timestpres.txt", "a+");
    fp3 = fopen("movingavg.txt", "a+");
    t = N_TIME;
    real l = CURRENT_TIME;
    Message("the time is \n%d\n", N_TIME);

    // Loop through faces to get pressure data
    begin_f_loop(f, thread)
    {
        c0 = F_C0(f, thread);
        t0 = THREAD_T0(thread);
        array[f] = F_P(c0, t0);
    }
    end_f_loop(f, thread)
    // Calculate sum and write instant pressure to file
    sum = 0.0;
    for (i = 0; i < size; i++)
    {
        fprintf(fp1, "%g\n", array[i]);
        sum += array[i];
    }
   // Calculate the timestep average pressure
    ttp = sum / 14;
    icount = N_TIME % 1000;
    // Update the moving average array and calculate the moving average
    ftp -= atp[icount] / 1000;
    atp[icount] = ttp;
    ftp += atp[icount] / 1000;

    Message("the timestep average is \n%g\n", ttp);
    fprintf(fp2, "%g\t\t%d\t\t%0.8g\t\n", ttp, N_TIME, CURRENT_TIME);
    Message("the totalsum for 10 timestep is \n%g\n", ftp);
    fprintf(fp3, "%g\t\t%d\t\t%0.8g\t\n", ftp, N_TIME, CURRENT_TIME);
    // Free allocated memory and close files
    free(array);
    fclose(fp1);
    fclose(fp2);
    fclose(fp3);
}
// Function to initialize the discrete phase model (DPM) injection
DEFINE_DPM_INJECTION_INIT(initdpm, I)
{
    FILE *fp4, *fp5;
    Particle *p;
    // Open files for writing data
    fp4 = fopen("instdpm.txt", "a+");
    fp5 = fopen("movingdpm.txt", "a+");
    s = N_TIME;
    real l = CURRENT_TIME;
    Message("the PHYSICAL TIME is \n%g\n", CURRENT_TIME);
    // Loop through particles to set flow rate based on pressure
    loop(p, I->p_init)
    {
```

```
        PP_FLOW_RATE(p) = (0.00000266 * (-ftp) + 0.2) / 12;
        dpm = 0.00000266 * (-ftp) + 0.2;
        fprintf(fp5, "%g\t\t%d\t\t%0.8g\t\n", dpm, N_TIME, CURRENT_TIME);
        fr = 0.00000266 * (-ftp) + 0.2;
        fprintf(fp4, "%g\t\t%d\t\t%0.8g\t\n", fr, N_TIME, CURRENT_TIME);
    }
    // Close files
    fclose(fp4);
    fclose(fp5);
}
```

9.6 Review of various CFD studies carried out on the CCGA process.

Author	2D/ 3D	Steady/ transient	Single/two -phase flow	Turbulence model	Secondary phase	Break-up model	Remarks
(Mi et al., 1996)	2D	Steady	Single-phase	*k-ε*	–	–	• Effect of gas inlet pressure was investigated. • Recirculation zone length increased with increase in pressure. But decreased with increase in pressure while operating at closed-wake condition.
(Mi et al., 1997)	2D	Steady	Single-phase	*k-ε*	–	–	• Effect of melt nozzle tip geometry on the gas-only flow was studied. • With increase in melt tip length, the second recirculation zone increased, but location of Mach-disk did not change. • Increase in melt nozzle taper angle pushed the Mach-disk downstream, and formed a weaker Mach-disk.
(Espina and Piomelli, 1998)	2D	Steady	Single-phase	*k-ε*	–	–	• Effect of varying model constants in the *k-ε* model, and were studied. • The model over-predicted *k*, under-predicted *ε,* hence resulting in under-predicted growth of the shear layers and reattachments.
(Ting and Anderson, 2004)	2D	Steady	Single-phase	*k-ε*	–	–	• The CFD model detailed the gas-only flow condition at different gas inlet pressure. • The model correctly captured the flow discontinuity immediate downstream in closed-wake condition. • The model displayed significant discrepancy between experimental and numerical results of aspiration pressure.
(Zeoli and Gu, 2006)	2D	Transient	Two-phase	RSM	DPM	TAB and KH	• Investigation of secondary break-up by employing TAB and KH breakup model. • Particle cooling on three different particle size - 1, 3 and 5 mm were studied.

							• The model well predicted that with increased particle size, the solidification time increases, and velocity decreases. • Weber number > 80, KH break-up, and for weber number < 80, TAB break-up was implemented. • Model lacked effective capturing of effect of gas-to-melt ratio.
(Zeoli and Gu, 2008a)	2D	Transient	Two-phase	RSM	DPM	TAB and KH	• Investigation of droplet cooling and break-up for different particle sizes - 1,3, and 5 mm. • Cooling and velocity profile of the particle are proportional. • Model captures the thermal history appropriately. Thermal history closely corresponds with the solid fraction observed during solidification. • The model over-predicts the solid fraction during solidification for bigger particle size.
(Zeoli and Gu, 2008b)	2D	Transient	Two-phase	RSM	DPM	TAB and KH	• Performance two different gas nozzle designs - annular slit and isentropic plug nozzle investigated. • The isentropic plug nozzle was investigated for different gas temperatures - 300K, 400K and 500K, for three different particle size - 1, 3 and 5 mm. • Formation and progression of strong oblique shocks absent in isentropic plug nozzle. • No significant change in the cooling rate observed for inlet gas with higher temperature. • Gas with higher temperature undergo finer atomisation compared to lower temperature.
(Tong and Browne, 2008)	2D	Unsteady	Two-phase	DNS	FTF	-	• The study reported the topology evolution of gas and melt flow using DNS for a flow where melt is first introduced followed by gas flow. • The model displayed simultaneous pinching of melt stream and formation fountain break-up. The discontinued melt stream further underwent a secondary fountain breakup.

							• Pressure greatly changed when liquid column discontinued, resulting in very high pressure within the wake. This is because of the closed-wake condition, where pressure rises sharply.
(Tong and Browne, 2009)	2D	transient	Single-phase	Combined unified procedure (CUP)	–	–	• The gas was modelled as a compressible flow via a novel CUP model. • The model outlined the transient gas flow dynamics • The model under-predicted the aspiration pressure.
(Aydin and Unal, 2011)	2D	Steady	Single-phase	*k-ε*	–	–	• Effect of gas inlet pressure was studied. • Although the trend in the aspiration pressure obtained between the experimental and theoretical runs were same, an offset in the value exists. • Increase in gas inlet pressure, produces more efficient flow separation within the gas delivery nozzle.
(Zhao et al., 2012)	2D	Steady and Transient	Two-phase	*k-ε* and RSM	VOF	CSF	• Comparison between k-ε and RSM turbulence models were carried out. • k-ε turbulence model under-predicted flow expansion. • RSM model better performed under steep pressure gradients. • VOF model validated the physical phenomenon of liquid column transforming into sheets while undergoing pre-filming.
(Zeoli et al., 2012)	3D	Steady & Transient	Two-phase	RSM & LES	VOF	CSF	• 3D Two-phase flow studied via two means: Steady state with RSM, and Transient state with LES model. • Steady state captures the mushroom-shaped melt entrainment from the nozzle. • Unsteady state captures the turbulence induced and unstable nature of the melt flow. • Although model captures the unstable nature of the flow around melt nozzle exit, it under-predicted the secondary atomisation even at higher gas-to-melt ratio.
(Motaman et al., 2013)	2D	steady	Single-phase	*k-ω*	–	–	• Effect of melt nozzle geometry was studied on gas-only flow. • The model effectively captured and reflected the experimental flow.

							• Increase in pressure impeded the back-streaming flow
(Urionabarrenetxea et al., 2013)	2D	Steady	Single-phase	*k-ε Realisable*	–	–	• Investigated the effect of different operating gas – Argon, Nitrogen, Helium and Carbon-di-oxide, and different gas inlet pressures to study the gas flow behaviour. • Helium gas at 50 bar produced twice the velocity as Nitrogen at 50 bar, and this is reflected on the fine particle size seen in experimental runs. Nitrogen, Argon, and Carbon-di-oxide resulted in a similar velocity range.
(Firmansyah et al., 2014)	2D	Transient	Two-phase	RSM	DPM	KH	• The study investigated the droplet break-up of three different sizes - 1, 3, and 5mm, all operated under an industry based GMR of 1.1. • The study reports increased secondary atomisation downstream compared to nozzle front. • The secondary atomisation occurs within a narrow spatial region radially, i.e., 12 mm from the axis. This is 1.5 times the nozzle diameter. • Both increase in gas pressure and temperature resulted in smaller particle size.
(Motaman et al., 2015)	2D	Steady	Single-phase	*k-ω SST*	–	–	• Investigated the gas flow behaviour using four different melt nozzle and two gas die designs, especially on wake-closure pressure. • Melt nozzles with tip profiles exhibited extended recirculation zone into the melt delivery tube compared to melt nozzle with a lip/tip. However, the recirculation length for the melt nozzle with tips were shorter compared to the nozzles with tip. • C-D nozzles generated smaller shock-cells compared to cylindrical/choked nozzles, but flow in C-D nozzle transitioned into closed-wake at higher gas pressure compared to cylindrical nozzles.

(Thompson et al., 2016)	3D	Transient	Two-phase	*k-ω SST*	DPM	KH-TAB and KHRT	• The study investigated the effect of two different droplet break-up models: KH-TAB and KHRT using injection droplets of 1 mm. • KH-TAB break-up model under-predicted the droplet break-up, whereas KHRT model closely predicted the droplet break-up compared with experimental runs. • KHRT model also well predicted the increase in particle size with increase in protrusion length and surface tension. s
(Schwenck et al., 2017)	2D	Steady	Single-phase	*k-ε*	–	–	• The effect of cylindrical and C-D nozzles and their slit width were investigated on the gas flow-field for different gas inlet pressures. • For a given gas pressure, a higher gas velocity is observed for a larger gas slit compared to larger gas slit. The velocity further increases when C-D nozzle is employed.
(Kaiser et al., 2018)	2D	unsteady	Two-phase	RSM	DPM	KH	• Comparison between annular slit nozzle and isentropic plug nozzle were conducted. • Computationally intensive simulation – compressible unsteady flow using the RSM turbulence model with a small timestep size of 1e-06 s. • Computational load reduced by decreased mesh elements. • Isentropic plug nozzle developed flow with reduced effects of shocks, but created a positive aspiration pressure at the melt nozzle tip.
(Arachchilage et al., 2019)	3D	Transient	Two-phase	LES	VOF	CSF	• The study reports a comprehensive description of the primary melt break-up and its mechanism. • The effect of gas pressure on the melt break-up details: low pressure gas shears the liquid column to result in melt break-up, whereas, high pressure gas impinges into the liquid column to break-up into ligaments. • Melt break-up occurs due to the action opposite direction vortex at the melt-gas interface.

(Ashokkumar, 2020)	2D & 3D	Steady and Transient	Single- and two-phase	*k-ω*	DPM	No break-up	• Effect of increasing gas inlet pressure was investigated for gas nozzles have with and without offset with the melt nozzle wall. • For case with offset, two significant recirculation zones were observed: one at the gas nozzle exit, and other one at the melt nozzle exit. Increasing pressure increase the length of the second recirculation zone, but unaffected the first recirculation zone. • For case without offset, only a recirculation zone at melt nozzle exit was observed; increase in gas pressure developed a stronger recirculation zone. • At higher gas inlet pressure, atomiser with offset developed lower aspiration pressure. • Presence of fluctuating aspiration pressure recorded during two-phase flow, and the recirculation of particles within the recirculation zone was captured.
(Wang et al., 2021)	3D	Transient	Two-phase	LES	VOF-DPM	CSF & KHRT	• A VOF-DPM model is employed with LES model to study the primary and secondary atomisation mechanism. • The study reports $F_p + F_g + F_d > F_f$ ensures smooth running of the process, whereas $F_p + F_g + F_d < F_f$ risks in melt freeze-off. • The study reports the melt droplets initially travel towards the axis and thereafter disperses radially outward. • Three different types of particle imperfection is reported: torn-surface, when ligament encloses solidified particle; fused powder, when two incomplete particle solidify together; and satellite powder, when smaller droplets impinges into solidified particle.
(Zhao et al., 2023)	2D	Steady	Single-phase	*k-ε*	–	–	• Effect of gas nozzle exit area on the gas flow-field was examined with same gas inlet pressure of 4 MPa. • With increase in nozzle exit area, the position of the Mach-disk moves upstream towards the melt nozzle. • Mach-disk becomes more profound at increased nozzle exit area.
(Liu et al., 2023a)	2D	Steady	Two-phase	*k-ω SST*	DPM	No break-up	• Investigated the effect of assisted gas nozzles (secondary gas nozzles) on gas flow and particle size.

							• At 200 m/s inlet velocity of AGN, the particles accelerate downstream much higher compared to without AGN. The droplet dispersion angle reduces, and particle cooling rate increases with AGN. However, in physical atomisation, this condition would lead to larger particles and satellite formation.
(Luo et al., 2023)	2D	Transient	Two-phase	*k-ω SST*	DPM	No break-up	• Elemental loss in the atomisation process was investigated by considering no melt break-up. • The study predicted bigger particles lose more element compared to smaller particles. • Decrease in melt over-heat resulted in reduced elemental loss. However, decrease in over-heat increased the particle size.
(Wang et al., 2023c)	2D	Transient	Two-phase	*k-ω SST*	DPM	KHRT	• Secondary atomisation is investigated for varying atomisation pressure, melt mass flow rates, and gas temperatures. • With constant gas pressure of 3 MPa, and increasing melt flow rate, from 0.025 to 0.1 kg/s, the d_{50} increased from 33.3 to 89.2 µm. • With constant melt flow rate of 0.05 kg/s and increasing gas pressure, from 1 to 3 MPa, the d_{50} decreased from 97.9 to 48.9 µm. • Two cases having same GMR were studied. 3 MPa with 0.1 kg/s, and 1.5 MPa with 0.05 kg/s, resulted in the same GMR. The form exhibited a d_{50} of 89.2 µm, and cooling rate of 5.81e+4, respectively. While the later displayed of a d_{50} of 82.7 µm, and cooling rate of 3.12e+4, respectively. • With increase in gas pressure, the droplet dispersion angle reduced from 29 to 16, indicating at high pressure the process is susceptible to increased collision and larger particle size. • With increase in gas temperature, the droplet dispersion angle decreases initially, but thereafter increases. Although, the mass flow rate of the gas decreases it reports a increase in the particle

							size, and this is due to the increased kinetic energy of gas at higher temperature.
(Zhang et al., 2023a)	2D	Transient	Two-phase	*k-ω SST*	DPM	TAB	• Investigation of secondary break-up models – TAB and KH models for a mono-sized droplet of 1 mm, and study on the satellite forming mechanism were reported. • The TAB model predicted particle diameter range from 7.35-1000 µm, whereas for the KH model the particle diameter ranged from 11.1-920 µm. However, TAB model displayed a symmetrical distribution similar to experimental recordings. • The satellite formation was attributed to the mesoscopic scale eddy in the gas flow leading to aggregation of droplets. • Three type of satellite morphology were reported. first might be because of larger particles colliding with smaller droplets; second might be because of smaller particles colliding with larger droplets; third might be because of two droplets colliding simultaneously and solidifying.
(Liu et al., 2023b)	2D	Transient	Two-phase	*k-ω SST*	VOF	CSF	• Primary break-up phenomenon was investigated under increasing melt flow rate, gas inlet pressure, and gas temperatures. • Based on the total forces acting on the liquid column, i.e., gravity (F_g), buoyancy (F_f), drag force (F_d), and pressure (F_p), the deformation mechanism of the liquid column is derived. • $F_p + F_f > F_d + F_g$ resulted in umbrella deformation (liquid film), where as $F_p + F_f < F_d + F_g$ resulted in fountain deformation. • Increase in gas pressure results in increased aspiration pressure, resulting in delayed entrainment of the melt from the melt nozzle.
(Wang et al., 2023b)	2D	Transient	Two-phase	*k-ε*	VOF	VOF	• Impact of gas inlet pressure is studied for varying melt bore diameter. • Low gas inlet induces nozzle clogging; and very high pressure induces melt freeze-off. • Intermediary gas pressure produces better particles.

(Wang et al., 2023e)	3D	Transient	Two-phase	LES	VOF	CSF	• The study investigated the gas inlet pressure and gas nozzle angle by implementing adaptive mesh refinement and modelling the nitrogen gas as incompressible flow. • At higher gas inlet pressure, the secondary atomisation occurs sooner compared to lower pressure, but higher pressures result in droplets travelling towards the axis, resulting in satellites and increased particle size. • At 20° and 60° gas nozzle angles, the secondary atomised droplets converged towards the axis, whereas for 40° nozzle angle, the droplets dispersed to result in finer atomised particles.
(Wang et al., 2023a)	3D	Transient	Two-phase	RSM	VOF and DPM	CSF & KHRT	• VOF and DPM models were implemented to investigate for two-phase flow. • No flow separation at the melt nozzle tip observed. • Flow of gas in recirculation zone reattaches with the flow-field at the stagnation point. • Particles with higher initial velocity travels significantly radially away, undergoing finer atomisation.
(Wang et al., 2024a)	2D	Transient	Two-phase	*k-ε* and LES	VOF	CSF	• The study investigated nozzle clogging phenomenon via two different melt entrainment sequence: Type1- gas flow followed by melt introduction; and type2 - melt flow introduction followed by gas flow. • Liquid film is observed at the melt nozzle exit when gas is first introduced, and gas impingement and liquid necking phenomena is observed when melt is first introduced. • Under increasing gas inlet pressure - 2.5, 3.5, and 4.5 MPa, type1 flow experiences nozzle clogging at low pressures, but type2 flow do not experience nozzle clogging for any of the pressures.
(Wang et al., 2024b)	3D	Transient	Two-phase	*k-ω SST*	VOF	CSF	• The study investigated the implementation of a supplementary gas nozzle in addition to the primary gas nozzles, and its effect on melt atomisation.

							• Implementation of secondary nozzles facilitated in lower aspiration pressure. However, lower pressures resulted in much lower aspiration compared to higher pressures. • Based on the pressure of secondary nozzles, the break-up progressed via different mechanism: at 1 MPa, break-up via ligament shedding, no significant droplet formation; at 2 MPa, break-up via ligaments, but only few droplets formation; at 3 MPa, upto 70% ligaments in liquid phase underwent droplet formation.
(Hua et al., 2024)	3D	Transient	Two-phase	LES	VOF-DPM	CSF & KHRT	• The study investigated the CFD model of gas atomisation by splitting into two domains: one near melt nozzle and other as rest of the domain. VOF model is applied via OpenFoam for the domain near to the melt nozzle, and DPM model is applied for the rest of the domain, and is simulated via ANSYS Fluent. • Operating gas is considered as incompressible for a GMR of 1.8, close to as used in the commercial atomisation. • The model predicted the liquid column flow undergoes umbrella (liquid film), and subsequently breaks-up into ligaments and droplets. Later, the liquid column flows without any deformation briefly before attacked by the gas jet. • The particle size distribution evaluated by considering the break-up model KHRT and WAVE were similar, but they underestimated particles less than 22 µm. TAB model well predicted breakup for particles less than 32 µm, but over-predicted particles 32-56 µm, and under-predicted for particles 56-140 µm.

10 Reference

AKSOY, A. & ÜNAL, R. 2006. Effects of gas pressure and protrusion length of melt delivery tube on powder size and powder morphology of nitrogen gas atomised tin powders. *Powder Metallurgy,* 49**,** 349-354.

ALOBAID, F., ALMOHAMMED, N., MASSOUDI FARID, M., MAY, J., RÖßGER, P., RICHTER, A. & EPPLE, B. 2022. Progress in CFD Simulations of Fluidized Beds for Chemical and Energy Process Engineering. *Progress in Energy and Combustion Science,* 91**,** 100930.

ANDERSON, I., FIGLIOLA, R. & MORTON, H. 1991. Flow mechanisms in high pressure gas atomization. *Materials Science and Engineering: A,* 148**,** 101-114.

ANDERSON, I., TERPSTRA, R. & FIGLIOLA, R. 2005. Visualization of enhanced primary atomization for powder size control. *Advances in powder metallurgy and particulate materials,* 1**,** 2.

ANDERSON, I. E. & ACHELIS, L. 2017. Two Fluid Atomization Fundamentals. *Metal Sprays and Spray Deposition.* Springer.

ANDERSON, I. E., BYRD, D. & MEYER, J. 2010. Highly tuned gas atomization for controlled preparation of coarse powder. *Materialwissenschaft und Werkstofftechnik,* 41**,** 504-512.

ANDERSON, I. E. & TERPSTRA, R. L. 2002. Progress toward gas atomization processing with increased uniformity and control. *Materials Science and Engineering: A,* 326**,** 101-109.

ANDERSON, I. E., WHITE, E. M. H. & DEHOFF, R. 2018. Feedstock powder processing research needs for additive manufacturing development. *Current Opinion in Solid State and Materials Science,* 22**,** 8-15.

ANSYSFLUENT®THEORY-GUIDE ANSYS Fluent Theory Guide. Release 19 ed.

ANTIPAS, G. S. E. 2009. Modelling of the break up mechanism in gas atomization of liquid metals Part II. The gas flow model. *Computational Materials Science,* 46**,** 955-959.

ANTONY, L. V. M. & REDDY, R. G. 2003. Processes for production of high-purity metal powders. *JOM,* 55**,** 14-18.

ARACHCHILAGE, K. H., HAGHSHENAS, M., PARK, S., ZHOU, L., SOHN, Y., MCWILLIAMS, B., CHO, K. & KUMAR, R. 2019. Numerical simulation of high-pressure gas atomization of two-phase flow: Effect of gas pressure on droplet size distribution. *Advanced Powder Technology,* 30**,** 2726-2732.

ASHGRIZ, N. 2011. *Handbook of atomization and sprays: theory and applications*, Springer Science & Business Media.

ASHOKKUMAR, A. P. 2020. *COMPUTATIONAL MODELLING OF CLOSE-COUPLED GAS ATOMIZATION.* PhD Doctoral theis, University of Leeds.

AYDIN, O. & UNAL, R. 2011. Experimental and numerical modeling of the gas atomization nozzle for gas flow behavior. *Computers & Fluids,* 42**,** 37-43.

BIGG, T. & MULLIS, A. 2020. Spatially Resolved Velocity Mapping of the Melt Plume During High-Pressure Gas Atomization of Liquid Metals. *Metallurgical and Materials Transactions B,* 51**,** 1973-1988.

BISWAS, S. & QIAO, L. 2017. A Numerical Investigation of Ignition of Ultra-Lean Premixed H 2 /Air Mixtures by Pre-Chamber Supersonic Hot Jet. *SAE International Journal of Engines,* 10.

CAI, Z.-Y., ZHANG, C., WANG, R.-C., PENG, C.-Q., QIU, K. & WANG, N.-G. 2016. Effect of pre-annealing on microstructure and compactibility of gas-atomized Al-Si alloy powders. *Transactions of Nonferrous Metals Society of China,* 26**,** 2355-2362.

CHANG, I. & ZHAO, Y. 2013. *Advances in powder metallurgy: Properties, processing and applications*, Elsevier.

CHIGIER, N. & FARAGO, Z. 1992. Morphological classification of disintegration of round liquid jets in a coaxial air stream. *Atomization and Sprays,* 2.

DESHPANDE, S. S., GURJAR, S. R. & TRUJILLO, M. F. 2015. A computational study of an atomizing liquid sheet. *Physics of Fluids,* 27**,** 082108.

DUNKLEY, J. J. 2019. Metal powder atomisation methods for modern manufacturing. *Johnson Matthey Technology Review,* 63**,** 226-232.

ESPINA, P. & PIOMELLI, U. Study of the gas jet in a close-coupled gas-metal atomizer. 36th AIAA Aerospace Sciences Meeting and Exhibit, 1998. 959.

FIRMANSYAH, D. A., KAISER, R., ZAHAF, R., COKER, Z., CHOI, T.-Y. & LEE, D. 2014. Numerical simulations of supersonic gas atomization of liquid metal droplets. *Japanese Journal of Applied Physics,* 53**,** 05HA09.

GALLAGHER, C., KERR, E. & MCFADDEN, S. 2023. Particle size distribution for additive manufacturing powder using stereological corrections. *Powder Technology,* 429**,** 118873.

GEPPERTH, S., GUILDENBECHER, D., KOCH, R. & BAUER, H.-J. Pre-filming primary atomization: Experiments and modeling. 23rd European Conference on Liquid Atomization and Spray Systems (ILASS-Europe 2010), Brno, Czech Republic, September, 2010. 6-8.

HSIANG, L.-P. & FAETH, G. M. 1992. Near-limit drop deformation and secondary breakup. *International journal of multiphase flow,* 18**,** 635-652.

HUA, J., GOBBER, F. S., ACTIS GRANDE, M., MORTENSEN, D. & ODDEN, J. O. 2024. A numerical modeling framework for predicting the effects of operational parameters on particle size distribution in the gas atomization process for Nickel-Silicon alloys. *Powder Technology,* 435**,** 119408.

JADIDI, M., MOGHTADERNEJAD, S. & DOLATABADI, A. 2015. A comprehensive review on fluid dynamics and transport of suspension/liquid droplets and particles in high-velocity oxygen-fuel (HVOF) thermal spray. *Coatings,* 5**,** 576-645.

JALAAL, M. & MEHRAVARAN, K. 2012. Fragmentation of falling liquid droplets in bag breakup mode. *International Journal of Multiphase Flow,* 47**,** 115-132.

JIANG, G., HENEIN, H. & SIEGEL, M. 1988. Intelligent sensors for atomization processing of molten metals and alloys. *Production and Processing of Fine Particles.* Elsevier.

KAISER, R., LI, C., YANG, S. & LEE, D. 2018. A numerical simulation study of the path-resolved breakup behaviors of molten metal in high-pressure gas atomization: With emphasis on the role of shock waves in the gas/molten metal interaction. *Advanced Powder Technology,* 29**,** 623-630.

KARLSSON, J., SNIS, A., ENGQVIST, H. & LAUSMAA, J. 2013. Characterization and comparison of materials produced by Electron Beam Melting (EBM) of two different Ti–6Al–4V powder fractions. *Journal of Materials Processing Technology,* 213**,** 2109-2118.

KUNDU, P. K., COHEN, I. M. & DOWLING, D. R. 2012. Chapter 15 - Compressible Flow. *In:* . (ed.) *Fluid Mechanics (Fifth Edition).* Boston: Academic Press.

LAUNDER, B. E. & SPALDING, D. B. 1974. PAPER 8 - THE NUMERICAL COMPUTATION OF TURBULENT FLOWS. *In:* PATANKAR, S. V., POLLARD, A., SINGHAL, A. K. & VANKA, S. P. (eds.) *Numerical Prediction of Flow, Heat Transfer, Turbulence and Combustion.* Pergamon.

LIU, J.-Q., DONG, Y.-N., WANG, P., ZHAO, H., PANG, J., LI, X.-Y. & ZHANG, J.-Q. 2023a. Simulation and experiment investigations on fabrication of Fe-based

amorphous powders by a novel atomization process equipped with assisted gas nozzles. *Journal of Iron and Steel Research International,* 30**,** 1142-1155.

LIU, J., WANG, P., DONG, Y., ZHAO, H., PANG, J. & ZHANG, J. 2023b. Investigation on close-coupled gas atomization for Fe-based amorphous powder production via simulation and industrial trials: Part I. Melt breakup behaviors during primary atomization. *Journal of Materials Research and Technology,* 27**,** 6568-6580.

LIU, Y.-Z., MINAGAWA, K., KAKISAWA, H. & HALADA, K. 2007. Melt film formation and disintegration during novel atomization process. *Transactions of Nonferrous Metals Society of China,* 17**,** 1276-1281.

LUBANSKA, H. 1970. Correlation of spray ring data for gas atomization of liquid metals. *Jom,* 22**,** 45-49.

ŁUKASZEWICZ, G. & KALITA, P. 2016. Navier–stokes equations. *Advances in Mechanics and Mathematics,* 34.

LUO, S., OUYANG, Y., YANG, H., WU, Y., PU, B., WANG, H. & WANG, H. 2023. Predicting the element loss in aluminum (AA2195) powder produced by gas atomization with a numerical model. *Powder Technology,* 430**,** 119013.

MANSOUR, A. & CHIGIER, N. 1990. Disintegration of liquid sheets. *Physics of Fluids A: Fluid Dynamics,* 2**,** 706-719.

MATES, S. P. & SETTLES, G. S. 1996. High-speed imaging of liquid metal atomization by two different close-coupled nozzles. *Advances in Powder Metallurgy and Particulate Materials--1996.,* 1**,** 1.

MATES, S. P. & SETTLES, G. S. 2005. A study of liquid metal atomization using close-coupled nozzles, Part 1: Gas dynamic behavior. *Atomization and Sprays,* 15.

MAZUMDAR, Y. C., DEMAURO, E. P., WAGNER, J., ARIENTI, M., GUILDENBECHER, D. R., FARIAS, P. A. & GRASSER, T. W. 2016. Aerodynamic Breakup and Secondary Drop Formation for a Liquid Metal Column in a Shock-Induced Cross-Flow. Sandia National Lab.(SNL-NM), Albuquerque, NM (United States); Sandia ….

MCCARTHY, I. N., ADKINS, N. J., ASLAM, Z., MULLIS, A. M. & COCHRANE, R. F. 2013. High speed imaging and Fourier analysis of the melt plume during close coupled gas atomisation. *Powder Metallurgy,* 52**,** 205-212.

MI, J., FIGLIOLA, R. & ANDERSON, I. 1997. A numerical investigation of gas flow effects on high-pressure gas atomization due to melt tip geometry variation. *Metallurgical and Materials transactions B,* 28**,** 935-941.

MI, J., FIGLIOLA, R. S. & ANDERSON, I. E. 1996. A numerical simulation of gas flow field effects on high pressure gas atomization due to operating pressure variation. *Materials Science and Engineering: A,* 208**,** 20-29.

MIYANAJI, H., RAHMAN, K. M., DA, M. & WILLIAMS, C. B. 2020. Effect of fine powder particles on quality of binder jetting parts. *Additive Manufacturing,* 36**,** 101587.

MOTAMAN, S. 2013. *High-speed imaging and computational modelling of close-coupled gas atomization*, University of Leeds.

MOTAMAN, S., MULLIS, A. M., COCHRANE, R. F. & BORMAN, D. J. 2015. Numerical and Experimental Investigations of the Effect of Melt Delivery Nozzle Design on the Open- to Closed-Wake Transition in Closed-Coupled Gas Atomization. *Metallurgical and Materials Transactions B,* 46**,** pp. 1990-2004.

MOTAMAN, S., MULLIS, A. M., COCHRANE, R. F., MCCARTHY, I. N. & BORMAN, D. J. 2013. Numerical and experimental modelling of back stream flow during close-coupled gas atomization. *Computers & Fluids,* 88**,** 1-10.

MOURA, A. F. & ROSA, M. A. P. A Computer Program for Calculating Normal and Oblique Shock Waves for Airflows in Chemical and Thermodynamic Equilibrium. 22nd International Congress of Mechanical Engineering, 2013. 2323-2333.

MULLIS, A., COCHRANE, R., ASLAM, Z., MCCARTHY, I. & ADKINS, N. 2007. High-Frame-Rate Analysis of Spray Cone Geometry during Close-Coupled Gas Atomization. *ADVANCES IN POWDER METALLURGY AND PARTICULATE MATERIALS,* 1**,** 02.

MULLIS, A., MCCARTHY, I. & COCHRANE, R. High speed imaging techniques for the analysis of close-coupled gas atomisation. Proceedings of the World Powder Metallurgy Congress and Exhibition, World PM 2010, 2010. European Powder Metallurgy Association (EPMA).

MULLIS, A. M., COCHRANE, R. F., MCCARTHY, I. N. & ADKINS, N. J. 2013a. Log-Normal Melt Pulsation in Close-Coupled Gas Atomization. *Metallurgical and Materials Transactions B,* 44**,** 789-793.

MULLIS, A. M., FARRELL, L., COCHRANE, R. F. & ADKINS, N. J. 2013b. Estimation of Cooling Rates During Close-Coupled Gas Atomization Using Secondary Dendrite Arm Spacing Measurement. *Metallurgical and Materials Transactions B,* 44**,** 992-999.

MULLIS, A. M., MCCARTHY, I. N. & COCHRANE, R. F. 2011. High speed imaging of the flow during close-coupled gas atomisation: Effect of melt delivery nozzle geometry. *Journal of Materials Processing Technology,* 211**,** 1471-1477.

NEGEED, E.-S. R., HIDAKA, S., KOHNO, M. & TAKATA, Y. 2011. Experimental and analytical investigation of liquid sheet breakup characteristics. *International Journal of Heat and Fluid Flow,* 32**,** 95-106.

OOSTHUIZEN, P. H. & CARSCALLEN, W. E. 1997. *Compressible fluid flow*, McGraw-Hill New York.

PAKSERESHT, P. & APTE, S. V. 2019. Modeling the dense spray regime using an euler-lagrange approach with volumetric displacement effects. *arXiv preprint arXiv:1910.00746*.

QU, Z., ZHANG, P., LAI, Y., WANG, Q., SONG, J. & LIANG, S. 2022. Influence of powder particle size on the microstructure of a hot isostatically pressed superalloy. *Journal of Materials Research and Technology,* 16**,** 1283-1292.

RATHAKRISHNAN, E. 2019. Applied gas dynamics.

ROSARIO, N. 2012. *Simulation of a Solid Rocket Exhaust System.*

SA, S. J. 2017. Flow-induced breakup of drops and bubbles. *arXiv preprint arXiv:1701.06157*.

SADHAL, S. S., AYYASWAMY, P. S. & CHUNG, J. N. 2012. *Transport phenomena with drops and bubbles*, Springer Science & Business Media.

SCHWENCK, D., ELLENDT, N., FISCHER-BÜHNER, J., HOFMANN, P. & UHLENWINKEL, V. 2017. A novel convergent–divergent annular nozzle design for close-coupled atomisation. *Powder Metallurgy,* 60**,** 198-207.

SHAO, C., LUO, K., CHAI, M. & FAN, J. 2018. Sheet, ligament and droplet formation in swirling primary atomization. *AIP Advances,* 8**,** 045211.

SHI, Y., LU, W., SUN, W., ZHANG, S., YANG, B. & WANG, J. 2022. Impact of gas pressure on particle feature in Fe-based amorphous alloy powders via gas atomization: Simulation and experiment. *Journal of Materials Science & Technology,* 105**,** 203-213.

SHINJO, J. & UMEMURA, A. 2010. Simulation of liquid jet primary breakup: Dynamics of ligament and droplet formation. *International Journal of Multiphase Flow,* 36**,** 513-532.

SI, C.-R., ZHANG, X.-J., WANG, J.-B. & LI, Y.-J. 2014. Design and evaluation of a Laval-type supersonic atomizer for low-pressure gas atomization of molten metals. *International Journal of Minerals, Metallurgy, and Materials,* 21**,** 627-635.

SILVA, F. C. D., LIMA, M. L. D. & COLOMBO, G. F. 2022. Evaluation of a Mathematical Model Based on Lubanska Equation to Predict Particle Size for Close-Coupled Gas Atomization of 316L Stainless Steel. *Materials Research,* 25.

SRIVASTAVA, V. C. & OJHA, S. N. 2006. Effect of aspiration and gas–melt configuration in close coupled nozzle on powder productivity. *Powder Metallurgy,* 49**,** 213-218.

THOMPSON, J. S., HASSAN, O., ROLLAND, S. A. & SIENZ, J. 2016. The identification of an accurate simulation approach to predict the effect of operational parameters on the particle size distribution (PSD) of powders produced by an industrial close-coupled gas atomiser. *Powder Technology,* 291**,** 75-85.

TING, J. A Pulsatile Atomization Model. 41st Aerospace Sciences Meeting and Exhibit, 2003. (p. 1283).

TING, J. & ANDERSON, I. E. 2004. A computational fluid dynamics (CFD) investigation of the wake closure phenomenon. *Materials Science and Engineering: A,* 379**,** 264-276.

TING, J., ANDERSON, I. E., TERPSTRA, R. & MI, J. 1998. Design and testing of an improved convergent-divergent discrete-jet high pressure gas atomization nozzle. *Metal Powder Industries Federation, Advances in Powder Metallurgy & Particulate Materials- 1998,* 3**,** 10.

TONG, M. & BROWNE, D. J. 2008. Direct numerical simulation of melt–gas hydrodynamic interactions during the early stage of atomisation of liquid intermetallic. *Journal of Materials Processing Technology,* 202**,** 419-427.

TONG, M. & BROWNE, D. J. 2009. Modelling compressible gas flow near the nozzle of a gas atomiser using a new unified model. *Computers & Fluids,* 38**,** 1183-1190.

ÜNAL, A. 1988. Influence of nozzle geometry in gas atomisation of rapidly solidified aluminium alloys. *Materials science and technology,* 4**,** 909-915.

ÜNAL, A. 1989a. Flow separation and liquid rundown in a gas-atomization process. *Metallurgical Transactions B,* 20**,** 613-622.

ÜNAL, A. 1989b. Influence of gas flow on performance of "confined" atomization nozzles. *Metallurgical and Materials Transactions B,* 20**,** 833-843.

ÜNAL, R. 2006. The influence of the pressure formation at the tip of the melt delivery tube on tin powder size and gas/melt ratio in gas atomization method. *Journal of Materials Processing Technology,* 180**,** 291-295.

ÜNAL, R. 2007a. Improvements to close coupled gas atomisation nozzle for fine powder production. *Powder metallurgy,* 50**,** 66-71.

ÜNAL, R. 2007b. Investigation on metal powder production efficiency of new convergent divergent nozzle in close coupled gas atomisation. *Powder Metallurgy,* 50**,** 302-306.

ÜNAL, R. & AYDıN, M. 2007. High Efficient Metal Powder Production by Gas Atomisation Process. *Materials Science Forum,* 534-536**,** 57-60.

URIONABARRENETXEA, E., MARTÍN, J., RIVAS, A., ITURRIZA, I. & CASTRO, F. Powder Manufacturing: EXPERIMENTAL STUDY AND SIMULATION OF THE GAS FLOW IN THE ATOMISATION CHAMBER DURING CLOSE-COUPLED GAS ATOMISATION. European Congress and Exhibition on Powder Metallurgy. European PM Conference Proceedings, 2013. The European Powder Metallurgy Association, 1.

URIONABARRENETXEA, E., MARTÍN, J., RIVAS, A., ITURRIZA, I. & CASTRO, F. Powder Manufacturing and Processing: Influence of Key Operational and Geometrical Variables on the Particle Size during Close-Coupled Gas Atomisation.

European Congress and Exhibition on Powder Metallurgy. European PM Conference Proceedings, 2014. The European Powder Metallurgy Association, 1.

URIONABARRENETXEA, E., MARTÍN, J. M., AVELLO, A. & RIVAS, A. 2022. Simulation and validation of the gas flow in close-coupled gas atomisation process: Influence of the inlet gas pressure and the throat width of the supersonic gas nozzle. *Powder Technology,* 407**,** 117688.

USLAN, I., SARITAS, S. & DAVIES, T. J. 2013. Effects of variables on size and characteristics of gas atomised aluminium powders. *Powder Metallurgy,* 42**,** 157-163.

VERSTEEG, H. K. 2007. *An introduction to computational fluid dynamics the finite volume method, 2/E*, Pearson Education India.

VOWINCKEL, B. 2021. Incorporating grain-scale processes in macroscopic sediment transport models. *Acta Mechanica,* 232**,** 2023-2050.

WANG, G., DENG, Y., ADJEI-KYEREMEH, F., ZHANG, J., RAFFEIS, I., BÜHRIG-POLACZEK, A., KALETSCH, A. & BROECKMANN, C. 2023a. Numerical analysis of droplet breakup, cooling, and solidification during gas atomisation. *Powder Metallurgy,* 66**,** 493-508.

WANG, J., XIA, M., WU, J. & GE, C. 2023b. Nozzle clogging in vacuum induction melting gas atomisation: influence of gas pressure and melt orifice diameter coupling. *Powder Metallurgy,* 66**,** 281-294.

WANG, J., XIA, M., WU, J., JIAN, X. & GE, C. 2024a. Precise control of atomization initial stage to address nozzle clogging issue in the vacuum induction-melting gas atomization process. *Journal of Materials Research and Technology,* 30**,** 1505-1517.

WANG, P., LI, J., WANG, X., LIU, H.-S., FAN, B., GAN, P., GUO, R.-F., GE, X.-Y. & WANG, M.-H. 2021. Close-coupled nozzle atomization integral simulation and powder preparation using vacuum induction gas atomization technology. *Chinese Physics B,* 30**,** 027502.

WANG, P., LIU, J., DONG, Y., ZHAO, H., PANG, J. & ZHANG, J. 2023c. Investigation on close-coupled gas atomization for Fe-based amorphous powder production via simulation and industrial trials: Part II. Particle flight and cooling during secondary atomization. *Journal of Materials Research and Technology,* 26**,** 9480-9498.

WANG, P., LIU, J., DONG, Y., ZHU, Z., PANG, J. & ZHANG, J. 2023d. Breakup process modeling and production of FeSiAl magnetic powders by close-coupled gas atomization. *Journal of Materials Research and Technology,* 23**,** 730-743.

WANG, P., ZHOU, X.-L., LI, X.-G., CHEN, Z.-P., HU, Q.-P., WANG, X. & YU, Z.-Y. 2024b. Numerical and experimental investigation of close-coupled twin-nozzle gas atomization towards fine high-entropy alloy powder production. *Journal of Materials Processing Technology,* 324**,** 118238.

WANG, Y., DANG, Y.-C., CHEN, X.-Q., WANG, B., LIU, Z.-Q., ZHOU, J.-A. & CHEN, C.-Y. 2023e. Numerical simulation of effect of various parameters on atomization in an annular slit atomizer. *Journal of Iron and Steel Research International,* 30**,** 1128-1141.

WIERZBA, A. 1990. Deformation and breakup of liquid drops in a gas stream at nearly critical Weber numbers. *Experiments in Fluids,* 9**,** 59-64.

WILCOX, D. C. 1998. *Turbulence modeling for CFD*, DCW industries La Canada, CA.

XIAO, F. 2012. *Large eddy simulation of liquid jet primary breakup.* © F. Xiao.

YULE, A. J. & DUNKLEY, J. J. 1994. *Atomization of melts for powder production and spray deposition*, Clarendon Press.

ZEOLI, N. & GU, S. 2006. Numerical modelling of droplet break-up for gas atomisation. *Computational Materials Science,* 38**,** 282-292.

ZEOLI, N. & GU, S. 2008a. Computational simulation of metal droplet break-up, cooling and solidification during gas atomisation. *Computational Materials Science,* 43**,** 268-278.

ZEOLI, N. & GU, S. 2008b. Computational validation of an isentropic plug nozzle design for gas atomisation. *Computational Materials Science,* 42**,** 245-258.

ZEOLI, N., TABBARA, H. & GU, S. 2012. Three-dimensional simulation of primary break-up in a close-coupled atomizer. *Applied Physics A,* 108**,** 783-792.

ZHANG, L.-C., XU, W.-Y., LI, Z., ZHENG, L., LIU, Y.-F. & ZHANG, G.-Q. 2023a. Mechanism of rapidly solidified satellites formation in gas atomized powders: Simulation and characterization. *Powder technology,* 418**,** 118162.

ZHANG, M., ZHANG, Z. & LIU, Q. 2023b. Research on the primary liquid atomization mechanism of a close-coupled vortical loop slit atomizer. *Acta Mechanica Sinica,* 39**,** 322476.

ZHAO, T., CHEN, C., LIU, X. & HAO, J. 2023. Effect of gas Mach number on the flow field of close-coupled gas atomization, particle size and cooling rate of as-atomized powder: Simulation and experiment. *Advanced Powder Technology,* 34**,** 104007.

ZHAO, W., CAO, F., NING, Z., ZHANG, G., LI, Z. & SUN, J. 2012. A computational fluid dynamics (CFD) investigation of the flow field and the primary atomization of the close coupled atomizer. *Computers & Chemical Engineering,* 40**,** 58-66.

ZHAO, X., XU, J., ZHU, X. & ZHANG, S. 2009. Effect of atomization gas pressure variation on gas flow field in supersonic gas atomization. *Science in China Series E: Technological Sciences,* 52**,** 3046-3053.